Clifford M. Krowne
Yong Zhang
Editors

SPRINGER SERIES IN MATERIALS SCIENCE 98

Physics of Negative Refraction and Negative Index Materials

Optical and Electronic Aspects and Diversified Approaches

Springer

Springer Series in
MATERIALS SCIENCE 98

Springer Series in

MATERIALS SCIENCE

Editors: R. Hull R. M. Osgood, Jr. J. Parisi H. Warlimont

C.M. Krowne Y. Zhang (Eds.)

Physics of Negative Refraction and Negative Index Materials

Optical and Electronic Aspects and Diversified Approaches

With 228 Figures

Springer

Dr. Clifford M. Krowne
Code 6851, Microwave Technology Branch
Electronics Science and Technology Division, Naval Research Laboratory
Washington, DC 20375-5347, USA
E-mail: krowne@webbsight.nrl.navy.mil

Dr. Yong Zhang
Materials Science Center, National Renewable Energy Laboratory (NREL)
1617 Cole Blvd., Golden, CO 80401, USA
E-mail: Yong_Zhang@nrel.gov

Series Editors:

Professor Robert Hull
University of Virginia
Dept. of Materials Science and Engineering
Thornton Hall
Charlottesville, VA 22903-2442, USA

Professor Jürgen Parisi
Universität Oldenburg, Fachbereich Physik
Abt. Energie- und Halbleiterforschung
Carl-von-Ossietzky-Strasse 9–11
26129 Oldenburg, Germany

Professor R. M. Osgood, Jr.
Microelectronics Science Laboratory
Department of Electrical Engineering
Columbia University
Seeley W. Mudd Building
New York, NY 10027, USA

Professor Hans Warlimont
Institut für Festkörper-
und Werkstofforschung,
Helmholtzstrasse 20
01069 Dresden, Germany

ISSN 0933-033X

ISBN 978-3-540-72131-4 Springer Berlin Heidelberg New York

Library of Congress Control Number: 2007925169

Typesetting: Data prepared by SPI Kolam using a Springer TEX macro package
Cover: eStudio Calamar Steinen

Printed on acid-free paper SPIN: 11810377 57/3180/SPI 5 4 3 2 1 0

Preface

There are many potentially interesting phenomena that can be obtained with wave refraction in the "wrong" direction, what is commonly now referred to as negative refraction. All sorts of physically new operations and devices come to mind, such as new beam controlling components, reflectionless interfaces, flat lenses, higher quality lens or "super lenses," reversal of lenses action, new imaging components, redistribution of energy density in guided wave components, to name only a few of the possibilities. Negative index materials are generally, but not always associated with negative refracting materials, and have the added property of having the projection of the power flow or Poynting vector opposite to that of the propagation vector. This attribute enables the localized wave behavior on a subwavelength scale, not only inside lenses and in the near field outside of them, but also in principle in the far field of them, to have field reconstruction and localized enhancement, something not readily found in ordinary matter, referred to as positive index materials.

Often investigators have had to create, even when using positive index materials, interfaces based upon macroscopic or microscopic layers, or even heterostructure layers of materials, to obtain the field behavior they are seeking. For obtaining negative indices of refraction, microscopic inclusions in a host matrix material have been used anywhere from the photonic crystal regime all the way into the metamaterial regime. These regimes take one from the wavelength size on the order of the separation between inclusions to that where many inclusions are sampled by a wavelength of the electromagnetic field. Generally in photonic crystals and metamaterials, a Brillouin zone in reciprocal space exists due to the regular repetitive pattern of unit cells of inclusions, where each unit cell contains an arrangement of inclusions, in analogy to that seen in natural materials made up of atoms. Only here, the arrangements consist of artificial "atoms" constituting an artificial lattice.

The first two chapters of this book (Chaps. 1 and 2) address the use of uniform media to generate the negative refraction, and examine what happens to optical waves in crystals, electron waves in heterostructures, and guided waves in bicrystals. The first chapter also contrasts the underlying physics in various approaches adopted or proposed for achieving negative refraction and examines the effects of anisotropy, as does the second chapter for negative index materials (left-handed materials). Obtaining left-handed material behavior by utilizing a permeability tensor modification employing magnetic material inclusions is investigated in Chap. 3. Effects of spatial dispersion in the permittivity tensor can be important to understanding excitonic–electromagnetic interactions (exciton–polaritons) and their ability to generate negative indices and negative refraction. This and other polariton issues are discussed in Chap. 4.

The next group of chapters, Chaps. 5 and 6, in the book looks at negative refraction in photonic crystals. This includes studying the effects in the microwave frequency regime on such lattices constructed as flat lenses or prisms, in two dimensional arrangements of inclusions, which may be of dielectric or metallic nature, immersed in a dielectric host medium, which could be air or vacuum. Even slight perturbations or crystalline disorder effects can be studied, as is done in Chap. 7 on quasi-crystals. Analogs to photonic fields do exist in mechanical systems, and Chap. 8 examines this area for acoustic fields which in the macroscopic sense are phonon fields on the large scale.

Finally, the last group of chapters investigates split ring resonator and wire unit cells to make metamaterials for creation of negative index materials. Chapter 9 does this as well as treating some of the range between metamaterials and photonic crystals by modeling and measuring split ring resonators and metallic disks. Chapter 10 looks at the effects of the split ring resonator and wire unit cells on left-handed guided wave propagation, finding very low loss frequency bands. Designing and fabricating split ring resonator and wire unit cells for lens applications is the topic of Chap. 11. This chapter has extensive modeling studies of various configurations of the elements and arrangements of their rectangular symmetry system lattice. The last chapter in this group and of the book, Chap. 12, delves into the area of nonlinear effects, expected with enhanced field densities in specific areas of the inclusions. For example, field densities may be orders of magnitude higher in the vicinity of the gaps in the split rings, than elsewhere, and it is here that a material could be pushed into its nonlinear regime.

The chapters here all report on recent research within the last few years, and it is expected that the many interesting fundamental scientific discoveries that have occurred and the applications which have resulted from them on negative index of refraction and negative index materials, will have a profound effect on the technology of the future. The contributors to this book prepared their chapters coming from very diversified backgrounds, and as such, provide the reader with unique perspectives toward the subject matter. Although the chapters are presented in the context of negative refraction and related phenomena, the contributions should be found relevant to broad areas in fundamental physics and material science beyond the original context of the research. We expect this area to continue to yield new discoveries, applications, and insertion into devices and components as time progresses.

Washington and Golden, June 2007

Clifford M. Krowne
Yong Zhang

Contents

List of Contributors

Vladimir M. Agranovich
The University of Texas at Dallas
NanoTech Institute
Richardson, TX 75083-0688 USA

and

Institute of Spectroscopy
Russian Academy of Sciences
Troitsk, Moscow obl. 142190, Russia
vladimir.agranovich@utdallas.edu

Che Ting Chan
Physics Department
Hong Kong University of Science
and Technology
Clear Water Bay, Hong Kong, China
phchan@ust.hk

Bingying Cheng
Institute of Physics
Chinese Academy of Sciences
Beijing 100080

Siu-Tat Chui
Department of Physics
and Astronomy
University of Delaware
Newark, DE 19716, USA
chui@bartol.udel.edu

Zhifang Feng
Institute of Physics
Chinese Academy of Sciences
Beijing 100080

K.H. Fung
Physics Department
Hong Kong University of Science
and Technology
Clear Water Bay, Hong Kong, China

Yuri N. Gartstein
Department of Physics
The University of Texas at Dallas
Richardson, Texas 75083, USA

Robert B. Greegor
Boeing Phantom Works
Seattle, WA 98124
Robert.b.greegor@boeing.com

L.B. Hu
Bartol Research Institute
and Department of Physics
and Astronomy
University of Delaware
Newark, DE 19711, USA

Yuri S. Kivshar
Nonlinear Physics Centre and Center for Ultra-High Bandwidth Devices for Optical Systems (CUDOS)
Research School of Physical Sciences and Engineering
Australian National University
Canberra, ACT 0200, Australia
ysk@internode.on.net

Clifford M. Krowne
Microwave Technology Branch
Electronics Science and Technology Division
Naval Research Laboratory
Washington, DC 20375-5347
krowne@webbsight.nrl.navy.mil

Jensen Li
Physics Department
Hong Kong University of Science and Technology
Clear Water Bay, Hong Kong, China

Zhi-Yuan Li
Institute of Physics
Chinese Academy of Sciences
Beijing 100080

Zifang Lin
Bartol Research Institute and Department of Physics and Astronomy
University of Delaware
Newark, DE 19711, USA

Z.Y. Liu
Physics Department
Wuhan University
Wuhan, China

Peter F. Loschialpo
Naval Research Laboratory
Washington, DC 20375

Wentao Lu
Department of Physics and Electronic Materials Research Institute
Northeastern University
Boston, MA 02115, USA
w.lu@neu.edu

Angelo Mascarenhas
Materials Science Center
National Renewable Energy Laboratory (NREL)
1617 Cole Blvd.
Golden, CO 80401, USA

Ekmel Ozbay
Nanotechnology Research Center
Department of Physics and Department of Electrical and Electronics Engineering
Bilkent University
Bilkent, 06800 Ankara, Turkey
ozbay@bilkent.edu.tr

Gonca Ozkan
Nanotechnology Research Center
Bilkent University
Bilkent 06800, Ankara, Turkey

Claudio G. Parazzoli
Boeing Phantom Works
Seattle, WA 98124

Frederic Rachford
Material Science and Technology Division
Naval Research Laboratory
Washington, DC 20375
rachford@anvil.nrl.navy.mil

Ilya V. Shadrivov
Nonlinear Physics Centre
Research School of Physical Sciences and Engineering
Australian National University
Canberra ACT 0200, Australia

Ping Sheng
Physics Department
Hong Kong University of Science
and Technology
Clear Water Bay, Hong Kong, China

Douglas L. Smith
Naval Research Laboratory
Washington, DC 20375

Srinivas Sridhar
Vice Provost for Research
Director, Electronic Materials
Research Institute
Arts and Sciences Distinguished
Professor of Physics
Northeastern University
360 Huntington Avenue,
Boston, MA 02115, USA
ssridhar@neu.edu

Minas H. Tanielian
Boeing Phantom Works
Seattle, WA 98124

P. Vodo
Department of Physics
and Electronic Materials
Research Institute
Northeastern University
Boston, MA 02115, USA

Yiquan Wang
Institute of Physics
Chinese Academy of Sciences
Beijing 100080

Dao-Zhong Zhang
Institute of Physics
Chinese Academy of Sciences
Beijing 100080

Xiangdong Zhang
Beijing Normal University
Beijing 100875, China
zhangxd@bnu.edu.cn

Yong Zhang
Materials Science Center
National Renewable Energy
Laboratory (NREL)
1617 Cole Blvd.
Golden, CO 80401
Yong_Zhang@nrel.gov

Lei Zhou
Bartol Research Institute
and Department of Physics
and Astronomy
University of Delaware
Newark, DE 19711, USA

1

Negative Refraction of Electromagnetic and Electronic Waves in Uniform Media

Y. Zhang and A. Mascarenhas

Summary. We discuss various schemes that have been used to realize negative refraction and zero reflection, and the underlying physics that dictates each scheme. The requirements for achieving both negative refraction and zero reflection are explicitly given for different arrangements of the material interface and different structures of the electric permittivity tensor $\boldsymbol{\varepsilon}$. We point out that having a left-handed medium is neither necessary nor sufficient for achieving negative refraction. The fundamental limitations are discussed for using these schemes to construct a perfect lens or "superlens," which is the primary context of the current interest in this field. The ability of an ideal "superlens" beyond diffraction-limit "focusing" is contrasted with that of a conventional lens or an immersion lens.

1.1 Introduction

1.1.1 Negative Refraction

Recently, negative refraction has attracted a great deal of attention, largely due to the realization that this phenomenon could lead to the development of a perfect lens (or superlens) [1]. A perfect lens is supposed to be able to focus all Fourier components (i.e., the propagating and evanescent modes) of a two-dimensional (2D) image without missing any details or losing any energy. Although such a lens has yet to be shown possible either physically and practically, the interest has generated considerable research in electromagnetism and various interdisciplinary areas in terms of fundamental physics and material sciences [2–4]. Negative refraction, as a physical phenomenon, may have much broader implications than making a perfect lens. Negative refraction achieved using different approaches may involve very different physics and may find unique applications in different technology areas. This chapter intends to offer some general discussion that distinguishes the underlying physics of various approaches, bridges the physics of different disciplines (e.g., electromagnetism and electronic properties of the material), and provides some detailed discussions for one particular approach, that is, negative refraction involving uniform media with conventional dielectric properties. By uniform medium we mean that other than the microscopic variation on the atomic or molecular scale the material is spatially homogeneous.

The concept of negative refraction was discussed as far back as 1904 by Schuster in his book *An Introduction to the Theory of Optics* [5]. He indicated that negative dispersion of the refractive index, n, with respect to the wavelength of light, λ, i.e., $\mathrm{d}n/\mathrm{d}\lambda < 0$, could lead to negative refraction when light enters such a material (from vacuum), and the group velocity, v_{g}, is in the opposite direction to the wave (or phase) velocity, v_{p}. Although materials with $\mathrm{d}n/\mathrm{d}\lambda < 0$ were known to exist even then (e.g., sodium vapor), Schuster stated that "in all optical media where the direction of the dispersion is reversed, there is a very powerful absorption, so that only thicknesses of the absorbing medium can be used which are smaller than a wavelength of light. Under these circumstances it is doubtful how far the above results have any application." With the advances in material sciences, researchers are now much more optimistic 100 years later. Much of the intense effort in demonstrating a "poor man's" superlens is directed toward trying to overcome Schuster's pessimistic view by using the spectral region normally having strong absorption and/or thin-film materials with film thicknesses in the order of (or even a fraction of) the wavelength of light [2]. However, with regard to the physics of refraction, for a "lens" of such thickness, one may not be well justified in viewing the transmission as refraction, because of various complications (e.g., the ambiguity in defining the layer parameters [6] and the optical tunnel effect [7]).

The group velocity of a wave, $\mathbf{v}_{\mathrm{g}}(\omega, \mathbf{k}) = \mathrm{d}\omega/\mathrm{d}\mathbf{k}$, is often used to describe the direction and the speed of its energy propagation. For an electromagnetic wave, strictly speaking, the energy propagation is determined by the Poynting vector $\mathbf{S}$. In certain extreme situations, the directions of $\mathbf{v}_{\mathrm{g}}$ and $\mathbf{S}$ could even be reversed [8]. However, for a quasimonochromatic wave packet in a medium without external sources and with minimal distortion and absorption, the direction of $\mathbf{S}$ does coincide with that of $\mathbf{v}_{\mathrm{g}}$ [9]. For simplicity, we will focus on the simpler case, where the angle between $\mathbf{v}_{\mathrm{g}}$ and wave vector $\mathbf{k}$ is of significance in distinguishing two types of media: when the angle is acute or $\mathbf{k} \cdot \mathbf{v}_{\mathrm{g}} > 0$, it is said to be a right-handed medium (RHM); when the angle is obtuse or $\mathbf{k} \cdot \mathbf{v}_{\mathrm{g}} < 0$, it is said to be a left-handed medium (LHM) [10]. If one prefers to define the direction of the energy flow to be positive, an LHM can be referred to as a material with a negative wave velocity, as Schuster did in his book. A wave with $\mathbf{k} \cdot \mathbf{v}_{\mathrm{g}} < 0$ is also referred to as a backward wave (with negative group velocity), in that the direction of the energy flow is opposite to that of the wave determined by $\mathbf{k}$ [11, 12]. Lamb was perhaps the first to suggest a one-dimensional mechanical device that could support a wave with a negative wave velocity [13], as mentioned in Schuster book [5]. Examples of experimental demonstrations of backward waves can be found in other review papers [4, 14]. Unusual physical phenomena are expected to emerge either in an individual LHM (e.g., a reversal of the group velocity and a reversal of Doppler shift) or jointly with an RHM (e.g., negative refraction that occurs at the interface of an LHM and RHM) [10]. The effect that has received most attention lately is the negative refraction at the interface of an RHM and LHM, which relies on the property $\mathbf{k} \cdot \mathbf{v}_{\mathrm{g}} < 0$ in the LHM.

There are a number of ways to realize negative refraction [4]. Most ways rely on the above-mentioned LH behavior, i.e., $\mathbf{k} \cdot \mathbf{v}_{\mathrm{g}} < 0$, although LH behavior is by no means necessary or even sufficient to have negative refraction. Actually, LH behavior can be readily found for various types of wave phenomena in crystals. Examples may include the negative dispersion of frequency $\omega(\mathbf{k})$ for phonons and of energy $E(\mathbf{k})$ for electrons; however, they are inappropriate to be considered as uniform media and thus to discuss refraction in the genuine sense, because the wave propagation in such media is diffractive in nature. For a simple electromagnetic wave, it is not trivial to find a crystal that exhibits LH behavior. By "simple electromagnetic wave," we refer to the electromagnetic wave in the transparent spectral region away from the resonant frequency of any elementary excitation in the crystal. In this case, the light–matter interaction is mainly manifested as a simple dielectric function $\varepsilon(\omega)$, as in the situation often discussed in crystal optics [15], where $\varepsilon(\omega)$ is independent of $\mathbf{k}$.

1.1.2 Negative Refraction with Spatial Dispersion

The first scheme to be discussed for achieving negative refraction relies on the $\mathbf{k}$ dependence of ε to produce the LH behavior. The dependence of $\varepsilon(\mathbf{k})$ or $n(\lambda)$ is generally referred to as spatial dispersion [16, 17], meaning that the dielectric parameter varies spatially. Thus, this scheme may be called the *spatial-dispersion scheme*. The negative refraction originally discussed by Schuster in 1904 could be considered belonging to this scheme, although the concept of spatial dispersion was only introduced later [17] and discussed in greater detail in a book by Agranovich and Ginzburg, *Spatial Dispersion in Crystal Optics and the Theory of Excitons* [9]. If one defines $v_{\mathrm{p}} = \omega/k = c/n$, and assumes $n > 0$, then according to Schuster, v_{g} is related to v_{p} by [5]

$$v_{\mathrm{g}} = v_{\mathrm{p}} - \lambda \frac{\mathrm{d}v_{\mathrm{p}}}{\mathrm{d}\lambda}, \tag{1.1}$$

and the condition for having a negative wave velocity is given as $\lambda\, \mathrm{d}v_{\mathrm{p}}/\mathrm{d}\lambda > v_{\mathrm{p}}$, which is equivalent to $\mathrm{d}n/\mathrm{d}\lambda < -n/\lambda < 0$. Negative group velocity and negative refraction were specifically associated with spatial dispersion by Ginzburg and Agranovich [9, 17]. Recently, a generalized version of this condition has been given by Agranovich et al. [18]. In their three-fields $(\mathbf{E}, \mathbf{D}, \mathbf{B})$ approach, with a generalized permittivity tensor $\tilde{\varepsilon}(\omega, \mathbf{k})$ (see the chapter of Agranovich and Gartstein for more details), the time-averaged Poynting vector in an isotropic medium is given as

$$\mathbf{S} = \frac{c}{8\pi}\mathrm{Re}(\mathbf{E}^* x \mathbf{B}) - \frac{\omega}{16\pi}\nabla_k \tilde{\varepsilon}(\omega, \mathbf{k})\mathbf{E}^*\mathbf{E}, \tag{1.2}$$

where the direction of the first term coincides with that of $\mathbf{k}$, and that of the second term depends on the sign of $\nabla_k\tilde{\varepsilon}(\omega,\mathbf{k})$, which could lead to the reversal of the direction of $\mathbf{S}$ with respect to $\mathbf{k}$ under certain conditions. If permeability $\mu = 1$ is assumed, the condition can be simplified to $\mathrm{d}\varepsilon/\mathrm{d}k > 2\varepsilon/k > 0$ (here, ε is the conventional permittivity or dielectric constant), which is essentially the same as that derived from (1.1). Spatial dispersion is normally very weak in a crystal, because it is characterized by a parameter a/λ, where a is the lattice constant of the crystal and λ is the wavelength in the medium. However, when the photon energy is near that of an elementary excitation (e.g., exciton, phonon, or plasmon) of the medium, the light–matter interaction can be so strong that the wave is neither pure electromagnetic nor electronic, but generally termed as a polariton [19, 20]. Thus, the spatial dispersion is strongly enhanced, as a result of coupling of two types of waves that normally belong to two very different physical scales. With the help of the polariton effect and the negative exciton dispersion $\mathrm{d}E(\mathbf{k})/\mathrm{d}k < 0$, one could, in principle, realize negative refraction for the polariton wave inside a crystal if the damping is not too strong [21]. Because damping or dissipation is inevitable near the resonance, similar to the case of sodium vapor noted by Schuster [5], a perfect lens is practically impossible with this *spatial-dispersion scheme*.

It is worth mentioning that the damping could actually provide another possibility to induce $\mathbf{k}\cdot\mathbf{v}_\mathrm{g} < 0$ for the polariton wave in a crystal, even though in such a case the direction of $\mathbf{v}_\mathrm{g}$ may not be exactly the same as that of $\mathbf{S}$. In the *spatial-dispersion scheme*, the need to have $\mathrm{d}E(\mathbf{k})/\mathrm{d}k < 0$ is based on the assumption of the ideal polariton model, i.e., with vanishing damping. However, with finite damping, even with the electronic dispersion $\mathrm{d}E(\mathbf{k})/\mathrm{d}k > 0$, one may still have one polariton branch exhibiting $\mathrm{d}\omega/\mathrm{d}\mathbf{k} < 0$ near the frequency window Δ_{LT}, splitting the longitudinal and transverse mode, and thus, causing the exhibiting of LH behavior [7].

1.1.3 Negative Refraction with Double Negativity

Mathematically, the simplest way to produce LH behavior in a medium is to have both $\varepsilon < 0$ and $\mu < 0$, as pointed out by Pafomov [22]. Double negativity, by requiring energy to flow away from the interface and into the medium, also naturally leads to a negative refractive index $n = -\sqrt{\varepsilon\mu}$, thus facilitating negative refraction at the interface with an RHM, as discussed by Veselago [10]. At first glance, this *double-negativity scheme* would seem to be more straightforward than the *spatial-dispersion scheme*. However, $\varepsilon < 0$ is only known to occur near the resonant frequency of a polariton (e.g., plasmon, optical phonon, exciton). Without damping and spatial dispersion, the spectral region of $\varepsilon < 0$ is totally reflective for materials with $\mu > 0$. $\mu < 0$ is also known to exist near magnetic resonances, but is not known to occur in the same material and the same frequency region where $\varepsilon < 0$ is found. Indeed, if in the same material and spectral region one could simultaneously have $\varepsilon < 0$ and $\mu < 0$ yet without any dissipation, the material would then turn transparent. In recent years, metamaterials have been developed to extend material response and thus allow effective ε and μ to be negative in an overlapped frequency region [3]. The hybridization of the metamaterials with, respectively, $\varepsilon_{\rm eff} < 0$ and $\mu_{\rm eff} < 0$ has made it possible to realize double negativity or $n_{\rm eff} < 0$ in a small microwave-frequency window, and to demonstrate negative refraction successfully [23]. However, damping or dissipation near the resonant frequency still remains a major obstacle for practical applications of metamaterials. There is a fundamental challenge to find any natural material with nonunity μ at optical frequencies or higher, because of the ambiguity in defying μ at such frequencies [18,24]. Although there have been a few demonstrations of metamaterials composed of “artificial atoms” exhibiting nonunity or even negative effective μ and negative effective refractive index at optical frequencies [25–29], no explicit demonstration of negative refraction or imaging has been reported, presumably because of the relative large loss existed in such materials. Thus, the *double-negativity scheme* essentially faces the same challenge that the *spatial-dispersion scheme* does in realizing the dream of making a perfect lens.

1.1.4 Negative Refraction Without Left-Handed Behavior

It is perhaps understandable that the general public might have the impression that negative refraction never occurs in nature [23,30]. One could only make such a claim if one insists on using isotropic media [4,31,32]. The simplest example of negative refraction is perhaps refraction of light at the interface of air and an anisotropic crystal without any negative components of ε and μ, as illustrated in Fig. 1.1 [32–36]. A standard application of such an optical component is a beam displacer. Thus, negative refraction is a readily observable phenomenon, if one simply allows the use of an anisotropic medium. This *anisotropy scheme* has enabled the demonstration of negative refraction in the most genuine sense – that is, the classic refraction phenomenon in uniform media or optical crystals in a broad spectral range and involving neither electronic nor magnetic resonances [31,34,35]. As in the case of the double-negativity scheme, to eliminate the reflection at the medium interface, the *anisotropy scheme* also needs to satisfy certain conditions for matching the dielectric properties of the two media, as illustrated by a special case of a bicrystal structure [31]. In general, eliminating the reflection loss requires material parameters to automatically ensure the continuity of the energy flux

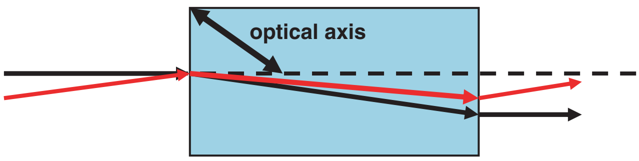

Fig. 1.1. Refraction of light at the interface of air and a (positive) uniaxial crystal

along the interface normal [32]. Generalization has been discussed for the interface of two arbitrary uniaxially anisotropic media [33, 37, 38]. Note that negative refraction facilitated by the anisotropy scheme does not involve any LH behavior and thus cannot be used to make a flat lens, in contrast to that suggested by Veselago, using a double-negativity medium [10], which is an important distinction from the other schemes based on negative group velocity. However, one could certainly envision various important applications other than the flat lens.

1.1.5 Negative Refraction Using Photonic Crystals

The last scheme we would like to mention is the *photonic crystal scheme*. Although it is diffractive in nature, one may often consider the electromagnetic waves in a photonic crystal as waves with new dispersion relations, $\omega_n(\mathbf{k})$, where n is the band index, and $\mathbf{k}$ is the wave vector in the first Brillouin zone. For a three-dimensional (3D) or 2D photonic crystal [39, 40], the direction of the energy flux, averaged over the unit cell, is determined by the group velocity $\mathrm{d}\omega_n(\mathbf{k})/\mathrm{d}\mathbf{k}$, although that might not be generally true for a 1D photonic crystal [40]. If the dispersion is isotropic, the condition $\mathbf{q}\cdot \mathrm{d}\omega_n(\mathbf{q})/\mathrm{d}\mathbf{q} < 0$, where $\mathbf{q}$ is the wave vector measured from a local extremum, must be satisfied to have LH behavior. Similar to the situations for the spatial-dispersion and double-negativity schemes, $\mathbf{q}\cdot \mathrm{d}\omega_n(\mathbf{q})/\mathrm{d}\mathbf{q} < 0$ also allows the occurrence of negative refraction at the interface of air and photonic crystal as well as the imaging effect with a flat photonic slab [4, 41–44]. However, similar to the situation for the anisotropy scheme, one may also achieve negative refraction with positive, but anisotropic, dispersions [40]. Because of the diffractive nature, the phase matching at the interface of the photonic crystal often leads to complications, such as the excitation of multiple beams [40, 45].

1.1.6 From Negative Refraction to Perfect Lens

Although the possibility of making a flat lens with the double-negativity material was first discussed by Veselago [10], the noted unusual feature alone, i.e., a lens without an optical axis, would not have caused it to receive such broad interest. It was Pendry who suggested perhaps the most unique aspect of the double-negativity material – the potential for realizing a perfect lens beyond negative refraction [1] – compared to other schemes that can also achieve negative refraction. Apparently, not all negative refractions are equal. To make Pendry's perfect lens, in addition to negative refraction, one also needs (1) zero dissipation, (2) amplification of evanescent waves, and (3) matching of the dielectric parameters between the lens and air. Exactly zero dissipation is physically impossible for any real material. For an insulator with an optical bandgap, one normally considers that there is no absorption for light with energy below the bandgap, if the crystal is perfect (e.g., free of defects). However, with nonlinear optical effects taken into account, there will always be some finite absorption below the bandgap due to harmonic transitions [46]. Although it is typically many orders of magnitude weaker than the above-bandgap linear absorption, it will certainly make the lens imperfect. Therefore, a perfect lens may simply be a physically unreachable singularity point. For the schemes working near the resonant frequencies of one kind or the other, the dissipation is usually strong, and thus more problematic to allow such a lens to be practically usable.

Mathematically, double-negativity material is the only one, among all the schemes mentioned above, that automatically provides a correct amount of amplification for each evanescent wave [1]. Unfortunately, this scheme becomes problematic at high frequencies because of the ambiguity in defining nonunity μ at high frequencies [18, 24]. The other schemes – spatial dispersion and photonic crystals – may also amplify the evanescent components when the effective refractive index $n_{\mathrm{eff}} < 0$, but typically with some complications (e.g., the amplification magnitude might not be exactly correct or the resolution is limited by the periodicity of the photonic crystal) [47, 48].

One important requirement of negative refraction for making a perfect lens is matching the dielectric parameters ("impedances") of the two media to eliminate reflection, as well as aberration [49], for instance, $n_1 = -n_2$ for the double-negativity scheme. In addition to the limitation caused by finite damping, another limitation faced by both the spatial-dispersion and double-negativity schemes is frequency dispersion, which prohibits the matching condition of the dielectric parameters to remain valid in a broad frequency range. For the spatial-dispersion scheme, the frequency dispersion $\varepsilon(\omega)$ is apparent [9]. It is less trivial for the double-negativity scheme, but it was pointed out by Veselago that "the simultaneous negative values of ε and μ can be realized only when there is frequency dispersion," in order to avoid the energy becoming negative [10]. For the photonic crystal, the effective index is also found to depend on frequency. Therefore, even for the ideal case of vanishing damping, the matching condition can be found at best for discrete frequencies, using any one of the three schemes discussed above.

However, even with the practical limitations on the three aspects – damping, incorrect magnitude of amplification, and dielectric mismatch – one can still be hopeful of achieving a finite improvement in "focusing" light beyond the usual diffraction limit [50], in addition to the benefits of having a flat lens. A widely used technique, an immersion lens [51], relies on turning as many evanescent waves as possible into propagating waves inside the lens, and it requires either the source or image to be in the near-field region. Compared to this immersion lens, the primary advantage of the "superlens" seems to be the ability to achieve subwavelength focusing with both the source and image at far field. An immersion lens can readily achieve $\sim \lambda/4$ resolution at $\sim$200 nm in semiconductor photolithography [52]. With a solid immersion lens, even better resolution has been achieved (e.g., $\sim 0.23\lambda$ at $\lambda = 436$ nm [53], $\sim\lambda/8$ at $\lambda = 515$ nm [54]). Thus far, using negative refraction, there have only been a few experimental demonstrations of non-near-field imaging with improved resolution (e.g., 0.4λ image size at 1.4λ away from the lens [55], using a 2D quasicrystal with $\lambda = 25$ mm; 0.36λ image size at 0.6λ away from the lens [56], using a 3D photonic crystal with $\lambda = 18.3$ mm). In addition, plasmonic systems (e.g., ultra thin metal film) have also be used for achieving subwavelength imaging in near field [57, 58], although not necessarily related to negative refraction.

Some further discussion is useful on the meaning of "focusing" as used by Pendry for describing the perfect lens [1]. The focusing power of a lens usually refers to the ability to provide an image smaller than the object. What the hypothetical flat lens can do is exactly reproduce the source at the image site, or equivalently, spatially translate the source by a distance of $2d$, where d is the thickness of the slab. Thus, mathematically, a δ-function source will give rise to a δ-function image, without being subjected to the diffraction limit of a regular lens, i.e., $\lambda/2$ [59]. And such a "superlens" can, in principle, resolve two objects with any nonzero separation, overcoming the Rayleigh criterion of 0.61λ for the resolving power of a regular lens [59]. However, what this "superlens" cannot do is focus an object greater than λ to an image smaller than λ; thus, it cannot bring a broad beam to focus for applications such as photolithography, whereas a regular lens or an immersion lens can, in principle, focus an object down to the diffraction limit $\lambda/2$ or $\lambda/(2n)$ (n is the refractive index of the lens material). Therefore, it might not be appropriate to call such optical device of no magnification a "lens," though it is indeed very unique. One could envision using the "superlens" to map or effectively translate a light source, while retaining its size that is already below the diffraction limit to begin with.

1.2 Conditions for Realizing Negative Refraction and Zero Reflection

Let us consider a fairly general case of refraction of light at the interface of two uniform media, as shown in Fig. 1.2. The media are assumed to have anisotropic permittivity tensors ε_L and ε_R, both with uniaxial symmetry,

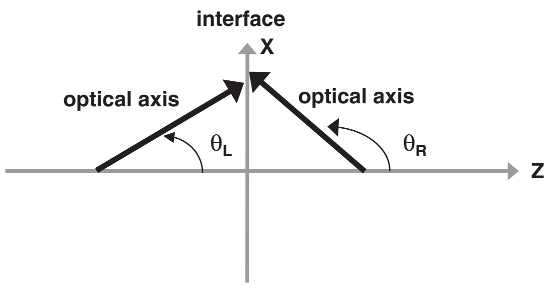

Fig. 1.2. The interface (the x–y plane) of two uniaxial anisotropic media

but isotropic permeabilities μ_{L} and μ_{R}, where L and R denote the left-hand and right-hand side, respectively. Their symmetry axes are assumed to lie in the same plane as the plane of incidence, which is also perpendicular to the interface, but nevertheless may incline at any angles with respect to the interface normal. In the principal coordinate system (x', y', z'), the relative permittivity tensors are given by

$$\varepsilon_{\mathrm{L,R}} = \begin{pmatrix} \varepsilon_1^{\mathrm{L,R}} & 0 & 0 \\ 0 & \varepsilon_1^{\mathrm{L,R}} & 0 \\ 0 & 0 & \varepsilon_3^{\mathrm{L,R}} \end{pmatrix}, \tag{1.3}$$

where ε_1 and ε_3 denote the dielectric components for electric field $\mathbf{E}$ polarized perpendicular and parallel to the symmetric axis. In the (x,y,z) coordinate system shown in Fig. 1.2, the tensor becomes

$$\varepsilon_{\mathrm{L,R}} = \begin{pmatrix} \varepsilon_1^{\mathrm{L,R}} \cos^2(\theta_{\mathrm{L,R}}) + \varepsilon_3^{\mathrm{L,R}} \sin^2(\theta_{\mathrm{L,R}}) & 0 & (\varepsilon_3^{\mathrm{L,R}} - \varepsilon_1^{\mathrm{L,R}}) \sin(\theta_{\mathrm{L,R}}) \cos(\theta_{\mathrm{L,R}}) \\ 0 & \varepsilon_1^{\mathrm{L,R}} & 0 \\ (\varepsilon_3^{\mathrm{L,R}} - \varepsilon_1^{\mathrm{L,R}}) \sin(\theta_{\mathrm{L,R}}) \cos(\theta_{\mathrm{L,R}}) & 0 & \varepsilon_3^{\mathrm{L,R}} \cos^2(\theta_{\mathrm{L,R}}) + \varepsilon_1^{\mathrm{L,R}} \sin^2(\theta_{\mathrm{L,R}}) \end{pmatrix}. \tag{1.4}$$

Rather generalized discussions for the reflection–refraction problem associated with the interface defined in Fig. 1.2 have been given in the literature for the situation of ε_1 and ε_3 both being positive [37,38]. For an ordinary wave with electric field $\mathbf{E}$ polarized in the y-direction, i.e., perpendicular to the plane of incidence (a TE wave), the problem is equivalent to an isotropic case with different dielectric constants $\varepsilon_1^{\mathrm{L}}$ and $\varepsilon_1^{\mathrm{R}}$ for the left-hand and right-hand side. It is the reflection and refraction of the extraordinary or **H**-polarized wave, i.e., with $\mathbf{E}$ polarized in the x–z plane (a TM wave), that has generally been found to be more interesting. For the E- and H-polarized waves, the dispersion relations are given below for the two coordinate systems:

$$k_x'^2 + k_z'^2 = \frac{\omega^2}{c^2}\mu\varepsilon_1, \tag{1.5E}$$

$$\frac{k_x'^2}{\varepsilon_3} + \frac{k_z'^2}{\varepsilon_1} = \frac{\omega^2}{c^2}\mu, \tag{1.5H}$$

and

$$k_x^2 + k_z^2 = \frac{\omega^2}{c^2}\mu\varepsilon_1, \tag{1.6E}$$

$$\frac{(k_x \cos\theta_0 - k_z \sin\theta_0)^2}{\varepsilon_3} + \frac{(k_x \sin\theta_0 + k_z \cos\theta_0)^2}{\varepsilon_1} = \frac{\omega^2}{c^2}\mu, \tag{1.6H}$$

where θ_0 is the inclined angle of the uniaxis of the medium with respect to the z-axis. The lateral component k_x is required to be conserved across the interface and the two solutions for k_z (of $\pm$) are found to be (with k in the unit of ω/c) the following:

$$k_z^{\pm} = \pm\sqrt{\mu\varepsilon_1 - k_x^2}, \tag{1.7E}$$

$$k_z^{\pm} = \frac{k_x\delta \pm 2\sqrt{\gamma(\beta\mu - k_x^2)}}{2\beta}, \tag{1.7H}$$

where $\gamma = \varepsilon_1\varepsilon_3$, $\beta = \varepsilon_1 \sin^2\theta_0 + \varepsilon_3 \cos^2\theta_0$, $\delta = \sin(2\theta_0)(\varepsilon_1 - \varepsilon_3)$. The Poynting vector $\mathbf{S} = \mathbf{E}^* \times \mathbf{H}$, corresponding to $k_z^{\pm}$, can be given as

$$S_x^{\pm} = |E_y|^2 \frac{k_x}{c\mu\mu_0}, \tag{1.8E}$$

$$S_x^{\pm} = |H_y|^2 \frac{2\gamma k_x \mp \delta\sqrt{\gamma(\beta\mu - k_x^2)}}{2c\varepsilon_0\beta\gamma}, \tag{1.8H}$$

and

$$S_z^{\pm} = \pm|E_y|^2 \frac{\sqrt{\mu\varepsilon_1 - k_x^2}}{c\mu\mu_0}, \tag{1.9E}$$

$$S_z^{\pm} = \pm|H_y|^2 \frac{\sqrt{\gamma(\beta\mu - k_x^2)}}{c\varepsilon_0\gamma}, \tag{1.9H}$$

where E_y and H_y are the y components of $\mathbf{E}$ and $\mathbf{H}$, respectively. If the incident beam is assumed to arrive from the left upon the interface (i.e., energy flows along the $+z$ direction), one should choose from (1.7) the solution that can give rise to a positive S_z. Note that (1.8) and (1.9) are valid for either side of the interface, and positive as well as negative ε_1, ε_3, and μ. With these equations, we can conveniently discuss the conditions for realizing negative refraction and zero reflection. Note that for the E-polarized wave, the sign of $\mathbf{k}\cdot\mathbf{S}$ is only determined by that of ε_1, since $\mathbf{k}\cdot\mathbf{S} = |E_y|^2\omega\varepsilon_0\varepsilon_1$; for the H-polarized wave, it is only determined by μ, since $\mathbf{k}\cdot\mathbf{S} = |H_y|^2\omega\mu_0\mu$.

Since S_z is always required to be positive, the condition to realize negative refraction is simply to request a sign change of S_x across the interface. For realizing zero reflection, if one can assure the positive component of S_z to be continuous across the interface, the reflection will automatically be eliminated. Therefore, one does not need to consider explicitly the reflection [32].

If both media are isotropic, i.e., $\varepsilon_1 = \varepsilon_3 = \varepsilon$, we have $S_x \propto k_x/\mu$ and $S_z^{\pm} \propto \pm\sqrt{\mu\varepsilon - k_x^2}/\mu$ for the E-polarized wave, $S_x \propto k_x/\varepsilon$ and $S_z^{\pm} \propto \pm\sqrt{\varepsilon^2(\varepsilon\mu - k_x^2)}/\varepsilon^2$ for the H-polarized wave. To have negative refraction for both of the polarizations, the only possibility is to have ε and μ changing sign simultaneously. To have zero reflection for any k_x, the conditions become $|\varepsilon^{\mathrm{L}}| = |\varepsilon^{\mathrm{R}}|$ and $|\mu^{\mathrm{L}}| = |\mu^{\mathrm{R}}|$, and $(\varepsilon\mu)^{\mathrm{L}} = (\varepsilon\mu)^{\mathrm{R}}$. Since $\varepsilon\mu > 0$ is necessary for the propagating wave, the conditions become $\varepsilon^{\mathrm{L}} = -\varepsilon^{\mathrm{R}}$ and $\mu^{\mathrm{L}} = -\mu^{\mathrm{R}}$, as derived by Veselago [10]. It is interesting to note that if one of the media is replaced with a photonic crystal with a negative effective refractive index, the "impedance" matching conditions become much more restrictive. In has been found that to minimize the reflection the surrounding medium has to have a pair of specific ε and μ for a given photonic crystal [60] and the values could even depend on the surface termination of the photonic crystal [61].

If the media are allowed to be anisotropic, several ways exist to achieve negative refraction, even if we limit ourselves to μ being isotropic. For the E-polarized wave, since $S_x \propto k_x/\mu$, negative refraction requires $\mu < 0$ on one side, assuming $\mu^{\mathrm{R}} < 0$ (the left-hand side is assumed to have everything positive). In the meantime, because $S_z \propto \pm\sqrt{\mu\varepsilon_1 - k_x^2}/\mu$, one also needs to have $\varepsilon_1^{\mathrm{R}} < 0$ to make the wave propagative. Thus, with $\varepsilon_1^{\mathrm{R}} < 0$ and $\mu^{\mathrm{R}} < 0$ while keeping $\varepsilon_3^{\mathrm{R}} > 0$, one can have negative refraction, and zero reflection for the E-polarized wave occurring for any k_x when $\mu^{\mathrm{R}} = -\mu^{\mathrm{L}}$ and $(\varepsilon_1\mu)^{\mathrm{L}} = (\varepsilon_1\mu)^{\mathrm{R}}$. This situation is similar to the isotropic case with $\varepsilon = \varepsilon_1$, although there will be no negative refraction for the H-polarized wave.

For the H-polarized wave, if both media are allowed to be anisotropic but the symmetry axes are required to be normal to the interface (i.e., $\theta_{\mathrm{L}} = \theta_{\mathrm{R}} = 0°$), we have $S_x \propto k_x/\varepsilon_3$ and $S_z \propto \pm\sqrt{\varepsilon_1\varepsilon_3(\varepsilon_3\mu - k_x^2)}/(\varepsilon_1\varepsilon_3) > 0$. Negative refraction requires $\varepsilon_3 < 0$ on one side, again assumed to be the right-hand side (the left-hand side is assumed to have everything positive). If $\varepsilon_1 < 0$, then $\mu^{\mathrm{R}} < 0$ is also needed to have a propagating wave; we have $S_z^R \propto \sqrt{\varepsilon_1^{\mathrm{R}}\varepsilon_3^{\mathrm{R}}(\varepsilon_3^{\mathrm{R}}\mu^{\mathrm{R}} - k_x^2)}/(\varepsilon_1^{\mathrm{R}}\varepsilon_3^{\mathrm{R}})$, and the conditions for zero reflection are $(\varepsilon_1\varepsilon_3)^{\mathrm{L}} = (\varepsilon_1\varepsilon_3)^{\mathrm{R}}$ and $(\varepsilon_3\mu)^{\mathrm{L}} = (\varepsilon_3\mu)^{\mathrm{R}}$. If $\varepsilon_1^{\mathrm{R}} > 0$, then $\mu^{\mathrm{R}} > 0$ is necessary to have a propagating wave; we have $S_z^{\mathrm{R}} \propto -\sqrt{\varepsilon_1^{\mathrm{R}}\varepsilon_3^{\mathrm{R}}(\varepsilon_3^{\mathrm{R}}\mu^{\mathrm{R}} - k_x^2)}/(\varepsilon_1^{\mathrm{R}}\varepsilon_3^{\mathrm{R}})$, but zero reflection is not possible except for $k_x = 0$ and when $(\varepsilon_1\varepsilon_3)^{\mathrm{L}} = |\varepsilon_1\varepsilon_3|^{\mathrm{R}}$ and $|\varepsilon_3\mu|^{\mathrm{L}} = |\varepsilon_3\mu|^{\mathrm{R}}$. The results for $\theta_{\mathrm{L}} = \theta_{\mathrm{R}} = 90°$ can be obtained by simply replacing ε_3 with ε_1 in the results for $\theta_{\mathrm{L}} = \theta_{\mathrm{R}} = 0°$. Similar or somewhat different cases have been discussed in the literature for either $\theta_{\mathrm{L}} = \theta_{\mathrm{R}} = 0°$ or $\theta_{\mathrm{L}} = \theta_{\mathrm{R}} = 90°$, leading to the conclusion that at least one component of either ε or $\boldsymbol{\mu}$ tensor needs to be negative to realize negative refraction [62–66].

However, the relaxation on the restriction of the optical axis orientations, allowing $0 < \theta_{\mathrm{L}} < 90°$ and $0 < \theta_{\mathrm{R}} < 90°$, makes negative refraction and zero reflection possible even if both ε and $\boldsymbol{\mu}$ tensors are positive definite. When ε is positive definite, we have $\gamma > 0$ and $\beta > 0$, and in this case $\mu > 0$ is necessary to have propagating modes. The condition for zero reflection can be readily found to be $\gamma^{\mathrm{L}} = \gamma^{\mathrm{R}}$, and $(\beta\mu)^{\mathrm{L}} = (\beta\mu)^{\mathrm{R}}$. For the case of the interface being that of a pair of twinned crystals [31], these requirements are automatically satisfied for any angle of incidence. The twinned structure assures that the zero-reflection condition is valid for any wavelength, despite the existence of dispersion; however, for the more-general case using two different materials, the condition can at best be satisfied at discrete wavelengths because the dispersion effect may break the matching condition, similar to the case of $\varepsilon = \mu = -1$. The negative-refraction condition can be derived from (1.8H) (since $\gamma > 0$, S_x^+ should be used). Note that $S_x^+ = 0$ at $k_{x0} = \delta\sqrt{\beta\mu}/\sqrt{4\gamma + \delta^2}$. If $k_{x0}^{\mathrm{L}} < k_{x0}^{\mathrm{R}}(k_{x0}^{\mathrm{L}} > k_{x0}^{\mathrm{R}})$, S_x changes sign across the interface or negative refraction occurs in the region $k_{x0}^{\mathrm{L}} < k_x < k_{x0}^{\mathrm{R}}(k_{x0}^{\mathrm{R}} < k_x < k_{x0}^{\mathrm{L}})$. For the crystal twin with $\theta_{\mathrm{L}} = \pi/4$ and $\theta_{\mathrm{R}} = -\pi/4$, $k_{x0}^{\mathrm{L}} = -k_{x0}^{\mathrm{R}} = (\varepsilon_1 - \varepsilon_3)/\sqrt{2(\varepsilon_1 + \varepsilon_3)}$. When $\varepsilon_3 > \varepsilon_1$ (i.e., positive birefringence) in the region of $k_{x0}^{\mathrm{L}} < k_x < k_{x0}^{\mathrm{R}}$, $S_x^{\mathrm{L}} > 0$ and $S_x^{\mathrm{R}} < 0$. For any given θ_{L}, ε_1, and ε_3, the maximum bending of the light beam or the strongest negative refraction occurs when $k_x = 0$ and $\sin^2 \theta_{\mathrm{L}} = \varepsilon_3/(\varepsilon_1 + \varepsilon_3)$, where the propagation direction of the light is given by $\phi = \arctan(S_x/S_z) = \arctan[-\delta/(2\beta)]$ for each side, and the amount of bending is measured by $\phi_{\mathrm{L}} - \phi_{\mathrm{R}} = 2\arctan[-\delta_{\mathrm{L}}/(2\beta)]$. For any given θ_{L} (as defined in Fig. 1.2), the maximum amount of bending is $2\theta_{\mathrm{L}}$ for positive crystal ($\varepsilon_3 > \varepsilon_1$ and $0 < \theta_{\mathrm{L}} < \pi/2$) or $2(\theta_{\mathrm{L}} - \pi/2)$ for negative crystal ($\varepsilon_1 > \varepsilon_3$ and $\pi/2 < \theta_{\mathrm{L}} < \pi$), when either $\varepsilon_1/\varepsilon_3 \to \infty$ or $\varepsilon_3/\varepsilon_1 \to \infty$. Figure 1.3 shows an experimental demonstration of amphoteric refraction with minimal reflection loss realized with a YVO_4 bicrystal [31], and Fig. 1.4 compares the experimental and theoretical results for the relationship between the angles of incidence and refraction (note that $\theta_{\mathrm{L}} = -\pi/4$ and $\theta_{\mathrm{R}} = \pi/4$ are assumed) [31].

As a special case of the general discussion with $0 < \theta_{\mathrm{L}} < 90°$ and $0 < \theta_{\mathrm{R}} < 90°$, zero reflection and/or negative refraction can also be realized at an isotropic–anisotropic interface [32–36]. Assuming $\mu = 1$, zero reflection occurs when $\varepsilon^{\mathrm{L}} = \sqrt{\varepsilon_1{}^{\mathrm{R}}\varepsilon_3{}^{\mathrm{R}}}$, which actually is the condition for the so-called perfectly matched layer [67]. The interface of air and a uniaxial crystal with

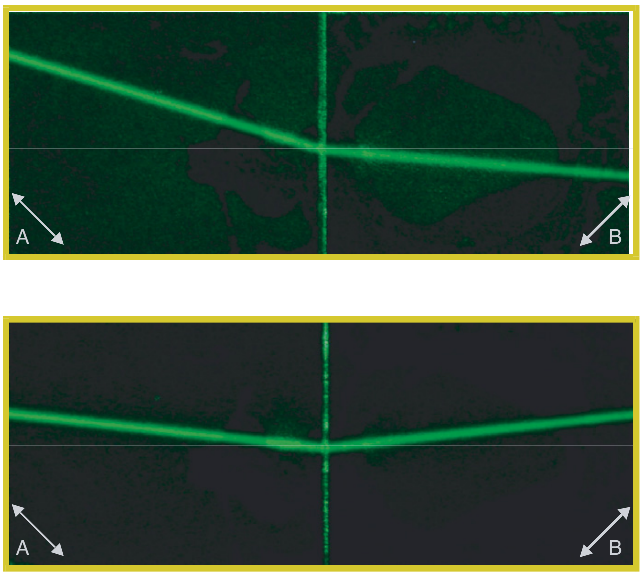

Fig. 1.3. Images of light propagation in a YVO_4 bicrystal. The *upper panel* shows an example of normal (positive) refraction, whereas the *lower panel* shows abnormal (negative) refraction. Note that no reflection at the bicrystal interface is visible to the naked eye. The interface is illuminated by inadvertently scattered light. The *arrows* indicate the orientations of the optical axes (A – *left*, B – *right*)

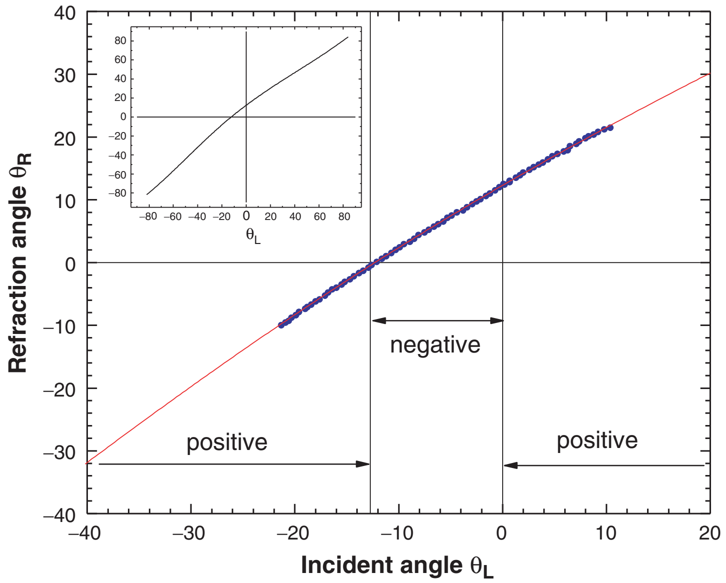

Fig. 1.4. Comparison of theoretical predictions with experimental data. Amphoteric refraction in a YVO_4 bicrystal is divided into three regions: one negative ($\theta_R/\theta_L < 0$) and two positive ($\theta_R/\theta_L > 0$). The data points are measured with a 532-nm laser light, and the curve is calculated with the refractive index of the material ($n_o = 2.01768$ and $n_e = 2.25081$). Inset: the full operation range of the device

its optical axis oriented at a nonzero angle to the interface normal is perhaps the simplest interface to facilitate negative refraction, as illustrated in Fig. 1.1. However trivial it might be, it is a genuine phenomenon of negative refraction.

If $\mu^R < 0$ and the ε^R tensor is indefinite or not positive definite, while allowing $0 < \theta_L < 90°$ and $0 < \theta_R < 90°$, we will have more unusual situations of refraction. Again, all parameters on the left-hand side are assumed positive, and, for simplicity, the left medium is assumed to be isotropic. If both $\varepsilon_1^R < 0$ and $\varepsilon_3^R < 0$, then the results are qualitatively similar to that of the isotropic case discussed above. However, when $\varepsilon_1^R < 0$ but $\varepsilon_3^R > 0$, or when ${\varepsilon_1}^R > 0$ but $\varepsilon_3^R < 0$, we thus have $\gamma^R < 0$; and by appropriately choosing θ_R to have $\beta^R > 0$, we have $\sqrt{\gamma^R(\beta^R\mu^R - k_x^2)} = \sqrt{|\gamma^R|\,(\beta^R\,|\mu^R| + k_x^2)}$, which indicates that all the real k_x components are propagating modes, and therefore, there will be no evanescent wave. For these cases, $(S_z^-)^R > 0$, and it is always possible to choose a value of θ_R (e.g., $\theta_R = 45°$ when ${\varepsilon_3}^R > |\varepsilon_1^R|$ or $\theta_R = -45°$ when ${\varepsilon_1}^R > |\varepsilon_3^R|$) such that $\delta^R < 0$; and thus, $(S_x^-)^R > 0$ for any k_x, which means that there will be no negative refraction for $k_x > 0$, in spite of the medium being left handed (because of $\mu^R < 0$), although refraction is negative for $k_x < 0$. Zero reflection only occurs at $k_x = 0$, when $\varepsilon^L = \sqrt{|\varepsilon_1^R\varepsilon_3^R|}$ and $(\varepsilon\mu)^L = |\beta\mu|^R$.

In summary, having an LHM is neither a necessary nor a sufficient condition for achieving negative refraction. The left-handed behavior does not always lead to evanescent wave amplification. It may not always be possible to match the material parameters to eliminate the interface reflection with an LHM. The double-negativity lens proposed by Veselago and Pendry represents the most-stringent material requirement to achieve negative refraction, zero reflection, and evanescent wave amplification. For a uniform medium, the left-handed behavior can only be obtained with at least one component of the ε or μ tensor being negative: ε_1 for the **E**-polarized wave and μ_1 for the **H**-polarized wave, if limited to materials with uniaxial symmetry [63]. However, once one of the components of either the ε or μ tensor becomes negative so as to have left-handed behavior, then at least one of the components of the other tensor needs to be negative to have propagating modes in the medium, and possibly to have evanescent wave amplification (as discussed above for the **H**-polarized wave and in the literature for the **E**-polarized wave [65]).

Analogous to the discussion of negative refraction in the photonic crystal, one could consider the propagation of a ballistic electron beam in a real crystal. It is perceivable that one could discuss how various types of electronic band structures might bend the electron beam negatively, in a manner similar to the negative "refraction" discussions for the photonic crystal [40]. Again, a domain twin interface, as the one shown in Fig. 1.5 for example, appears to be a simple case that can give rise to negative refraction and zero reflection for a ballistic electron beam [31]. It is a genuine refraction when light goes through such an interface; but for the electron beam, it is fundamentally a phenomenon of diffraction. Complex structures of this type of domain twin could be of great interest for both optics and electronics. Examples of such super structures created by stacking domain twins in a linear manner

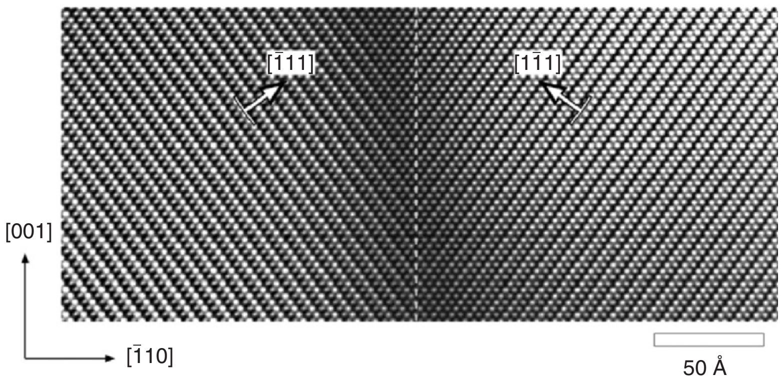

Fig. 1.5. A typical high-resolution cross-sectional transmission electron microscopy (TEM) image of domain twin structures frequently observed in CuPt-ordered III–V semiconductor alloys (e.g., GaInAs). The ordering directions are [$\bar{1}$11] (*left*) and [1$\bar{1}$1] (*right*). The *vertical dashed line* indicates the twin boundary

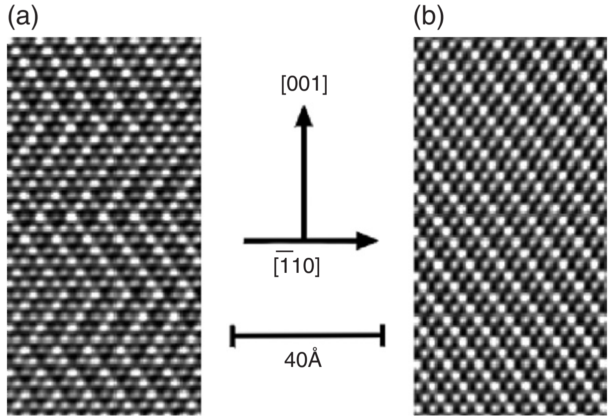

Fig. 1.6. High-resolution cross-sectional TEM images of ordered GaInP alloys: (**a**) double-variant ordered structure with quasiperiodic stacking of domain twins along the [001] direction, and (**b**) single-variant ordered domain

can be found in the literature, though not in the context of negative refraction. For instance, a zig-zag structure found in the so-called "sculptured" thin film is ideally a periodic one-dimensional stacking of the domain twins. Zero reflection for the TM polarized electromagnetic wave was indicated in the literature (for normal incidence [68] and arbitrary angle of incidence [69]). For electronics, an unusual type of semiconductor superlattice, termed an "orientational superlattice," was found in spontaneously ordered semiconductor alloys, and their electronic structures and optical properties were also investigated [70–72]. Figure 1.6 shows a quasiperiodic structure of ordered domain twins, which is an orientational superlattice, in a $Ga_{1-x}In_xP$ alloy [72].

1.3 Conclusion

Negative refraction, as an interesting physical phenomenon, can be observed in a number of circumstances possibly facilitated by very different physical mechanisms. The interest in this field has provided great opportunities for fundamental physics research, material developments, and novel applications.

Acknowledgments

We thank Drs. V.M. Agranovich, C.M. Krowne, B. Fluegel, and S. Smith for helpful discussions. This work was funded by the US Department of Energy, Office of Science, Basic Energy Sciences, under Contract No. DE-AC36-99GO10337 to NREL.

References

1. J.B. Pendry, Phys. Rev. Lett. **85**, 3966 (2000)
2. J.B. Pendry, Science **305**, 788 (2005)
3. J.B. Pendry, D.R. Smith, Phys. Today **57**, 37 (2004)
4. Y. Zhang, A. Mascarenhas, Mod. Phys. Lett. B **18** (2005)
5. A. Schuster, *An Introduction to the Theory of Optics* (Edward Arnold, London, 1904)
6. E.I. Rashba, J. Appl. Phys. **79**, 4306 (1996)
7. C.F. Klingshirn, *Semiconductor Optics* (Springer, Berlin Heidelberg New York, 1995)
8. G. Dolling, C. Enkrich, M. Wegener, C.M. Soukoulis, S. Linden, Science **312**, 892 (2006)
9. V.M. Agranovich, V. L. Ginzburg, *Spatial Dispersion in Crystal Optics and the Theory of Excitons* (Wiley, London, 1966)
10. V.G. Veselago, Sov. Phys. Usp. **10**, 509 (1968)
11. A.I. Viktorov, *Physical Principles of the Use of Ultrasonic Raleigh and Lamb Waves in Engineering* (Nauka, Russia, 1966)
12. P.V. Burlii, I.Y. Kucherov, JETP Lett. **26**, 490 (1977)
13. H. Lamb, Proc. London Math. Soc. Sec. II **1**, 473 (1904)
14. C.M. Krowne, *Encyclopedia of Rf and Microwave Engineering*, vol. 3 (Wiley, New York, 2005), p. 2303
15. M. Born, E. Wolf, *Principles of Optics* (Cambridge University Press, Cambridge, 1999)
16. J. Neufeld, R.H. Ritchie, Phys. Rev. **98**, 1955 (1955)
17. V.L. Ginzburg, JETP **34**, 1096 (1958)
18. V.M. Agranovich, Y.R. Shen, R.H. Baughman, A.A. Zakhidov, Phys. Rev. B **69**, 165112 (2004)
19. M. Born, K. Huang, *Dynamical Theory of Crystal Lattices* (Clarendon, Oxford, 1954)
20. J.J. Hopfield, Phys. Rev. **112**, 1555 (1958)
21. V.M. Agranovich, Y.R. Shen, R.H. Baughman, A.A. Zakhidov, J. Lumin. **110**, 167 (2004)
22. V.E. Pafomov, Sov. Phys. JETP **36**, 1321 (1959)
23. R.A. Shelby, D.R. Smith, S. Schultz, Science **292**, 77 (2001)
24. L.D. Landau, E.M. Lifshitz, L.P. Pitaevskii, *Electrodynamics of Continuous Media* (Butterworth-Heinemann, Oxford, 1984)
25. C. Enkrich, M. Wegener, S. Linden, S. Burger, L. Zschiedrich, F. Schmidt, J.F. Zhou, T. Koschny, C.M. Soukoulis, Phys. Rev. Lett. **95** (2005)
26. A.N. Grigorenko, A.K. Geim, H.F. Gleeson, Y. Zhang, A.A. Firsov, I.Y. Khrushchev, J. Petrovic, Nature **438**, 335 (2005)
27. S. Zhang, W.J. Fan, N.C. Panoiu, K.J. Malloy, R.M. Osgood, S.R.J. Brueck, Phys. Rev. Lett. **95** (2005)
28. S. Linden, C. Enkrich, M. Wegener, J.F. Zhou, T. Koschny, C.M. Soukoulis, Science **306**, 1351 (2004)
29. V.M. Shalaev, W.S. Cai, U.K. Chettiar, H.K. Yuan, A.K. Sarychev, V.P. Drachev, A.V. Kildishev, Opt. Lett. **30**, 3356 (2005)
30. J.B. Pendry, Science **306**, 1353 (2004)
31. Y. Zhang, B. Fluegel, A. Mascarenhas, Phys. Rev. Lett. **91**, 157404 (2003)
32. Y. Zhang, A. Mascarenhas, in *Mat. Res. Soc. Symp. Proc.*, vol. 794 (MRS Fall Meeting, Boston, 2003), p. T10.1

33. L.I. Perez, M.T. Garea, R.M. Echarri, Opt. Commun. **254**, 10 (2005)
34. X.L. Chen, H. Ming, D. YinXiao, W.Y. Wang, D.F. Zhang, Phys. Rev. B **72**, 113111 (2005)
35. Y.X. Du, M. He, X.L. Chen, W.Y. Wang, D.F. Zhang, Phys. Rev. B **73**, 245110 (2006)
36. Y. Lu, P. Wang, P. Yao, J. Xie, H. Ming, Opt. Commun. **246**, 429 (2005)
37. Z. Liu, Z.F. Lin, S.T. Chui, Phys. Rev. B **69**, 115402 (2004)
38. Y. Wang, X.J. Zha, J.K. Yan, Europhys. Lett. **72**, 830 (2005)
39. K. Sakoda, *Optical Properties of Photonic Crystals* (Springer, Berlin Heidelberg New York, 2001)
40. S. Foteinopoulou, C.M. Soukoulis, Phys. Rev. B **72**, 165112 (2005)
41. M. Notomi, Phys. Rev. B **62**, 10696 (2000)
42. P.V. Parimi, W.T.T. Lu, P. Vodo, S. Sridhar, Nature **426**, 404 (2003)
43. C. Luo, S.G. Johnson, J.D. Joannopoulos, J.B. Pendry, Phys. Rev. B **65**, 201104 (2002)
44. E. Cubukcu, K. Aydin, E. Ozbay, S. Foteinopoulou, C.M. Soukoulis, Nature **423**, 604 (2003)
45. A.B. Pippard, *The Dynamics of Conduction Electrons* (Gordon and Breach, New York, 1965)
46. Y.R. Shen, *The Principles of Nonlinear Optics* (Wiley, New York, 1984)
47. L. Silvestri, O.A. Dubovski, G.C. La Rocca, F. Bassani, V.M. Agranovich, Nuovo Cimento Della Societa Italiana Di Fisica C-Geophysics and Space Physics **27**, 437 (2004)
48. C. Luo, S.G. Johnson, J.D. Joannopoulos, J.B. Pendry, Phys. Rev. B **68**, 45115 (2003)
49. A.L. Pokrovsky and A.L. Efros, Phys. B **338**, 333 (2003)
50. D.R. Smith, D. Schurig, M. Rosenbluth, S. Schultz, S.A. Ramakrishna, J.B. Pendry, Appl. Phys. Lett. **82**, 1506 (2003)
51. I. Ichimura, S. Hayashi, G.S. Kino, Appl. Opt. **36**, 4339 (1997)
52. http://www.semiconductor-technology.com/features/section290/
53. S.M. Mansfield, G.S. Kino, Appl. Phys. Lett. **57**, 2615 (1990)
54. I. Smolyaninov, J. Elliott, A.V. Zayats, C.C. Davis, Phys. Rev. Lett. **94** (2005)
55. Z.F. Feng, X.D. Zhang, Y.Q. Wang, Z.Y. Li, B.Y. Cheng, D.Z. Zhang, Phys. Rev. Lett. **94** (2005)
56. Z. Lu, J.A. Murakowski, C.A. Schuetz, S. Shi, G.J. Schneider, D.W. Prather, Phys. Rev. Lett. **95**, 153901 (2005)
57. N. Fang, H. Lee, C. Sun, X. Zhang, Science **308**, 534 (2005)
58. D.O.S. Melville, R.J. Blaikie, Opt. Express **13**, 2127 (2005)
59. J.M. Vigoureux, D. Courjon, Appl. Opt. **31**, 3170 (1992)
60. A.L. Efros, A.L. Pokrovsky, Solid State Commun. **129**, 643 (2004)
61. T. Decoopman, G. Tayeb, S. Enoch, D. Maystre, B. Gralak, Phys. Rev. Lett. **97** (2006)
62. I.V. Lindell, S.A. Tretyakov, K.I. Nikoskinen, S. Ilvonen, Microw. Opt. Technol. Lett. **31**, 129 (2001)
63. L.B. Hu, S.T. Chui, Phys. Rev. B **66**, 085108 (2002)
64. L. Zhou, C.T. Chan, P. Sheng, Phys. Rev. B **68**, 115424 (2003)
65. D.R. Smith, D. Schurig, Phys. Rev. Lett. **90**, 077405 (2003)
66. T. Dumelow, J.A.P. da Costa, V.N. Freire, Phys. Rev. B **72** (2005)
67. S.D. Gedney, IEEE Trans. Antennas Propagat. **44**, 1630 (1996)

68. A. Lakhtakia, R. Messier, Opt. Eng. **33**, 2529 (1994)
69. G.Y. Slepyan, A.S. Maksimenko, Opt. Eng. **37**, 2843 (1998)
70. Y. Zhang, A. Mascarenhas, Phys. Rev. B **55**, 13100 (1997)
71. Y. Zhang, A. Mascarenhas, S.P. Ahrenkiel, D.J. Friedman, J. Geisz, J.M. Olson, Solid State Commun. **109**, 99 (1999)
72. Y. Zhang, B. Fluegel, S.P. Ahrenkiel, D.J. Friedman, J. Geisz, J.M. Olson, A. Mascarenhas, Mat. Res. Soc. Symp. Proc. **583**, 255 (2000)

2

Anisotropic Field Distributions in Left-Handed Guided Wave Electronic Structures and Negative Refractive Bicrystal Heterostructures

C.M. Krowne

Summary. Effect of anisotropy in the physical tensor description of the negative index of refraction material acting as a substrate is found on the electromagnetic field distributions. This is done for the case of a microstrip structure whose configuration is commonly used in microwave and millimeter wave integrated circuits. These ab initio studies have been done self-consistently with a computer code using a full-wave integral equation numerical method based upon a generalized anisotropic Green's function utilizing appropriate boundary conditions. Field distributions are provided over two decades of frequency in the cross-section of the uniform guided wave structure, from 0.2 to 20 GHz. It is found that modifying the tensor can allow control because the wave changes volumetrically, or switches from volumetric to surface, in its distribution of fields. It has also been discovered that heterostructure bicrystal arrangements lead to field asymmetry in guided wave structures. A study is conducted over a range of nominal permittivity values to see if the effect is present in widely varying dielectric materials. Marked shifts of the field distribution occurs in some cases, and this can be the basis of an all electronic device that provides beam steering or a device that gives directional action. Such all electronic devices could be fixed or even constructed as control components using materials with electrostatically controllable permittivity. Distributions have been obtained to demonstrate the effect using an anisotropic Green's function solver.

2.1 Anisotropic Field Distributions in Left-Handed Guided Wave Electronic Structures

2.1.1 Introduction

Although considerable physics has been learned about the dispersion behavior and electromagnetic fields for propagation down guided wave microstrip structures loaded with DNM (double-negative materials with simultaneous negative permittivity and permeability) which are also referred to LHM (left-handed materials for the left-handed orientation of the electric, magnetic, and propagation phase constant) [1, 2] nothing is known about what happens to the field distributions as anisotropy is introduced. This is an extremely interesting area since maintenance of isotropy has been recognized to be essential for 3D imaging possibilities [3, 4], and such isotropy should also be necessary for arbitrary field contouring or arrangement of fields in small electronic devices which are created especially to employ the unique properties of DNM. It should also be noted here that these materials can be referred to as NIRM (negative index of refraction materials) or NIM (negative index materials). Furthermore, because the essential property of these materials is opposite orientations of the phase velocity and the Poynting vector (giving the power flow direction), they may be referred to as alternatively as negative phase velocity materials (NPV materials or simply NPVM) [5].

Because we are not going to further examine 3D imaging issues, but 3D behavior of fields in electronic devices, we will restrict the use of notation when referring to these materials as DNM or NPVM. Although maintaining isotropy for many integrated circuit applications may be desirable as mentioned above, it may also be desirable to introduce anisotropy [6, 7], or at least find it acceptable to have some anisotropy in certain device configurations, where because of the particular applications, the effective dimensions of the device is reduced from 3D to 2D or even 1D. This is not some idle speculation, as quasilumped element realizations using distributed and/or lumped sections have been used to make components employing backward wave behavior, one of the hallmarks of DNM or NPVM [8–11]. Thus, whether or not we want to examine what the effect is of some deviation from isotropy, or wish to intentionally introduce anisotropy, it would be very instructive to undertake such an investigation.

In pursuing this quest, the backdrop of already studied field distributions for isotropic DNM in the C-band, X-band, Ka and V-bands, and W-band broadcast frequency regions gives us some basis upon which to begin these studies. In the C-band region, electromagnetic field line plots of $\mathbf{E}_\mathrm{t}$ and $\mathbf{H}_\mathrm{t}$ for the transverse fields in the cross-section perpendicular to the propagation direction were provided at 5 GHz [2]. Also given were simultaneous magnitude and arrow vector distributions plots for $E/\mathbf{E}_\mathrm{t}$ and $H/\mathbf{H}_\mathrm{t}$ at the same frequency. Finally, a Poynting vector distribution plot P_z was provided at 5 GHz. In the X-band region, electromagnetic field line plots of $\mathbf{E}_\mathrm{t}$ and $\mathbf{H}_\mathrm{t}$ were provided at 10 GHz [12]. Also given were simultaneous magnitude and arrow vector distributions plots for $E/\mathbf{E}_\mathrm{t}$ and $H/\mathbf{H}_\mathrm{t}$ at the same frequency. Finally, a Poynting vector distribution plot P_z was provided at 10 GHz. In the overlap region between the Ka and V-bands, electromagnetic field plots of simultaneous magnitude and arrow vector distributions plots for $E/\mathbf{E}_\mathrm{t}$ and $H/\mathbf{H}_\mathrm{t}$ were given at 40 GHz [12, 13]. Simultaneous line and magnitude distribution plots for $E/\mathbf{E}_\mathrm{t}$ and $H/\mathbf{H}_\mathrm{t}$ were also provided at 40 GHz [12]. Lastly, a Poynting vector distribution plot P_z was provided at the same frequency [12].

Sections 2.1.2 and 2.1.3 cover, respectively, the governing equations/acquisition of the anisotropic Green's function, and use of basis current functions/determination of the propagation constant and electromagnetic fields, for the guided wave microstrip structure with anisotropic DNM. With a complete development in hand, numerical calculations are performed in Sect. 2.1.4 for a microstrip structure at three frequencies offset from each other by decade steps. Each study is begun by first examining an isotropic tensor to provide a reference standard for looking at the effects of introducing anisotropy through a permittivity tensor. Once the electromagnetic distributions have been obtained for the isotropic case, distributions for anisotropy are calculated. This process of first finding the isotropic result, then proceeding on to the anisotropic situation, is done at each frequency.

2.1.2 Anisotropic Green's Function Based Upon LHM or DNM Properties

Maxwell's time varying equations describe the electromagnetic field behavior in a medium if they are combined with constitutive relationships embedding the physical properties of the medium in them. Maxwell's two curl equations are

$$\nabla \times \mathbf{E}(t,\mathbf{x}) = -\frac{\partial \mathbf{B}(t,\mathbf{x})}{\partial t}, \quad \nabla \times \mathbf{H}(t,\mathbf{x}) = \frac{\partial \mathbf{D}(t,\mathbf{x})}{\partial t} + \mathbf{J}(t,\mathbf{x}). \tag{2.1}$$

Constitutive relationships are

$$\mathbf{D}(t,\mathbf{x}) = \bar{\bar{\varepsilon}}\mathbf{E}(t,\mathbf{x}) + \bar{\bar{\rho}}\mathbf{H}(t,\mathbf{x}), \quad \mathbf{B}(t,\mathbf{x}) = \bar{\bar{\rho}}'\mathbf{E}(t,\mathbf{x}) + \bar{\bar{\mu}}\mathbf{H}(t,\mathbf{x}). \tag{2.2}$$

Here $\mathbf{x} = (\mathrm{x}_1, \mathrm{x}_2, \mathrm{x}_3) = (\mathrm{x}, \mathrm{y}, \mathrm{z})$. Most general NPV medium can have all constitutive tensors in (2.2) nonzero, including the magnetoelectric or optical activity tensors $\bar{\bar{\rho}}$ and $\bar{\bar{\rho}}'$, as they are sometimes called. The formulation is therefore kept general in order to retain the most flexibility for studying materials with widely varying physical properties. Because many problems are often transparent in the frequency domain, and because nonharmonic problems can be resolved into a superposition of time-harmonic components, we elect to study here time harmonic electromagnetic wave propagation through the solid state LHM–RHM structure (RHM, right-handed medium or ordinary medium). Taking the time harmonic variation to be of a form $\mathrm{e}^{\mathrm{i}\omega t}$, Maxwell's equation become

$$\nabla \times \mathbf{E}(\mathbf{x}) = -\mathrm{i}\omega\mathbf{B}(\mathbf{x}), \quad \nabla \times \mathbf{H}(\mathbf{x}) = \mathrm{i}\omega\mathbf{D}(\mathbf{x}) + \mathbf{J}(\mathbf{x}) \tag{2.3}$$

with the constitutive relationships dropping the explicit t-dependence

$$\mathbf{D}(\mathbf{x}) = \bar{\bar{\varepsilon}}(\omega)\mathbf{E}(\mathbf{x}) + \bar{\bar{\rho}}(\omega)\mathbf{H}(\mathbf{x}), \quad \mathbf{B}(\mathbf{x}) = \bar{\bar{\rho}}'(\omega)\mathbf{E}(\mathbf{x}) + \bar{\bar{\mu}}(\omega)\mathbf{H}(\mathbf{x}). \tag{2.4}$$

Dependence of the constitutive parameters on radian frequency is a well-recognized fact and that is why explicit variation on ω is shown. However, for the study to be conducted here at specific frequencies, we do not need to call out this dependence explicitly. We will be setting for, example $\bar{\bar{\varepsilon}}(\omega) = v$ for $\omega = \omega_v$. Therefore, we set

$$\mathbf{D}(\mathbf{x}) = \bar{\bar{\varepsilon}}\mathbf{E}(\mathbf{x}) + \bar{\bar{\rho}}\mathbf{H}(\mathbf{x}), \quad \mathbf{B}(\mathbf{x}) = \bar{\bar{\rho}}'\mathbf{E}(\mathbf{x}) + \bar{\bar{\mu}}\mathbf{H}(\mathbf{x}) \tag{2.5}$$

and understand it means (2.2).

Curl equations (2.1) may be combined into a single sourceless governing equation [14],

$$L_{\mathrm{T}}(\mathbf{x})\mathbf{V}_{\mathrm{L}}(\mathbf{x}) = \mathrm{i}\omega\mathbf{V}_{\mathrm{R}}(\mathbf{x}), \tag{2.6}$$

where the matrix partial differential operator acting on the **E**–**H** column vector is

$$L_{\mathrm{T}}(\mathbf{x}) = \begin{bmatrix} 0 & L_{\mathrm{q}}(\mathbf{x}) \\ -L_{\mathrm{q}}(\mathbf{x}) & 0 \end{bmatrix}, \tag{2.7}$$

where the quadrant operator is

$$L_{\mathrm{q}}(\mathbf{x}) = \begin{bmatrix} 0 & -\dfrac{\partial}{\partial z} & \dfrac{\partial}{\partial y} \\ \dfrac{\partial}{\partial z} & 0 & -\dfrac{\partial}{\partial x} \\ -\dfrac{\partial}{\partial y} & \dfrac{\partial}{\partial x} & 0 \end{bmatrix}. \tag{2.8}$$

Current **J** effects are introduced later through a Green's function process [see (2.80)]. Vectors in (2.6) are

$$\mathbf{V}_{\mathrm{L}}(\mathbf{x}) = \begin{bmatrix} E_x \\ E_y \\ E_z \\ H_x \\ H_y \\ H_z \end{bmatrix} = \begin{bmatrix} \mathbf{E} \\ \mathbf{H} \end{bmatrix}, \quad \mathbf{V}_{\mathrm{R}}(\mathbf{x}) = \begin{bmatrix} D_x \\ D_y \\ D_z \\ B_x \\ B_y \\ B_z \end{bmatrix} = \begin{bmatrix} \mathbf{D} \\ \mathbf{B} \end{bmatrix}. \tag{2.9}$$

Restricting ourselves to a guided wave structure with the wave traveling in a uniform cross-section in the z-direction, that is the wave has the form $\mathrm{e}^{\mathrm{i}\omega t - \gamma z}$, $\gamma = \gamma(\omega)$, simplifies (2.6)–(2.8) to

$$L_{\mathrm{T}}(x,y)\mathbf{V}_{\mathrm{L}}(x,y) = \mathrm{i}\omega\mathbf{V}_{\mathrm{R}}(x,y), \tag{2.10}$$

$$L_{\mathrm{T}}(x,y) = \begin{bmatrix} 0 & L_{\mathrm{q}}(x,y) \\ -L_{\mathrm{q}}(x,y) & 0 \end{bmatrix}, \tag{2.11}$$

$$L_{\mathrm{q}}(x,y) = \begin{bmatrix} 0 & \gamma & \dfrac{\partial}{\partial y} \\ -\gamma & 0 & -\dfrac{\partial}{\partial x} \\ -\dfrac{\partial}{\partial y} & \dfrac{\partial}{\partial x} & 0 \end{bmatrix}. \tag{2.12}$$

Finally, there are certain advantages for approaching the problem in the Fourier transform domain, not the least of which is that real space convolution integrals reduce to products, and so for the integral equation technique to be applied to a finite enclosed region in the x-direction, with layering in the y-direction, the finite Fourier transform pair

$$\mathbf{F}(k_x, y) = \int_{-b}^{b} \mathbf{F}(x, y)\mathrm{e}^{-\mathrm{i}k_x x}\mathrm{d}x, \quad F_i(k_x, y) = \int_{-b}^{b} F_i(x, y)\mathrm{e}^{-\mathrm{i}k_x x}\mathrm{d}x; \tag{2.13}$$

$$\mathbf{F}(x, y) = \frac{1}{2b}\sum_{k_x=-\infty}^{\infty} \mathbf{F}(k_x, y)\mathrm{e}^{\mathrm{i}k_x x}, \quad F_i(x, y) = \frac{1}{2b}\sum_{k_x=-\infty}^{\infty} F_i(k_x, y)\mathrm{e}^{\mathrm{i}k_x x} \tag{2.14}$$

is applied to the fields, converting (2.10)–(2.12) into

$$L_\mathrm{T}(k_x, y)\mathbf{V}_\mathrm{L}(k_x, y) = \mathrm{i}\omega\mathbf{V}_\mathrm{R}(k_x, y), \tag{2.15}$$

$$L_\mathrm{T}(k_x, y) = \begin{bmatrix} 0 & L_\mathrm{q}(k_x, y) \\ -L_\mathrm{q}(k_x, y) & 0 \end{bmatrix}, \tag{2.16}$$

$$L_\mathrm{q}(k_x, y) = \begin{bmatrix} 0 & \gamma & \dfrac{\partial}{\partial y} \\ -\gamma & 0 & -\mathrm{i}k_x \\ -\dfrac{\partial}{\partial y} & \mathrm{i}k_x & 0 \end{bmatrix}. \tag{2.17}$$

Constitutive relationships (2.2) can be combined into a super-tensor,

$$\mathbf{V}_\mathrm{R}(\boldsymbol{t}, \mathbf{x}) = \mathbf{M}\mathbf{V}_\mathrm{L}(\boldsymbol{t}, \mathbf{x}), \quad \mathbf{M} = \begin{bmatrix} \bar{\bar{\varepsilon}} & \bar{\bar{\rho}} \\ \bar{\bar{\rho}}' & \bar{\bar{\mu}} \end{bmatrix} \tag{2.18}$$

and using the harmonic transformation leading to (2.5),

$$\mathbf{V}_\mathrm{R}(\mathbf{x}) = \mathbf{M}(\omega)\mathbf{V}_\mathrm{L}(\mathbf{x}). \tag{2.19}$$

Characterization of the wave by the complex propagation constant reduces (2.19) to

$$\mathbf{V}_\mathrm{R}(x, y) = \mathbf{M}(\omega)\mathbf{V}_\mathrm{L}(x, y). \tag{2.20}$$

When the finite Fourier transform is applied to (2.20),

$$\mathbf{V}_\mathrm{R}(k_x, y) = \mathbf{M}(\omega)\mathbf{V}_\mathrm{L}(k_x, y). \tag{2.21}$$

Inserting this formula describing the material physics into electromagnetic equation yields, after eliminating $\mathbf{V}_\mathrm{R}$,

$$L_\mathrm{T}(k_x, y)\mathbf{V}_\mathrm{L}(k_x, y) = \mathrm{i}\omega\mathbf{M}(\omega)\mathbf{V}_\mathrm{L}(k_x, y). \tag{2.22}$$

This matrix equation can in principle be solved for the normal mode eigenvectors and eigenvalues $\gamma = \gamma(k_x, \omega)$, realizing that the 1×6 column vectors and the 6×6 operator and material tensor square matrices use the full electromagnetic field component set. However, because we will restrict ourselves to canonical layered structures (layered in the y-direction), it is very convenient to extract the perpendicular field components from (2.22) using rows 2 and 5 which do not possess differential operator $\mathrm{d}/\mathrm{d}y$:

$$-\gamma V_4 - \mathrm{i}k_x V_6 = \mathrm{i}\omega \sum_{i=1}^{6} m_{2i} V_i, \tag{2.23}$$

$$\gamma V_1 + \mathrm{i}k_x V_3 = \mathrm{i}\omega \sum_{i=1}^{6} m_{5i} V_i. \tag{2.24}$$

Solution of (2.23) and (2.24) is

$$V_i = \sum_{j=1}^{6} a_{ij}(1-\delta_{2,j})(1-\delta_{5,j})V_j, \quad i = 2, 5, \tag{2.25}$$

where $\delta_{i,j}$ is the Kronecker delta function, or

$$E_y = a_{21}E_x + a_{23}E_z + a_{24}H_x + a_{26}H_z, \tag{2.26}$$

$$H_y = a_{51}E_x + a_{53}E_z + a_{54}H_x + a_{56}H_z. \tag{2.27}$$

Here a_{ij} are given by

$$a_{ij} = \frac{a'_{ij}}{D_a}, \tag{2.28}$$

$$D_a = m_{22}m_{55} - m_{25}m_{52}, \tag{2.29}$$

$$a'_{21} = m_{25}\left(m_{51} + \frac{\mathrm{i}\gamma}{\omega}\right) - m_{21}m_{55}, \tag{2.30}$$

$$a'_{23} = m_{25}\left(m_{53} - \frac{k_x}{\omega}\right) - m_{23}m_{55}, \tag{2.31}$$

$$a'_{24} = m_{25}m_{54} - m_{55}\left(m_{24} - \frac{\mathrm{i}\gamma}{\omega}\right), \tag{2.32}$$

$$a'_{26} = m_{25}m_{56} - m_{55}\left(m_{26} + \frac{k_x}{\omega}\right), \tag{2.33}$$

$$a'_{51} = m_{52}m_{21} - m_{22}\left(m_{51} + \frac{\mathrm{i}\gamma}{\omega}\right), \tag{2.34}$$

$$a'_{53} = m_{52}m_{23} - m_{22}\left(m_{53} - \frac{k_x}{\omega}\right), \tag{2.35}$$

$$a'_{54} = m_{52}\left(m_{24} - \frac{\mathrm{i}\gamma}{\omega}\right) - m_{22}m_{54}, \tag{2.36}$$

$$a'_{56} = m_{52}\left(m_{26} + \frac{k_x}{\omega}\right) - m_{22}m_{56}. \tag{2.37}$$

Here $\mathbf{M}$ consists of the set $\{m_{ij}\}$ of elements. For the case when the optical activities are turned off, $\bar{\bar{\rho}} = 0$ and $\bar{\bar{\rho}}' = 0$, (2.29)–(2.37) become

$$D_a = \varepsilon_{22}\mu_{22} - \rho_{22}\rho'_{22} = \varepsilon_{22}\mu_{22}, \tag{2.38}$$

$$a'_{21} = \rho_{22}\left(\rho'_{21} + \frac{\mathrm{i}\gamma}{\omega}\right) - \varepsilon_{21}\mu_{22} = -\varepsilon_{21}\mu_{22}, \tag{2.39}$$

$$a'_{23} = \rho_{22}\left(\rho'_{23} - \frac{k_x}{\omega}\right) - \varepsilon_{23}\mu_{22} = -\varepsilon_{23}\mu_{22}, \tag{2.40}$$

$$a'_{24} = \rho_{22}\mu_{21} - \mu_{22}\left(\rho_{21} - \frac{\mathrm{i}\gamma}{\omega}\right) = \mu_{22}\frac{i\gamma}{\omega}, \tag{2.41}$$

$$a'_{26} = \rho_{22}\mu_{23} - \mu_{22}\left(\rho_{23} + \frac{k_x}{\omega}\right) = -\mu_{22}\frac{k_x}{\omega}, \tag{2.42}$$

$$a'_{51} = \rho'_{22}\varepsilon_{21} - \varepsilon_{22}\left(\rho'_{21} + \frac{\mathrm{i}\gamma}{\omega}\right) = -\varepsilon_{22}\frac{\mathrm{i}\gamma}{\omega}, \tag{2.43}$$

$$a'_{53} = \rho'_{22}\varepsilon_{23} - \varepsilon_{22}\left(\rho'_{23} - \frac{k_x}{\omega}\right) = \varepsilon_{22}\frac{k_x}{\omega}, \tag{2.44}$$

$$a'_{54} = \rho'_{22}\left(\rho_{21} - \frac{\mathrm{i}\gamma}{\omega}\right) - \varepsilon_{22}\mu_{21} = -\varepsilon_{22}\mu_{21}, \tag{2.45}$$

$$a'_{56} = \rho'_{22}\left(\rho_{23} + \frac{k_x}{\omega}\right) - \varepsilon_{22}\mu_{23} = -\varepsilon_{22}\mu_{23}. \tag{2.46}$$

For biaxial electric and magnetic crystalline properties in a principal axis system, only the diagonal elements of the subtensors of $\mathbf{M}$ survive, making (2.39)–(2.46) become

$$a'_{21} = a'_{23} = 0, \quad a'_{24} = \mu_{22}\frac{\mathrm{i}\gamma}{\omega}, \quad a'_{26} = -\mu_{22}\frac{k_x}{\omega} \tag{2.47}$$

$$a'_{51} = -\varepsilon_{22}\frac{\mathrm{i}\gamma}{\omega}, \quad a'_{53} = \varepsilon_{22}\frac{k_x}{\omega}, \quad a'_{54} = a'_{56} = 0. \tag{2.48}$$

Governing equation of the problem can be acquired by realizing that rows 1, 3, 4, and 6 of (2.22) contain first-order linear differential equations

$$\gamma V_5 + \frac{\mathrm{d}V_6}{\mathrm{d}y} = \mathrm{i}\omega\sum_{i=1}^{6} m_{1i}V_i, \tag{2.49}$$

$$-\frac{\mathrm{d}V_4}{\mathrm{d}y} + \mathrm{i}k_x V_5 = \mathrm{i}\omega\sum_{i=1}^{6} m_{3i}V_i, \tag{2.50}$$

$$-\gamma V_2 - \frac{\mathrm{d}V_3}{\mathrm{d}y} = \mathrm{i}\omega\sum_{i=1}^{6} m_{4i}V_i, \tag{2.51}$$

$$\frac{\mathrm{d}V_1}{\mathrm{d}y} - \mathrm{i}k_x V_2 = \mathrm{i}\omega\sum_{i=1}^{6} m_{6i}V_i. \tag{2.52}$$

With the help of (2.25) to remove V_2 and V_5 from (2.49)–(2.52),

$$\frac{\mathrm{d}\aleph}{\mathrm{d}y} = \mathrm{i}\omega \mathbf{R}\aleph, \tag{2.53}$$

$$\aleph = \begin{bmatrix} V_1 \\ V_3 \\ V_4 \\ V_6 \end{bmatrix} = \begin{bmatrix} E_x \\ E_z \\ H_x \\ H_z \end{bmatrix}, \tag{2.54}$$

$$r_{1j} = m_{6\theta} + a_{5\theta} m_{65} + a_{2\theta}\left(m_{62} + \frac{k_x}{\omega}\right), \tag{2.55}$$

$$r_{2j} = -\left\{m_{4\theta} + a_{5\theta} m_{45} + a_{2\theta}\left(m_{42} - \frac{\mathrm{i}\gamma}{\omega}\right)\right\}, \tag{2.56}$$

$$r_{3j} = -\left\{m_{3\theta} + a_{2\theta} m_{32} + a_{5\theta}\left(m_{35} - \frac{k_x}{\omega}\right)\right\}, \tag{2.57}$$

$$r_{4j} = m_{1\theta} + a_{2\theta} m_{12} + a_{5\theta}\left(m_{15} + \frac{\mathrm{i}\gamma}{\omega}\right). \tag{2.58}$$

Here the $\theta(j)$ index on a_{ij} is defined by

$$\theta(j) = \begin{cases} \dfrac{3}{2} j, & j = 2, 4; \\ \dfrac{3j-1}{2}, & j = 1, 3. \end{cases} \tag{2.59}$$

Here $\mathbf{R}$ consists of the set $\{r_{ij}\}$ of elements. For the case when the optical activities are turned off, $\bar{\bar{\rho}} = 0$ and $\bar{\bar{\rho}}' = 0$,

$$r_{11} = \rho'_{31} + a_{51}\mu_{32} + a_{21}\left(\rho'_{32} + \frac{k_x}{\omega}\right) = -\frac{\mathrm{i}\gamma}{\omega}\frac{\mu_{32}}{\mu_{22}} - \frac{\varepsilon_{21}}{\varepsilon_{22}}\frac{k_x}{\omega}, \tag{2.60}$$

$$\begin{aligned} r_{12} &= \rho'_{33} + a_{53}\mu_{32} + a_{23}\left(\rho'_{32} + \frac{k_x}{\omega}\right) = \frac{k_x}{\omega}\frac{\mu_{32}}{\mu_{22}} - \frac{\varepsilon_{23}}{\varepsilon_{22}}\frac{k_x}{\omega} \\ &= \frac{k_x}{\omega}\left(\frac{\mu_{32}}{\mu_{22}} - \frac{\varepsilon_{23}}{\varepsilon_{22}}\right), \end{aligned} \tag{2.61}$$

$$r_{13} = \mu_{31} + a_{54}\mu_{32} + a_{24}\left(\rho'_{32} + \frac{k_x}{\omega}\right) = \mu_{31} - \frac{\mu_{21}}{\mu_{22}}\mu_{32} + \frac{1}{\varepsilon_{22}}\frac{\mathrm{i}\gamma}{\omega}\frac{k_x}{\omega}, \tag{2.62}$$

$$r_{14} = \mu_{33} + a_{56}\mu_{32} + a_{26}\left(\rho'_{32} + \frac{k_x}{\omega}\right) = \mu_{33} - \frac{\mu_{23}}{\mu_{22}}\mu_{32} - \frac{1}{\varepsilon_{22}}\frac{k_x}{\omega}\frac{k_x}{\omega}, \tag{2.63}$$

$$\begin{aligned} r_{21} &= -\left\{\rho'_{11} + a_{51}\mu_{12} + a_{21}\left(\rho'_{12} - \frac{\mathrm{i}\gamma}{\omega}\right)\right\} = \frac{\mathrm{i}\gamma}{\omega}\frac{\mu_{12}}{\mu_{22}} - \frac{\varepsilon_{21}}{\varepsilon_{22}}\frac{\mathrm{i}\gamma}{\omega} \\ &= \frac{\mathrm{i}\gamma}{\omega}\left(\frac{\mu_{12}}{\mu_{22}} - \frac{\varepsilon_{21}}{\varepsilon_{22}}\right), \end{aligned} \tag{2.64}$$

$$r_{22} = -\left\{\rho'_{13} + a_{53}\mu_{12} + a_{23}\left(\rho'_{12} - \frac{\mathrm{i}\gamma}{\omega}\right)\right\} = -\frac{k_x}{\omega}\frac{\mu_{12}}{\mu_{22}} - \frac{\varepsilon_{23}}{\varepsilon_{22}}\frac{\mathrm{i}\gamma}{\omega}, \tag{2.65}$$

$$r_{23} = -\left\{\mu_{11} + a_{54}\mu_{12} + a_{24}\left(\rho'_{12} - \frac{\mathrm{i}\gamma}{\omega}\right)\right\} = -\mu_{11} + \frac{\mu_{21}}{\mu_{22}}\mu_{12} + \frac{1}{\varepsilon_{22}}\frac{\mathrm{i}\gamma}{\omega}\frac{\mathrm{i}\gamma}{\omega}, \tag{2.66}$$

$$r_{24} = -\left\{\mu_{13} + a_{56}\mu_{12} + a_{26}\left(\rho'_{12} - \frac{\mathrm{i}\gamma}{\omega}\right)\right\} = -\mu_{13} + \frac{\mu_{23}}{\mu_{22}}\mu_{12} - \frac{1}{\varepsilon_{22}}\frac{k_x}{\omega}\frac{\mathrm{i}\gamma}{\omega}, \tag{2.67}$$

$$r_{31} = -\left\{\varepsilon_{31} + a_{21}\varepsilon_{32} + a_{51}\left(\rho_{32} - \frac{k_x}{\omega}\right)\right\} = -\varepsilon_{31} + \frac{\varepsilon_{21}}{\varepsilon_{22}}\varepsilon_{32} - \frac{1}{\mu_{22}}\frac{\mathrm{i}\gamma}{\omega}\frac{k_x}{\omega}, \tag{2.68}$$

$$r_{32} = -\left\{\varepsilon_{33} + a_{23}\varepsilon_{32} + a_{53}\left(\rho_{32} - \frac{k_x}{\omega}\right)\right\} = -\varepsilon_{33} + \frac{\varepsilon_{23}}{\varepsilon_{22}}\varepsilon_{32} + \frac{1}{\mu_{22}}\frac{k_x}{\omega}\frac{k_x}{\omega}, \tag{2.69}$$

$$r_{33} = -\left\{\rho_{31} + a_{24}\varepsilon_{32} + a_{54}\left(\rho_{32} - \frac{k_x}{\omega}\right)\right\} = -\frac{\mathrm{i}\gamma}{\omega}\frac{\varepsilon_{32}}{\varepsilon_{22}} - \frac{\mu_{21}}{\mu_{22}}\frac{k_x}{\omega}, \tag{2.70}$$

$$\begin{aligned} r_{34} &= -\left\{\rho_{33} + a_{26}\varepsilon_{32} + a_{56}\left(\rho_{32} - \frac{k_x}{\omega}\right)\right\} = \frac{k_x}{\omega}\frac{\varepsilon_{32}}{\varepsilon_{22}} - \frac{\mu_{23}}{\mu_{22}}\frac{k_x}{\omega} \\ &= \frac{k_x}{\omega}\left(\frac{\varepsilon_{32}}{\varepsilon_{22}} - \frac{\mu_{23}}{\mu_{22}}\right), \end{aligned} \tag{2.71}$$

$$r_{41} = \varepsilon_{11} + a_{21}\varepsilon_{12} + a_{51}\left(\rho_{12} + \frac{\mathrm{i}\gamma}{\omega}\right) = \varepsilon_{11} - \frac{\varepsilon_{21}}{\varepsilon_{22}}\varepsilon_{12} - \frac{1}{\mu_{22}}\frac{\mathrm{i}\gamma}{\omega}\frac{\mathrm{i}\gamma}{\omega}, \tag{2.72}$$

$$r_{42} = \varepsilon_{13} + a_{23}\varepsilon_{12} + a_{53}\left(\rho_{12} + \frac{\mathrm{i}\gamma}{\omega}\right) = \varepsilon_{13} - \frac{\varepsilon_{23}}{\varepsilon_{22}}\varepsilon_{12} + \frac{1}{\mu_{22}}\frac{k_x}{\omega}\frac{\mathrm{i}\gamma}{\omega}, \tag{2.73}$$

$$\begin{aligned} r_{43} &= \rho_{11} + a_{24}\varepsilon_{12} + a_{54}\left(\rho_{12} + \frac{\mathrm{i}\gamma}{\omega}\right) = \frac{\mathrm{i}\gamma}{\omega}\frac{\varepsilon_{12}}{\varepsilon_{22}} - \frac{\mu_{21}}{\mu_{22}}\frac{\mathrm{i}\gamma}{\omega} \\ &= \frac{\mathrm{i}\gamma}{\omega}\left(\frac{\varepsilon_{12}}{\varepsilon_{22}} - \frac{\mu_{21}}{\mu_{22}}\right), \end{aligned} \tag{2.74}$$

$$r_{44} = \rho_{13} + a_{26}\varepsilon_{12} + a_{56}\left(\rho_{12} + \frac{\mathrm{i}\gamma}{\omega}\right) = -\frac{k_x}{\omega}\frac{\varepsilon_{12}}{\varepsilon_{22}} - \frac{\mu_{23}}{\mu_{22}}\frac{\mathrm{i}\gamma}{\omega}. \tag{2.75}$$

For biaxial electric and magnetic crystalline properties in a principal axis system, only the diagonal elements of the subtensors of $\mathbf{M}$ survive again [see a'_{ij} in (2.47) and (2.48)], making (2.60)–(2.75) become

$$r_{11} = 0, \quad r_{12} = 0, \quad r_{13} = \frac{1}{\varepsilon_{22}} \frac{\mathrm{i}\gamma}{\omega} \frac{k_x}{\omega}, \quad r_{14} = \mu_{33} - \frac{1}{\varepsilon_{22}} \frac{k_x}{\omega} \frac{k_x}{\omega}; \tag{2.76}$$

$$r_{21} = 0, \quad r_{22} = 0, \quad r_{23} = -\mu_{11} + \frac{1}{\varepsilon_{22}} \frac{\mathrm{i}\gamma}{\omega} \frac{\mathrm{i}\gamma}{\omega}, \quad r_{24} = -\frac{1}{\varepsilon_{22}} \frac{k_x}{\omega} \frac{\mathrm{i}\gamma}{\omega}; \tag{2.77}$$

$$r_{31} = -\frac{1}{\mu_{22}} \frac{\mathrm{i}\gamma}{\omega} \frac{k_x}{\omega}, \quad r_{32} = -\varepsilon_{33} + \frac{1}{\mu_{22}} \frac{k_x}{\omega} \frac{k_x}{\omega}, \quad r_{33} = 0, \quad r_{34} = 0; \tag{2.78}$$

$$r_{41} = \varepsilon_{11} - \frac{1}{\mu_{22}} \frac{\mathrm{i}\gamma}{\omega} \frac{\mathrm{i}\gamma}{\omega}, \quad r_{42} = \frac{1}{\mu_{22}} \frac{k_x}{\omega} \frac{\mathrm{i}\gamma}{\omega}, \quad r_{43} = 0, \quad r_{44} = 0. \tag{2.79}$$

The Green's function problem is posed by placing a Dirac delta forcing function

$$\mathbf{J}_{\mathrm{s}\delta}(x) = (\hat{x} + \hat{z})\delta(x - x') \tag{2.80}$$

on the strip conductor (could be an ordinary metal, a low-temperature superconductor, a medium-temperature MgB_2 superconductor, or a ceramic perovskite high-temperature superconductor HTSC, for example) and solving the partial differential equation system in space subject to appropriate boundary and interfacial conditions. Figure 2.1 shows an example structure with two layers, one interface and one strip conductor (this particular structure will be numerically studied in Sect. 2.1.4). Equation (2.80) says that a surface current of unit delta magnitude is impressed in the x- and z-directions. This is consistent with the strip having width w in the x-direction, infinitesimal extent in

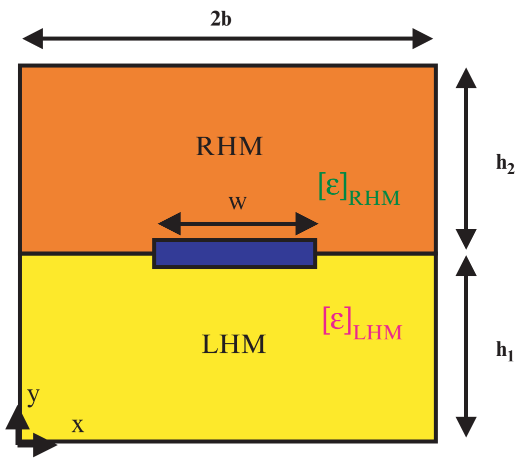

Fig. 2.1. Cross-sectional diagram of the double-layered structure, with the strip sandwiched between the upper RLM and the lower LHM substrate, which is generally a principal axis biaxial LHM crystal for this study. Propagation is perpendicular to the cross-section

the y-direction, and extending infinitely in the z-direction corresponding to a uniform cross-section. Because we have Fourier transformed the problem into the spectral domain, the impressed delta current now appears as

$$\mathbf{J}_{s\delta}(k_x) = (\hat{x} + \hat{z}) \int_{-b}^{b} \delta(x - x')\mathrm{e}^{-\mathrm{i}k_x x'}\mathrm{d}x' = (\hat{x} + \hat{z})\mathrm{e}^{-\mathrm{i}k_x x'}, \tag{2.81}$$

where $2b$ is the finite width of the enclosure bounding the x extent. Of course, the actual current is a continuous superposition of weighted contributions over the strip width,

$$\mathbf{J}_\mathrm{s}(x) = \int_{-w/2}^{w/2} \left[J_{\mathrm{s}x}(x')\hat{x} + J_{\mathrm{s}z}(x')\hat{z}\right] \delta(x - x')\mathrm{d}x = \int_{-w/2}^{w/2} \mathbf{J}_\mathrm{s}(x')\delta(x - x')\mathrm{d}x. \tag{2.82}$$

Here we have used the fact that current exists only on the strip. Equation (2.82) merely states that scanning the extent of the strip (with the delta function) will reproduce the correct current distribution function. Now one can state that (2.3) and (2.19) having assumed a time-harmonic variation, or (2.10) and (2.20) assuming a z-directed propagation constant also, form a complete set of partial differential equations subject to the interfacial conditions

$$\hat{y} \times \left(\mathbf{H}^+ - \mathbf{H}^-\right) = \mathbf{J}_s(x), \tag{2.83}$$

$$\mathbf{E}_\mathrm{t}^+ = \mathbf{E}_\mathrm{t}^- \tag{2.84}$$

and boundary conditions

$$E_y(x, y) = E_z(x, y) = 0, \qquad x = \pm b; \tag{2.85}$$

$$E_x(x, y) = E_z(x, y) = 0, \qquad y = 0, h_\mathrm{T}. \tag{2.86}$$

Equation (2.83), which arose from curl equation (2.3), says that the tangential **H** field above the interface minus that below is related to the surface current at that interface. If we take this interface to be where there are conductor strips, $\mathbf{J}_\mathrm{s}(x) \neq 0$, but at other interfaces without strips, $\mathbf{J}_\mathrm{s}(x) = 0$ and tangential **H** field continuity occurs. Equation (2.84) assures tangential electric field **E** continuity at any interface. Equation (2.85) enables the finite Fourier transform, and (2.86) constrains the device to be fully enclosed with actual (or computational) walls, where h_T is the total vertical structure thickness.

In the Green's function construction, (2.80) is impressed on the system through (2.83) which creates the field solution

$$\bar{\bar{\mathbf{G}}}(x, y; x') = F_\mathrm{L}\left[\delta(x - x')\right]. \tag{2.87}$$

Here the system linear operator F_L takes the delta function $\delta(x - x')$ applied in either the $\hat{x}$ or $\hat{z}$ directions and determines the field component responses, making a two-indexed tensor (dyadic) of size 6×2. Multiply (2.87) on the right by $\mathbf{J}_{\mathrm{s}}(x')$ and integrate, and because F_{L} is a linear operator, the current vector along with the integral operator may be pulled inside it, giving

$$\int_{-b}^{b} \bar{\bar{\mathbf{G}}}(x, y; x') \cdot \mathbf{J}_{\mathrm{s}}(x') \mathrm{d}x' = F_{\mathrm{L}} \left[\int_{-b}^{b} \mathbf{J}_{\mathrm{s}}(x') \delta(x - x') \mathrm{d}x' \right] . \tag{2.88}$$

The left-hand side is the field solution of the problem $\mathbf{F}(x, y)$, and because the argument of the linear operator by (2.82) is the total vector surface current, (2.88) yields

$$\mathbf{F}(x, y) = F_{\mathrm{L}} \left[\mathbf{J}_{\mathrm{s}}(x) \right] . \tag{2.89}$$

Therefore, with knowledge of $\bar{\bar{\mathbf{G}}}(x, y; x')$, the field solution is immediately known,

$$\mathbf{F}(x, y) = \int_{-b}^{b} \bar{\bar{\mathbf{G}}}(x, y; x') \cdot \mathbf{J}_{\mathrm{s}}(x') \mathrm{d}x' . \tag{2.90}$$

Considering $\mathbf{J}_{\mathrm{s}}$ as a form of a field, as well as $\mathbf{F}$ being a field, makes (2.90) an integral equation of the homogeneous Fredholm type of the second kind [15]. Neither $\mathbf{J}_{\mathrm{s}}$ nor $\mathbf{F}$ are known. They must be found by solving (2.90), with the understanding that the kernel $\bar{\bar{\mathbf{G}}}(x, y; x')$ can be acquired before finding the unknowns. Because we will be working in the spectral domain, the integral equation of the problem (2.90) must be converted to this domain also. Before we do this, note that if the delta function sources were anywhere in the cross-section, it would be written as $\delta(\underline{\rho} - \underline{\rho'})$, implying then by extension of (2.87) with it being operated on by F_{L}, that the spatial Green's function will also be a function of $\underline{\rho} - \underline{\rho'}$, where $\underline{\rho} = x\hat{x} + y\hat{y}$. That is,

$$\bar{\bar{\mathbf{G}}}(\underline{\rho} - \underline{\rho'}) = F_{\mathrm{L}}[\delta(\underline{\rho} - \underline{\rho'})]. \tag{2.91}$$

Equation (2.90) would then be written as

$$\mathbf{F}(x, y) = \int_{-b}^{b} \mathrm{d}x' \int_{0}^{h_T} \mathrm{d}y' \bar{\bar{\mathbf{G}}}(\underline{\rho} - \underline{\rho'}) \cdot \mathbf{J}_{\mathrm{s}}(\underline{\rho'}). \tag{2.92}$$

This integral equation is very general and can be solved for any number of interfacial layers with conductor strips. However, because later in the paper we are restricting ourselves to the guiding of waves in a multilayered structure with one interface containing a guiding conductor, it is only the form of (2.92) which is instructive – it is a multidimensional convolution integral. In (2.92) the differential integration element $\rho\, \mathrm{d}\theta\, \mathrm{d}\rho$ was not used in order to explicitly indicate the cross-sectional dimensions. Clearly, as before, the kernel $\bar{\bar{\mathbf{G}}}(\underline{\rho} - \underline{\rho'})$ can be acquired, and (2.92) solved for the unknown fields. However, there are several ways to find the entire field solution, and one effective way, which does not require obtaining the dyadic Green's function over the whole cross-sectional spatial domain, uses the fact that the strip is a perfect conductor with

$$\mathbf{E}_{\mathrm{t}}(x,y) = 0 : |x| < w, \quad y = y_{\mathrm{I}}. \tag{2.93}$$

Here w is the physical width of the strip , and y_{I} its location along the y-axis. A smaller piece of the $\bar{\bar{\mathbf{G}}}$ must be used, $\bar{\bar{\mathbf{G}}}_{EJ}^{xz}$, which relates the driving surface current to the two tangential electric field components. At the $y = y_{\mathrm{I}}$ interface, (2.92) is cast into the form

$$\mathbf{E}(x,y_{\mathrm{I}}) = \int_{-b}^{b} \bar{\bar{\mathbf{G}}}_{EJ}^{xz}(x-x';y_{\mathrm{I}}) \cdot \mathbf{J}_{\mathrm{s}}(x')\mathrm{d}x'. \tag{2.94}$$

Forms (2.92) and (2.94) of the integral equation are convolution integrals of the kernel and the driving surface current. They both have the wonderful property that transformation into the spectral domain for, respectively, 2D and 1D removes the integral operation. The solution procedure employed requires us to take a finite Fourier transform of (2.94),

$$\begin{aligned}
\int_{-b}^{b} \mathbf{E}(x)\mathrm{e}^{-\mathrm{i}k_x x}\mathrm{d}x &= \int_{-b}^{b} \mathrm{e}^{-\mathrm{i}k_x x}\mathrm{d}x \left\{ \int_{-b}^{b} \bar{\bar{\mathbf{G}}}_{EJ}^{xz}(x-x') \cdot \mathbf{J}_{\mathrm{s}}(x')\mathrm{d}x' \right\} \\
&= \int_{-b}^{b} \left\{ \int_{-b}^{b} \bar{\bar{\mathbf{G}}}_{EJ}^{xz}(x-x')\mathrm{e}^{-\mathrm{i}k_x x}\mathrm{d}x \right\} \cdot \mathbf{J}_{\mathrm{s}}(x')\mathrm{d}x' \\
&= \int_{-b}^{b} \left\{ \int_{-b}^{b} \bar{\bar{\mathbf{G}}}_{EJ}^{xz}(x'')\mathrm{e}^{-\mathrm{i}k_x (x'+x'')}\mathrm{d}x'' \right\} \cdot \mathbf{J}_{\mathrm{s}}(x')\mathrm{d}x' \\
&= \int_{-b}^{b} \left\{ \int_{-b}^{b} \bar{\bar{\mathbf{G}}}_{EJ}^{xz}(x'')\mathrm{e}^{-\mathrm{i}k_x x''}\mathrm{d}x'' \right\} \cdot \mathbf{J}_{\mathrm{s}}(x')\mathrm{e}^{-\mathrm{i}k_x x'}\mathrm{d}x' \\
&= \left\{ \int_{-b}^{b} \bar{\bar{\mathbf{G}}}_{EJ}^{xz}(x'')\mathrm{e}^{-\mathrm{i}k_x x''}\mathrm{d}x'' \right\} \cdot \left\{ \int_{-b}^{b} \mathbf{J}_{\mathrm{s}}(x')\mathrm{e}^{-\mathrm{i}k_x x'}\mathrm{d}x' \right\} \\
&= \bar{\bar{\mathbf{G}}}_{EJ}^{xz}(k_x) \cdot \mathbf{J}_{\mathrm{s}}(k_x)
\end{aligned} \tag{2.95}$$

or

$$\mathbf{E}(k_x) = \bar{\bar{\mathbf{G}}}_{EJ}^{xz}(k_x) \cdot \mathbf{J}_{\mathrm{s}}(k_x). \tag{2.96}$$

In (2.95) $x'' = x - x'$, $\mathrm{d}x'' = \mathrm{d}x$, led to the third step, and (2.13) to the final step. $\bar{\bar{\mathbf{G}}}^{xz}_{EJ}$ is given by [16]

$$\tilde{G}_{xx}(k_x, \gamma) = \frac{P^{(1)}_{13}\left[P^{(21)}_{24}P^{(2)}_{14} - P^{(21)}_{14}P^{(2)}_{24}\right]}{P^{(21)}_{14}P^{(21)}_{23} - P^{(21)}_{13}P^{(21)}_{24}} + \frac{P^{(1)}_{14}\left[P^{(21)}_{13}P^{(2)}_{24} - P^{(21)}_{23}P^{(2)}_{14}\right]}{P^{(21)}_{14}P^{(21)}_{23} - P^{(21)}_{13}P^{(21)}_{24}}, \tag{2.97}$$

$$\tilde{G}_{xz}(k_x, \gamma) = \frac{P^{(1)}_{13}\left[P^{(21)}_{24}P^{(2)}_{13} - P^{(21)}_{14}P^{(2)}_{23}\right]}{P^{(21)}_{14}P^{(21)}_{23} - P^{(21)}_{13}P^{(21)}_{24}} - \frac{P^{(1)}_{14}\left[P^{(21)}_{13}P^{(2)}_{23} - P^{(21)}_{23}P^{(2)}_{13}\right]}{P^{(21)}_{14}P^{(21)}_{23} - P^{(21)}_{13}P^{(21)}_{24}}, \tag{2.98}$$

$$\tilde{G}_{zx}(k_x, \gamma) = \frac{P^{(1)}_{23}\left[P^{(21)}_{24}P^{(2)}_{14} - P^{(21)}_{14}P^{(2)}_{24}\right]}{P^{(21)}_{14}P^{(21)}_{23} - P^{(21)}_{13}P^{(21)}_{24}} + \frac{P^{(1)}_{24}\left[P^{(21)}_{13}P^{(2)}_{24} - P^{(21)}_{23}P^{(2)}_{14}\right]}{P^{(21)}_{14}P^{(21)}_{23} - P^{(21)}_{13}P^{(21)}_{24}}, \tag{2.99}$$

$$\tilde{G}_{zz}(k_x, \gamma) = \frac{P^{(1)}_{23}\left[P^{(21)}_{24}P^{(2)}_{13} - P^{(21)}_{14}P^{(2)}_{23}\right]}{P^{(21)}_{14}P^{(21)}_{23} - P^{(21)}_{13}P^{(21)}_{24}} - \frac{P^{(1)}_{24}\left[P^{(21)}_{13}P^{(2)}_{23} - P^{(21)}_{23}P^{(2)}_{13}\right]}{P^{(21)}_{14}P^{(21)}_{23} - P^{(21)}_{13}P^{(21)}_{24}} \tag{2.100}$$

with

$$P^{(1)} = P^{(1)}(h_1), \quad P^{(2)} = P^{(2)}(h_2), \quad P^{(21)} = P^{(2)}(h_2)P^{(1)}(h_1), \tag{2.101}$$

$$P(y) = \mathrm{e}^{\mathrm{i}\omega\mathbf{R}y}, \tag{2.102}$$

where h_i is the thickness of the ith layer. Note that $\mathbf{R}$ is the same matrix operator first introduced in (2.53), governing the field behavior variation in the y direction. It contains both the physical properties of the LHM (or RHM) and the electromagnetic field equations.

2.1.3 Determination of the Eigenvalues and Eigenvectors for LHM or DNM

Formulas (2.97)–(2.100) were found utilizing (2.53) which has a solution in the ith layer of

$$\aleph_i = \aleph(y_i) = P^{(i)}(y_i)\aleph_i(h_{\mathrm{T}i}) \tag{2.103}$$

using the global y coordinate. It is very convenient to convert to the local coordinates y' where for the ith layer now the local coordinate ($h_0 \equiv 0$) is

$$y'_i = y_i - h_{\mathrm{T}i}\ ;\ h_{\mathrm{T}i} = \sum_{k=0}^{i-1} h_k \tag{2.104}$$

with $\mathrm{h}_{\mathrm{T}i}$ being the total thickness of all the layers prior to the ith layer. In the local coordinate system, (2.103) appears as

$$\aleph_i = \aleph(y'_i) = P^{(i)}(y'_i)\aleph_i(0). \tag{2.105}$$

This equation is applied repeatedly to each layer throughout the structure, being careful to impose (2.83)–(2.86) in the spectral domain:

$$\hat{y} \times \left[\mathbf{H}^+(k_x, y) - \mathbf{H}^-(k_x, y)\right] = \mathbf{J}_\mathrm{s}(k_x), \quad y = y_\mathrm{I}; \tag{2.106}$$

$$\mathbf{E}_\mathrm{t}^+(k_x, y) = \mathbf{E}_\mathrm{t}^-(k_x, y), \quad y = h_i + h_{\mathrm{T}i} = \sum_{k=0}^{i} h_k \tag{2.107}$$

and boundary conditions

$$E_x(k_x, y) = E_z(k_x, y) = 0, \quad y = 0, h_\mathrm{T}. \tag{2.108}$$

Boundary condition on the side walls (2.85) get converted to the spectral domain in a process which generates the discretization of k_x. The detailed derivation will be given since the whole technique hinges on it.

By (2.14), the spatial electric field components $E_{y,z}$ are expressed as

$$E_{y,z}(x, y) = \frac{1}{2b} \sum_{k_x=-\infty}^{\infty} E_{y,z}(k_x, y)\mathrm{e}^{\mathrm{i}k_x x}. \tag{2.109}$$

Consider first the case where $E_{y,z}(x, y)$ has even symmetry with respect to the x-axis. (Symmetry choices will be covered in more detail after the derivation of the discretization k_x values.) For even symmetry,

$$E_{y,z}(x, y) = E_{y,z}(-x, y). \tag{2.110}$$

Invoking (2.109), this becomes

$$\begin{aligned} \frac{1}{2b} \sum_{k_x=-\infty}^{\infty} E_{y,z}(k_x, y)\mathrm{e}^{\mathrm{i}k_x x} &= \frac{1}{2b} \sum_{k_x=-\infty}^{\infty} E_{y,z}(k_x, y)\mathrm{e}^{-\mathrm{i}k_x x} \\ &= \frac{1}{2b} \sum_{k_x=+\infty}^{-\infty} E_{y,z}(-k_x, y)\mathrm{e}^{\mathrm{i}k_x x}, \end{aligned} \tag{2.111}$$

$$\frac{1}{2b} \sum_{k_x=-\infty}^{\infty} [E_{y,z}(k_x, y) - E_{y,z}(-k_x, y)]\mathrm{e}^{\mathrm{i}k_x x} = 0. \tag{2.112}$$

Equation (2.112) is true for any x if the bracketed term is zero, namely that

$$E_{y,z}(k_x, y) = E_{y,z}(-k_x, y). \tag{2.113}$$

Now we must insert this back into the expansion (2.109), obtaining

$$
\begin{aligned}
&E_{y,z}(x,y) \\
&\quad = \frac{1}{2b}\sum_{k_x=-\infty}^{\infty} E_{y,z}(k_x,y)\mathrm{e}^{\mathrm{i}k_x x} \\
&\quad = \frac{1}{2b}\sum_{k_x=-\infty}^{0^-} E_{y,z}(k_x,y)\mathrm{e}^{\mathrm{i}k_x x} + E_{y,z}(0,y) + \frac{1}{2b}\sum_{k_x=0^+}^{\infty} E_{y,z}(k_x,y)\mathrm{e}^{\mathrm{i}k_x x} \\
&\quad = \frac{1}{2b}\sum_{k_x=+\infty}^{0^+} E_{y,z}(-k_x,y)\mathrm{e}^{-\mathrm{i}k_x x} + E_{y,z}(0,y) + \frac{1}{2b}\sum_{k_x=0^+}^{\infty} E_{y,z}(k_x,y)\mathrm{e}^{\mathrm{i}k_x x} \\
&\quad = \frac{1}{2b}\sum_{k_x=0^+}^{\infty} E_{y,z}(k_x,y)\mathrm{e}^{-\mathrm{i}k_x x} + E_{y,z}(0,y) + \frac{1}{2b}\sum_{k_x=0^+}^{\infty} E_{y,z}(k_x,y)\mathrm{e}^{\mathrm{i}k_x x} \\
&\quad = \frac{1}{2b}\sum_{k_x=0^+}^{\infty} E_{y,z}(k_x,y)\left[\mathrm{e}^{-\mathrm{i}k_x x} + \mathrm{e}^{\mathrm{i}k_x x}\right] + E_{y,z}(0,y) \\
&\quad = \frac{1}{b}\sum_{k_x=0^+}^{\infty} E_{y,z}(k_x,y)\cos(k_x x) + E_{y,z}(0,y).
\end{aligned}
\tag{2.114}
$$

In (2.114), (2.113) was used for the third step. Imposition of boundary condition (2.85) forces (2.114) to obey

$$\frac{1}{b}\sum_{k_x=0^+}^{\infty} E_{y,z}(k_x,y)\cos(k_x x) + E_{y,z}(0,y) = 0 \tag{2.115}$$

or

$$\cos(k_x b) = 0, \quad E_{y,z}(0,y) = 0. \tag{2.116}$$

The first constraint in (2.116) restricts k_x to

$$k_x = \frac{2n-1}{2b}\pi, \quad n = 0, \pm 1, \pm 2, \ldots \tag{2.117}$$

showing that $k_x \neq 0$, allowing us to drop the second (2.116) constraint. For odd symmetry,

$$E_{y,z}(x,y) = -E_{y,z}(-x,y). \tag{2.118}$$

Invoking (2.109), this becomes

$$
\begin{aligned}
\frac{1}{2b}\sum_{k_x=-\infty}^{\infty} E_{y,z}(k_x,y)\mathrm{e}^{\mathrm{i}k_x x} &= -\frac{1}{2b}\sum_{k_x=-\infty}^{\infty} E_{y,z}(k_x,y)\mathrm{e}^{-\mathrm{i}k_x x} \\
&= -\frac{1}{2b}\sum_{k_x=+\infty}^{-\infty} E_{y,z}(-k_x,y)\mathrm{e}^{\mathrm{i}k_x x},
\end{aligned}
\tag{2.119}
$$

$$\frac{1}{2b}\sum_{k_x=-\infty}^{\infty}[E_{y,z}(k_x,y)+E_{y,z}(-k_x,y)]\mathrm{e}^{\mathrm{i}k_x x}=0. \tag{2.120}$$

Equation (2.112) is true for any x if the bracketed term is zero, namely that

$$E_{y,z}(k_x,y)=-E_{y,z}(-k_x,y). \tag{2.121}$$

Now we must insert this back into the expansion (2.109), obtaining

$$\begin{aligned}
&E_{y,z}(x,y)\\
&=\frac{1}{2b}\sum_{k_x=-\infty}^{\infty}E_{y,z}(k_x,y)\mathrm{e}^{\mathrm{i}k_x x}\\
&=\frac{1}{2b}\sum_{k_x=-\infty}^{0^-}E_{y,z}(k_x,y)\mathrm{e}^{\mathrm{i}k_x x}+E_{y,z}(0,y)+\frac{1}{2b}\sum_{k_x=0^+}^{\infty}E_{y,z}(k_x,y)\mathrm{e}^{\mathrm{i}k_x x}\\
&=\frac{1}{2b}\sum_{k_x=+\infty}^{0^+}E_{y,z}(-k_x,y)\mathrm{e}^{-\mathrm{i}k_x x}+E_{y,z}(0,y)+\frac{1}{2b}\sum_{k_x=0^+}^{\infty}E_{y,z}(k_x,y)\mathrm{e}^{\mathrm{i}k_x x}\\
&=-\frac{1}{2b}\sum_{k_x=0^+}^{\infty}E_{y,z}(k_x,y)\mathrm{e}^{-\mathrm{i}k_x x}+E_{y,z}(0,y)+\frac{1}{2b}\sum_{k_x=0^+}^{\infty}E_{y,z}(k_x,y)\mathrm{e}^{\mathrm{i}k_x x}\\
&=\frac{1}{2b}\sum_{k_x=0^+}^{\infty}E_{y,z}(k_x,y)\left[-\mathrm{e}^{-\mathrm{i}k_x x}+\mathrm{e}^{\mathrm{i}k_x x}\right]+E_{y,z}(0,y)\\
&=\frac{\mathrm{i}}{b}\sum_{k_x=0^+}^{\infty}E_{y,z}(k_x,y)\sin(k_x x)+E_{y,z}(0,y).
\end{aligned} \tag{2.122}$$

In (2.122), (2.121) was used in the third step. Imposition of boundary condition (2.85) forces (2.122) to obey

$$\pm\frac{\mathrm{i}}{b}\sum_{k_x=0^+}^{\infty}E_{y,z}(k_x,y)\sin(k_x b)+E_{y,z}(0,y)=0 \tag{2.123}$$

or

$$\sin(k_x b)=0,\quad E_{y,z}(0,y)=0. \tag{2.124}$$

The first constraint in (2.124) restricts k_x to

$$k_x=\frac{n}{b}\pi,\quad n=0,\pm1,\pm2,\dots. \tag{2.125}$$

Since the first constraint allows $k_x=0$, technically the first summation in (2.123) does not have $n=0$ in its domain, but by widening its domain to cover $k_x = 0$, the second constraint may be dropped. That is, (2.123) becomes

$$\pm\frac{\mathrm{i}}{b}\sum_{k_x=0}^{\infty} E_{y,z}(k_x, y)\sin(k_x b) = 0 \tag{2.126}$$

and rule (2.125) is exact.

Next we treat the origin of the symmetry choices. Go to the harmonic equations (2.3), using $\nabla\times\mathbf{F} = \varepsilon^{ijk}\nabla_i E_j \hat{x}_k$ to expand them out by components for the doubly biaxial case (biaxial for $\bar{\bar{\varepsilon}}$ and $\bar{\bar{\mu}}$ with principal axes in the coordinate directions), find

$$\frac{\partial H_z}{\partial y} - \frac{\partial H_y}{\partial z} = \mathrm{i}\omega\varepsilon_{xx}E_x + J_x, \quad \frac{\partial H_x}{\partial z} - \frac{\partial H_z}{\partial x} = \mathrm{i}\omega\varepsilon_{yy}E_y,$$
$$\frac{\partial H_y}{\partial x} - \frac{\partial H_x}{\partial y} = \mathrm{i}\omega\varepsilon_{zz}E_z + J_z; \tag{2.127}$$

$$\frac{\partial E_z}{\partial y} - \frac{\partial E_y}{\partial z} = -\mathrm{i}\omega\mu_{xx}H_x, \quad \frac{\partial E_x}{\partial z} - \frac{\partial E_z}{\partial x} = -\mathrm{i}\omega\mu_{yy}H_y,$$
$$\frac{\partial E_y}{\partial x} - \frac{\partial E_x}{\partial y} = -\mathrm{i}\omega\mu_{zz}H_z. \tag{2.128}$$

Setting $J_z(x, y)$ even for the impressed current, we find that (2.127) requires that $E_z(x, y)$ is even, $H_y(x, y)$ is odd, and $H_x(x, y)$ is even in its third equation; $H_z(x, y)$ is odd and $E_y(x, y)$ is even in its second equation; and $E_x(x, y)$ is odd and $J_x(x, y)$ is odd in its first equation. These selections are consistent with (2.128). For $J_z(x, y)$ odd, all of the selections are reversed. To see that great care must be exercised in this process, look at the ferrite spin system which for principal axes (defined by three orthogonal bias fields) in the three coordinate directions, $\bar{\bar{\mu}}$ is given by [17] (see also [18] for a magnetized semiconductor with similar permittivity tensor)

$$\bar{\bar{\mu}}(H_0\hat{x}) = \begin{bmatrix} \mu_\mathrm{e} & 0 & 0 \\ 0 & \mu & -\mathrm{i}\kappa \\ 0 & \mathrm{i}\kappa & \mu \end{bmatrix}, \quad \bar{\bar{\mu}}(H_0\hat{y}) = \begin{bmatrix} \mu & 0 & \mathrm{i}\kappa \\ 0 & \mu_\mathrm{e} & 0 \\ -\mathrm{i}\kappa & 0 & \mu \end{bmatrix}, \quad \bar{\bar{\mu}}(H_0\hat{z}) = \begin{bmatrix} \mu & -\mathrm{i}\kappa & 0 \\ \mathrm{i}\kappa & \mu & 0 \\ 0 & 0 & \mu_\mathrm{e} \end{bmatrix}. \tag{2.129}$$

Now for (2.3) with the static bias field $\mathrm{H}_0\hat{x}$ in (2.129), (2.127) is still valid for the permittivity biaxial, but (2.128) is changed to

$$\frac{\partial E_z}{\partial y} - \frac{\partial E_y}{\partial z} = -\mathrm{i}\omega\mu_\mathrm{e}H_x, \quad \frac{\partial E_x}{\partial z} - \frac{\partial E_z}{\partial x} = -\mathrm{i}\omega\mu H_y - \kappa H_z,$$
$$\frac{\partial E_z}{\partial y} - \frac{\partial E_y}{\partial z} = -\mathrm{i}\omega\mu H_z - \kappa H_y. \tag{2.130}$$

Again imposing $J_z(x, y)$ even, the same results are obviously seen from (2.127) for the electrically biaxial ferrite case, with these selections being now consistent also with (2.130). With the bias field being $H_0\hat{y}$, (2.128) changes to

$$\frac{\partial E_z}{\partial y}-\frac{\partial E_y}{\partial z}=-\mathrm{i}\omega\mu H_x-\kappa H_z,\quad \frac{\partial E_x}{\partial z}-\frac{\partial E_z}{\partial x}=-\mathrm{i}\omega\mu_{\mathrm{e}}H_y,$$
$$\frac{\partial E_z}{\partial y}-\frac{\partial E_y}{\partial z}=-\mathrm{i}\omega\mu H_z-\kappa H_x. \tag{2.131}$$

Utilizing the choices found from (2.127) for $J_z(x,y)$ even makes (2.131) symmetry wise inconsistent, as can be easily verified by inspection. This means that for the $H_0\hat{y}$ bias case, all of the fields must be a superposition of both symmetries. Finally for the third tensor permeability in (2.129), (2.128) changes to

$$\frac{\partial E_z}{\partial y}-\frac{\partial E_y}{\partial z}=-\mathrm{i}\omega\mu H_x-\kappa H_y,\quad \frac{\partial E_x}{\partial z}-\frac{\partial E_z}{\partial x}=-\mathrm{i}\omega\mu H_y-\kappa H_x,$$
$$\frac{\partial E_z}{\partial y}-\frac{\partial E_y}{\partial z}=-\mathrm{i}\omega\mu_{\mathrm{e}} H_z. \tag{2.132}$$

This last case for $H_0\hat{z}$ bias also has the symmetry inconsistency between (2.127) and curl equation (2.132) with the magnetic constitutive information, requiring all fields to be a superposition of both symmetry types.

The surface currents which drive the problem self-consistently, can be chosen in a number of ways, it only being necessary to prepare complete sets of basis functions which are used to construct them. They are selected in the real space domain to display some advantageous property, for example, edge singularity behavior due to charge repulsion. For the complete set of cosinusoidal basis functions modified by the edge condition, we have for a strip with even mode symmetry (determined by the z-component symmetry as just discussed above)

$$J_{zm}(x)=\xi_{\mathrm{em}}(x)=\begin{cases}\dfrac{\cos\left(\pi\dfrac{x}{w}[m-1]\right)}{\sqrt{1-(x/w)^2}}, & |x|\le w\\ 0, & w<|x|\end{cases} \tag{2.133}$$

$$J_{xm}(x)=\eta_{\mathrm{em}}(x)=\begin{cases}\dfrac{\sin\left(\pi\dfrac{x}{w}m\right)}{\sqrt{1-(x/w)^2}}, & |x|\le w\\ 0, & w<|x|\end{cases} \tag{2.134}$$

and for odd mode symmetry,

$$J_{zm}(x)=\xi_{\mathrm{om}}(x)=\begin{cases}\dfrac{\sin\left(\dfrac{\pi}{2}\dfrac{x}{w}[2m-1]\right)}{\sqrt{1-(x/w)^2}}, & |x|\le w\\ 0, & w<|x|\end{cases} \tag{2.135}$$

$$J_{xm}(x)=\eta_{\mathrm{om}}(x)=\begin{cases}\dfrac{\cos\left(\dfrac{\pi}{2}\dfrac{x}{w}[2m-1]\right)}{\sqrt{1-(x/w)^2}}, & |x|\le w\\ 0, & w<|x|\end{cases}. \tag{2.136}$$

Superposition of the complete set forms the total surface current (and constitutes the moment method when unknown currents/fields are expanded using basis sets and then inner products with weights are then taken on the structure governing equation to derive a linear system to be solved).

$$J_{xe}(x) = \sum_{m=1}^{n_x} a_{em}\eta_{em}(x), \quad J_{ze}(x) = \sum_{m=1}^{n_z} b_{em}\xi_{em}(x); \tag{2.137}$$

$$J_{xo}(x) = \sum_{m=1}^{n_x} a_{om}\eta_{om}(x), \quad J_{zo}(x) = \sum_{m=1}^{n_z} b_{om}\xi_{om}(x). \tag{2.138}$$

Fourier transforming (2.137) and (2.138) according to (2.13) gives

$$J_{xe}(n) = \sum_{m=1}^{n_x} a_{em}\eta_{em}(n), \quad J_{ze}(n) = \sum_{m=1}^{n_z} b_{em}\xi_{em}(n); \tag{2.139}$$

$$J_{xo}(n) = \sum_{m=1}^{n_x} a_{om}\eta_{om}(n), \quad J_{zo}(n) = \sum_{m=1}^{n_z} b_{om}\xi_{om}(n) \tag{2.140}$$

with

$$\xi_{em}(n) = \xi_{em}(k_x[n]) = \frac{\pi w}{2}\{J_0(k_x w+[m-1]\pi)+J_0(k_x w-[m-1]\pi)\}, \tag{2.141}$$

$$\eta_{em}(n) = \eta_{em}(k_x[n]) = -\frac{i\pi w}{2}\{J_0(k_x w + m\pi) - J_0(k_x w - m\pi)\}, \tag{2.142}$$

$$\begin{aligned}\xi_{om}(n) &= \xi_{om}(k_x[n]) \\ &= -\frac{i\pi w}{2}\left\{J_0\left(k_x w + [2m-1]\frac{\pi}{2}\right) - J_0\left(k_x w - [2m-1]\frac{\pi}{2}\right)\right\},\end{aligned} \tag{2.143}$$

$$\begin{aligned}\eta_{om}(n) &= \eta_{om}(k_x[n]) \\ &= \frac{\pi w}{2}\left\{J_0\left(k_x w + [2m-1]\frac{\pi}{2}\right) + J_0\left(k_x w - [2m-1]\frac{\pi}{2}\right)\right\}.\end{aligned} \tag{2.144}$$

An exact solution is obtained only when n_x and $n_z \to \infty$. However, a finite number of them may be used, depending on the propagating eigenmode modeled, to find a reasonably accurate numerical result. In (2.141)–(2.144), J_0 denotes the Bessel function of the first kind.

Eigenvalues γ and eigenvectors of the propagating problem can now be found from (2.96), the interfacial strip equation (drop all interfacial indexes and use subscripts to label elements),

$$\begin{aligned}E_x(n,\gamma) &= G_{xx}(\gamma,n)J_x(n,\gamma) + G_{xz}(\gamma,n)J_z(n,\gamma), \\ E_z(n,\gamma) &= G_{zx}(\gamma,n)J_x(n,\gamma) + G_{zz}(\gamma,n)J_z(n,\gamma)\end{aligned} \tag{2.145}$$

by substituting for the surface currents using expressions (2.139) or (2.140) depending upon the mode symmetry to be studied. (We drop the explicit mode symmetry type notation since we will only treat one or the other type of pure symmetry solution here.)

$$
\begin{aligned}
E_x(n,\gamma) &= G_{xx}(\gamma,n)\sum_{i=1}^{n_x} a_i\eta_i(n) + G_{xz}(\gamma,n)\sum_{i=1}^{n_z} b_i\xi_i(n),\\
E_z(n,\gamma) &= G_{zx}(\gamma,n)\sum_{i=1}^{n_x} a_i\eta_i(n) + G_{zz}(\gamma,n)\sum_{i=1}^{n_z} b_i\xi_i(n).
\end{aligned}
\tag{2.146}
$$

Next multiply the first equation of (2.146) by η_j and the second by ξ_j, then summing over the spectral index n (this is the inner product part of the moment method)

$$
\begin{aligned}
\sum_{n=-\infty}^{\infty}\eta_j(n)E_x(n,\gamma) &= \sum_{n=-\infty}^{\infty}\left[\eta_j(n)G_{xx}(\gamma,n)\sum_{i=1}^{n_x} a_i(n)\eta_i(n)\right]\\
&\quad+\sum_{n=-\infty}^{\infty}\left[\eta_j(n)G_{xz}(\gamma,n)\sum_{i=1}^{n_z} b_i(n)\xi_i(n)\right],\\
\sum_{n=-\infty}^{\infty}\xi_j(n)E_z(n,\gamma) &= \sum_{n=-\infty}^{\infty}\left[\xi_j(n)G_{zx}(\gamma,n)\sum_{i=1}^{n_x} a_i(n)\eta_i(n)\right]\\
&\quad+\sum_{n=-\infty}^{\infty}\left[\xi_j(n)G_{zz}(\gamma,n)\sum_{i=1}^{n_z} b_i(n)\xi_i(n)\right].
\end{aligned}
\tag{2.147}
$$

Interchanging the order of the basis function and spectral summations in (2.147),

$$
\begin{aligned}
\sum_{n=-\infty}^{\infty}\eta_j(n)E_x(n,\gamma) &= \sum_{i=1}^{n_x} a_i(n)\left[\sum_{n=-\infty}^{\infty}\eta_j(n)G_{xx}(\gamma,n)\eta_i(n)\right]\\
&\quad+\sum_{i=1}^{n_z} b_i(n)\left[\sum_{n=-\infty}^{\infty}\eta_j(n)G_{xz}(\gamma,n)\xi_i(n)\right],\\
\sum_{n=-\infty}^{\infty}\xi_j(n)E_z(n,\gamma) &= \sum_{i=1}^{n_x} a_i(n)\left[\sum_{n=-\infty}^{\infty}\xi_j(n)G_{zx}(\gamma,n)\eta_i(n)\right]\\
&\quad+\sum_{i=1}^{n_z} b_i(n)\left[\sum_{n=-\infty}^{\infty}\xi_j(n)G_{zz}(\gamma,n)\xi_i(n)\right].
\end{aligned}
\tag{2.148}
$$

Examine the left-hand sides of this paired set of equations (2.148):

$$\begin{aligned}
&\begin{bmatrix} -1 & 1 \\ 1 & -1 \end{bmatrix} \sum_{n=-\infty}^{\infty} \begin{Bmatrix} \eta_{e,o;j} \\ \xi_{e,o;j} \end{Bmatrix} (n) E_{x,z}(n,\gamma) \\
&\quad = \sum_{n=-\infty}^{\infty} \begin{Bmatrix} \eta_j^* \\ \xi_j^* \end{Bmatrix} (n) E_{x,z}(n,\gamma) \\
&\quad = \sum_{n=-\infty}^{\infty} \left[\int_{-b}^{b} \begin{Bmatrix} \eta_j \\ \xi_j \end{Bmatrix} (x) \mathrm{e}^{-\mathrm{i}k_x x} \mathrm{d}x \right]^* E_{x,z}(n,\gamma) \\
&\quad = \sum_{n=-\infty}^{\infty} \int_{-b}^{b} \begin{Bmatrix} \eta_j^* \\ \xi_j^* \end{Bmatrix} (x) \mathrm{e}^{\mathrm{i}k_x x} \mathrm{d}x \, E_{x,z}(n,\gamma) \\
&\quad = \sum_{n=-\infty}^{\infty} \int_{-b}^{b} \begin{Bmatrix} \eta_j \\ \xi_j \end{Bmatrix} (x) \mathrm{e}^{\mathrm{i}k_x x} \mathrm{d}x \, E_{x,z}(n,\gamma) \\
&\quad = \int_{-b}^{b} \begin{Bmatrix} \eta_j \\ \xi_j \end{Bmatrix} (x) \left[\sum_{n=-\infty}^{\infty} E_{x,z}(n,\gamma) \mathrm{e}^{\mathrm{i}k_x x} \right] \mathrm{d}x \\
&\quad = 2b \int_{-b}^{b} \begin{Bmatrix} \eta_j \\ \xi_j \end{Bmatrix} (x) E_{x,z}(x,\gamma) \mathrm{d}x \\
&\quad = 0,
\end{aligned} \tag{2.149}$$

where the first and second rows in the left-hand side matrix corresponds, respectively, to even and odd symmetry. Right-hand equalities in the first, second, fourth, sixth, and last lines used, respectively, (2.141)–(2.144), (2.13), (2.133)–(2.136), (2.14), and (2.92) with (2.133)–(2.136). Equation (2.149) amounts to a Parseval theorem [19] for the problem at hand. Enlisting this theorem, (2.148) can be rewritten as

$$\begin{aligned}
&\sum_{i=1}^{n_x} a_i(n) \left[\sum_{n=-\infty}^{\infty} \eta_j(n) G_{xx}(\gamma,n) \eta_i(n) \right] + \sum_{i=1}^{n_z} b_i(n) \left[\sum_{n=-\infty}^{\infty} \eta_j(n) G_{xz}(\gamma,n) \xi_i(n) \right] = 0, \\
&\sum_{i=1}^{n_x} a_i(n) \left[\sum_{n=-\infty}^{\infty} \xi_j(n) G_{zx}(\gamma,n) \eta_i(n) \right] + \sum_{i=1}^{n_z} b_i(n) \left[\sum_{n=-\infty}^{\infty} \xi_j(n) G_{zz}(\gamma,n) \xi_i(n) \right] = 0.
\end{aligned} \tag{2.150}$$

Since (2.150) is true for any jth basis test function, it may be condensed into the form

$$\begin{aligned}
&\sum_{i=1}^{n_x} a_i(n) X_{xx}^{ji}(\gamma) + \sum_{i=1}^{n_z} b_i(n) X_{xz}^{ji}(\gamma) = 0, \quad j = 1,2,\ldots n_x, \\
&\sum_{i=1}^{n_x} a_i(n) X_{zx}^{ji}(\gamma) + \sum_{i=1}^{n_z} b_i(n) X_{zz}^{ji}(\gamma) = 0, \quad j = 1,2,\ldots n_z,
\end{aligned} \tag{2.151}$$

where (this is referred to as the Galerkin technique since $\{\eta_i, \xi_i\} = \{\eta_j, \xi_j\}$)

$$\begin{aligned} X_{xx}^{ji}(\gamma) &= \sum_{n=-\infty}^{\infty} \eta_j(n) G_{xx}(\gamma, n) \eta_i(n), \\ X_{xz}^{ji}(\gamma) &= \sum_{n=-\infty}^{\infty} \eta_j(n) G_{xz}(\gamma, n) \xi_i(n), \\ X_{zx}^{ji}(\gamma) &= \sum_{n=-\infty}^{\infty} \xi_j(n) G_{zx}(\gamma, n) \eta_i(n), \\ X_{zz}^{ji}(\gamma) &= \sum_{n=-\infty}^{\infty} \xi_j(n) G_{zz}(\gamma, n) \xi_i(n). \end{aligned} \tag{2.152}$$

In matrix form, (2.151) appears as

$$\begin{aligned} \begin{bmatrix} X_{xx} & X_{xz} \\ X_{zx} & X_{zz} \end{bmatrix} \begin{bmatrix} a \\ b \end{bmatrix} = 0, \quad \mathbf{X} \begin{bmatrix} a \\ b \end{bmatrix} = 0, \quad \mathbf{X}\mathbf{v} = 0; \\ \mathbf{X} = \begin{bmatrix} X_{xx} & X_{xz} \\ X_{zx} & X_{zz} \end{bmatrix}, \quad \mathbf{v} = \begin{bmatrix} a \\ b \end{bmatrix}. \end{aligned} \tag{2.153}$$

Once system of equations (2.153) is solved, vector $\mathbf{v}$ containing the coefficients needed to construct the surface current, and from them the electromagnetic field, is known, which is the problem eigenvector. The eigenvalue, γ, is determined from this system also (from the determinant of $\mathbf{X}$ being set to zero). From (2.137) and (2.138), the total vector surface current is obtained. Defining $\alpha_n = k_x(n)$,

$$\mathbf{J}(x, y) = \frac{1}{2b} \sum_{n=-n_{\max}}^{n_{\max}} \mathbf{J}(n; y) \mathrm{e}^{\mathrm{i}\alpha_n x}. \tag{2.154}$$

Once the total surface current is available, the total eigenvector field solution follows from $\bar{\bar{\mathbf{G}}}(\rho - \rho')$ in (2.92) [12],

$$\mathbf{E}(x, y) = \frac{1}{2b} \sum_{n=-n_{\max}}^{n_{\max}} \mathbf{E}(n; y) \mathrm{e}^{\mathrm{i}\alpha_n x}, \quad \mathbf{H}(x, y) = \frac{1}{2b} \sum_{n=-n_{\max}}^{n_{\max}} \mathbf{H}(n; y) \mathrm{e}^{\mathrm{i}\alpha_n x}. \tag{2.155}$$

Spectral expansion is truncated at the same maximum number of terms $n = n_{\max}$ for all vector components. Basis function summation limits n_x and n_z for the x and z components ($m = m_{\max}$) [see (2.139) and (2.140) for the surface current expansion] can be truncated at different values. Current and fields are real physical quantities, so they must be converted through

$$\begin{aligned} \mathbf{J}_{\mathrm{p}}(x, y, z) = \mathrm{Re}[\mathbf{J}(x, y) \mathrm{e}^{\mathrm{i}\omega t - \gamma z}], \quad \mathbf{E}_{\mathrm{p}}(x, y, z) = \mathrm{Re}[\mathbf{E}(x, y) \mathrm{e}^{\mathrm{i}\omega t - \gamma z}], \\ \mathbf{H}_{\mathrm{p}}(x, y, z) = \mathrm{Re}[\mathbf{H}(x, y) \mathrm{e}^{\mathrm{i}\omega t - \gamma z}], \end{aligned} \tag{2.156}$$

which reasserts both the time and z-dependence down the guiding structure. At a particular z plane, say $z = 0$, we may drop out the explicit z-dependence. And if we do not wish to watch the time evolution of the harmonic wave, which is sufficient for plotting purposes, we may further set $t = 0$, and write (2.156) as

$$\mathbf{J}_{\mathrm{p}}(x, y) = \mathrm{Re}[\mathbf{J}(x, y)], \quad \mathbf{E}_{\mathrm{p}}(x, y) = \mathrm{Re}[\mathbf{E}(x, y)], \quad \mathbf{H}_{\mathrm{p}}(x, y) = \mathrm{Re}[\mathbf{H}(x, y)]. \tag{2.157}$$

2.1.4 Numerical Calculations of the Electromagnetic Field for LHM or DNM

To enable us to assess the effect of varying the anisotropy on the propagation constant and the field patterns, we will study the single biaxial crystal case, which has the anisotropy in the permittivity. The permeability will be left alone, set to a scalar value of $u = -2.5$ (relative to the free space value). To further simplify the interpretation, the electric crystalline properties will be chosen with principle axis orientation. Thus the material tensors are

$$\bar{\bar{\varepsilon}} = \begin{bmatrix} \varepsilon_{xx} & 0 & 0 \\ 0 & \varepsilon_{yy} & 0 \\ 0 & 0 & \varepsilon_{zz} \end{bmatrix}, \quad \bar{\bar{\mu}} = \begin{bmatrix} \mu_{xx} & 0 & 0 \\ 0 & \mu_{yy} & 0 \\ 0 & 0 & \mu_{zz} \end{bmatrix} = \mu \begin{bmatrix} 1 & 0 & 0 \\ 0 & 1 & 0 \\ 0 & 0 & 1 \end{bmatrix}. \tag{2.158}$$

The structure to be modeled is a single microstrip guided wave device (Fig. 2.1), with the wave propagating in the z-direction, with the cross-section of the device being uniform in every xy-planar cut. Substrate material is the LHM (NIM or NPV) with $h_1 = 5\,\mathrm{mm}$, which rests over a ground plane, above it is a conductor strip of perfect conductivity with insignificant thickness and width $w = 5\,\mathrm{mm}$, and then above it is placed an overlayer of RHM with unity permittivity and permeability with $h_2 = 20\,\mathrm{mm}$ (perfect air or vacuum). This stacking is done in the y-direction. Initially we start out with a nominal permittivity value of $\varepsilon_n = -2.5$ (relative to the free space value) making ($\mu_n = -2.5$)

$$\bar{\bar{\varepsilon}} = \begin{bmatrix} \varepsilon_n & 0 & 0 \\ 0 & \varepsilon_n & 0 \\ 0 & 0 & \varepsilon_n \end{bmatrix}, \quad \bar{\bar{\mu}} = \mu_n \begin{bmatrix} 1 & 0 & 0 \\ 0 & 1 & 0 \\ 0 & 0 & 1 \end{bmatrix}. \tag{2.159}$$

For the nominal values of this device, we are looking at the lowest order mode possible. Spectral terms in (2.152), and in (2.154) and (2.155), are summed to $n = n_{\max} = 200$, and the basis function limits are set $n_x = n_z = 1$. Further terms in the expansion are not expected to have a large effect on either the current or field distribution because this number of basis functions is enough to capture the current variation for the lowest order mode which is symmetric. Another salutary effect of being able to use so few basis function terms is that unwanted higher order modes would not be available to create the surface current which excites the structure. Nevertheless, for each propagation constant γ eigenvalue found below, other higher order solutions were found (up to six in some situations) to verify that our γ was the desired one. We will pick out three frequencies to study spanning two decades, each frequency within a range. In the 0.1–0.3 GHz range, we select 0.2 GHz, which lies within a range possessing imaginary propagation constants with the phase value β (relative to the free space value) varying from 3.5 to 4.5 [nominal case of (2.159)]. An order of magnitude higher is the next frequency value at 2.0 GHz, which lies within the 0.3–10 GHz range, whose propagation constants γ are complex ($\gamma = \alpha + \mathrm{i}\beta$) with α varying in value from 1.7 to 0.35 and β varying over 4.0 to 0.8 [nominal case of (2.159)]. Finally, the last frequency chosen is yet one more order of magnitude higher at 20 GHz, in the frequency range 10–40 GHz, where again $\gamma = \mathrm{i}\beta$ giving pure phase behavior with β varying from 2.0 to 2.5 [nominal case of (2.159)]. None of the γ vs. f variations is linear in any of these three ranges. All results displayed below were done by partitioning the structure into 45 divisions per layer vertically, and 90 divisions horizontally, producing a mesh with grid points having field values calculated at each of them. Field mesh values were then sent through another processing step to produce the magnitude field distributions. Arrow distributions were produced in the second processing stage by attaching arrows to a courser grid point mesh created from the first meshing scheme, which was on the order of 20×20 in size.

Figure 2.2a–d shows the electric field magnitude $E = \left[\sum_{i=1}^{3} E_i^2\right]^{1/2}$ at $f = 0.2\,\mathrm{GHz}$ for

$$\bar{\bar{\varepsilon}}(a) = \begin{bmatrix} \varepsilon_n & 0 & 0 \\ 0 & \varepsilon_n & 0 \\ 0 & 0 & \varepsilon_n \end{bmatrix}, \quad \bar{\bar{\varepsilon}}(b) = \begin{bmatrix} \varepsilon_n & 0 & 0 \\ 0 & 2\varepsilon_n & 0 \\ 0 & 0 & \varepsilon_n \end{bmatrix}, \quad \bar{\bar{\varepsilon}}(c) = \begin{bmatrix} \varepsilon_n & 0 & 0 \\ 0 & 2\varepsilon_n & 0 \\ 0 & 0 & 2\varepsilon_n \end{bmatrix},$$

$$\bar{\bar{\varepsilon}}(d) = \begin{bmatrix} 2\varepsilon_n & 0 & 0 \\ 0 & 2\varepsilon_n & 0 \\ 0 & 0 & \varepsilon_n \end{bmatrix}. \tag{2.160}$$

Notice that the first tensor $\bar{\bar{\varepsilon}}(a)$ case represents isotropy so that any deviation from the distributions shown for it, the cases $\bar{\bar{\varepsilon}}(b)$–$\bar{\bar{\varepsilon}}(d)$, indicate the effect of anisotropy. With mostly phase behavior except for the last case, complex propagation constant is for these four cases $\alpha(a), \beta(a) = 0, 3.753$; $\alpha(b), \beta(b) = 6.261 \times 10^{-4},\ 5.910$; $\alpha(c), \beta(c) = 8.112 \times 10^{-4},\ 5.960$; $\alpha(d), \beta(d) = 0.7835, 7.456$. Surface current expansion coefficients (complex, x and z components [see (2.139)]) for the cases are, respectively, $\{a_{\mathrm{e}1}, b_{\mathrm{e}1}\} = \{(0, -7.859 \times 10^{-4}); (1, 0)\}$, $\{(0, -2.159 \times 10^{-3}); (1, 0)\}$, $\{(-3.171 \times 10^{-6}, -2.202 \times 10^{-3}); (1, 0)\}$, $\{(-8.875 \times 10^{-5}, -1.133 \times 10^{-3}); (1, 0)\}$. Very little change in the electric magnitude distribution occurs until we get to case (d), which has a rather noticeable increase in intensity above the interface, and the shape of the distribution changed or enlarged

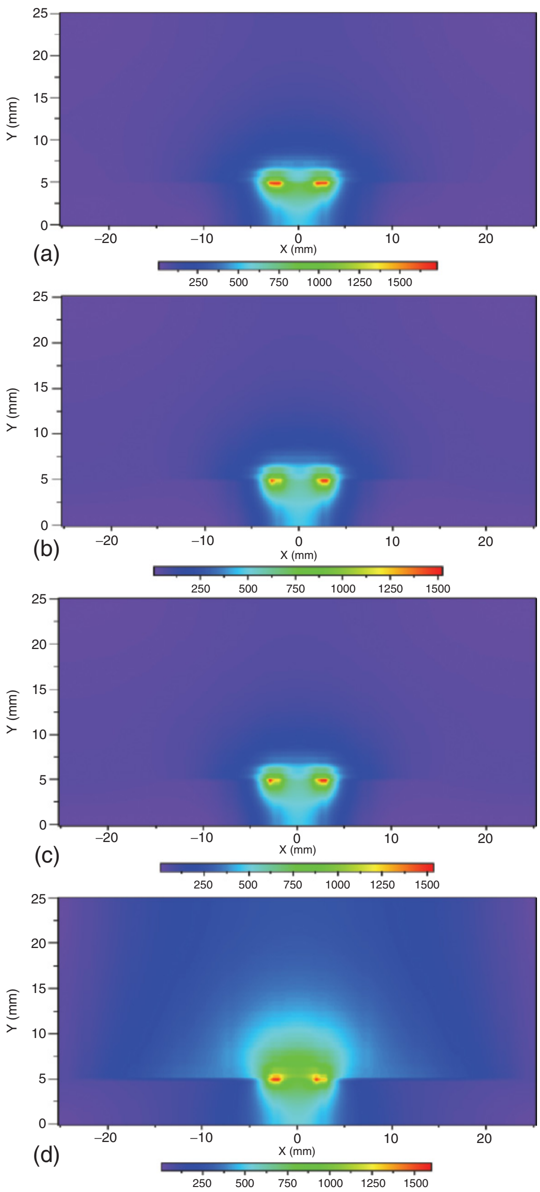

Fig. 2.2. Color distribution of the E field for a microstrip guided wave structure, with an LHM substrate $h_1 = 5\,\mathrm{mm}$ thick, and a vacuum overlayer $h_2 = 20\,\mathrm{mm}$ thick, with 50 mm side wall separation. Calculation is done at $f = 0.2\,\mathrm{GHz}$. Tensor cases have scalar permeability $\mu = \mu_n = -2.5$ and biaxial permittivity which are chosen as (**a**) $\varepsilon_{xx} = \varepsilon_{yy} = \varepsilon_{zz} = \varepsilon_n = -2.5$; (**b**) $\varepsilon_{xx} = \varepsilon_{zz} = \varepsilon_n$, $\varepsilon_{yy} = 2\varepsilon_n$; (**c**) $\varepsilon_{yy} = \varepsilon_{zz} = 2\varepsilon_n$, $\varepsilon_{xx} = \varepsilon_n$; (**d**) $\varepsilon_{xx} = \varepsilon_{yy} = 2\varepsilon_n$, $\varepsilon_{zz} = \varepsilon_n$

to look like more of a bubble immediately around and on top of the strip. Substantial $\alpha(d)$ indicates lateral wave motion due to a wave attached to the interface and having some surface wave character, or bulk nature, or both, and must correspond to the energy being carried by a large portion of the top region seen in the Fig. 2.2d. (At the end of this section, we will return to this question by examining field cuts.) Figure 2.3a–d shows the magnetic field magnitude $H = [\sum_{i=1}^{3} H_i^2]^{1/2}$ for (2.160). Magnetic magnitude distribution is seen to keep the same basic shape, but the intensity of the field is seen to progressively rise just above the interface, and below it beneath the strip and immediately to either side of the strip. Figure 2.4a–d shows electric field arrow plots of $\mathbf{E}_{\rm t}$, the field in the plane transverse to the z-direction, with the arrow length indicating the cross-sectional magnitude and the orientation the direction [maximum arrow size is shown below the device cross-section – this value is correlated with the field intensity values shown in Figs. 2.2 and 2.3 for the same $\bar{\bar{\varepsilon}}$ cases]. Nominal case for $\mathbf{E}_{\rm t}$ is given in Fig. 2.4a, b which provide, respectively, the actual arrow distribution and the scaled distribution, with the scaled plot lifting the small magnitude arrows out of obscurity so one can study their directions. Scaling is done according to a formula using an inverse trigonometric function,

$$E_i = \frac{E_i}{E_{\rm t}}\left[\left|\tan^{-1}\left(\frac{E_{\rm t}}{E_{\rm av}}\right)\right| + 0.75\right], \quad H_i = \frac{H_i}{H_{\rm t}}\left[\left|\tan^{-1}\left(\frac{H_{\rm t}}{H_{\rm av}}\right)\right| + 0.75\right]; \tag{2.161}$$

$$E_{\rm t}^2 = E_x^2 + E_y^2, \quad H_{\rm t}^2 = H_x^2 + H_y^2. \tag{2.162}$$

One should be very careful in using scaled plots to understand anything other than direction behavior. Arrow plots of $\mathbf{E}_{\rm t}$ for cases $\bar{\bar{\varepsilon}}(b)$ and $\bar{\bar{\varepsilon}}(c)$ look similar to $\bar{\bar{\varepsilon}}(a)$, and because it is much harder to resolve subtle trends in arrow plots vs. color magnitude distribution plots, as we have just seen, we omit them and go on to the last $\bar{\bar{\varepsilon}}(d)$ case of (2.160). Figure 2.4c, d provide, respectively, the unscaled and scaled distributions of $\mathbf{E}_{\rm t}$ for this last case $\bar{\bar{\varepsilon}}(d)$. Significant change is seen from the $\bar{\bar{\varepsilon}}(a)$ case. Electric field pointing into the conductor strip from the RHM indicates that the charge on the upper part of the strip is negative. However, electric field pointing into the strip from the LHM means the charge on the lower part of the strip is positive. This previously seen behavior of the charge is not inconsistent with a single surface current flow $\mathbf{J}_{\rm s}$, because, for argument sake, if the bottom charge flows in the $+\hat{z}$ direction, and the top charge in the $-\hat{z}$ direction, they will add and produce a net current. Figure 2.5a–d shows field arrow plots of $\mathbf{H}_{\rm t}$, the magnetic field in the plane transverse to the z-direction. Again we show the nominal $\bar{\bar{\varepsilon}}(a)$ case [Fig. 2.5a, b provide, respectively, the actual arrow distribution and the scaled distribution in (2.161)] and the $\bar{\bar{\varepsilon}}(d)$ case (in Fig. 2.5c, d). (For this frequency at 0.2 GHz, and the frequencies to follow, (2.161) has been used with $E_{\rm av} = 100\,{\rm V\,m^{-1}}$ and $H_{\rm av} = 0.1\,{\rm A\,m^{-1}}$.)

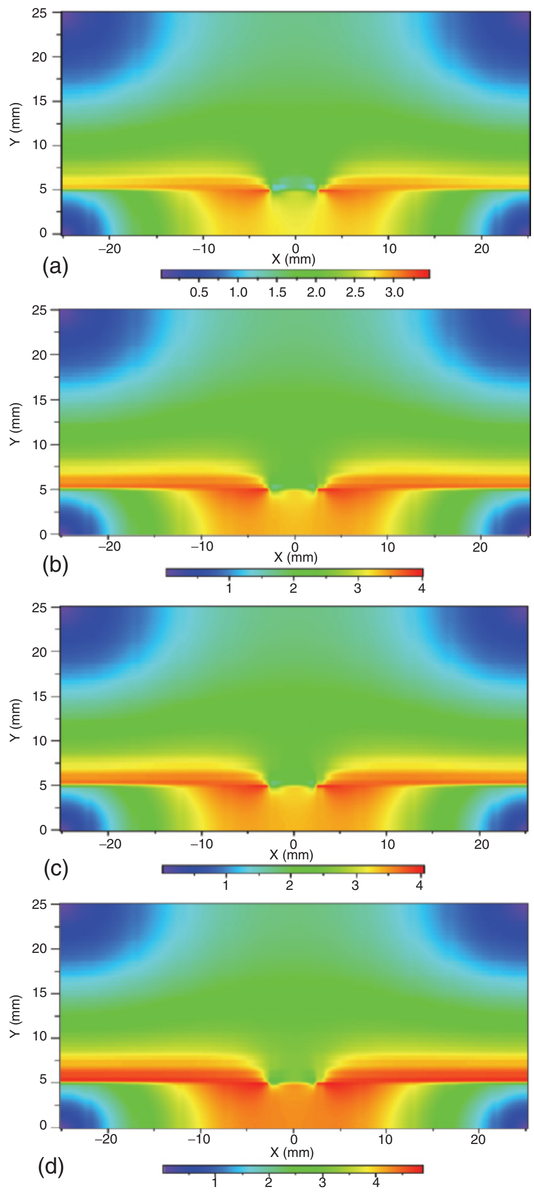

Fig. 2.3. Color distribution of the H field for a microstrip guided wave structure, with an LHM substrate $h_1 = 5\,\mathrm{mm}$ thick, and a vacuum overlayer $h_2 = 20\,\mathrm{mm}$ thick, with 50 mm side wall separation. Calculation is done at $f = 0.2\,\mathrm{GHz}$. Tensor cases have scalar permeability $\mu = \mu_n = -2.5$ and biaxial permittivity which are chosen as (**a**) $\varepsilon_{xx} = \varepsilon_{yy} = \varepsilon_{zz} = \varepsilon_n = -2.5$; (**b**) $\varepsilon_{xx} = \varepsilon_{zz} = \varepsilon_n$, $\varepsilon_{yy} = 2\varepsilon_n$; (**c**) $\varepsilon_{yy} = \varepsilon_{zz} = 2\varepsilon_n$, $\varepsilon_{xx} = \varepsilon_n$; (**d**) $\varepsilon_{xx} = \varepsilon_{yy} = 2\varepsilon_n$, $\varepsilon_{zz} = \varepsilon_n$

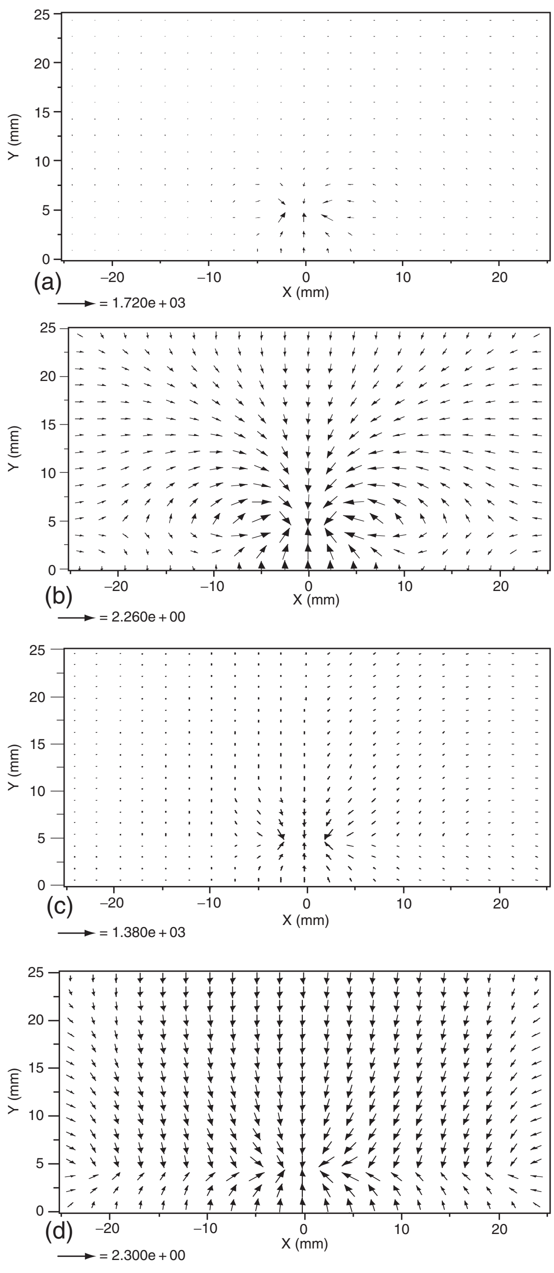

Fig. 2.4. *Arrow* distribution plots at $f = 0.2\,\mathrm{GHz}$ for the transverse electric $\mathbf{E}_\mathrm{t}$ vector for the LHM device in Figs. 2.2 and 2.3. (**a**) Unscaled plot for nominal case with $\bar{\bar{\varepsilon}} = \varepsilon_n I$ and $\bar{\bar{\mu}} = \mu_n I$; (**b**) scaled plot for parameters in (**a**); (**c**) unscaled plot with $\varepsilon_{xx} = \varepsilon_{yy} = 2\varepsilon_n$, $\varepsilon_{zz} = \varepsilon_n = -2.5$; (**d**) scaled plot for parameters in (**c**)

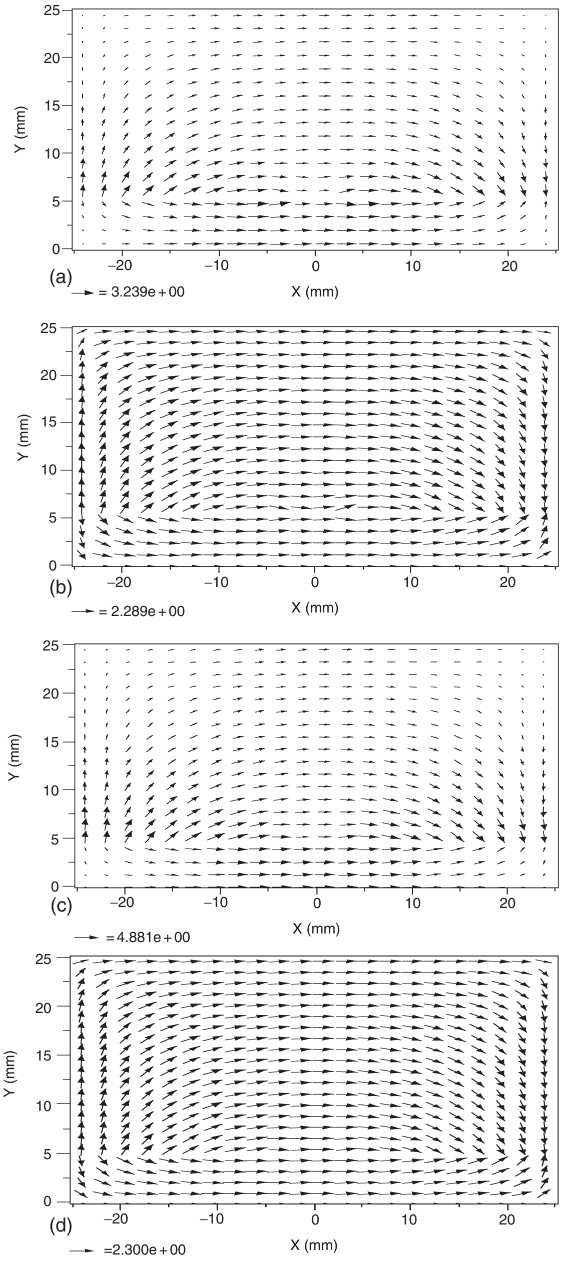

Fig. 2.5. *Arrow* distribution plots at $f = 0.2\,\text{GHz}$ for the transverse magnetic $\mathbf{H}_\text{t}$ vector for the LHM device in Figs. 2.2 and 2.3. (**a**) Unscaled plot for nominal case with $\bar{\bar{\varepsilon}} = \varepsilon_n I$ and $\bar{\bar{\mu}} = \mu_n I$; (**b**) scaled plot for parameters in (**a**); (**c**) unscaled plot with $\varepsilon_{xx} = \varepsilon_{yy} = 2\varepsilon_n$, $\varepsilon_{zz} = \varepsilon_n = -2.5$; (**d**) scaled plot for parameters in (**c**)

At the second frequency $f = 2.0\,\mathrm{GHz}$, we consider the permittivity tensor cases

$$\bar{\bar{\varepsilon}}(a) = \begin{bmatrix} \varepsilon_n & 0 & 0 \\ 0 & \varepsilon_n & 0 \\ 0 & 0 & \varepsilon_n \end{bmatrix}, \quad \bar{\bar{\varepsilon}}(b) = \begin{bmatrix} \varepsilon_n & 0 & 0 \\ 0 & 4\varepsilon_n & 0 \\ 0 & 0 & \varepsilon_n \end{bmatrix}, \quad \bar{\bar{\varepsilon}}(c) = \begin{bmatrix} \varepsilon_n & 0 & 0 \\ 0 & \varepsilon_n & 0 \\ 0 & 0 & 4\varepsilon_n \end{bmatrix},$$
$$\bar{\bar{\varepsilon}}(d) = \begin{bmatrix} \varepsilon_n & 0 & 0 \\ 0 & 4\varepsilon_n & 0 \\ 0 & 0 & 4\varepsilon_n \end{bmatrix}, \quad \bar{\bar{\varepsilon}}(e) = \begin{bmatrix} 4\varepsilon_n & 0 & 0 \\ 0 & 4\varepsilon_n & 0 \\ 0 & 0 & 4\varepsilon_n \end{bmatrix}. \tag{2.163}$$

Again, the first tensor $\bar{\bar{\varepsilon}}(a)$ represents isotropy, and the next three tensors $[\bar{\bar{\varepsilon}}(b), \bar{\bar{\varepsilon}}(c)$, and $\bar{\bar{\varepsilon}}(d)]$ are anisotropic, so their field distribution deviations from $\bar{\bar{\varepsilon}}(a)$ show the effect of anisotropy. Finally, the last tensor $\bar{\bar{\varepsilon}}(e)$, returns to the isotropic situation. Propagation constant is complex for these five cases, being $\alpha(a), \beta(a) = 1.133, 1.424; \alpha(b), \beta(b) = 1.999, 2.338; \alpha(c), \beta(c) = 1.226, 1.692; \alpha(d), \beta(d) = 1.722, 2.568; \alpha(e), \beta(e) = 1.728, 2.428$. Surface current expansion coefficients (complex, x and z components [see (2.139)]) for the cases are, respectively, $\{a_{\mathrm{e1}}, b_{\mathrm{e1}}\} = \{(-3.273 \times 10^{-3}, -6.645 \times 10^{-3}); (1, 0)\}, \{(-1.685 \times 10^{-2}, -2.973 \times 10^{-2}); (1, 0)\}, \{(-6.278 \times 10^{-3}, -9.416 \times 10^{-3}); (1, 0)\}, \{(-1.602 \times 10^{-2}, -3.243 \times 10^{-2}); (1, 0)\}, \{(-7.989 \times 10^{-3}, -3.058 \times 10^{-2}); (1, 0)\}$. Because we are modeling the problem with the LHM lossless, as well as no losses in the strip, bottom ground plane, top cover, or side wall conductors, the presence of a finite α means that some of the power must be flowing in the x-direction as bulk or surface waves as we saw at one-tenth of the frequency value before. Confirmation of this behavior comes from examining the electric magnitude E distributions in Fig. 2.6a–e, which show marked intensity above the interface but hugging it along much of the surface for cases $\bar{\bar{\varepsilon}}(a), \bar{\bar{\varepsilon}}(c)$, and $\bar{\bar{\varepsilon}}(e)$ (see further discussion of this subject at the section's end). Figure 2.6a, c has E similar in shape in that a substantial intensity exists below the strip all the way to the ground plane, just above the strip, and to either side of the strip just above the interface. Figure 2.6b, d, and e are similar because substantial intensity exists between the strip and ground plane, and above the strip in a half bubble shape. Figure 2.7a–e shows the magnetic field magnitude H. Figure 2.7a–d shows substantial intensity along the interface and above it, again lending strength to the argument that wave propagation normal to the guided wave direction is occurring. All cases of Fig. 2.7 show significant distribution shape variation from one case to another. Figure 2.8a–e shows transverse electric field $\mathbf{E}_{\mathrm{t}}$ arrow plots, in scaled format. Figure 2.9a–e shows transverse magnetic field $\mathbf{H}_{\mathrm{t}}$ arrow plots, in scaled format.

One of the more easily identifiable trends, amongst the anisotropic effects seen above, caused by the change from isotropy to anisotropy, is the enhancement of the E field distribution in the y-direction for those tensors which have enhanced the corresponding tensor element [see $\bar{\bar{\varepsilon}}(b)$ and $\bar{\bar{\varepsilon}}(d)$]. When the last tensor $\bar{\bar{\varepsilon}}(e)$ returns the LHM to isotropy, one sees a field pattern similar to that in $\bar{\bar{\varepsilon}}(a)$ (the initial isotropy, but with lower nominal permittivity value

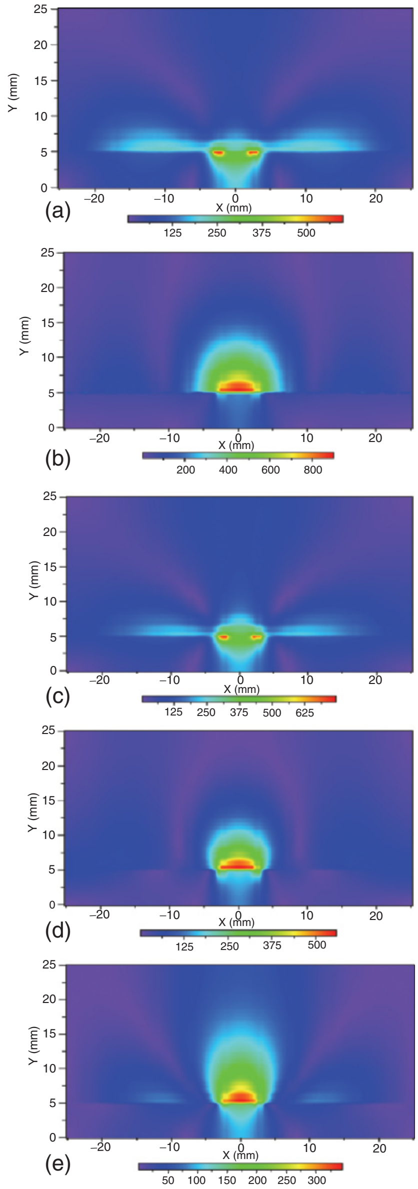

Fig. 2.6. Color distribution of the E field for a microstrip guided wave structure, with an LHM substrate $h_1 = 5\,\mathrm{mm}$ thick, and a vacuum overlayer $h_2 = 20\,\mathrm{mm}$ thick, with 50 mm side wall separation. Calculation is done at $f = 2.0\,\mathrm{GHz}$. Tensor cases have scalar permeability $\mu = \mu_n = -2.5$ and biaxial permittivity which are chosen as (**a**) $\varepsilon_{xx} = \varepsilon_{yy} = \varepsilon_{zz} = \varepsilon_n = -2.5$; (**b**) $\varepsilon_{xx} = \varepsilon_{zz} = \varepsilon_n$, $\varepsilon_{yy} = 4\varepsilon_n$; (**c**) $\varepsilon_{xx} = \varepsilon_{yy} = \varepsilon_n$, $\varepsilon_{zz} = 4\varepsilon_n$; (**d**) $\varepsilon_{yy} = \varepsilon_{zz} = 4\varepsilon_n$, $\varepsilon_{xx} = \varepsilon_n$; (**e**) $\varepsilon_{xx} = \varepsilon_{yy} = \varepsilon_{zz} = 4\varepsilon_n$

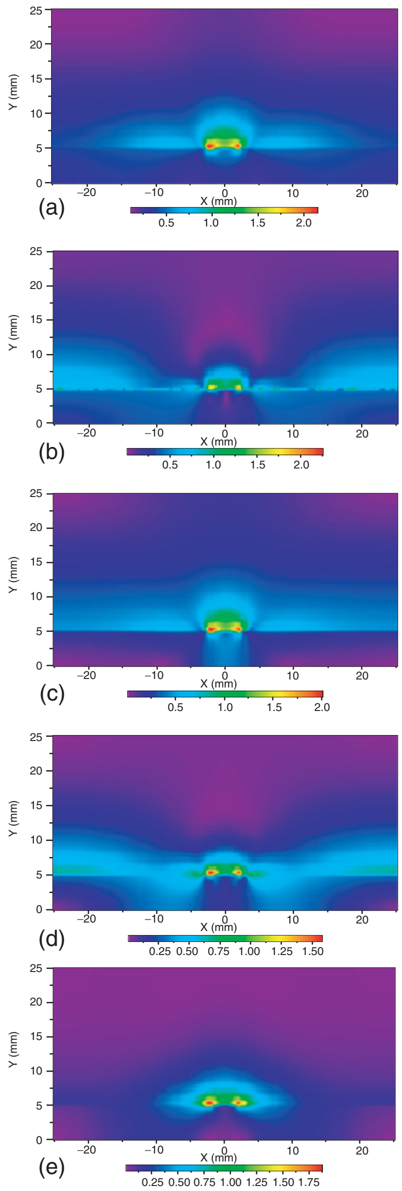

Fig. 2.7. Color distribution of the H field for a microstrip guided wave structure, with an LHM substrate $h_1 = 5\,\text{mm}$ thick, and a vacuum overlayer $h_2 = 20\,\text{mm}$ thick, with 50 mm side wall separation. Calculation is done at $f = 2.0\,\text{GHz}$. Tensor cases have scalar permeability $\mu = \mu_n = -2.5$ and biaxial permittivity which are chosen as (**a**) $\varepsilon_{xx} = \varepsilon_{yy} = \varepsilon_{zz} = \varepsilon_n = -2.5$; (**b**) $\varepsilon_{xx} = \varepsilon_{zz} = \varepsilon_n$, $\varepsilon_{yy} = 4\varepsilon_n$; (**c**) $\varepsilon_{xx} = \varepsilon_{yy} = \varepsilon_n$, $\varepsilon_{zz} = 4\varepsilon_n$; (**d**) $\varepsilon_{yy} = \varepsilon_{zz} = 4\varepsilon_n$, $\varepsilon_{xx} = \varepsilon_n$; (**e**) $\varepsilon_{xx} = \varepsilon_{yy} = \varepsilon_{zz} = 4\varepsilon_n$

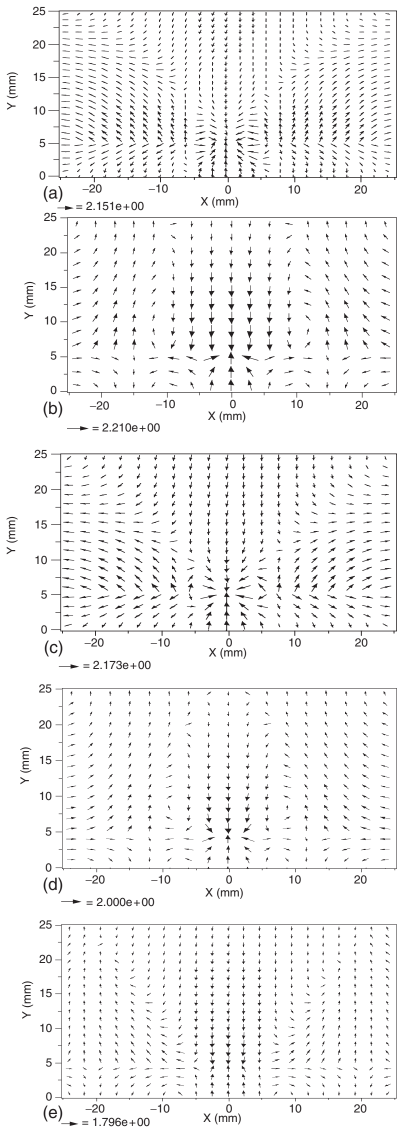

Fig. 2.8. *Arrow* distribution plots at $f = 2.0\,\mathrm{GHz}$ for the transverse electric $\mathbf{E}_\mathrm{t}$ vector for the LHM device in Figs. 2.2 and 2.3. All plots are scaled – tensor cases have scalar permeability $\mu = \mu_n = -2.5$ and biaxial permittivity which are chosen as (**a**) $\varepsilon_{xx} = \varepsilon_{yy} = \varepsilon_{zz} = \varepsilon_n = -2.5$; (**b**) $\varepsilon_{xx} = \varepsilon_{zz} = \varepsilon_n$, $\varepsilon_{yy} = 4\varepsilon_n$; (**c**) $\varepsilon_{xx} = \varepsilon_{yy} = \varepsilon_n$, $\varepsilon_{zz} = 4\varepsilon_n$; (**d**) $\varepsilon_{yy} = \varepsilon_{zz} = 4\varepsilon_n$, $\varepsilon_{xx} = \varepsilon_n$; (**e**) $\varepsilon_{xx} = \varepsilon_{yy} = \varepsilon_{zz} = 4\varepsilon_n$

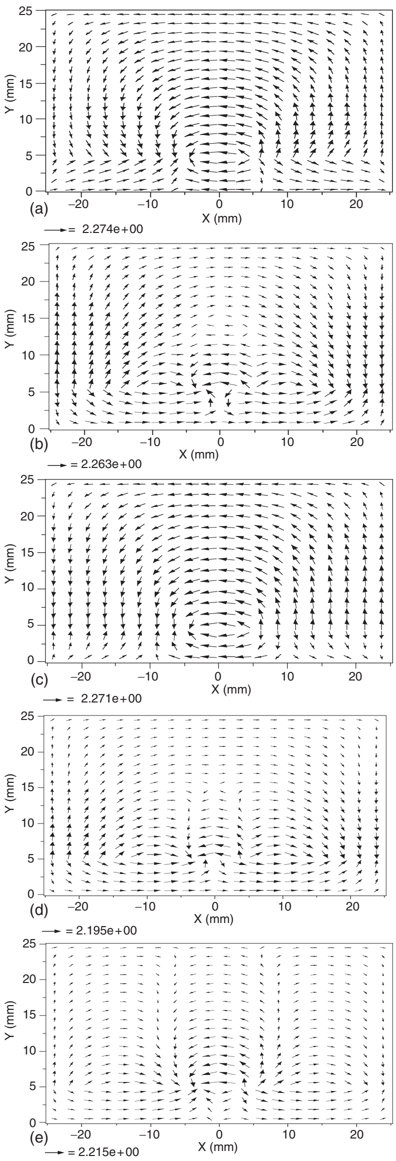

Fig. 2.9. *Arrow* distribution plots at $f = 2.0\,\text{GHz}$ for the transverse magnetic $\mathbf{H}_\text{t}$ vector for the LHM device in Figs. 2.2 and 2.3. All plots are scaled – tensor cases have scalar permeability $\mu = \mu_n = -2.5$ and biaxial permittivity which are chosen as (**a**) $\varepsilon_{xx} = \varepsilon_{yy} = \varepsilon_{zz} = \varepsilon_n = -2.5$; (**b**) $\varepsilon_{xx} = \varepsilon_{zz} = \varepsilon_n$, $\varepsilon_{yy} = 4\varepsilon_n$; (**c**) $\varepsilon_{xx} = \varepsilon_{yy} = \varepsilon_n$, $\varepsilon_{zz} = 4\varepsilon_n$; (**d**) $\varepsilon_{yy} = \varepsilon_{zz} = 4\varepsilon_n$, $\varepsilon_{xx} = \varepsilon_n$; (**e**) $\varepsilon_{xx} = \varepsilon_{yy} = \varepsilon_{zz} = 4\varepsilon_n$

than the final tensor), but with the added effect of enhanced E field behavior in the y-direction above the strip, as seen in the intervening anisotropic cases.

To gain some idea of the vast differences between LHM and RHM substrates affecting the field distribution, the last figure after the LHM figures (Figs. 2.2–2.16), Fig. 2.17 gives the electric field distributions for an RHM substrate with the same nominal permittivity magnitude value as the LHM, making its $\varepsilon_n = 2.5$ ($\mu = 1.0$ nonmagnetic) at $f = 2.0\,\text{GHz}$. Again five tensors are treated as in (2.163) (here the multiplicative factor used was 2). One notes that in all the cases shown, $\bar{\bar{\varepsilon}}(a)$–$\bar{\bar{\varepsilon}}(e)$, the primary feature is the preponderance of electric field magnitude in the RHM substrate and below the metal strip. Secondary feature, arising from the presence of the inflated y tensor element ε_{yy}, is the notch effect, that is, the appearance of a dimple or notch between the edges of the strip above the substrate corresponding to a field magnitude reduction, which is also associated with enhancement of the field magnitude below the interface under the strip. Comparison of the cases in Fig. 2.17 with those in Fig. 2.6 shows that an LHM substrate allows vast changes in the field distributions, and that its anisotropy directly affects the field distribution.

Finally, at the third frequency $f = 20\,\text{GHz}$, we consider the permittivity tensor cases

$$\bar{\bar{\varepsilon}}(a) = \begin{bmatrix} \varepsilon_n & 0 & 0 \\ 0 & \varepsilon_n & 0 \\ 0 & 0 & \varepsilon_n \end{bmatrix}, \quad \bar{\bar{\varepsilon}}(b) = \begin{bmatrix} \varepsilon_n & 0 & 0 \\ 0 & 4\varepsilon_n & 0 \\ 0 & 0 & \varepsilon_n \end{bmatrix}, \quad \bar{\bar{\varepsilon}}(c) = \begin{bmatrix} \varepsilon_n & 0 & 0 \\ 0 & 4\varepsilon_n & 0 \\ 0 & 0 & 4\varepsilon_n \end{bmatrix},$$
$$\bar{\bar{\varepsilon}}(d) = \begin{bmatrix} 4\varepsilon_n & 0 & 0 \\ 0 & 4\varepsilon_n & 0 \\ 0 & 0 & \varepsilon_n \end{bmatrix}, \quad \bar{\bar{\varepsilon}}(e) = \begin{bmatrix} 4\varepsilon_n & 0 & 0 \\ 0 & 4\varepsilon_n & 0 \\ 0 & 0 & 4\varepsilon_n \end{bmatrix}. \tag{2.164}$$

As in the previous frequency cases, here again one starts out with isotropy, and finishes with isotropy for this frequency as in the last case. Deviation from these two bounding cases demonstrates the effects of anisotropy. Propagation constant reverts back to a pure phase characteristic for all but the second and third cases in these five cases, being $\beta(a) = 2.394$; $\alpha(b)$, $\beta(b) = 1.324 \times 10^{-3}$, 3.653; $\alpha(c), \beta(c) = 1.630 \times 10^{-3}$, 3.721; $\beta(d) = 3.699$; $\beta(e) = 3.730$. Surface current expansion coefficients (complex, x and z components [see (2.139)]) for the cases are, respectively, $\{a_{e1}, b_{e1}\} = \{(0, -0.5338); (1, 0)\}$, $\{(1.110 \times 10^{-3}, -0.4390); (1, 0)\}$, $\{(-2.505 \times 10^{-3}, -0.2248); (1, 0)\}$, $\{((1, 0); (0, 0.5368)\}$, $\{(0, -0.5371); (1, 0)\}$. All of the electric magnitudes E look different from each other as seen in Fig. 2.10a–e. But some of the overall trends can be discerned. For example, below the interface intensity maxima and minima occur periodically. This x-variation must be due to the effective wavelength in that direction. Although it must be determined numerically, and its value found by counting two successive maxima and minima in the plot, an estimate can be calculated as $\lambda = \lambda_0/\sqrt{\varepsilon_{xx}} = 15\,\text{mm}/\sqrt{\varepsilon_{xx}}$ at 20 GHz. For cases (a) and (d), $\sqrt{\varepsilon_{xx}(a)} = \sqrt{\varepsilon_n} = \sqrt{2.5} = 1.58$ making $\lambda(a) = 9.5\,\text{mm}$, and

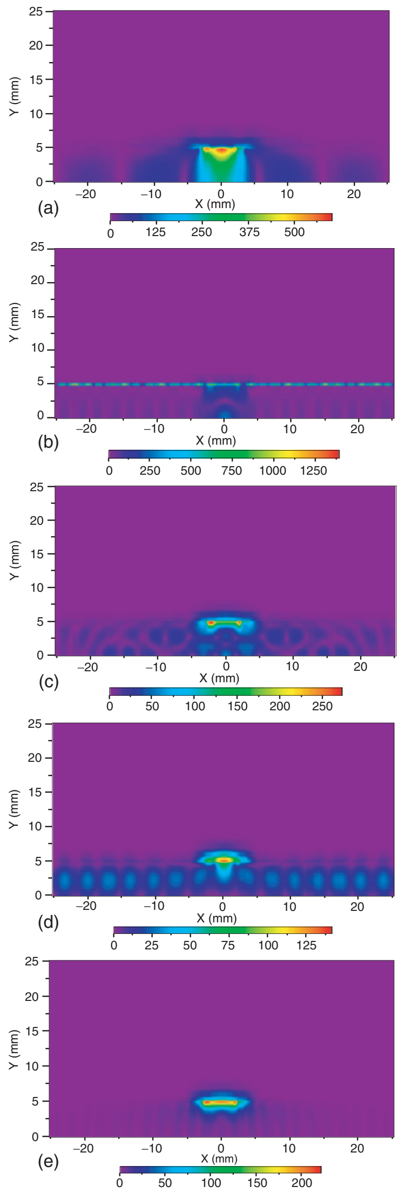

Fig. 2.10. Color distribution of the E field for a microstrip guided wave structure, with an LHM substrate $h_1 = 5\,\mathrm{mm}$ thick, and a vacuum overlayer $h_2 = 20\,\mathrm{mm}$ thick, with 50 mm side wall separation. Calculation is done at $f = 20\,\mathrm{GHz}$. Tensor cases have scalar permeability $\mu = \mu_n = -2.5$ and biaxial permittivity which are chosen as (**a**) $\varepsilon_{xx} = \varepsilon_{yy} = \varepsilon_{zz} = \varepsilon_n = -2.5$; (**b**) $\varepsilon_{xx} = \varepsilon_{zz} = \varepsilon_n$, $\varepsilon_{yy} = 4\varepsilon_n$; (**c**) $\varepsilon_{yy} = \varepsilon_{zz} = 4\varepsilon_n$, $\varepsilon_{xx} = \varepsilon_n$; (**d**) $\varepsilon_{xx} = \varepsilon_{yy} = 4\varepsilon_n$, $\varepsilon_{zz} = \varepsilon_n$; (**e**) $\varepsilon_{xx} = \varepsilon_{yy} = \varepsilon_{zz} = 4\varepsilon_n$

$\sqrt{\varepsilon_{xx}(d)} = \sqrt{4\varepsilon_n} = 2\sqrt{2.5} = 3.16$ making $\lambda(d) = 4.75\,\text{mm}$. This translates into about five periods for case (a) and 10.5 periods for case (d) in the $2b = 50\,\text{mm}$ width. Inspection of Fig. 2.10a, d shows that the actual number is slightly less, roughly 3.25 and 7.5. All cases except (b) have the largest intensity around the strip, with significant field below the strip for cases (a) and (d), with case (a) being much more than case (d). Cases (c)–(e) in Fig. 2.10 have some field just above the strip. Finally, case (b) in Fig. 2.10 has only a remnant of a field around the strip, but very noticeable field along the interface, extending all the way to both side walls. Case (b) in Fig. 2.10 appears to be a clear example of a surface wave, although it is not obvious based upon the α/β ratio being so small. However, this could occur if the surface wave is predominantly in the same direction as the guided wave, the z-direction (see section end for more discussion). Figure 2.11a–e shows the magnetic field magnitude H, and like the E field plots the periodicity variation along the x-direction is seen here also, as well as all cases having significant field around the strip. Surface wave characteristic is again clearly demonstrated in Fig. 2.11b. Figure 2.12a–e shows transverse electric field $\mathbf{E}_\text{t}$ arrow plots, in scaled format. We notice that in all cases except $\bar{\bar{\varepsilon}}(b)$, the arrows immediately above and below the strip point in or out, indicating opposite charges on the two sides of the conductor strip, an observation made earlier in regard to behavior at $f = 0.2\,\text{GHz}$. However, for $\bar{\bar{\varepsilon}}(b), \mathbf{E}_\text{t}$ arrows point upward above and below the strip, indicating positive charge on both sides of the conductor. Figure 2.13a–e shows transverse magnetic field $\mathbf{H}_\text{t}$ arrow plots, in scaled format. As seen for the previous frequency case, tensor element enhancement of the y element tends to push the E field distribution to being just below the strip or above the strip. However, at this frequency, the bubble shape is more squished in appearance.

In order to discern the field variation in the LHM structure in another way, other than the cross-sectional 2D visualization techniques already covered, simple cuts for specific x or y values may be taken. Here an x cut at $x = 15\,\text{mm}$ will be done, purposely with $x \neq 0$ to avoid going through the strip, with the interval broken into 100 points. One case is chosen from each frequency previously studied, to illustrate the cross-sectional field component variations against x. The cases are $\bar{\bar{\varepsilon}}(d)$ for $f = 0.2\,\text{GHz}$, $\bar{\bar{\varepsilon}}(c)$ for $f = 2\,\text{GHz}$, and $\bar{\bar{\varepsilon}}(b)$ for $f = 20\,\text{GHz}$. All results are for $n_x = n_z = 1, n = 200$, except for Figs. 2.14a and 2.15a done with $n_x = n_z = 5, n = 600$ to capture the interfacial E_x continuity better and for Fig. 2.16c to capture the interfacial H_x continuity better (see Table 2.1 for the surface current coefficients used for these exceptions). At $f = 0.2\,\text{GHz}$ (Fig. 2.14), other than the sign switches in E_y and H_y which occur because of continuity of normal components of $\mathbf{D}$ or $\mathbf{B}$ across the interface at $x = 15\,\text{mm}$ (magnitude and sign of the difference in values of the normal electric field component on either side of the interface is controlled by $\varepsilon_\text{top}E_\text{ytop} = \varepsilon_\text{LHM}E_\text{yLHM}$, or the permittivity ratio $1/2\varepsilon_n = -1/5$; magnitude and sign of the difference in values of the normal magnetic field component on either side of the interface is controlled by $\mu_\text{top}H_\text{ytop} = \mu_\text{LHM}H_\text{yLHM}$,

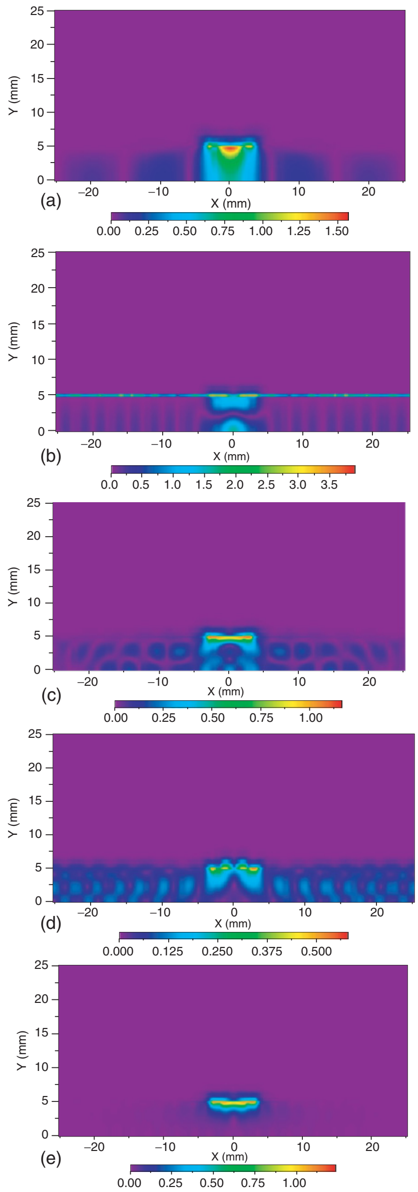

Fig. 2.11. Color distribution of the H field for a microstrip guided wave structure, with an LHM substrate $h_1 = 5\,\mathrm{mm}$ thick, and a vacuum overlayer $h_2 = 20\,\mathrm{mm}$ thick, with 50 mm side wall separation. Calculation is done at $f = 20\,\mathrm{GHz}$. Tensor cases have scalar permeability $\mu = \mu_n = -2.5$ and biaxial permittivity which are chosen as (**a**) $\varepsilon_{xx} = \varepsilon_{yy} = \varepsilon_{zz} = \varepsilon_n = -2.5$; (**b**) $\varepsilon_{xx} = \varepsilon_{zz} = \varepsilon_n$, $\varepsilon_{yy} = 4\varepsilon_n$; (**c**) $\varepsilon_{yy} = \varepsilon_{zz} = 4\varepsilon_n$, $\varepsilon_{xx} = \varepsilon_n$; (**d**) $\varepsilon_{xx} = \varepsilon_{yy} = 4\varepsilon_n$, $\varepsilon_{zz} = \varepsilon_n$; (**e**) $\varepsilon_{xx} = \varepsilon_{yy} = \varepsilon_{zz} = 4\varepsilon_n$

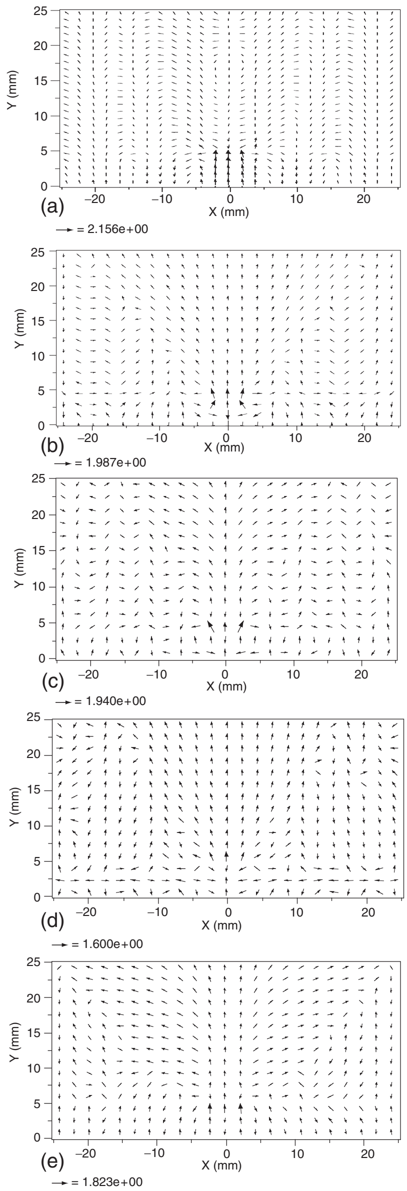

Fig. 2.12. *Arrow* distribution plots at $f = 20\,\text{GHz}$ for the transverse electric $\mathbf{E}_\text{t}$ vector for the LHM device in Figs. 2.2 and 2.3. All plots are scaled – tensor cases have scalar permeability $\mu = \mu_n = -2.5$ and biaxial permittivity which are chosen as (**a**) $\varepsilon_{xx} = \varepsilon_{yy} = \varepsilon_{zz} = \varepsilon_n = -2.5$; (**b**) $\varepsilon_{xx} = \varepsilon_{zz} = \varepsilon_n$, $\varepsilon_{yy} = 4\varepsilon_n$; (**c**) $\varepsilon_{yy} = \varepsilon_{zz} = 4\varepsilon_n$, $\varepsilon_{xx} = \varepsilon_n$; (**d**) $\varepsilon_{xx} = \varepsilon_{yy} = 4\varepsilon_n$, $\varepsilon_{zz} = \varepsilon_n$; (**e**) $\varepsilon_{xx} = \varepsilon_{yy} = \varepsilon_{zz} = 4\varepsilon_n$

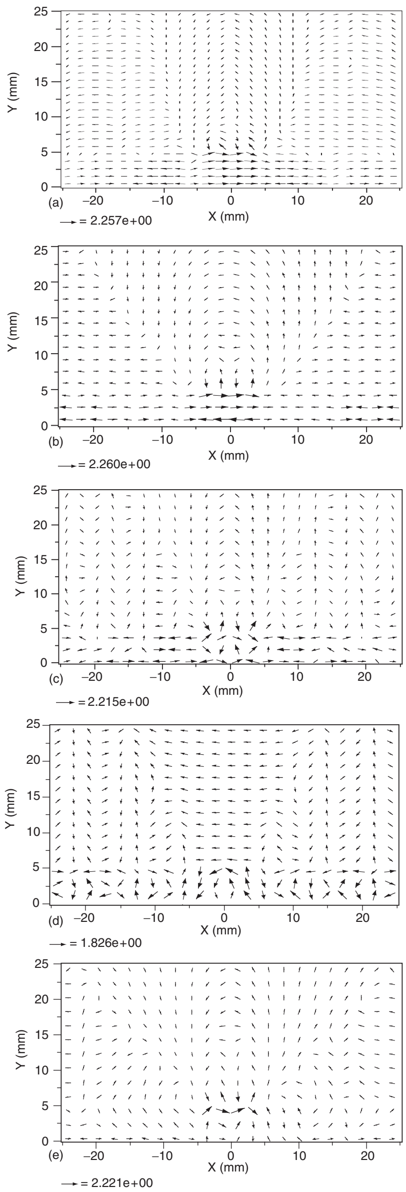

Fig. 2.13. *Arrow* distribution plots at $f = 20\,\mathrm{GHz}$ for the transverse magnetic $\mathbf{H}_\mathrm{t}$ vector for the LHM device in Figs. 2.2 and 2.3. All plots are scaled – tensor cases have scalar permeability $\mu = \mu_n = -2.5$ and biaxial permittivity which are chosen as (**a**) $\varepsilon_{xx} = \varepsilon_{yy} = \varepsilon_{zz} = \varepsilon_n = -2.5$; (**b**) $\varepsilon_{xx} = \varepsilon_{zz} = \varepsilon_n$, $\varepsilon_{yy} = 4\varepsilon_n$; (**c**) $\varepsilon_{yy} = \varepsilon_{zz} = 4\varepsilon_n$, $\varepsilon_{xx} = \varepsilon_n$; (**d**) $\varepsilon_{xx} = \varepsilon_{yy} = 4\varepsilon_n$, $\varepsilon_{zz} = \varepsilon_n$; (**e**) $\varepsilon_{xx} = \varepsilon_{yy} = \varepsilon_{zz} = 4\varepsilon_n$

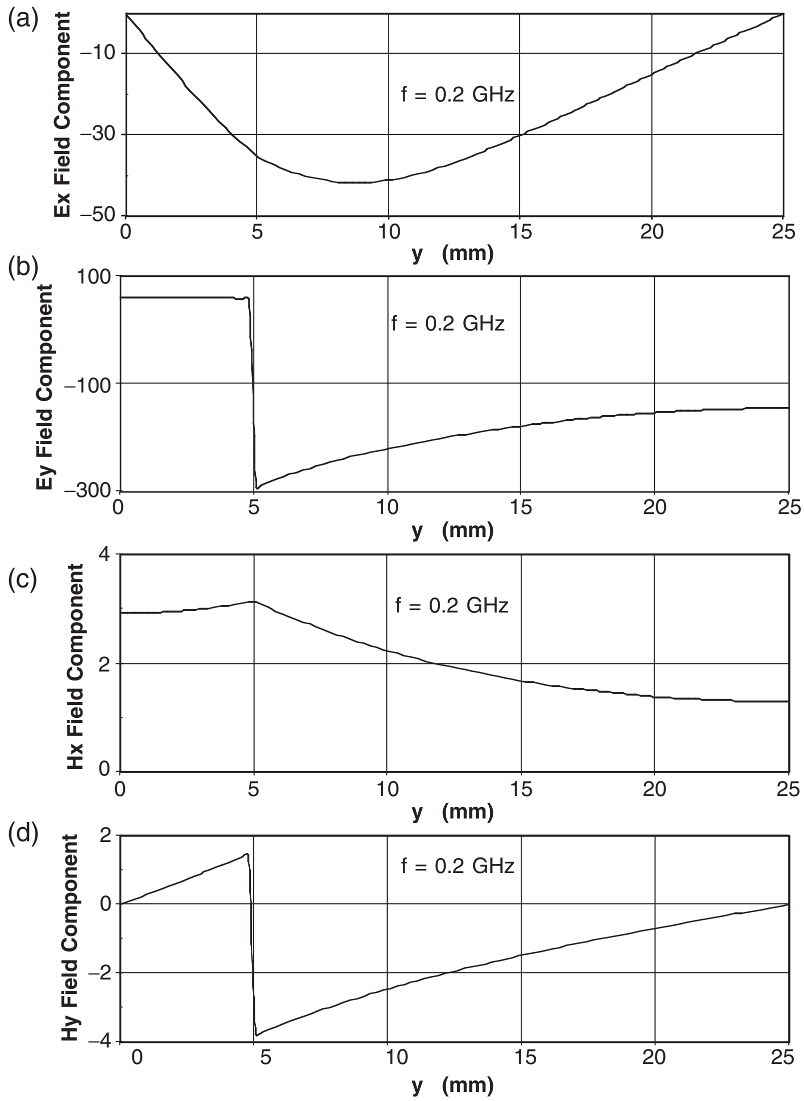

Fig. 2.14. Field component variations vs. y (mm) along the cut $x = 15\,\text{mm}$ for a microstrip guided wave structure, with an LHM substrate $h_1 = 5\,\text{mm}$ thick, and a vacuum overlayer $h_2 = 20\,\text{mm}$ thick, with 50 mm side wall separation. The frequency is $f = 0.2\,\text{GHz}$ for permittivity case $\bar{\bar{\varepsilon}}(d)$ with $\varepsilon_{xx} = \varepsilon_{yy} = 2\varepsilon_n$, $\varepsilon_{zz} = \varepsilon_n = -2.5$. (**a**) E_x component, (**b**) E_y component, (**c**) H_x component, (**d**) H_y component

or the permeability ratio $1/\mu_n = -1/2.5$), the field variation is linear (in the LHM substrate) or if nonlinear, having moderate variation. (E_x and H_x [as well as E_z and H_z] are continuous across the interface due to **E** and **H** tangential component continuity.) At $f = 2\,\text{GHz}$ (Fig. 2.15), similar field

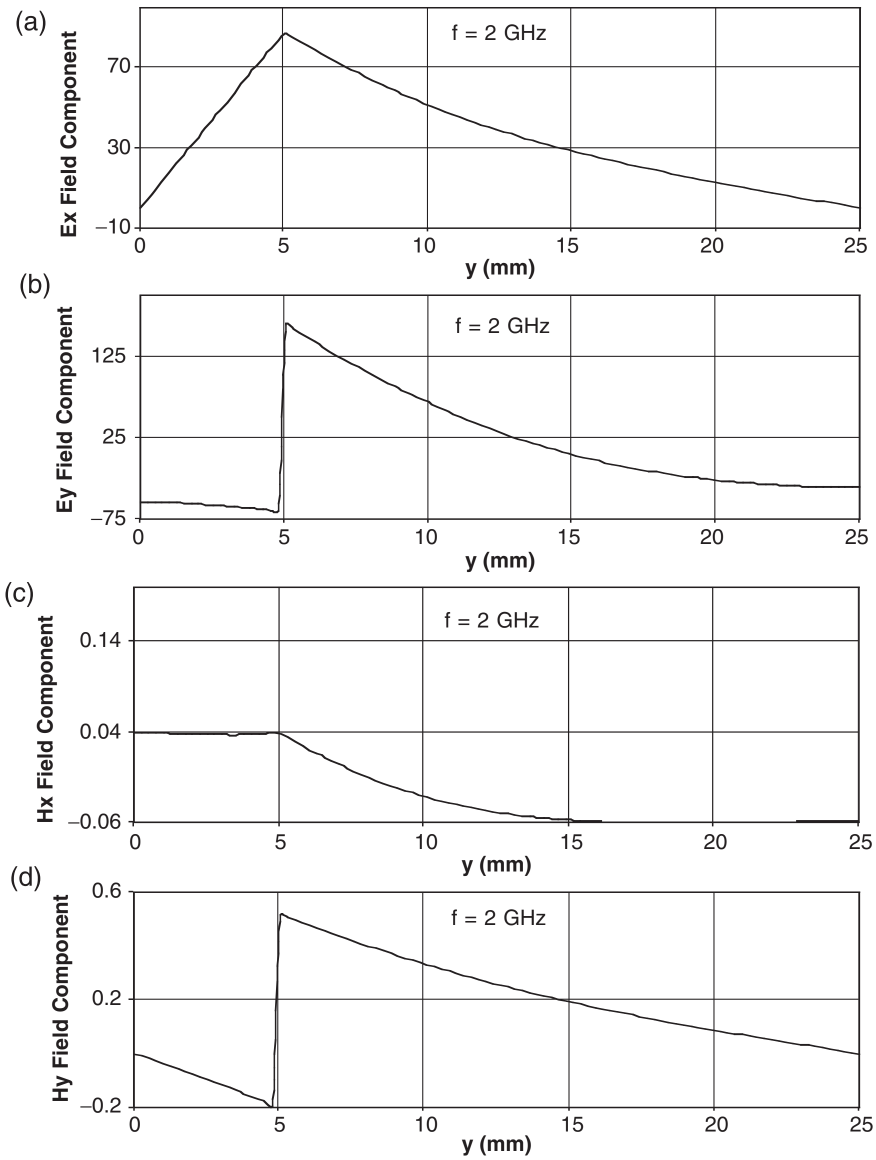

Fig. 2.15. Field component variations vs. y (mm) along the cut $x = 15\,\mathrm{mm}$ for the LHM microstrip guided wave structure of Fig. 2.14. The frequency is $f = 2\,\mathrm{GHz}$ for permittivity case $\bar{\bar{\varepsilon}}(c)$ with $\varepsilon_{xx} = \varepsilon_{yy} = \varepsilon_n = -2.5$, $\varepsilon_{zz} = 4\varepsilon_n$. (**a**) E_x component, (**b**) E_y component, (**c**) H_x component, (**d**) H_y component

component behavior to the lower frequency case is seen, with sign switches (and magnitude) of the normal field components obeying **D** or **B** continuity (permittivity ratio $\varepsilon_{\mathrm{top}}/\varepsilon_{\mathrm{LHM}} = 1/\varepsilon_n = -1/2.5$; again permeability ratio

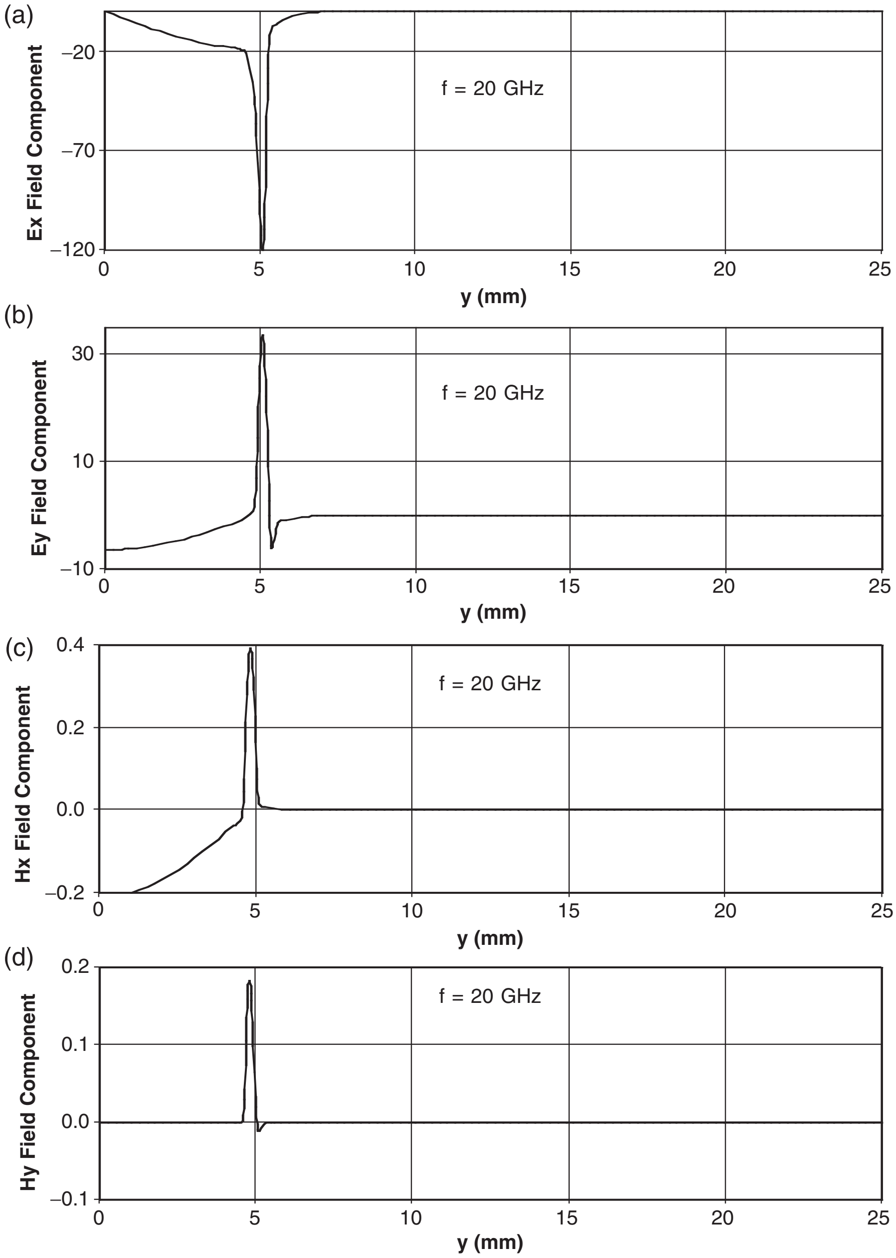

Fig. 2.16. Field component variations vs. y (mm) along the cut $x = 15\,\text{mm}$ for the LHM microstrip guided wave structure of Fig. 2.14. The frequency is $f = 20\,\text{GHz}$ for permittivity case $\bar{\bar{\varepsilon}}(b)$ with $\varepsilon_{xx} = \varepsilon_{zz} = \varepsilon_n = -2.5, \varepsilon_{yy} = 4\varepsilon_n$. (**a**) E_x component, (**b**) E_y component, (**c**) H_x component, (**d**) H_y component

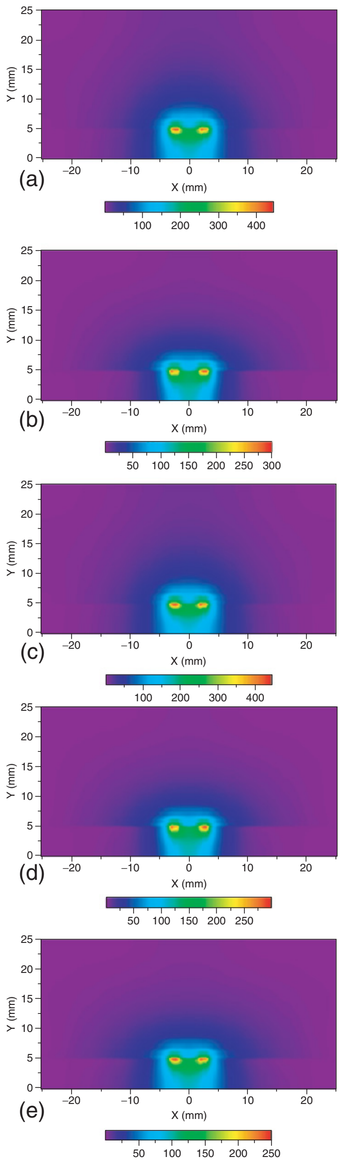

Fig. 2.17. Color distribution of the E field for a microstrip guided wave structure, with an RHM dielectric substrate $h_1 = 5$ mm thick, and a vacuum overlayer $h_2 = 20$ mm thick, with 50 mm side wall separation. Calculation is done at $f = 2.0$ GHz. Tensor cases have scalar permeability $\mu = \mu_n = 1.0$ and biaxial permittivity which are chosen as (**a**) $\varepsilon_{xx} = \varepsilon_{yy} = \varepsilon_{zz} = \varepsilon_n = 2.5$; (**b**) $\varepsilon_{xx} = \varepsilon_{zz} = \varepsilon_n$, $\varepsilon_{yy} = 2\varepsilon_n$; (**c**) $\varepsilon_{xx} = \varepsilon_{yy} = \varepsilon_n$, $\varepsilon_{zz} = 2\varepsilon_n$; (**d**) $\varepsilon_{yy} = \varepsilon_{zz} = 2\varepsilon_n$, $\varepsilon_{xx} = \varepsilon_n$; (**e**) $\varepsilon_{xx} = \varepsilon_{yy} = \varepsilon_{zz} = 2\varepsilon_n$. βs are, respectively, 1.4052, 1.8188, 1.4053, 1.8198, 1.9219

Table 2.1. Surface current coefficients for $n_x = n_z = 5$ and $n = 600$ [see (2.137) or (2.139)] corresponding to Figs. 2.13a, 2.14a, and 2.15c

	$f = 0.2\,\mathrm{GHz}$ $\bar{\bar{\varepsilon}}(d)$	$f = 2\,\mathrm{GHz}$ $\bar{\bar{\varepsilon}}(c)$	$f = 20\,\mathrm{GHz}$ $\bar{\bar{\varepsilon}}(b)$
i	J_{xe}, a_{ei}	J_{xe}, a_{ei}	J_{xe}, a_{ei}
1	$(1.8351 \times 10^{-3}$, $4.3927 \times 10^{-3})$	$(-1.4428 \times 10^{-3}$, $-1.0938 \times 10^{-2})$	$(-6.0329 \times 10^{-3}$, $-9.5096 \times 10^{-1})$
2	$(-2.3666 \times 10^{-4}$, $-5.5963 \times 10^{-4})$	$(-1.9032 \times 10^{-4}$, $1.3574 \times 10^{-3})$	$(1.5952 \times 10^{-3}$, $-2.9726 \times 10^{-1})$
3	$(8.4232 \times 10^{-5}$, $1.4838 \times 10^{-4})$	$(5.7020 \times 10^{-5}$, $-4.3501 \times 10^{-4})$	$(-9.5447 \times 10^{-3}$, $1.2971 \times 10^{-1})$
4	$(-1.8509 \times 10^{-5}$, $-1.4672 \times 10^{-4})$	$(-3.0738 \times 10^{-5}$, $2.6851 \times 10^{-4})$	$(-2.1657 \times 10^{-2}$, $1.3878 \times 10^{-1})$
5	$(6.5200 \times 10^{-6}$, $4.8388 \times 10^{-5})$	$(1.7669 \times 10^{-5}$, $3.0188 \times 10^{-6})$	$(2.0023 \times 10^{-4}$, $1.7385 \times 10^{-2})$
i	J_{ze}, b_{ei}	J_{ze}, b_{ei}	J_{ze}, b_{ei}
1	(1, 0)	(1, 0)	$(-1.7115 \times 10^{-1}$, $-1.1041 \times 10^{-3})$
2	$(1.5983 \times 10^{-1}$, $-3.5862 \times 10^{-2})$	$(3.5268 \times 10^{-2}$, $-6.7151 \times 10^{-2})$	(1, 0)
3	$(-3.9399 \times 10^{-2}$, $9.9047 \times 10^{-3})$	$(-7.7496 \times 10^{-3}$, $1.7510 \times 10^{-2})$	$(2.3721 \times 10^{-1}$, $-1.0963 \times 10^{-2})$
4	$(1.3619 \times 10^{-2}$, $-6.8264 \times 10^{-3})$	$(5.8341 \times 10^{-4}$, $-9.0669 \times 10^{-3})$	$(1.4831 \times 10^{-1}$, $3.2868 \times 10^{-2})$
5	$(-1.8171 \times 10^{-2}$, $7.3621 \times 10^{-5})$	$(6.0421 \times 10^{-3}$, $8.7917 \times 10^{-3})$	$(5.8148 \times 10^{-1}$, $7.2386 \times 10^{-2})$

$\mu_{\mathrm{top}}/\mu_{\mathrm{LHM}} = 1/\mu_n = -1/2.5$). Radically different field behavior occurs at $f = 20\,\mathrm{GHz}$ (Fig. 2.16), where exponentially decaying field away from the interface occurs. If we use exponential functional variation as a definition of pure surface wave behavior, then only this third frequency case qualifies as strictly a surface wave. Sign switches and magnitude differences of the normal field components obey permittivity ratio $\varepsilon_{\mathrm{top}}/\varepsilon_{\mathrm{LHM}} = 1/4\varepsilon_n = -1/10$ and permeability ratio $\mu_{\mathrm{top}}/\mu_{\mathrm{LHM}} = 1/\mu_n = -1/2.5$. Note that for Figs. 2.14–2.16, E_i and H_i, $i = x, y$, the units are E_y ($\mathrm{V\,m^{-1}}$) and H_y ($\mathrm{A\,m^{-1}}$) which is mks, but because the solution is rf, small signal, it really can be scaled arbitrarily, making the units really arbitrary. The size of the field components for a particular permittivity and permeability tensor pair choice in a computer simulation run are related because they were solved simultaneously, but field sizes may not be directly compared for different tensor cases run separately. Thus Figs. 2.2d, 2.3d and 2.14 all correspond to the same $\bar{\bar{\varepsilon}}(d)$ run at $f = 0.2\,\mathrm{GHz}$, and may be directly compared in regard to field component magnitudes.

2.1.5 Conclusion

In this Section a complete treatment of the theoretical process for modeling anisotropic left-handed materials (LHM) in guided wave structures has been given. With that formulation, a specific structure had been chosen to study, the single microstrip guided wave device loaded with LHM. Three frequency bands were identified to study, and calculations done at three frequency points within those bands. Field magnitude color distribution plots have been produced for electric E and magnetic H fields. Also, arrow plots have been generated. We have identified propagation of guided waves with and without the generation of surface waves. The surface wave is coupled to the guided wave and extracts energy from the guided wave and results in both a real part of the propagation constant and a concomitant field distribution showing sideway extraction of energy. Use of LHM substrates produces field distributions considerably different from ordinary media (right-handed materials, RHM), and it has been shown here that anisotropy can have a significant effect on those distributions. Not studied here explicitly, but known for the nominal structure considered in this paper, backward waves occur (propagation along the z-axis) over part of the frequency spectrum (in regions of the 0.3–10 and 30–40 GHz bands), by examining the dispersion diagram. Such LHM character of the whole device itself may be of great interest for devices in electronic circuits.

Also seen here is that anisotropy introduced through specific tensor elements can have identifiable aspects displayed in the electromagnetic field distributions. For example, transverse plane anisotropy produces different results than longitudinal anisotropy, and examination of the electric field magnitude distribution shows this behavior. All the field distributions produced in this research on anisotropy were done against a backdrop of isotropy for the initial tensors describing the physical properties of the LHM. The ability to redistribute the volumetric fields of a bulk-like wave, or convert a volumetric wave into a surface wave, as found here suggests potential LHM device applications. It may be possible to introduce a new class of control components based upon distortion of the LHM permittivity tensor. Such LHM tensor distortion could be produced by stress or strain, or through an analogy to ferroelectric behavior in materials, for example. Much of the work reported in this section may be found, although with less complete derivations of the theoretical background, in [20]. Also, related material may be found in [21].

Closely tied in with our study here, the negative refractive property of LHMs has also been examined, as covered in Sect. 2.2, in a related class of anisotropic crystals in regard to guided wave propagation in microwave structures which produce newly found asymmetric redistributions of fields. Interesting device applications may result, and this demonstrates that the study of anisotropy in negative refractive materials may be just at its beginning. More interesting physics is expected to be discovered, with other applications.

2.2 Negative Refractive Bicrystal Heterostructures

2.2.1 Introduction

Recently it has been shown that a bicrystalline pair of materials leads to field asymmetry [22, 23]. This was accomplished by realizing that a similar arrangement consisting of two crystals, properly oriented with respect to each other, provides a structure capable of producing negative refraction for some directions of the incoming wave in an optical scattering numerical and experimental test [24,25]. Field asymmetry arises from some properties of the broken symmetry, only available by using a heterostructure. The simplest arrangement is the bicrystal pair, with the crystals chosen as uniaxial, possessing two ordinary principal axes, and one extraordinary principal axis. Although the original discovery of field asymmetric was for nominal values of permittivity $\varepsilon = 5$, there is no reason why the effect cannot be found in other crystalline materials. It is only necessary to utilize the uniaxial properties of the crystal.

In fact, it is this universality of the effect, which leads us to the next conclusion, that it is possible to produce the effect starting with isotropic crystals if they are ferroelectric. Logic is as follows. Start with a ferroelectric crystal which is isotropic. Apply a static electric bias field E_0 in some direction, and increase the field until the desired reduction in permittivity occurs in the bias direction. The artificially induced preferred direction becomes the extraordinary direction and is a principal axis direction. Permittivity tensor element in that direction is the extraordinary permittivity diagonal value ε_{e}. Two other principal axis directions, normal to this preferred biased direction, become the ordinary directions and in those directions is the unbiased original permittivity, equal to the ordinary permittivity ε_{o}.

Ferroelectric behavior of permittivity change is based upon a phase transition, going from a cubic to tetragonal atomic crystalline arrangement, which takes the crystal from a paraelectric state to a ferroelectric state. This is why ferroelectric materials are so attractive for electronic applications, because huge percentage changes in the dielectric constant may be made.

So two possibilities exist. The first one is simply to acquire uniaxial crystals, properly orient their crystalline planes (to be covered in detail in Sect. 2.2.2), and build the structure to provide a fixed given asymmetry. Second possibility, is to work with a ferroelectric crystalline system, and implement biasing configurations dc isolated from the rf characteristics of the electromagnetic structure, allowing variable asymmetry. First structure realized does not need any external static electric field biasing. Second structure realized requires biasing configurations, and is more complicated, but has the tremendous quality of being a variable control component. The second structure, creates what is termed a negative crystal [26], because the extraordinary permittivity value is deflated compared to the ordinary permittivity value.

2.2.2 Theoretical Crystal Tensor Rotations

Bicrystal layering which produces the effect has two adjacent layers with opposite rotations of the principal cross-sectional axes, the rotation angles denoted by θ, where the positive angle corresponds to a counterclockwise rotation of the cross-sectional xy axes about the z-axis [see Fig. 2.1a]. Electromagnetic waves propagate down the z-axis, the longitudinal axis of the uniform guiding structure. To utilize the negative refractive property, the guiding metal is placed between the two crystals. In such an arrangement, one crystal is the bottom substrate, the other crystal the superstrate on top. Treatment of the tensors of the crystals is given in [17, 23]. Here $\theta = \pm 45$ is selected.

2.2.3 Guided Stripline Structure

Structure to be studied numerically here is a single stripline configuration with bounding vertical walls and a ground plane and a top cover. Although results will be obtained for the symmetric geometric placement of the strip with respect to all the bounding walls, better to unambiguously show that any asymmetry of the fields must come from the crystalline properties of the bi-layer arrangement, there is no reason in principle why, for example, each crystal layer cannot be of unequal thickness, causing the field to be unsymmetric in the vertical direction. Figure 2.18 shows a cross-sectional drawing of the structure. For calculations to be done in Sect. 2.2.4, we take $w = \mathrm{h}_\mathrm{T} = h_\mathrm{B} = 5\,\mathrm{mm}, b = 50\,\mathrm{mm}$, making $h_\mathrm{TOTAL} = h_\mathrm{T} + h_\mathrm{B} = 10\,\mathrm{mm}$. $b/w = 10$. Cross-hatching in Fig. 2.18a is meant to show the crystalline planes, and parallel to and normal to them indicates principal axis directions for each one of the crystals. Strip thickness is taken to be vanishing small.

2.2.4 Beam Steering and Control Component Action

Beam steering can be enabled by taking advantage of the asymmetric electromagnetic field distribution with controllable asymmetry utilizing ferroelectric crystals. Isolator action can be enabled by inserting a lossy strip, a second strip, beside the symmetrically located guiding strip, so that it is off – centered and positioned correctly so as to attenuate the wave when the direction is reversed from the low loss direction (Fig. 2.18b). This concept is well known, and is referred to as the field displacement effect, and has been widely employed in nonreciprocally based isolation devices, often utilizing ferrite material [27].

If the field displacement effect is employed in the bicrystal heterostructure, a device can be built without the need of magnets. Even for the bicrystal heterostructure with tuning capability based upon ferroelectric materials [28–30], only electric fields are used to bias the device. (See Fig. 2.18, top crystal, which shows biasing dc circuit.) A special advantage may accrue to using ferroelectric materials, in that even for the situation where one has amorphous

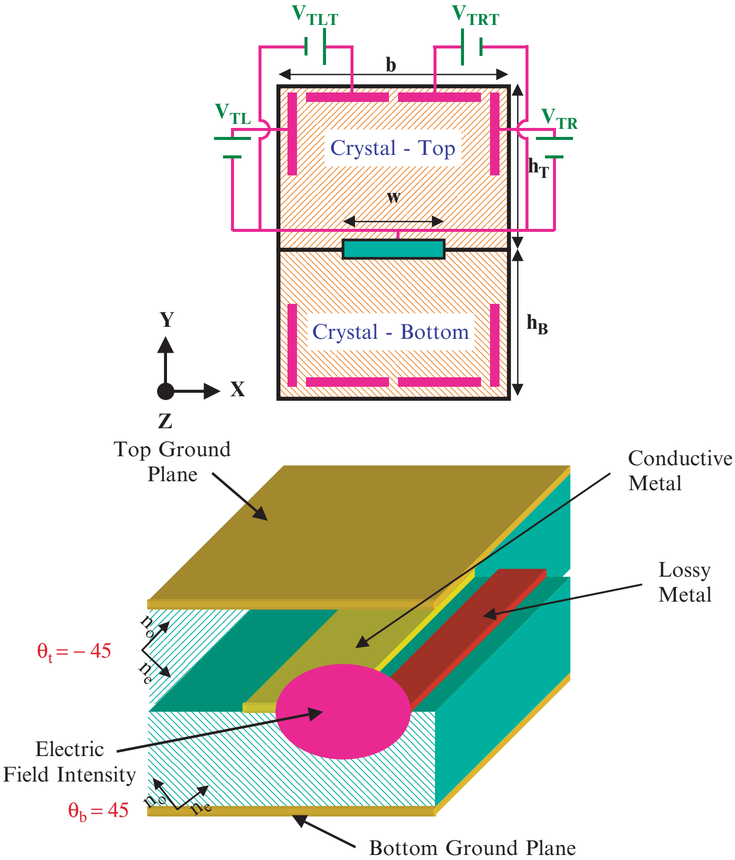

Fig. 2.18. (**a**) Cross-section of the bicrystal structure. Differently oriented crystals sandwich the strip. Biasing circuit shown for the upper half of the structure – lower half is similar. (**b**) Perspective drawing of the structure minus the biasing circuits, showing schematically a shifted field intensity relative to a lossy line

material with random microcrystal orientations, imposition of a biasing field may allow artificial creation of the principal axes, a requirement for getting the bicrystal to exist.

It may be desirable to actively sense whether the wave enters from port 1 (into the page – see Fig. 2.18) or port 2 (out of the page) and electronically bias the ferroelectric crystals to shift the rf field magnitude to be low loss or high loss with regard to the lossy strip. This may be necessary since the anisotropic reaction theorem [31], applied to a two terminal device, says that $\langle b, c\rangle = \langle \tilde{a}, b\rangle$ using that paper's notation, which implies reciprocal behavior of the crystals since their permittivities satisfy $\bar{\bar{\varepsilon}}^{\mathrm{T}} = \bar{\bar{\varepsilon}}$, and therefore of a composite of such crystals making up a structure.

The reaction theorem tells us that the asymmetry in field distribution can be used for beam steering, but to achieve control component action, or unequal transmission through a device going in either longitudinal direction, the asymmetry location must be shifted by 180° by electronic bias control. This is the major difference between the present effect and that obtained using a longitudinally biased ferrite spin ceramic material. Such a control component may have use as a variable attenuator in phase shifter applications.

2.2.5 Electromagnetic Fields

Starting with the structure in Fig. 2.18, computations using an anisotropic Green's function spectral domain method [2, 12], were run for nominal values of the permittivity $\varepsilon = 500$, 140, and 30. Figure 2.19 shows the electromagnetic field distribution for the transverse electric field $\mathbf{E}_\mathrm{t}$ in the cross-section. $\mathbf{H}_\mathrm{t}$ is similar and will not be shown here due to space limitations. Frequency was $f = 10\,\mathrm{GHz}$ and the propagation constant pure phase with $\gamma = \alpha + \mathrm{j}\beta = \mathrm{j}\beta, \beta = 4.392$ normalized to the free space value. Number of even and odd current basis functions was $n_x = n_z = 1$ for currents in the x and z directions. Both parities of the basis functions are needed to allow for asymmetric current distributions in the x-direction. Number of spectral terms was $n = 200$. Permittivity values were $\varepsilon_\mathrm{e} = 15$ and $\varepsilon_\mathrm{o} = 30$, making $\varepsilon_a = 22.5$ and $\varepsilon_d = 7.5$. $\varepsilon_d/\varepsilon_a = 33\%$. Distribution in Fig. 2.19 seems to be a fundamental mode fixed about the strip, with a cycloid shape, and the major intensity of the distribution shifted to the left. (Strip located at $|x| \le 2.5\,\mathrm{mm}$ or $-2.5 \le x \le 2.5$.)

Figure 2.20 shows the transverse electric field $\mathbf{E}_\mathrm{t}$ for $f = 10\,\mathrm{GHz}$. Permittivity values were $\varepsilon_\mathrm{e} = 110$ and $\varepsilon_\mathrm{o} = 140$, making $\varepsilon_a = 125$ and $\varepsilon_d = 15$. $\varepsilon_d/\varepsilon_a = 12\%$. Distribution in Fig. 2.20 also seems to be a fundamental mode but with less of a pronounced cycloid shape than before. Overall intensity of the entire distribution is even more shifted to the left. Again the propagation constant is pure phase with $\beta = 10.38$ normalized to the free space value.

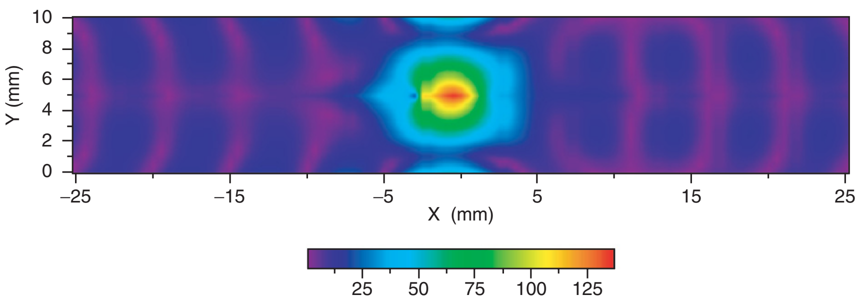

Fig. 2.19. Electric field bicrystal distribution for nominal $\varepsilon = 30$ at a frequency of $f = 10\,\mathrm{GHz}$

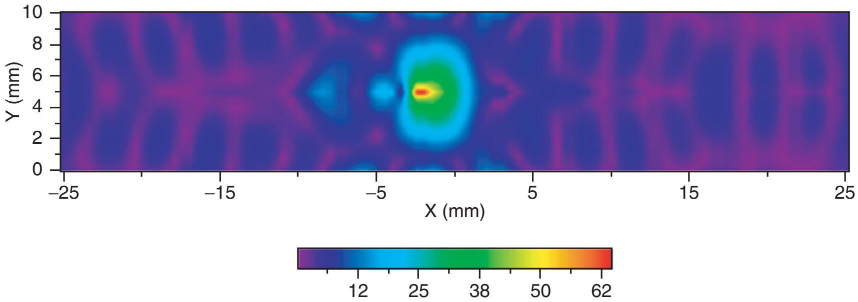

Fig. 2.20. Electric field bicrystal distribution for nominal $\varepsilon = 140$ at a frequency of $f = 10\,\mathrm{GHz}$

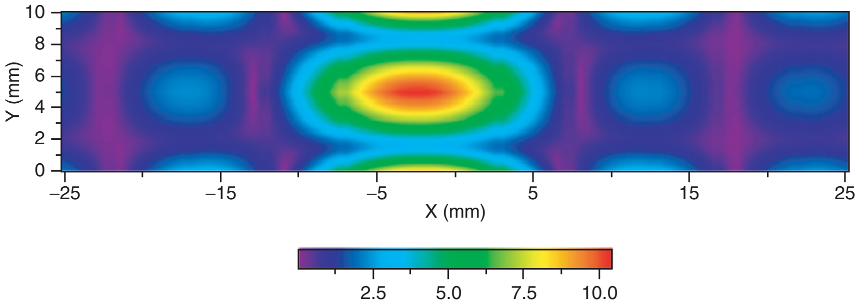

Fig. 2.21. Electric field bicrystal distribution for nominal $\varepsilon = 500$ at a frequency of $f = 2\,\mathrm{GHz}$

Lastly, Fig. 2.21 shows the transverse electric field $\mathbf{E}_\mathrm{t}$ for $f = 2\,\mathrm{GHz}$. Permittivity values were $\varepsilon_\mathrm{e} = 250$ and $\varepsilon_\mathrm{o} = 500$, making $\varepsilon_a = 375$ and $\varepsilon_d = 125$. $\varepsilon_d/\varepsilon_a = 33\%$. Distribution in Fig. 2.21 seems to be a fundamental mode, or at least one that is close to being the fundamental, as the majority of the distribution's highest strength is located about the strip. Elliptical distribution shapes appear. Marked shift of the overall distribution to the left is apparent. Again the propagation constant is pure phase with $\beta = 17.888$ normalized to the free space value.

2.2.6 Surface Current Distributions

As one would suspect, the surface current distributions for each of the cases just examined for the electric field distributions in Figs. 2.19–2.21 are asymmetric. Figures 2.22–2.24 provide the surface current distributions corresponding, respectively, to Figs. 2.19–2.21.

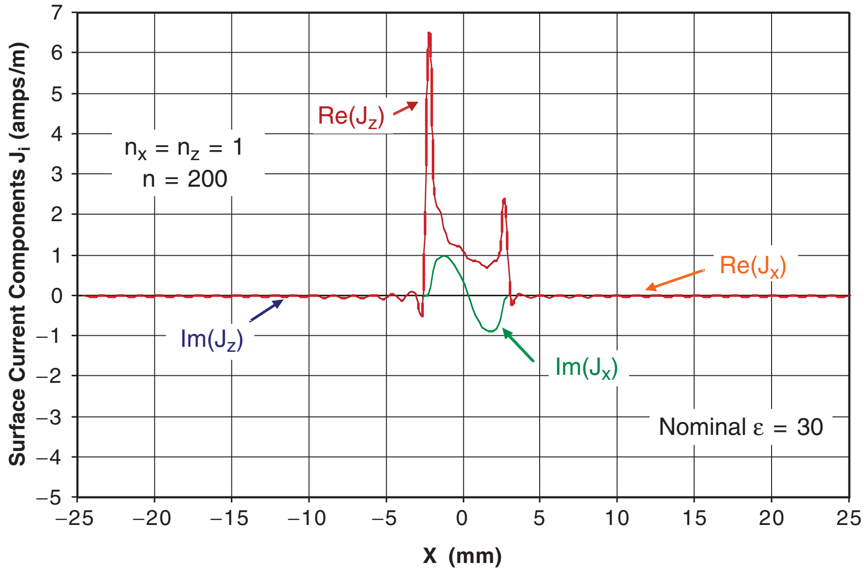

Fig. 2.22. Surface current bicrystal distribution corresponding to Fig. 2.19 with nominal $\varepsilon = 30$ at 10 GHz

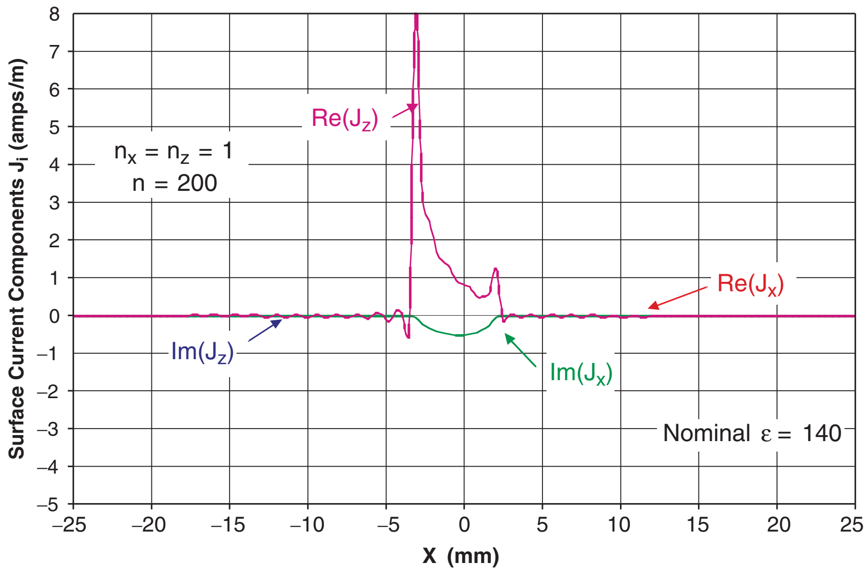

Fig. 2.23. Surface current bicrystal distribution corresponding to Fig. 2.20 with nominal $\varepsilon = 140$ at 10 GHz

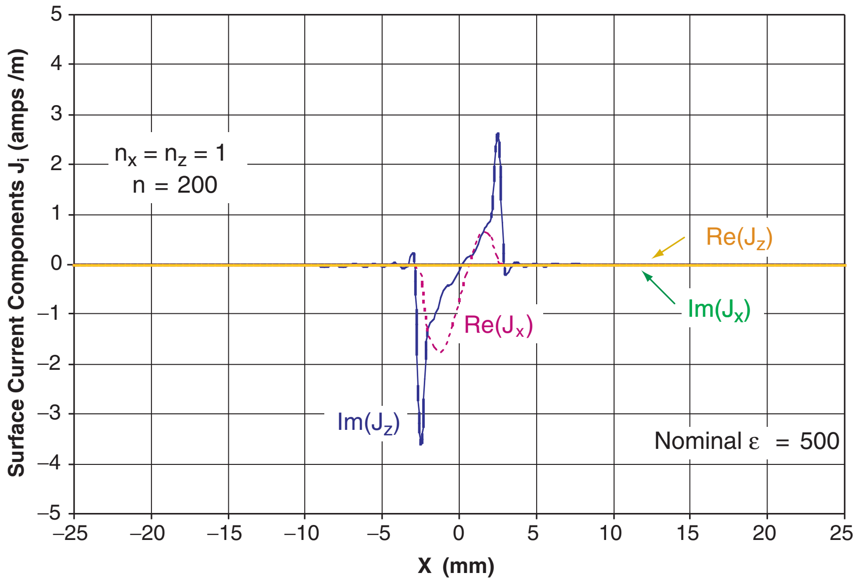

Fig. 2.24. Surface current bicrystal distribution corresponding to Fig. 2.21 with nominal $\varepsilon = 500$ at 2 GHz

2.2.7 Conclusion

It has been demonstrated here that a new arrangement of crystals into heterostructures can produce asymmetric field distributions, with the potential of leading to new beam steering and directional control component devices at microwave frequencies. A structure capable of doing this with only voltage biasing has been proposed. Most of the work reported in this section was taken from [32].

References

1. C.M. Krowne, Bull. Am. Phys. Soc. **48**, Pt. 1, 580 (Mar. 2003)
2. C.M. Krowne, Phys. Rev. Lett. **92**(5), 053901-1 to 4 (Feb. 3, 2004). Also on Cornell Univ. Archive arXiv.org/abs/physics/0305004, May 5, 2003
3. F.J. Rachford, D.L. Smith, P.L. Loschialpo, D.W. Forester, Phys. Rev. E **66**, 036613-1 to 5 (2002)
4. P.L. Loschialpo, D.L. Smith, D.W. Forester, F.J. Rachford, Phys. Rev. E **67**, 025602(R)-1 to 4 (2003)
5. A. Lakhtakia, C.M. Krowne, Optik **114**(7), 305–307 (2003). Also on Cornell Univ. arXiv, physics/0308043, Aug. 11, 2003
6. A. Alu, N. Engheta, Microw. Opt. Tech. Lett. **35**, 460–463 (2002)
7. L. Hu, S.T. Chui, Phys. Rev. B **66**, 085108-1 to 7 (2002)
8. C. Caloz, A. Sanada, L. Liu, T. Itoh, IEEE MTT-S Int. Microw. Symp. Dig. 317–320 (June 2003)

9. R. Islam, G.V. Eleftheriades, IEEE MTT-S Int. Microw. Symp. Dig. 321–324 (June 2003)
10. I.-H. Lin, C. Caloz, T. Itoh, IEEE MTT-S Int. Microw. Symp. Dig. 325–328 (June 2003)
11. H. Okabe, C. Caloz, T. Itoh, IEEE MTT-S Int. Microw. Symp. Dig. 329–332 (June 2003)
12. C.M. Krowne, IEEE Trans. Microw. Theory Tech. **51**, 2269–2283 (Dec. 2003)
13. C.M. Krowne, M. Daniel, IEEE Int. Microw. Symp. Dig. 309–312 (June 2003)
14. C.M. Krowne, IEEE Trans. Microw. Theory Tech. **32**, 1617–1625 (Dec. 1984)
15. P.M. Morse, H. Feshbach, *Methods of Theoretical Physics*, repr. 1978 (McGraw-Hill, New York, 1953)
16. A.A. Mostafa, C.M. Krowne, K.A. Zaki, IEEE Trans. Microw. Theory Tech. **35**, 1399–1407 (Dec. 1987)
17. C.M. Krowne, Microw. Opt. Technol. Letts. **28**(1), 63–69 (Jan. 5, 2001)
18. C.M. Krowne, Theoretical considerations for full-wave electromagnetic-media interactions in layered structures with ferroelectric or ferromagnetic materials, Invited paper, Proc. SPIE (Soc. Photo-Optical Instrum. Eng.), Complex Mediums, Microwave Materials **4097**, 70–84 (July 30, 2000)
19. C.M. Krowne, A.A. Mostafa, K.A. Zaki, IEEE Trans. Microw. Theory Tech. **36**, 1850–1860 (Dec. 1988)
20. C.M. Krowne, J. Appl. Phys. **99**, 044914-1 to 19 (15 Feb. 2006). Also on Cornell Univ. Archive, arXiv.org/abs/physics/cond-mat/0406219
21. C.M. Krowne, *Encyclopedia of RF and Microwave Engineering*, vol. 3 (Wiley, New York, 2005), pp. 2303–2320
22. C.M. Krowne, Bull. Am. Phys. Soc. **49**, Pt. 2, 928 (Mar. 2004)
23. C.M. Krowne, Phys. Rev. Lett. **93**(5), 053902–1 to 4 (July 2004)
24. Y. Zhang, B. Fluegel, A. Mascarenhas, Bull. Am. Phys. Soc. **49**, Pt. 2, 928 (Mar. 2004)
25. Y. Zhang, B. Fluegel, A. Mascarenhas, Phys. Rev. Lett. **91**, 157404-1 to 4 (Oct. 2003)
26. J.F. Nye, *Physical Properties of Crystals* (Oxford University Press, Oxford, 1979). First published 1957
27. F.J. Rosenbaum, *Advances Microwaves*, vol. 8 (Academic, New York, 1974), pp. 203–294
28. M.E. Lines, A.M. Glass, *Principles and Applications of Ferroelectrics and Related Materials* (Clarendon, Oxford, 2001). First published 1977
29. K. Uchino, *Ferroelectric Devices* (Dekker, New York, 2000)
30. C.M. Krowne, M. Daniel, S.W. Kirchoefer, J.M. Pond, IEEE Trans. Microw. Theory Tech. **50**(2), 537–548 (Feb. 2002)
31. C.M. Krowne, IEEE Trans. Antennas Propagat. **32**, 1224–1230 (Nov. 1984)
32. C.M. Krowne, Appli. Phys. Lett. **91**, 022902 (2007).

3

"Left-Handed" Magnetic Granular Composites

S.T. Chui, L.B. Hu, Z. Lin and L. Zhou

Summary. We investigate the possibility of preparing left-handed materials in metallic magnetic granular composites. Based on the effective medium approximation, we show that by incorporating metallic magnetic nanoparticles into an appropriate insulating matrix and controlling the directions of magnetization of metallic magnetic components and their volume fraction, it may be possible to prepare a composite medium which is left handed for electromagnetic waves propagating in some special direction and polarization in a frequency region near the ferromagnetic resonance frequency. This composite may be easier to make on an industrial scale. In addition, its physical properties may be easily tuned by rotating the magnetization locally. The anisotropic characteristics of this material is discussed. The exactly solvable example of the multilayer system is used to illustrate the results of the effective medium calculation.

3.1 Introduction

In classical electrodynamics, the response (typically frequency dependent) of a material to electric and magnetic fields is characterized by two fundamental quantities, the permittivity ϵ and the permeability μ. The permittivity relates the electric displacement field $\boldsymbol{D}$ to the electric field $\boldsymbol{E}$ through $\boldsymbol{D} = \epsilon\boldsymbol{E}$, and the permeability μ relates the magnetic fields $\boldsymbol{B}$ and $\boldsymbol{H}$ by $\boldsymbol{B} = \mu\boldsymbol{H}$. If we do not take losses into account and treat ϵ and μ as real numbers, according to Maxwell's equations, electromagnetic waves can propagate through a material only if the index of refraction n, given by $(\epsilon\mu)^{1/2}$, is real.

Although all our everyday transparent materials have both positive ϵ and positive μ, from the theoretical point of view, in a medium with ϵ and μ both negative, the index of refraction is also real and electromagnetic waves can also propagate through, moreover, if such media exist, the propagation of waves through them should give rise to several peculiar properties. This was first pointed out by Veselago over 30 years ago [1,1–4]. For example, the cross product of $\boldsymbol{E}$ and $\boldsymbol{H}$ for a plane wave in regular media gives the direction of both propagation and energy flow, and the electric field $\boldsymbol{E}$, the magnetic field

$\boldsymbol{H}$, and the wave vector $\boldsymbol{k}$ form a right-handed triplet of vectors. In contrast, in a medium with ϵ and μ both negative, $\boldsymbol{E} \times \boldsymbol{H}$ for a plane wave still gives the direction of energy flow, but the wave itself (that is, the phase velocity) propagates in the opposite direction, i.e., wave vector $\boldsymbol{k}$ lies in the opposite direction of $\boldsymbol{E} \times \boldsymbol{H}$ for propagating waves. In this case, electric field $\boldsymbol{E}$, magnetic field $\boldsymbol{H}$, and wave vector $\boldsymbol{k}$ form a left-handed triplet of vectors. Recently, progress has been achieved in preparing a "left-handed" material artificially. Following the suggestion of Pendry [1], Smith and coworkers reported that a medium made up of an array of conducting nonmagnetic split ring resonators and continuous thin wires can have both an effective negative permittivity ϵ and negative permeability μ for electromagnetic waves propagating in some special direction and special polarization at microwave frequencies [6]. This is the one of the first experimental realizations of an artificial preparation of a left-handed material. Motivated by this progress, we have investigated the possibility of preparing left-handed materials in another type of system-metallic magnetic granular composites. The idea is that, by incorporating metallic ferromagnetic nanoparticles into an appropriate insulating matrix and controlling the directions of magnetization of metallic magnetic particles and their volume fraction, it may be possible to achieve a composite medium that has simultaneously negative ϵ and negative μ. This idea was based on the fact that on the one hand, the permittivity of metallic particles is automatically negative at frequencies less than the plasma frequency, and on the other hand, the effective permeability of ferromagnetic materials for electromagnetic waves propagating in some particular direction and polarization can be negative at a frequency in the vicinity of the ferromagnetic resonance frequency ω_0, which is usually in the frequency region of microwaves. So, if we can prepare a composite medium in which one component is both metallic and ferromagnetic and other component insulating, and we can control the directions of magnetization of metallic magnetic particles and their volume fraction, it may be possible to achieve a left-handed composite medium for electromagnetic waves propagating in some special direction and polarization. This composite may be easier to make on an industrial scale. In addition, its physical properties may be easily tuned by rotating the magnetization locally.

3.2 Description of "Left-Handed" Electromagnetic Waves: The Effect of the Imaginary Wave Vector

To illustrate the above idea more clearly, we have performed calculations based on the effective medium theory (Bruggeman) [7]. Let us consider an idealized metallic magnetic granular composite consisting of two types of spherical particles, in which one type of particles are metallic ferromagnetic grains of radius R_1, the other type are non-magnetic dielectric (insulating) grains of radius R_2. Each grain is assumed to be homogeneous. The directions of magnetization of all metallic magnetic grains are assumed to be in the same direction. In length scales much larger than the grain sizes, the composite can be considered as a homogeneous magnetic system. The permittivity and permeability of nonmagnetic dielectric grains are both scalars, and will be denoted as ϵ_1 and μ_1. The permittivity of metallic magnetic grains will be denoted as ϵ_2 and will be taken to have a Drude form: $\epsilon_2 = 1 - \omega_p^2/\omega(\omega + \mathrm{i}/\tau)$, where ω_p is the plasma frequency of the metal and τ is a relaxation time. Such a form of ϵ is representative of a variety of metal composites [8]. The permeability of metallic magnetic grains are second-rank tensors and will be denoted as $\hat{\mu}_2$, which can be derived from the Landau–Lifschitz equations [9]. Assuming that the directions of magnetization of all magnetic grains are in the direction of the z-axis, $\hat{\mu}_2$ will have the following form [9]:

$$\hat{\mu_2} = \begin{bmatrix} \mu_a & -\mathrm{i}\mu' & 0 \\ \mathrm{i}\mu' & \mu_a & 0 \\ 0 & 0 & 1 \end{bmatrix}, \tag{3.1}$$

where

$$\mu_a = 1 + \frac{\omega_m(\omega_0 - \mathrm{i}\alpha\omega)}{(\omega_0 - \mathrm{i}\alpha\omega)^2 - \omega^2}, \tag{3.2}$$

$$\mu' = -\frac{\omega_m \omega}{(\omega_0 - \mathrm{i}\alpha\omega)^2 - \omega^2}, \tag{3.3}$$

$\omega_0 = \gamma H_0$ is the ferromagnetic resonance frequency, H_0 is the effective magnetic field in magnetic particles and is a sum of the external magnetic field, the effective anisotropy field and the demagnetization field; $\omega_m = \gamma M_0$, where γ is the gyromagnetic ratio, M_0 is the saturation magnetization of magnetic particles; α is the magnetic damping coefficient; ω is the frequency of incident electromagnetic waves. We shall only consider incident electromagnetic waves propagating in the direction of the magnetization. This is the most interesting case in the study of magneto-optical effects in ferromagnetic materials. We also assume that the grain sizes are much smaller compared with the characteristic wavelength λ, and consequently, electromagnetic waves in the composite can be treated as propagating in a homogeneous magnetic system. According to Maxwell's equations, electromagnetic waves propagating in the direction of magnetization in a homogeneous magnetic material is either positive or negative transverse circularly polarized. If the composite can truly be treated as a homogeneous magnetic system in the case of grain sizes much smaller than the characteristic wavelength, electric and magnetic fields in the composite should also be either positive or negative circularly polarized and can be expressed as :

$$\boldsymbol{E}(\boldsymbol{r}, t) = \boldsymbol{E}_0^{(\pm)} \mathrm{e}^{\mathrm{i}kz - \beta z - \mathrm{i}\omega t}, \tag{3.4}$$

$$\boldsymbol{H}(\boldsymbol{r}, t) = \boldsymbol{H}_0^{(\pm)} \mathrm{e}^{\mathrm{i}kz - \beta z - \mathrm{i}\omega t}, \tag{3.5}$$

where $\boldsymbol{E}_0^{(\pm)} = \hat{x} \mp \mathrm{i}\hat{y}$, $\boldsymbol{H}_0^{(\pm)} = \hat{x} \mp \mathrm{i}\hat{y}$, $k = \mathrm{Real}[k_{\mathrm{eff}}]$ is the effective wave number, $\beta = \mathrm{Im}[k_{\mathrm{eff}}]$ is the effective damping coefficient caused by the eddy current,

$k_{\text{eff}} = k + \text{i}\beta$ is the effective propagation constant. In (3.4) and (3.5) the signs of k and β can both be positive or negative depending on the directions of the wave vector and the energy flow. For convenience we assume that the direction of energy flow is in the positive direction of the z-axis, i.e., we assume $\beta > 0$ in (3.4) and (3.5), but the sign of k still can be positive or negative. In this case, if $k > 0$, the phase velocity and energy flow are in the same directions, and from Maxwell's equation, one can see that the electric and magnetic field $\boldsymbol{E}$ and $\boldsymbol{H}$ and the wave vector $\boldsymbol{k}$ will form a right-handed triplet of vectors. This is the usual case for right-handed materials. In contrast, if $k < 0$, the phase velocity and energy flow are in opposite directions, and $\boldsymbol{E}$, $\boldsymbol{H}$, and $\boldsymbol{k}$ will form a left-handed triplet of vectors. This is just the peculiar case for left-handed materials. So, for incident waves of a given frequency ω, we can determine whether wave propagations in the composite is right handed or left handed through the relative sign changes of k and β. We have determined the effective propagation constant $k_{\text{eff}} = k + \text{i}\beta$ by means of the effective medium approximation [7].

3.3 Electromagnetic Wave Propagations in Homogeneous Magnetic Materials

The details of various kinds of effective medium approximations have been discussed in a series of references [8, 10–13], here we only list the main points. First, if the composite can truly be considered as a homogeneous magnetic system in the case of grain sizes much smaller than the characteristic wavelength, then for waves (positive or negative circularly polarized) propagating through the composite in the direction of magnetization, their propagations can be described by an effective permittivity ϵ_{eff} and an effective permeability μ_{eff}, which satisfy the following relations

$$\int \boldsymbol{D}(\boldsymbol{r}, \omega)\text{e}^{\text{i}k_{\text{eff}}z}\text{d}\boldsymbol{r} = \epsilon_{\text{eff}} \int \boldsymbol{E}(\boldsymbol{r}, \omega)\text{e}^{\text{i}k_{\text{eff}}z}\text{d}\boldsymbol{r}, \tag{3.6}$$

$$\int \boldsymbol{B}(\boldsymbol{r}, \omega)\text{e}^{\text{i}k_{\text{eff}}z}\text{d}\boldsymbol{r} = \mu_{\text{eff}} \int \boldsymbol{H}(\boldsymbol{r}, \omega)\text{e}^{\text{i}k_{\text{eff}}z}\text{d}\boldsymbol{r}, \tag{3.7}$$

where k_{eff} and ω are related by $k_{\text{eff}} = \omega[\epsilon_{\text{eff}}\mu_{\text{eff}}]^{1/2}$. Although these relations are simple and in principle exact, it is very difficult to calculate the integrals in them because the fields in the composite are spatially varying in a random way. One therefore must resort to various types of approximations. The simplest approximation is the effective medium approximation. In this approximation, we calculate the fields in each grain as if the grain were embedded in an effective medium of dielectric constant ϵ_{eff} and magnetic permeability μ_{eff}. Consider, for example, the ith grain. Under the embedding assumption, the electric and magnetic fields incident on the grain are the form of (3.4) and (3.5):

$$\boldsymbol{E}_{\text{inc}} = \boldsymbol{E}_0^{(\pm)} \mathrm{e}^{\mathrm{i}k_{\text{eff}}z - \mathrm{i}\omega t}, \tag{3.8}$$

$$\boldsymbol{H}_{\text{inc}} = \boldsymbol{H}_0^{(\pm)} \mathrm{e}^{\mathrm{i}k_{\text{eff}}z - \mathrm{i}\omega t}, \tag{3.9}$$

where $\boldsymbol{E}_0^{(\pm)} = \hat{x} \mp \mathrm{i}\hat{y}$ and $\boldsymbol{H}_0^{(\pm)} = \hat{x} \mp \mathrm{i}\hat{y}$, corresponding to the positive(+) or negative(−) circularly polarized waves. If the fields inside the grain can be found, then the inside fields can be used to calculate the integral over the grain volume

$$\boldsymbol{I}_i = \int_{v_i} \boldsymbol{E}_i(\boldsymbol{r}, \omega) \mathrm{e}^{\mathrm{i}k_{\text{eff}}z} \mathrm{d}\boldsymbol{r}/v_i, \tag{3.10}$$

$$\boldsymbol{J}_i = \int_{v_i} \boldsymbol{H}_i(\boldsymbol{r}, \omega) \mathrm{e}^{\mathrm{i}k_{\text{eff}}z} \mathrm{d}\boldsymbol{r}/v_i, \tag{3.11}$$

which is required to find the integral in (3.6) and (3.7). For the positive or negative circularly polarized incident waves described by (3.8) and (3.9), the integral $\boldsymbol{I}_i$ and $\boldsymbol{J}_i$ can be written as

$$\boldsymbol{I}_i = (\hat{x} \mp \mathrm{i}\hat{y}) I_i, \tag{3.12}$$

$$\boldsymbol{J}_i = (\hat{x} \mp \mathrm{i}\hat{y}) J_i, \tag{3.13}$$

where I_i and J_i are scalars. If I_i and J_i can be found, then from (3.6) and (3.7), the effective permittivity ϵ_{eff} and effective permeability μ_{eff} can be calculated by

$$\epsilon_{\text{eff}} = \frac{f_1 \epsilon_1 I_1 + f_2 \epsilon_2 I_2}{f_1 I_1 + f_2 I_2}, \tag{3.14}$$

$$\mu_{\text{eff}} = \frac{f_1 \mu_1 J_1 + f_2 \mu_2^{(\pm)} J_2}{f_1 J_1 + f_2 J_2}, \tag{3.15}$$

where f_1 and f_2 are the volume fractions of the two types of grains, μ_1 is the permeability of nonmagnetic dielectric grains, $\mu_2^{(+)} = \mu_a - \mu'$ and $\mu^{(-)} = \mu_a + \mu'$ (see 3.1–3.3) are the effective permeability of magnetic grains for positive and negative circularly polarized waves, respectively. As for the calculation of I_i and J_i, we can follow the method of expanding interior and exterior fields in a multipole series and matching the boundary conditions [14]. After the coefficients of the multipole expansion of interior and exterior fields are obtained by matching the boundary conditions, I_i and J_i can be found and subsequently be substituted into (3.14) and (3.15). Since this method is standard, we shall not present the details. In the final results, (3.14) and (3.15) reduce to one self-consistent equation:

$$\sum_{i=1,2} f_i \sum_{l=1}^{\infty} (2l+1) \left[\frac{(\mu_{\text{s}}/\mu_{\text{eff}}) k_{\text{eff}} \psi_l'(k_i R_i) \psi_l(k_{\text{eff}} R_i) - k_i \psi_l(k_i R_i) \psi_l'(k_{\text{eff}} R_i)}{(\mu_{\text{s}}/\mu_{\text{eff}}) k_{\text{eff}} \psi_l'(k_i R_i) \zeta_l(k_{\text{eff}} R_i) - k_i \psi_l(k_i R_i) \zeta_l'(k_{\text{eff}} R_i)} \right.$$
$$\left. + \frac{k_i \psi_l'(k_i R_i) \psi_l(k_{\text{eff}} R_i) - (\mu_{\text{s}}/\mu_{\text{eff}}) k_{\text{eff}} \psi_l(k_i R_i) \psi_l'(k_{\text{eff}} R_i)}{k_i \psi_l'(k_i R_i) \zeta_l(k_{\text{eff}} R_i) - (\mu_{\text{s}}/\mu_{\text{eff}}) k_{\text{eff}} \psi_l(k_i R_i) \zeta_l'(k_{\text{eff}} R_i)} \right] = 0, \tag{3.16}$$

where R_i is the radius of the ith type of grains, and

$$k_1 = \omega[\epsilon_1 \mu_1]^{1/2}, \tag{3.17}$$

$$k_2 = \omega[\epsilon_2 \mu_2^{(\pm)}]^{1/2}, \tag{3.18}$$

$$\psi_l(x) = x j_l(x), \tag{3.19}$$

$$\zeta_l(x) = x h_l^{(1)}(x), \tag{3.20}$$

$j_l(x)$ and $h_l(x)$ are the usual spherical Bessel and Hankel functions. Equation (3.16) determines the effective product of $(\epsilon\mu)_{\mathrm{eff}}$, or equivalently k_{eff}. This equation was solved numerically [7]. It was found that the relative signs between the real and the imaginary part of the wave vector changes sign near the FMR frequency.

3.4 Some Characteristics of Electromagnetic Wave Propagation in Anisotropic "Left-Handed" Materials

Both our system and that previously studied by the UCSD group are anisotropic in nature. Veselago's original paper and recent theoretical works discussed only the characteristics of electromagnetic wave propagation in isotropic "left-handed" media. In classical electrodynamics, it is well known that the electrodynamic properties of anisotropic materials are significantly different from that of isotropic materials. The simplest and most common form of anisotropy is the uniaxial anisotropy. In this section, we shall show that the characteristics of electromagnetic wave propagation in uniaxial anisotropic "left-handed" media are also significantly different from that in isotropic "left-handed" media.

3.4.1 "Left-Handed" Characteristic of Electromagnetic Wave Propagation in Uniaxial Anisotropic "Left-Handed" Media

For isotropic materials, the permittivity and permeability are both scalars, and if the permittivity and permeability of an isotropic medium are both negative, electromagnetic wave propagation in such a medium would be "left-handed" for any propagation direction. For anisotropic materials, one or both of the permittivity and permeability are second-rank tensors. In this section, we shall discuss in what conditions electromagnetic wave propagation in uniaxially anisotropic media shall be "left-handed." For clarity, we first consider the case that one of the permittivity and permeability is uniaxially anisotropic but the other is isotropic. We assume that the permittivity is isotropic and the permeability is uniaxially anisotropic. In this case, the permittivity is a scalar (denoted as ϵ) and the permeability is a second-rank tensor (denoted as $\hat{\mu}$). For uniaxial anisotropy, $\hat{\mu}$ can be expressed as [10]:

$$\hat{\mu} = \begin{bmatrix} \mu_\perp & 0 & 0 \\ 0 & \mu_\perp & 0 \\ 0 & 0 & \mu_z \end{bmatrix}. \tag{3.21}$$

Consider the propagation of a plane wave of frequency ω with $\boldsymbol{E} = \boldsymbol{E}_0 \mathrm{e}^{\mathrm{i}\boldsymbol{k}\cdot\boldsymbol{r}-\mathrm{i}\omega t}$, $\boldsymbol{H} = \boldsymbol{H}_0 \mathrm{e}^{\mathrm{i}\boldsymbol{k}\cdot\boldsymbol{r}-\mathrm{i}\omega t}$, Maxwell's equations becomes

$$\boldsymbol{k} \times \boldsymbol{E} = \omega\hat{\mu} \cdot \boldsymbol{H}, \tag{3.22}$$

$$\boldsymbol{k} \times \boldsymbol{H} = -\omega\epsilon\boldsymbol{E}. \tag{3.23}$$

Substituting (3.21) into (3.22) and (3.23), one can see that there are two types of linearly polarized plane waves, namely the E-polarized and H-polarized plane waves. The E-polarized plane waves satisfy the conditions $\boldsymbol{k}\cdot\boldsymbol{E} = 0$ and $E_z = 0$, the H-polarized waves satisfy the conditions $\boldsymbol{k}\cdot\boldsymbol{H} = 0$ and $H_z = 0$. Assuming that the wave vector is in the x–z plane, then for the E-polarized plane waves one gets

$$\boldsymbol{E} = E_0 \mathbf{y} \mathrm{e}^{\mathrm{i}\boldsymbol{k}\cdot\boldsymbol{r}-\mathrm{i}\omega t}, \tag{3.24}$$

$$\boldsymbol{H} = \left[-\frac{E_0 k_z}{\omega\mu_\perp}\mathbf{x} + \frac{E_0 k_x}{\omega\mu_z}\mathbf{z}\right] \mathrm{e}^{\mathrm{i}\boldsymbol{k}\cdot\boldsymbol{r}-\mathrm{i}\omega t}, \tag{3.25}$$

where $\mathbf{x}$, $\mathbf{y}$, and $\mathbf{z}$ are unit vectors along the x-, y-, and z-axis. Similarly, the H-polarized waves can be expressed as

$$\boldsymbol{H} = H_0 \mathbf{y} \mathrm{e}^{\mathrm{i}\boldsymbol{k}\cdot\boldsymbol{r}-\mathrm{i}\omega t}, \tag{3.26}$$

$$\boldsymbol{E} = \left[\frac{H_0 k_z}{\omega\epsilon}\mathbf{x} - \frac{H_0 k_x}{\omega\epsilon}\mathbf{z}\right] \mathrm{e}^{\mathrm{i}\boldsymbol{k}\cdot\boldsymbol{r}-\mathrm{i}\omega t}. \tag{3.27}$$

The dispersion relation for the E-polarized waves is determined by

$$\frac{k_x^2}{\mu_z} + \frac{k_z^2}{\mu_\perp} = \omega^2\epsilon \tag{3.28}$$

and the dispersion relation for the H-polarized waves is given by

$$k^2 = \omega^2\epsilon\mu_\perp. \tag{3.29}$$

The energy density current $\boldsymbol{S}$ and its inner product with the wave vector $\boldsymbol{k}$ are given by

$$\begin{aligned} \boldsymbol{S} &= \frac{1}{2}\boldsymbol{E}^* \times \boldsymbol{H} \\ &= \frac{|E_0|^2 k_x}{2\omega\mu_z}\mathbf{x} + \frac{|E_0|^2 k_z}{2\omega\mu_\perp}\mathbf{z}, \end{aligned} \tag{3.30}$$

$$\boldsymbol{k} \cdot \boldsymbol{S} = \frac{1}{2}\omega\epsilon|E_0|^2 \tag{3.31}$$

for E-polarized plane waves, and

$$\boldsymbol{S} = \frac{|H_0|^2 k_x}{2\omega\epsilon}\mathbf{x} + \frac{|H_0|^2 k_z}{2\omega\epsilon}\mathbf{z}, \tag{3.32}$$

$$\boldsymbol{k}\cdot\boldsymbol{S} = \frac{1}{2}\omega\mu_\perp |H_0|^2 \tag{3.33}$$

for H-polarized waves. From (3.24) to (3.32), we can get the following conclusions:

1. From (3.29), we can see that the propagation of the H-polarized waves requires the ϵ and $\mu_\perp$ must have same sign. If ϵ and $\mu_\perp$ are both negative, for any propagation direction, the energy density current $\boldsymbol{S}$ of the H-polarized waves shall be in the exact opposite direction of the wave vector $\boldsymbol{k}$, and $\boldsymbol{E}$, $\boldsymbol{H}$, and $\boldsymbol{k}$ shall form a left-handed triplet of vectors. This can be seen from (3.26) and (3.27) and (3.32) and (3.33). So, if ϵ and $\mu_\perp$ are both negative, the H-polarized waves shall be "left-handed" for any propagation direction. An interesting fact is that μ_z including its sign has no effect on the propagation and the "left-handed" characteristic of the H-polarized waves.
2. If ϵ is and $\mu_\perp$ are both negative, in the direction of the z-axis, the E-polarized waves are exactly "left-handed" if the wave vector $\boldsymbol{k}$ is in the direction of the z-axis, as can be seen from (3.24) and (3.25) and (3.30) and (3.31). But if the wave vector $\boldsymbol{k}$ is not in the direction of the z-axis, the E-polarized waves cannot be exactly "left-handed" but be approximately "left-handed," in the sense that the energy density current $\boldsymbol{S}$ could be in backward but not the exact opposite direction of the wave vector, i.e., the angle between the directions of energy flow and wave vector $\boldsymbol{k}$ is larger than $\pi/2$ but smaller than π, and $\boldsymbol{E}$, $\boldsymbol{H}$, and $\boldsymbol{k}$ form an approximate but not a strict "left-handed" triplet of vectors. Unlike the H-polarized waves, μ_z including its sign have effects on the propagation of the E-polarized waves. From (3.28), (3.30), and (3.31), we can see that if $\epsilon < 0$, $\mu_\perp < 0$, and $\mu_z < 0$, the E-polarized waves can propagate in any direction and be approximately "left-handed." If $\epsilon < 0$, $\mu_\perp < 0$, and $\mu_z > 0$, the E-polarized waves could propagate and be approximately "left-handed" if the angle θ between the wave vector and the z-axis is smaller than $\arctan(|\mu_z/\mu_\perp|)$. If $\theta > \arctan(|\mu_z/\mu_\perp|)$, the E-polarized waves could not propagate since in this case the wave vector $\boldsymbol{k}$ is imaginary.
3. If $\epsilon < 0$ but $\mu_\perp > 0$, the wave vector of the H-polarized waves shall be imaginary for any propagation direction [see (3.29)] no matter what sign μ_z has, hence the H-polarized waves cannot propagate in any direction. For the E-polarized waves, if $\mu_z > 0$, the wave vector is also imaginary as can be seen from (3.28), and hence the E-polarized waves cannot propagate in any direction. If $\mu_z < 0$, the E-polarized waves can propagate if the angle

between the wave vector and the z-axis is larger than $\arctan(|\mu_z/\mu_\perp|)$. In this case the waves are approximately "left-handed" since the angle between the directions of energy flow and wave vector $\boldsymbol{k}$ is larger than $\pi/2$.

4. If $\mu_\perp < 0$ and $\epsilon > 0$, the H-polarized waves cannot propagate in any direction. For the E-polarized waves, if $\mu_z > 0$, the E-polarized waves can propagate if the angle between the wave vector and the z-axis is smaller than $\arctan(|\mu_z/\mu_\perp|)$. In this case, the waves are not "left-handed" since the angle between the directions of energy flow and wave vector $\boldsymbol{k}$ is larger than $\pi/2$.
5. Similar results as shown in (1)–(4) can also be obtained in the case that the permittivity is uniaxial anisotropic and the permeability is isotropic. From these results, we can see that for anisotropic materials, the propagation and the "left-handed" characteristic of electromagnetic waves do not require all elements of the permittivity and the permeability tensors to be of the same sign. This is an important difference between isotropic and anisotropic media. For isotropic media, the propagation of electromagnetic waves require the permittivity and permeability to have the same signs and the media is left-handed only if the permittivity and permeability are both negative.

Next, we discuss the more complicated case that both the permittivity and permeability exhibit uniaxial anisotropy. In this case, the permittivity is also a second-rank tensor having the similar form as $\hat{\mu}$:

$$\hat{\epsilon} = \begin{bmatrix} \epsilon_\perp & 0 & 0 \\ 0 & \epsilon_\perp & 0 \\ 0 & 0 & \epsilon_z \end{bmatrix}. \tag{3.34}$$

Following the same procedure as above, one can see that in this case there are also two types of linearly polarized plane waves, i.e., the E-polarized and the H-polarized plane waves. The E-polarized plane waves also satisfy the condition $\boldsymbol{k} \cdot E = 0$ and $E_z = 0$, the H-polarized plane waves satisfy $\boldsymbol{k} \cdot H = 0$ and $H_z = 0$. The dispersion relation for the E-polarized waves is determined by

$$\frac{k_x^2}{\mu_z} + \frac{k_z^2}{\mu_\perp} = \omega^2 \epsilon_\perp, \tag{3.35}$$

the dispersion relation for the H-polarized waves is determined by

$$\frac{k_x^2}{\epsilon_z} + \frac{k_z^2}{\epsilon_\perp} = \omega^2 \mu_\perp. \tag{3.36}$$

The energy current density $\boldsymbol{S}$ and its inner product with the wave vector $\boldsymbol{k}$ are given by

$$\boldsymbol{S} = \frac{|E_0|^2 k_x}{2\omega\mu_z}\mathbf{x} + \frac{|E_0|^2 k_z}{2\omega\mu_\perp}\mathbf{z}, \tag{3.37}$$

$$\boldsymbol{k} \cdot \boldsymbol{S} = \frac{1}{2}\omega\epsilon_{\perp}|E_0|^2 \tag{3.38}$$

for E-polarized plane waves, and

$$\boldsymbol{S} = \frac{|H_0|^2 k_x}{2\omega\epsilon_z}\mathbf{x} + \frac{|H_0|^2 k_z}{2\omega\epsilon_{\perp}}\mathbf{z}, \tag{3.39}$$

$$\boldsymbol{k} \cdot \boldsymbol{S} = \frac{1}{2}\omega\mu_{\perp}|H_0|^2 \tag{3.40}$$

for H-polarized waves. From (3.35) and (3.36), we can get the following conclusions:

1. If the wave vector $\boldsymbol{k}$ is in the direction of the z-axis, the propagation of both the E- and H-polarized waves require the product of $\epsilon_{\perp}$ and $\mu_{\perp}$ to be positive. In this case, if $\epsilon_{\perp} < 0$ and $\mu_{\perp} < 0$, both the E- and H-polarized waves are "left-handed," and ϵ_z and μ_z do not have effect on the "left-handed" characteristic of both the E- and H-polarized waves.
2. If the propagation is not in the direction of the z-axis, both the E-polarized and H-polarized waves cannot be exactly "left-handed" since in this case the energy flow cannot be in the exact opposite direction of the wave vector if $\mu_{\perp} \neq \mu_z$ and $\epsilon_{\perp} \neq \epsilon_z$. But if some conditions are satisfied, the wave propagation can be approximately "left-handed," i.e., the direction of energy flow is in the backward but not exactly opposite direction of wave vector.
3. The necessary condition for the E-polarized waves being approximately "left-handed" is that $\epsilon_{\perp} < 0$ but it is not necessary that $\mu_{\perp}$ and μ_z are both negative, and ϵ_z has no effect on the propagation of the E-polarized waves. If $\mu_{\perp}$ and μ_z are both negative, the E-polarized waves are approximately "left-handed" no matter what the angle between $\boldsymbol{k}$ and the z-axis is. If $\mu_{\perp} < 0$ and $\mu_z > 0$, the E-polarized waves can propagate only if the angle between $\boldsymbol{k}$ and the z-axis is smaller than $\arctan(|\mu_z/\mu_{\perp}|)$, or else the wave vector is imaginary and the E-polarized waves cannot propagate. Similarly, if $\mu_{\perp} > 0$ and $\mu_z < 0$, the E-polarized waves can propagate also only if the angle between $\boldsymbol{k}$ and the z-axis is smaller $\arctan(|\mu_z/\mu_{\perp}|)$.
4. The necessary condition for the H-polarized waves being approximately "left-handed" is that $\mu_{\perp} < 0$ but it is not necessary that $\epsilon_{\perp}$ and ϵ_z are both negative. If $\epsilon_{\perp}$ and ϵ_z are both negative, the H-polarized waves are approximately "left-handed" no matter what the angle between $\boldsymbol{k}$ and the z-axis is. If $\epsilon_{\perp} < 0$ and $\epsilon_z > 0$, the H-polarized waves can propagate only if the angle between $\boldsymbol{k}$ and the z-axis is smaller than $\arctan(|\epsilon_z/\epsilon_{\perp}|)$, or else the wave vector is imaginary and the E-polarized waves cannot propagate. Similarly, if $\epsilon_{\perp} > 0$ and $\epsilon_z < 0$, the E-polarized waves can propagate also only if the angle between $\boldsymbol{k}$ and the z-axis is smaller $\arctan(|\epsilon_z/\epsilon_{\perp}|)$.

3.4.2 Characteristics of Refraction of Electromagnetic Waves at the Interfaces of Isotropic Regular Media and Anisotropic “Left-Handed” Media

When a beam of light passes from one regular medium into a second regular medium, the ray undergoes refraction at the interface between the two media, and the refracted ray should bent toward the normal of the interface but never emerge on the same side of the normal as the incident ray (Snell’s law). Veselago predicted that if the second medium is an isotropic “left-handed” medium, the refracted ray should lie on the same side of the normal of the interface as the incident ray due to the “left-handed” characteristic of the refracted waves in the second medium [2]. This anomalous refraction is one of the most interesting peculiar properties of isotropic “left-handed” media and has been verified experimentally very recently [6]. It has been shown that this anomalous refraction could lead to some strange optics [1, 17, 28]. In this section, we discuss the characteristics of refraction when a beam of light passing from one isotropic regular medium into another uniaxial anisotropic “left-handed” medium. In what follows we shall only discuss the case that both the permittivity and the permeability of the second medium are uniaxially anisotropic with the forms of (3.21) and (3.34). The results for the case that either the permittivity or the permeability is isotropic can be obtained similarly.

Before we discuss whether the refraction is ordinary or anomalous, we shall first discuss under what conditions the incident waves shall be refracted or totally reflected in the case that some of the elements of the permittivity and(or) permeability tensors of the second medium are negative. In the following we denote the permittivity and permeability of the isotropic regular media as ϵ_1 and μ_1(both positive) and denote the wave vectors of the incident waves as $\boldsymbol{k} = k_x\mathbf{x} + k_z\mathbf{z}$ and the incident angles as θ. The wave vectors of the refracted waves are denoted as $\boldsymbol{k}' = k'_x\mathbf{x} + k'_z\mathbf{z}$ and the refraction angles with respect to the surface normal are denoted as ϕ. The refracted waves satisfy the following boundary conditions whether or not the second medium is regular or “left-handed”

$$\boldsymbol{n} \times \boldsymbol{E}_1 = \boldsymbol{n} \times \boldsymbol{E}_2, \quad \boldsymbol{n} \cdot \boldsymbol{D}_1 = \boldsymbol{n} \cdot \boldsymbol{D}_2, \tag{3.41}$$

$$\boldsymbol{n} \times \boldsymbol{H}_1 = \boldsymbol{n} \times \boldsymbol{H}_2, \quad \boldsymbol{n} \cdot \boldsymbol{B}_1 = \boldsymbol{n} \cdot \boldsymbol{B}_2. \tag{3.42}$$

It follows from (3.41) and (3.42) that the refracted waves shall maintain the same polarization (E or H) as the incident waves, and the x and y components of the wave vector of the refracted waves is equal to that of the incident waves, i.e, $k'_x = k_x$. Then from (3.35) and (3.36), the z component of the wave vector of the refracted waves can be obtained by

$$k_z'^{\,2} = \omega^2\epsilon_\perp\mu_\perp - \frac{\mu_\perp}{\mu_z}k_x^2 \tag{3.43}$$

for E-polarized incident waves, and

$$k_z'^{\,2} = \omega^2 \epsilon_\perp \mu_\perp - \frac{\epsilon_\perp}{\epsilon_z} k_x^2 \tag{3.44}$$

for H-polarized incident waves. One necessary condition for the occurrence of refraction is that k_z' must be real, or else the incident waves shall be totally reflected. This requires that the incident angle $\theta = \tan^{-1} k_x/k_z$ should satisfy the following inequality

$$\frac{\mu_\perp}{\mu_z} \sin^2\theta < \frac{\epsilon_\perp \mu_\perp}{\epsilon_1 \mu_1} \tag{3.45}$$

for E-polarized incident waves, and

$$\frac{\epsilon_\perp}{\epsilon_z} \sin^2\theta < \frac{\epsilon_\perp \mu_\perp}{\epsilon_1 \mu_1} \tag{3.46}$$

for H-polarized incident waves. From (3.43) and (3.44), we can see that:

1. For E-polarized incident waves, if $\mu_\perp/\mu_z$ is positive, the occurrence of refraction requires that $\epsilon_\perp \mu_\perp$ is also positive and the incident angle θ must be smaller than a critical angle $\theta_\mathrm{c} = \arcsin \sqrt{\frac{\epsilon_\perp \mu_z}{\epsilon_1 \mu_1}}$, or else the incident waves shall be totally reflected. If $\mu_\perp/\mu_z$ is negative, $\epsilon_\perp \mu_\perp$ can be either positive or negative. In this case, if $\epsilon_\perp \mu_\perp$ is positive, for any incident angle, the incident waves shall be refracted. If $\epsilon_\perp \mu_\perp$ is negative, the incident angle θ must be *larger* than $\arcsin \sqrt{\frac{|\epsilon_\perp \mu_z|}{\epsilon_1 \mu_1}}$, or else the incident waves shall be totally reflected.
2. For H-polarized incident waves, if $\epsilon_\perp/\epsilon_z$ is positive, the occurrence of refraction requires that $\epsilon_\perp \mu_\perp$ is also positive and the incident angle θ must be small than $\theta_\mathrm{c} = \arcsin \sqrt{\frac{\mu_\perp \epsilon_z}{\epsilon_1 \mu_1}}$, or else the incident ray shall be totally reflected. If $\epsilon_\perp/\epsilon_z$ is negative, $\epsilon_\perp \mu_\perp$ can be either positive or negative. In this case, if $\epsilon_\perp \mu_\perp$ is positive, refraction will occur for any incident angle. If $\epsilon_\perp \mu_\perp$ is negative, the occurrence of refraction shall require the incident angle θ must be *larger* than $\arcsin \sqrt{\frac{|\mu_\perp \epsilon_z|}{\epsilon_1 \mu_1}}$.
3. From these results, we can see that in the case that some of the elements of the permittivity and(or) permeability tensors of the second medium are negative, the incident waves may be totally reflected if the incident angle is smaller but not larger than a critical incident angle. This is a very interesting peculiar characteristic which should never occur if the second media are regular materials.

Now we discuss under what conditions anomalous refraction shall occur. For a plane incident wave, whether the refraction is ordinary or anomalous depends on the direction of energy flow of the refracted waves, or equivalently, the signs of the x and z components of energy density current $\boldsymbol{S}$ of the refracted waves. Causality requires that in the second medium, energy current should be transmitted away from the interface of two media but never toward the interface. This requires that in the second medium the z component of energy density current $\boldsymbol{S}$ must be always positive, and in order to keep the sign of S_z always negative, the z components of the wave vectors of the refracted waves can be either positive or negative and shall be determined by the signs of $\epsilon_\perp$ and $\mu_\perp$, as can be seen from (3.37) and (3.39). Unlike the z component of energy current density $\boldsymbol{S}$, the x component of energy density current $\boldsymbol{S}$ of the refracted waves need not necessarily be negative. Since S_z is always positive, if $S_x > 0$, the refracted ray shall lie on the opposite side of the normal of the interface of two media as incident ray and the refraction shall be ordinary. If $S_x < 0$, the refracted ray shall lie on the opposite side of the normal of the interface of two media as incident ray and the refraction shall be anomalous. Considering that the x components of the wave vectors of the refracted waves always maintain the same direction as the incident waves due to the boundary condition, then from (3.37)-(3.40), we can obtain the following conclusions:

1. For E-polarized incident waves, the occurrence of anomalous refraction requires that $\mu_z < 0$ but does not necessarily require that other elements of the permittivity and(or) permeability tensors are also negative. From (3.37, we can see that if $\mu_z > 0$, then $S_x > 0$, and the refracted ray shall lie on the opposite side of the normal of the interface of two media; if $\mu_z < 0$, then $S_x < 0$, and the refracted ray shall lie on the same side of the normal of the interface. *In the case that the second medium is anisotropic, the system is not "left-handed" even if the refraction is anomalous, as is described in the previous section.* For example, if $\mu_z < 0$ and $\epsilon_\perp > 0$, then from (3.37) and (3.38), we can see that $S_x < 0$ and $\boldsymbol{k} \cdot \boldsymbol{S} > 0$. In this case the refraction is anomalous but the refracted ray is not "left-handed" since in this case the energy flow is the forward but not the backward direction of the wave vector.
2. For H-polarized incident waves, the occurrence of anomalous refraction requires that $\epsilon_z < 0$ but the other elements of the permittivity and(or) permeability tensors need not be also negative. From (3.39), we can see that if $\epsilon_z < 0$, then $S_x < 0$, and the refracted ray shall lie on the same side of the normal of the interface of two media. Like E-polarized incident waves, in the case that the second medium is anisotropic, the refracted waves are not necessarily "left-handed" even if the refraction is anomalous. For example, if $\epsilon_z < 0$ and $\mu_\perp > 0$, from (3.39)-(3.40), we can see that $S_x < 0$ but $\boldsymbol{k} \cdot \boldsymbol{S} > 0$. In this case the refraction is anomalous but the refracted waves are not "left-handed."
3. If the incident rays are not either E-polarized or H-polarized, there shall be two refracted rays with different propagation directions, and one ray is E-polarized and the other ray is H-polarized. In this case, if μ_z and ϵ_z are both negative, the two refracted rays shall both lie on the same side of the normal of the interface as the incident rays. If one of μ_z and ϵ_z is negative, one refracted ray shall lie on the opposite side of the normal of

the interface but the other refracted ray shall lie on the same side of the normal as incident ray. If μ_z and ϵ_z are both positive, the two refracted rays shall both lie on the opposite site of the normal of the interface of two media as the incident ray.

3.5 Multilayer Structures Left-Handed Material: An Exact Example

In this section, we examine ferromagnet insulator multilayer structures as left-handed materials. In multilayer structures, the propagation of electromagnetic waves can be exactly analytically calculated. This will provide us with some assessment of different approximations that has been used in this area.

We found that when the wave vector is parallel (perpendicular) to the layers, the square of the phase velocity is inversely proportional to $\langle\mu\rangle_{\mathrm{a}}\langle\epsilon\rangle_{\mathrm{h}}$ ($\langle\epsilon\rangle_{\mathrm{a}}\langle\mu\rangle_{\mathrm{a}}$), where the angular brackets with subscripts a, h stand for the arithmetic and the harmonic mean, respectively. *Different* averages of ϵ and μ come into play. For example: $\langle\epsilon\rangle_{\mathrm{a}} = c_m\epsilon_m + c_i\epsilon_i$, $1/\langle\epsilon\rangle_{\mathrm{h}} = c_m/\epsilon_m + c_i/\epsilon_i$ where c_j stands for the volume fraction of component j. $\langle\epsilon\rangle_{\mathrm{a}}$ is of the same order of magnitude of the metal dielectric constant, whereas $\langle\epsilon\rangle_{\mathrm{h}}$ is of the order of magnitude of the insulator dielectric constant. These two are very different. The different averages of the dielectric constant obtained here in the long wavelength limit is very similar to the "form birefringence" discussed by Born and Wolf [18]. The form birefringence focuses on the dielectric constants only. Here we have included the magnetic susceptibility at the same time. We now explain our results in detail.

We begin by considering the propagation of electromagnetic waves in the multilayer structure consisting of periodic arrays of two materials of thicknesses d_m, d_i with $d = d_m + d_i$. The dielectric constant and the magnetic permeability of the two components are denoted by ϵ_m, μ_m (ϵ_i, μ_i). There are two types of eigenstates for Maxwell's equation: the H (E) polarization where the macroscopic magnetic field H (electric field E) is perpendicular to the wave vector and parallel to the layers. Our goal is to derive the dispersion relationships of the radiation for these two polarizations in the long wavelength limit. For the H (E) polarization we denote the direction of $\mathbf{H}$ ($\mathbf{E}$) as the y-direction and the normal to the multilayers as the x-direction. Any wavevector $\mathbf{k}$ can be decomposed into a component perpendicular to the planes and a component parallel to the planes. The wave vector is in the xz plane with $\mathbf{k} = (k_x, 0, k_z)$. There is no y component because the wave vector is perpendicular to the direction of $\mathbf{H}$ ($\mathbf{E}$). The frequency of the radiation will be denoted by ω. We define a "vacuum wave vector" $k_0 = \omega/c$ where c is the speed of light.

To calculate the dispersion we solve Maxwell's equation in each of the components separately. The solution is then matched across the boundary [19,20]. The solution of Maxwell's equation in each region $j = m, i$ can be written in separable form as $E_{zj} = V_j(x)\exp(\mathrm{i}k_z z)$, $H_{yj} = X_j(x)\exp(\mathrm{i}k_z z)$ for the H polarization and $H_{zj} = V_j(x)\exp(\mathrm{i}k_z z)$, $E_{yj} = X_j(x)\exp(\mathrm{i}k_z z)$ for the E polarization. The wave vector k_z, the component of the wave vector parallel to the planes, is the same in both regions. The functions V, X are linear combinations of plane wave solutions. $X_j = A_j\cos(p_j x') + B_j\sin(p_j x')$, $V_j = \mathrm{i}[-p_j A_j \sin(p_j x') + p_j B_j \cos(p_j x')]/(k_0\tau_j)$, where $p_j = (\epsilon_j \mu_j k_0^2 - k_z^2)^{0.5}$. $\tau_j = \epsilon_j$ $(-\mu_j)$ for the H (E) polarization. $x' = x$ for $0 < x < d_m$, $x' = x - d_m$ for $d_m < x < d_i + d_m$. The constant coefficients A_j, B_j can be determined from the continuity of the tangential components of E and H across the boundaries and the "periodic boundary condition": $E(x+d) = \exp(\mathrm{i}k_x d)E(x)$, $H(x+d) = \exp(\mathrm{i}k_x d)H(x)$. Across the first interface, we get from the continuity conditions

$$\begin{bmatrix} X_m(x=d_m) \\ V_m(x=d_m) \end{bmatrix} = \mathbf{T}(p_m, d_m, \tau_m) \begin{bmatrix} X_m(x=0) \\ V_m(x=0) \end{bmatrix},$$

where

$$\mathbf{T}(p,d,\tau) = \begin{bmatrix} \cos(pd) & -\mathrm{i}\sin(pd)\tau k_0/p \\ -\mathrm{i}\sin(pd)p/\tau k_0 & \cos(pd) \end{bmatrix}.$$

From the "periodic boundary condition," we get

$$\begin{aligned} \begin{bmatrix} X_i(d) \\ V_i(d) \end{bmatrix} &= \exp[\mathrm{i}\,\mathrm{d}k_x] \begin{bmatrix} X_i(0) \\ V_i(0) \end{bmatrix} = \mathbf{T}(p_i, d_i, \tau_i) \begin{bmatrix} X_i(d_m) \\ V_i(d_m) \end{bmatrix} \\ &= \mathbf{T}(p_i, d_i, \tau_i) \begin{bmatrix} X_m(d_m) \\ V_m(d_m) \end{bmatrix}. \end{aligned}$$

From the above equations, we obtain an eigenvalue problem:

$$\begin{bmatrix} X_i(0) \\ V_i(0) \end{bmatrix} = \exp[-\mathrm{i}\,\mathrm{d}k_x]\mathbf{T}(p_i, d_i, \tau_i)\mathbf{T}(p_m, d_m, \tau_m) \begin{bmatrix} X_i(0) \\ V_i(0) \end{bmatrix}.$$

Simplifying the algebra [21], we obtain finally the eigenvalue equation

$$\begin{aligned} \cos(k_x d) &= \cos\phi_i \cos\phi_m \\ &\quad - 0.5[\kappa p_i/p_m + p_m/(p_i\kappa)]\sin\phi_i \sin\phi_m, \end{aligned} \tag{3.47}$$

where $\phi_j = p_j d_j$, $\kappa = \tau_m/\tau_i$. The corresponding eigenvector is given by

$$A_m = 1, \tag{3.48}$$

$$B_m = \mathrm{i}W_0 \tau_m k_0/p_m, \tag{3.49}$$

where

$$W_0 = [\exp(\mathrm{i}k_x d) - M]/N.$$

$$M = \cos(\phi_m)\cos(\phi_i) - p_m\tau_i \sin(\phi_i)\sin(\phi_m)/(\tau_m p_i),$$

$$N = \mathrm{i}k_0[\cos(\phi_m)\sin(\phi_i)\tau_i/p_i + \cos(\phi_i)\sin(\phi_m)\tau_m/p_m].$$

$$A_i = U_1, \tag{3.50}$$

$$B_i = \mathrm{i}W_1 \tau_i k_0 / p_i, \tag{3.51}$$

where $U_1 = \cos(p_m d_m) + \mathrm{i}W_0 \tau_m k_0 \sin(p_m d_m)/p_m$, $W_1 = V_0 \cos(p_m d_m) + \mathrm{i}p_m \sin(p_m d_m)/(\tau_m k_0)$.

We next examine these results in the long wavelength limit with $p_j d_j \ll 1$. Using the approximation $\cos(x) \approx 1 - x^2/2$, $\sin(x) \approx x$ we get from (3.47) after some algebra

$$\begin{aligned} &k_z^2(d_i\sqrt{\kappa} + d_m/\sqrt{\kappa}) + (k_x d)^2/(d_i/\sqrt{\kappa} + d_m\sqrt{\kappa}) \\ &\qquad = k_0^2(\mu_i \epsilon_i d_i \sqrt{\kappa} + \mu_m \epsilon_m d_m/\sqrt{\kappa}). \end{aligned} \tag{3.52}$$

Putting in the expression for κ and simplifying, we get for the H polarization

$$k_z^2/\langle\epsilon\rangle_\mathrm{h} + k_x^2/\langle\epsilon\rangle_\mathrm{a} = k_0^2 \langle\mu\rangle_\mathrm{a}, \tag{3.53}$$

where the angular brackets with a subscript "a" stands for the arithmetic mean: $\langle\epsilon\rangle_\mathrm{a} = (d_m\epsilon_m + d_i\epsilon_i)/d$, $\langle\mu\rangle_\mathrm{a} = (d_m\mu_m + d_i\mu_i)/d$. Similarly, angular brackets with a subscript "h" stands for the harmonic mean: $1/\langle\epsilon\rangle_\mathrm{h} = (d_m/\epsilon_m + d_i/\epsilon_i)/d$.

For the E polarization, one interchanges ϵ with μ. From (3.53), we get the long wavelength dispersion:

$$k_z^2/\langle\mu\rangle_\mathrm{h} + k_x^2/\langle\mu\rangle_\mathrm{a} = k_0^2 \langle\epsilon\rangle_\mathrm{a}. \tag{3.54}$$

The system is also anisotropic. The real part of $\langle\epsilon\rangle_\mathrm{a}$ is negative. In this long wavelength limit the corresponding eigenvector becomes

$$A_m = 1,\ B_m = \mathrm{i}V_0 \tau_m k_0/p_m, \tag{3.55}$$

where $V_0 = [1 + \mathrm{i}k_x d - M]/N$. $M = 1 - (p_m d_m)^2/2 - (p_i d_i)^2/2 - p_m^2 \tau_i d_i d_m/\tau_m$, $N = \mathrm{i}k_0[1 - (p_m d_m)^2/2] d_i \tau_i + [1 - (p_i d_i)^2/2] d_m \tau_m$. $V_0 = k_x/[k_0 < \tau >_\mathrm{a}]$. $B_m = \mathrm{i}k_x \tau_m/[p_m < \tau >_\mathrm{a}]$.

$A_i = U_1$, $B_i = \mathrm{i}V_1 \tau_i k_0/p_i$, where $U_1 = 1 - (p_m d_m)^2/2 + \mathrm{i}V_0 \tau_m k_0 d_m$, $V_1 = V_0[1 - (p_m d_m)^2/2] + \mathrm{i}p_m^2 d_m/(\tau_m k_0)$ $V_1 = k_x/[k_0 < \tau >_\mathrm{a}]$ $U_1 = 1$, $A_i = 1$, $B_i = ik_x \tau_i/[p_i < \tau >_\mathrm{a}]$. To summarize

$$X_m = \cos(p_m x) + \mathrm{i}k_x \tau_m \sin(p_m x)/[p_m \langle\tau\rangle_\mathrm{a}], \tag{3.56}$$

$$X_i = \cos(p_i x') + \mathrm{i}k_x \tau_i \sin(p_i x')/[p_i \langle\tau\rangle_\mathrm{a}]. \tag{3.57}$$

We next look at the Poynting vector of the system. We first discuss the case of the H polarization. We get,

$$\boldsymbol{H_j} = H_0 \mathbf{y} \mathrm{e}^{\mathrm{i}k_z z - \mathrm{i}\omega t} X_j(x), \tag{3.58}$$

$$\boldsymbol{E_j} = H_0 \left[\frac{k_z}{k_0 \epsilon_j} \mathbf{x} X_j(x) + \mathrm{i}\frac{1}{k_0 \epsilon_j} \mathbf{z} X_j'(x)\right] \mathrm{e}^{\mathrm{i}k_z z - \mathrm{i}\omega t} \tag{3.59}$$

The corresponding Poynting vector $\mathbf{S}_j = \mathbf{E}_j \times \mathbf{H}^*{}_j$ is given by (as usual [22], it is the real part of this expression that is of interest)

$$\boldsymbol{S_j} = H_0^2 \left(-\frac{\mathrm{i} X_j^* X_j'}{2k_0\epsilon_j}\mathbf{x} + \frac{|X_j|^2 k_z}{2k_0\epsilon_j}\mathbf{z} \right),$$

X_j is a function of the spatial variable x. We calculate the mean Poynting vector by averaging expressions involving X_m, X_m' (X_i, X_i') in the interval $0 < x < d_m$ ($d_m < x < d + m + d_i$). From (3.53) and (3.57), we can calculate the averages of expressions involving the function X: $\langle |X|^2 \rangle = 1$, $\langle X^* X' \rangle = \mathrm{i} k_x \tau / \langle \tau \rangle_\mathrm{a}$,

The Poynting vector in the corresponding region is

$$\boldsymbol{S_j} = H_0^2 \left(\frac{k_x}{2k_0\langle\epsilon\rangle_\mathrm{a}}\mathbf{x} + \frac{k_z}{2k_0\epsilon_j}\mathbf{z} \right),$$

Averaging over the two types of layers, we get

$$\boldsymbol{S} = H_0^2 \left(\frac{k_x}{2k_0\langle\epsilon\rangle_\mathrm{a}}\mathbf{x} + \frac{k_z}{2k_0\langle\epsilon\rangle_h}\mathbf{z} \right). \tag{3.60}$$

This Poynting vector is parallel (antiparallel) to the normal of the constant ω contour, $\partial\omega/\partial\mathbf{k}$, if $\langle\mu\rangle_\mathrm{a}$ is positive (negative). If the imaginary part of the susceptibilities are small so that the wave vector is mostly real, the dot product of the wave vector and the Poynting vector is given by

$$\boldsymbol{k}^* \cdot \boldsymbol{S} \approx \frac{1}{2} k_0 \langle\mu\rangle_\mathrm{a} |H_0|^2. \tag{3.61}$$

Thus if we can find a material with a negative average $\langle\mu\rangle_\mathrm{a}$, Real$[\mathbf{k}^* \cdot \mathbf{S}] < 0$, the system will be left handed. This may be achievable with ferromagnetic materials above the ferromagnetic resonance frequency. We shall come back to this point later.

We next discuss the case of the E polarization. The electric and magnetic fields are given by

$$\boldsymbol{E_j} = E_0 \mathbf{y} \mathrm{e}^{\mathrm{i}k_z z - \mathrm{i}\omega t} X_j(x), \tag{3.62}$$

$$\boldsymbol{H_j} = E_0 \left[-\frac{k_z}{k_0\mu_j}\mathbf{x} X_j(x) - \mathrm{i}\frac{1}{k_0\mu_j}\mathbf{z} X_j'(x) \right] \mathrm{e}^{\mathrm{i}k_z z - \mathrm{i}\omega t}. \tag{3.63}$$

The Poynting vector is now given by

$$\boldsymbol{S_j} = E_0^2 \left(-\frac{\mathrm{i} X_j^* X_j'}{2k_0\mu_j}\mathbf{x} + \frac{|X_j|^2 k_z}{2k_0\mu_j}\mathbf{z} \right).$$

Substituting in the average of the function X_j, we get

$$\boldsymbol{S_j} = E_0^2 \left(\frac{k_x}{2k_0\langle\mu\rangle_\mathrm{a}}\mathbf{x} + \frac{k_z}{2k_0\mu_j}\mathbf{z} \right).$$

Averaging over the two components we get

$$\boldsymbol{S} = |E_0|^2 \left(\frac{k_x}{2k_0\langle\mu\rangle_\mathrm{a}}\mathbf{x} + \frac{k_z}{2k_0\langle\mu\rangle_\mathrm{h}}\mathbf{z} \right), \tag{3.64}$$

$$\boldsymbol{k}^* \cdot \boldsymbol{S} = \frac{1}{2}k_0\langle\epsilon\rangle_\mathrm{a}|E_0|^2. \tag{3.65}$$

The Poynting vector is again anisotropic. The same results are obtained if one approximates the multilayer system as an anisotropic homogeneous system [23]. If the imaginary part $\langle\epsilon\rangle_\mathrm{a}$ is small $\mathrm{Re}[\mathbf{k}^* \cdot \mathbf{S}] < 0$.

We close with a discussion of how to make $\langle\mu\rangle_\mathrm{a}$ negative. The obvious choice is to use a ferromagnetic metal as one of the components of the multilayer system [7, 24, 25]. When the magnetization is aligned along the z-direction, the magnetic susceptibility of a ferromagnet is a tensor given by (3.1)–(3.3). It is still possible to solve Maxwell's equations for the multilayer system analytically. The results are algebraically complicated and not very illuminating physically. Here we consider the case when the remanent magnetization of the ferromagnet is zero. The system consists of domains with the magnetization forced by the shape anisotropy to lie in the yz plane but otherwise randomly oriented. For frequencies of the order of GHz, the domain size is usually much less than the wavelength. The magnetic susceptibility can be obtained by averaging $\hat{\mu}_\mathrm{F}$ over the different orientations of the magnetizations of the domains. The resulting magnetic susceptibility becomes diagonal but anisotropic [26]:

$$\hat{\mu}_{\mathbf{M}=0} = \begin{bmatrix} \mu_d & 0 & 0 \\ 0 & \mu_{yz} & 0 \\ 0 & 0 & \mu_{yz} \end{bmatrix}, \tag{3.66}$$

where $\mu_{yz} = (\mu_d + 1)/2$. It is still possible to solve analytically Maxwell's equation. For the H polarization, the magnetic susceptibility μ_m is now replaced by μ_{yz}. Above the ferromagnetic resonance frequency ω_0, if μ_d becomes negative enough that $\langle\mu\rangle_\mathrm{a}$ is also negative, then the system can be considered a left-handed material.

For the E polarization,

$$\boldsymbol{E} = E_0\mathbf{y}\mathrm{e}^{\mathrm{i}k_z z - \mathrm{i}\omega t}X(x), \tag{3.67}$$

$$\boldsymbol{H} = E_0 \left[-\frac{k_z}{k_0\mu_d}\mathbf{x}X(x) - \mathrm{i}\frac{1}{k_0\mu_{yz}}\mathbf{z}X'(x) \right] \mathrm{e}^{\mathrm{i}k_z z - \mathrm{i}\omega t}. \tag{3.68}$$

Now $p_m = (k_0^2\epsilon_m\mu_{yz} - k_z^2\mu_{yz}/\mu_d)^{0.5}$, $\tau_m = \mu_{yz}$. The functional form for the dispersion, (3.54), remains the same except now the different averages of the magnetic susceptibilities involve different components of the tensor: $1/\langle\mu\rangle_\mathrm{h} = c_i/\mu_i + c_m/\mu_d$; $\langle\mu\rangle_\mathrm{a} = c_i\mu_i + c_m\mu_{yz}$. The conclusions reached previously remain qualitatively unchanged.

In this paper we have assumed that $k_j d_j \ll 1$. Typically, in multilayers d_j can easily be made to be of the order of 10 Å. k_j is of the order of

$2\pi(\epsilon)^{0.5}/(wavelength)$. For microwaves with wavelengths of the order of millimeters (10^6 Å), ϵ is of the order of 10^5 [27], no matter what the angle of incidence is, the largest value of $kd \approx 10^{-2}$. For infrared radiation, the wavelength is of the order of micrometer (10^4 Å) and ϵ is of the order of 10. Again, for all possible angle of incidence, the largest possible $kd \approx 10^{-3}$. Thus at different frequencies our condition can be easily satisfied. The transmission in these types of systems can be estimated from the reflectivity previously calculated [20]. In the infrared, for a Cu–Ge system, the reflectivity can be made as low as 10%. For a thin enough system, a high transmission of 90% can be obtained. Typical interface roughness is of the order of Angstroms, whereas the wavelengths of interest is more than thousands of Angstroms. The interface roughness is much less than a wavelength.

STC is partly supported by the NSF, ZL, and LZ are partly supported by the Chinese NSF.

References

1. J.B. Pendry, A.J. Holden, W.J. Stewart, I. Youngs, Phys. Rev. Lett. **76**, 4773 (1996)
2. R.H. Ritchie, A. Howie, Philos. Mag. A **44**, 931 (1981)
3. T.L. Ferrell, P.M. Echenique, Phys. Rev. Lett. **55**, 1526 (1985)
4. A.W. Howie, C.A. Walsh, Microsc. Microanal. Microstruct. **2**, 171 (1991)
5. V.G. Veselago, Sov. Phys. Usp. **10**, 509 (1968)
6. D.R. Smith, W.J. Padilla, D.C. Vier, S.C. Nemet-Nasser, S. Schultz, Phys. Rev. Lett. **67**, 3578 (2000)
7. S.T. Chui, L.B. Hu, Phys. Rev. B **65**, 144407 (2002)
8. R. Burridge, S. Childress, G. papanicolaou (eds.), *Macroscopic Properties of Disordered Media* (Springer, Berlin Heidelberg New York, 1982)
9. C.P. Slichter, *Principle of Magnetic Resonance* (Springer, Berlin Heidelberg New York, 1978)
10. J.C. Garland, D.B. Tanner (eds.), *Electrical Transport and Optical Properties of Inhomogeneous Media* (American Institute of Physics, New York, 1978)
11. D. Stroud, F.P. Pan, Phys. Rev. B **20**, 455 (1979)
12. P. Sheng, Phys. Rev. Lett **45**, 60 (1980)
13. W. Lamb, D.M. Wood, N.W. Ashcroft, Phys. Rev. B **21**, 2248 (1980)
14. H.C. Van de Hulst, *Light Scattering by Small Particles*, chap. 9 (Dover, New York, 1981); J.D. Jackson, *Classical Electrodynamics*, 2nd ed. (Wiley, New York, 1975)
15. L.D. Landau, E.M. Lifshitz, *Electrodynamics of Continuous Media*, chap. 11 (Pergamon, Oxford, 1960)
16. J.B. Pendry, Phys. Rev. Lett. **85**, 3966 (2000)
17. D.R. Smith, N. Kroll, Phys. Rev. Lett. **85**, 2933 (2000)
18. M. Born, E. Wolf, *Principles of Optics*, 7th edn. (Cambridge University Press, Cambridge, 1999), p. 837
19. P. Sheng, R.S. Stepleman, P.N. Sanda, Phys. Rev. B **26**, 2907 (1982)
20. S.T. Chui, M.Y. Zhou, P. Sheng, Z. Chen, J. Appl. Phys. **69**, 3366 (1989)

21. Define a matrix $U = T(p_i, d_i, \tau_i)T(p_m, d_m, \tau_m)$. One can show by direct computation that the determinant of the matrix U is 1. The eigenvalue equation $det(U - \lambda) = 0$ reduces to a quadratic equation $\lambda^2 - 2z\lambda + 1 = 0$, where z is the right-hand side of Eq. (1). The solution of this equation is $\lambda = z \pm (z^2 - 1)^{0.5}$. If one calls $z = \cos kl$, then $\lambda = \exp(\pm ikl)$, as claimed
22. J.D. Jackson, *Classical Electrodynamics*, section 6.9, 3rd edn. (Wiley, New York, 1999)
23. L.B. Hu, S.T. Chui, Phys. Rev. B **66**, 085108 (2002); L. Zhou, C.T. Chan, P. Sheng, Phys. Rev. B **68**, 115424 (2003)
24. R.X. Wu, X.K. Zhang, Z.F. Lin, S.T. Chui, J.Q. Xiao, J. Magn. Magn. Mater. **271**(2–3), 180–183 (2004)
25. S.T. Chui, L.B. Hu, Z.F. Lin, Phys. Lett. A **319**, 85 (2003)
26. This result is obtained from the condition that the matrix becomes diagonal and the trace of the submatrix is invariant under rotation.
27. M.A. Ordal et al., Appl. Opt. **22**, 1099 (1983)

4

Spatial Dispersion, Polaritons, and Negative Refraction

V.M. Agranovich and Yu.N. Gartstein

Summary. Negative refraction occurs at an interface as a natural consequence of negative group velocity waves in one of the interfacing media. We briefly comment on the history of this understanding of the phenomenon. Several physical systems are discussed that may be capable of exhibiting normal electromagnetic waves (polaritons) with negative group velocities at optical frequencies. These systems are analyzed in a unified way on the basis of a framework provided by spatial dispersion. This framework utilizes the notion of the generalized dielectric tensor $\varepsilon_{ij}(\omega, \boldsymbol{k})$ representing the electromagnetic response of the medium to perturbations of frequency ω and wave vector $\boldsymbol{k}$. Polaritons with negative group velocity can occur in the medium (whether in natural materials or in artificial metamaterials) when spatial dispersion is strong enough. Our examples include both chiral and nonchiral systems, and bulk and surface polariton waves. We also discuss the relationship between the spatial dispersion approach and the more familiar description based on the dielectric permittivity $\varepsilon(\omega)$ and magnetic permeability $\mu(\omega)$.

4.1 Introduction

In this chapter the phenomenon of negative refraction (NR) is discussed in terms of the dispersion $\omega(\boldsymbol{k})$ of *polaritons*, namely normal electromagnetic waves propagating in the medium. Our focus will be on the case of a macroscopically uniform and isotropic medium with negligible dissipation, where the basic physics is especially transparent. In this context, "macroscopically" means on the scale of the wavelength λ of the waves in the medium. In an isotropic medium, the frequency ω of the wave is a function of the magnitude $k = |\boldsymbol{k}|$ of the wave vector $\boldsymbol{k}$ and, therefore, the group velocity of the wave packet

$$\boldsymbol{v}_{\mathrm{g}} = \frac{\mathrm{d}\omega(\boldsymbol{k})}{\mathrm{d}\boldsymbol{k}} = \frac{\boldsymbol{k}}{k}\frac{\mathrm{d}\omega(k)}{\mathrm{d}k} \tag{4.1}$$

is directed along either $\boldsymbol{k}$ or $-\boldsymbol{k}$ depending on the sign of $\mathrm{d}\omega(k)/\mathrm{d}k$. The latter direction is the case of "negative group velocity" (NGV), $\mathrm{d}\omega(k)/\mathrm{d}k < 0$, and it is related to the phenomenon of NR as was clearly discussed by Mandelstam [1–3].

As is well known (see, e.g., [3–6]), in a medium with *small dissipation*, the velocity of energy propagation coincides with the group velocity so that the energy flux vector (the Poynting vector for electromagnetic waves) is the product

$$\boldsymbol{S} = U \cdot \boldsymbol{v}_{\mathrm{g}}, \tag{4.2}$$

where U is the time-averaged energy density. In *thermodynamic equilibrium*, $U > 0$ and, hence, for waves with NGV, the energy flux vector $\boldsymbol{S}$ is directed oppositely to the wave vector $\boldsymbol{k}$. Negative refraction and other unusual properties of NR materials are a very natural consequence of such a relationship. While our real interest is, of course, in NR of electromagnetic waves, Mandelstam's analysis (see Sect. 4.2.1) showed that NR is a general wave phenomenon for waves with NGV.

Later in this chapter we will discuss several physical systems that can exhibit polaritons with NGV and are therefore candidates for the realization of NR, including in the optical region of frequencies. Polaritons with NGV are possible for strong enough *spatial dispersion* of the dielectric properties of the medium [6–8]. Spatial dispersion signifies a nonlocal dielectric response and is reflected in a dependence of the generalized dielectric tensor $\varepsilon_{ij}(\omega, \boldsymbol{k})$ on the wave vector $\boldsymbol{k}$ [5, 6].

As will be shown in more detail below, the spatial dispersion framework in fact also covers the more widely studied case of NR in media with simultaneously negative dielectric permittivity $\varepsilon(\omega) < 0$ and magnetic permeability $\mu(\omega) < 0$ conventionally referred to in the context of Veselago's work [9] on left-handed materials. That the group velocity of the waves displaying NR in this case is negative has been discussed (e.g., [10]), and is explicitly illustrated in Fig. 4.1 (figures in this chapter are not to be scaled). The illustration of Fig. 4.1a uses model resonance behavior expressions for the permittivity

$$\varepsilon(\omega) = 1 + \frac{F_{\mathrm{e}}}{\omega_{\perp}^2 - \omega^2} = \frac{\omega_{\parallel}^2 - \omega^2}{\omega_{\perp}^2 - \omega^2}, \quad \omega_{\parallel}^2 = \omega_{\perp}^2 + F_{\mathrm{e}}, \tag{4.3}$$

and for the permeability

$$\mu(\omega) = 1 + \frac{F_{\mathrm{m}}}{\omega_{\mathrm{mp}}^2 - \omega^2} = \frac{\omega_{\mathrm{mz}}^2 - \omega^2}{\omega_{\mathrm{mp}}^2 - \omega^2}, \quad \omega_{\mathrm{mz}}^2 = \omega_{\mathrm{mp}}^2 + F_{\mathrm{m}}, \tag{4.4}$$

to determine the dispersion law $\omega(k)$ of transverse polaritons from the familiar equation

$$\omega^2 \varepsilon(\omega)\mu(\omega) = \omega^2 n^2(\omega) = c^2 k^2, \tag{4.5}$$

where $n(\omega)$ is the refractive index. Among the resulting three polariton branches in Fig. 4.1a there is one indicated by an arrow that evidently exhibits NGV, as the polariton frequency ω decreases with increasing k. Of course, this is exactly the region of frequencies where both $\varepsilon(\omega)$ from (4.3) and $\mu(\omega)$ from

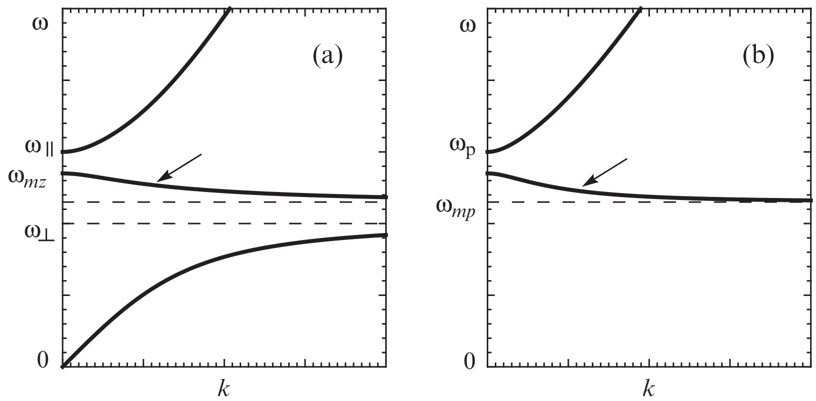

Fig. 4.1. Dispersion $\omega(k)$ of transverse polaritons in materials described by model magnetic permeability (4.4) and dielectric permittivities (**a**) from (4.3) and (**b**) from (4.6) for a specific arrangement of characteristic frequencies. Polariton branches with NGV are indicated by *arrows*. Note that neither this figure nor the following figures are to be scaled – numerical parameters have been chosen with the only purpose to better display qualitative features

(4.4) are negative. For the particular choice of parameters used for Fig. 4.1, the pole ω_{mp} and zero ω_{mz} of the magnetic permeability fall inside the well-known transverse ($\omega_{\perp}$)–longitudinal ($\omega_{\parallel}$) splitting gap due to the resonance of the dielectric permittivity. Other orderings of these frequencies are also possible.

For the result presented in Fig. 4.1b we used the same expression (4.4) for $\mu(\omega)$ but, instead of (4.3), the metal-like model dielectric permittivity

$$\varepsilon(\omega) = 1 - \frac{\omega_{\mathrm{p}}^2}{\omega^2}, \tag{4.6}$$

where ω_{p} is the effective plasma frequency. Among the two polariton branches that occur in this case, one possesses a NGV.

4.2 Nature of Negative Refraction: Historical Remarks

4.2.1 Mandelstam and Negative Refraction

The recent explosion of interest in NR materials, spawned to a large extent by the experimental observation [11] of the NR of microwaves and the theoretical prediction [12] of perfect lensing, has resulted in a very large number of articles published in scientific and popular journals and even in newspapers. Very often the origin of the subject is traced back to the already mentioned 1968 work of Veselago [9]. It is therefore interesting to note that the actual history of NR and its relationship to NGV is much longer going back to the beginning of the twentieth century. Relevant historical references and discussions can be found in [13, 14]. A brief account of the history of NGV is also given in [15] referring to early discussions by Lamb [16] and von Laue [17]. It appears that Schuster [18] was the first to discuss implications of NGV for optical refraction.

A deep understanding of the essence of the phenomenon of NR demonstrated by Mandelstam in the 1940s [1,2] influenced a lot of subsequent studies performed in the former Soviet Union. The forefather of a remarkable Moscow physical school [19], Mandelstam gave a series of informal courses of lectures that started in the 1930s and continued for many years. The lectures covered many important and subtle topics in optics, relativity and quantum mechanics, and were famous for their in-depth analysis. They were well attended not only by students but also by many senior professors. Thanks to lecture notes taken by Mandelstam's collaborators Rytov and Leontovich, the lectures were then published as part of Mandelstam's Complete Works [1] and, much later, separately [3].

It is in one of his 1944 lectures on the theory of oscillations [1] that Mandelstam gave a detailed analysis of negative refraction as it occurs at a plane interface with a medium supporting waves with NGV. As neither of the publications [1, 3] has been translated from the original Russian, we will now provide the reader with an excerpt from Mandelstam's lecture. After discussing conditions under which the group velocity does represent the velocity of energy propagation, Mandelstam continues:

"Let these conditions be satisfied and, hence, the energy propagates with the group velocity. But we know that the group velocity can be negative. This means that the group (and the energy) propagates in the direction opposite to the propagation direction of the phase of the wave. Is this possible in reality?

In 1904, Lamb invented some artificial mechanical models of one-dimensional "media" in which the group velocity can be negative. He himself probably did not think that his examples may have physical applications. It turns out, however, that there exist real media where the phase and the group velocities are directed opposite to each other in some frequency regions. This happens for the so-called "optical" branches of the vibrational spectrum of the crystal lattice considered by Born. The existence of situations like this allows one to look from a different angle at such seemingly well-known phenomena as reflection and refraction of a plane wave at the interface between two nonabsorbing media. While traditional discussions of this process do not even mention the notion of the group velocity, the way it occurs significantly depends on the sign of the group velocity.

Indeed, what is the idea behind the derivation of Fresnel's formulae?

One considers a sinusoidal plane wave incident at angle φ on the interface plane $y = 0$:

$$E_{\text{inc}} = \mathrm{e}^{\mathrm{i}[\omega t - k(x\,\sin\varphi + y\,\cos\varphi)]},$$

and, in addition, two other waves: reflected

$$E_{\text{refl}} = \mathrm{e}^{\mathrm{i}\left[\omega t - k(x\,\sin\varphi' - y\,\cos\varphi')\right]}$$

and refracted

$$E_{\mathrm{refr}} = \mathrm{e}^{\mathrm{i}[\omega t - k_1(x\ \sin\varphi_1 + y\ \cos\varphi_1)]}.$$

At the plane $y = 0$ these waves should obey so called boundary conditions. For elastic bodies those are conditions of continuity for the stress and displacements on both sides of the interface. In the electromagnetic problem the tangential components of the fields and the normal components of the inductions should be continuous across the interface. It is easy to show that with only the reflected wave (or with only the refracted wave) these boundary conditions cannot be satisfied. In contrast, with both the reflected and refracted waves, the boundary conditions can always be satisfied. From this consideration, however, it does not follow that there should be only *three* waves involved and not a larger number of waves: in fact, the boundary conditions permit one more, a fourth wave propagating in the second medium at the angle $\pi - \varphi_1$. Conventionally it is tacitly assumed that this wave is not involved and that there is only *one* wave that propagates in the second medium.

From the boundary conditions immediately follow the laws of reflection:

$$\sin\varphi = \sin\varphi' \quad \text{or} \quad \varphi = \varphi',$$

and of refraction:

$$k\ \sin\varphi = k_1\ \sin\varphi_1.$$

The last equation, however, is satisfied not only by the angle φ_1 but also by the angle $\pi - \varphi_1$. The wave corresponding to φ_1 propagates in the second medium away from the interface (left panel of Fig. 4.2). In contrast, the wave corresponding to $\pi - \varphi_1$ propagates toward the interface (right panel of Fig. 4.2). It is considered self-evident that the second wave cannot be involved as the light is incident from the first medium on the second medium and, hence, the *energy* in the second medium should flow away from the interface. But what is the relationship to the energy? The direction of wave propagation is determined by its *phase* velocity while the energy propagates with the

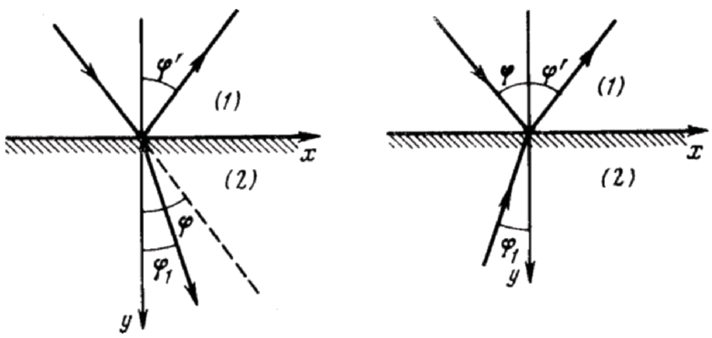

Fig. 4.2. Drawings of reflection and refraction of the incident plane wave as they were used in Mandelstam's lectures [1, 3]

group velocity. A leap of logic is thus made here which goes undetected just because we are used to the notion that the directions of the energy and of the phase propagation coincide. If these directions indeed coincide, i.e., if the group velocity is positive, then everything is correct. If, however, we have the case of negative group velocity, quite a realistic case as I have already discussed, then everything changes. Still requiring that the energy in the second medium flows away from the interface, we conclude that the phase in this case should propagate toward the interface and, therefore, the refracted wave would propagate at the angle $\pi - \varphi_1$ (as shown on the right panel of Fig. 4.2). However unusual, there is, of course, nothing surprising in this conclusion since the phase velocity does not say anything yet about the direction of the energy propagation."

The above remarks by Mandelstam made more than 60 years ago actually explain the physical origin and the nature of negative refraction. It is instructive that in his explanation of the nature of NR, Mandelstam speaks in terms of the wave vector, group velocity, and causality principle and not in terms of the quite popular nowadays negative refractive index. It follows from the same causality that the intensity of the wave propagating away from the interface can only decay in the medium in thermodynamic equilibrium. This rule definitely determines the sign of the imaginary part of the refractive index and, thereby, the sign of its real part, as both would result simultaneously from the sign in the expression $n(\omega) = \pm\sqrt{\varepsilon(\omega)\mu(\omega)}$ following from (4.5).

The relationship of NR to a negative group velocity as discussed by Mandelstam clearly identifies NR as a general wave phenomenon, and also indicates a way of looking at candidate NR materials through the dispersion $\omega(k)$ of the waves they can support. It is worth noting here, however, that the notion of waves with NGV has a broader scope and would not be always applicable to the phenomenon of NR.

As far as we know, Sivukhin [20] and Pafomov [21] were the first to note that in a medium with simultaneously negative $\varepsilon(\omega) < 0$ and $\mu(\omega) < 0$ the Poynting vector $\boldsymbol{S}$ and wave vector $\boldsymbol{k}$ are directed opposite to each other and, thus, the group velocity in this case is negative. The importance of the notion of the group velocity for crystal optics has been extensively explored in the monograph [6], and NR occurring at an interface with a chiral medium was explicitly indicated already in its 1966 edition accompanied by the now so familiar picture of Fig. 4.2 (see p. 252 of [6]).

4.2.2 Cherenkov Radiation

Negative group velocity waves can lead to a peculiar nature of some other electromagnetic phenomena such as the Cherenkov and Doppler effects (see the discussion in [22]). In particular, as was understood a long time ago [23], Cherenkov radiation in media with NGV waves would have an "unusual" directional behavior. This can be readily seen from the theory of Cherenkov radiation (e.g., [5, 22, 24]) and from the sign of the group velocity. Suppose a charged particle moves in a transparent medium along the x-axis with velocity v. As a result, the medium could emit electromagnetic waves with frequency ω and wave vector $\boldsymbol{k}$ such that $\omega = k_x v$. On the other hand, the wave vector and frequency are related by $k = n\,\omega/c$, where n is the refractive index. Since $k > k_x$, it follows that one must have $v > v_{\mathrm{ph}} = c/n(\omega)$, i.e., radiation of waves of frequency ω would occur if the velocity of the particle exceeds the phase velocity v_{ph}. If θ is the angle between the direction of the particle motion and the radiation wave vector $\boldsymbol{k}$, one immediately finds that

$$\cos\theta = c/n(\omega)v. \tag{4.7}$$

Quoting from [5], "the radiation of each frequency is emitted forwards, and is distributed over the surface of a cone with vertical angle 2θ, where θ is given by (4.7)."

From the logic of the above derivation, it is clear that the conclusion on the direction of the emission was based on the tacit assumption that the group velocity $\boldsymbol{v}_{\mathrm{g}}$ corresponding to the wave vector $\boldsymbol{k}$ was positive, that is, directed along $\boldsymbol{k}$ – this is the situation depicted in Fig. 4.3a. If, instead, the group velocity was negative, so that $\boldsymbol{v}_{\mathrm{g}}$ was directed opposite to $\boldsymbol{k}$, the direction of the emission (energy flow $\boldsymbol{S}$) would in fact be opposite. The radiation in the latter case forms an obtuse angle with the direction of the particle motion, as first discussed by Pafomov [23]. The illustration of Cherenkov radiation emitted backward is shown in Fig. 4.3b; it would be distributed over the surface of a cone with the same vertical angle.

As will be discussed in more detail later, waves with NGV may occur in crystals due to effects of spatial dispersion. Various manifestations of spatial dispersion in Cherenkov radiation have been discussed in the monograph [6] (see pp. 400–401). Particularly interesting effects have been indicated both in chiral [6, 25] and nonchiral [6] media in the vicinity of excitonic resonances: how the direction of the Cherenkov cone is modified from forward radiation to backward radiation upon a decrease of the velocity of a moving charge.

Another interesting effect of NGV is on the transition radiation of a charged particle crossing the boundary between two media with different

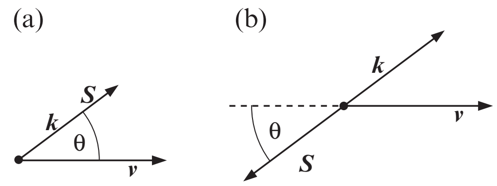

Fig. 4.3. Illustration of the directionality of Cherenkov radiation in media with (**a**) positive and (**b**) negative group velocity. Here $\boldsymbol{v}$ denotes the direction of the particle velocity, $\boldsymbol{k}$ the direction of the wave vector of the emitted radiation, and $\boldsymbol{S}$ the direction of the Poynting vector. $\boldsymbol{S}$ is *along* the group velocity $\boldsymbol{v}_{\mathrm{g}}$ and shows the actual direction of the emission

dielectric constants (see, e.g., [5, 22]). The important role of the sign of the group velocity for the transition radiation and features of the "inverse" Doppler effect were originally clarified in papers by Frank [26], Barsukov [27], and Pafomov [21].

4.3 Maxwell Equations and Spatial Dispersion

4.3.1 Dielectric Tensor

Macroscopic Maxwell equations forming the basis of electrodynamics of continuous media [5] are derived by averaging microscopic electromagnetic fields, charge and current densities, and have to be supplemented by constitutive material relations between the averaged fields that are determined by the response of the medium to the fields. Following Landau and Lifshitz [5] (see also [6,28,29]), we find it more appropriate for our goals to use a (very general for nonferromagnetic bodies) spatial dispersion approach utilizing only *three* macroscopic fields: $\boldsymbol{E}, \boldsymbol{D}, \boldsymbol{B}$ while the fourth field $\boldsymbol{H}$ is set equal to $\boldsymbol{B}$ and does not appear in the formalism. This framework assumes that the results of the averaging of *all* induced microscopic currents are absorbed in the definition of the field $\boldsymbol{D}$. The macroscopic Maxwell equations for monochromatic plane waves in this approach take the following form:

$$\begin{aligned} c\boldsymbol{k} \times \boldsymbol{E} &= \omega \boldsymbol{B} \\ c\boldsymbol{k} \times \boldsymbol{B} &= -\omega \boldsymbol{D} \\ \boldsymbol{k} \cdot \boldsymbol{D} &= 0 \\ \boldsymbol{k} \cdot \boldsymbol{B} &= 0, \end{aligned} \tag{4.8}$$

while the material relation between the components of the fields $\boldsymbol{D}$ and $\boldsymbol{E}$ in such waves is given by

$$D_i = \varepsilon_{ij}(\omega, \boldsymbol{k}) E_j. \tag{4.9}$$

The generalized dielectric tensor $\varepsilon_{ij}(\omega, \boldsymbol{k})$ in (4.9) can depend not only on the frequency ω but also on the wave vector $\boldsymbol{k}$. The latter dependence would signify *spatial dispersion* that is the fact that the electric induction $\boldsymbol{D}$ at a given spatial point is affected by the electric field $\boldsymbol{E}$ not only at the same spatial point (local medium response) but also by the electric field in some neighborhood (nonlocal response). The tensor $\varepsilon_{ij}(\omega, \boldsymbol{k})$ describes both dielectric and magnetic responses of the medium, the latter through a natural account of the response to spatial derivatives of $\boldsymbol{E}$ (see below in greater detail). Spatial dispersion comes in addition to the more familiar temporal, or frequency ω, dispersion of the response. Ordinarily spatial dispersion effects are much weaker than those from frequency dispersion but they can lead to qualitatively new phenomena like additional electromagnetic waves. The consideration of spatial dispersion is simplified if the relevant parameter $ka \sim a/\lambda$ is small, where a is the characteristic microscopic length or the mean free path of charge carriers. The smallness of ka allows one in many cases to use only the first terms (linear and/or quadratic) in the expansion of the tensor $\varepsilon_{ij}(\omega, \boldsymbol{k})$ *or* of the inverse tensor $\varepsilon_{ij}^{-1}(\omega, \boldsymbol{k})$ in powers of the components of the wave vector $\boldsymbol{k}$ [5,6]

$$\varepsilon_{ij}(\omega, \boldsymbol{k}) = \varepsilon_{ij}(\omega) + \mathrm{i}\gamma_{ijl}(\omega)k_l + \alpha_{ijlm}(\omega)k_l k_m, \tag{4.10}$$

$$\varepsilon_{ij}^{-1}(\omega, \boldsymbol{k}) = \varepsilon_{ij}^{-1}(\omega) + \mathrm{i}\delta_{ijl}(\omega)k_l + \beta_{ijlm}(\omega)k_l k_m. \tag{4.11}$$

The various tensors appearing in expansions (4.10) and (4.11) reflect the symmetries of the system under consideration. They also satisfy the Onsager principle of symmetry of kinetic coefficients [5,6,28,29] which, in the absence of a static magnetic field, states that

$$\varepsilon_{ij}(\omega, \boldsymbol{k}) = \varepsilon_{ji}(\omega, -\boldsymbol{k}). \tag{4.12}$$

In systems with inversion symmetry, the second terms of the expansions (proportional to the first power of k_l) vanish.

Maxwell equations (4.8) immediately lead to the $\boldsymbol{D}$–$\boldsymbol{E}$ relationship:

$$\boldsymbol{D} = \frac{c^2k^2}{\omega^2}\left[\boldsymbol{E} - \frac{\boldsymbol{k}(\boldsymbol{k}\cdot\boldsymbol{E})}{k^2}\right]. \tag{4.13}$$

Taken together, (4.13) and (4.9) determine the *dispersion relations* $\omega(\boldsymbol{k})$ for the electromagnetic waves propagating in the medium with a given dielectric tensor $\varepsilon_{ij}(\omega, \boldsymbol{k})$.

The time-averaged energy density and the Poynting vector in the $\boldsymbol{E}, \boldsymbol{D}, \boldsymbol{B}$ approach discussed are found via an analysis of wave packets [5,6] and are given, respectively, by

$$U = \frac{1}{16\pi}\left[\frac{\partial(\omega\varepsilon_{ij})}{\partial\omega}E_iE_j^* + |\boldsymbol{B}|^2\right] \tag{4.14}$$

and

$$\boldsymbol{S} = \frac{c}{8\pi}\mathrm{Re}(\boldsymbol{E}^* \times \boldsymbol{B}) - \frac{\omega}{16\pi}\frac{\partial\varepsilon_{ij}}{\partial\boldsymbol{k}}E_i^*E_j, \tag{4.15}$$

where $\boldsymbol{E}^*$ stands for the complex conjugate of the field $\boldsymbol{E}$ and Re denotes the real part. Expressions (4.14) and (4.15) satisfy energy conservation (no dissipation). Equation (4.15) features an additional (second) term [30,31] entirely due to spatial dispersion, which in fact plays a crucial role for waves with NGV described within the framework we use.

It is important to note that the fields $\boldsymbol{D}$ and $\boldsymbol{H}$ $(= \boldsymbol{B})$ of the spatial dispersion approach are, in general, different from the $\boldsymbol{D}$ and $\boldsymbol{H}$ fields employed in the more familiar "symmetric" approach based on an explicit consideration of all four fields $\boldsymbol{E}, \boldsymbol{D}, \boldsymbol{B}, \boldsymbol{H}$. To clearly delineate this difference and illustrate relationships, we will denote here the $\boldsymbol{D}$ and $\boldsymbol{H}$ fields of the symmetric approach by $\boldsymbol{D}'$ and $\boldsymbol{H}'$, respectively. With the set of four fields, Maxwell equations for plane waves read

$$
\begin{aligned}
c\,\boldsymbol{k} \times \boldsymbol{E} &= \omega \boldsymbol{B} \\
c\,\boldsymbol{k} \times \boldsymbol{H}' &= -\omega \boldsymbol{D}' \\
\boldsymbol{k} \cdot \boldsymbol{D}' &= 0 \\
\boldsymbol{k} \cdot \boldsymbol{B} &= 0\,,
\end{aligned}
\tag{4.16}
$$

where spatially local and isotropic material relations are assumed to hold for the two pairs of the fields:

$$
\boldsymbol{D}' = \varepsilon(\omega)\boldsymbol{E}, \quad \boldsymbol{B} = \mu(\omega)\boldsymbol{H}'. \tag{4.17}
$$

We will be referring to the framework of (4.17) as the $\varepsilon(\omega)$–$\mu(\omega)$ description. In both sets of (4.8) and (4.16), no explicit separation has been made of the macroscopic current due to free charges: free charges are assumed to be treated on the same footing with bound charges in the term $\partial \boldsymbol{D}/\partial t$ in the time-dependent Maxwell equations. With this assumption, the sets (4.8) and (4.16) are applicable to both dielectrics and conductors.

To cast (4.16) in the form of (4.8), let us add $c\,[1 - 1/\mu(\omega)]\,\boldsymbol{k} \times \boldsymbol{B}$ to both sides of the second line in (4.16) and introduce new (combination) fields

$$
\boldsymbol{D} = \boldsymbol{D}' - \frac{c}{\omega}\left(1 - \frac{1}{\mu(\omega)}\right)\boldsymbol{k} \times \boldsymbol{B} \tag{4.18}
$$

and

$$
\boldsymbol{H} = \boldsymbol{H}' + \left(1 - \frac{1}{\mu(\omega)}\right)\boldsymbol{B}. \tag{4.19}
$$

This transformation of the fields obviously preserves the form of the second and third lines in (4.16): $c\,\boldsymbol{k} \times \boldsymbol{H} = -\omega \boldsymbol{D}$ and $\boldsymbol{k} \cdot \boldsymbol{D} = 0$. Using the material relations (4.17) in the definitions (4.18) and (4.19) of the new fields yields "new" material relations:

$$
\boldsymbol{H} = \boldsymbol{B} \tag{4.19a}
$$

and

$$
\begin{aligned}
\boldsymbol{D} &= \varepsilon(\omega)\boldsymbol{E} - \frac{c}{\omega}\left(1 - \frac{1}{\mu(\omega)}\right)\boldsymbol{k} \times \boldsymbol{B} \\
&= \varepsilon(\omega)\boldsymbol{E} - \frac{c^2}{\omega^2}\left(1 - \frac{1}{\mu(\omega)}\right)\boldsymbol{k} \times (\boldsymbol{k} \times \boldsymbol{E}).
\end{aligned}
\tag{4.20}
$$

In obtaining (4.20) the first Maxwell equation from set (4.16) has been used, signifying an inherent relationship of the time-dependent magnetic field to spatial derivatives of the electric field. Given (4.19a), we end up with (4.8) employing the newly defined field $\boldsymbol{D}$. Thus the description of the electromagnetic behavior of the system provided by (4.16) and (4.17) of the symmetric approach is equivalent to the description provided by (4.8) of the $\boldsymbol{E}, \boldsymbol{D}, \boldsymbol{B}$ framework where the material relation has the form of (4.20). Equation (4.20) is a particular case of the general linear material relation (4.9) displaying a specific type of spatial dispersion whenever $\mu(\omega)$ deviates from unity. The spatial dispersion of $\varepsilon_{ij}(\omega, \boldsymbol{k})$ in this case is a result of absorbing a purely magnetic response of the system in the field $\boldsymbol{D}$ – local responses for the two fields in (4.17) have been converted into a nonlocal response of a single field. Of course, relation (4.9) can in general describe other types of spatial dispersion ($\boldsymbol{k}$-dependence) due to different physical reasons, some of which will be discussed in this chapter.

The reader interested in various viewpoints, arguments, and details related to a comparison of the $\boldsymbol{E}, \boldsymbol{D}, \boldsymbol{B}$ and $\boldsymbol{E}, \boldsymbol{D}, \boldsymbol{B}, \boldsymbol{H}$ approaches to macroscopic electrodynamics, may find useful discussions in books [28,29], reviews [32–34], and a recent paper [8].

4.3.2 Isotropic Systems with Spatial Inversion

With account of spatial dispersion, the dielectric response should be described by a tensor even in isotropic systems, as the vector $\boldsymbol{k}$ selects a certain direction. So for an isotropic medium possessing inversion symmetry (a nongyrotropic or nonchiral medium), the general form of the dielectric tensor is [5]

$$\varepsilon_{ij}(\omega, \boldsymbol{k}) = \varepsilon_{\perp}(\omega, k)\left[\delta_{ij} - \frac{k_i k_j}{k^2}\right] + \varepsilon_{\parallel}(\omega, k)\frac{k_i k_j}{k^2}, \tag{4.21}$$

where the *transverse* $\varepsilon_{\perp}(\omega, k)$ and *longitudinal* $\varepsilon_{\parallel}(\omega, k)$ dielectric functions now depend on $\boldsymbol{k}$ only through its magnitude k, and provide a complete description of this medium. In accordance with (4.13) and (4.9), the dispersion $\omega(k)$ of transverse ($\boldsymbol{E} \perp \boldsymbol{k}$) polaritons is then found from

$$\omega^2 \varepsilon_{\perp}(\omega, k) = c^2 k^2, \tag{4.22}$$

while the equation

$$\varepsilon_{\parallel}(\omega, k) = 0 \tag{4.23}$$

determines the dispersion of longitudinal ($\boldsymbol{E} \parallel \boldsymbol{k}$, $\boldsymbol{D} = 0$, $\boldsymbol{B} = 0$) waves.

It can be shown [5] that the $\varepsilon(\omega)$–$\mu(\omega)$ description of this medium would then correspond only to the limiting $\boldsymbol{k} \to 0$ behavior in the full spatial dispersion framework:

$$\varepsilon(\omega) = \varepsilon_{\perp}(\omega, 0) = \varepsilon_{\parallel}(\omega, 0) \tag{4.24}$$

and

$$1 - \frac{1}{\mu(\omega)} = \lim_{k \to 0} \frac{\omega^2 \left[\varepsilon_{\perp}(\omega, k) - \varepsilon_{\parallel}(\omega, k)\right]}{c^2 k^2}. \tag{4.25}$$

Consistently with (4.24) and (4.25), the material relation (4.20) we derived in the field conversion procedure is equivalent to a particular choice of the transverse function,

$$\varepsilon_{\perp}(\omega, k) = \varepsilon(\omega) + \frac{c^2 k^2}{\omega^2}\left[1 - \frac{1}{\mu(\omega)}\right], \tag{4.26}$$

while the longitudinal function $\varepsilon_{\parallel}(\omega, k) = \varepsilon(\omega)$ displays no spatial dispersion. Using (4.26) in dispersion equation (4.22) for transverse polaritons would make (4.22) *identical* to (4.5) derived in the $\varepsilon(\omega)$–$\mu(\omega)$ description. This again demonstrates that results derivable for transverse waves in the $\varepsilon(\omega)$–$\mu(\omega)$ framework are recovered in the spatial dispersion approach for a specific k-dependence ($\propto k^2$) in $\varepsilon_{\perp}(\omega, k)$. Even within the k^2-accuracy, however, one has to be aware of the following.

In the isotropic system under consideration, the response tensor α_{ijlm} of (4.10) is in general characterized by *two independent* parameters. These parameters (a and b) can, for instance, be chosen via the representation

$$\alpha_{ijlm} = a\,\delta_{ij}\delta_{lm} + \frac{b}{2}\left(e_{ril}e_{rjm} + e_{rim}e_{rjl}\right), \tag{4.27}$$

where e_{ril} denotes the antisymmetric unit tensor of rank three. Equation (4.27) is written explicitly symmetric in both the first (ij) and second (lm) pairs of indices, and it leads to

$$\varepsilon_{\perp}(\omega, k) = \varepsilon(\omega) + [a(\omega) + b(\omega)]k^2, \quad \varepsilon_{\parallel}(\omega, k) = \varepsilon(\omega) + a(\omega)k^2 \tag{4.28}$$

in expansions for the transverse and longitudinal dielectric functions. The corresponding material relation (4.9), as follows from (4.10) and (4.27), is

$$\boldsymbol{D} = [\varepsilon(\omega) + a(\omega)k^2]\boldsymbol{E} + b(\omega)\boldsymbol{k} \times (\boldsymbol{E} \times \boldsymbol{k}). \tag{4.29}$$

Equations (4.20), (4.28), and (4.29) make it clear that the parameter $b(\omega)$ can be loosely thought of as quantifying spatial dispersion due to a "magnetic response" of the system: It is related to the magnetic permeability (see (4.20) and (4.25)) through $\omega^2 b(\omega)/c^2 = 1 - 1/\mu(\omega)$. The parameter $a(\omega)$, on the other hand, would then quantify spatial dispersion due to an "electric response." This latter dispersion could not be properly taken into account within the $\varepsilon(\omega)$–$\mu(\omega)$ description, as both types of responses contribute similarly to the dispersion of transverse polaritons [(4.28) and (4.22)] but only the electric response affects the longitudinal waves [(4.28) and (4.23)]. Particularly noteworthy is that polaritons with NGV and subsequent negative refraction may occur in systems with $\mu(\omega) = 1$ (i.e., with $b(\omega) = 0$) if the response coefficient $a(\omega)$ has an appropriate frequency behavior.

4.3.3 Connection to Microscopics

The dielectric tensor $\varepsilon_{ij}(\omega, \boldsymbol{k})$ describes the response of the medium to electromagnetic perturbations of *arbitrary* frequencies ω and wave vectors $\boldsymbol{k}$. As such, it has certain well-known analytic properties and can, in principle, be derived from a microscopic description of elementary excitations of the medium by the use of various methods; see, e.g., [6, 28, 35–37] for discussions of many important aspects. Our limited illustration here follows the derivation in [6] where more details can be found.

Consider a crystalline medium of volume V containing N electrons of charge e and mass m. The ground state $|0\rangle$ of this system is being perturbed by the external vector potential $\boldsymbol{A}(\boldsymbol{r},t) = \boldsymbol{A}_0\,\mathrm{e}^{\mathrm{i}(\boldsymbol{k}\cdot\boldsymbol{r}-\omega t)}$ + c.c. to the time-dependent state $|\widetilde{0}\rangle$. The corresponding perturbing electric field $\boldsymbol{E} = -(1/c)\partial\boldsymbol{A}/\partial t$ is characterized by the amplitude $\boldsymbol{E}_0 = \mathrm{i}(\omega/c)\boldsymbol{A}_0$. In the linear approximation, the perturbation operator is then

$$H_{\mathrm{int}} = F\mathrm{e}^{-\mathrm{i}\omega t} + F^{\dagger}\mathrm{e}^{\mathrm{i}\omega t}, \quad F = -\frac{\mathrm{i}c}{\omega}\,\boldsymbol{M}(\boldsymbol{k})\cdot\boldsymbol{E}_0, \tag{4.30}$$

where

$$\boldsymbol{M}(\boldsymbol{k}) = -\frac{e}{2mc}\sum_{\alpha}(\boldsymbol{p}^{\alpha}\,\mathrm{e}^{\mathrm{i}\boldsymbol{k}\cdot\boldsymbol{r}^{\alpha}} + \mathrm{e}^{\mathrm{i}\boldsymbol{k}\cdot\boldsymbol{r}^{\alpha}}\boldsymbol{p}^{\alpha}) \tag{4.31}$$

comprises effects on all electrons, with $\boldsymbol{r}^{\alpha}$ the coordinate of the αth electron and $\boldsymbol{p}^{\alpha} = -\mathrm{i}\hbar\partial/\partial\boldsymbol{r}^{\alpha}$ its momentum operator.

As a result of the perturbation (4.30), an electric current will be induced in the system, whose average induced current density is

$$\boldsymbol{J}(\boldsymbol{r},t) = \frac{e}{2}\left\langle \widetilde{0}\right|\sum_{\alpha}\left(\boldsymbol{v}^{\alpha}\delta(\boldsymbol{r}-\boldsymbol{r}^{\alpha}) + \delta(\boldsymbol{r}-\boldsymbol{r}^{\alpha})\boldsymbol{v}^{\alpha}\right)\left|\widetilde{0}\right\rangle, \tag{4.32}$$

where $m\boldsymbol{v}^{\alpha} = \boldsymbol{p}^{\alpha} - (e/c)\boldsymbol{A}(\boldsymbol{r}^{\alpha},t)$ and only terms linear in $\boldsymbol{A}$ are supposed to be retained. One applies the ordinary first-order time-dependent perturbation theory to evaluate (4.32) in terms of the ground state $|0\rangle$ and various excited states $|n\rangle$ of the unperturbed system. These "bare" excited states, which we will be calling *excitons*, have excitation energies $\hbar\omega_n$ and are assumed to have been calculated without account of the macroscopic electromagnetic field (in the terminology of [6], these are "mechanical excitons"). Restricting ourselves to the same Fourier harmonics, one then finds $\boldsymbol{J} = \boldsymbol{J}_0\mathrm{e}^{\mathrm{i}(\boldsymbol{k}\cdot\boldsymbol{r}-\omega t)}$ + c.c., where the amplitude $\boldsymbol{J}_0$ of the induced current determines the conductivity tensor σ via its relationship to the amplitude of the perturbing electric field:

$$J_{0i} = \sigma_{ij}(\omega,\boldsymbol{k})E_{0j}. \tag{4.33}$$

The dielectric tensor is related to the conductivity tensor in (4.33) in a standard way:

$$\varepsilon_{ij}(\omega,\boldsymbol{k}) = \delta_{ij} + \frac{4\pi\mathrm{i}}{\omega}\,\sigma_{ij}(\omega,\boldsymbol{k}). \tag{4.34}$$

Collecting all the terms contributing to (4.34), one ends up with the following expression for the dielectric tensor:

$$\begin{aligned}\varepsilon_{ij}(\omega,\boldsymbol{k}) = &\left(1 - \frac{4\pi e^2 N}{m\omega^2 V}\right)\delta_{ij}\\ &- \frac{4\pi c^2}{\hbar\omega^2 V}\sum_{n}\left[\frac{M_i^{n*}(\boldsymbol{k})M_j^{n}(\boldsymbol{k})}{\omega-\omega_n} - \frac{M_i^{n}(-\boldsymbol{k})M_j^{n*}(-\boldsymbol{k})}{\omega+\omega_n}\right],\end{aligned} \tag{4.35}$$

where $M_i^n(\boldsymbol{k})$ are the Cartesian components of the matrix elements of the vector operator (4.31):

$$\boldsymbol{M}^n(\boldsymbol{k}) = \langle n|\boldsymbol{M}(\boldsymbol{k})|0\rangle. \tag{4.36}$$

By using Onsager relation (4.12), one can further explicitly symmetrize expression (4.35): $\varepsilon_{ij}(\omega, \boldsymbol{k}) \to [\varepsilon_{ij}(\omega, \boldsymbol{k}) + \varepsilon_{ji}(\omega, -\boldsymbol{k})]/2$.

It is instructive to look now at the microscopic origin of expressions like (4.26) and (4.28) in isotropic systems with inversion, for which we expand the matrix elements (4.36) in powers of the components of the wave vector $\boldsymbol{k}$:

$$M_i^n(\boldsymbol{k}) = P_i^n + \mathrm{i}k_l X_{il}^n + \cdots \tag{4.37}$$

A set of atoms or molecules can be a useful, although not necessary, model picture of the system (for an extensive relevant discussion of molecular transitions, see, e.g., [38,39]). In accordance with (4.28) and (4.35), the dielectric permittivity $\varepsilon(\omega)$ is determined by the $\boldsymbol{M}^n(\boldsymbol{k}=0)$ elements

$$P_i^n = -\frac{e}{mc}\sum_\alpha \langle n|p_i^\alpha|0\rangle\,, \tag{4.38}$$

yielding

$$\frac{4\pi c^2}{\hbar\omega^2 V}\sum_n \frac{\omega_n\left(P_i^{n*}P_j^n + P_i^n P_j^{n*}\right)}{\omega_n^2-\omega^2} \tag{4.39}$$

in the second line of (4.35). Transitions with nonzero P_i^n are *electric-dipole allowed* transitions (otherwise called E1 transitions) and only they contribute to $\varepsilon(\omega)$.

Equation (4.39) can be transformed employing the quantum-mechanical relationships

$$\langle n|p_i^\alpha|0\rangle = \mathrm{i}m\omega_n\langle n|r_i^\alpha|0\rangle \tag{4.40}$$

and

$$\sum_{n\alpha\beta}\frac{m\omega_n}{\hbar}\Big(\langle 0|r_i^\alpha|n\rangle\langle n|r_j^\beta|0\rangle + \langle 0|r_j^\beta|n\rangle\langle n|r_i^\alpha|0\rangle\Big) = N\delta_{ij}. \tag{4.41}$$

The sum rule, (4.41), of course, follows immediately from the commutator $[r_i^\alpha, p_j^\beta] = \mathrm{i}\hbar\delta_{\alpha\beta}\delta_{ij}$ using the completeness of the set of states $|n\rangle$ and (4.40). Since

$$\frac{\omega_n^2}{\omega_n^2-\omega^2} = 1 + \frac{\omega^2}{\omega_n^2-\omega^2},$$

one can use the sum rule (4.41) to conveniently separate from (4.39) the term $(4\pi e^2 N/m\omega^2 V)\delta_{ij}$, which exactly cancels the diamagnetic contribution in the first line of (4.35). In isotropic systems, the rest of (4.39) would also be proportional to δ_{ij} so that the resulting permittivity is

$$\varepsilon(\omega) = 1 + \sum_{en}\frac{F_{en}}{\omega_{en}^2-\omega^2}, \tag{4.42}$$

where we have used the index en to emphasize that the actual summation is over electric-dipole allowed transitions only. The corresponding transition frequencies are denoted by ω_{en} while the "oscillator strengths" F_{en}, in accordance with (4.41), satisfy the sum rule $\sum_{en} F_{en} = \omega_{\mathrm{p}}^2$, where the plasma frequency is $\omega_{\mathrm{p}} = \left(4\pi e^2 N/mV\right)^{1/2}$. In the vicinity of a single resonance frequency $\omega_\perp$, (4.42) exhibits the behavior

$$\varepsilon(\omega) = \epsilon_{\mathrm{b}} + \frac{F_{\mathrm{e}}}{\omega_\perp^2 - \omega^2} = \epsilon_{\mathrm{b}} \frac{\omega_\parallel^2 - \omega^2}{\omega_\perp^2 - \omega^2}, \quad \omega_\parallel^2 = \omega_\perp^2 + F_{\mathrm{e}}/\epsilon_{\mathrm{b}}, \tag{4.43}$$

where the background constant ϵ_{b} comes from other allowed transitions ($\epsilon_{\mathrm{b}} = 1$ in (4.3)).

A qualitatively different contribution to the dielectric tensor comes from *electric-dipole forbidden* transitions. In expansion (4.37) of the matrix elements the first term for these transitions vanishes. It is the second term with

$$X_{il}^n = -\frac{e}{2mc} \sum_\alpha \langle n | p_i^\alpha r_l^\alpha + r_l^\alpha p_i^\alpha | 0 \rangle \tag{4.44}$$

that is responsible now for the transition intensity. It is useful to distinguish the magnetic-dipole transitions (M1 transitions) that would be caused by the antisymmetric magnetic-dipole combination

$$r_l^\alpha p_i^\alpha - r_i^\alpha p_l^\alpha \tag{4.45}$$

in the brackets of (4.44). The actual combination in those brackets differs from (4.45) by

$$p_i^\alpha r_l^\alpha + r_i^\alpha p_l^\alpha . \tag{4.46}$$

The combination in (4.46) is well known to correspond to electric-quadrupole transitions (E2 transitions). The difference of the magnetic-dipole and electric-quadrupole transitions is reflected in the symmetry of the tensor X_{il}^n: the tensor is antisymmetric, $X_{il}^{n(m)} = -X_{li}^{n(m)}$, for the former; but symmetric, $X_{il}^{n(q)} = X_{li}^{n(q)}$, for the latter. As follows from (4.35) and (4.37), both types of transitions can contribute to the tensor α_{ijlm} (4.27) via the following term:

$$\frac{4\pi c^2}{\hbar \omega^2 V} \sum_n \frac{\omega_n \left(X_{il}^{n*} X_{jm}^n + X_{jl}^{n*} X_{im}^n \right)}{\omega_n^2 - \omega^2} . \tag{4.47}$$

One notes, however, that, because of their symmetry, purely magnetic-dipole combinations like $X_{il}^{n(m)*} X_{jm}^{n(m)}$ in (4.47) contribute only to the magnetic-response coefficient $b(\omega)$ in (4.27). On the other hand, the electric-quadrupole combinations like $X_{il}^{n(q)*} X_{jm}^{n(q)}$ can contribute to both response coefficients $a(\omega)$ and $b(\omega)$ in (4.27). (For examples of other symmetry applications see, e.g., [6]; for a general discussion of the electric quadrupole polarization in macroscopic electrodynamics see [24].)

Equation (4.47) explicitly shows that magnetic-dipole and electric-quadrupole transitions (and, in general, their mix) can lead to contributions of the same type to the transverse dielectric function $\varepsilon_\perp(\omega, k)$, of the general form

$$\frac{c^2k^2}{\omega^2}\sum_{fn}\frac{F_{fn}}{\omega_{fn}^2-\omega^2}\,, \tag{4.48}$$

as follows from (4.27), (4.28), and (4.47). We used the index fn in (4.48) to indicate that the sum is over electric-dipole forbidden transitions with frequencies ω_{fn} and intensities determined by the parameters F_{fn}. Combining a contribution from a single isolated resonance of frequency ω_f in (4.48) with (4.43) leads to

$$\varepsilon_\perp(\omega,k)=\epsilon_\mathrm{b}+\frac{F_\mathrm{e}}{\omega_\perp^2-\omega^2}+\frac{c^2k^2}{\omega^2}\frac{F_\mathrm{f}}{\omega_\mathrm{f}^2-\omega^2}\,. \tag{4.49}$$

The general behavior featured in (4.49) arises from the interplay of two resonances: one, which is electric-dipole allowed (frequency $\omega_\perp$), and the other, which is electric-dipole forbidden (frequency ω_f). This is the interplay that can lead to polaritons with NGV as shown in Fig. 4.1a. One easily finds from (4.26), (4.3), and (4.4) that this is indeed the case by associating $[1-1/\mu(\omega)]$ in (4.26) with $F_\mathrm{f}/(\omega_\mathrm{f}^2-\omega^2)$ in (4.49). For the model expression (4.4), the correspondence is that the zero ω_mz of the magnetic permeability $\mu(\omega)$ is the frequency ω_f of the forbidden transition, while the parameter $F_\mathrm{m}=F_\mathrm{f}$.

(We note that, of course, contributions $\propto k^2$ in (4.28) can also come through corrections to matrix elements from electric-dipole allowed transitions; they are, however, of no interest for the discussion at hand.)

The derivation leading to (4.49) also indicates that the strength of the forbidden electronic transitions in atomic/molecular materials is generally much weaker than the strength of the electric-dipole allowed transitions. Assuming, e.g., that the allowed and forbidden transitions in (4.49) arise from the same molecular species, one can estimate the matrix elements (4.40) and (4.44), leading to

$$\frac{F_\mathrm{f}}{F_\mathrm{e}}\sim\frac{1}{c^2}\frac{\omega_\mathrm{f}^3a^4}{\omega_\perp a^2}\sim\frac{v^2}{c^2}\ll 1, \tag{4.50}$$

where a is the characteristic molecular size and v a typical electron velocity ($\omega_\perp\sim\omega_\mathrm{f}$). In this regard, we recall that $F_\mathrm{e}/\epsilon_\mathrm{b}$ determines the magnitude of the $\omega_\parallel-\omega_\perp$ splitting in Fig. 4.1a, while $F_\mathrm{f}=F_\mathrm{m}$ defines the frequency width of the polariton branch with NGV.

4.3.4 Isotropic Systems Without Spatial Inversion

In media with broken spatial inversion symmetry (gyrotropic or chiral media) the tensors γ_{ijl} and δ_{ijl} [from (4.10) and (4.11)] do not vanish, and spatial dispersion manifests itself already in terms of the first-order smallness with respect to the wave vector $\boldsymbol{k}$. Important features of the polariton dispersion in such media can be readily delineated even if only these linear terms are retained [6,40]. In isotropic systems the general tensors γ_{ijl} and δ_{ijl} reduce to the unit antisymmetric tensor and the expansions take the forms

$$\varepsilon_{ij}(\omega,\boldsymbol{k}) = \varepsilon(\omega)\,\delta_{ij} + \mathrm{i}\,\gamma(\omega)e_{ijl}k_l, \tag{4.51}$$

$$\varepsilon_{ij}^{-1}(\omega,\boldsymbol{k}) = \frac{1}{\varepsilon(\omega)}\,\delta_{ij} + \mathrm{i}\,\delta(\omega)e_{ijl}k_l. \tag{4.52}$$

As discussed later, (4.51) is appropriate to use in the vicinity of the longitudinal frequency $\omega_{\parallel}$: $\varepsilon(\omega_{\parallel}) = 0$, while (4.52) is useful in the vicinity of the resonance frequency $\omega_{\perp}$: $1/\varepsilon(\omega_{\perp}) = 0$.

Once again, it is instructive to see the microscopic origin of the behavior in (4.51). For a set of chiral molecules, for instance, it is well known (see, e.g., [37–39]) that optical activity results from transitions to states $|n\rangle$ with nonvanishing matrix elements of both types (4.38) and (4.44). Using expansion (4.37) in (4.35), one indeed easily finds a microscopic representation of the tensor γ_{ijl} in (4.10) as

$$\frac{4\pi c^2}{\hbar\omega^2 V}\sum_n \frac{\omega_n\left(P_i^n X_{jl}^{n*} - P_j^n X_{il}^{n*} + \mathrm{c.c.}\right)}{\omega_n^2 - \omega^2}. \tag{4.53}$$

In isotropic systems it is only the antisymmetric magnetic-dipole $X_{il}^{n(m)}$ matrix elements that actually contribute to (4.53), whose tensor structure reduces to the antisymmetric tensor in (4.51). The microscopic meaning of $\delta(\omega)$ in (4.52) will be addressed in Sect. 4.4.2.

4.4 Polaritons with Negative Group Velocity

As has already been mentioned, it is the second term in expression (4.15) for the Poynting vector $\boldsymbol{S}$ that explicitly shows how spatial dispersion can "invert" the direction of energy propagation with respect to the wave vector $\boldsymbol{k}$. Indeed the first term in (4.15) in an isotropic medium is a vector directed along $\boldsymbol{k}$. For the group velocity to become negative, the second term has to be along $-\boldsymbol{k}$ and larger in magnitude. This, in particular, implies that the spatial dispersion $\partial\varepsilon_{\perp}(\omega,k)/\partial k$ should be strong enough. This is precisely the case occurring in the situation of (4.49) below the forbidden frequency ω_{f}. In what follows we will discuss several other instances of substantial spatial dispersion of the dielectric function leading to polaritons with negative group velocities in potentially broader regions of frequency ω.

4.4.1 Excitons with Negative Effective Mass in Nonchiral Media

Pekar [41] was the first to suggest in 1957 that spatial dispersion of the dielectric function near the excitonic resonance could lead to the appearance of an additional propagating exciton–polariton wave. This possibility has to do with the fact that excitons in the medium have their own dispersion, that is, the exciton in the medium can move (e.g., from one molecule to another) and its energy depends on the wave vector $\boldsymbol{k}$. Consider expression (4.43) for the transverse dielectric function featuring a response due to an isolated electric-dipole allowed excitonic transition of frequency $\omega_\perp$. In fact, however, the matrix elements (4.36) "select" excitonic states $|n\rangle$ with (quasi)momentum $\hbar\boldsymbol{k}$, hence the energies ω_n should correspond to such a momentum. In the effective mass approximation, the exciton energy–momentum relationship has the form

$$\hbar\widetilde{\omega}_\perp(k) = \hbar\omega_\perp + \frac{\hbar^2 k^2}{2M_{\mathrm{exc}}}. \tag{4.54}$$

Correspondingly, the transverse dielectric function is

$$\varepsilon_\perp(\omega, k) = \epsilon_{\mathrm{b}} + \frac{F_{\mathrm{e}}}{\widetilde{\omega}_\perp^2(k) - \omega^2}, \tag{4.55}$$

which would coincide with (4.43) only for immobile excitons: $M_{\mathrm{exc}} = \infty$. Of course, the oscillator strength F_{e} would also acquire some k dependence. We limit our discussion, however, to a stronger effect in the resonance denominator in (4.55). We emphasize again that spatial dispersion exhibited in the response function (4.55) is due to the energy–momentum relationship of excitons in the medium. It is (4.22) that would describe how excitons couple with photons to form polaritons, mixed light–matter excitations. The resulting dispersion curves for transverse polaritons found from (4.22) and (4.55) are illustrated in Fig. 4.4.

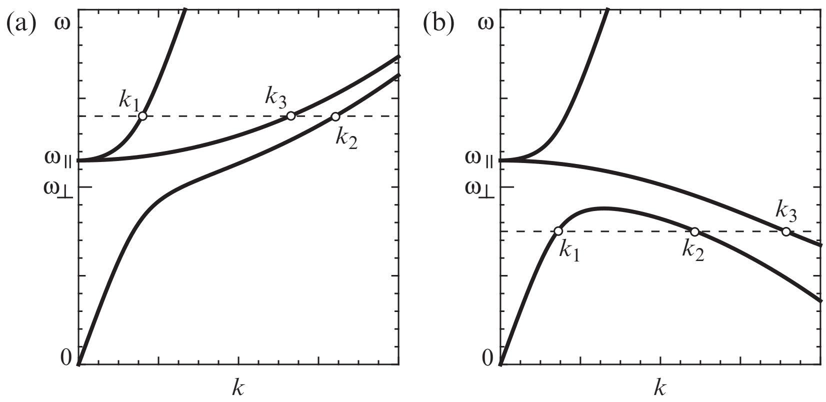

Fig. 4.4. Dispersion of two transverse polariton branches and of the longitudinal wave in a system with exciton dispersion (4.54): (**a**) Positive exciton effective mass, $M_{\mathrm{exc}} > 0$; (**b**) Negative effective mass, $M_{\mathrm{exc}} < 0$. Crossings of *dashed lines* with *dispersion curves* indicate wave vectors k of the waves at a given frequency ω: k_1 and k_2 are for transverse polaritons and k_3 for the longitudinal wave. In case (**b**) k_2 corresponds to polaritons with NGV

Figure 4.4 shows that, for a range of frequencies ω, there indeed can be two different values of k for each ω representing two transverse polariton waves of the same polarization, the one with a larger k (denoted as k_2) being the additional wave pointed out by Pekar. The existence of additional exciton–polariton waves has been demonstrated in many crystals; the most convincing experiments were conducted in semiconductors near the Wannier–Mott exciton resonances (see [6] for references and discussion). Of principal importance for the sign of the polariton group velocity is the sign of the exciton effective mass. The effective mass of Wannier–Mott excitons is ordinarily positive: $M_{\mathrm{exc}} = m_{\mathrm{e}} + m_{\mathrm{h}} > 0$, where m_{e} and m_{h} are the effective masses of electrons and holes, respectively. This is the situation depicted in Fig. 4.4a. Evidently, the additional exciton–polariton waves in this case have positive group velocities.

In organic crystals, however, Frenkel excitons typically have a small radius. The resonant intermolecular interaction then strongly depends on molecular orientation, leading to different signs of the exciton effective mass in different directions. We expect that the use of powders could provide a material with an effectively isotropic behavior and negative $M_{\mathrm{exc}} < 0$. The situation with negative exciton mass is depicted in Fig. 4.4b. It clearly illustrates that for a range of frequencies ω the additional transverse polariton waves (k_2-wave in the figure) have negative group velocities. These are the transverse waves that would exhibit the negative refraction behavior.

Also shown in Fig. 4.4 is the dispersion of the longitudinal waves determined by (4.23). For specificity we assumed $\varepsilon_{\parallel}(\omega, k) = \varepsilon_{\perp}(\omega, k)$ in this illustration. The wave vector k for the longitudinal waves is denoted by k_3. In the case $M_{\mathrm{exc}} < 0$, longitudinal waves also possess negative group velocities. In general all three waves (two transverse and one longitudinal) can be excited in a medium by an incident wave of an appropriate frequency. The solution of reflection/refraction problems in such circumstances requires one to specify so-called additional boundary conditions (ABCs), as the usual Maxwell-type boundary conditions would obviously be insufficient to find amplitudes of all the waves involved. The form of ABCs does depend on the microscopic nature of excitons, which was extensively discussed in [6] for molecular crystals.

A direct numerical study of reflection/refraction by a planar slab of a medium supporting excitons with negative $M_{\mathrm{exc}} < 0$ (Fig. 4.4b) has been recently performed in [42]. The results reassuringly show that such a slab can indeed act as a Veselago-type lens due to the negative refraction behavior of the waves with NGV. The simulation [42] also indicates that for an experimental realization of such a lens one needs to have crystals with a large oscillator strength of the excitonic transition and a rather weak dissipation of the additional polaritons below the resonance exciton frequency.

4.4.2 Chiral Systems in the Vicinity of Excitonic Transitions

Chiral (gyrotropic) systems, well known for the phenomena of optical activity and circular dichroism, naturally lend themselves as candidate media to support polaritons with NGV in certain regions of frequency ω. We start our discussion from the case of a frequency region in the vicinity of the exciton transition frequency $\omega_\perp$. As the transition frequency corresponds to the pole of the dielectric permittivity $\varepsilon(\omega)$, a more convenient way to consider this region is by using the expansion (4.52) for the inverse dielectric tensor. The inverse dielectric function vanishes at the transition frequency: $\varepsilon^{-1}(\omega_\perp) = 0$, making clear the qualitative importance of the next, spatially dispersive, term in that expansion.

Equation (4.52) corresponds to the material relation

$$\boldsymbol{E} = \frac{1}{\varepsilon(\omega)}\boldsymbol{D} + \mathrm{i}\,\delta(\omega)\boldsymbol{D} \times \boldsymbol{k} \tag{4.56}$$

between the $\boldsymbol{E}$ and $\boldsymbol{D}$ fields, where the parameter $\delta(\omega)$ defines the "strength" of the chirality. Relation (4.56) combined with the wave equation (4.13) for *transverse* waves leads to the equation

$$\left(\frac{\omega^2}{c^2k^2}\right)\boldsymbol{D} = \frac{1}{\varepsilon(\omega)}\boldsymbol{D} + \mathrm{i}\,\delta(\omega)\boldsymbol{D} \times \boldsymbol{k}\,, \tag{4.57}$$

whose nontrivial solutions describe transverse polaritons in this system. These solutions are known to correspond to circularly polarized waves: e.g., $D_y/D_x = \pm\mathrm{i}$ for waves propagating in the z-direction. The polariton dispersion $\omega(k)$ is determined from the condition that the determinant of the system of equations (4.57) vanishes:

$$\left(\frac{1}{\varepsilon(\omega)} - \frac{\omega^2}{c^2k^2}\right)^2 = \delta^2(\omega)k^2 \tag{4.58}$$

or, for waves of different circular polarizations,

$$\frac{1}{\varepsilon(\omega)} - \frac{\omega^2}{c^2k^2} = \pm|\delta(\omega)|k. \tag{4.58a}$$

Figure 4.5a illustrates the two branches of the transverse polariton dispersion resulting from (4.58a) when the model dielectric function $\varepsilon(\omega)$ of (4.43) and a constant $\delta(\omega) = \delta$ are used.

Qualitatively (see [6,43]) this two-branch polariton spectrum can be understood as being due to the dispersion of excitons, that is, due to the fact that the exciton energies themselves can depend on the wave vector k, similarly to the effect we discussed in Sect. 4.4.1 in connection with (4.54). In a chiral medium, however, electric-dipole active excitons (or optical phonons) would have their dispersion split into two branches corresponding to the two different circular

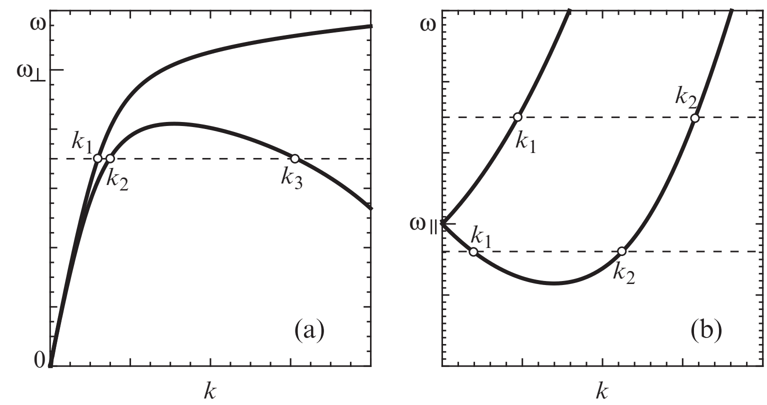

Fig. 4.5. Dispersion branches of transverse polaritons in chiral media. Note distinctly different ranges of frequencies (and wave vectors) in panels (**a**) and (**b**). Shown in (**a**) is a range around the frequency $\omega_\perp$ and below, a neighborhood of $\omega_\parallel$ would be above this plot. Shown in (**b**) is a range around the frequency $\omega_\parallel$ and above, a neighborhood of $\omega_\perp$ would be below this plot. The crossing of *dashed lines* with *dispersion curves* show allowed values k of the wave vector at a given frequency ω. Both panels feature polaritons with NGV

polarizations. One can easily see the connection by analyzing a region of ω in the vicinity of the resonance frequency $\omega_\perp$ where the inverse permittivity can be linearly approximated by

$$\varepsilon^{-1}(\omega) \simeq A_\perp(\omega_\perp - \omega), \quad A_\perp = 2\omega_\perp/F_\mathrm{e}, \tag{4.59}$$

as follows from the model expression (4.43). Using the approximation (4.59) in (4.58a) one rewrites the latter as $A_\perp(\omega_\perp - \omega \mp |\delta|k/A_\perp) = \omega^2/c^2k^2$, which is exactly the transverse polariton dispersion equation that would be obtained for excitons possessing their own dispersion law

$$\widetilde{\omega}_\perp(k) = \omega_\perp \mp \frac{|\delta|}{A_\perp}\, k. \tag{4.60}$$

One can compare (4.60) with (4.54). The linear behavior in (4.60) represents the first terms of the k-expansion of the exciton dispersion in the chiral medium with the chirality parameter δ determining the splitting effect in the vicinity of the resonance. When these dispersing excitons couple with light of two different circular polarizations, they form two of the polariton branches displayed in Fig. 4.5a. The first experimental observation of this branching and of a linear dependence of the frequency of dipole-active excitations on the wave vector was made for optical phonons propagating along the optical axis in quartz [44].

As is evident in Fig. 4.5a, the lower polariton branch features waves with negative group velocity whose wave vector is denoted by k_3. It is also transparent that there would be two other waves excited at the same frequency

ω whose wave vectors are denoted by k_1 and k_2. The relative amplitudes of these three waves depend on the matching of the incident wave vector to the wave vectors of the individual waves. An experimental realization of negative refraction due to k_3-waves again necessitates a large oscillator strength of the excitonic transition as well as a large rotatory power and a rather small dissipation of the additional polaritons below the resonance frequency.

4.4.3 Chiral Systems in the Vicinity of the Longitudinal Frequency

A "chiral route" to negative refraction has been specifically emphasized by Pendry [45] recently in a different frequency region: that in the vicinity of the longitudinal frequency $\omega_\parallel$. Related is the theoretical work on negative refraction in chiral materials with certain material parameters [46, 47], including demonstrations of focusing for circularly polarized waves [48,49]. Our consideration is based on the spatial dispersion approach. For more details we refer the reader to paper [50].

As the longitudinal frequency corresponds to the zero of the dielectric permittivity $\varepsilon(\omega)$, it is appropriate to use now expansion (4.51) of the dielectric tensor. Once again, the vanishing of $\varepsilon(\omega_\parallel)$ makes it clear that the next, spatially dispersive, term in that expansion is going to be qualitatively important. With the model dielectric permittivity (4.43),

$$\omega_\parallel = \sqrt{\omega_\perp^2 + F_{\mathrm{e}}/\epsilon_{\mathrm{b}}},$$

and $\varepsilon(\omega)$ behaves linearly as

$$\varepsilon(\omega) \simeq A_\parallel(\omega - \omega_\parallel), \quad A_\parallel = 2\epsilon_{\mathrm{b}}^2\omega_\parallel/F_{\mathrm{e}}, \tag{4.61}$$

in the immediate vicinity of the frequency $\omega_\parallel$.

Equation (4.51) corresponds to the material relation

$$\boldsymbol{D} = \varepsilon(\omega)\boldsymbol{E} + \mathrm{i}\gamma(\omega)\boldsymbol{E} \times \boldsymbol{k} \tag{4.62}$$

between the fields. Now it is the parameter $\gamma(\omega)$ that determines the magnitude of the chirality. The wave equation (4.13) then requires that *transverse* polaritons satisfy the equation

$$\left(\frac{c^2k^2}{\omega^2}\right)\boldsymbol{E} = \varepsilon(\omega)\boldsymbol{E} + \mathrm{i}\,\gamma(\omega)\boldsymbol{E} \times \boldsymbol{k}. \tag{4.63}$$

Of course, one can draw parallels between (4.63) and (4.57). Nontrivial solutions of (4.63) are circularly polarized waves whose dispersion has to be determined from

$$\varepsilon(\omega) - \frac{c^2k^2}{\omega^2} = \pm|\gamma(\omega)|k, \tag{4.64}$$

the plus and minus signs corresponding to waves of opposite handedness. Figure 4.5b illustrates the transverse polariton dispersion in this case in the region of frequencies around and above $\omega_{\|}$ resulting from (4.64) when using the model dielectric function $\varepsilon(\omega)$ of (4.43) and a model dependence of $\gamma(\omega) = \gamma_1/(\omega^2 - \omega_\perp^2)$.

The qualitative nature of the polariton spectrum in Fig. 4.5b is easily understood when using the linear approximation (4.61) in the dispersion equation (4.64), which immediately yields polariton dispersion curves in the form of "displaced parabolas":

$$\omega_\pm(k) \simeq \omega_{\|} + \frac{c^2}{A_{\|}\omega_{\|}^2}k^2 \pm \frac{\gamma}{A_{\|}}k, \tag{4.65}$$

where $\gamma = \gamma(\omega_{\|})$. As is evident in (4.65) and in Fig. 4.5b, for each frequency ω, where waves can exist there are two types of solutions with k-values denoted by k_1 and k_2 such that $k_1 \leq k_2$. For frequencies $\omega > \omega_{\|}$, k_1- and k_2-waves belong to different polarization branches ($\omega_+(k)$ and $\omega_-(k)$), while for $\omega < \omega_{\|}$, they belong to the same branch: $\omega_-(k)$ for $\gamma > 0$. The latter has a minimum of $\omega_-(k_{\min}) = \omega_{\|} - \Delta$ (the minimum of the allowed frequencies for the propagating waves) achieved at $k = k_{\min} \simeq (\omega_{\|}^2/2c^2)\gamma$. The depth of this minimum

$$\Delta = \omega_{\|} - \omega_-(k_{\min}) \simeq \gamma^2\omega_{\|}^2/4A_{\|}c^2, \tag{4.66}$$

strongly depends not only on $\omega_{\|}$ and γ but also on the value of $A_{\|}$. Clearly, it is the part $\omega_-(k < k_{\min})$ of the polariton spectrum, that is, k_1-waves at $\omega < \omega_{\|}$, that exhibits negative group velocities as the frequency in that part decreases with growing k_1. All other parts of the spectrum in (4.65) correspond to polaritons with positive group velocities. At the bottom of the allowed frequency range $\omega_{\|} - \Delta$, the wave vectors $k_1 = k_2 = k_{\min}$, and the polariton's group velocity vanishes.

It is interesting to note that, similarly to the case illustrated in Fig. 4.1, the negative group velocity waves in Fig. 4.5b appear in the region of frequencies that would be forbidden for electromagnetic waves – in the absence of the magnetic resonance in the system of Fig. 4.1 and in the absence of chirality in the system we consider now. In the former case, however, waves of arbitrary polarization have negative group velocities, while the chiral system supports negative group velocities for circularly polarized waves of one handedness only, waves of the other handedness have positive group velocities.

As left- and right-hand polarized waves propagate with different phase velocities, a linearly polarized light wave will experience a rotation of its plane of polarization. It is quantified by parameter ρ giving the rotation of the polarization plane per unit length of ray passage. It is useful to note that an exact (for unspecified $\omega-$dependences of $\varepsilon(\omega)$ and $\gamma(\omega)$) relationship follows from (4.64) for the difference between wave vector magnitudes at the same frequency $\omega > \omega_{\|}$:

$$k_2 - k_1 = \gamma(\omega)\omega^2/c^2. \tag{4.67}$$

Its exact counterpart for frequencies $\omega < \omega_{\|}$ relates the sum of wave vector magnitudes at the same frequency:

$$k_2 + k_1 = \gamma(\omega)\omega^2/c^2. \tag{4.68}$$

Equations (4.67) and (4.68) then lead [50] to the same result

$$\rho = \frac{\gamma(\omega)\omega^2}{2c^2}$$

in a given chiral medium both below and above the frequency $\omega_{\|}$. Measuring ρ thus provides experimental access to the chirality parameter $\gamma(\omega)$.

Dissipation can have a substantial detrimental effect on the possibility of realizing negative refraction conditions. A quantitative illustration for the case we consider now follows from the physically transparent statement that the dispersion of the waves shown in Fig. 4.5b retains its physical significance only if the minimum depth Δ in (4.66) is large enough in comparison with the dissipative width Γ of *transverse* electromagnetic waves in the region of frequencies around $\omega_{\|}$. As we have discussed in [50] for several examples, this restriction in fact leads to quite demanding requirements on the "allowed" magnitudes of gyrotropy (chirality) and dissipation.

We have shown [50] that ordinary specular reflection can be useful in experimental studies of candidate chiral materials: The interesting region of frequencies around $\omega_{\|}$ would be directly detectable in features of the frequency-dependent pattern of the reflection of linearly polarized incident light.

4.4.4 Surface Polaritons

Negative group velocity waves can also occur in two-dimensional wave propagation. We consider here an example of surface polariton waves in near resonance with modes of the surface transition layer. It is known that a surface transition layer (e.g., a thin film on a substrate) can drastically alter the dispersion of surface polaritons when the latter resonate with vibrational or electronic excitations of the layer [51]. If chosen properly, the transition layer can give rise to surface polariton dispersion curves exhibiting regions of negative group velocities.

Consider a system composed of a thin film of thickness $d \gg a$ (where a is the lattice constant) and dielectric function $\varepsilon(\omega)$, that is sandwiched between two semi-infinite media of dielectric functions $\varepsilon_1(\omega) > 0$ and $\varepsilon_2(\omega) < 0$. Surface polaritons in this system exist in a certain frequency range, and their dispersion curve $\omega(k)$ is determined by the equation [51]

$$\frac{\kappa_1}{\varepsilon_1} + \frac{\kappa_2}{\varepsilon_2} + k^2 p + \frac{\kappa_1}{\varepsilon_1}\frac{\kappa_2}{\varepsilon_2}\, q = 0. \tag{4.69}$$

Here k is the magnitude of the *two-dimensional* wave vector of the surface polaritons along the interface, which is assumed to be planar-isotropic. The parameters in (4.69) are defined as

$$\kappa_i = \sqrt{k^2 - \frac{\omega^2}{c^2}\,\varepsilon_i}, \quad i = 1, 2,$$

$$q = (\varepsilon - \varepsilon_2)\, d, \quad p = \left(\frac{1}{\varepsilon} - \frac{1}{\varepsilon_2}\right) d,$$

and $kd \ll 1$ has been assumed. For $d = 0$, the parameters p and q vanish, and (4.69) reduces to the familiar equation for the dispersion of surface polaritons at a single interface between two semi-infinite media. The effect we describe is due to the thin film, that is, due to $d \neq 0$. However, since $kd \ll 1$, it is clear that the terms proportional to d in (4.69) should become especially significant for frequency regions where either the dielectric function $\varepsilon(\omega) \simeq 0$ (longitudinal resonance) or its inverse $\varepsilon^{-1}(\omega) \simeq 0$ (transverse resonance). Often it is the former region where the effect of a thin film on the surface polariton dispersion of the substrate is much stronger.

To explicitly illustrate a significant effect of a thin film overlayer on surface polaritons near a resonance, let us consider the case of a thin film of metal covering a metal substrate. Then $\varepsilon_1 = 1$ and one can approximate the optical response of both metals by the Drude model expressions:

$$\varepsilon(\omega) = 1 - \frac{\omega_{\mathrm{p}}^2}{\omega^2}, \quad \varepsilon_2(\omega) = 1 - \frac{\omega_{2\mathrm{p}}^2}{\omega^2}. \tag{4.70}$$

In the absence of the thin film, the surface plasmon–polaritons of the substrate would exist in the frequency range

$$0 < \omega < \omega_{2\mathrm{p}}/\sqrt{2}.$$

Let us now choose conditions such that $\omega_{\mathrm{p}} \ll \omega_{2\mathrm{p}}$ so that a longitudinal resonance would be occurring at frequencies $\omega \simeq \omega_{\mathrm{p}}$. This is a resonance between the surface polaritons of the substrate and the plasmons of the thin metal film.

An illustrative example of the resulting dispersion of polaritons in this system is shown in Fig. 4.6 for the ratio $(\omega_{2\mathrm{p}}/\omega_{\mathrm{p}})^2 = 15.2$ and a film thickness d representative of experiments [52] where an aluminum substrate is coated by a silver film. As a consequence of the resonance, the polariton spectrum in Fig. 4.6 is split into two branches with a frequency gap appearing between them. Evidently, the lower branch of the polariton spectrum exhibits two modes for a given frequency ω. It is the modes with the larger k (denoted by k_2) that are additional surface polariton waves possessing NGV. The origin of the apparently linear negative slope can be readily revealed by the following analysis.

Indeed, for the conditions $\omega \simeq \omega_{\mathrm{p}} \ll \omega_{2\mathrm{p}}$, the magnitudes of the dielectric functions (4.70) would satisfy

$$-\varepsilon_2(\omega) \gg 1, \quad |\varepsilon(\omega)| \ll 1.$$

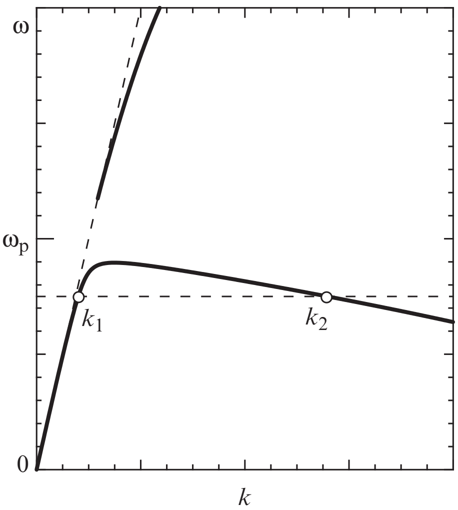

Fig. 4.6. Dispersion of surface polaritons due to a resonance at frequency ω_p with modes of a thin overlayer. Both a gap in the polariton spectrum and a branch with NGV (exemplified by the wave vector k_2 at a given frequency) are clearly seen

Then the second and fourth terms in (4.69) can be neglected because $|\kappa_2/\varepsilon_2| \ll \kappa_1$ and $|(\kappa_1\kappa_2/\varepsilon_1\varepsilon_2)\,q| \ll k^2|p|$. At large enough k, $\kappa_1 \simeq k$ and (4.69) immediately yields

$$\omega(k) \simeq \omega_\mathrm{p}(1 - kd/2) \tag{4.71}$$

for the corresponding polariton dispersion. Equation (4.71) describes the negative group velocity behavior seen in the lower polariton branch of Fig. 4.6.

We note the experimental observation [53] of the thermally excited radiation from such surface polaritons with NGV in systems of ZnSe films on Al and Cr. Also, experiments [54] for thin films of LiF on a sapphire substrate confirmed the square root dependence of the frequency gap on the film thickness d as follows from (4.69). This gap can increase substantially as the resonant plasma frequency increases and, in fact, a gap of 0.4 eV has been reported in [52] for surface plasmons on aluminum coated by a silver film of $d = 2.6\,\mathrm{nm}$, in good agreement with theory. Splitting of the surface polariton dispersion curve has also been observed in systems of organic monolayers [55] and thin films [56] on the surface of silver. In the latter case the observed splitting reached 0.18 eV.

Analysis of the propagation of surface waves requires a more complicated study of the ABCs because at the edge of the film one has to take into account diffraction and conversion of surface waves into bulk radiation [57].

4.5 Magnetic Permeability at Optical Frequencies

In Sect. 4.3 of this chapter we have already discussed certain aspects of the correspondence between two approaches used in the electrodynamics of continuous media. In this section, we continue with a more detailed look at the notion of magnetic permeability $\mu(\omega)$ used in the standard, symmetric, approach employing all four fields $\boldsymbol{E}, \boldsymbol{D}, \boldsymbol{B}, \boldsymbol{H}$. The Maxwell equations for plane waves in this approach are given by (4.16), and material relations by (4.17). As no ambiguity will arise, the notation $\boldsymbol{D}$ and $\boldsymbol{H}$ is now restored for the fields of the symmetric approach:

$$\boldsymbol{D} = \varepsilon(\omega)\boldsymbol{E}, \quad \boldsymbol{B} = \mu(\omega)\boldsymbol{H}. \tag{4.72}$$

The use of (4.72) with the Maxwell equations leads to the standard dispersion law (4.5) for plane waves propagating in a *spatially uniform* medium.

Our aim will be to discuss conditions under which the magnetic permeability $\mu(\omega)$ in (4.72) may retain its traditional direct physical meaning in the description of a continuous material. An analysis of this question for natural materials has been provided in Landau and Lifshitz's textbook [5] with the conclusion that "unlike $\varepsilon(\omega)$, the magnetic permeability $\mu(\omega)$ ceases to have any physical meaning at relatively low frequencies." We therefore feel that the issue is relevant as the quest for natural and artificial negatively refracting materials moves into the optical domain.

As is well known, a macroscopic description involves spatial averaging and, therefore, necessitates that a microscopic length (there can be more than one such length) characterizing the medium, a, is much smaller than the length of the spatial variation of macroscopic electromagnetic fields, that is, the wavelength λ for the electromagnetic waves in the medium. For natural materials, a is ordinarily of an atomic/molecular size, such as a crystal lattice constant, or of the order of the mean free path of charge carriers.

In many recent papers sparked by Pendry's work [58] (for references to earlier studies, see [13]), macroscopic Maxwell equations have been used to study wave propagation and negative refraction in artificial periodic or amorphous structures (metamaterials) that are composites consisting of various objects such as nonoverlapping split-ring resonators, small metallic or dielectric spheres, rods, pillars, etc. The geometrical sizes of these constituent objects, so to say artificial "molecules," and corresponding lattice constants (establishing the length scale a) can be hundreds of times larger than in natural materials. As an example, we will mention here the structure of pairs of gold nanopillars with various geometrical elements measuring 80–200 nm studied in [59] within the range of vacuum wavelengths from 400 to 700 nm. In another example of recent work [60], a doubly periodic array of pairs of parallel gold nanorods has been used, with the rods measuring $780 \times 220 \times 50$ nm with the illuminating light wavelength between 500 and 2,000 nm. The structures used in [59, 60] have been developed with the goal to fabricate metamaterials with a negative index of refraction at optical frequencies.

One could distinguish two different ways to analyze properties of the composite. As the size of the objects is much larger than actual atomic sizes, each of the objects would be describable within the framework of the ordinary macroscopic theory by appropriate choices for $\varepsilon(\omega)$ and $\mu(\omega)$. Wave propagation in the composite can then be studied by applying the Maxwell boundary conditions on the objects' surfaces within, e.g., the finite-difference time domain (FDTD) method of computational electrodynamics [61]. Evidently in this powerful straightforward approach there is no need to evaluate effective material constants of the metamaterial, while the ordinary $\varepsilon(\omega)$ and $\mu(\omega)$ would be spatially variable. Any restriction on the meaning of $\mu(\omega)$ here would be the same as for natural materials.

A different but conceptually and analytically attractive way is to perform a "secondary averaging" over the composite's structure, and to use the picture of an effectively uniform medium, which would be applicable so long as $\lambda \gg a$, with the corresponding *effective* medium permittivity and permeability. We will be commenting on the applicability of the notion of an effective $\mu(\omega)$ in this case.

4.5.1 Magnetic Moment of a Macroscopic Body

As analyzed by Landau and Lifshitz [5], a difficulty with the physical meaning of $\mu(\omega)$ at higher frequencies has to do with the fact that one may not be able to "measure" permeability by measuring the *total* induced magnetic moment of a macroscopic body. In the case of static fields, it is this total magnetic moment per unit volume that corresponds to the magnetization $\boldsymbol{M}$:

$$\boldsymbol{M} = (\boldsymbol{B} - \boldsymbol{H})/4\pi, \tag{4.73}$$

and allows one to introduce the permeability μ as a well-defined system response coefficient via (4.72). In the case of *time-dependent* fields, however, the total induced magnetic moment is contributed to not only by the magnetization (4.73) but also by the time-dependent dielectric polarization $\boldsymbol{P} = (\boldsymbol{D} - \boldsymbol{E})/4\pi$. The induced current density $\boldsymbol{J} = \langle \rho \boldsymbol{v} \rangle$, as a result of spatial averaging of the microscopic current density $\rho \boldsymbol{v}$ due to all charges in the system, now consists of two parts:

$$\boldsymbol{J} = c\nabla \times \boldsymbol{M} + \frac{\partial \boldsymbol{P}}{\partial t}. \tag{4.74}$$

A microscopic picture for this splitting of the induced current density using positions and velocities of charged particles in the medium is explicitly discussed, e.g., in [24, 38]. Equation (4.74) also follows directly from the macroscopic Maxwell equations. Indeed, consider the standard form

$$\nabla \times \boldsymbol{H} = \frac{1}{c}\frac{\partial \boldsymbol{D}}{\partial t} \tag{4.75}$$

that leads to the second line of (4.16) for plane waves. On the other hand, the exact microscopic Maxwell equation reads

$$\nabla \times \boldsymbol{b} = \frac{4\pi}{c}\rho\boldsymbol{v} + \frac{1}{c}\frac{\partial \boldsymbol{e}}{\partial t}, \tag{4.76}$$

where microscopic field values are denoted by lower-case characters. Spatial averaging yields $\boldsymbol{B} = \langle \boldsymbol{b} \rangle$, $\boldsymbol{E} = \langle \boldsymbol{e} \rangle$, and, hence, for (4.76):

$$\nabla \times \boldsymbol{B} = \frac{4\pi}{c}\boldsymbol{J} + \frac{1}{c}\frac{\partial \boldsymbol{E}}{\partial t}. \tag{4.77}$$

Subtracting (4.75) from (4.77) and using the definitions of $\boldsymbol{M}$ and $\boldsymbol{P}$ results in (4.74). We recall that the macroscopic current due to free charge carriers in conductors has been included in $\partial \boldsymbol{P}/\partial t$.

As the total induced current (4.74) consists of two parts, so does the total induced magnetic moment

$$\boldsymbol{M}^{\mathrm{tot}} = \frac{1}{2c}\int (\boldsymbol{r} \times \boldsymbol{J})\mathrm{d}V$$

of a macroscopic body:

$$\boldsymbol{M}^{\mathrm{tot}} = \boldsymbol{M}_1^{\mathrm{tot}} + \boldsymbol{M}_2^{\mathrm{tot}}, \tag{4.78}$$

where

$$\boldsymbol{M}_1^{\mathrm{tot}} = \int \boldsymbol{M}\,\mathrm{d}V \tag{4.79}$$

and

$$\boldsymbol{M}_2^{\mathrm{tot}} = \frac{1}{2c}\int \left(\boldsymbol{r} \times \frac{\partial \boldsymbol{P}}{\partial t}\right)\mathrm{d}V. \tag{4.80}$$

The association of the magnetization $\boldsymbol{M}$ with the magnetic moment of a unit volume of the body thus depends on the possibility to neglect in (4.78) the contribution (4.80) from the time-dependent dielectric polarization. Only then could the permeability $\mu(\omega)$ be "measured" separately to retain its traditional physical meaning as an independent system response coefficient related to the magnetic moment induced by the applied magnetic field according to (4.72) and (4.73). Another way to put it is the requirement of a physically meaningful separation of the magnetic current $c\,\nabla \times \boldsymbol{M}$ from the total induced current $\boldsymbol{J}$ in (4.74); see, e.g., [28] for estimates of various physical contributions to the total induced current.

By using the Maxwell equation (4.75) and the definitions of $\boldsymbol{M}$ and $\boldsymbol{P}$, one can, for instance, immediately evaluate the relative contributions to the induced current (4.74) taking place in the fields of a monochromatic electromagnetic wave. For the magnetic current to dominate,

$$|c\,\nabla \times \boldsymbol{M}| \gg \left|\frac{\partial \boldsymbol{P}}{\partial t}\right|,$$

would then require

$$R(\omega) = \left| \frac{\varepsilon(\omega) \, [\mu(\omega) - 1]}{\varepsilon(\omega) - 1} \right| \gg 1. \tag{4.81}$$

An electromagnetic wave, however, does not provide the most favorable conditions for separating the magnetic effect, as the electric field in the wave is relatively strong. Following Landau and Lifshitz [5], one would, instead, place a *small* macroscopic body in a time-dependent (monochromatic) magnetic field produced by some external current density $\boldsymbol{J}_{\text{ext}}$. For an explicit analytic treatment, let us take a cylindrical sample of length L and radius l that is positioned coaxially within a solenoid driven by an external current. The smallness of the sample in this geometry means

$$l \ll \lambda. \tag{4.82}$$

The sample, however, should still be macroscopic, that is, be much larger than the microscopic length scale a,

$$l \gg a, \tag{4.83}$$

for the very notion of (an effective) macroscopic permeability to be valid.

With (4.82) satisfied, the magnetic field in the sample is mostly produced by the external current. Let H be the magnitude of that uniform field. It leads to the uniform magnetization $M = [\mu(\omega) - 1]H/4\pi$ of the sample and its contribution (4.79)

$$M_1^{\text{tot}} = \left| \, l^2 L \, [\mu(\omega) - 1] \, H/4 \right| \tag{4.84}$$

to the total magnetic moment. The time-dependent magnetic field would also induce an electric field in the sample according to the Maxwell equation

$$\nabla \times \boldsymbol{E} = -\frac{1}{c} \frac{\partial \boldsymbol{B}}{\partial t}.$$

In our geometry the magnitude of this "circular" field varies with the distance x from the cylinder axis as $E = |\omega\mu(\omega)Hx/2c|$. The magnitude of the dielectric polarization current density is therefore $|\partial P/\partial t| = \left|\omega^2\mu(\omega)[\varepsilon(\omega) - 1]Hx/8\pi c\right|$, making the second contribution (4.80) to the total magnetic moment equal to

$$M_2^{\text{tot}} = \left| \, l^4 L \, \omega^2 \mu(\omega)[\varepsilon(\omega) - 1]H/32c^2 \right|. \tag{4.85}$$

For the magnetization contribution to dominate:

$$\left| \boldsymbol{M}_1^{\text{tot}} \right| \gg \left| \boldsymbol{M}_2^{\text{tot}} \right|,$$

Equations (4.84) and (4.85) now require

$$\frac{8c^2}{\omega^2 l^2} \left| \frac{1 - \frac{1}{\mu(\omega)}}{\varepsilon(\omega) - 1} \right| \gg 1. \tag{4.86}$$

Using, instead of the frequency ω, the corresponding wavelength $\lambda(\omega) = 2\pi c/\omega\sqrt{\varepsilon\mu}$ for plane waves in the medium, criterion (4.86) can be rewritten as

$$\frac{2}{\pi^2}\, R(\omega) \left(\frac{\lambda(\omega)}{l}\right)^2 \gg 1, \tag{4.87}$$

which is "weaker" than (4.81) by virtue of the condition (4.82). Frequency segments where condition (4.82) is not met should be excluded from the above consideration. Needless to say, the numerical coefficients in (4.86) and (4.87) are affected by the particular shape of the sample considered.

It is instructive to recognize that inequalities (4.81) and (4.86) would also follow naturally from a comparison of the medium response contributions to the transverse dielectric function in (4.26). Since the quantity $\varepsilon_\perp(\omega, k) - 1$ is proportional to the generalized dielectric susceptibility, one clearly sees two contributions to it in (4.26): One is the dielectric term $\propto [\varepsilon(\omega) - 1]$, and the other, $\propto k^2$, which determines the magnetic effect. The inequalities discussed above arise from the requirement that the latter contribution be larger than the former. The magnitude of the magnetic term, however, depends on the wave vector k. For a given frequency ω, inequality (4.81) would follow if, in (4.26), one uses the wave vector k that the transverse electromagnetic wave would have in this medium. Inequality (4.86), on the other hand, would follow if one takes wave vectors $k \sim 1/l$, of the order of the inverse sample size.

For inequality (4.86) to be better satisfied, the size l of the sample can be made as small as possible but still consistent with it comfortably remaining macroscopic, (4.83). Evidently, the smaller the microscopic scale a, the smaller l could be. The smallest magnitudes of a are of atomic/molecular sizes featured by natural materials. The presence of the factor ω^2 in the denominator of the combination in criterion (4.86) clearly shows that, while this criterion is safely satisfied at low enough frequencies, it becomes in general harder and harder to meet as the frequency ω increases. Of course, the criterion would also reflect the details of the frequency dispersions of $\varepsilon(\omega)$ and $\mu(\omega)$: using the model behavior in (4.3) and (4.4), for instance, would make the LHS of (4.86) equal to

$$\frac{8c^2}{\omega^2 l^2}\,\frac{F_\mathrm{m}}{F_\mathrm{e}} \left|\frac{\omega_\perp^2 - \omega^2}{\omega_\mathrm{mz}^2 - \omega^2}\right|. \tag{4.88}$$

The magnitude of expression (4.88) is enhanced in a narrow region around the zero-permeability frequency ω_mz, which would in reality be substantially mitigated by dissipation. Apart from that, the overall scale of expression (4.88) is determined by the factor

$$\frac{c^2}{\omega^2 l^2}\,\frac{F_\mathrm{m}}{F_\mathrm{e}} \sim \frac{\omega_\perp^2}{\omega^2}\,\frac{a^2}{l^2} \quad \rightarrow \quad \frac{a^2}{l^2} \quad (\text{for } \omega \sim \omega_\perp), \tag{4.89}$$

where the estimate has been made by using (4.50) for natural atomic or molecular materials with $\omega_\perp \sim \omega_\mathrm{mz}$. These molecular transition frequencies $\omega_\perp$ are in the range of optical frequencies. In view of condition (4.83), it is then clear from (4.89) that at optical frequencies $\omega \sim \omega_\perp$, inequality (4.86) cannot, in general, be satisfied in such materials. A measurement of the *total* magnetic moment of a macroscopic body in this frequency region would have a substantial contribution from polarization currents, (4.80), and, therefore, would not yield "independent" information on the magnetization $\boldsymbol{M}$ (except, perhaps, in some frequency intervals).

It seems reasonable to assume that an estimate similar to (4.89) would also be valid for a metamaterial built of small ($a \ll \lambda$) plasmonic structures, provided that the electric and magnetic resonance frequencies are of the order of ω_{p}, while the quantity equivalent to $F_{\mathrm{m}}/F_{\mathrm{e}}$ is of the order of $\omega_{\mathrm{p}}^2 a^2/c^2$. Results for various structural shapes suggested in the literature could be verified with respect to conditions like (4.86) to establish the range of frequencies where the permeability $\mu(\omega)$ retains its traditional physical meaning in a description of a macroscopic sample. Given the increased (in comparison with atomic) length scale a in metamaterials (tens and hundred(s) of nanometers), it is obvious, however, that the range of frequencies ω where one could have a reasonably satisfied ordering

$$a \ll l \ll \lambda(\omega), \tag{4.90}$$

would in general move to lower frequencies as the size a grows. In fact, it is possible that in metamaterials with larger a, the ordering (4.90) could not be established in a wide range of frequencies while the wavelength λ is still appreciably larger than a. Then the solenoidal setup to measure permeability becomes useless and one essentially is left with a criterion like (4.81). We are not aware of a better configuration to "measure" permeability.

As long as $\lambda(\omega) \gg a$, natural or metamaterials can, of course, still be described as continuous uniform bodies. The spatial dispersion approach using the tensor $\varepsilon_{ij}(\omega, \boldsymbol{k})$ then presents itself as a flexible way of providing such a description, including at frequencies where $\mu(\omega)$ would lose its physical significance and where magnetic effects would be indistinguishable from the spatial dispersion of dielectric effects. In the spatial dispersion framework one considers the total induced current without (artificially or arbitrarily) breaking it into parts – in the absence of a physically meaningful way to measure/address all the contributions separately. This framework allows one to analyze various material relations in a unified fashion. The overall response of the system in the spatial dispersion approach is described by as many phenomenological constants as are required by the symmetry of the system under consideration and by the "type" of the spatial dispersion. From our discussion in Sect. 4.3, it should be clear that, whenever spatial dispersion is restricted to the $\propto k^2$ terms as in (4.28), a description of *transverse polaritons* in an isotropic medium requires only two phenomenological parameters at each frequency ω, that is, only two coefficients in the expansion of $\varepsilon_\perp(\omega, k)$ in powers of k. The coefficient in front of k^2 can then be formally postulated to be related to $\mu(\omega)$ as in (4.26), independently of the physical origin of this coefficient. The standard expression (4.5) for the refractive index then also follows. This is the case where the phenomenology of the $\varepsilon(\omega)$–$\mu(\omega)$ formalism *is adequate*. One could then use this phenomenology to extract information on the so defined "effective" $\mu(\omega)$ from data on the refractive index $n(\omega)$ and separate measurements of $\varepsilon(\omega)$.

With structural sizes a in metamaterials becoming comparable with the wavelength λ in the medium, the continuum electrodynamics analysis of wave propagation in a composite as in a uniform body ceases to be possible, and one has to resort to descriptions using spatially variable (position-dependent) material response functions.

As more actual data on $\varepsilon(\omega)$ and $\mu(\omega)$ in 3D metamaterials become available, it will be interesting to analyze those data from the standpoint of the discussion in this section.

4.6 Related Interesting Effects

4.6.1 Generation of Harmonics from a Nonlinear Material with Negative Refraction

Generation of harmonics in media with a negative group velocity can have features that are worthwhile to discuss and investigate. Here we, following [7], will just give a brief qualitative account of one of these interesting effects. Consider a semi-infinite medium that supports negative refraction in some frequency range. Ordinarily one should expect that the spectral width $\Delta\omega$ of this range is relatively narrow: $\Delta\omega \ll \omega$. Suppose a laser beam of frequency ω_{l} is incident on the medium from vacuum, where ω_{l} is within the range $\Delta\omega$. Then the frequencies of the second ($2\omega_{\mathrm{l}}$) and higher harmonics will fall into regions of the spectrum where the medium supports waves with positive group velocities. Optical nonlinear susceptibilities $\chi^{(2)}, \chi^{(3)}, \ldots$, determine the sources of harmonics generation and, in the simplest approximation, such sources depend only on the incoming refracted wave. As the latter wave is in the frequency range of negative refraction, its wave vector $\boldsymbol{k}$ is directed *from* the bulk of the medium toward its surface, as depicted in Fig. 4.7a. Then the wave vector of the source, for instance of the second harmonic (SH), is $2\boldsymbol{k}$ and is also directed toward the vacuum–medium interface. The transmitted wave at frequency $2\omega_{\mathrm{l}}$, on the other hand, will have its wave vector directed from the interface into the bulk of the medium. Therefore, the wave vectors of the source of the harmonic and of this transmitted wave will be strongly phase mismatched and these waves will interact only weakly. This mismatch will then cause the dominant part of the energy from the source of the SH to be transferred to the *reflected* second harmonic propagating in vacuum away from the interface, as schematically shown in Fig. 4.7a. This effect could provide for an effective "quadratic mirror" that reflects the SH component generated by an incident laser beam in a medium with negative refraction. Details of the

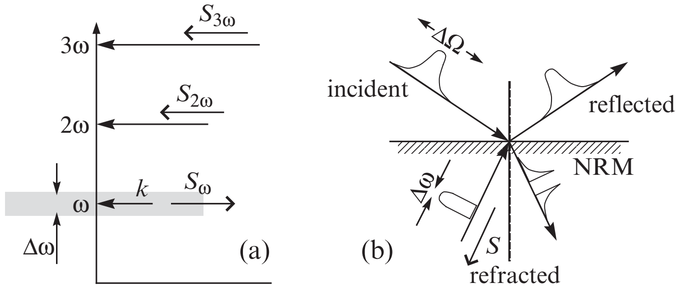

Fig. 4.7. Schematic illustrations for the effects discussed in Sect. 4.6. (**a**) Harmonics generation. The incident wave frequency ω falls within a narrow window $\Delta\omega$ of frequencies for negative group velocity waves in the medium. The energy transferred to higher harmonics at 2ω and 3ω will mostly propagate (Poynting vector $\boldsymbol{S}$) in the reflection mode. (**b**) An ultra-short pulse ($\Delta\Omega > \Delta\omega$) incident on a NRM leads to two refracted pulses of different spectral contents

corresponding calculations can be found in [7, 62]. (For a discussion of the generation of acoustic wave harmonics in one-dimensional phononic crystals with negative refraction, see [63].) Experimental studies of nonlinear effects are only in their beginning; we can mention paper [64] where an enhancement has been found of the intensity of the reflected SH in nonlinear left-handed transmission line media. Other nonlinear properties of artificial left-handed materials have been discussed in [65–67].

4.6.2 Ultra-Short Pulse Propagation in Negative Refraction Materials

Ultra-short pulses are currently available in a wide range of frequencies from THz to far UV. An interesting manifestation of negative refraction may occur when the spectral width $\Delta\Omega$ of a pulse is appreciably larger than the spectral width $\Delta\omega$ of the window where waves with negative group velocity exist in a negative refraction material (NRM). Qualitatively, one can think of the ultra-short pulse decomposed into frequency Fourier components, and can then follow the propagation of each component and compose the components back after the propagation. With $\Delta\Omega \gg \Delta\omega$, the pulse incident on the NRM is expected to split into three outgoing pulses with different spectral content as schematically shown in Fig. 4.7b. The reflected pulse would approximately have the spectral content of the incident pulse. The two transmitted pulses would have both different propagation directions and different spectral contents. A central part of the pulse spectrum (of width $\Delta\omega$) experiences negative refraction at the interface, but the "side" frequency components outside of the $\Delta\omega$ window propagate according to the rules of ordinary "positive" refraction. A spectroscopic study can therefore be used for the determination of the frequency interval $\Delta\omega$.

Interesting effects can also be expected for harmonics generation and wave mixing with ultra-short pulses – the harmonics would also propagate in an unusual way. As only some part of the spectrum of the input or output experiences negative refraction, the output pulses in transmission and reflection can be drastically different in terms of the energy, pulse shape, spectral composition, and direction, from those expected in an ordinary nonlinear medium. The details are complicated, and depend on the spectral contents of the ultra-short pulse and the NRM.

4.7 Concluding Remarks

In writing this chapter we have been very pleased to have an opportunity to pay our respect to L. I. Mandelstam who clearly analyzed how negative refraction occurs at an interface as a consequence of negative group velocity waves in one of the interfacing media [1–3]. Realizing that negative group velocity is at the heart of negative refraction, one finds it quite useful to look at various factors that may affect the dispersion law $\omega(\boldsymbol{k})$ of the waves propagating in the medium.

A natural and flexible way to analyze such factors for electromagnetic waves in effectively uniform media is within the spatial dispersion framework utilizing the notion of the generalized dielectric tensor $\varepsilon_{ij}(\omega, \boldsymbol{k})$ representing the electromagnetic response of the medium to perturbations of frequency ω and wave vector $\boldsymbol{k}$. Normal waves (polaritons) with negative group velocity can occur in the medium (whether in natural or in artificial metamaterials) when spatial dispersion ($\boldsymbol{k}$-dependence of the dielectric tensor) is strong enough. One particular situation of this kind (corresponding to spatial dispersion $\propto k^2$) is more familiar as the case of simultaneously negative dielectric susceptibility $\varepsilon(\omega)$ and magnetic permeability $\mu(\omega)$. The spatial dispersion approach assists in substantiating the description of such a situation at optical frequencies when $\mu(\omega)$ loses its traditional physical meaning, and even when no magnetic-dipole type response takes place in the medium.

Within the framework of the tensor $\varepsilon_{ij}(\omega, \boldsymbol{k})$ one can analyze in a *unified* fashion more complex types of material relations and the resulting qualitatively new effects, such as additional polariton waves. We have used this approach in this chapter to discuss several physical systems that may be capable of exhibiting polaritons with negative group velocity at optical frequencies. Our examples included both chiral and nonchiral systems, and bulk and surface polariton waves. We hope these examples will be helpful in identifying appropriate candidate media for experimental studies.

In order to focus on the physical origin of the negative group velocity polaritons in these systems, we left out many important issues that affect the possibility of practical realizations. One of these is the attenuation of waves due to dissipation, which, of course, is a common problem for different frequency regions. Crystals with sharp and strong excitonic resonances could therefore be good candidates among natural materials. Another problem is the low efficiency of utilization of additional polariton waves due to wave vector mismatch. Certain schemes, however, have been developed to improve this efficiency for positive group velocity waves, and such schemes are likely to be also useful for negative refraction.

Acknowledgments

This work was supported by AFOSR grant FA 9550-05-1-0409. VMA also thanks the Russian Foundation of Basic Research and the Ministry of Science and Technology of the Russian Federation for partial support. The authors are grateful to R.H. Baughman, A.A. Zakhidov, and especially Y.R. Shen for collaboration and discussion of various problems of negative refraction, and also to V.L. Ginzburg, C.M. Krowne, A.A. Maradudin, and Y. Zhang for reading the manuscript and making many useful suggestions.

References

1. L.I. Mandelstam, *Complete Works*, vol. 5 (USSR Academy of Sciences, Moscow, 1950), Lectures given on 26 February 1940 and on 5 May 1944
2. L.I. Mandelstam, *Zh. Eksp. Teor. Fiz.*, **15**, 475 (1945)
3. L.I. Mandelstam, *Lectures on Optics, Relativity and Quantum Mechanics* (Nauka, Moscow, 1972)
4. L. Brillouin, *Wave Propagation and Group Velocity* (Academic, New York, 1960)
5. L.D. Landau, E.M. Lifshitz, *Electrodynamics of Continuous Media* (Butterworth-Heinemann, Oxford, 1984)
6. V.M. Agranovich, V.L. Ginzburg, *Crystal Optics with Spatial Dispersion, and Excitons* (Springer, Berlin Heidelberg New York, 1984)
7. V.M. Agranovich, Y.R. Shen, R. Baughman, A.A. Zakhidov, *Phys. Rev. B*, **69**, 165112 (2004)
8. V.M. Agranovich, Y.R. Shen, R. Baughman, A.A. Zakhidov, J. Lumin. **110**, 167 (2004)
9. V.G. Veselago, Sov. Phys. Uspekhi **10**, 509 (1968)
10. A.L. Pokrovsky, A.L. Efros, Solid State Commun. **124**, 283 (2002)
11. R.A. Shelby, D.R. Smith, S. Schultz, Science **292**, 77 (2001)
12. J.B. Pendry, Phys. Rev. Lett. **85**, 3966 (2000)
13. A. Moroz, `http://www.wave-scattering.com/negative.html`
14. A. Boardman, N. King, L. Velasco, Electromagnetics **25**, 365 (2005)
15. K.T. McDonald, Am. J. Phys. **69**, 607 (2001)
16. H. Lamb, Proc. Lond. Math. Soc. **1**, 473 (1904)
17. M. Laue, Ann. Phys. (Leipzig) **18**, 523 (1905)
18. A. Schuster, *An Introduction to the Theory of Optics* (Edward Arnold, London, 1904)
19. E.L. Feinberg, Phys. Uspekhi **45**, 81 (2002)
20. D.V. Sivukhin, Opt. Spektrosk. **3**, 308 (1957)

21. V.E. Pafomov, Sov. Phys. JETP **9**, 1321 (1959)
22. V.L. Ginzburg, *Applications of Electrodynamics in Theoretical Physics and Astrophysics* (Gordon and Breach, New York, 1989), Chap. 7
23. V.E. Pafomov, Sov. Phys. JETP **5**, 307 (1957)
24. J.D. Jackson, *Classical Electrodynamics* (Wiley, New York, 1975)
25. V.M. Agranovich, V.E. Pafomov, A.A. Rukhadze, Sov. Phys. JETP **9**, 160 (1959)
26. I.M. Frank, Sov. Phys. JETP **9**, 580 (1959)
27. K.A. Barsukov, Sov. Phys. JETP **9**, 1052 (1959)
28. Yu.A. Il'inskii, L.V. Keldysh, *Electromagnetic Response of Material Media* (Plenum, New York, 1994)
29. D.B. Melrose, R.C. McPhedran, *Electromagnetic Processes in Dispersive Media* (Cambridge University Press, Cambridge, 1991)
30. S.M. Rytov, Zh. Eksp. Teor. Fiz. **17**, 930 (1947)
31. M.E. Gertsenshtein, Zh. Eksp. Teor. Fiz. **26**, 680 (1954)
32. A.A. Golubkov, V.A. Makarov, Phys. Uspekhi **38**, 325 (1995)
33. A.P. Vinogradov, Phys. Uspekhi **45**, 331 (2002)
34. D. Bedeaux, M. Osipov, J. Vlieger, J. Opt. Soc. Am. A **12**, 2431 (2004)
35. L. Keldysh, D. Kirzhnitz, A. Dolgov (eds.), *The Dielectric Function of Condensed Systems* (North-Holland, Amsterdam, 1989)
36. G.D. Mahan, *Many-Particle Physics* (Kluwer, New York, 2000)
37. Y. Toyozawa, *Optical Processes in Solids* (Cambridge University Press, Cambridge, 2003)
38. D.P. Craig, T. Thirunamachandran, *Molecular Quantum Electrodynamics* (Academic, London, 1984)
39. L.D. Barron, *Molecular Light Scattering and Optical Activity* (Cambridge University Press, Cambridge, 2004)
40. V.L. Ginzburg, Sov. Phys. JETP **7**, 1096 (1958)
41. S.I. Pekar, Sov. Phys. JETP **6**, 785 (1958)
42. L. Silvestri, O.A. Dubovski, G.C. La Rocca, F. Bassani, V.M. Agranovich, Nuovo Cimento Soc. Ital. Fis. C **27**, 437 (2004)
43. V.M. Agranovich, Sov. Phys. Uspekhi **3**, 427 (1961)
44. V.S. Pine, G. Dresselhaus, Phys. Rev. **188**, 1489 (1969)
45. J.B. Pendry, Science **306**, 1353 (2004)
46. S. Tretyakov, I. Nefedov, A. Sihvola, S. Maslovski, C. Simovski, J. Electromagn. Waves Appl. **17**, 695 (2003)
47. T.G. Mackay, Microw. Opt. Technol. Lett. **45**, 120 (2005)
48. Y. Jin, S. He, Opt. Express **13**, 4974 (2005)
49. C. Monzon, D.W. Forester, Phys. Rev. Lett. **95**, 123904 (2005)
50. V.M. Agranovich, Yu.N. Gartstein, A.A. Zakhidov, Phys. Rev. B **73**, 045114 (2006)
51. V.M. Agranovich, in *Surface Polaritons*, ed. by V.M. Agranovich, D.L. Mills (North-Holland, Amsterdam, 1982), p. 187
52. T. Lopez-Rios, F. Abeles, G. Vuye, J. Physique **39**, 645 (1978)
53. E.A. Vinogradov, T.A. Leskova, Phys. Rep. **194**, 273 (1990)
54. V.A. Yakovlev, G.N. Zhizhin, Opt. Commun. **15**, 293 (1975)
55. I. Pockrand, A. Brillante, D. Mobius, J. Chem. Phys. **77**, 6289 (1982)
56. J. Bellessa, C. Bonnand, J.C. Plenet, J. Mugnier, Phys. Rev. Lett. **93**, 036404 (2004)

57. V.M. Agranovich, T.A. Leskova, Prog. Surf. Sci. **29**, 169 (1988)
58. J.B. Pendry, Phys. Rev. Lett. **85**, 3965 (2000)
59. A.N. Grigorenko, A.K. Geim, H.F. Gleeson, Y. Zhang, A.A. Firsov, I.Y. Khrushchev, J. Petrovic, Nature **438**, 355 (2005)
60. V.M. Shalaev, W. Cai, U. Chettiar, H.K. Yuan, A.K. Sarychev, V.P. Drachev, V. KIldishev, Opt. Lett. **30**, 3356 (2005)
61. A. Taflove, *Computational Electrodynamics: The Finite-Difference Time-Domain Method* (Artech House, Boston, 1995)
62. I.V. Shadrivov, A.A. Zharov, Yu.S. Kivshar, arXiv:physics/0506092 (2005)
63. O.S. Tarasenko, S.V. Tarasenko, V.M. Yurchenko, JETP Lett. **80**, 484 (2004)
64. A.B. Kozyrev, H. Kim, A. Karbassi, D.W. van der Weide, Appl. Phys. Lett. **87**, 121109 (2005)
65. M. Lapin, M. Gorkunov, K.H. Rinhofer, Phys. Rev. E **67**, 065601 (2003)
66. A.A. Zharov, I.V. Shadrivov, Yu.S. Kivshar, Phys. Rev. Lett. **91**, 037401 (2003)
67. S. O'Brien, D. McPeake, S.A. Ramakrishna, J.B. Pendry, Phys. Rev. B **69**, 241101(R) (2004)

5

Negative Refraction in Photonic Crystals

W.T. Lu, P. Vodo, and S. Sridhar

Summary. The phenomenon of negative refraction (NR) by 2D photonic crystals (PCs) is demonstrated in microwave experiments. NR by PCs is observed in 2D parallel-plate waveguide and in 3D free space measurements. Results are in excellent agreement with band structure calculation and numerical simulation.

5.1 Introduction

The optical properties of isotropic materials that are transparent to electromagnetic (EM) waves can be characterized by a refractive index n. Given the direction of the incident beam θ_1 at the interface of vacuum and the material, the direction θ_2 of the outgoing beam can be determined using Snell's law, $\sin\theta_1 = n\sin\theta_2$. All naturally available transparent materials possess a positive refractive index, $n > 0$. Although we do know that materials with negative permittivity (ε) or negative permeability (μ) are available but do not allow light transmission, it was Veselago who in 1968 realized that double negative indices media with $\varepsilon, \mu < 0$ are consistent with Maxwell's equations [1]. This idea was largely ignored till 2001 when it was demonstrated that certain composite metamaterials refract microwaves negatively ($\theta_2 < 0$, $\theta_1 > 0$) and consequently a negative index of refraction $n < 0$ can be assigned to such materials [2].

Negative refractive index materials (NIM) exhibit some unusual propagation characteristics of EM waves. The most striking property is that of left-handed electromagnetism (LHE). Since for a plane wave, the electric field $\mathbf{E}$ and the magnetic field $\mathbf{H}$ are related to each other through $\mathbf{H} = (c/\mu\omega)\mathbf{k}\times\mathbf{E}$ and $\mathbf{E} = -(c/\varepsilon\omega)\mathbf{k}\times\mathbf{H}$, thus $\mathbf{E}$, $\mathbf{H}$, and $\mathbf{k}$ form a left-handed triplet in a NIM. Consequently the Poynting vector $\mathbf{S} = \mathbf{E}\times\mathbf{H}$ is antiparallel to the wave vector $\mathbf{k}$, so that $\mathbf{S}\cdot\mathbf{k} < 0$. A material possessing simultaneously negative permittivity $\varepsilon < 0$ and permeability $\mu < 0$ can be shown to necessarily have $n \equiv \sqrt{\varepsilon}\sqrt{\mu} < 0$ [1]. NIM are also referred to as left-handed metamaterials (LHM). In contrast $\mathbf{E}$, $\mathbf{H}$, $\mathbf{k}$ form a right-handed set corresponding to right-handed electromagnetism (RHE), and $\mathbf{S}\cdot\mathbf{k} > 0$ for conventional $n > 0$ materials.

The negative refraction (NR) of EM waves allows new approaches to control EM wave propagation, such as flat lens imaging [3] and planoconcave lens focusing [4]. These demonstrations of principles open the door for new approaches to a variety of applications from microwave to optical frequencies.

In this chapter, we first discuss the types of materials exhibiting NR. Then we focus on NR by PCs in microwave experiments. NR is reported in microwave experiments for metallic PCs in parallel-plate waveguide and in free space. We finally conclude with some remarks on applications of NR.

5.2 Materials with Negative Refraction

Currently all the materials showing NR have periodic structures. Depending on the ratio of the wavelength to the lattice constant and the underlying mechanism, these materials are loosely classified as two types of NIM.

The first type of NIM is the so-called metamaterial [2,5,6]. In these materials, the wavelength is much larger than the lattice constant. It is this type of artificial materials which initiated the whole field of NR. The prototype metamaterial consists of periodic split-ring resonators which lead to negative μ and periodic metallic wires which lead to negative ε. Since the metamaterial is operated near the magnetic resonance, high loss is expected. The push for this material to higher frequencies may be limited to the THz range [7–9]. The physics behind this limit is that any material will have $\mu \to 1$ since the electrons will not keep pace with the frequency of visible light [10], thus the split-ring resonators will cease to function at optical frequencies due to shrinking sizes. Also the metallic wires should be dense enough to give negative permittivity, otherwise the effective permittivity will be positive in the visible spectrum.

NR has also been shown in a network of LC circuits at microwave frequencies [11, 12]. This system also belongs to the class of metamaterials. NR is achieved through a high-pass LC network which supports backward waves, that is the Poynting vector is antiparallel to the wave vector. Materials supporting backward waves including NIM are also called backward-wave media [13]. This approach is inherently limited to RF and microwave frequencies. However, this transmission line concept has been used by Engheta et al. [14] to design NR materials in optics.

The second type of NIM is the photonic crystal (PC). PCs provide another way to manipulate EM waves [15]. A PC is an artificial periodic structure [16], usually made of a dielectric or metal, designed to control photons similar to the way a solid-state crystal controls electrons. It has since been proposed that NR can be achieved in PCs with lattice constant comparable to the wavelength [17, 18]. Locally both $\varepsilon, \mu > 0$ everywhere in a PC. The physical principles that allow NR in the PC [19–22] arise from the dispersion characteristics of wave propagation in a periodic medium, and are very different from that of the metamaterial in [2]. To have the desired dispersion characteristics for NR, large dielectric constant contrast is required which poses no problem on the availability of materials even in visible frequency range. Thus there is no fundamental limit on pushing NR in PC toward the visible. NR by PC has been recently reported in infrared spectral range [23].

Recently NR was also shown in anisotropic media, such as uniaxial crystals [24]. This type of material occurs naturally. The mechanism of NR in anisotropic media [24–26] is that the wave vector and group velocity are not parallel to each other. Thus with an appropriate orientation of surface cut, the parallel components of the wave vector and the group velocity will have opposite sign. This is similar to the PCs with certain designed wave vector–frequency dispersion relation. But NR in uniaxial crystals can be achieved only within certain small range of angles [27].

The most striking consequence of NR is the possible existence of "Perfect lens" [28], although causality and dissipation do pose some restriction [10, 29, 30] on the NIM. All of the above types of materials have been shown experimentally to have NR and planoconcave lens focusing [4]. Flat lens imaging using PC was first demonstrated in microwave experiments [3, 31] and preliminary results showed flat lens imaging in metamaterial and LC circuits [6, 12] as well. However, the uniaxial materials cannot lead to flat lens focusing due to the lack of all-angle negative refraction [18].

5.3 Negative Refraction in Microwave Metallic Photonic Crystals

In this section we present experimental evidence of NR in metallic PCs. Two kinds of microwave experiments were performed on PC prisms. One where the PC prisms were placed in a parallel-plate waveguide (PPW) with only transverse magnetic (TM) wave excitation and the other in free space for both TM and transverse electric (TE) microwaves. Parallel theoretical and numerical investigations of the band structure and simulations of wave propagation through the PC prisms were performed and exceptionally good agreement was found with the experimental results.

5.3.1 Metallic PC in Parallel-Plate Waveguide

In these experiments, the microwave metallic PC was an array of cylindrical copper rods of height $d = 1.26\,\mathrm{cm}$ and radius $r = 0.63\,\mathrm{cm}$ forming a triangular lattice. The lattice constant a is such that $r/a = 0.2$. Refraction measurements are carried out in a PPW made of a pair of metallic plates. The excitation in the PPW is only TM mode up to a cutoff frequency $c/2d \simeq 12\,\mathrm{GHz}$ such that the electric field $\mathbf{E}$ is parallel to and constant along the rod axis. A coax-to-waveguide adaptor is employed to couple microwave radiation into

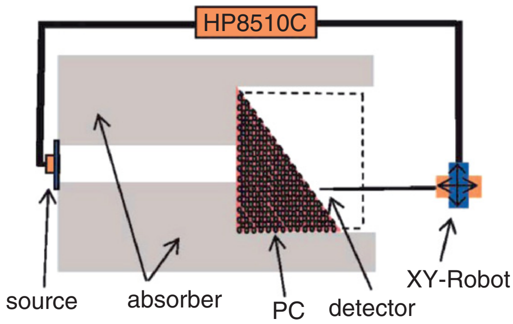

Fig. 5.1. Schematic diagram of microwave refraction experimental setup (not to scale). The X–Y plane is in the paper and the Z-axis is out of the paper

the parallel plate waveguide. Microwave absorbers are placed on either side to avoid spurious reflections and to collimate the propagating beam of width 9 cm, which is incident normally to a right angle prism of PC. On the far side a dipole antenna, attached to an X–Y robot, maps the electric field $\mathbf{E}$ through the transmission coefficient S_{21} using a microwave network analyzer HP8510C. A schematic diagram of the setup is shown in Fig. 5.1.

The measurements on the triangular lattice PC were carried out with the incident wave vector $\mathbf{k}_i$ along directions $\Gamma \to K$ and $\Gamma \to M$ of the lattice (these directions in the reciprocal space and in the real space are shown in Fig. 5.3). The angles of incidence, $\theta_K = 30°$ for $\Gamma \to K$ and $\theta_M = 60°$ for $\Gamma \to M$, are chosen in such a way that the periodicity on the surface of refraction is minimum to prevent higher-order Bragg diffraction. Accurate angles of refraction are obtained by fitting the emerging wave front with a plane wave, with the refraction angle θ_r as the fit parameter. Figure 5.2a illustrates the negatively refracted wave front at a refracted angle $\theta_{\mathrm{r}K} = -11.5°$ for $f = 9.77$ GHz with incidence along $\Gamma \to K$. Using Snell's law $n_\mathrm{eff} \sin\theta_K = \sin\theta_{\mathrm{r}K}$ with $\theta_K = 30°$ and $\theta_{\mathrm{r}K} = -11.5°$, we obtain an *effective* refractive index of $n_\mathrm{eff} = -0.4$ at this frequency. A second wave front can also be seen emerging from the top edge of the PC. We attribute this wave front to the edge effect due to the finite sample size. Figure 5.2b shows NR for the incident beam along $\Gamma \to M$ direction. In Fig. 5.2c, an illustrative example of positive refraction at $f = 6.62$ GHz is presented.

The refraction experiment was validated by data on a polystyrene prism having similar dimensions as that of the PC prisms. In Fig. 5.2d the direction of the emerging beam can be clearly seen at an angle $\theta_\mathrm{r} = +52.2°$ from the normal to the surface of refraction, corresponding to a positive refractive index $n = 1.58$ ($n \sin\theta = \sin\theta_\mathrm{r}$) for an incident angle $\theta = 30°$.

An understanding of NR and its relation to LHM in a PC can be achieved by examining the band structure and equifrequency surface (EFS) of an infinite PC (see Fig. 5.3). We have calculated the band structure using the

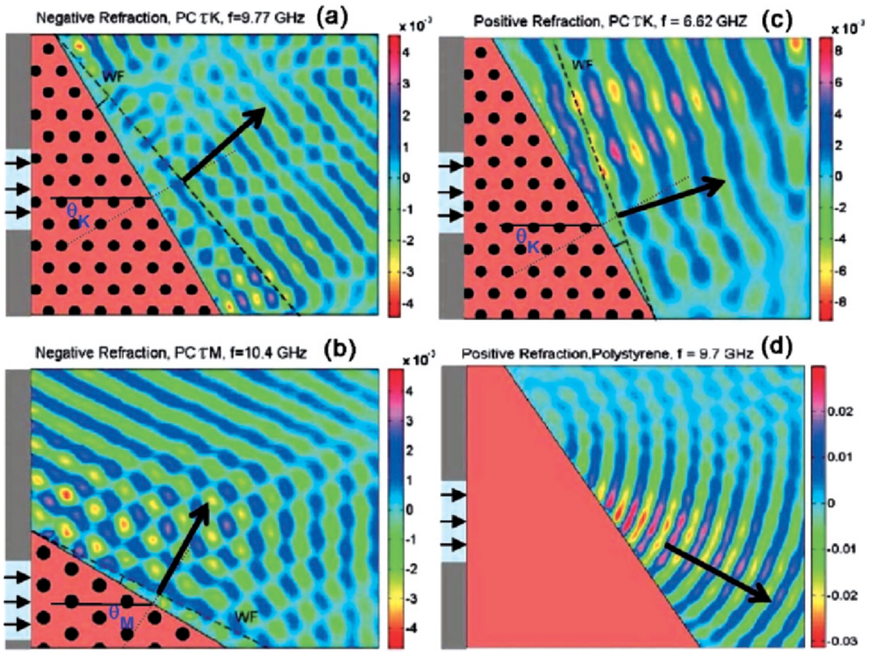

Fig. 5.2. (**a**)–(**d**) Measured electric field (real part of S_{21}) of the microwave. (**a**) Negative and (**c**) positive refraction by the metallic PC prism for the incident beam along $\Gamma \rightarrow K$ forming an angle of incidence 30° with the refraction surface. Wave front (WF) is shown as a *dashed line*. (**b**) NR for the incident beam along $\Gamma \rightarrow M$ forming an angle of incidence 60°. (**d**) Positive refraction by a polystyrene prism. In all the field maps, approximate area of each field map is $43 \times 40\,\mathrm{cm}^2$. The PC prisms and incident beams shown above are schematic and do not correspond to the actual scale

standard plane wave expansion method [16]. The EFS and band structure of the TM modes for the triangular lattice metallic PC are shown in Figs. 5.3a and 5.4a, respectively.

For a plane wave with wave vector $\mathbf{k}_i$ and frequency ω incident normally to an air–PC interface, the wave vector $\mathbf{k}_f$ inside the PC is parallel or antiparallel to $\mathbf{k}_i$ as determined by the band structure. If $\mathrm{d}\omega/\mathrm{d}k_f > 0$, $\mathbf{k}_f$ is parallel to $\mathbf{k}_i$ and consequently the EM field in the PC is right handed (RHE). Otherwise $\mathbf{k}_f$ is antiparallel to $\mathbf{k}_i$ and the EM field in the PC is left handed (LHE). For a general case the phase and group velocities in a medium are $\mathbf{v}_\mathrm{p} = (c/|n_\mathrm{p}|)\hat{\mathbf{k}}_f$ with $\hat{\mathbf{k}}_f = \mathbf{k}_f/k_f$ and $\mathbf{v}_\mathrm{g} = \nabla_\mathbf{k}\omega$. It can be proved analytically that the direction of group velocity $\mathbf{v}_\mathrm{g}$ in an infinite PC coincides with that of the energy flow $\mathbf{S}$ [32]. An effective refractive index can be defined as

$$n_\mathrm{p} = \mathrm{sgn}(\mathbf{v}_\mathrm{g} \cdot \mathbf{k}_f)ck_f/\omega \tag{5.1}$$

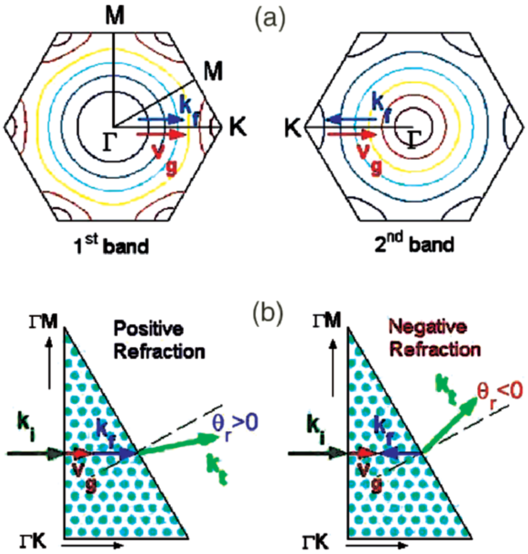

Fig. 5.3. (**a**) The EFS for the first and second bands of TM modes for the triangular lattice metallic PC with $r/a = 0.2$. Blue (red) color represents lower (higher) frequency. (**b**) Propagation wave vectors and group velocity for positive and negative refraction

and calculated from the band structure. The sign of n_{p} is determined from the behavior of the EFS. The EFS plots for the first and second bands of the triangular lattice are shown in Fig. 5.3a. The EFS that move outward from the center with increasing frequency correspond to RHE with $\mathbf{v}_{\mathrm{g}} \cdot \mathbf{k}_f > 0$ and inward moving surface correspond to LHE with $\mathbf{v}_{\mathrm{g}} \cdot \mathbf{k}_f < 0$. In the case of LHE (RHE) conservation of $\mathbf{k}_f$ component along the surface of refraction would result in negative (positive) refraction. The resulting refractive index n_{p} determined from the band structure and EFS using Eq. (5.1) for a beam incident along $\Gamma \rightarrow K$ (dashed line) and $\Gamma \rightarrow M$ (solid line) is shown in Fig. 5.4c. NR is predicted for regions in the second and third bands and positive refraction in the first and fourth bands. They are confirmed experimentally and shown in Fig. 5.4c.

We note the salient features of the experimental results and comparison to the band structure:

(I) In the first band between 6.2 and 7.7 GHz the EFS moves outward with increasing frequency (left panel of Fig. 5.3a), so that $n_{\mathrm{p}} > 0$ corresponding to RHE with $\mathbf{v}_{\mathrm{g}} \cdot \mathbf{k}_f > 0$. A representative field map at $f = 6.62$ GHz in Fig. 5.2c confirms the positive refraction as expected. The measured n_{p} are in good agreement with the theoretical calculations (Fig. 5.4c).

(II) In the second band between 7.7 and 11 GHz, the EFS moves inward with increasing frequency (right panel of Fig. 5.3a), consistent with $n_{\mathrm{p}} < 0$

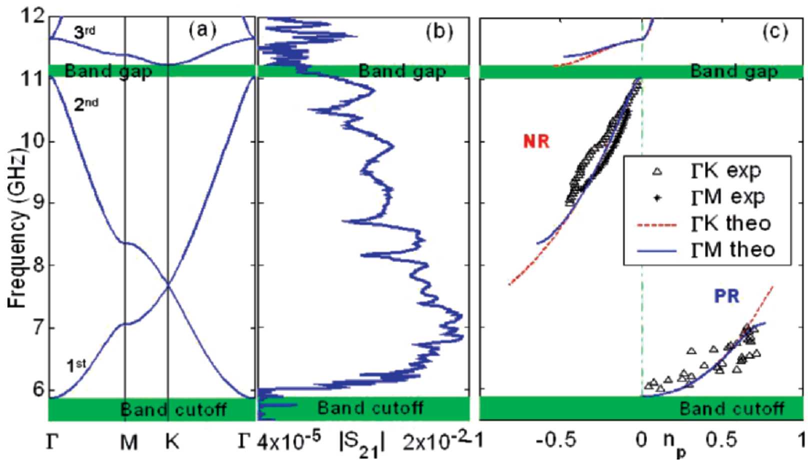

Fig. 5.4. (**a**) Band structure of TM modes for the triangular lattice metallic PC with $r/a = 0.2$ and $r = 0.63\,\text{cm}$. (**b**) Microwave transmission amplitude S_{21} vs. frequency f (GHz) on the far side. (**c**) Refractive index n_p determined from the experimental results for a beam incident along $\Gamma \rightarrow K$ ($\triangle$) and $\Gamma \rightarrow M$ (*) and compared with theory (*dashed* and *solid lines*)

corresponding to LHE with $\mathbf{v}_\text{g} \cdot \mathbf{k}_f < 0$. An illustrative field map in Fig. 5.2a at $f = 9.77\,\text{GHz}$ shows the emerging wave front in the negative direction. The experimental results of refraction for the incident beam along both $\Gamma \rightarrow K$ and $\Gamma \rightarrow M$ are in excellent agreement with the band structure calculations as shown in Fig. 5.4c.

(III) In certain frequency ranges in which the EFS is circular and frequency is not so high, the first-order Bragg diffraction is very weak. For the zeroth-order Bragg peak, n_p is frequency independent and consequently Snell's law is applicable. The index of refraction n_p shown in Fig. 5.4c in the region 9–11 GHz determined from the experimental wave field scans for different angles of incidence, viz., $\theta_{1K} = 30°$ for $\Gamma \rightarrow K$ and $\theta_{1M} = 60°$ for $\Gamma \rightarrow M$, is nearly angle independent due to the circular nature of the EFS, confirming the validity of Snell's law in this frequency region. Thus we have confirmed the validity of Snell's law both experimentally and theoretically (Fig. 5.4c). A noteworthy point is that the strong dielectric constant contrast in the metallic PC leads to near circular EFS (Fig. 5.3a) and results in NR in a wider frequency range than that of a dielectric PC.

(IV) The band cutoff at 6.2 GHz, transmission between 6.2–11.1 GHz and bandgap region 11.1-11.3 GHz, all of which are seen in the spectral transmission intensity shown in Fig. 5.4b, are in excellent agreement with the band structure calculations shown in Fig. 5.4a.

5.3.2 Numerical Simulation of TM Wave Scattering

The metallic PC prism experiment in PPW can be viewed as n-disk wave scattering in two dimensions [33]. While the system is chaotic in the short wavelength limit, the periodic structure in the n-disk system will give rise to coherent scattering phenomena such as NR.

Direct numerical simulations (see Fig. 5.5) of TM wave refraction were carried out and are in good agreement with the experimental results and band structure calculations. The simulation is done using a Green's function boundary wall approach originally developed for hard wall potentials in quantum mechanics [34]. The identification between the TM waves in a PPW and quantum wave function in two-dimensional hard wall potential lies in the fact that both the electric field $E_z(x, y)$ and quantum wave function $\psi(x, y)$ satisfy the same equation and the same boundary condition if the frequency in the waveguide is below the cutoff frequency $c/2d$ with d being the thickness of the PPW.

The simulations are carried out using a potential that is nonvanishing only on the boundary of the disks, that is

$$V(\mathbf{r}) = \gamma \sum_{\mathbf{R}} \delta(|\mathbf{r} - \mathbf{R}| - r_0). \tag{5.2}$$

Here r_0 is the radius of the disks located at $\mathbf{R}$, γ is the strength of the δ-function potential. As $\gamma \to \infty$, the wave function will vanish on the boundary of the disks. In this limit, whether there will be nonvanishing wave function inside the disks is of no concern to us.

With this potential model, the numerical implementation of the Green's function scattering is quite straight forward. Details and numerical accuracy can be found in [34].

As shown in Fig. 5.5, the simulation results in NR for $f = 9.7$ GHz in the second band, and positive refraction for $f = 6.6$ GHz in the first band, both in agreement with the experimental results shown in Fig. 5.2.

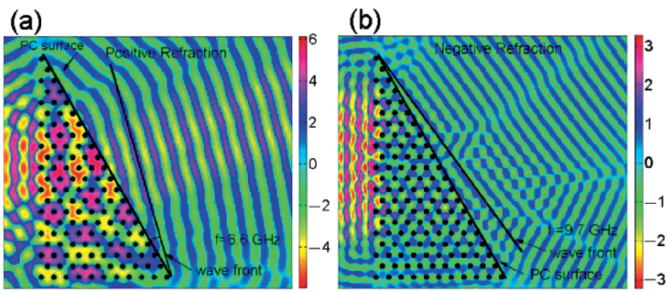

Fig. 5.5. Simulations of wave refraction showing the wave front emerging from a metallic PC: (**a**) positive refraction at 6.6 GHz and (**b**) negative refraction at 9.7 GHz. The PC used in the simulations has the same size as that used in the experiment. The electric field is plotted as $E_z^{1/3}$ for better visibility

5.3.3 Metallic PC in Free Space

In Sect. 5.3.2, we have demonstrated NR by metallic PC in PPW. This approach has the advantage to map out all the waves coming out of the PC, thus being able to probe not only the far field but also the near field feature around the surface of refraction. This study is limited to the TM modes.

In this subsection we describe NR for both TM ($\mathbf{E}_{\parallel}$ to the rod axis) and TE ($\mathbf{E}_{\perp}$ to the rod axis) mode propagation, in a metallic PC prism suspended in free space [35]. The angle of the refracted beam was measured directly, similar to the prism experiments in optics. The results show that a PC can exhibit NR with tailor made refractive indices in a large frequency range. The propagation in different bands of the PC can be tuned with frequency to obtain either negative or positive refraction. Thus the present tailor made PC can be utilized for a variety of applications.

The microwave metallic PC consists of an array of cylindrical copper tubes of height 60 cm and outer radius $r = 0.63$ cm arranged on a triangular lattice with $r/a = 0.2$. Refraction experiments were performed in an anechoic chamber of dimensions $5 \times 8 \times 4\,\mathrm{m}^3$ to prevent reflections from the walls. A square X-band horn placed at 3 m from the PC acts as a plane wave source (Fig. 5.6). Placing a piece of microwave absorber with a 6×6 in.^{2} aperture in front of the PC narrows the incident beam. On the far side another square horn attached to a goniometer swings around in two-degree steps to receive the emerging beam. Refraction is considered positive (negative) if the emerging signal is received to the right (left) of the normal to the surface of refraction of the PC. Measurements were carried out with the incident wave vector $\mathbf{k}_i$ along $\Gamma \to M$ direction of the first Brillouin zone of the PC and in both TM and TE modes. The angle of incidence $\theta = 60°$ for $\Gamma \to M$ is chosen in order to

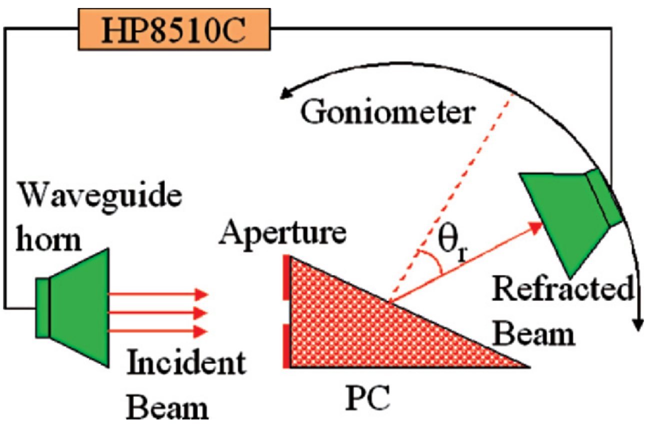

Fig. 5.6. Microwave free-space refraction experiment setup in an anechoic chamber. Negative or positive refraction is determined from the direction of the emerging signal with the normal to the surface of refraction

minimize surface periodicity along the surface of refraction, thus eliminating higher-order Bragg waves.

Figure 5.7a shows a plot of the transmitted intensity measured at different angles and incident frequencies for the TM mode propagation. The angle θ_r of the refracted beam is converted into the refractive index n_p through Snell's law $\sin\theta_\mathrm{r} = n_\mathrm{p}\sin\theta$ with $\theta = \pi/3$. As can be seen from the figure between 6 and 7.1 GHz the signal emerges on the positive side of the normal to the surface corresponding to positive refraction. No transmission is observed between 7.1 and 8.3 GHz. Between 8.3 and 11 GHz two signals are observed, one on the positive and the other on the negative side of the normal. The negatively refracted signal is strongest around 10.7 GHz and positively refracted signal around 8.6 GHz. Although both positively and negatively refracted signals

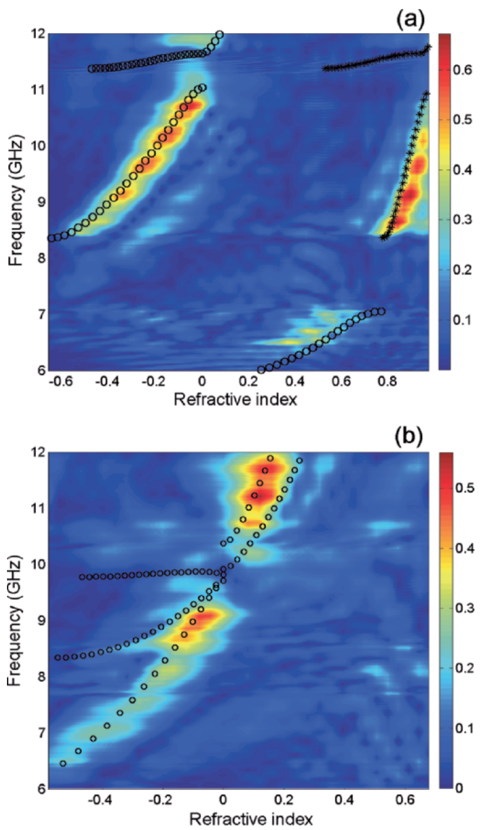

Fig. 5.7. (**a**) Plot of refracted wave intensity measured at various angles, for TM mode propagation. (**b**) Similar plot for TE mode. *Circles* are the theoretically calculated refractive indices corresponding to the zeroth order Bragg wave and *stars* are for the first-order Bragg wave

are observed, with the increase in frequency positive signal gets weaker while negative signal gets stronger.

We have also carried out measurements of refraction for TE mode propagation. The results for these modes are shown in Fig. 5.7b. Here NR is observed between 6.4 and 9.8 GHz and positive refraction between 9.8 and 12 GHz. It is important to note that NR is possible for both TM and TE modes; such a freedom in the choice of modes provides a crucial advantage of using the metallic PC over the split-ring and wire array metamaterial.

The band structures of the 2D triangular PC for both TM and TE modes are shown in Fig. 5.8. From the band structure for TM modes of propagation NR is predicted for the second and third band regions, with positive refraction in the first band. In the first TM band between 6 and 7.1 GHz the EFS moves outward with increasing frequency, so that $\mathbf{v}_\mathrm{g} \cdot \mathbf{k}_f > 0$. In the second TM band between 8.3 and 11 GHz, the EFS moves inward with increasing frequency, consistent with $n_\mathrm{p} < 0$ corresponding to LHE with $\mathbf{v}_\mathrm{g} \cdot \mathbf{k}_f < 0$. The bandgap is in the frequency range 7.1–8.3 GHz (partial gap along $\Gamma \rightarrow M$ direction) between the first and second passbands and from 11 to 11.2 GHz (complete gap) between the second and third bands. For the TE modes, NR is predicted for the second, third, and fourth bands. Partial bandgap along $\Gamma \rightarrow M$ direction is between 4.5 and 6 GHz.

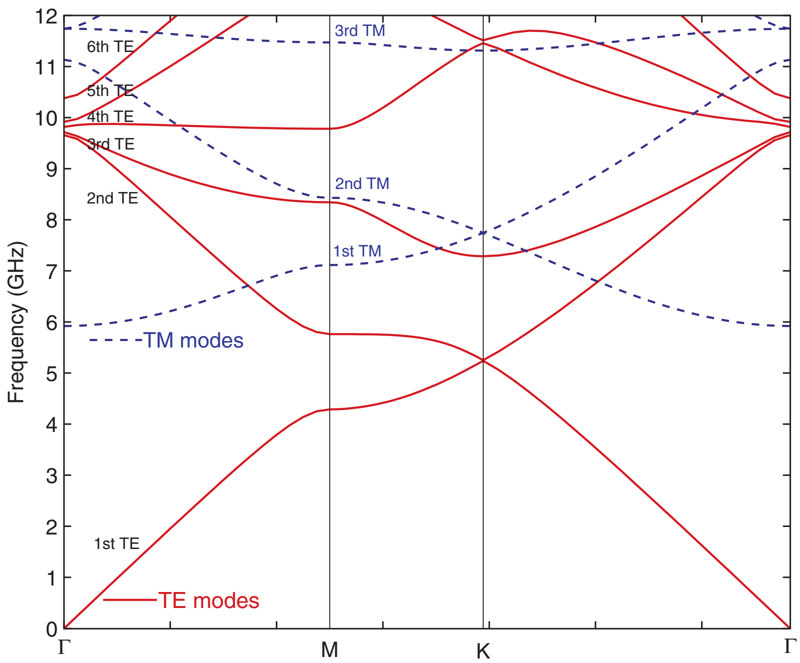

Fig. 5.8. Band structures of the triangular metallic PC with $r/a = 0.2$ and $r = 0.63\,\mathrm{cm}$ for both TM (*dashed lines*) and TE (*solid lines*) modes

In Fig. 5.7a, b the refractive indices n_p defined in (5.1) and determined from the band structure are plotted with experimental data. The close match between the theory and experiments is striking. All the predicted features including bandgap, negative and positive refraction are observed in the experiments. The degeneracy observed in the case of TE modes is due to multiple bands for a single frequency, which results in multiple propagation $\mathbf{k}$ vectors. It is an interesting observation that different intensities are associated with different propagation vectors for TE modes. For these modes with $\Gamma \to M$ propagation, as shown in Fig. 5.7, it can be seen that the higher the slope of the curve the more intense the beam.

A particular feature of interest is the bandwidth for NR and LHE. From Fig. 5.8 it can be deduced that the bandwidth for TE modes is 42% and for TM modes 27%. In comparison, a relatively weakly modulated dielectric PC has a bandwidth estimated to be 6.3% which is very narrow and the experimentally obtained bandwidth for metamaterials [2, 5] to date is only 10%. The present bandwidths for both TE and TM modes are higher than that in metamaterial. Bandwidth puts stringent restrictions on the tunability and functional range of the devices based on the LHM. In particular in our recent work we have shown that in the LHM, EM wave propagation is slow with group velocity of $0.02c$, where c is the speed of light in vacuum. This slow group velocity [36] combined with large bandwidth can be used for designing a delay line filter with a large passband.

In the case of TE modes, for an incident angle of 60°, the refractive index is found to vary from 0 to -0.48, which is a 200% change for a frequency change of 42%. Such a large $\mathrm{d}n/\mathrm{d}\omega$ results in a large $\mathrm{d}\phi/\mathrm{d}\omega$ which can be used in designing ultrasensitive phase shifters.

5.3.4 High-Order Bragg Waves at the Surface of Metallic Photonic Crystals

In this subsection we will discuss in detail the situation for all orders of Bragg diffraction and show that even with the presence of high-order Bragg diffraction, the appearance of NR is unambiguous and the direction of the Bragg wave beam determined from theory matches well with the experimental observation.

At the second interface between the PC prism and the air, the waves penetrate into the air through all orders of Bragg waves. The parallel and vertical components of the mth-order Bragg wave vector along the surface are

$$k_{t\|m} = k_f \sin\theta + 2m\pi/a_\mathrm{s}, \quad k_{t\perp m} = \sqrt{\omega^2/c^2 - k_{t\|m}^2}. \tag{5.3}$$

Here k_f is the wave number in the PC and a_s is the surface periodicity. For the band with NR, k_f is negative. The electric field of the outgoing waves from this interface can thus be written as a summation over all orders of Bragg wave $\mathbf{k}_{tm}$

$$E_{zt} = a_0 e^{i\mathbf{k}_{t0}\cdot\mathbf{r}} + a_1 e^{i\mathbf{k}_{t1}\cdot\mathbf{r}} + \cdots . \tag{5.4}$$

Depending on the a_{s} and the incident angle θ, only the first few Bragg waves will have real $k_{t\perp m}$ and can propagate. The refracted angle can be obtained from $\theta_{\mathrm{r}} = \arctan(k_{t\|}/k_{t\perp})$ for each beam. In all of the prescribed experiments, the surface periodicity is $a_{\mathrm{s}} = 3.15\,\mathrm{cm}$.

Let us first consider the TM modes. For the incident beam along the $\Gamma \to K$ direction, $\theta = \pi/6$. In the first band, if the frequency is below 7.12 GHz, only the zeroth-order Bragg wave will propagate in the air. For the incident beam along the $\Gamma \to M$ direction, $\theta = \pi/3$, the first-order Bragg diffraction will be suppressed for frequency below 6.70 GHz in the first band. For the second band along either $\Gamma \to K$ or $\Gamma \to M$ direction, the zeroth- and the first-order Bragg diffraction will propagate. Even if present, the first-order Bragg wave is much weaker than the zeroth-order Bragg wave as can be seen in Figs. 5.2a, b, 5.5b, and 5.7a. Thus we were able to determine n_{p} which corresponds to the zeroth-order Bragg wave. The measured angles for the first-order Bragg waves match perfectly with the theory as shown in Fig. 5.7a.

For the TE modes with incident beam along $\Gamma \to M$ direction, one has $\theta = \pi/3$. For all the first three bands which are below 9.52 GHz, only the zeroth-order Bragg wave will propagate. For frequencies above 9.52 GHz, higher-order Bragg diffraction will be present. This can be clearly seen in Fig. 5.7b.

5.4 Conclusion and Perspective

In this chapter, NR was demonstrated experimentally for both TM and TE mode propagation in metallic PCs. Two approaches were used, one was measuring the energy beam direction and the other by mapping out the electric field with magnitude and phase to determine the wave front of the refracted beam. Thus the verification of NR is unambiguous. A major feature is the extraordinary level of control exemplified by the convergence between the experimental data, band structure calculations, and simulations. The ease and low cost of fabrication of the metallic PC compared with a dielectric PC and metamaterials makes them ideal for a wide range of applications. Precise control over the geometry, choice of mode, and scalability to submicron dimensions of PCs show promise for applications from microwave to optical frequencies. This means that a variety of tailor-made structures are feasible to be designed and constructed.

Numerous possibilities open up by the present results. For applications such as imaging, one requires index matching between the negative index material and surroundings accompanied by negligible losses. These requirements are more easily met with PCs than with metamaterials. Metallic PC offers additional advantages of the high dielectric constant contrast compared with dielectric PC and low attenuation compared with metamaterial. Furthermore the microwave PC can be easily scaled to 3D [37,38], and to optical frequencies which is highly unlikely with metamaterials [2]. Thus the advantages of NR and LHE, such as imaging by flat lenses, planoconcave lens focusing, beam steerers, couplers, and others, are feasible with PCs from microwave to optical frequencies. With large group dispersion [39], slow light [36], and nonlinear properties [40] in PCs, the all-optical circuits computer is closer to becoming a reality.

NR provides a new arena for physics and technology to emerge and enhance each other. New ideas of NR [41,42] continue to emerge in this expanding field of physics. Though Pendry's perfect lens is an ideal limit and may never be realized due to loss [30], the poor man's lens using the near field of metallic thin film has produced improved subwavelength imaging [43, 44]. This may enhance the performance of lithography [45]. Optical components utilizing NR are expected to have several advantages. Examples are flat lenses without optical axis [28,31], subwavelength resolution imaging [46], and improved lens performance due to reduced aberrations [47, 48]. In addition light weight and compact structures offer additional advantages in a variety of applications.

Acknowledgment

This work was supported by the National Science Foundation and the Air Force Research Laboratories, Hanscom, MA.

References

1. V. Veselago, Sov. Phys. Usp. **10**, 509 (1968)
2. R.A. Shelby, D.R. Smith, S. Schultz, Science **292**, 77 (2001)
3. P.V. Parimi, W.T. Lu, P. Vodo, S. Sridhar, Nature (London) **426**, 404 (2003)
4. P. Vodo, P.V. Parimi, W.T. Lu, S. Sridhar, Appl. Phys. Lett. **86**, 201108 (2005)
5. C.G. Parazzoli, R.B. Greegor, K. Li, B.E.C. Koltenbah, M. Tanielian, Phys. Rev. Lett. **90**, 107401 (2003)
6. A.A. Houck, J.B. Brock, I.L. Chuang, Phys. Rev. Lett. **90**, 137401 (2003); J.B. Brock, A.A. Houck, I.L. Chuang, Appl. Phys. Lett. **85**, 2472 (2004)
7. C. Enkrich, M. Wegener, S. Linden, S. Burger, L. Zschiedrich, F. Schmidt, J.F. Zhou, Th. Koschny, C.M. Soukoulis, Phys. Rev. Lett. **95**, 203901 (2005)
8. J. Zhou, Th. Koschny, M. Kafesaki, E.N. Economou, J.B. Pendry, C.M. Soukoulis, Phys. Rev. Lett. **95**, 223902 (2005)
9. W.J. Padilla, A.J. Taylor, C. Highstrete, M. Lee, R.D. Averitt, Phys. Rev. Lett. **96**, 107401 (2006)
10. L. Landau, I.M. Lifshitz, *Electrodynamics of Continuous Media*, 2nd edn. (Elsevier, Amsterdam, 1984)
11. G.V. Eleftheriades, A.K. Iyer, P.C. Kremer, IEEE Trans. Microw. Theory Tech. **50**, 2702 (2002)
12. A. Grbic, G.V. Eleftheriades, Phys. Rev. Lett. **92**, 117403 (2004); J. Appl. Phys. **98**, 043106 (2005)
13. I.V. Lindell, S.A. Tretyakov, K.I. Nikoskines, S. Ilvonen, Microw. Opt. Tech. Lett. **31**, 129 (2001)
14. N. Engheta, A. Salandrino, A. Alù, Phys. Rev. Lett. **95**, 095504 (2005)

15. J.D. Joannopoulos, P.R. Villeneuve, S. Fan, Nature **386**, 143 (1997)
16. J.D. Joannopoulos, R.D. Meade, J.N. Winn, *Photonic Crystals: Molding the Flow of Light* (Princeton University Press, Princeton, 1995)
17. M. Notomi, Phys. Rev. B **62**, 10696 (2000); Opt. Quant. Electron. **34**, 133 (2002)
18. C. Luo, S.G. Johnson, J.D. Joannopoulos, J.B. Pendry, Phys. Rev. B **65**, 201104 (2002)
19. S. Foteinopoulou, E.N. Economou, C.M. Soukoulis, Phys. Rev. Lett. **90**, 107402 (2003)
20. S. Foteinopoulou, C.M. Soukoulis, Phys. Rev. B **67**, 235107 (2003)
21. E. Cubukcu, K. Aydin, E. Ozbay, S. Foteinopoulou, C.M. Soukoulis, Nature **423**, 604 (2003)
22. P.V. Parimi, W.T. Lu, P. Vodo, J. Sokoloff, J.S. Derov, S. Sridhar, Phys. Rev. Lett. **92**, 127401 (2004)
23. A. Berrier, M. Mulot, M. Swillo, M. Qiu, L. Thyln, A. Talneau, S. Anand, Phys. Rev. Lett. **93**, 073902 (2004)
24. Y. Zhang, B. Fluegel, A. Mascarenhas, Phys. Rev. Lett. **91**, 157404 (2003)
25. Z. Liu, Z. Lin, S.T. Chui, Phys. Rev. B **69**, 115402 (2004)
26. X.L. Chen, M. He, Y. Du, W.Y. Wang, D.F. Zhang, Phys. Rev. B **72**, 113111 (2005)
27. H. Kosaka, T. Kawashima, A. Tomita, M. Notomi, T. Tamamura, T. Sato, S. Kawakami, Phys. Rev. B **58**, R10096 (1998)
28. J.B. Pendry, Phys. Rev. Lett. **85**, 3966 (2000)
29. D.R. Smith, N. Kroll, Phys. Rev. Lett. **85**, 2933 (2000)
30. N. Garcia, M. Nieto-Vesperinas, Phys. Rev. Lett. **88**, 207403 (2002)
31. W.T. Lu, S. Sridhar, Opt. Express **13**, 10673 (2005)
32. K. Sakoda, *Optical Properties of Photonic Crystal* (Springer, Berlin Heidelberg New York, 2001)
33. W. Lu, L. Viola, K. Pance, M. Rose, S. Sridhar, Phys. Rev. E **61**, 3652 (2000)
34. M.G.E. Da Luz, A.S. Lupu-Sax, E.J. Heller, Phys. Rev. E **56**, 2496 (1997)
35. P. Vodo, P.V. Parimi, W.T. Lu, S. Sridhar, R. Wing, Appl. Phys. Lett. **85**, 1858 (2004)
36. E. Di Gennaro, P.V. Parimi, W.T. Lu, S. Sridhar, J.S. Derov, B. Turchinetz, Phys. Rev. B **72**, 033110 (2005)
37. D.F. Sievenpiper, M.E. Sickmiller, E. Yablonovitch, Phys. Rev. Lett. **76**, 2480 (1996)
38. C. Luo, S.G. Johnson, J.D. Joannopoulos, Appl. Phys. Lett. **81**, 2352 (2002)
39. M. Notomi, K. Yamada, A. Shinya, J. Takahashi, C. Takahashi, I. Yokohama, Phys. Rev Lett. **87**, 253902 (2001)
40. M. Soljačić, J.D. Joannnopoulos, Nat. Mater. **3**, 211 (2004)
41. V.A. Podolskiy, E.E. Narimanov, Phys. Rev. B **71**, 201101 (2005)
42. H. Shin, S. Fan, Phys. Rev. Lett. **96**, 073907 (2006)
43. W.T. Lu, S. Sridhar, Microw. Opt. Tech. Lett. **39**, 282 (2003)
44. N. Fang, H. Lee, C. Sun, X. Zhang, Science **308**, 534 (2005)
45. D.O.S. Melville, R.J. Blaikie, C.R. Wolf, Appl. Phys. Lett. **84**, 4403 (2004)
46. C. Luo, S.G. Johnson, J.D. Joannopoulos, J.B. Pendry, Phys. Rev. B **68**, 045115 (2003)
47. D. Schurig, D.R. Smith, Phys. Rev. E **70**, 065601 (2004)
48. J. Chen, C. Radu, A. Puri, Appl. Phys. Lett. **88**, 071119 (2006)

6

Negative Refraction and Subwavelength Focusing in Two-Dimensional Photonic Crystals

E. Ozbay and G. Ozkan

Summary. We experimentally and theoretically demonstrate negative refraction and focusing on electromagnetic (EM) waves by using two-dimensional photonic crystal slabs at microwave frequencies. Negative refraction is observed both for transverse magnetic (TM) and transverse electric (TE) polarized incident EM waves. Gaussian beam shifting method is used to verify negative refractive index. Subwavelength imaging and flat lens behavior of photonic crystals are successfully demonstrated. We have been able to overcome the diffraction limit and focus the EM waves to a spot size of 0.21λ. Metallodielectric photonic crystals are employed to increase the range of angles of incidence that results in negative refraction. Experimental results and theoretical calculations are in good agreement throughout the work.

6.1 Introduction

Materials which possess negative index of refraction have become a remarkable research area in recent years [1–10]. One approach taken is to construct a composite metamaterial [2–5] consisting of two components which have a negative permittivity [11] ($\varepsilon(\omega) < 0$) and negative permeability [12] ($\mu(\omega) < 0$) simultaneously over a certain frequency range, respectively, so that the resulting index of refraction of the effective medium becomes $n_{\text{eff}} = \sqrt{\varepsilon}\sqrt{\mu} < 0$ [6–10]. Such structures are able to behave like a perfect lens, where both the propagating and evanescent waves contribute to the focusing [13]. Another path is revealed by the photonic crystals (PCs), where the band structure can lead to negative dispersion for electromagnetic (EM) waves.

Photonic crystals are periodic dielectric or metallic structures that have photonic bands exhibiting arbitrarily different dispersions for the propagation of EM waves, and band gaps, where the propagation is prohibited at certain range of wavelengths [14–18]. In this respect, there is a close analogy between a photon in a photonic crystal, and an electron in a semiconductor. Based on these properties, photonic crystals provide a medium where the propagation of light can be modified virtually in any way in a controllable manner [19–31]. Their application potential covers the existing electromagnetic technologies for improvement, and extends beyond for advancement. From the fundamental physics point of view, photonic crystals provide access to novel and unusual optical properties. It has been theoretically shown that photonic crystals may possess negative refraction although they have a periodically modulated positive permittivity and permeability of unity [32–35]. Cubukcu et al. has been first to demonstrate negative refraction phenomenon in two-dimensional (2D) PCs in the microwave region [36]. Further experimental studies proved that carefully designed PCs are candidates for obtaining negative refraction at microwave [37] and infrared [38] frequency regimes. Superprism effect is another exciting property arising from photonic crystals [39,40]. Subwavelength imaging and resolution [41] and flat lens behavior [42] of PCs have been experimentally demonstrated. Extensive numerical [43–46] and experimental studies [47–52] helped to have a better understanding of negative refraction, focusing, and subwavelength imaging in photonic crystal structures.

In this chapter, we review certain recent studies on the negative refraction and imaging of EM waves by photonic crystal slabs in the microwave frequency regime. We first report on the negative refraction and the subwavelength imaging with transverse magnetic (TM) polarized EM waves. Then we show that it is also possible to have negative refraction with transverse electric (TE) polarized EM waves. Fifth band of the photonic crystal is utilized for purpose of achieving negative refraction. A spectral negative refraction and focusing behavior will be provided. Finally we demonstrate a metallodielectric PC that possesses negative refraction and imaging through a slab. Throughout the work two basic mechanisms arising from the band structure of PCs are employed to obtain negative refraction. We found that focusing abilities of a PC slab can surpass that of conventional (i.e., positive refractive) materials, providing both subwavelength imaging and true flat lens behavior.

6.2 Negative Refraction and Subwavelength Imaging of TM Polarized Electromagnetic Waves

Refraction is perhaps one of the most basic topics of electromagnetic phenomena, whereby when a beam of radiation is incident on an interface between two media at an arbitrary angle, the direction of propagation of the transmitted beam is altered by an amount related to the indices of refraction of the two media. Although all of the known naturally occurring materials exhibit positive indices of refraction, the possibility of materials with negative refractive index has been explored theoretically by Victor Veselago [1]. In his seminal work, he concluded that such materials did not violate any fundamental physical laws. These materials were termed left-handed materials (LHMs), and it was further shown that some of the most fundamental electromagnetic properties of an LHM would be opposite to that of ordinary right-handed materials (RHM), resulting in unusual and nonintuitive optics [5,8]. Photonic crystals are alternatives to LHM structures, being a candidate for negative refractive media. Recent experimental and theoretical works indicate that negative refraction phenomena in photonic crystals are possible. Luo et al. demonstrated theoretically all-angle negative refraction of two-dimensional PCs [34].

The 2D photonic crystal structure that we use in our experiments consists of a square array of dielectric rods in air having a dielectric constant $\varepsilon = 9.61$, radius $r = 1.6\,\text{mm}$, and length $l = 150\,\text{mm}$ [36]. The periodicity of the structure in both directions is $a = 4.79\,\text{mm}$. The analysis of Luo et al [34] is followed to determine the negative refraction frequency range of our structure, which is calculated to be 13.10–15.44 GHz. Propagation properties of the EM wave within the crystal can be described by studying equal-frequency contours (EFCs) in k-space. The TM polarized band diagram of the photonic crystal calculated by plane wave expansion method is shown in Fig. 6.1a. We focus on the first band for the experimental and theoretical demonstration of single-beam negative refraction in 2D photonic crystals. EFCs of the photonic crystal and air at 13.698 GHz are schematically drawn in Fig. 6.1b. The conservation of the surface-parallel wave vector gives the direction of the refracted waves inside the PC [34]. The negative refraction effect is present at this frequency.

The refraction spectrum is measured by a setup consisting of an HP 8510C network analyzer, a standard high-gain microwave horn antenna as the transmitter, and a monopole antenna as the receiver (Fig. 6.2a). The size of the monopole antenna is 11 mm, which is half of the operation wavelength

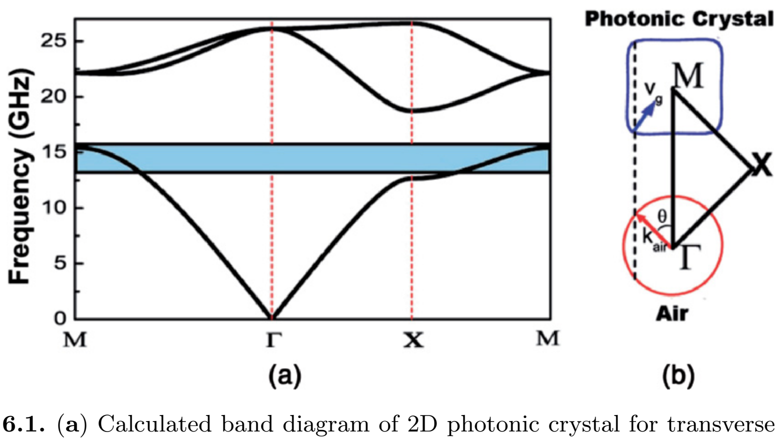

Fig. 6.1. (**a**) Calculated band diagram of 2D photonic crystal for transverse magnetic (TM) polarization. (**b**) Equal-frequency contours in k-space of PC and air at 13.698 GHz. θ is the incident angle and v_g is the group velocity inside the PC

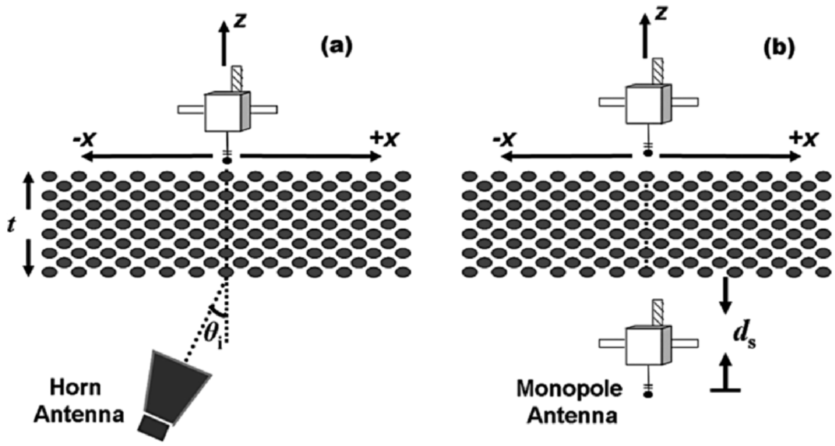

Fig. 6.2. Schematic drawing of the experimental setup for observing (**a**) negative refraction phenomenon, (**b**) focusing effect of a slab of negative refractive 2D PC

($\lambda \sim 22$ mm) of the EM wave at a working frequency of $f = 13.698$ GHz. The top view of the experimental setup is given in Fig. 6.2a. The x and z directions are shown in the figure, whereas the y is directed out of the page. The electric field is along the y-direction (i.e., parallel to the rods), whereas the magnetic field and wave-vector are on the x–z plane. The horn antenna is oriented such that the incident waves make an angle of 45° with the normal of Γ–M interface.

The spatial distributions of the time-averaged incident field intensity along the second (PC–air) interface are measured (Fig. 6.3a). The PC used in negative refraction experiments has 17 layers along the propagation direction (z) and 21 layers along the lateral direction (x). For a direct comparison of theoretical predictions and experimental results, simulation of the structure based on experimental parameters using a finite difference time domain (FDTD) method is performed. The incident EM wave has a Gaussian beam profile centered at $x = 0$. Therefore, by measuring the shift of the outgoing beam as given in Fig. 6.3a, one can easily deduce whether the structure has a positive or negative refractive index.

Figure 6.3b plots the measured (solid) and simulated (dashed-dotted) spatial distributions of intensity at the interfaces for the slabs of PC (black) and randomly filled polystyrene pellets (gray). As clearly seen in Fig. 6.3b, the center of the outgoing Gaussian beam is shifted to the left side of the center of the incident Gaussian beam for the PC structure. Due to Snell's law, this behavior corresponds to negative refraction. Experimental results and numerical simulations agree well. Refractive index of PC at 13.698 GHz determined from the experiment is -1.94, which is very close to the theoretical value of -2.06 computed by the FDTD method. For comparison purposes, the measurements and the simulations are repeated with a slab that contains only polystyrene

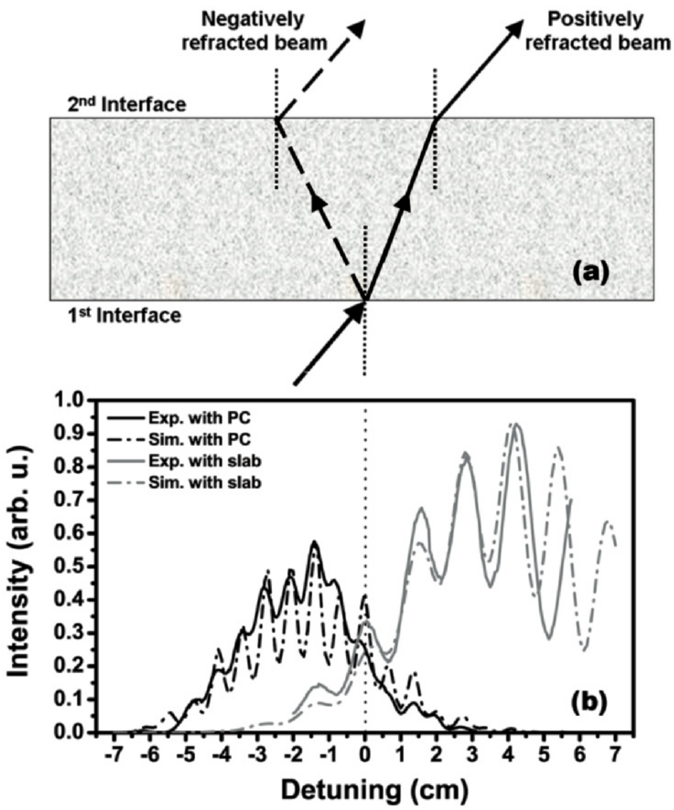

Fig. 6.3. (**a**) Schematics of refraction of the incident beam through positive and negative media for TM polarization. (**b**) Refraction spectrum of incident beam through negative refractive PC (*black lines*) and positive refractive polystyrene pallets (*gray lines*). The *solid lines* and the *dashed-dotted lines* correspond to the experimental measurements and theoretical simulations, respectively

pellets, which has a positive refractive index (n=1.46). The refracted beam emerges from the right-hand side of the incident beam as plotted in Fig. 6.3b. The positive refractive index determined from the experiment is 1.52, which is close to the tabulated value of 1.46.

A negative refractive index allows a flat lens to bring EM waves into focus, whereas positive refractive index materials always require curved surfaces to focus EM waves [1, 13]. One interesting physical behavior of negative index materials is that they can restore the amplitude of evanescent waves and therefore enable subwavelength focusing [13, 43]. Subwavelength resolution was experimentally verified for negative index materials made of PCs [36]. To investigate the focusing ability of the present PC, a slab of the same PC (with 15×21 layers) is employed. The operation frequency is set to 13.698 GHz, having the largest angular range for negative refraction [36]. FDTD simulations

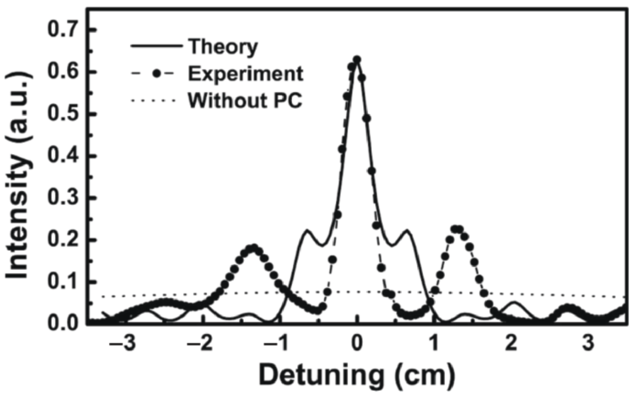

Fig. 6.4. Measured power distribution (*large dotted-dashed line*) and calculated average intensity (*solid line*) at the focal point for TM polarization. *Dashed line* is the spatial power distribution without PC

with experimental parameters predict the formation of an image 0.7 mm away from the PC–air interface for a point source that is placed 0.7 mm away from the air–PC interface. We first simulated the distribution of time-averaged intensity along the PC–air interface with and without the PC (solid curve and thin dotted curve in Fig. 6.4). In the experiment, a monopole antenna is used as the point source (Fig. 6.2b). The measured (large dotted-dashed) and calculated (solid) power distribution along the interface is depicted in Fig. 6.4. The full width at half maximum (FWHM) of the measured focused beam is found to be 0.21λ, which is in good agreement with the calculated FWHM. In contrast, the calculated FWHM of the beam at this plane in the absence of the PC is found to be 5.94λ (dashed line in Fig. 6.4). This implies an enhancement of the transmitted field about 25 times compared to that of free space.

6.3 Negative Refraction and Point Focusing of TE Polarized Electromagnetic Waves

In Sect. 6.2 the negative refraction originating from the convex EFCs of the first band around the M-point in k-space was investigated. The first band has a partial gap around Γ-point, and the EM waves are forced to move along the Γ–M-direction, where the conservation of the surface-parallel component of the wave vector causes negative refraction (Fig. 6.1a). In this section, we employ a different band topology of a 2D PC to obtain negative refraction [47]. We aim to achieve negative refractive index with higher isotropy. Based on the analysis presented in [45], we utilize a TE polarized upper band of the PC where the magnetic field is parallel to the dielectric rods. A similar study using the TM polarized band was recently reported by Martinez et al. [49]

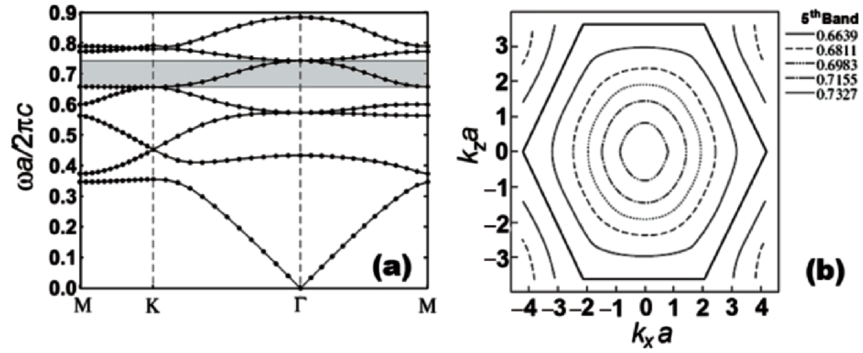

Fig. 6.5. (**a**) Calculated TE polarized band structure. *Shaded band* (fifth band) covers the frequencies where the structure possesses negative index of refraction. (**b**) Equal-frequency contours of the fifth band in the full Brillouin zone. The contours are nearly circular (i.e., isotropic) and shrink with increasing frequency

We used the same photonic crystal structure as analyzed in Sect. 6.2. The only difference is that we calculated the band diagram for TE polarized EM waves. Figure 6.5a depicts the calculated band diagram in the first Brillouin zone. The transverse direction is taken to be in the plane of 2D PC. We scaled frequency with $\widetilde{f} = f(a/c)$. The fifth band as shaded in the Fig. 6.5a extends from $\widetilde{f} = 0.65(f = 40.65\,\text{GHz})$ to $\widetilde{f} = 0.74(f = 46.27\,\text{GHz})$. Figure 6.5b plots the EFCs in the full Brillouin zone. The EFCs of the band shrink with increasing frequency, contrary to the EFCs in air ($n = 1$).

The refraction spectra are measured by using same setup as in Fig. 6.2a. Since the EM wave is TE polarized in this case, the horn and the monopole antennas are rotated by 90°. Therefore the magnetic field is parallel to the dielectric rods. The PC structure consists of seven layers along the propagation direction (z) and 31 layers along the lateral direction (x). The horn antenna is on the negative side of the PC with respect to its central axis. The scanning is performed along the second PC–air interface by $\Delta x = 1.27\,\text{mm}$ steps. Refraction spectra of the EM waves with three different incident angles are measured and the results are plotted in Fig. 6.6. The top part of Fig. 6.6 gives the field distribution along the PC–air interface as a function of frequency. It is evident that the refracted beam appears (for θ_i=15° (a), θ_i=30° (b), and θ_i=45° (c)) on the negative side, meaning that the PC structure has negative refractive index between 40.0 and 43.0 GHz.

When the incidence angle is increased, the transmission shifts to the left accordingly. To investigate the beam profiles, the spatial cross-sections at f=41.7 GHz are plotted in the middle part of Fig. 6.6. The intensities are normalized with respect to the maximum intensity for the incident angle $\theta_\text{i} = 15°$. It is apparent that the lateral shift is accompanied by a decrease in the transmission intensity. This is due to the higher reflection at the interface for larger incidence angles and the diffraction-induced out-of-plane losses, which increase

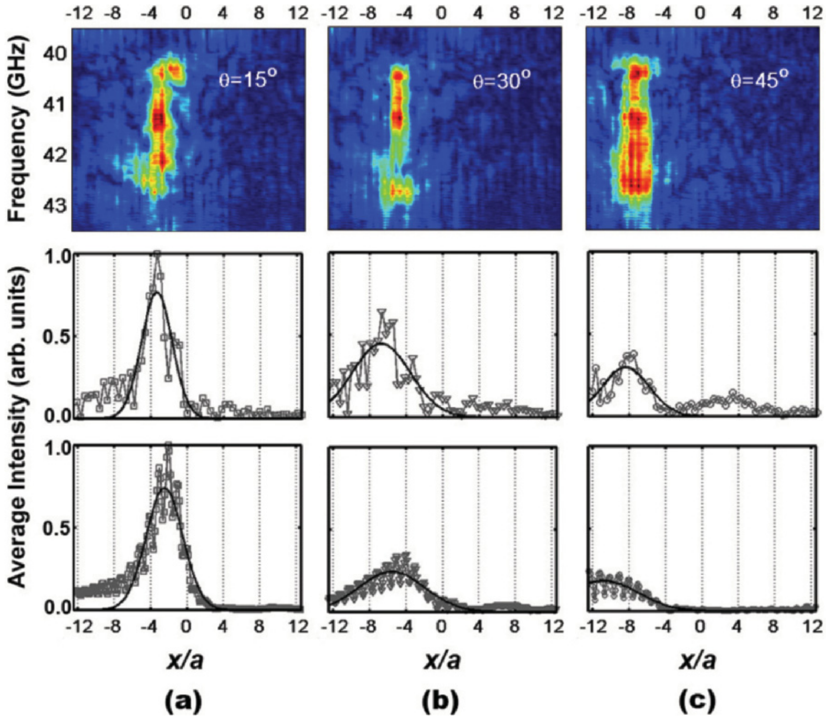

Fig. 6.6. Measured refraction spectra of the fifth band along the PC–air interface for incidence angles of (**a**) θ_{i}=15°, (**b**) θ_{i}=30°, and (**c**) θ_{i}=45° is given on the *top* figures. *Middle* figures are the measured, whereas the *bottom* figures are the simulated intensity profiles at 41.7 GHz for the respective angles of incidence. *Solid curves* indicate the Gaussian fits of the data. All results are for TE polarization

with increasing path length through the lattice. The bottom part of Fig. 6.6 displays the simulated average field intensity at f=41.7 GHz. Experimental results agree well with the FDTD simulations. By using Snell's law, index of refraction is obtained to be $n_{\mathrm{eff}} = -0.52$, -0.66, and -0.86 from the experiment for $\theta_{\mathrm{i}} = 15°$, 30°, and 45°, respectively. The simulation results for the same incidence angles give $n_{\mathrm{eff}} = -0.66$, -0.72, and -0.80. The experimental and theoretical results agree quite well. We observed that the band manages to provide a negative refracted uniform beam within the measured frequency range both from the experiments and simulations.

We have also checked the imaging properties of our PC slab for TE polarized EM waves. FDTD simulations are performed at f=42.07 GHz located at a distance $d_{\mathrm{s}} = 2\lambda$ away from air–PC interface. Omnidirectional (point) source is used to excite the first interface. Figure 6.7a displays the resulting spatial intensity distribution in the image plane, normalized to the value of maximum intensity. The PC–air interface is located at $z = 0$. The peak indicates focusing behavior unambiguously. We would like to emphasize that the focusing

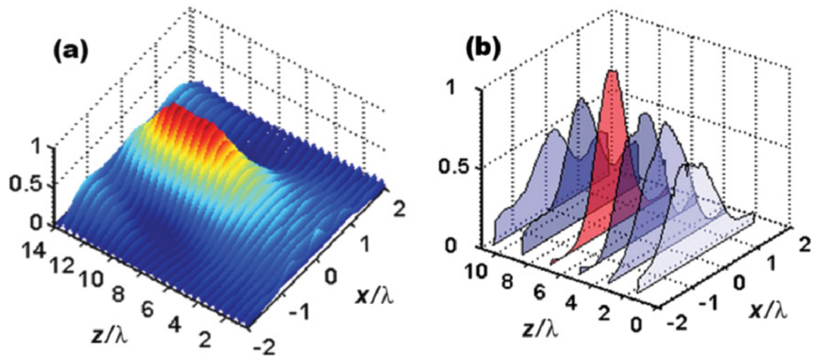

Fig. 6.7. (**a**) Simulated 2D intensity profile in the image plane. z=0 corresponds to the PC–air interface. (**b**) Measured lateral intensity profiles along the propagation direction. Measurements are performed at six different positions z/λ = 1.78, 3.56, 5.34, 7.12, 8.90, and 10.68 for TE polarization

occurs away from the PC–air interface, observed at $z \approx 8\lambda$. Therefore, unlike the focusing discussed in Sect. 6.2 for TM polarized EM wave, this PC does not perform imaging in the strict sense. Also a subwavelength imaging as presented in Fig. 6.4 is not present since the focal point is quite far away from the interface.

Experimental setup for verifying focusing through a slab of PC is similar to the one discussed in Sect. 6.2 (Fig. 6.2b). But to imitate a TE polarized monopole antenna, we employed a waveguide aperture as the source. The waveguide aperture provides sufficiently omnidirectional radiation due to the diffraction at the aperture [47]. The intensity distribution in the focusing plane is measured by the monopole antenna. For $d_s = 2\lambda$, first a scan is performed along the propagation direction (z) to locate the maximum intensity, i.e., the focal point. Then, lateral cross-sections (along x) of field intensity at several z points around the peak position are measured. As seen in Fig. 6.7b, the beam is focused both in lateral and longitudinal directions. The maximum intensity is observed at $z \approx 8\lambda$, the focal point. The longitudinal extent of the focusing indicates that index of refraction deviates from negative unity, and bears a certain amount of anisotropy. We stress that even when refractive indices were perfectly isotropic and uniform, a value different from $n = -1$ would not generate point focusing and would induce an aberration of the image.

6.4 Negative Refraction and Focusing Analysis for a Metallodielectric Photonic Crystal

In Sects. 6.2 and 6.3 we have dealt with dielectric photonic crystals. Photonic crystal structures can also be made of metals. But it is not easy to obtain negative refraction from the metallic photonic crystal structures since the EFCs of the metallic PCs are larger than the EFCs of air. Luo et al. theoretically demonstrated that it is indeed possible to obtain all-angle negative refraction by embedding metallic rods into a high-dielectric constant medium [44]. The main idea for using a medium with high dielectric permittivity is to increase the effective index of the photonic crystal. The advantage is that the EFCs will be lowered in frequency but the area occupied by EFCs in k space will not change. Following this basic idea, we used a different approach for constructing the PC structure. Instead of embedding metallic rods into a high-dielectric medium, we combined dielectric rods and metallic rods together to form a metallodielectric PC. Metallodielectric PC could be considered as a metallic PC with a periodic dielectric perturbation. Positive dielectric constant is an attractive perturbation and causes lowering the frequency of the bands [50].

The metallodielectric photonic crystal is a square lattice of metallic and dielectric rods where the basis of the PC consists of a metallic and a dielectric rod placed along the diagonal of the square unit cell as given in the inset of Fig. 6.8b. Cylindrical alumina rods with a radius of 1.55 mm are used as the dielectric rods with $\varepsilon = 9.61$. The metallic rods are made of aluminum and have a radius of 1.5 mm. Both the metallic and dielectric rods have a height of 150 mm.

We have computed the band diagrams of the metallic photonic crystal (Fig. 6.8a) and metallodielectric photonic crystal (Fig. 6.8b) for TM polarized EM waves. The radius of the dielectric rod is $0.136a$, and the radius

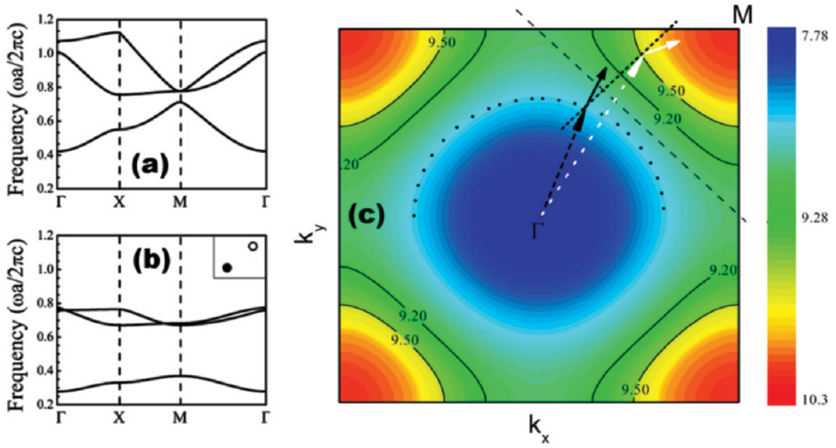

Fig. 6.8. (**a**) Calculated TM-polarized bands for the metallic photonic crystal, and (**b**) the metallodielectric crystal. (**c**) Equal-frequency contours (*solid curves*) are shown for the metallodielectric PC. *Dotted circle* is the free-space equal-frequency contour at 9.5 GHz. Free-space wave vector (*black dashed arrow*), free-space group velocity (*black solid arrow*), wave vector of the refracted waves in the PC (*white dashed arrow*), group velocity inside the PC (*white solid arrow*) are drawn

of the metallic rod is $0.14a$, where a is the lattice constant and is equal to 11.0 mm. Lattice constant is taken to be same in both structures. By comparing Fig. 6.8a and b we can conclude that the bands of the metallodielectric photonic crystal are lowered in frequency compared to the bands of the metallic photonic crystal.

Equal-frequency contours of the metallodielectric PC for TM polarization over the first Brillouin zone is plotted in Fig. 6.8c. The dotted circle is the EFC of air. The PC surface is aligned such that the normal vector to the air–PC interface is along the ΓM direction. Since the surface-parallel component of the wave vector is conserved, the wave vectors of the refracted beam can easily be obtained, as given in the figure. The group velocity of the incident waves and the group velocity of the transmitted waves fall on opposite sides of the surface normal. Therefore the incident waves are negatively refracted [34]. For the plotted EFCs, the magnitude of the largest surface-parallel wave vector component in air is smaller than the largest surface-parallel wave vector component in the photonic crystal. The range of incidence angles that are negatively refracted can be increased by lowering the bands without modifying the lattice parameters [50].

The electric field intensities are measured along the PC–air interface to demonstrate the negative refraction experimentally. The measurement method is same with the measurements indicated in the previous sections (Fig. 6.2a). Waves that are positively refracted are expected to emerge from the positive side of the surface, whereas negatively refracted waves are to emerge from the negative side. Measurement results for incidence angles of $\theta_{\mathrm{i}}=15°, 25°, 35°$, and $45°$ are provided in Fig. 6.9a–d, respectively. Between the frequencies 9.20 and 10.30 GHz waves exit from the negative side of the PC meaning that EM waves are negatively refracted by the PC in this frequency range. Up to 9.20 GHz the waves are positively refracted.

We have also performed FDTD simulations to see how the EM wave is refracted by the metallodielectric PC. We have sent an incident Gaussian beam to the air–PC interface and calculated electric field intensities inside and outside the PC at 9.70 GHz. The simulation results for two different incident angles $\theta_{\mathrm{i}}=15°$ (Fig. 6.10a) and $\theta_{\mathrm{i}}=45°$ (Fig. 6.10b) clearly show that the negative refraction takes place at this frequency. The effect of reflection is also clear in this picture. For higher incident angle the intensity (therefore the transmission) is lower due to the high reflections from the air–PC interface. Note that 9.70 GHz is in the negative refraction frequency regime as calculated from the EFCs (Fig. 6.8c).

We have compared the experimental and theoretical results of the values of refractive indices at $\theta_{\mathrm{i}}=25°$ incidence angle in Fig. 6.11. Between 9.00 and 9.19 GHz the refractive indices are found to be positive. Around 9.20 GHz there is an abrupt change in the values and the sign of the index of refraction. In the close vicinity of 9.20 GHz the indices of refraction are found to be high, $+18$ and -12 due to the flatness of EFS contours around 9.20 GHz (Fig. 6.8c). The refractive indices are negative in the frequency range

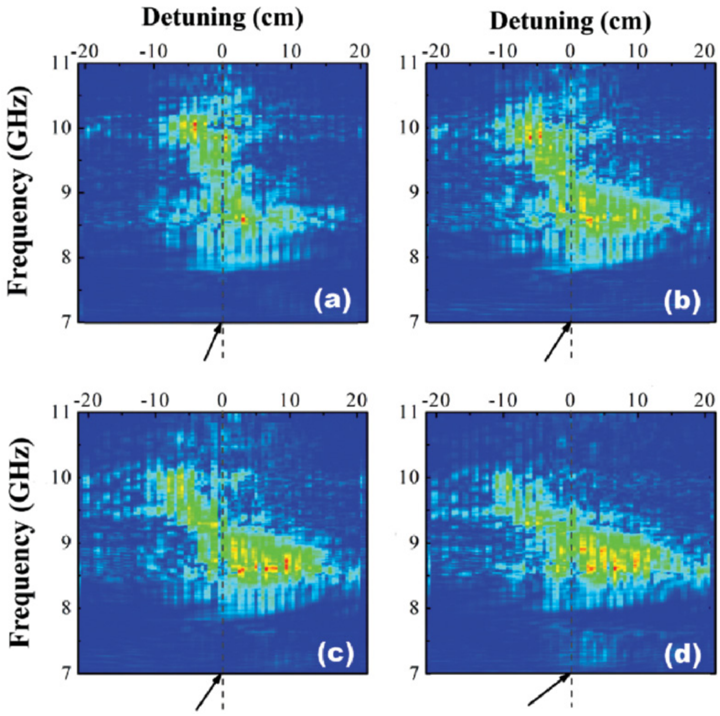

Fig. 6.9. Measured electric field intensities along the PC–air interface for incident angles of (**a**) θ=15°, (**b**) θ=25°, (**c**) θ=35°, and (**d**) θ=45° for the metallodielectric PC. The intensities are plotted as a function of frequency. Up to 9.2 GHz the structure is positively refracting and between 9.2 and 10.3 GHz the structure refracts negatively

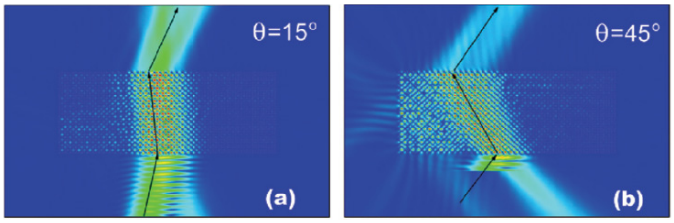

Fig. 6.10. Simulated electric field distributions for both angles of incidence. Incident angles of (**a**) θ=15° and (**b**) θ=45° for the metallodielectric PC. Negative refraction phenomenon is clearly observed for both angles of incidence

9.25–10.00 GHz. As seen in Fig. 6.11 the refractive indices depend strongly on the frequency. This is an expected behavior since the EFCs (Fig. 6.8c) are anisotropic throughout the frequency range of interest. Measured refractive index values are −0.65, −0.85, −0.88, and −0.96 for four different incidence

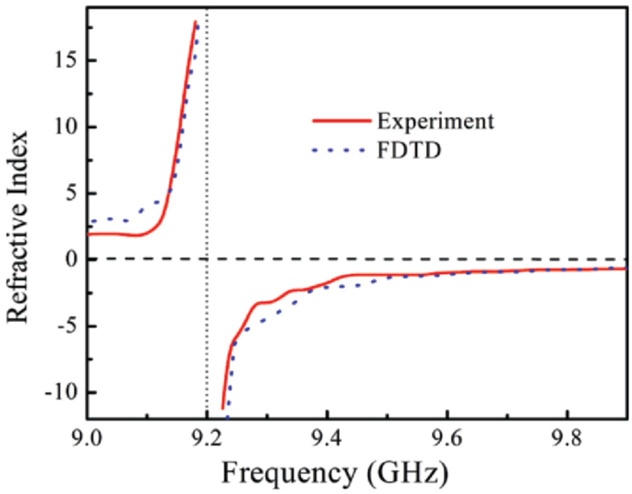

Fig. 6.11. Measured (*solid line*) and calculated (*dashed line*) refractive indices at an angle of incidence 15° for the metallodielectric PC

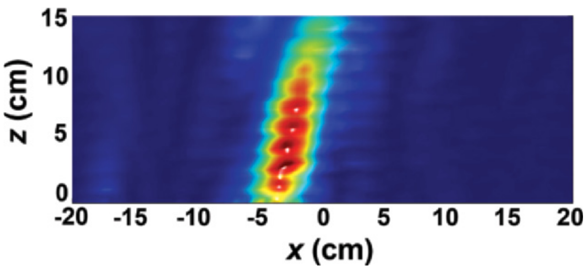

Fig. 6.12. Spatial intensity distribution of an outgoing EM wave at 3.70 GHz along the x–z plane of the metallodielectric PC. The wave is refracted negatively since the beam emerges from the negative side of the normal

angles of $15°, 25°, 35°$, and $45°$, respectively, at 9.70 GHz. These results clearly show that refractive index also depends on the incidence angle. To obtain uniform angle-independent negative indices of refraction two conditions must be satisfied. First, a circular EFC centered at the origin of the Brillouin zone is required. Second, the radius of the circular EFC must be decreasing with increasing frequency [50].

We have also scanned the intensity distribution of the EM wave by a monopole antenna mounted to a 2D scanning table with $\Delta x = \Delta z = 2.5$ mm steps. In our experiments we can only measure the power at a certain point, which corresponds to the time-averaged intensity at that point. Note that up to this point we have only scanned the field along PC–air interface for measuring the index of refraction. The resulting scanned field profile at 9.70 GHz is plotted in Fig. 6.12. We can clearly see how the wave propagates after being refracted

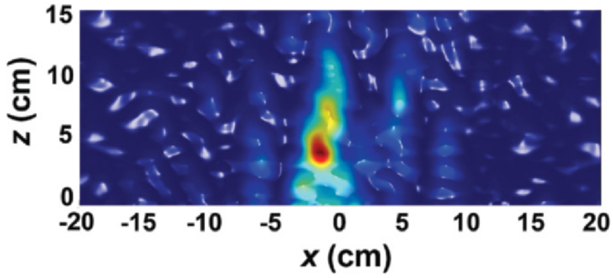

Fig. 6.13. Spatial intensity distribution of an omnidirectional source at 3.70 GHz along the $x - -z$ plane of the metallodielectric PC. Focusing through a slab of metallodielectric photonic crystal is observed

from the PC–air interface. The intensities are normalized with respect to the maximum intensity. The incident EM wave has a Gaussian beam profile centered at $x = 0$. Gaussian beam is shifted by 40 mm to the negative side of the normal as expected from a negatively refracting medium.

A similar field scan is performed for the observation of focusing through a PC slab lens. In this case we have used a monopole antenna as a point source to shine the air–PC interface (refer to Fig. 6.2b for setup). EM waves emerging from a point source located near a lens with negative refractive index will first be refracted through the first air–PC interface and will come into focus inside the PC. Then outgoing EM waves will face refraction again at the second PC–air interface and the refracted beam will meet the optical axis of flat lens, where the second focusing will occur. If the lens is not thick enough, the focusing may not occur inside the lens, which in turn will result in a diverging beam instead of a converging beam, even if the material is negatively refracting. Therefore, the thickness of the lens plays a crucial role for observing flat lens behavior.

Figure 6.13 provides the transmission spectrum for the omnidirectional source located at $d_s = 7$ cm away from the PC lens. Number of layers along the propagation direction is $N_z = 10$. As seen in Fig. 6.13, an image is formed at a focal length of $z = 4$ cm. Focusing is obtained both in the lateral and the propagation direction. If the slab was made of a positive refractive material, it would not be possible to observe a point focusing. For such positive refractive index slab lenses the beam will diverge as expected from ray optics. Therefore flat lens focusing is available only for negative refractive media.

6.5 Conclusion

In this chapter, the negative refraction and the focusing abilities of 2D dielectric and metallodielectric photonic crystals were investigated both experimentally and theoretically. We have observed that an effective index of refraction can be defined from the band structure of the PC, which, under convex EFCs, can take negative values and can be associated with refraction of EM waves through the PC. The isotropy and spectral range of the refractive indices depend strongly on the details of the band structure. The focusing abilities associated with negative refractive index are promising. We have observed that the subwavelength imaging and far-field focusing are achievable using PC with appropriate band structures. Our studies showed that negative refraction is available both for TM and TE polarized incident EM waves. Metallodielectric crystals are used to obtain negative refractive indices over a wide range of angles. Dielectric rods are inserted within metallic crystal, and the resulting band diagram is calculated and a lowering in frequency of the bands is observed.

The advantage of using photonic crystals as negative refractive media is that the transmission is higher compared to lossy LHM. Also the electromagnetic phenomena discussed here depend only on the refractive index of the dielectric material and on the geometrical parameters of the 2D PC, hence it is scalable across the electromagnetic spectrum. With advancing fabrication techniques, photonic crystals are now seen as essential building blocks of applications in the infrared and optical frequencies. It is much more difficult to scale the LHM that are made of metallic structures.

Acknowledgments

This work is supported by the European Union under the projects EU-DALHM, EU-NOE-METAMORPHOSE, EU-NOE-PHOREMOST, and TUBITAK under Project No. 104E090. Ekmel Ozbay acknowledges partial support from the Turkish Academy of Sciences.

References

1. V.G. Veselago, Sov. Phys. Usp. **10**, 504 (1968)
2. D.R. Smith, W.J. Padilla, D.C. Vier, S.C. Nemat-Nasser, S. Schultz, Phys. Rev. Lett. **84**, 4184 (2000)
3. R.A. Shelby, D.R. Smith, S.C. Nemat-Nasser, S. Schultz, Appl. Phys. Lett. **78**, 489 (2001)
4. M. Bayindir, K. Aydin, P. Markos, C.M. Soukoulis, E. Ozbay, Appl. Phys. Lett. **81**, 120 (2002)
5. K. Aydin, K. Guven, M. Kafesaki, L. Zhang, C.M. Soukoulis, E. Ozbay, Opt. Lett. **29**, 2623 (2004)
6. R.A. Shelby, D.R. Smith, S. Schultz, Science **292**, 77 (2001)
7. C.G. Parazzoli, R.B. Greegor, K. Li, B.E. Koltenbah, M. Tanielian, Phys. Rev. Lett. **90**, 107401 (2003)
8. A.A. Houck, J.B. Brock, I.L. Chuang, Phys. Rev. Lett. **90**, 137401 (2003)
9. K. Aydin, K. Guven, C.M. Soukoulis, E. Ozbay, Appl. Phys. Lett. **86**, 124102 (2005)

10. K. Aydin, I. Bulu, E. Ozbay, Opt. Express **13**, 8753 (2005)
11. J.B. Pendry, A.J. Holden, D.J. Robbins, W.J. Stewart, J. Phys. Condens. Matter **10**, 4785 (1998)
12. J.B. Pendry, A.J. Holden, D.J. Robbins, W.J. Stewart, IEEE Trans. Microw. Theory Tech. **47**, 2075 (1999)
13. J.B. Pendry, Phys. Rev. Lett. **85**, 3966 (2000)
14. E. Yablonovitch, Phys. Rev. Lett. **58**, 2059 (1987)
15. S. John, Phys. Rev. Lett. **58**, 2486 (1987)
16. J.D. Joannopoulos, R.D. Meade, J.N. Winn, *Photonic Crystals: Molding the Flow of Light* (Princeton University Press, Princeton, NJ, 1995)
17. C.M. Soukoulis (ed.), *Photonic Crystals and Light Localization in the 21st Century* (Kluwer, Norwell, MA, 2001)
18. K. Sakoda, *Optical Properties of Photonic Crystals* (Springer, Berlin Heidelberg New York, 2001)
19. E. Ozbay, G. Tuttle, R. Biswas, K.M. Ho, J. Bostak, D.M. Bloom, Appl. Phys. Lett. **65**, 1617 (1994)
20. E. Ozbay, B. Temelkuran, Appl. Phys. Lett. **69**, 743 (1996)
21. A. Mekis, J.C. Chen, I. Kurland, S. Fan, P.R. Villeneuve, and J.D. Joannapoulos, Phys. Rev. Lett. **77**, 3787 (1996)
22. P.R. Villeneuve, D.S. Abrams, S. Fan, J.D. Joannopoulos, Opt. Lett. **21**, 2017 (1996)
23. B. Temelkuran, E. Ozbay, J.P. Kavanaugh, G. Tuttle, K.M. Ho, Appl. Phys. Lett. **72**, 2376 (1998)
24. H. Kosaka, T. Kawashima, A. Tomita, M. Notomi, T. Tamamura, T. Sato, S. Kawakamib, Appl. Phys. Lett. **74**, 1370 (1999)
25. M. Bayindir, E. Ozbay, Phys Rev. B **62**, R2247 (2000)
26. M. Loncar, D. Nedeljkovic, T. Doll, J. Vuckovic, A. Scherer, T.P. Pearsall, Appl. Phys. Lett. **77**, 1937 (2000)
27. S. Noda, M. Yokoyama, M. Imada, A. Chutinan, M. Mochizuki, Science **293**, 1123 (2001)
28. M. Bayindir, S. Tanriseven, E. Ozbay, Appl. Phys. A-Mater. Sci. Process. **72**, 117 (2001)
29. E. Ozbay, M. Bayindir, I. Bulu, E. Cubukcu, IEEE J. Quantum Electron. **38**, 837 (2002)
30. S. Enoch, B. Gralak, G. Tayeb, Appl. Phys. Lett. **81**, 1588 (2002)
31. M.F. Yanik, S. Fan, Phys. Rev. Lett. **92**, 083901 (2004)
32. B. Gralak, S. Enoch, G. Tayeb, J. Opt. Soc. Am. A **17**, 1012 (2000)
33. M. Notomi, Phys. Rev. B **62**, 10696 (2000)
34. C. Luo, S.G. Johnson, J.D. Joannopoulos, J.B. Pendry, Phys. Rev. B **65**, 201104 (2002)
35. S. Foteinopoulou, E.N. Economou, C.M. Soukoulis, Phys. Rev. Lett. **90**, 107402 (2003)
36. E. Cubukcu, K. Aydin, E. Ozbay, S. Foteinopoulou, C.M. Soukoulis, Nature **423**, 604 (2003)
37. P.V. Parimi, W.T. Lu, P. Vodo, J. Sokoloff, J.S. Derov, S. Sridhar, Phys. Rev. Lett. **92**, 127401 (2004)
38. A. Berrier, M. Mulot, M. Swillo, M. Qiu, L. Thylén, A. Talneau, S. Anand, Phys. Rev. Lett. **93**, 073902 (2004)
39. H. Kosaka, T. Kawashima, A. Tomita, M. Notomi, T. Tamamura, T. Sato, S. Kawakami, Phys. Rev. B **58**, R10096 (1998)

40. S. Foteinopoulou, C.M. Soukoulis, Phys. Rev. B **67**, 235107 (2003)
41. E. Cubukcu, K. Aydin, E. Ozbay, S. Foteinopoulou, C.M. Soukoulis, Phys. Rev. Lett. **91**, 207401 (2003)
42. P.V. Parimi, W.T. Lu, P. Vodo, S. Sridhar, Nature **426**, 404 (2003)
43. C. Luo, S.G. Johnson, J.D. Joannopoulos, J.B. Pendry, Phys. Rev. B **68**, 045115 (2003)
44. C. Luo, S.G. Johnson, J.D. Joannopoulos, J.B. Pendry, Opt. Express **11**, 746 (2003)
45. S. Foteinopoulou, C.M. Soukoulis, Phys. Rev. B **72**, 165112 (2005)
46. R. Moussa, S. Foteinopoulou, L. Zhang, G. Tuttle, K. Guven, E. Ozbay, C.M. Soukoulis, Phys. Rev. B **71**, 085106 (2005)
47. K. Guven, K. Aydin, K.B. Alici, C.M. Soukoulis, E. Ozbay, Phys. Rev. B **70**, 205125 (2004)
48. E. Ozbay, K. Guven, E. Cubukcu, K. Aydin, B.K. Alici, Mod. Phys. Lett. B **18**, 1275 (2004)
49. A. Martínez, H. Míguez, A. Griol, J. Martí, Phys. Rev. B **69**, 165119 (2004)
50. I. Bulu, H. Caglayan, E. Ozbay, Phys. Rev. B **72**, 045125 (2005)
51. P. Vodo, P.V. Parimi, W.T. Lu, S. Sridhar, R. Wing, Appl. Phys. Lett. **85**, 1858 (2005)
52. P. Vodo, P.V. Parimi, W.T. Lu, S. Sridhar, Appl. Phys. Lett. **86**, 201108 (2005)

7

Negative Refraction and Imaging with Quasicrystals

X. Zhang, Z. Feng, Y. Wang, Z.-Y. Li, B. Cheng and D.-Z. Zhang

Summary. Recently, negative refraction of electromagnetic waves in photonic crystals was demonstrated experimentally and subwavelength images were observed. However, these investigations all focused on the periodic structure. In fact, the negative refraction exists not only in periodic structure, but also in nonperiodic structures such as quasicrystalline arrangement of dielectric. Here, we discuss the negative refraction and imaging based on some transparent quasicrystalline photonic structures. The high-symmetric photonic quasicrystals (PQCs) can exhibit an effective refractive index close to -1 in a certain frequency window. The index shows small spatial dispersion, consistent with the nearly homogeneous geometry of the quasicrystal. Thus, a flat lens based on the 2D PQCs can form a non-near-field image whose position varies with the thickness of the sample and the source distance. At the same time, the focus and image for both polarized waves at the same structure and parameters can also be realized by such a flat lens. In addition, the negative refraction behaviors of acoustic wave in phononic quasicrystal are also discussed.

7.1 Introduction

In recent years, negative refraction and left-hand materials (LHMs) have attracted a great deal of attention from both the theoretical and experimental sides due to their implication for realizing so-called subwavelength focusing and many other unusual wave propagation phenomena [1–31]. Properties of LHMs were analyzed theoretically by Veselago over 30 years ago [1, 2], but only recently they were demonstrated experimentally [3, 4]. It was pointed out lately that negative refraction can also be achieved at an interface associated with periodic photonic crystal (PC) [13–29] or uniaxially anisotropic medium [30]. The physical principles that allow negative refraction in them arise from the dispersion characteristics of wave propagation in a periodic medium, which can be well described by analyzing the equifrequency surface (EFS) of the band structures [13–29].

In the PC structures, there are two kinds of cases for negative refraction occurring [16]. The first is the left-handed behavior as being described above [26–29]. In this case, $\vec{k}$, $\vec{E}$ and $\vec{H}$ form a left-handed set of vectors (i.e., $\vec{S} \cdot \vec{k} < 0$, where $\vec{S}$ is the Poynting vector). Another case is that the negative refraction can be realized without employing the backward wave effect [17–25]. In this case, the PC is behaving much like a uniform right-handed medium (i.e., $\vec{S} \cdot \vec{k} > 0$). In fact, there is the same usefulness for both cases. For example, they all can be applied to design the flat lens and realize the focusing of the wave. Very recently, the subwavelength focusing and image by 2D PC slab have been demonstrated experimentally [17–29].

There are two aspects relating to the image and focusing. One is position (in near-field region or non-near-field region), and the other is resolution (full width at half maximum of the focus spot). The position of the image depends on the effective refractive index n of the sample and the homogeneity of the materials. For the case with $n = -1$ and single-mode transmission, the imaging behavior depends on the slab thickness and the object distance, explicitly following the well-known wave-beam negative refraction law as [26–28] had pointed out. However, due to the anisotropy of dispersion in some 2D PCs, the refraction angles are not linearly proportional to the incident angles when a plane wave is incident from vacuum to the PC. This is the reason why only the near-field images were observed in some works [18–25]. The position of the image does not depend on whether or not the evanescent waves are amplified. That is to say, the focus and image can still be observed if only the propagating waves are considered. In such a case, the image resolution cannot beat the diffraction limit. In contrast, the superlensing effect comes from the evanescent waves (or resonance transmission). The excitation of surface mode (or the appearance of resonant transmission) can improve the image resolution [18, 28]. This rule holds not only for the images in the near-field region, but also for the images in the non-near-field region [28].

It is evident that the anisotropy of the dispersion is dependent on the symmetry of the PC lattice. In order to obtain homogeneous dispersion and realize the non-near-field focus, we should use the structures with high symmetry to construct flat lens. However, the highest level of symmetry that can be found in a periodic lattice is six. In contrast, the high geometric symmetry in photonic quasicrystals (PQCs) can reach 12. The problem is whether or not the negative refraction exists in these PQCs. If it exists, what kind of properties does it possess? Based on these problems, we perform detailed theoretical and experimental investigations on the phenomenon of the negative refraction in the PQCs [31].

7.2 Negative Refraction by High-Symmetric Quasicrystal

In the past few years the photonic band gaps (PBGs) in some quasiperiodic structures have been investigated and some interesting results have been obtained [32–34]. One found that the PBGs exist not only in periodic

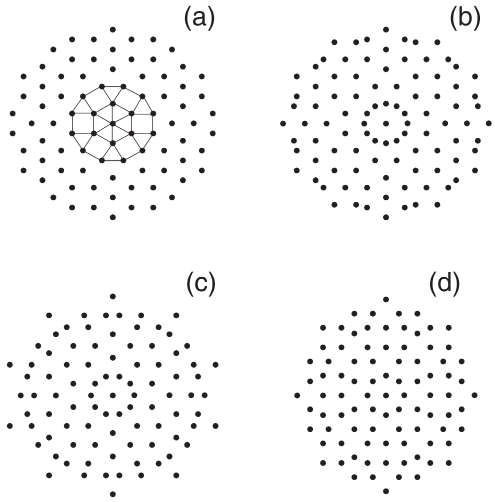

Fig. 7.1. Schemes of the basic quasicrystal structures. (**a**) 12-fold quasicrystal with a random square–triangle tiling system. (**b**) 12-fold quasicrystal with a general rotated symmetry. (**c**) tenfold quasicrystal. (**d**) eightfold quasicrystal

structures, but also in some quasiperiodic structures. In contrast to the PBGs, in this chapter we investigate the transport properties of electromagnetic wave in the band region of the high-symmetric PQC. According to the level of symmetry, the PQCs can be divided into fivefold, eightfold, tenfold, and 12-fold structures. Figure 7.1a, b describes two kinds of structure with 12-fold symmetry. The PQC structures with eightfold and tenfold symmetry are shown in Fig. 7.1c, d, respectively.

We first consider the 12-fold PQC based on a random square–triangle tiling system which is shown in the Fig. 7.1a. We have fabricated the 12-fold PQC samples. The samples consist of a number of dielectric cylinders with dielectric constant 8.6 and radii 3.0 mm embedded in a styrofoam template with a lattice constant of $a = 10$ mm. In order to gain understanding of the band and gap regions for the electromagnetic wave transport in such a quasiperiodic structure, we first explore the transmission spectrum. A rectangular sample 110 mm thick and 400 mm wide was made for microwave measurements. The measurements were carried out in a wide scattering chamber by using an HP8757E scalar network analyzer and an HP8364A series synthesized sweeper, which was similar to our previous experimental setup [34]. The measured transmission data for the above sample are plotted in Fig. 7.2 by the dotted line. In all our measurements the electric field is kept parallel to the cylinders. The wave incident on the cylinders with normal direction, and the lengths of the cylinders are 100 times as big as their radii. Thus, such a system can be theoretically regarded as a two-dimensional PC consisting of infinite-length cylinders embodied in the styrofoam background. The solid line represents the numerical results obtained by the multiple-scattering method [23, 28].

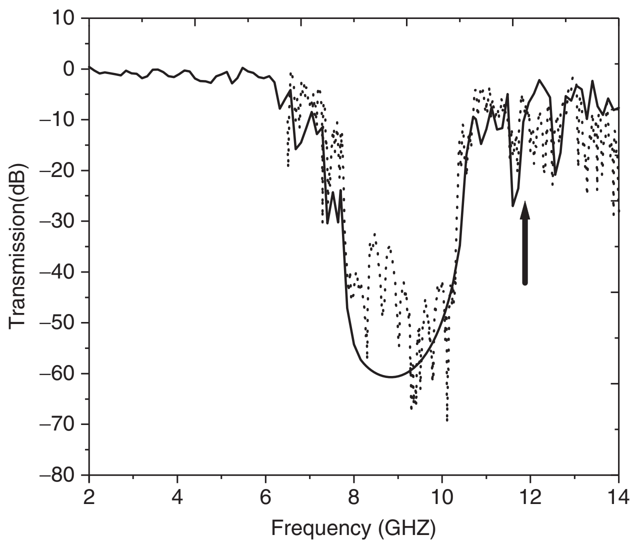

Fig. 7.2. The measured (*dotted lines*) and calculated (*solid lines*) transmission coefficients for the 12-fold quasicrystal with a random square–triangle tiling system. The lattice constant of the system is $a = 10$ mm. The radii and the dielectric constant of the dielectric cylinder are 3.0 mm and 8.6, respectively

The multiple-scattering method is best suited for a finite collection of cylinders with a continuous incident wave of fixed frequency. For circular cylinders, the scattering property of the individual cylinder can be obtained analytically, relating the scattered fields to the incident fields. The total field, which includes the incident plus the multiple-scattered field, can then be obtained by solving a linear system of equations, whose size is proportional to the number of cylinders in the system. Both the near-field and the far-field radiation patterns can be obtained straightforwardly. So, such a method is a very efficient way of handling the scattering problem of a finite sample containing cylinders of circular cross-sections, which should be regarded as exact numerical simulation. Comparing the solid line with the dotted line, we find that excellent agreement between the measured and calculated results is apparent. Both results show one gap and two bands between the frequency $f = 5.0$ and 14 GHz. Because we aim at the refraction feature of wave transport in the quasicrystal structure, in the following we focus our measurement on the band region.

To study the refraction behavior of wave transport through the quasicrystal–air interface, we have fabricated some wedge samples with different shapes characterized by the wedge angle θ_0. In experiment, all the wedge samples always have the left surface kept perpendicular to the incident direction in order to avoid multiple refraction. A $\theta_0 = 30°$ wedge sample is schematically shown in the inset of Fig. 7.3a. When a slit wave beam of

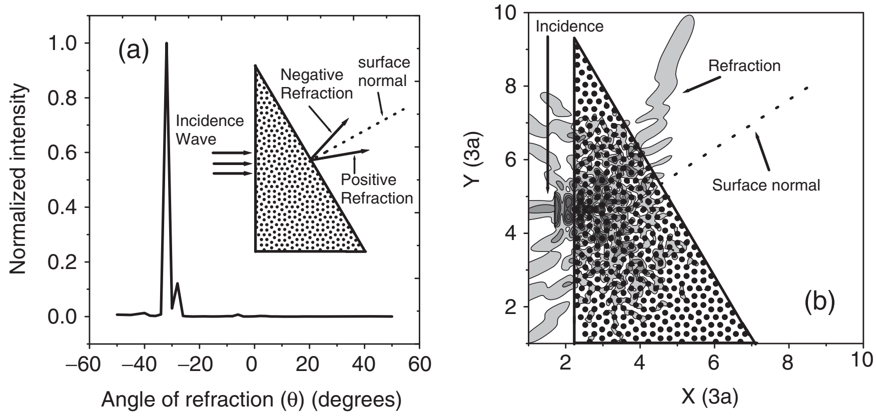

Fig. 7.3. (**a**) The measured transmission intensity as a function of refractive angle (θ) at $f = 11.82\,\text{GHz}$ and $\theta_0 = 30°$ incidence. A wedged sample is shown in the inset graph. (**b**) The corresponding simulation result of wave intensity showing the negative refraction behavior. The boundaries of the sample are marked with the *black frame*. The crystal and parameters are identical to those in Fig. 7.2

certain frequency is incident normal to the left surface of the sample, it transports along the incident direction until it meets the wedge surface of the sample. A part of the beam will refract out of the sample and the other is reflected inside. The refracted wave either travels on the right side (positive refraction) or the left side (negative refraction) of the surface normal. The incident angle of the wave beam impinging upon the wedge interface is equal to θ_0. Therefore, by choosing different shapes of the wedge sample, we can extract the information of the refraction angle θ vs. the incident angle θ_0 for this quasicrystal structure.

The refraction experiments were performed in a semicircular cavity. A dipole antenna was mounted on a goniometer that runs along the semicircular outer edge of the parallel plate waveguide to detect the refraction beam. Figure 7.3a shows the measured transmission intensity as a function of θ for the 30° wedge sample at an incident wave frequency 11.82 GHz. A peak is clearly seen at $\theta = -32°$ corresponding to a negative refractive index $n = -1.06$. To understand the experiment results, we still implement the multiple-scattering theory [23, 28] to calculate wave propagation and scattering in the quasicrystal sample. The simulation results of the field energy patterns of the incidence and refraction waves are plotted in Fig. 7.3b. It can be clearly seen that the energy flux of the refraction wave travels on the negative refraction side of the surface normal. The calculated refraction angle and the corresponding refractive index is consistent with the measured results.

The simulation and experimental results of θ vs. θ_0 at 11.82 GHz are summarized in Fig. 7.4 by the solid line and dark dots, respectively. Near all-angle

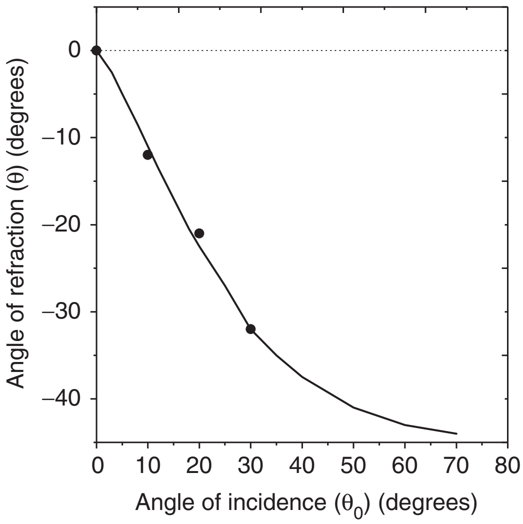

Fig. 7.4. Comparison of measured (*dark dot*) and calculated (*solid line*) angles of refraction (θ) vs. angles of incidence (θ_0) at $f = 11.82$ GHz

negative refraction can be observed at this frequency. In addition, θ is largely linearly proportional to θ_0, which means that the quasicrystal sample has a negative refractive index close to -1 and is only weakly dependent on the wave propagation direction in a rather wide range of incidence angles. In other words, the structure exhibits small spatial dispersion, which is consistent with the nearly homogeneous geometry of such a quasicrystal. This all-angle negative refraction feature for PQC can make it serve as a flat lens [1, 2].

The origin of the negative refraction in the PQCs can be understood similar to the cases in the periodic PCs. The physical principle that allows negative refraction in the periodic PCs is based on complex Bragg scattering effects [13–29]. Recently, some experiments [35] have shown that analogous concepts to Bloch functions and Bloch-like states in the periodic structures can be applied to some quasicrystals. In particular, the 12-fold PQC is composed of two basic composite units (triangle and square) tiling together. One is convinced that each unit, when arranged in a periodic lattice, can show negative refraction. If we bring the triangle and square together into a quasicrystal, the negative refraction phenomenon is still expected. In fact, the present results have demonstrated such an analysis.

7.3 Focus and Image by High-Symmetric Quasicrystal Slab

It is well known that an important application of negative refraction materials is the flat lens [1, 2]. Ideally, such a lens can focus a point source on one side of the lens into a real point image on the other side even for the case of a parallel sided slab of material. It possesses some advantages over conventional lenses. For example, it can break through the traditional limitation on lens performance and focus light on to an area smaller than a square wavelength. The focus and image by the flat lens consisting of the periodic PC have been investigated extensively [17, 18, 20–29].

To see whether the lens effect indeed exists in our quasicrystal structure, we investigate the image formation of a point source against a quasicrystal slab. A 400-mm wide and 70-mm thick slab sample was taken as the first example. A monochromatic point source radiating at frequency 11.82 GHz was placed at a distance 35 mm (half thickness of the sample) from the left surface of the slab. We still employ the multiple-scattering method [23, 28] to calculate the propagation of emitted waves in such a slab sample. A typical field intensity pattern for the wave across the slab is plotted in Fig. 7.5a. X and Y represent the vertical and transverse directions of wave propagation, respectively. Only data in the 300 mm $\times$ 300 mm domain around the center of the sample are displayed here. The geometry of the quasicrystal slab is also shown for clarity of view. One can see that a very high-quality image is formed in the opposite side of the slab. A closer look at the data reveals a transverse size (half width at half maximum) of the image spot about 10 mm in diameter at a distance of 35 mm from the right surface of the slab, which is 0.4λ ($\lambda = 25$ mm being the wavelength of the radiation), well below the conventional diffraction limit (0.5λ) [36]. Such a subwavelength resolution might imply amplification of evanescent waves inside the PQC slabs. Although it is difficult to discern the evanescent wave components within the slab from the total-field pattern due

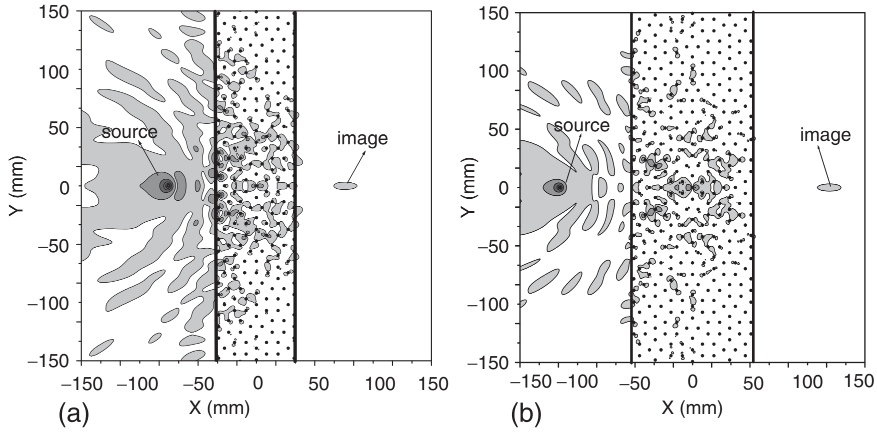

Fig. 7.5. (**a**) The intensity distributions of point source and its image across a slabs with 70-mm thick PQC slab at frequency $f = 11.82$ GHz. (**b**) The corresponding case for a slab with 110-mm thick slab. The crystal and parameters are identical to those in Fig. 7.2

to the existence of complex standing and propagating wave components, the problem can be well solved by looking into the dependence of the imaging and focusing on the sample thickness. If the decay in the free space could be offset by the amplification within the slab as Ref. [2] has pointed out, a subwavelength resolution can be achieved in any distance from the slab by varying the slab thickness accordingly.

In order to clarify such a dependence of the imaging and focusing, we have checked a series of slab samples of different thicknesses. Figure 7.5b shows the calculated field pattern for a 110-mm thick sample. A monochromatic point source at 11.82 GHz is placed at a distance of half thickness of the sample (55 mm) from the left surface of the slab and its image is found near the symmetric position in the opposite side of the slab. More interestingly, a bright point is also seen at the center of the sample. We have continued to increase the thickness of the sample, and found that the image also moves farther away from the slab, a strong evidence of the amplification of evanescent waves by the quasicrystal slab. These phenomena of imaging and focusing are very close to the results predicted by Veselago [1] and Pendry [2] for an ideal LHM with $n = -1.0$. As a comparison, in the previous studies on PC structures [17, 18, 20–25], the image mostly appears in the near-field region, with little dependence of the image distance on the source distance.

We have also performed experiments to verify the above theoretical observations. In the experiment, a monopole antenna is used as the point source. The power distribution at the image plane is measured by scanning and recording the transmission intensity along a line parallel to the surface of the slab at the focus plane. The measurement results at 11.82 GHz are shown as dark dots in Fig. 7.6a, b, where the calculated results (solid lines) are also displayed for comparison. Good agreement between theory and experiment can be observed. Using the same method, we have investigated the imaging properties at different frequencies, and found that negative refraction and focusing can appear in a frequency range between 11.78 and 11.9 GHz (marked by arrow in Fig. 7.2). However, the best focus occurs at 11.82 GHz. At this frequency, the quasicrystal sample shows small spatial dispersion. This feature can be attributed to the high geometric symmetry in the 12-fold quasicrystal.

The above results are only for 12-fold PQC with a random square-triangle tiling system. For other kinds of the PQCs, similar phenomena can be observed. Figure 7.7 describes the case of the PQC with tenfold symmetry. Solid line in Fig. 7.7a represents the transmission coefficients of the tenfold quasicrystal slab with 7a thickness as a function of the frequency. The radii and the dielectric constant of the cylinders are taken as 0.3a and 8.9, respectively. If we take suitable frequency such as $\omega = 0.4(2\pi a/c)$ (marked by an arrow in Fig. 7.7a), the non-near-field focus can also be realized by a flat lens consisting of such a PQC structure. The numerical results for the intensity distributions of point source and its image across such a lens with $11a$ thickness are plotted in Fig. 7.7b. The fields in figures are over $30a \times 30a$ region around the center of the sample. The point source is placed at a distance

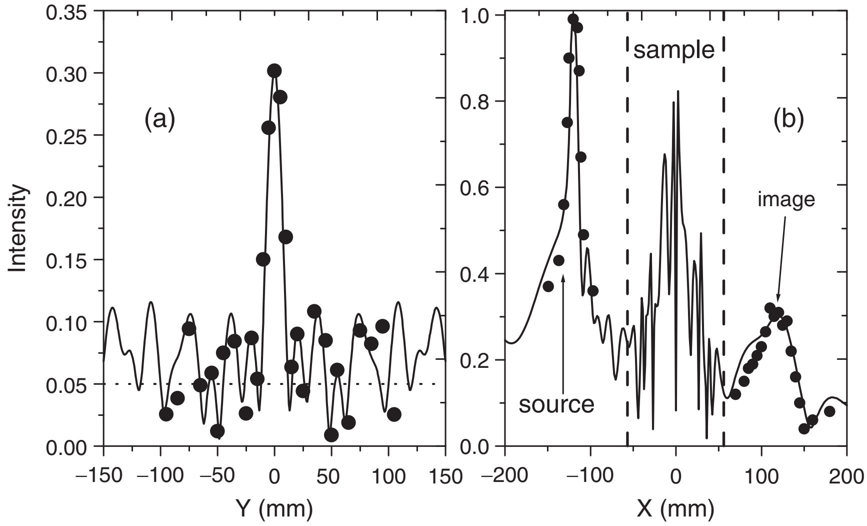

Fig. 7.6. The measured (*dark dots*) and calculated (*solid lines*) intensity distribution along the transverse (Y)-direction at the image plane (**a**), and the vertical (X)-direction. (**b**). Spatial power distribution without PQC is also shown (*dotted line*). Note that the experimental data have been normalized such that the maximum value is the same as the theoretical maximum intensity

of $5.5a$ from the left surface of the sample and a high-quality image formed in the opposite side of the slab. The corresponding results of the PQC with eightfold symmetry are plotted in Fig. 7.8a, b. Here, the radii and the dielectric constant of the cylinders are taken as $0.3a$ and 8.4, respectively. As seen from the figures, the similar non-near-field focus at $\omega = 0.436(2\pi a/c)$ has also been obtained.

It is well known that the electromagnetic wave can be decomposed into E-polarization (S wave) and H-polarization (P wave) modes for the 2D PC structures [23, 28]. However, the above discussions about the negative refraction and the focusing of the wave in the 2D PQCs all focused on a certain S-polarized wave. In fact, similar phenomena can also appear for the P wave. It is more interesting that the non-near-field focus and images for both polarized waves with the same structure and parameters can be realized by using such a high-symmetry PQC slab.

We take a PQC slab with $11a$ thickness and $40a$ width. The slab is made by the 12-fold PQC with a general rotated symmetry which is shown in Fig. 7.1b. A continuous-wave point source is still placed at a distance $5.5a$ (half thickness of the sampled) from the left surface of the slab. The frequency of the incident wave emitting from such a point source is $\omega = 0.4375(2\pi a/c)$. The calculated intensity distributions of E_Z field for the S wave and H_Z field for the P wave of the point sources and their images across such a slab are plotted in Fig. 7.9a, b, respectively. The parameters of the cylinders are identical to those in Fig. 7.8b.

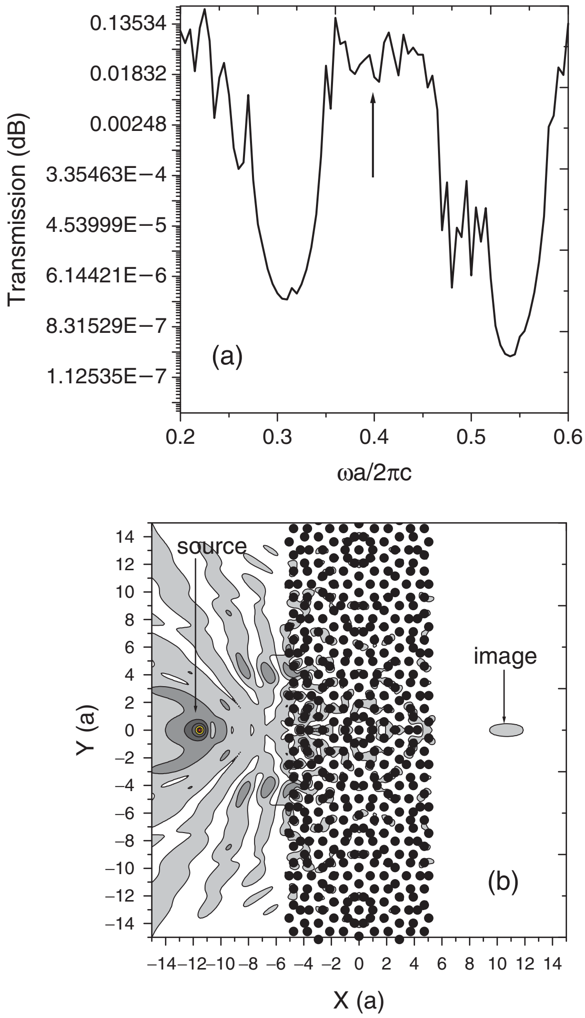

Fig. 7.7. (**a**) Transmission coefficients as a function of frequency for the tenfold quasicrystal. The radii and the dielectric constant of the cylinder are $0.3a$ and 8.9. (**b**) The intensity distributions of point source and its image across the tenfold PQC slab with $11a$ thickness at frequency $\omega = 0.4(2\pi a/c)$

The fields in figures are over $30a \times 30a$ region around the center of the sample. One can find that the positions of the images for both polarized waves are approximately the same. They are about at a distance of $5.5a$ from the right surface of the slab. That is to say, the image of the unpolarized wave point source can be realized by such a 2D PC slab.

We would like to point out that the PQC is not better than the periodic PC in all aspects. In fact, the above phenomena all can be observed by the flat

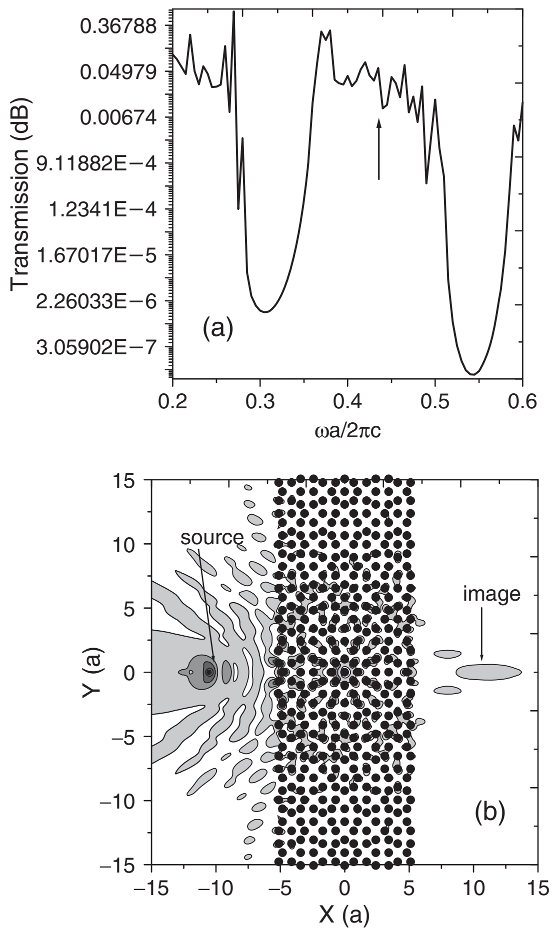

Fig. 7.8. (**a**) Transmission coefficients as a function of frequency for the eightfold quasicrystal. The radii and the dielectric constant of the cylinder are $0.3a$ and 8.4. (**b**) The intensity distributions of point source and its image across the eightfold PQC slab with $11a$ thickness at frequency $\omega = 0.436(2\pi a/c)$

lens consisting of some periodic PC [26–28]. Furthermore, it is more difficult to control the interface reflection of the PQC than that of the PC with the periodic interface. However, the PQC has some advantages in producing the non-near-field images due to their higher rotational symmetry. For example, it is very difficult to construct a flat lens by using pure dielectric cylinder of periodic structure to realize the non-near-field focus for the S wave, but it is easy to complete by high-symmetry PQC slab as has been shown in this chapter. Thus, the investigation on the negative refraction and focus of the PQC can open a new window in the realistic application of such a phenomenon.

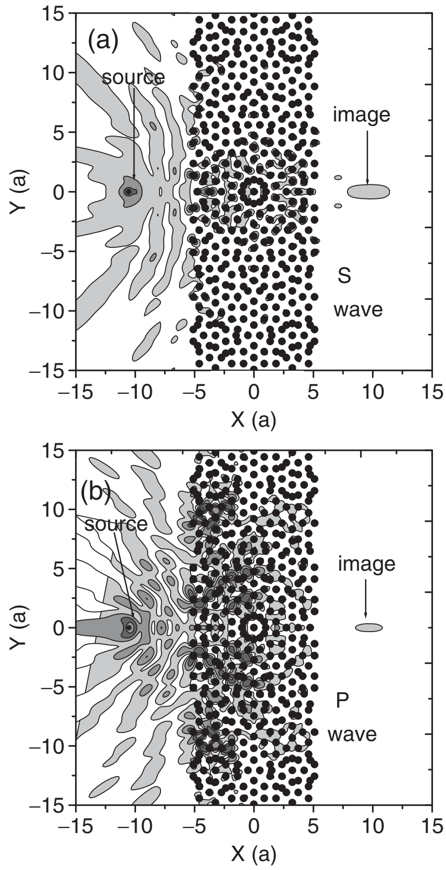

Fig. 7.9. The intensity distributions of E_Z field for S wave (**a**) and H_Z field for P wave (**b**) of point sources and their images across a $11a$ 2D PQC slab with 12-fold symmetry at frequency $\omega = 0.4375(2\pi a/c)$. The radii and the dielectric constant of the cylinder are $0.3a$ and 8.4, respectively

In addition, we would like to point out that our PQC structures are composed of pure dielectric materials and therefore are not subject to loss of absorption. Our results all can be scaled to any range of the frequency. Thus, we have used the normalization units in all figures with the exception of Figs. 7.2–7.6. The reason to use the physical units of millimeter from Figs. 7.2 to 7.6 is that it is convenient to compare the calculated results to the experimental measurements. This is different from the metal-based LHMs and PCs, where increased absorption in metals prohibits the scaling of these structures to the optical wavelengths. As a result, the effective negative refractive index can be maintained in an optical quasicrystal structure, and many negative refraction phenomena that have been observed in the microwave regime can also be found in the optical wavelengths. All these superior features make

PQC promising for application in a range of optical devices, such as a flat lens for visible light.

7.4 Negative Refraction and Focusing of Acoustic Wave by High-Symmetric Quasiperiodic Phononic Crystal

In analogy with the negative-refraction behavior of the electromagnetic wave in the PC, the phenomena of the negative-refraction for other classical waves have also been investigated [37–41]. Negative-refraction and imaging effects of a water surface wave by a periodic structure were theoretically and experimentally demonstrated recently [37]. We have also observed the negative-refraction behavior and imaging effect of acoustic wave in the periodic phononic crystals by exact numerical simulations [38,39]. The experimental demonstrations have been given in [40, 41].

Similar to the case of the electromagnetic wave, the phenomena of negative refraction and focusing for the acoustic wave can also be found in some phononic quasicrystal. Figure 7.10 describes the intensity distributions of pressure field of a sonic point source and its image across a 12-fold PQC slab with $7a$ thickness. The pressure fields in figures are over $20a \times 20a$ region around the center of the sample. They are obtained by the multiple-scattering numerical simulations similar to the case of the electromagnetic wave in the PCs. The slab consists of some steel cylinders embedded in the air background with the random square–triangle tiling structure. The radius of the steel cylinder is $0.36a$. The ratios of density and velocity between the steel and the air

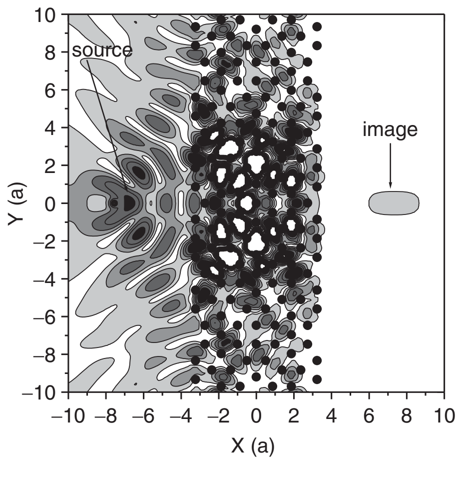

Fig. 7.10. The intensity distributions of pressure field of a point source and its image across a 12-fold PQC slab with $7a$ thickness. The radii of the steel cylinders are $0.36a$

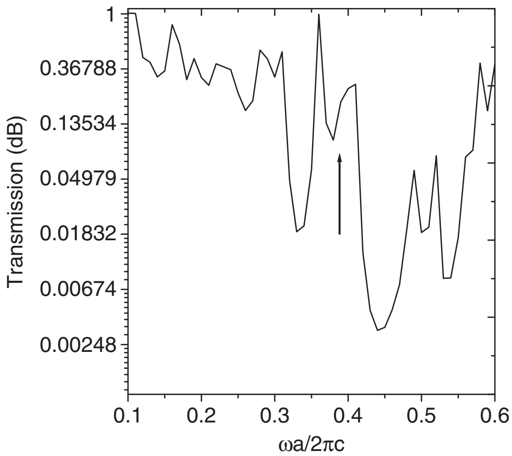

Fig. 7.11. Transmission coefficients of acoustic wave as a function of frequency for steel cylinders in air background with the random square–triangle tiling structure. The crystal and parameters are identical to those in Fig. 7.10

are taken as 7,800 and 17.9, respectively. A continuous sonic point source is placed at a distance $3.5a$ from the left surface of the slab. The frequency of the incident wave emitting from such a point source is $\omega = 0.386(2\pi a/c)$ which is marked as an arrow in Fig. 7.11. Figure 7.11 represents the transmission coefficient of acoustic wave as a function of frequency for such a system. The frequency is in the region of the second band which is similar to the case of the electromagnetic wave. One can find that the position of the image is approximately $3.5a$ from the right surface of the slab which is also similar to the case of the electromagnetic wave.

7.5 Summary

We have theoretically and experimentally investigated the negative refraction and focusing of the electromagnetic wave by two-dimensional high-symmetric photonic quasiperiodic structures. Three kinds of PQCs (12-fold, tenfold, and eightfold) have been considered. We have found that the negative refractions can exist in these PQCs. The high-symmetric PQCs can exhibit an effective refractive index close to -1 in a certain frequency window. The index shows small spatial dispersion, consistent with the nearly homogeneous geometry of the quasicrystal. Thus, a flat lens based on the 2D PQCs can form a non-near-field image whose position varies with the thickness of the sample and the source distance. At the same time, the focus and image for both polarized waves with the same structure and parameters can also be realized by such a flat lens due to its high symmetry. In addition, the negative refraction behaviors and focusing of the acoustic wave in phononic quasicrystal have also been simulated.

Acknowledgments

This work was supported by the National Key Basic Research Special Foundation of China at No. 2001CB610402, 2004CB719804 and the National Natural Science Foundation of China at No. 10374009. The project was supported by NCET.

References

1. V.G. Veselago, Sov. Phys. Usp. **10**, 509 (1968)
2. J.B. Pendry, Phys. Rev. Lett. **85**, 3966 (2000)
3. R.A. Shelby, D.R. Smith, S. Schultz, Science **292**, 77 (2001)
4. D.R. Smith, W.J. Padilla, D.C. View, S.C. Nemat-Nasser, S. Schultz, Phys. Rev. Lett. **84**, 4184 (2000); D.R. Smith, N. Kroll, Phys. Rev. Lett. **84**, 2933 (2000)
5. P. Markos, C.M. Soukoulis, Phys. Rev. E **65**, 036622 (2002); Phys. Rev. B **65**, 033401 (2002)
6. J. Pacheco Jr., T.M. Grzegorczyk, B.L. Wu, Y. Zhang, J.A. Kong, Phys. Rev. Lett. **89**, 257401 (2002)
7. R. Marques, J. Martel, F. Mesa, F. Medina, Phys. Rev. Lett. **89**, 183901 (2002)
8. S. Foteinopoulou, E.N. Economou, C.M. Soukoulis, Phys. Rev. Lett. **90**, 107402 (2003)
9. D.R. Smith, D. Schurig, Phys. Rev. Lett. **90**, 077405 (2003)
10. A.A. Houck, J.B. Brock, I.L. Chuang, Phys. Rev. Lett. **90**, 137401 (2003)
11. C.G. Parazzoli, R.B. Greegor, K. Li, B.E.C. Koltenbah, M. Tanielian, Phys. Rev. Lett. **90**, 107401 (2003)
12. A. Grbic, G.V. Eleftheriades, Phys. Rev. Lett. **92**, 117403 (2004)
13. H. Kosaka, T. Kawashima, A. Tomita, M. Notomi, T. Tamamura, T. Sato, S. Kawakami, Phys. Rev. B **58**, 10096 (1998)
14. M. Notomi, Phys. Rev. B **62**, 10696 (2000)
15. B. Gralak, S. Enoch, G. Tayeb, J. Opt. Soc. Am. A **17**, 1012 (2000)
16. S. Foteinopoulou, C.M. Soukoulis, Phys. Rev. B **67**, 235107 (2003)
17. C. Luo, S.G. Johnson, J.D. Joannopoulos, J.B. Pendry, Phys. Rev. B **65**, 201104 (2002); Opt. Express **11**, 746 (2003); C. Luo, S.G. Johnson, J.D. Joannopoulos, Appl. Phys. Lett. **83**, 2352 (2002)
18. C. Luo, S.G. Johnson, J.D. Joannopoulos, J.B. Pendry, Phys. Rev. B **68**, 045115 (2003)
19. E. Cubukcu, K. Aydin, E. Ozbay, S. Foteinopoulou, C.M. Soukoulis, Nature (London) **423**, 604 (2003)
20. P.V. Parimi, W.T. Lu, P. Vodo, S. Sridhar, Nature **426**, 404 (2003)
21. E. Cubukcu, K. Aydin, E. Ozbay, S. Foteinopoulou, C.M. Soukoulis, Phys. Rev. Lett. **91**, 207401 (2003)
22. Z.Y. Li, L.L. Lin, Phys. Rev. B **68**, 245110 (2003)
23. X. Zhang, Phys. Rev. B **70**, 205102 (2004); Appl. Phys. Lett. **86**, 121103 (2005)
24. S.L. He, Z.C. Ruan, L. Chen, J. Shen, Phys. Rev. B **70**, 115113 (2004)
25. P. Belov, C. Simovski, P. Ikonen, Phys. Rev. B **71**, 193105 (2005)
26. X. Wang, Z.F. Ren, K. Kempa, Opt. Express **12**, 2919 (2004); Phys. Rev. B **71**, 085101 (2005)

27. X. Hu, C.T. Chan, Appl. Phys. Lett. **85**, 1520 (2004)
28. X. Zhang, Phys. Rev. B **70**, 195110 (2004); Phys. Rev. B **71**, 235103 (2005); Phys. Rev. E **71**, 037601 (2005); Phys. Rev. B **71**, 165116 (2005)
29. A. Berrier, M. Mulot, M. Swillo, M. Qiu, L. Thylen, A. Talneau, S. Anand, Phys. Rev. Lett. **93**, 073902 (2004)
30. Y. Zhang, B. Fluegel, A. Mascarenhas, Phys. Rev. Lett. **91**, 157404 (2003); Z. Liu, Z. Lin, S.T. Chui, Phys. Rev. B **69**, 115402 (2004)
31. Z. Feng, X. Zhang, Y.Q. Wang, Z.Y. Li, B.Y. Cheng, D.Z. Zhang, Phys. Rev. Lett. **94**, 247402 (2005)
32. M.E. Zoorob, M.D.B. Chartton, G.J. Parker, J.J. Baumberg, M.C. Nettl, Nature (London) **404**, 740 (2000)
33. X. Zhang, Z.Q. Zhang, C.T. Chan, Phys. Rev. B **63**, 081105 (2001)
34. C. Jin, B. Cheng, B. Man, Z. Li, D.Z. Zhang, S. Ban, B. Sun, Appl. Phys. Lett. **75**, 1848 (1999)
35. E. Rotenberg, W. Theis, K. Horn, P. Gille, Nature (London) **406**, 602 (2000)
36. M. Born, E. Wolf, *Principles of Optics*, chapter VIII, 7th edn. (Cambridge University Press, Cambridge, 1999), p. 462
37. X. Hu, Y. Shen, X. Liu, R. Fu, J. Zi, Phys. Rev. E **69**, 030201 (2004)
38. X. Zhang, Z. Liu, Appl. Phys. Lett. **85**, 341 (2004)
39. C. Qiu, X. Zhang, Z. Liu, Phys. Rev. B **71**, 054302 (2005)
40. S. Yang, J.H. Page, Z. Liu, M.L. Cowan, C.T. Chan, P. Sheng, Phys. Rev. Lett. **93**, 024301 (2004)
41. L. Feng, X.-P. Liu, Y.-B. Chen, Z.-P. Huang, Y.-W. Mao, Y.-F. Chen, J. Zi, Y.-Y. Zhu, Phys. Rev. B **72**, 033108 (2005)

8

Generalizing the Concept of Negative Medium to Acoustic Waves

J. Li, K.H. Fung, Z.Y. Liu, P. Sheng and C.T. Chan

Summary. Electromagnetic metamaterials are artificial materials exhibiting simultaneously negative permeability and permittivity, and the "double negativity" gives rise to many interesting phenomena such as negative refraction, backward waves and superlensing effects. We will see that the concept can be extended to acoustic waves. We will show the existence of acoustic metamaterial, in which both the effective density and bulk modulus are simultaneously negative at some particular frequency range, in the sense of an effective medium. Such a double negative acoustic system is an acoustic analog of Veselogo's medium in electromagnetism, and shares many novel consequences such as negative refractive index, flat slab focusing and super-resolution. The double negativity in acoustics is derived from low frequency resonances, as in the case of electromagnetism, but the negative density and modulus can come from a single resonance structure, as distinct from electromagnetism in which the negative permeability and negative permittivity originates from different resonance mechanisms.

8.1 Introduction

Novel concepts of "negative" media, having negative refraction and/or "double negativity" [1] and their physical consequences and plausible applications are drawing excitement from researchers in many fields. In the past few years, considerable progress has been made on realizing such materials for electromagnetic (EM) waves [2]. Since the concepts of negative refraction, negative constitutive relationships, and "double negativity" originate from electromagnetics, we will use EM waves to qualify these concepts before discussing acoustic waves. For EM waves, we know that the electric permittivity (ε) and magnetic permeability (μ) dictate the response of a medium to external EM fields and these constitutive parameters collectively govern the propagation of EM waves. In particular, the refractive index (n) is given by $n^2 = \varepsilon\mu$. If either ε or μ is negative, then n becomes imaginary and the wave cannot propagate. If, however, *both* ε and μ are simultaneously negative [1] (*double negativity*), then waves can propagate through the media, but with a negative n and hence the phenomenon of *negative refraction*. Many amazing effects, such as Doppler shifts with reversed signs, backward Cherenkov radiation [1], and superlensing effects [3] are consequences of double negativity. These "double-negative" media are characterized by the phenomenon that the Poynting vector and the wavevector are in opposite directions ($\boldsymbol{S} \cdot \boldsymbol{k} < 0$), and they are also called backward wave media. For EM waves, negative ε can be found in natural materials, but negative μ has to be made artificially using resonating units that respond to magnetic fields. The realization of negative effective μ using "split ring" type resonators [4] leads to realization of "double negativity" in EM wave experimentally [5], and those materials are frequently called metamaterials. For EM waves, these "Veselago" media are sometimes called left-handed media (LHM) since the $\{\boldsymbol{E}, \boldsymbol{H}, \boldsymbol{k}\}$ forms a left-handed set, but the term "double negative" medium is more informative.

We will see that such concepts can be generalized to other kinds of classical waves such as acoustic waves [6]. For acoustic waves traveling with a wave vector $\boldsymbol{k}$ inside a homogeneous medium, the refractive index n is given by

$$k = |n|\,\omega \quad \text{with } n^2 = \frac{\rho}{\kappa}, \tag{8.1}$$

where ρ and κ are the mass density and the bulk modulus of the medium, respectively. Therefore, in order to have propagating plane waves inside the medium, we should intuitively have either *both* positive ρ and κ or *simultaneously* negative ρ and κ. Moreover, the time-averaged Poynting vector for a propagating plane wave is given by

$$\boldsymbol{S} = \frac{\mathrm{i}}{2\omega\rho}\psi\,\nabla\psi^* = \frac{|\psi|^2\,\boldsymbol{k}}{2\omega\rho}, \tag{8.2}$$

where ψ is the pressure. Now, if we can have a "negative" medium in acoustic waves, a negative effective ρ means that we have a backward wave in which $\boldsymbol{S}$ and $\boldsymbol{k}$ should point in the opposite directions. And simultaneous negativity in κ and ρ ensures the existence of propagating waves. Although the analogy between acoustic and EM waves can be made, the realization of such "negative" acoustic wave is in fact less obvious than EM waves. For EM waves, at least negative ε can be found in nature. It is the negative μ that has to be made artificially. For acoustic waves, neither negative ρ nor negative κ can be found in naturally occurring materials. They have to be derived from artificial resonances through composite materials. Physically, this means that the medium displays anomalous response at some frequencies such that it expands upon compression (negative modulus) and accelerates to the left when being pushed to the right (negative density). We need to show that negative effective density and negative effective modulus are "allowable," at least mathematically, and we need to give explicit configurations and perform calculations to show that they indeed have the "negative" backward wave properties. This is not an easy task because (even for composite materials) the effective bulk modulus and density are normally bounded by the Hashin and Shtrikman bounds [7]. Therefore, we still expect positive bulk modulus and density. For instance, let us examine the prototypical case of spherical particles dispersed in a fluid with filling ratio f. In the long-wavelength and small-filling-ratio limit, the effective bulk modulus, κ_{eff}, and effective density, ρ_{eff}, are governed by the Berryman's equations [8]:

$$\frac{1}{\kappa_{\text{eff}}} = \frac{f}{\kappa_{\text{s}}} + \frac{1-f}{\kappa_0} \quad \text{and} \quad \frac{\rho_{\text{eff}} - \rho_0}{2\rho_{\text{eff}} + \rho_0} = f \frac{\rho_{\text{s}} - \rho_0}{2\rho_{\text{s}} + \rho_0}, \tag{8.3}$$

where the subscripts "s" and "0" denotes, respectively, the parameters of the sphere and the background fluid. It can be shown from the formulae that κ_{eff} and ρ_{eff} are positive definite for natural materials. However, the above effective medium formulae and the traditional bounds on the effective parameters do not apply if there are low frequency resonances, and we will see that within the context of effective medium theories, negative values of κ_{eff} and ρ_{eff} are mathematically "allowed" at finite but low frequencies. The task then is to find physical systems (with explicit configurations) to realize them so that κ_{eff} and ρ_{eff} are simultaneously negative in the same frequency range and the frequency should be low enough for a meaningful effective medium description. One possibility is to create strong Mie-type resonances [9]. That can in principle be achieved by finding two components that have very different sound speeds. When the configuration is given, the effective constitutive parameters and the wave propagation properties can be computed as shown below.

Before we go into the specific details, we would like to emphasize that the double negative acoustic medium is not necessarily a "phononic crystal" [10]. To distinguish the two, it helps first to distinguish a double negative EM wave medium ("Veselago" medium) from a photonic crystal [11]. A comparison is given in Table 8.1. We are aiming here at a "Veselago"-type medium,

Table 8.1. Comparison of a photonic crystal with a double negative electromagnetic medium

photonic crystal	Veselago/metamaterial
$\lambda \approx a$ (lattice constant)	$\lambda >> a$
negative group velocity originates from band folding, can get negative refraction ($n < 0$, but ε, μ may not even be well defined)	Double Negative constitutive parameters ($\varepsilon, \mu < 0$) Double negativity implies negative refraction, subwavelength imaging...
Bragg scattering	Resonance
Band structure description	Effective medium description

The concept of photonic crystal has an analog in acoustic waves in the form of phononic crystals, which are crystals with a periodic variation of elastic constants/density. The purpose of this chapter is to examine the analog of Veselago medium in acoustic waves, which is expected to be a system containing subwavelength resonators that permits a long-wavelength description, having double negative constitutive relationships which derives the negative refraction from "double negativity" (negative κ_{eff} and ρ_{eff}). "Double negativities" are typically resonance based and are rather different from negative refraction observed in phononic crystals [12, 13] in which the mechanism is derived from Bragg scattering. "Double negativity" in constitutive relationships will lead to negative refraction, and "negativity" refers to negative constitutive parameters. For an inhomogeneous system, the wavelength must be long compared with the embedded inhomogeneity before we can meaningfully employ effective constitutive parameters (after proper homogenization) to describe the response of the medium to incident waves. The "double-negative" medium should be viewed within the context of an effective medium. However, if we are interested in the phenomenon of negative refraction only, it can also be derived from other mechanisms. One example is that we have a highly anisotropic medium and that the principal axis is "misaligned" with another medium. We can observe negative refraction for some angles at the interface, but many novel phenomena (such as the superlens effect) cannot occur. All-angle negative refraction can also be achieved by using band structure effects (arising from Bragg scattering [14]) in periodic structures. These have been demonstrated in photonic [15] and phononic [13] bandgap systems. While an "effective parameter" description is not necessarily meaningful in these cases, some novel effects, such as point source imaging with near-field subwavelength resolution, are also possible.

8.2 A Simple Model

In order to give an intuitive understanding of the problem, we start with a simple model (see Fig. 8.1) to understand the meaning of "negative mass" and demonstrate a way to realize negative effective mass by resonance. We will then move on to real systems and consider acoustic waves.

This model system is a chain of identical "resonant" units connected together by springs with a spring constant K as illustrated in the figure. Each "resonant" unit consists of a shell and a core with, respectively, masses

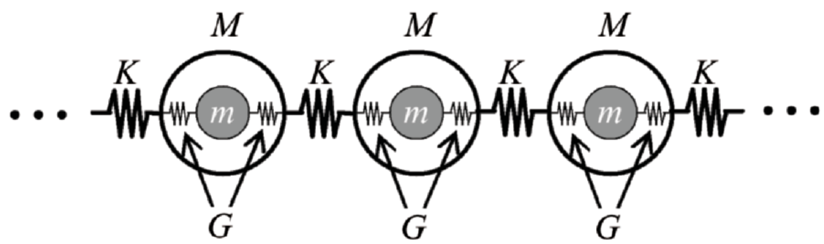

Fig. 8.1. Schematic structure of the spring-mass model with resonance effect on the effective mass

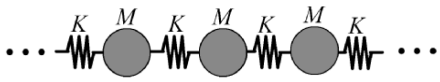

Fig. 8.2. A simple textbook spring-mass model

M and m. The core is connected internally, through two springs with spring constant G, to the shell. It can be shown easily that the dispersion relation for acoustic waves on this infinite chain is

$$\omega^2 \left(M + \frac{m\omega_0^2}{\omega_0^2 - \omega^2} \right) = 4K \sin^2 \left(\frac{ka}{2} \right), \tag{8.4}$$

where $\omega_0 = \sqrt{2G/m}$, k is the Bloch wavenumber, and ω is the angular frequency. We may compare this dispersion relation with that of the usual textbook example [16] (see Fig. 8.2) which is an infinite chain of identical masses with mass M.

The dispersion relation of this system is

$$\omega^2 = \frac{4K}{M} \sin^2 \left(\frac{ka}{2} \right). \tag{8.5}$$

Comparing (8.4) and (8.5), we see that (8.4) can be obtained by replacing the quantity M in (8.5) with a frequency-dependent effective mass

$$M_{\text{eff}} = M + \frac{m\omega_0^2}{\omega_0^2 - \omega^2}. \tag{8.6}$$

We see immediately the possibility of a negative effective mass near resonance. One may argue that (8.4) can also be obtained by keeping the mass M in (8.5) unchanged, but replacing K with the effective spring constant of the form

$$K_{\text{eff}} = \frac{K}{1 + \dfrac{m}{M} \dfrac{\omega_0^2}{\omega_0^2 - \omega^2}}. \tag{8.7}$$

By just looking at the dispersion relation, it thus seems to be different ways to choose effective parameters from (8.6) and (8.7). However, a more physical derivation (shown below) suggests that the effective mass in (8.6) is the correct choice. Let F be the external (longitudinal) force acting on the shell. Then, assuming harmonic time dependence, the equations of motion are

$$\begin{cases} -M\omega^2 u = F + 2G(v - u) \\ -m\omega^2 v = \quad 2G(u - v) \end{cases}. \tag{8.8}$$

where u and v are the displacements of, respectively, the shell M and the mass core m with respect to their equilibrium positions. Eliminating v, we get a single equation of motion for the shell:

$$F = -\left(\frac{2Gm}{2G - m\omega^2} + M\right)\omega^2 u. \tag{8.9}$$

Now, suppose that the observers cannot "see" the internal structure of the resonant unit, then the only information that the observers know about this black box is its displacement and the force acting on it. If we still consider the whole black box as a rigid body with mass M_{eff}, the equation of motion of such an object is

$$F = -M_{\mathrm{eff}}\omega^2 u. \tag{8.10}$$

Comparing (8.9) with (8.10), we get an equation which is exactly the same as (8.6). This effective mass shows a familiar form $1/\left(\omega_0^2 - \omega^2\right)$, which indicates a resonant effect at $\omega = \omega_0$ similar to the dielectric constant in the EM theory.

The resonant feature of M_{eff} indicates that there is a range of frequencies in which M_{eff} is negative (see Fig. 8.3b). Making analogy with the negative dielectric constant, we see that this represents a frequency range in which there is no propagating wave solution inside the media and incoming wave decays inside the negative-mass media. For a composite material possessing such a negative effective mass, there exists a phononic bandgap due to resonance (see, e.g., Fig. 8.3).

A typical band structure with a resonance in the effective mass is shown in Fig. 8.3a. The figure compares the dispersion relations described by (8.4) (solid curve) and (8.5) (dashed curve). The resonance frequency $\omega_0 = 1$ unit

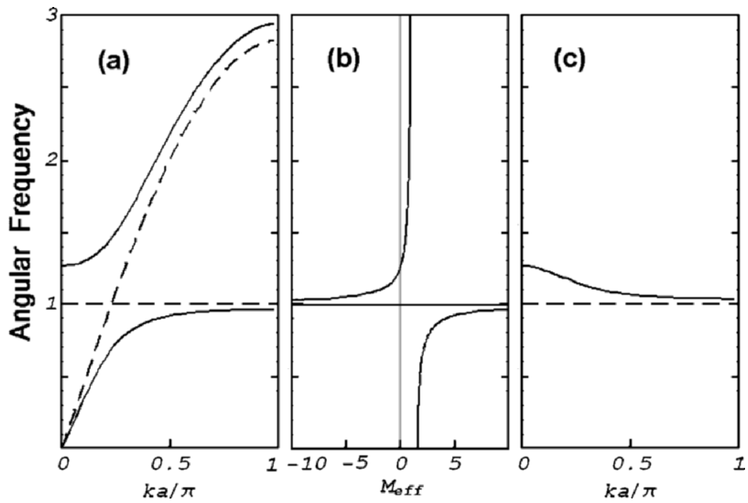

Fig. 8.3. Band structure of the spring-mass model shown in Fig. 8.1. (**a**) $K > 0$. (**b**) Effective mass of a resonant unit. (**c**) $K < 0$

is also indicated by another dashed horizontal straight line. The hybridization effect opens a bandgap near the resonance frequency. In the effective medium picture, bandgap region (bounded by $M_{\text{eff}} = 0$ and $M_{\text{eff}} \to -\infty$) corresponds to a range of negative effective mass. This can be seen clearly by comparing Fig. 8.3a, b.

Now suppose that the force constant can also be made to be negative in the same frequency range as the $M_{\text{eff}} < 0$ region. The dispersion will be changed to that shown in Fig. 8.3c. The range of forbidden transmission due to the negative effective mass ($M_{\text{eff}} < 0, K > 0$) becomes a passband with negative group velocity when we have both $M_{\text{eff}} < 0$ and $K < 0$. This very simple model already tells some useful information (1) Dynamical negative effective mass can be obtained by resonance; (2) "Single negative" ($M_{\text{eff}} < 0$) implies a bandgap; and (3) "Double negative" ($K > 0$) implies a passband with negative group velocity.

A medium with negative effective mass due to resonance can block the transmission of waves near the resonance frequency because of the bandgap effect. However, the transmission properties for thin slabs are somewhat different from that of a phononic crystal in which the bandgap is derived from Bragg scattering. Here, we make a digression to look at the transmission spectra for the spring-mass model with built-in resonance resulting in a frequency-dependent effective mass. A comparison between the transmission amplitude (T) spectra and the bulk band structure is shown in Fig. 8.4.

For a relatively long chain of resonance units, the overall transmission spectrum follows the band structure with high transmission in the passband and low transmission in the bandgap. The oscillatory feature of the transmission

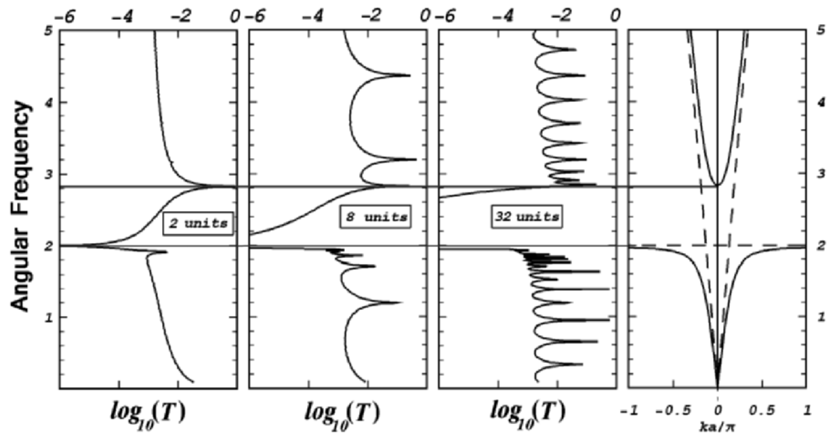

Fig. 8.4. Transmission spectra of the spring-mass model shown in Fig. 8.1. The three panels on the left correspond to chains of 2, 8, and 32 resonant units, respectively. On the right most panel, *solid lines* show the band structure of an infinitely long chain. *Dashed lines* show the resonance frequency and the dispersion relation of the model when there is no core mass

spectrum inside the passband is due to the Fabry–Perot effect. However, for a short chain, the bandgap is not fully developed and the wave is highly attenuated only near the resonance frequency. Exactly at the resonance frequency, the transmittance is a dip, followed by a peak marking the band-edge of the second passband.

8.3 An Example of Negative Mass

We have shown in our simple ball-and-spring model that resonance structures can lead to a negative effective mass. Such materials can in fact be fabricated experimentally and one of the realizations of such material is called locally resonant sonic materials [17] (LRSM), which is a composite made up of three components: a heavy core, a light and soft cladding layer, and a passive matrix. In the samples fabricated, an array of lead spheres, coated by soft silicone rubber, is embedded periodically inside an epoxy matrix (see Fig. 8.5). The lead sphere and the epoxy matrix correspond to the core and shell in the simple model, respectively. The silicone rubber acts like springs connecting the "shells" and the "cores." Such LRSM can block low frequency sound waves by resonance-induced sonic bandgaps. An example for the transmission spectra (air–LRSM–air) and the elastic wave band structure of the LRSM in bcc (100)-direction are shown in Fig. 8.6. Results are calculated by using the multiple scattering theory (MST) [18, 19] for elastic waves. The band structure in Fig. 8.6 is very similar to that in Fig. 8.4. A noticeable difference is that there are two bandgaps in LRSM while there is a single bandgap in our simple model. The lower and the upper bandgaps are due to the resonances of the lead spheres and the silicone rubber, respectively (see Fig. 8.7). Also,

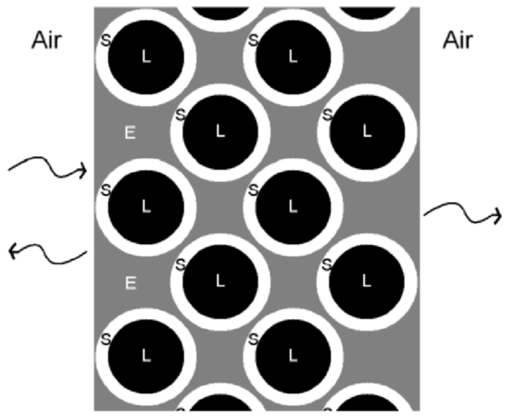

Fig. 8.5. Schematic structure of LRSM which possesses negative effective mass due to resonance structures. "L," "S," and "E" denote lead, silicone rubber, and epoxy, respectively

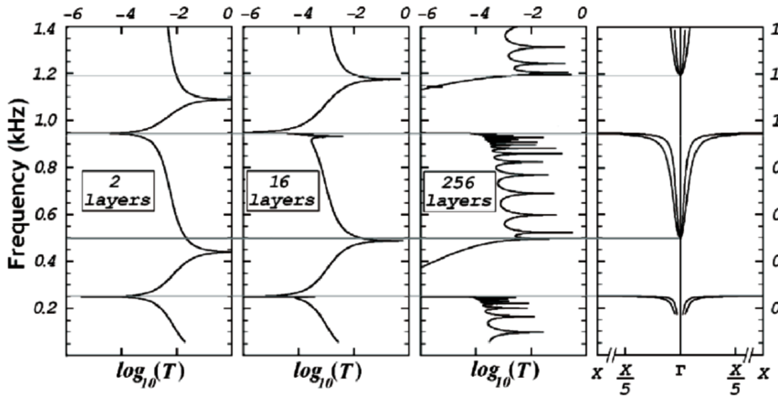

Fig. 8.6. Transmission spectra of an LRSM in bcc structure in the (100)-direction. The three panels on the left correspond, respectively, to a slab of LRSM with 2, 16, and 256 layers. The right most panel shows the band structure of the infinite crystal. The x-axis of band structure is not in uniform scale

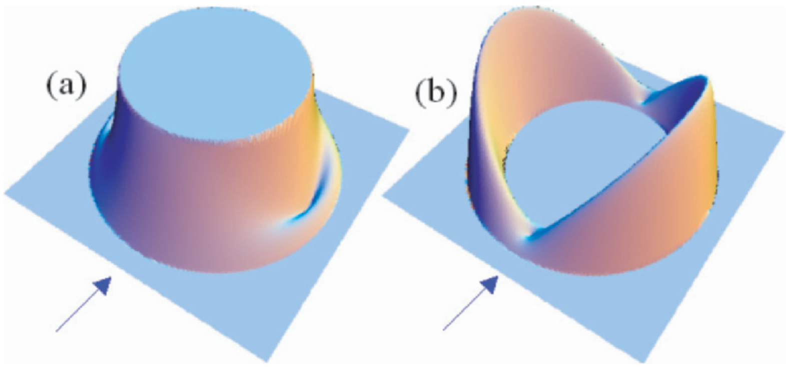

Fig. 8.7. Displacement amplitude plot of the silicone-coated lead sphere at resonance. The *arrows* show the propagation directions of the incident wave. (**a**) Resonance of lead sphere at 250 Hz. (**b**) Resonance of silicone rubber at 950 Hz

for LRSM, there are two separate branches shown in each passband region (see the right-hand panel in Fig. 8.6). The upper one is the longitudinal mode while the lower one corresponds to the doubly degenerate transverse modes. The transmission curves are also similar to that of the simple model. For a thick LRSM slab, the transmission amplitude (T) is high (with Fabry–Perot peaks) in the passband region while it is nearly zero in the bandgap region. For a thin LRSM slab, there are two transmission dips marking exactly the bottom of each bandgap. These frequencies are the resonance frequencies of each resonance unit. There is also a peak located directly above each dip. According to the simple model, these should mark the top of the bandgaps.

However, these peaks are now inside the bulk bandgaps. This very strange phenomenon of having a "$T = 1$" transmission peak inside the bandgap is an effect due to the interface [20]. For a thick slab of the simple model, it can be shown that a transmission peak exists when the effective mass $M_{\text{eff}} = 0$, with a frequency of

$$\omega_{\text{p}} = \sqrt{2G\left(\frac{1}{m} + \frac{1}{M}\right)}. \tag{8.11}$$

For a thin slab of LRSM with high filling ratio (such as the schematic picture shown in Fig. 8.5), we cannot ignore the extra volume occupied by the matrix materials near the interfaces between LRSM and air. This can affect the effective mass of a thin slab of LRSM (but not a thick one). By taking into account the extra mass near the surfaces, we get

$$\omega_{\text{p}} = \sqrt{K\left(\frac{1}{M_{\text{lead}}} + \frac{n}{M'_{\text{epo}} + nM_{\text{epo}}}\right)}, \tag{8.12}$$

where n is the number of layers, K is the "effective" spring constant of silicone rubber, M_{epo} and M_{lead} are the epoxy mass and lead mass in a unit cell of the crystal, respectively, M'_{epo} is the mass of extra epoxy near the surface of the sample. Equation (8.12) fits the peak frequencies inside the lower bandgap very well (see Fig. 8.8). Here we showed that the effective mass can be used to understand why there is a transmission peak in the slab transmission spectrum with frequency within the bulk bandgap. We can also use similar physics to explain the peak inside the upper bandgap.

So, we see that a "negative mass" is conceptually rather transparent, and has indeed been realized. However, to achieve a "negative spring" is much more challenging. We thus seek another route (using Mie resonances) to achieve double negativity in acoustic waves.

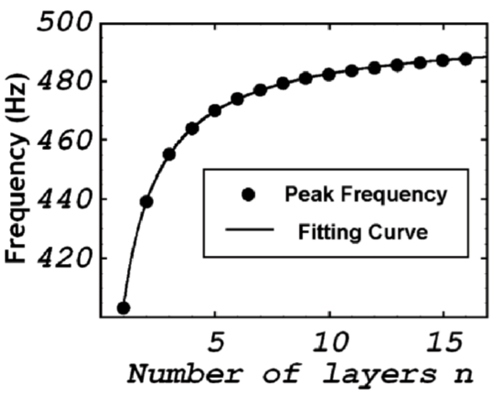

Fig. 8.8. Frequency of the first peak above the first dip of bcc structured LRSM vs. number of layers. *Filled circles* are the data obtained from the transmission curve. The *solid line* is the fitting to the data with (8.12)

8.4 Acoustic Double-Negative Material

We now generalize the concept of double negativity in electromagnetic waves to acoustic waves by using Mie resonances. The acoustic wave equation (with time dependence $e^{-i\omega t}$) is written as [21]

$$\begin{aligned} &\nabla \cdot \boldsymbol{u} + \frac{1}{\kappa(\boldsymbol{r})}\psi = 0, \\ &\nabla \psi - \rho(\boldsymbol{r})\omega^2 \boldsymbol{u} = 0. \end{aligned} \tag{8.13}$$

The first equation is the continuity equation where ψ is the pressure field (deviation from equilibrium), $\boldsymbol{u}$ is the displacement field, and κ is the position-dependent bulk modulus. The second equation is the Newton's second law where ρ is the position-dependent density. Suppose we have a closed region V of constant bulk modulus and constant density, by integrating (8.13), we obtain

$$\begin{aligned} \Delta V &= \oint \boldsymbol{u} \cdot \mathrm{d}\boldsymbol{A} = -\frac{1}{\kappa}\int \psi \, \mathrm{d}V, \\ \boldsymbol{F} &= -\int \psi \, \mathrm{d}\boldsymbol{A} = -\rho\omega^2 \int \boldsymbol{u} \, \mathrm{d}V, \end{aligned} \tag{8.14}$$

where ΔV is the volume dilation and F is the total force on the volume V. Therefore, we see that a negative bulk modulus means that the volume expands when the system is pressed, and a negative density means that the volume element accelerates to the opposite direction of the total force.

To make the mathematics tractable, the composite material is assumed to be of the form of small particles dispersed in a homogeneous background material. The ratio κ/ρ is different from the background value κ_0/ρ_0 only in the regions of the particles. By defining the secondary source functions Q and $\boldsymbol{P}$, the wave equation can be written with respect to the background by

$$\begin{aligned} \nabla \cdot \boldsymbol{u} + \frac{1}{\kappa_0}\psi &= -\frac{Q(\boldsymbol{r})}{\omega^2} = \left(\frac{1}{\kappa_0} - \frac{1}{\kappa(\boldsymbol{r})}\right)\psi, \\ \frac{1}{\rho_0}\nabla\psi - \omega^2 \boldsymbol{u} &= \boldsymbol{P}(\boldsymbol{r}) = \left(\frac{1}{\rho_0} - \frac{1}{\rho(\boldsymbol{r})}\right)\nabla\psi. \end{aligned} \tag{8.15}$$

The fields outside a particular particle can be expanded by partial waves in response to the incident wave so that the particle can be regarded effectively as a point particle. Up to the dipole approximation, the secondary sources are approximated by their monopolar (Q) and dipolar ($\boldsymbol{P}$) contributions as

$$\begin{aligned} Q(\boldsymbol{r}) &\approx \sum_{\boldsymbol{R}} q_{\boldsymbol{R}}\delta(\boldsymbol{r} - \boldsymbol{R}), \\ \boldsymbol{P}(\boldsymbol{r}) &\approx \sum_{\boldsymbol{R}} \boldsymbol{p}_{\boldsymbol{R}}\delta(\boldsymbol{r} - \boldsymbol{R}), \end{aligned} \tag{8.16}$$

where $\boldsymbol{R}$ are the position vectors of the particles. On the other hand, for the scattering problem of a single isotropic particle up to the dipole approximation, the induced sources at the particles are related to the local fields by

$$\begin{aligned} \frac{\kappa_0 q_{\boldsymbol{R}}}{\omega^2 V} &= \frac{3}{\mathrm{i}k_0^3 r_0^3} D_0 \psi_{\mathrm{local},\boldsymbol{R}}, \\ \frac{\rho_0 \boldsymbol{p}_{\boldsymbol{R}}}{3V} &= \frac{3}{\mathrm{i}k_0^3 r_0^3} D_1 (\nabla\psi)_{\mathrm{local},\boldsymbol{R}}, \end{aligned} \tag{8.17}$$

where $k_0 = \omega\sqrt{\rho_0/\kappa_0}$ is the wave number in the background medium and $V = 4\pi r_0^3/3$ is defined as the average volume occupied by one particle. If the particles are arranged in a lattice, it is the volume of one primitive unit cell. D_0 and D_1 are the scattering coefficients of the particle in the partial wave expansion of angular momentum $L = 0$ and $L = 1$. On the other hand, the local field at each particle is related to the macroscopic field by

$$\begin{aligned} &\psi_{\mathrm{local},\boldsymbol{R}} \approx \langle\psi\rangle(\boldsymbol{R}), \\ &(\nabla\psi)_{\mathrm{local},\boldsymbol{R}} \approx \langle\nabla\psi\rangle(\boldsymbol{R}) - \frac{\rho_0 \boldsymbol{p}_{\boldsymbol{R}}}{3V}, \end{aligned} \tag{8.18}$$

where the angle brackets denote spatial averaging. It is the series expansion of the local field in frequency with only the static term being kept for simplicity. For a periodic lattice of the particles, we should also keep the third order term, which is usually called "radiative correction." For a disordered system, the third order term vanishes due to the incoherent addition of the scattered fields from the particles [22, 23].

By substituting (8.17) and (8.18) into (8.16) and applying spatial averaging, we obtain

$$\begin{aligned} \langle\boldsymbol{P}\rangle &= \left(\frac{1}{\rho_0} - \frac{1}{\rho_{\mathrm{eff}}}\right)\langle\nabla\psi\rangle, \\ \frac{\langle Q\rangle}{\omega^2} &= \left(\frac{1}{\kappa_{\mathrm{eff}}} - \frac{1}{\kappa_0}\right)\langle\psi\rangle, \end{aligned} \tag{8.19}$$

where the effective density and bulk modulus are given by

$$\begin{aligned} -1 + \frac{\kappa_0}{\kappa_{\mathrm{eff}}} &= \frac{3}{\mathrm{i}k_0^3 r_0^3} D_0, \\ \frac{\rho_{\mathrm{eff}} - \rho_0}{2\rho_{\mathrm{eff}} + \rho_0} &= \frac{3}{\mathrm{i}k_0^3 r_0^3} D_1. \end{aligned} \tag{8.20}$$

By putting (8.19) back into the spatially averaged version of (8.15), we finally obtain the macroscopic wave equation

$$\begin{aligned} &\nabla\cdot\langle\boldsymbol{u}\rangle + \frac{1}{\kappa_{\mathrm{eff}}}\langle\psi\rangle = 0, \\ &\langle\nabla\psi\rangle - \rho_{\mathrm{eff}}\omega^2\langle\boldsymbol{u}\rangle = 0. \end{aligned} \tag{8.21}$$

It has the same form as the microscopic equation, and we need negative effective bulk modulus together with negative effective density to have a propagating plane wave whose energy and phase are propagating in the opposite directions. Note that the imaginary part of the effective density and bulk modulus accounts for both the dissipative loss and the diffusive scattering loss in the system. If the system is periodic, adding the radiative correction in (8.18) gives

$$
\begin{aligned}
-1 + \frac{\kappa_0}{\kappa_{\text{eff}}} &= \frac{3}{\mathrm{i}k_0^3 r_0^3} \frac{D_0}{1 + D_0}, \\
\frac{\rho_{\text{eff}} - \rho_0}{2\rho_{\text{eff}} + \rho_0} &= \frac{3}{\mathrm{i}k_0^3 r_0^3} \frac{D_1}{1 + D_1}.
\end{aligned} \tag{8.22}
$$

In this case, we note that the right-hand sides of (8.22) and hence the effective density and bulk modulus remain purely real for nonabsorbing system.

We note that in the case of anisotropic particles, the macroscopic acoustic wave equation should be written as

$$
\begin{aligned}
\nabla \cdot \langle \boldsymbol{u} \rangle + \frac{1}{\kappa_{\text{eff}}} \langle \psi \rangle &= 0, \\
\langle \nabla \psi \rangle - \overleftrightarrow{\rho}_{\text{eff}}\, \omega^2 \langle \boldsymbol{u} \rangle &= 0,
\end{aligned} \tag{8.23}
$$

since the dipolar scattering coefficient is a tensor rather than a scalar.

The effective-medium formulae can also be derived by using the techniques commonly used in the coherent potential approach (CPA). This method is more elegant in the sense that we need not define the sources and set up the somewhat tedious homogenization scheme step by step as above. In the spirit of a single-site mean-field theory, the inhomogeneity is represented by a single spherical particle dispersed in a background fluid of volume equal to the average volume a single particle occupies. It is represented by a sphere of radius r_0 in Fig. 8.9 and it shares the same center with the particle. The "coated sphere," which represents the inhomogeneous media, is further embedded in an effective medium which carries effective parameters that represent the bulk homogenized medium. The self-consistency we require is that the inhomogeneity embedded within the effective medium generates no scattering. In the following we will demonstrate this self-consistency can be fulfilled if we expand the scattering in the lowest order of frequency and (8.20) and (8.22) can be derived using the CPA method.

Inside the layer of the background medium, the pressure field can be written as

$$
\psi(\boldsymbol{r}) = \sum_{L,m} \left(a_{Lm}^{(0)} j_L(k_0 r) + b_{Lm}^{(0)} h_L(k_0 r) \right) Y_{Lm}(\hat{r}), \tag{8.24}
$$

where $j_L(x)/h_L(x)$ is the spherical Bessel/Hankel function and $Y_{Lm}(\hat{r})$ are the spherical harmonics. The pressure field in the effective medium can be

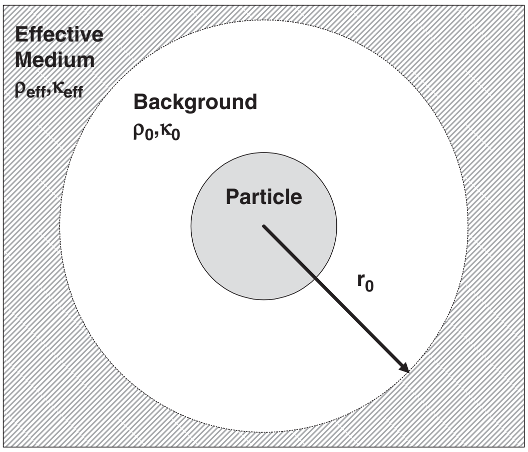

Fig. 8.9. CPA condition for particles in matrix for acoustic wave. The effective medium is defined to be a homogeneous medium with values of ρ_{eff} and κ_{eff} such that there is no scattering (lowest order) from the particle coated with the matrix material

written by the same formula with $a_{Lm}^{(0)}/b_{Lm}^{(0)}$ replaced by $a_{Lm}^{(\text{eff})}/b_{Lm}^{(\text{eff})}$ and k_0 replaced by k_{eff}. We assume the particle to be isotropic so that each (L, m) wave scatters independently. The scattering cross-section of the coated particle (that represents that inhomogeneity) is then given by

$$C_{\text{sca}} = \frac{4\pi}{k_{\text{eff}}^2} \sum_{L=0}^{\infty} (2L+1) \left| D_L^{(\text{tot})} \right|^2, \tag{8.25}$$

where $D_L^{(\text{tot})} = b_{Lm}^{(\text{eff})}/a_{Lm}^{(\text{eff})}$ is the Mie scattering coefficient of the whole coated particle. In the long wavelength expansion of (8.25), the scattering cross-section is dominated by the "$L = 0$" and "$L = 1$" terms. Therefore, the CPA self-consistent condition is

$$D_0^{(\text{tot})} = D_1^{(\text{tot})} = 0. \tag{8.26}$$

Actually, we can rewrite (8.26) in a more useful form. Since there are no monopolar and dipolar outgoing fields in the effective medium, the field matching (continuous normal displacement $(\partial\psi/\partial r)/\rho$ and pressure ψ) on the radius r_0 is thus equivalent to another situation that wave is scattered in the background medium by an "effective sphere" (a sphere made of the effective medium of radius r_0). Therefore, we have

$$D_L^{(\text{eff})} = b_{Lm}^{(0)}/a_{Lm}^{(0)} \quad \text{for } L = 0, 1, \tag{8.27}$$

where $D_L^{(\text{eff})}$ is defined as the scattering coefficient of the effective sphere in background. By recognizing the right-hand side of (8.27) is the scattering coefficient of the central particle in background, the CPA self-consistent condition now becomes

$$D_0^{(\mathrm{eff})} = D_0 \quad \text{and } D_1^{(\mathrm{eff})} = D_1. \tag{8.28}$$

In the limit $k_{\mathrm{eff}} r_0, k_0 r_0 \ll 1$, we can approximate $D_0^{(\mathrm{eff})}$ and $D_1^{(\mathrm{eff})}$ by

$$\begin{aligned} \frac{1}{D_0^{(\mathrm{eff})}} &\approx \frac{3}{\mathrm{i}k_0^3 r_0^3} \frac{\kappa_{\mathrm{eff}}}{-\kappa_{\mathrm{eff}} + \kappa_0} - 1 \\ \frac{1}{D_1^{(\mathrm{eff})}} &\approx \frac{3}{\mathrm{i}k_0^3 r_0^3} \frac{2\rho_{\mathrm{eff}} + \rho_0}{\rho_{\mathrm{eff}} - \rho_0} - 1. \end{aligned} \tag{8.29}$$

The term "-1" in the two right-hand sides of (8.29) is the radiative correction [24]. Combining (8.28) and (8.29) gives (8.22) while combining (8.28) and (8.29) without the radiative correction gives (8.20).

If the particles are made from a homogeneous material (a fluid particle) such that the long-wavelength limit is valid within this particle ($k_{\mathrm{s}} r_{\mathrm{s}} \ll 1$ where k_{s} is the wave number of the particle and r_{s} is the radius of it), (8.20) and (8.22) reduce to the familiar Berryman formula (8.3).

If the particle is a solid particle, in the limit $k_{\mathrm{s}} r_{\mathrm{s}} \ll 1$ and $q_{\mathrm{s}} r_{\mathrm{s}} \ll 1$ where q_{s} is the wave number of shear wave within the particle, (8.20) and (8.22) still reduce to (8.3). In such a case,

$$\kappa_{\mathrm{s}} = \lambda_{\mathrm{s}} + 2\mu_{\mathrm{s}}/3, \tag{8.30}$$

where λ_{s}, μ_{s} are the Lamé constants of the particle with μ_{s} (also denoted as the shear modulus) being zero for fluid and nonzero for solid.

8.4.1 Construction of Double-Negative Material by Mie Resonances

For EM waves, we are familiar with the notion that double-negative metamaterials can be constructed from a combination of "plasmonic wires" which give negative effective ε and "split rings" that give negative effective μ. Thus, two different types of structures are needed to give two different types of resonances. In fact, there is another strategy to realize double negativity. Resonances can be derived from the Mie resonances from one single structure. In the absence of Mie resonances, the effective medium formula is well represented by (8.3) for a small filling ratio of spherical particles dispersed in a background fluid. (We note that for solid particles in a solid matrix, the density should be volume averaged.) The formulae imply that the effective bulk modulus and the effective density can only be positive in the absence of resonances. In fact, we can obtain the physical properties of the medium by considering the effective sphere introduced in the last section. For ease in discussion, let us ignore the radiative correction, which is usually small. Then, it is easy to find the relationship between the local and the macroscopic fields, and (8.21) can be written as

$$\begin{aligned} \rho_0 \omega^2 \langle \boldsymbol{u} \rangle &= \frac{3\rho_0}{2\rho_{\mathrm{eff}} + \rho_0} (\nabla \psi)_{\mathrm{local}} = \frac{\rho_0}{\rho_{\mathrm{eff}}} \langle \nabla \psi \rangle, \\ \kappa_0 \frac{\Delta V}{V} &= -\frac{\kappa_0}{\kappa_{\mathrm{eff}}} \psi_{\mathrm{local}} = -\frac{\kappa_0}{\kappa_{\mathrm{eff}}} \langle \psi \rangle. \end{aligned} \tag{8.31}$$

Without resonance, the fractional volume dilation $\Delta V/V$ always has the same sign as $-\psi_{\mathrm{local}}$ if $\kappa_{\mathrm{eff}} > 0$ while the displacement $\langle \boldsymbol{u} \rangle$ is bounded by 0 and $3(\nabla\psi)_{\mathrm{local}}/\left(\rho_0\omega^2\right)$ if $\rho_{\mathrm{eff}} > 0$. We say that the medium can only have a positive monopolar and a bounded positive dipolar response to the local field.

However, due to the possibility of high contrast in sound speed or in density between different materials, we may be able to work in a frequency regime where the wavelength in the background fluid is much longer than the average interparticle distance but the wavelength within the particle is comparable to its size. This allows for the possibility of Mie resonances at very low frequencies. In such a case, the system can still be homogenized to an effective medium and the corresponding analytical formulae for low filling ratio of particles should be (8.20). In general, a higher sound speed contrast between the particle and the background pushes the Mie resonances to lower frequencies and ensures a good effective medium description. In fact, the displacement and the volume dilation of the medium and the particles are linked by spatial averaging on the structural unit:

$$\begin{aligned} \rho_0 \omega^2 \langle \boldsymbol{u} \rangle &\approx f \rho_0 \omega^2 \boldsymbol{u}_{\mathrm{s}} + (1-f)(\nabla\psi)_{\mathrm{local}}, \\ \kappa_0 \frac{\Delta V}{V} &\approx f \kappa_0 \left(\frac{\Delta V}{V} \right)_{\mathrm{s}} + (1-f)(-\psi_{\mathrm{local}}), \end{aligned} \tag{8.32}$$

where $(\Delta V/V)_{\mathrm{s}}$ is the fractional volume dilation of the particle, $\boldsymbol{u}_{\mathrm{s}}$ is the displacement of the particle, and f is the volume filling ratio of the particle. Through Mie resonances, the particle can have a negative response ($(\Delta V/V)_{\mathrm{s}}, -\psi_{\mathrm{local}}$ having opposite sign). If it is negative enough to compensate for the background, we can have a negative medium response ($\Delta V/V$ and $-\psi_{\mathrm{local}}$ having opposite sign) and it gives us negative effective bulk modulus according to (8.31). For the dipolar response, we have two scenarios. The first corresponds to the case $\rho_{\mathrm{eff}} < -\rho_0/2$. From (8.31), we see that the local field and the macroscopic field are in the same direction and both are opposite to the $\langle \boldsymbol{u} \rangle$, and from (8.32), we must have a negative particle response ($\boldsymbol{u}_{\mathrm{s}}$ and $(\nabla\psi)_{\mathrm{local}}$ in opposite sign) which is large enough to compensate the background so that $\langle \boldsymbol{u} \rangle$ and $(\nabla\psi)_{\mathrm{local}}$ point in the opposite directions. The second scenario corresponds to $-\rho_0/2 < \rho_{\mathrm{eff}} < 0$. Here, the local field points to the opposite direction to the macroscopic field. Note that in both scenarios, $\boldsymbol{u}_{\mathrm{s}}$ and $\langle \nabla\psi \rangle$ point in opposite directions.

To give a concrete example, let us consider a system of rubber spherical particles suspended in water. The rubber spheres have a low filling ratio of 0.1 such that (8.20) is reasonably accurate. We have ignored the shear wave inside the particles due to the high velocity contrast [25] for simplicity and the main features remain the same if we include the shear wave within the

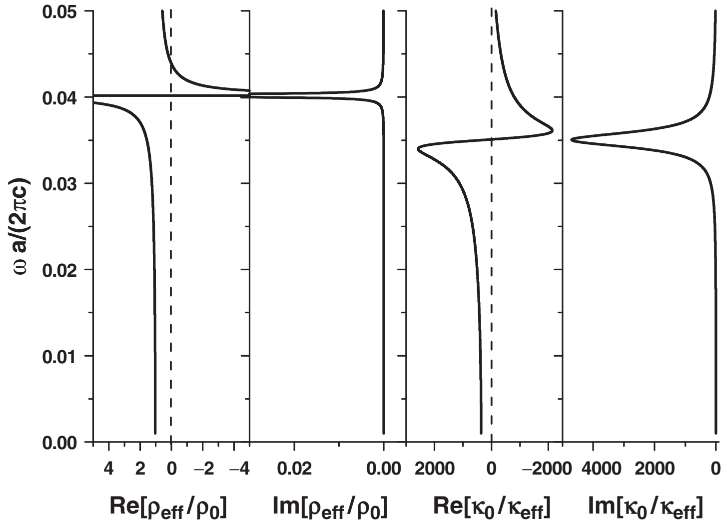

Fig. 8.10. Effective density and bulk modulus for rubber ($\rho = 1,300\,\mathrm{kg\,m^{-3}}, \kappa = 6.27 \times 10^5\,\mathrm{Pa}$) spheres of filling ratio $f = 0.1$ within water ($\rho = 1,000\,\mathrm{kg\,m^{-3}}, \kappa = 2.15 \times 10^9\,\mathrm{Pa}$)

particles. The spheres are made of a kind of soft silicone rubber whose data is taken from [18]. The effective medium result using (8.20) is shown in Fig. 8.10.

From the figure, the effective bulk modulus and density near the static limit are both positive as predicted by (8.3). The frequency is normalized and is given as $\omega a/(2\pi c)$ where a is the lattice constant if the spheres are assembled into an fcc lattice and c is the sound speed in the background fluid. The monopolar resonance creates an effective dynamic negative bulk modulus above the normalized frequency about 0.035 while the dipolar resonance creates an effective negative density above the normalized frequency about 0.04. Hence, there is a narrow frequency range where the monopolar and dipolar resonances overlap and we have both negative bulk modulus and negative density. The imaginary part of the effective parameters is due to the diffusive scattering loss.

The Mie resonances at low frequency in acoustics are the analogue of the resonances created by the split-rings and bars in an electromagnetic left-handed medium. In the case of electromagnetic metamaterial, the bars and split-rings create negative electric dipolar and magnetic dipolar responses. In the case of double negativity in acoustic waves, the rubber spheres create two types of resonances at the same time. One is the monopolar resonance which gives a negative response such that the volume of the medium expands when it is pressed. The same structure gives a dipolar resonance which gives a negative response such that the medium accelerates to the opposite direction of the force acting on it.

Under the condition that the background wavelength is much larger than the average interparticle distance and for slow spatially varying volume-averaged wave field, the homogenization of the composite guarantees that it is valid to replace the whole composite by a homogeneous medium in considering its acoustic properties. In the following, we demonstrate it is indeed meaningful to assign both negative bulk modulus and negative density by considering the transmittance at different incidence angles through a slab of eight layers ((111) planes) of an fcc colloidal crystal of silicone rubber spheres suspended in water. The high contrast between the sound speed in silicone rubber and water allows for very low frequency Mie resonances, which in turn allows for the treatment as an effective medium. Here, for simplicity, we assume the density of the rubber spheres ($1,000\,\mathrm{kg\,m^{-3}}$) matched with that of water but the sound speed within the rubber is $46.4\,\mathrm{ms^{-1}}$ which is much lower than the one ($1,466\,\mathrm{ms^{-1}}$) in water. The radius of the rubber spheres is fixed at 1 cm. We look at two different cases with $f = 40\%$ and $f = 74\%$ (nearly closely packed), respectively. The filling ratios are much higher than the case we have considered previously, leading to higher strength of resonances and thus wider frequency regime of double negativity. However, the CPA formulae (8.20) are not quantitatively accurate in such a high filling ratio, although they give the physical origin of the double negativity. Here, we use another way to extract the effective parameters. We first calculate the dispersion at zero transverse wave vector $k_z(\omega; \boldsymbol{k}_t = \boldsymbol{0})$ using the MST where the fcc (111) planes of the crystal are aligned perpendicular to the z-axis. The square of the effective refractive index $n_{\mathrm{eff}}^2(\omega)$ is then extracted from it by

$$k_z^2 = \left(\frac{\omega}{c}\right)^2 n_{\mathrm{eff}}^2, \tag{8.33}$$

where c is the speed of sound in the background medium. Note that the eigenstate can be spanned by plane-wave components consisting of both the normal and the diffracted plane waves. Conventionally, we can only extract the refractive index from the dispersion curve. In fact, by recognizing that the information of half-space reflection amplitude is already embedded in the details of the eigenmode, we can get one additional parameter. The half-space reflection amplitude can be proved to be the ratio between the amplitudes of the backward and forward propagating normal plane-wave components at the middle between two (111) planes of spheres. Therefore, we can extract the effective surface impedance $Z_{\mathrm{eff}}(\omega)$ by

$$r_{\mathrm{h.s.}} = \frac{\psi_{\boldsymbol{g}=0}^-}{\psi_{\boldsymbol{g}=0}^+} = \frac{Z_{\mathrm{eff}} - c\rho_0}{Z_{\mathrm{eff}} + c\rho_0}, \tag{8.34}$$

where $\psi_{\boldsymbol{g}}^{\pm}$ is the coefficient of the plane-wave expansion of the eigenstate within one single layer. Here, $\boldsymbol{g}$ is a reciprocal lattice vector in the x–y plane. Since we have assumed that the crystal can be effectively replaced by a homogeneous medium, the effective density and the effective bulk modulus are finally found from the relationship

$$
\begin{aligned}
Z_{\text{eff}} &= \frac{\omega \rho_{\text{eff}}}{k_z}, \\
n_{\text{eff}}^2 &= \frac{\rho_{\text{eff}}}{\rho_0} \frac{\kappa_0}{\kappa_{\text{eff}}}.
\end{aligned} \tag{8.35}
$$

Figure 8.11a shows the effective bulk modulus and the effective density of the colloidal crystal while Fig. 8.11b shows the dispersion of the colloidal crystal calculated using MST for the case of a filling ratio of 0.4. From Fig. 8.11a, we see that for the frequency below 2.65 kHz, both the effective bulk modulus and density are negative so that there is a singly degenerate band of effective medium with a negative group velocity. For the normalized frequency above 2.65 kHz, the effective density becomes positive and it results in a bandgap in the dispersion.

There is a deaf band of double degeneracy just above the band of effective medium and they meet at the zone center. The physical origin of the deaf band can be understood also from the effective medium. When we put the plane wave solution into the macroscopic wave equation for homogeneous medium:

$$
\begin{aligned}
\nabla \cdot \boldsymbol{u} + \frac{1}{\kappa}\psi &= 0, \\
\nabla \psi - \rho\omega^2 \boldsymbol{u} &= 0
\end{aligned} \tag{8.36}
$$

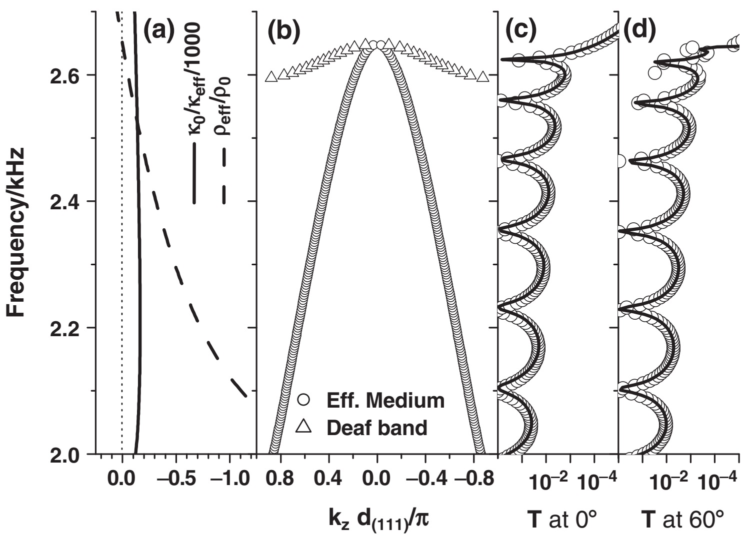

Fig. 8.11. Panel (**a**) shows the ρ_{eff} and κ_{eff} extracted (see text), showing negative values of ρ_{eff} and κ_{eff}. Panel (**b**) shows the band structure of a rubber-in-water fcc colloidal crystal of filling ratio 40%. *Open circles* in panels (**c**) and (**d**) are the transmittance (T) through eight layers of the (111) planes calculated by the multiple scattering method and the *solid line* is the approximation using homogeneous media. Note the agreement between the exact multiple scattering and the effective medium for both normal and 60° off-normal incidence

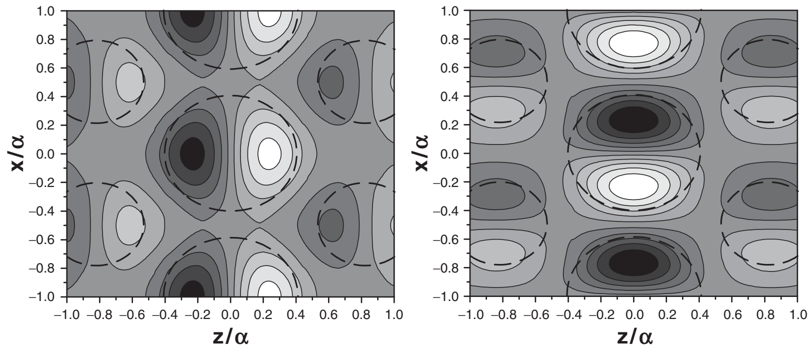

Fig. 8.12. Pressure field at 2.64679 kHz on the z–x plane of (**a**) a normal longitudinal mode and (**b**) one of the two transverse modes of the deaf band. *White/black region* denotes positive/negative values

we obtain the expected longitudinal mode where the displacement vector (the polarization of the mode) is parallel with the wave vector and the dispersion is $k^2 = \omega^2\rho/\kappa$. We also get two extra transverse modes when the effective density is zero. In this case, the macroscopic pressure field is zero, the displacement vector and the wave vector are arbitrary as long as they are perpendicular to each other. Therefore, it should be a dispersion-less flat band at the frequency of zero effective density. It becomes slightly dispersive away from the Brillouin Zone center as shown in Fig. 8.11 due to the spatial dispersion effect in the colloidal crystal. Figure 8.12a, b shows, respectively, the pressure field on the z–x plane of the longitudinal mode and the transverse mode of x-polarization at 2.647 kHz. It verifies the prediction from the effective medium theory as the longitudinal mode shows that the pressure field has the p-like orbitals aligning in the z-direction while the p-like orbitals align in the x-direction for the transverse mode of x-polarization.

In fact, from symmetry analysis, the deaf band has a Λ_3 symmetry. This deaf band cannot be excited by a normally incident wave [26], which has a Λ_1 symmetry and it couples weakly even to an incident wave of an oblique incidence angle. Also, any state of Λ_3 symmetry contributes zero macroscopic pressure field as expected from effective medium theory. Since we know that this deaf band does not couple with incident wave and it is not the expected longitudinal mode, we do not use the deaf band in calculating the effective parameters. It avoids ambiguity in calculating effective parameters in the frequency regime where the normal longitudinal band and the deaf band overlap.

In Fig. 8.11c, d, we compare, respectively, the transmittance at normal incidence and 60° off normal incidence across the eight layers of particles calculated by MST and the one calculated by replacing the colloidal crystal with our effective medium of the same thickness. We found that the effective medium results agree very well with the results from the MST. Therefore, it demonstrated the usefulness of the negative effective bulk modulus and density

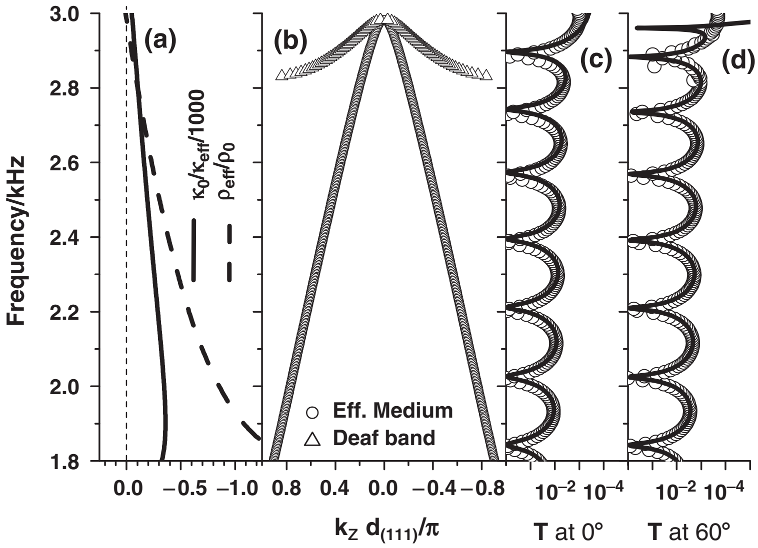

Fig. 8.13. Panel (**a**) shows the ρ_{eff} and κ_{eff} extracted (see text), showing negative values of ρ_{eff} and κ_{eff}. Panel (**b**) shows the band structure of a rubber-in-water fcc colloidal crystal of filling ratio 74%. *Open circles* in panels (**c**) and (**d**) are the transmittance (T) through eight layers of the (111) planes calculated by the multiple scattering method (using $L_{\max} = 7$) and the *solid line* is the approximation using homogeneous media with effective ρ_{eff} and κ_{eff} shown in panel (**a**)

extracted. We emphasize here that the result of the negative refractive band is not a band-folding effect from Bragg scattering. The colloidal crystal can be treated as a homogeneous medium the same way as the "Veselago" medium for electromagnetic waves.

When the filling ratio is further increased, the resonance is more pronounced. Figure 8.13 shows the band structure, effective density/bulk modulus, and the transmittance through 0 or 60° across eight layers of colloidal crystal when the filling ratio is increased to 74%. As the concentration of particles becomes higher, the resonance becomes stronger. It results in an increased band width of the negative refractive band of negative density and bulk modulus. We see that the effective medium also represents the colloidal crystal very well in calculating the transmittance of various incidence angles. Again, this is an evidence that the colloidal crystal can be really treated as a homogeneous medium.

As we have pointed out that the high contrast between sound speed in rubber and water creates a negative refractive band at a very low frequency so that it is meaningful to talk about a negative density and negative bulk modulus. In the case where the contrast in sound speed becomes smaller, we should expect the effective medium description degrades in the intermediate frequency regime. This can be seen by increasing the sound speed in the rubber

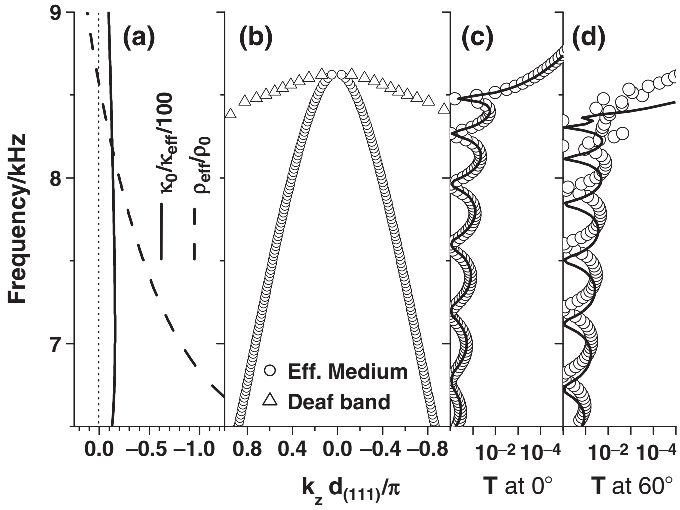

Fig. 8.14. Panel (**a**) shows the ρ_{eff} and κ_{eff} extracted (see text), showing negative values of ρ_{eff} and κ_{eff}. Panel (**b**) shows the band structure of a rubber-in-water fcc colloidal crystal of filling ratio 40%. The sound speed in rubber is $150\,\text{ms}^{-1}$. *Open circles* in panels (**c**) and (**d**) are the transmittance (T) through eight layers of the (111) planes calculated by the multiple scattering method (using $L_{\max} = 7$) and the *solid line* is the approximation using homogeneous media with effective ρ_{eff} and κ_{eff} shown in panel (**a**)

to a higher value of $150\,\text{ms}^{-1}$. Figure 8.14 shows the corresponding dispersion and transmittance at both normal and 60° degrees off-normal incidence. In this case, the negative refractive band is shifted to higher frequencies such that the effective medium description degrades. We can see that the impedance extracted cannot represent the colloidal crystal so well at large incidence angle.

Here, we have demonstrated theoretically the concept of double-negative media (Poynting vector in opposite direction with wave vector) in acoustic waves for the media that can be properly homogenized. Such medium is effectively having both negative effective bulk modulus and negative density. This double negativity is created by monopolar and dipolar resonance of the building blocks and it remains true even if we include shear wave components within the particles. It is possible to have two different types of particles giving two resonances separately to have a larger degree of freedom in designing the material as in the case of the electromagnetic left-handed medium. In our case, since the monopolar resonance is in general broader than the dipolar resonance, we can have just one type of particles to give double negativity. Finally, the realization of this acoustic left-handed medium relies on the low sound speed in rubber.

8.5 Focusing Effect Using Double-Negative Acoustic Material

In this section, we will investigate the focusing property of a slab of material that can be described by an effective negative density and modulus, which will have a negative group velocity. The problem can be reduced to a one-dimensional (1D) problem. By characterizing each layer using a refractive index and impedance, both the electromagnetic and acoustic wave problems can be treated in a unified language. We note that such a homogeneous medium description gives a divergent field at the perfect lens condition. This is because such a description ignores the spatial dispersion inherent with the microscopic features of the double-negative medium.

8.6 Focusing by Uniaxial Effective Medium Slab

For the acoustic wave, when we have an additional source, the macroscopic wave equation [see (8.23)] becomes

$$\nabla \cdot \frac{1}{\overleftrightarrow{\rho}(\boldsymbol{r})} \nabla \psi + \frac{\omega^2}{\kappa(\boldsymbol{r})} \psi = -\frac{1}{\rho_0} s, \tag{8.37}$$

where ψ is the macroscopic pressure, s represents the source, $\overleftrightarrow{\rho}$ is the effective density tensor, and κ is the effective bulk modulus which are position dependent. The two effective parameters are constant within the same piece of acoustic composite which is treated as a homogeneous medium under the length-scale of this macroscopic wave equation. In this section, we assume that the medium is uniaxial, such as planes of different materials stacking along the z-direction. Each medium is characterized by a density tensor

$$\overleftrightarrow{\rho}_i = \begin{pmatrix} \rho_{t,i} & 0 & 0 \\ 0 & \rho_{t,i} & 0 \\ 0 & 0 & \rho_i \end{pmatrix} \tag{8.38}$$

and an index ellipsoid

$$\omega^2 = k_t^2 c_i^2 + k_z^2 c_i^2 \gamma_i^2, \quad \gamma_i > 0, \tag{8.39}$$

where z-axis is the "optical" axis, $\boldsymbol{k} = (k_t, k_z)$ is the wave vector, $\gamma_i^2 = \rho_{t,i}/\rho_i$ is the anisotropy factor which becomes one for isotropic medium, and i is the medium index. The dispersion relationship can be obtained by substituting a plane wave solution $\psi = \psi_0 \exp(\mathrm{i}\boldsymbol{k} \cdot \boldsymbol{r})$ into the wave equation. Both the density tensor and the dispersion surface are assumed to be isotropic on the x–y

plane. On a planar interface between two mediums, the boundary condition (which is already embedded in (8.37) is the continuity of

$$\psi \quad \text{and} \quad \hat{z} \cdot \frac{1}{\overleftrightarrow{\rho}} \nabla \psi = \frac{1}{\rho} \frac{\partial \psi}{\partial z}. \tag{8.40}$$

In this section, we would like to solve the Green's function satisfying

$$\left(\nabla \cdot \frac{1}{\overleftrightarrow{\rho}\ (\boldsymbol{r})} \nabla + \frac{\omega^2}{\kappa(\boldsymbol{r})} \right) G(\boldsymbol{r}, \boldsymbol{r}') = -\frac{1}{\rho_0} \delta(\boldsymbol{r} - \boldsymbol{r}'), \tag{8.41}$$

where the source is situated at $\boldsymbol{r}' = z'\hat{z}$ within the region of background medium of (isotropic) density ρ_0 and sound speed c. Since the transverse wave vector is conserved across the planar interfaces, it is convenient to expand the Green's function as

$$G(\boldsymbol{r}, \boldsymbol{r}') = \int \frac{\mathrm{d}\boldsymbol{k}_t}{(2\pi)^2} \mathrm{e}^{\mathrm{i}\boldsymbol{k}_t \cdot \boldsymbol{r}} g(\boldsymbol{k}_t;\ z, z'), \tag{8.42}$$

where the z-axis is along the normal direction of the interface, and t labels the vectors parallel to the interface. This expansion decouples the problem into a 1D problem, where $g(\boldsymbol{k}_t;\ z, z')$ is the 1D Green's function for waves at a fixed transverse wave vector, satisfying

$$\left(\rho(z) \frac{\mathrm{d}}{\mathrm{d}z} \frac{1}{\rho(z)} \frac{\mathrm{d}}{\mathrm{d}z} + k_z^2(z) \right) g(\boldsymbol{k}_t\ ; z, z') = -\delta(z - z'). \tag{8.43}$$

In a source-free region, this equation becomes the 1D wave equation

$$-\frac{Z}{n_z} \frac{\mathrm{d}}{\mathrm{d}z} \left(\frac{1}{Z n_z} \frac{\mathrm{d}}{\mathrm{d}z} g(\boldsymbol{k}_t\ ; z, z') \right) = \left(\frac{\omega}{c} \right)^2 g(\boldsymbol{k}_t\ ; z, z'), \tag{8.44}$$

where the acoustic surface impedance and the refractive index are defined by

$$\begin{aligned} Z &= \frac{\omega \rho}{k_z}, \\ n_z &= \frac{c k_z}{\omega}. \end{aligned} \tag{8.45}$$

The sign of k_z is determined by the sign of impedance which is conventionally taken to be positive here similar to the case of electromagnetic wave.

We now first consider the focusing effect of a single interface separating an ordinary isotropic medium (medium 1), such as air on the left and a uniaxial double-negative medium (medium 2) on the right, as shown in Fig. 8.15. The interface is located at $z = 0$. Medium 2 has a negative group velocity in the sense that the dispersion surface (an ellipsoid) shrinks when frequency increases. The optical axes of the two media are both aligned to the z-axis.

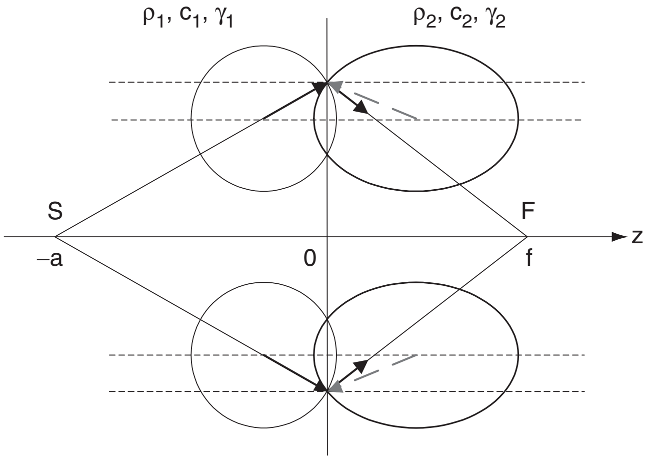

Fig. 8.15. Configuration for half space focusing. ρ_i, c_i, γ_i are the density, the phase velocity, and the anisotropy factor of the corresponding mediums. "S" is the source. "F" is the focus. *Dashed arrows* show the direction of the wave vectors while the *solid arrows* show the direction of the Poynting vectors

Causality mandates the choice of a solution for $z > 0$ such that the energy flows to the right.

The dispersion surfaces for the two media are both described by (8.39). By having all geometric rays coming out from the source S on the left-hand side focused to the same point F on the right-hand side, it can be proved that the focusing condition is

$$c_1 = c_2 = c. \tag{8.46}$$

The subscripts "1" and "2" means that the quantity refers to the medium 1 and medium 2, respectively. From here on, we will use similar notations. It is equivalent to say that the two dispersion surfaces should have the same radius on the transverse plane. If the focusing condition is satisfied, the ratio of k_z becomes independent of k_t and the focal length is governed by

$$\frac{f}{a} = \left|\frac{k_{1z}}{k_{2z}}\right| = \frac{\gamma_2}{\gamma_1}. \tag{8.47}$$

A remark should be added here that for the same problem in electromagnetic waves, the dispersion surfaces of TE and TM polarizations are in general different so that it may have focus for one polarization but not the other. However, if both polarizations have focus for the same uniaxial media, the two foci are essentially at the same point and the uniaxial crystal falls into a special kind of "affinely isotropic" medium in which the permittivity and permeability tensors are proportional to each other.

The focusing condition is valid in general for putting two uniaxial media together but from now on, we will assume the medium 1 is always a usual isotropic medium, $\gamma_1 = 1$, with positive group velocity for ease of discussion and we just write $\gamma_2 = \gamma$.

In solving (8.43), we express the solution as

$$\begin{array}{ll} z < z', & g = A\mathrm{e}^{-\mathrm{i}k_{1z}z}, \\ z' < z < 0, & g = B\mathrm{e}^{\mathrm{i}k_{1z}z} + C\mathrm{e}^{-\mathrm{i}k_{1z}z}, \\ z > 0, & g = D\mathrm{e}^{\mathrm{i}k_{2z}z}, \end{array} \tag{8.48}$$

and impose the following boundary conditions:

$$\begin{array}{ll} z = 0, & \begin{array}{l} \mathrm{g}|_{\mathrm{z=0+}} = \mathrm{g}|_{\mathrm{z=0-}}, \\ \dfrac{1}{\rho_2}\dfrac{\partial g}{\partial z}|_{z=0+} = \dfrac{1}{\rho_1}\dfrac{\partial g}{\partial z}|_{z=0-}, \end{array} \\ z = z', & \begin{array}{l} \mathrm{g}|_{\mathrm{z=z'+}} = \mathrm{g}|_{\mathrm{z=z'-}}, \\ \dfrac{\partial g}{\partial z}|_{z=z'-}^{z=z'+} = -1. \end{array} \end{array} \tag{8.49}$$

Then, the 1D Green's Function (in the region $z > 0$) is obtained as

$$g(\boldsymbol{k}_t;\ z, z') = \frac{1}{1 + Z_1/Z_2}\frac{\mathrm{i}}{k_{1z}}\mathrm{e}^{\mathrm{i}k_{2z}\left(z+\gamma z'\right)}, \tag{8.50}$$

which shows the phase information is also conserved when the rays arrive at the focus. Figure 8.16 shows an example of the numerical Green's function with γ_2 set to 0.5. It is formulated using (8.42) by integrating all the 1D Green's function for every k_t, satisfying the boundary condition (8.40). The image is formed in medium 2 at half the source distance as expected from

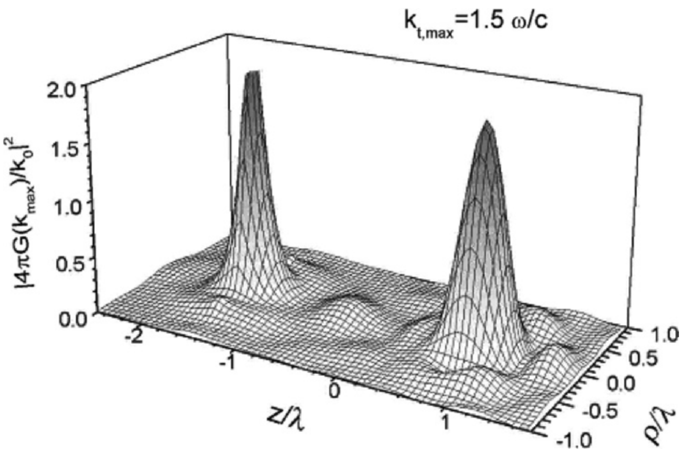

Fig. 8.16. Square magnitude of the half-space Green's function with configuration: $\gamma_2 = 0.5, Z_2 = 2Z_1$. The source is at -1.5λ and the image is at 0.75λ. ρ is the distance in the x–y plane. The maximum k_t included in the calculation of the Green's function is $1.5\omega/c$ which is large enough to have convergent results

the geometric ray diagram. By using the Green's function formulation, we can now include the phase information and also the evanescent waves from the source in the plot of the Green's function. As the ratio of the surface impedance between the two media is independent of the incidence angle, the transmission amplitude is a constant from the source to the image so that plane waves of any incidence angle from the source arrive at the image at the same phase. All the phase information of the source is conserved. It is clearly shown when we plot the contour of the Green's function only up to all propagating components from the source as in Fig. 8.17. The image is exactly the same replica of the source when we only include up to $k_{t,\max} = \omega/c$ in the integration in (8.42). On the other hand, since we can only choose a decaying wave within medium 2, all the evanescent waves from the source are lost in the far field limit. In this case, as shown from Fig. 8.16, even at a distance of 0.75λ away from the interface, the evanescent waves are lost already. Information carried by the evanescent wave components cannot reach the image since there is no mechanism to induce growing waves in the steady state. The diffraction limit can only be broken by near field if we move the source (i.e., the image) closer to the interface.

After investigating the principle for focusing on one single interface between two media of positive and negative group velocity, the case of slab focusing is considered in the following example. When the medium of negative group velocity has a finite thickness and the wave then returns to the same medium 1 again, the focusing condition still holds on the second interface and a second focus is expected to form.

We repeat the procedure above to get the Green's function for a slab of negative group velocity material of thickness d in an ordinary material (see Figs. 8.18 and 8.19). The second interface is set to $z = 0$, the 1D Green's function (on the side of the image) can be found as

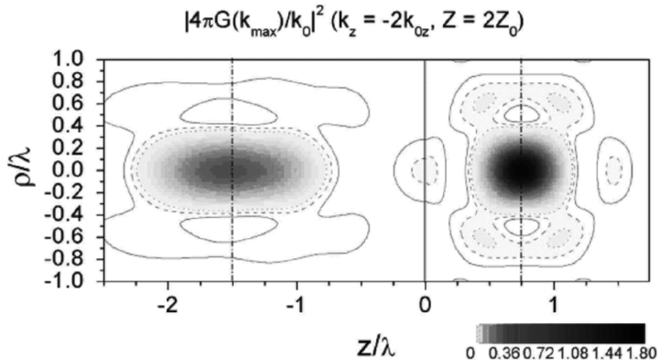

Fig. 8.17. Contour plot of the half-space Green's function with the same configuration as Fig. 8.16. The Green's function here only includes all the propagating waves from source but excludes all evanescent waves from the source

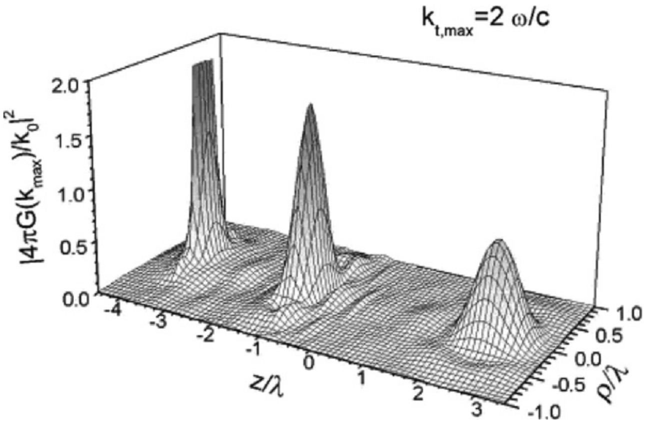

Fig. 8.18. Square magnitude of the slab Green's function (3D plot) with configuration: $\gamma_2 = 0.5, Z_2 = 2Z_1$. The slab extends from $z = -2\lambda$ to $z = 0$. The source is placed at -3.5λ and the image is at 2.5λ. The maximum k_t included in the calculation of the Green's function is $2\omega/c$ which is large enough to have convergent results

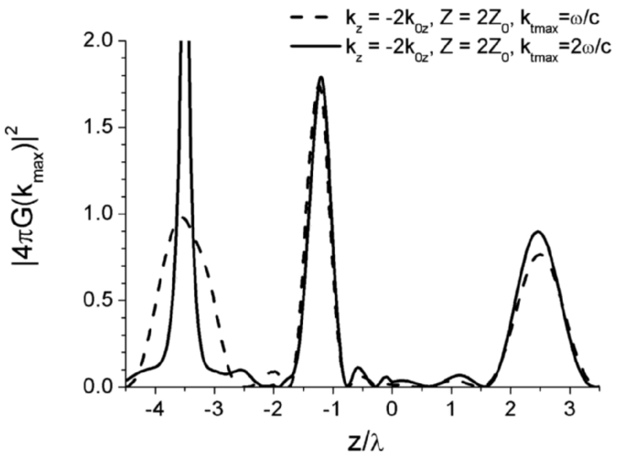

Fig. 8.19. The square magnitude of the slab Green's function (along z-axis) with configuration: $\gamma_2 = 0.5, Z_2 = 2Z_1$. The slab extends from $z = -2\lambda$ to $z = 0$. The source is at -3.5λ and the image is at 2.5λ

$$g(\boldsymbol{k}_t;\ z, z') = \frac{\mathrm{i}}{2k_{1z}} \frac{4\mathrm{e}^{\mathrm{i}k_{1z}(z-z'-d)}}{\left(2 - \dfrac{Z_1}{Z_2} - \dfrac{Z_2}{Z_1}\right)\mathrm{e}^{\mathrm{i}k_{2z}d} + \left(2 + \dfrac{Z_1}{Z_2} + \dfrac{Z_2}{Z_1}\right)\mathrm{e}^{-\mathrm{i}k_{2z}d}}. \quad (8.51)$$

Although the transmission amplitude from the source to the image position for the slab case is not incidence-angle independent when the impedance of

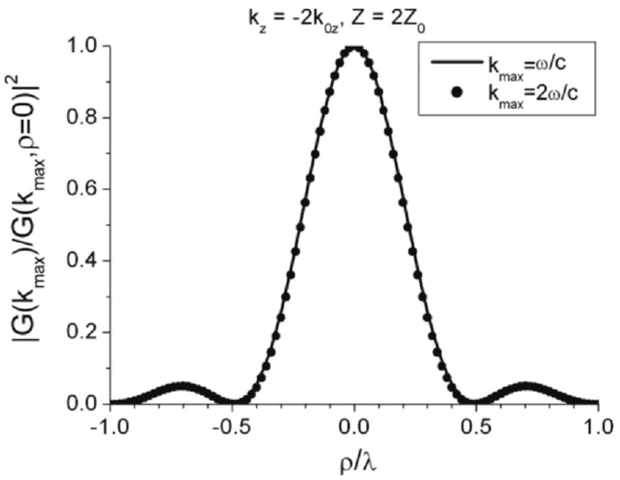

Fig. 8.20. Normalized square magnitude of the slab Green's function at the image with configuration: $\gamma_2 = 0.5, Z_2 = 2Z_1$. The slab is situated from $z = -2\lambda$ to $z = 0$. The source is at -3.5λ and the image is at 2.5λ

the two media are not equal to each other, an image at position z'' still forms at the exact position geometrical rays predict, which is

$$z'' = z' + d + d/\gamma. \tag{8.52}$$

Note that in order to have a second focus, one must have the first focus forming inside the slab. Otherwise, z'' obtained from (8.52) will become negative, which means that the image is virtual.

When we plot the cross-section of the Green's function at the image on the x–y plane as shown in Fig. 8.20, the result with evanescent waves included is exactly the same as the result with only propagating waves included. Both image profiles have the width of about one wavelength. It indicates that the diffraction limit has not been broken in this case. On the contrary, if the evanescent waves contribute to the resolution up to $k_{\max} = 2\omega/c$, we should expect the width of the image profile should be about half a wavelength.

In the above example, the image still forms although it is not an exact replica of the source. In the case that the impedance mismatch is due to absorption, an image can still form if the absorption of the medium is not too large as shown in Fig. 8.21.

The above analysis is done in stationary wave formulation. It is expected that the stationary image will disappear if the impedance of the slab deviates too much from the impedance of the outside material. In such a case, imaging is still possible and meaningful if a wave packet is used instead of a continuous source, provided that the pulse is short enough and the slab is thick enough so that the multiple-scattered train of pulses is much delayed after the first transmitted train of pulses.

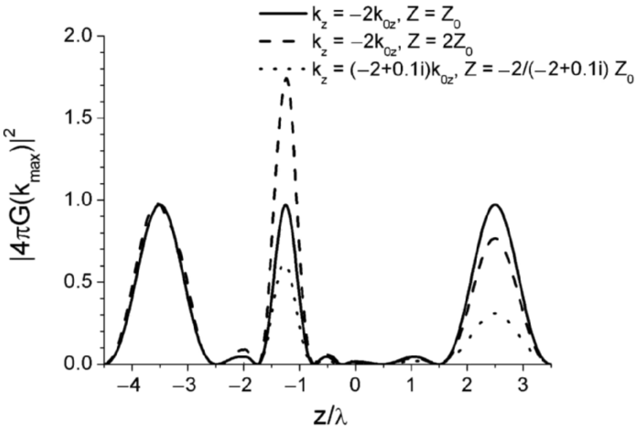

Fig. 8.21. Square magnitude of the slab Green's function along z-axis with configuration: (**a**) $\gamma_2 = 0.5, Z_2 = Z_1$; (**b**) $\gamma_2 = 0.5, Z_2 = 2Z_1$; (**c**) $\gamma_2 = 1/(-2+0.1\mathrm{i})$, $Z_2 = -2/(-2+0.1\mathrm{i})Z_1$. The slab is situated from $z = -2\lambda$ to $z = 0$. The source is at -3.5λ and the image is at 2.5λ. Note that only propagating components of the Green's function are included here

As indicated from the denominator of the 1D Green's function, there is one value of $k_t > \omega/c$ which can make the Green's function diverge and it is a signature of a coupled-surface mode at this particular magnitude of transverse wave vector. In the numerical calculation of the three-dimensional (3D) Green's function, we have put a maximum value of k_t as the upper limit of the integral. In this case, we should take the maximum value much larger than that of the coupled-surface mode in order to have a convergent result. In fact, the transmission amplitude from the source to image drops rapidly beyond the k_t of the coupled-surface mode. It means that the resolution of the image is dictated by this k_t [27]. In the example $Z_2 = 2Z_1$ we have considered, the impedance mismatch between the slab and the outside medium is too high so that the k_t of the coupled-surface mode is only slightly larger than ω/c. This is the reason why there is essentially no enhancement of resolution as observed in Fig. 8.20.

However, if we adjust the two media so that they nearly match in impedance, $Z_2 \approx Z_1$. Then, we have

$$g(\boldsymbol{k}_t;\ z, z') = \frac{\mathrm{i}}{2k_{1z}} \mathrm{e}^{\mathrm{i}k_{1z}(z-z'')}, \tag{8.53}$$

such that we have transmission amplitude exactly equal to one at the image from the source. For $z > z''$, the Green function is the same as that of a point source located at the image point z'', so that the whole amplitude and phase information of the source is reconstructed at the image. This is the effect of perfect focusing, as pointed out by Pendry. Since there is no reflection at either interface of the slab, the incident evanescent wave from the source

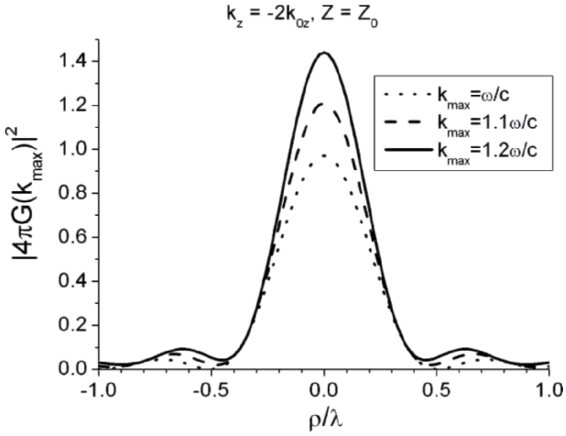

Fig. 8.22. Square magnitude of the slab Green's function (the transverse plane at image) with configuration: $\gamma_2 = 0.5, Z_2 = Z_1$. The slab is situated from $z = -2\lambda$ to $z = 0$. The source is at -3.5λ and the image is at 2.5λ

directly triggers a surface mode on the second interface. This surface mode provides a mechanism which is not available in half-space configuration to amplify the evanescent wave within the slab to compensate exactly the decay in the region between the source and the first interface and the region between the second interface and the image. When we plot the Green's function on the transverse plane at the image point as shown in Fig. 8.22, the Green's function on the transverse plane at the location of the image becomes sharper and sharper as the maximum value of k_t increases. However, as $k_t > \omega/c$, a surface mode of larger amplitude is required to compensate the decay of the evanescent wave. Therefore, as shown in Fig. 8.23, the field between the first and second focus in fact increases without bound if we increase $k_{t,\max}$ to infinity. In this case, several assumptions (such as ignoring nonlocal effects and ignoring nonlinear effects) actually breaks down, and it can be shown that such a final state requires a very long time [28] to establish in practice even if we assume the effective medium description remains valid.

Finally, we calculate the field pattern using multiple point sources instead of only one. As shown in Fig. 8.24, we purposely only integrate up to all propagating wave components in the Green's function, and we see that the same image shape forms. The image formed outside has the same aspect ratio and is fully restored as the source although the image within the slab can be elongated or compressed in the z-direction depending on the anisotropy factor.

In this section, we investigated the focusing problem of double negative acoustic media with a negative refraction index. Two cases are analyzed with the Green's function method, one involves only one interface, and another is a slab with finite thickness. For the former, acoustic waves from a point source outside the crystal can be focused to a diffraction-limited spot inside this

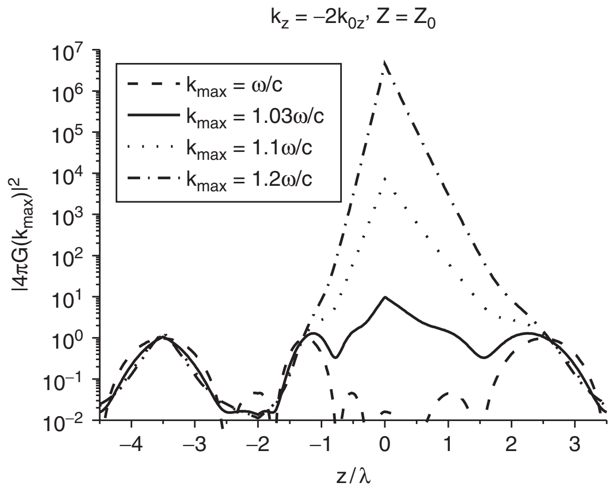

Fig. 8.23. Square magnitude of the slab Green's function (along z-axis) with configuration: $\gamma_2 = 0.5, Z_2 = Z_1$. The slab is situated from $z = -2\lambda$ to $z = 0$. The source is at -3.5λ and the image is at 2.5λ

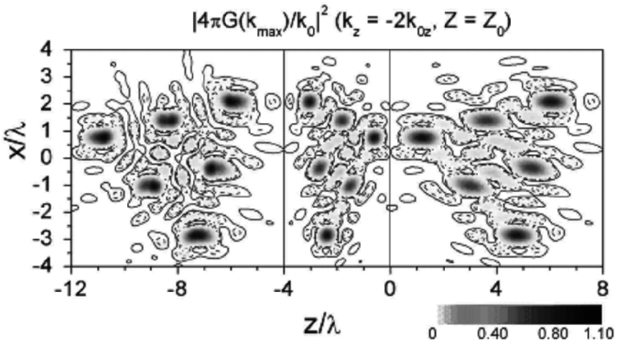

Fig. 8.24. Contour plot of the field due to six point sources at one side of the slab. The Green's function here only includes all the propagating waves from the sources but excludes all evanescent waves from the sources

crystal if it possesses a particular elliptical constant-frequency surface. For the latter, the crystal can focus an object to a resolution-limited but undistorted 3D replica on the other side. The effect of impedance matching and absorption is also discussed under the assumption of local effective medium description.

Acknowledgment

We gratefully acknowledge funding support from Hong Kong RGC through grant 600305.

References

1. V.C. Veselago, Sov. Phys. Usp. **10**, 509 (1968)
2. D.R. Smith, J.B. Pendry, M.C.K. Wiltshire, Science **305**, 788 (2004)
3. J.B. Pendry, Phys. Rev. Lett. **85**, 3966 (2000)
4. J.B. Pendry, A.J. Holden, D.J. Robins, W.J. Stewart, IEEE Trans. Microw. Theory Tech. **47**, 2075 (1999)
5. R.A. Shelby, D.R. Smith, S. Schultz, Science **292**, 77 (2001)
6. J. Li, C.T. Chan, Phys. Rev. E **70**, 055602 (2004)
7. Z. Hashin, S. Shtrikman, J. Appl. Phys. **33**, 3125 (1962)
8. J.G. Berryman, J. Acoust. Soc. Am. **68**, 1809 (1980)
9. G. Mie, Ann. Phys. (Leipzig) **25**, 377 (1908)
10. J.H. Page, A. Sukhovich, S. Yang, M.L. Cowan, F. Van Der Biest, A. Tourin, M. Fing, Z. Liu, C.T. Chan, P. Sheng, Phys. Status Solidi B **241**, 3454 (2004)
11. For an introduction to photonic crystal, see, e.g., J.D. Joannopoulos, R.D. Meade, J.N. Winn, *Photonic Crystals: Molding the Flow of Light* (Princeton University Press, Princeton, 1995)
12. S. Yang, J.H. Page, Z.Y. Liu, M.L. Cowan, C.T. Chan, P. Sheng, Phys. Rev. Lett. **93**, 024301 (2004)
13. X. Zhang, Z.Y. Liu, Appl. Phys. Lett. **85**, 341 (2004)
14. L. Feng, X.P. Liu, M.H. Lu, Y.B. Chen, Y.F. Chen, Y.W. Mao, J. Zi, Y.Y. Zhu, S.N. Zhu, N.B. Ming, Phys. Rev. Lett. **96**, 14301 (2006)
15. See, e.g., C. Luo, S.G. Johnson, J.D. Joannopoulos, J.B. Pendry, Phys. Rev. B **65,** 201104(R) (2002)
16. See, e.g., N.W. Ashcroft, N.D. Mermin, *Solid State Physics* (Saunders, Philadelphia, 1976)
17. Z.Y. Liu, X.X. Zhang, Y. Mao, Y.Y. Zhu, Z. Yang, C.T. Chan, P. Sheng, Science **289**, 1641 (2000)
18. Z.Y. Liu, C.T. Chan, P. Sheng, A.L. Goertzen, J.H. Page, Phys. Rev. B **62**, 2446 (2000)
19. Z.Y. Liu, C.T. Chan, P. Sheng, Phys. Rev. B **65**, 165116 (2002)
20. K.H. Fung, Z.Y. Liu, C.T. Chan, Zeitschrift Fur Kristallographie **220**, 871 (2005)
21. See, e.g., A.L. Fetter, J.D. Walecka, *Theoretical Mechanics of Particles and Continua* (McGraw-Hill, New York, 1980)
22. J.E. Sipe, J. Van Kranendonk, Phys. Rev. A **9**, 1806 (1974)
23. S. Tretyakov, *Analytical Modeling in Applied Electromagnetics* (Artech House, Boston, 2003)
24. L. Tsang, J.A. Kong, K.-H. *Ding, Scattering of Electromagnetic Waves: Theories and Applications* (Wiley, New York, 2000)
25. M. Kafeski, E.N. Economou, Phys. Rev. B **60**, 1 (1993)
26. E. Psarobas, A. Modinos, R. Sainidou, N. Stefanou, Phys. Rev. B **65**, 064307 (2002)
27. D.R. Smith, D. Schurig, M. Rosenbluth, S. Schultz, S.A. Ramakrishna, J.B. Pendry, Appl. Phys. Lett. **82**, 1506 (2003)
28. L. Zhou, C.T. Chan, Appl. Phys. Lett. **86**, 101104 (2005)

9

Experiments and Simulations of Microwave Negative Refraction in Split Ring and Wire Array Negative Index Materials, 2D Split-Ring Resonator and 2D Metallic Disk Photonic Crystals

F.J. Rachford, D.L. Smith and P.F. Loschialpo

Summary. In this chapter, we describe a series of simulations and experiments on composites displaying negative refraction. The materials consist of both split ring resonator/wire structures and 2D photonic crystals. The finite difference time domain simulations were found to closely correspond to our microwave frequency measurements. Our exploration of photonic structures evolved from the serendipitous experimental observation that our early split ring resonators exhibited planar slab focusing in the absence of a wire grid. Although split ring resonator/wire grid composites were shown to display negative index behavior over a vary narrow band-pass, the photonic crystal structures display negative phase propagation and negative refraction over a much larger frequency band.

9.1 Introduction

Our group at the Naval Research Laboratory initiated a program of measurement, simulation, and analytic analysis of composite materials having a negative index (NIM) soon after the pioneering publications of Smith et al. [1–4]. Smith et al. performed microwave transmission measurements combining two artificial media devised by Pendry [5–7]: A conducting wire array to introduce a controllable composite plasma frequency and negative permittivity in the microwave region and a double-split-ring resonator (SRR) array to provide a sharp narrow band negative permeability at a limited frequency band above the SRR resonance. Ideally the composite geometry is arranged so that the plasma frequency and the magnetic antiresonance (the frequency where the permeability recrosses zero above magnetic resonance) coincide. These structured composites were predicted to exhibit a (mean field) negative refractive index over a narrow frequency band above the SRR resonance [8–10]. Prism refraction [11] and planar slab focusing experiments have confirmed the existence of negative refraction for the SRR/wire composites in a narrow frequency band.

These early publications demonstrated that composites of split-ring resonators (SRRs) and wires could realize Veselogo's [12] prediction that a medium with simultaneous negative permittivity and permeability will produce a "left-handed" material with unusual refractive properties. Critiques and controversy [13–16] ensued after the initial work leading us to a detailed investigation of the effect. In this chapter, we present results of accurate finite difference time domain (FDTD) simulations and experiments. The FDTD work employed idealized but causal constitutive parameters with Lorentzian frequency and Drude type frequency dependences as well as detailed metallic SRR and wire structure representations and detailed photonic crystal constructs. The experimental work investigated these SRR/wire structures and metallic disk photonic crystal assemblies.

In the course of our investigations we noted that some of our composites displayed negative refraction at frequencies above the plasma frequency and also in structures without wire arrays to provide a negative permittivity. FDTD and experimental work indicated that these structures were acting as negatively refracting photonic crystals. Notomi [17] and others [18–23] have also shown that photonic crystals can evidence negative refraction near the bandgap edge. Recent simulations and experiments have indicated that focusing by planar slabs [24] and other manifestations of negative refractive index can be observed in photonic crystals at microwave frequencies. In addition, other unusual refractive phenomena such as superprism effects [25] have also be seen in PC materials.

We find that arrays of Pendry type SRRs *without wires* displayed refraction and focusing indicative of negative index behavior with GHz wide bandwidths [26]. Replacing SRRs with metal disks having the same outside diameter and arrayed on the same scale also displayed focusing and refraction associated with negative index behavior over the same wide frequency band. We follow the displacement of the focus with increasing frequency from near field to more than ten wavelengths behind the arrays. FDTD simulations [27] of hexagonal disk arrays and hexagonal annulus arrays display similar behavior and demonstrate that wave propagation in our structures is refractive rather than diffractive in nature. Although the metallic structures described in this work are on the order of a third of a free space wavelength, the FDTD simulation of the wave propagation in the composite does not display multiple beam formation or coherent scattering characteristic of a diffractive medium but shows a continuous propagation in the medium that can be accurately characterized by an anisotropic index of refraction. Close inspection of the electric and magnetic fields in proximity to the small structures of the metallic rings and disks shows very complicated behavior. Averaging the fields on a coarser scale we find a regular progression of electromagnetic amplitude and phase. It is in this sense that we can assign an index and an averaged permittivity and permeability to these media. Experimentally, we derive estimates of the effective index of refraction for the disk array from the displacement of an off normal microwave beam emerging from the stack.

In this chapter we first examine negative refraction in an idealized NIM. Then we review simulations and measurements on a SRR/wire composite. This led to the observation that a hexagonal SRR array can act as a negatively refracting 2D photonic crystal. Replacing the SRR constructs with metal disks of the same outer diameter reduced the complexity of the transmission spectrum and enabled detailed simulations of negative refraction in these 2D structures. Measurements then confirmed simulations and led to estimates for the frequency-dependent index.

9.2 Theory

The Pendry wire array plasma frequency for a wire array suspended in free space is given by

$$f_{\mathrm{p}} = \frac{c}{a\sqrt{2\pi \ln\left(\dfrac{a}{r}\right)}}, \tag{9.1}$$

where a is the wire lattice spacing and r is the wire radius. The double-split-ring resonance frequency (free space) is given by

$$f_{\mathrm{o}} = \frac{c}{2\pi}\sqrt{\frac{3\ell}{\pi\varepsilon r^3 \ln\left(\dfrac{2w}{d}\right)}}, \tag{9.2}$$

with ℓ being the ring layer spacing, w the width of the rings, d is the gap width between inner and outer rings, r is the inner ring radius, ε is the permittivity of the inter-ring gap, and c is the velocity of light. In a medium the effective spacing of the array and the self-inductance of the array are affected by the index and local permeability. Similarly the resonant frequency of the SRRs modified by the local values of μ and ε: In practice the plasma frequency and SRR resonance in string wire structures are strongly influenced by the interaction between the wire array and the SRRs and cannot be accurately calculated with simple modifications to the Pendry formulae.

In Smith's first realization of the wire/split-ring (WSR) medium the three-dimensional orthogonally interpenetrating Pendry wire array is replaced by a monodirectional square lattice array of wires separated from the SRRs by free space. As long as the microwave radiation transmitted through this wire assembly is confined to propagation in the plane normal to the wire axis with electric polarization along the wire axis there will be a plasma resonance and the plasma frequency should be approximated by (9.1).

Smith's split-ring structures were first created as stacked planar square arrays [1] and later as two orthogonal stacked arrays [4]. The wire axes were structured to lie parallel to the split-ring array plane. The combined WSR stacks were confined in a parallel plate transmission line and measurements were limited to a small portion of a waveguide band. They reported negative index for a narrow transmission peak identified with the split-ring resonance in their composite. In fact the first realization of the SRR/wire medium employed large diameter wires that were capacitively tuned by varying the spacing of their ends from the top face of the parallel plate waveguide containing the structure and propagating microwave fields [28]. The Pendry formulae were only used as first estimates of the f_p and f_o, and the structure was tuned experimentally.

Here we first study idealized functional permittivity and permeability in the double negative regime and then proceed to analysis and experiments on simple SRR/wire array structures and eventually to photonic crystals constructed of SRR structures and simple metal disks.

9.3 FDTD Simulations in an Ideal Negative Index Medium

Initial realizations of NIM composite materials have employed metallic elements imbedded in dielectric that are often a substantial fraction of a free space wavelength. In most cases the structures are inherently anisotropic and lossy and in some cases, diffractive effects and impedance boundary mismatches obscure the negative index of refraction [29–32]. To answer several fundamental issues we ran FDTD simulations involving idealized isotropic fully causal representations of permittivity and permeability. We choose the time step for all FDTD simulations in this paper to satisfy the Courant–Friederichs–Lewy condition [33]:

$$c\,\Delta t = \frac{1}{\sqrt{\left(\frac{1}{\Delta x}\right)^2 + \left(\frac{1}{\Delta y}\right)^2 + \left(\frac{1}{\Delta z}\right)^2}}, \tag{9.3}$$

where c is the velocity of light Δt is the time step, Δx, Δy, and Δz are the simulation grid increments.

We set $\mu = \varepsilon = -1$ to eliminate boundary impedance mismatches. Negative permittivity or permeability requires strong dispersion which we model using the same Lorentzian form and parameters for both:

$$F(f) = 1 + \frac{K-1}{1 - \mathrm{i}\left(\dfrac{fG}{f_\mathrm{o}^2}\right) - \left(\dfrac{f}{f_\mathrm{o}}\right)^2}, \tag{9.4}$$

where $\mu(f) = \varepsilon(f) = F(f)$ and $\mu_\mathrm{dc} = \varepsilon_\mathrm{dc} = K$. The FDTD code [27] used to perform the numerical experiments was validated extensively with laboratory experiments some of which are described below. In the following simulations the code employs perfectly matched layer [34] type of absorbing boundaries in the dimensions of finite extent and periodic boundary conditions in the dimensions of infinite extent.

Veselago [12] pointed out that if a diverging radiation source is placed a distance d before a slab (thickness t) of index $n = -1$ material, images will form a distance d inside the slab and a distance $t - d$ in free space on the opposite side of the slab. Initial simulations by Ziolkowski [35] indicated that the foci would not be stable in time. And arguments of Valanju [13] suggested that such images could not be produced by divergent pulse radiation. To test these assertions we chose physically plausible Lorentzian parameters (9.4) $f_o = 6.3\,\text{GHz}$, $\varepsilon_{dc} = \mu_{dc} = 4.0$, and $G = 0.04\,\text{GHz}$. With this selection of parameters the index at 10 GHz is $n = -1.001 + 0.013i$.

We first simulate the arrival and steady state transmission of a 10 GHz plane wave impinging on a planar slab of our causal negative index medium. The slab is semi-infinite in the lateral directions and 9.8 cm thick in the direction of propagation. Plotting the amplitude of the instantaneous electric field with time vs. distance taken along the center line of propagation through the simulation space (Fig. 9.1) we note that the slope of the wave crests are equal amplitude in air and in the slab but the sign of the slope is reversed in the slab indicative of negative phase propagation. In the transition region where the ramp initiated plane wave initially propagates through the slab the slope of amplitude distribution is positive and approximately equal to the (positive) group velocity, $v_g = 0.18c$.

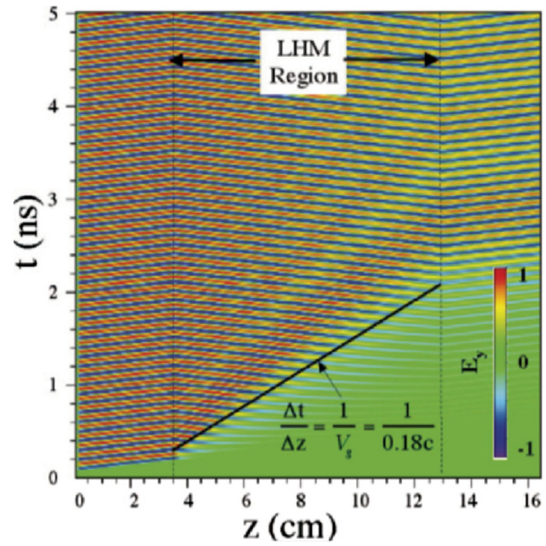

Fig. 9.1. Color electric field amplitude vs. time for a ramp-initiated CW plane wave traveling in the z-direction. A left-handed material with index $n = -1.001 + 0.013i$ at the particular 10 GHz chosen is situated between the two *dashed lines*. The inverse of the slopes of the crests gives the phase velocity. On either side of the slab the phase velocity is the speed of light, c. Inside the LHM the phase velocity is also approximately the speed of light, but is negative. The slope of the early time arriving impulse corresponds to the group velocity of $0.18c$ and is positive

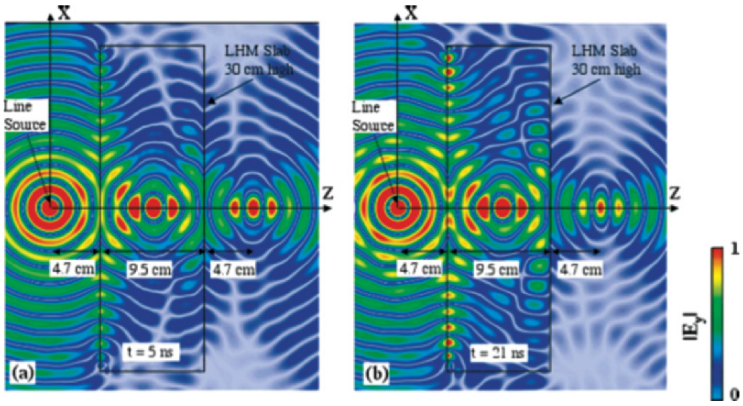

Fig. 9.2. FDTD snapshots of the electric field magnitude at (**a**) $t = 5\,\text{ns}$ and (**b**) $21\,\text{ns}$ for a planar slab with line source illumination at 10 GHz (LHM regime). The position of both focal points is in agreement with Snell's law. The stability of the foci images is established by comparison of (**a**) with (**b**). The *rectangle* shown in the figures represents the slab contour

The stability of the focus was investigated in a series of 10 GHz simulations employing negative index blocks of varying size. The NIM blocks had the same causal ε and μ as above. In Fig. 9.2 we present snapshots of a sample simulation at two different times after steady state is achieved. The foci are apparent both inside and external to the idealized LHM slab. Varying the dimensions of the NIM blocks demonstrate that the foci continue to be stable and obey Snell's law with index of -1. For blocks of ten wavelengths or greater lateral size edge diffraction did not affect the location or stability of the foci. Our foci are consistent with standard diffraction limit and do not show the Pendry superfocusing [36, 37] proposed for NIM planar lenses. Evanescent mode amplification required for superlensing is not expected to occur in the presence of loss exemplified by our choice of complex index nor is it expected for focal distances greater than a wavelength [38].

Next we simulate pulse propagation through a laterally semi-infinite idealized NIM slab [39, 40]. In this example the pulse is a Gaussian modulated 10 GHz signal emanating from a line source located to the left of the NIM slab. The pulse was described by the equation

$$\frac{E(t-t_0)}{E_{\text{max}}} = \mathrm{e}^{-1/2((t-t_0)/\tau_{\mathrm{B}})^2} \sin\left(\frac{2\pi(t-t_0)}{\tau_{\mathrm{p}}}\right) \tag{9.5}$$

with parameters $\tau_{\mathrm{B}} = 1.67\,\text{ns}, \tau_{\mathrm{p}} = 0.10\,\text{ns}$. The pulse peaks at time $t_0 = 6.8\,\text{ns}$. In Fig. 9.3 we plot the pulse progression in time vs. distance on the centerline of the simulation through the line source and normal to the slab interfaces. The pulse propagates through the NIM material focusing inside the slab as well as to the right on the far side. Chromatic aberration smears

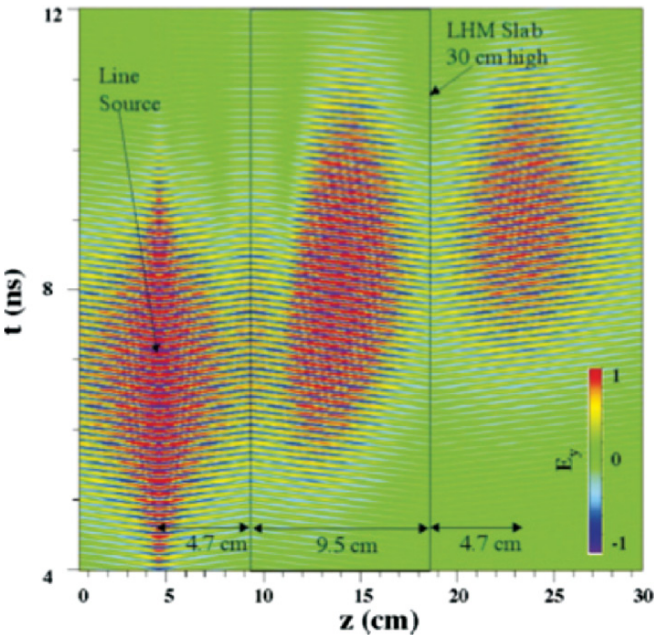

Fig. 9.3. E_y component amplitude as a function of z and time for a Gaussian pulse propagating in the z-direction through a 2D left-handed material slab. The pulse shape has a narrow bandwidth and peaks at $t = 7$ ns at the line source location. At a later time the amplitude peaks at a focal region at the slab center. Still later it peaks at a second focal region, 4.7 cm to the right of the slab. Inspection of the phase fronts clearly shows the negative phase velocity noted earlier for the CW case

the focus to some extent but the effect is essentially the same as seen in CW steady state in Fig. 9.2. The slope of the wave fronts is reversed in the NIM indicative of backward progressing wavefronts. Power is transmitted through the sample opposite to the phase movement. Our group [39] and others have reported many other interesting case simulations supporting and clarifying NIM refractive properties first proposed by Veselago [12].

9.4 Simulations and Experiments with Split-Ring Resonators and Wire Arrays

Shortly after noting the UCSD group's early publications [1] on this subject we fabricated a SRR/wire structure. Our SRRs were close to the same dimensions as the early work but more densely populated. Our thought was to increase the magnetic fill factor in hopes of broadening the operational bandwidth while keeping the SRR resonance in the accessible microwave frequency region with SRR gap sizes set to commercially reproducible dimensions. Initially,

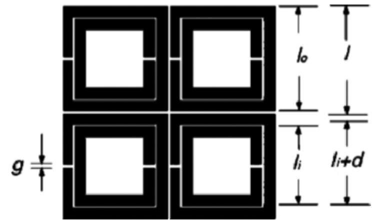

Fig. 9.4. Square double ring geometry. Lattice constant $l = 1.04$ cm, ring's outer dimensions $l_\mathrm{o} = 0.99$ cm, etched line-width 1 mm, inner ring's outer dimensions $l_\mathrm{i} = 0.75$ cm, inter-ring gap of 0.02 cm, and ring gap $g = 0.04$ cm

we chose a square geometry for our SRRs in order to accurately model their performance with our FDTD code which requires a quadrangular grid. Figure 9.4 describes our initial SRR geometry.

This copper SRR pattern is roughly 1 µm thick on a 0.015-cm polyimide substrate. The outer square side length is 0.99 cm while the inner square side length is 0.55 cm. The width of the etched copper segments is 0.10 cm. The gap spacing between inner and outer rings is $d = 0.02$ cm. Over 100 planar arrays with 9×40 elements were stacked, carefully aligned, and spaced 0.32 cm apart by high-density polyethylene (HDPE) spacers. Midway between SRR layers we positioned monodirectional arrays of 36 µm diameter copper wires spaced 0.32 cm apart producing a square wire lattice. The wire array was incommensurate with the SRR period. In our FDTD modeling we were forced to make a 3% adjustment to the wire spacing to commensurate with the SRRs.

Measurements were conducted between 4 and 14 GHz using a focused beam apparatus. The microwave electric field was carefully aligned with the wire and SRR plane direction since the orthogonal polarization should not display NIM behavior. Initially we measured the HDPE stack without SRRs or wires and found the frequency independent dielectric response, $\varepsilon_\mathrm{HDPE} = 2.35 + 0.014\mathrm{i}$. Next we measured the stack with the wire array present and no SRRs. Inverting the complex transmission coefficient we find the response shown in Fig. 9.5 which is in excellent agreement with the simple Pendry formula (9.1) offset by the HDPE susceptibility $\chi_\mathrm{HDPE} = \varepsilon_\mathrm{HDPE} - 1$.

Results for SRRs in HDPE and the combination of SRRs and wires are shown in Fig. 9.6. We note the complexity of the SRR and combined SRR/wire array transmission spectra. We call attention to the two high-lighted regions where transmission nulls are replaced by narrow transmission peaks reminiscent of the expected behavior. Namely, microwave undergoes a null at SRR resonance placing an absorption band in the transmission spectrum at those frequencies. Then with the addition of the wire arrays, a transmission peak is created in the absorption band where both $\mathrm{Re}(\varepsilon)$ and $\mathrm{Re}(\mu)$ are negative. To further investigate the character of the transmission spectrum we selected several frequencies (arrows) for further FDTD analysis including the frequency peaks that appear in the SRR only absorption bands. As seen in Table 9.1 the peak that appears in the absorption band at 9.98 GHz displays negative index.

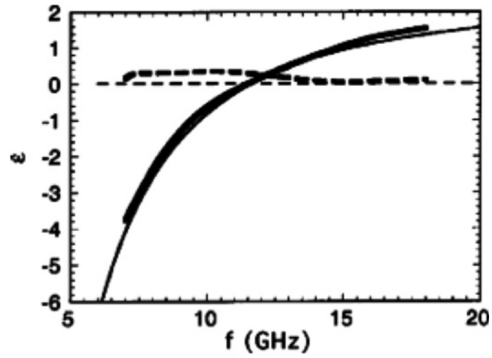

Fig. 9.5. The measured complex permittivity of our wire array embedded in HDPE. The *heavy solid line* is the measured real part and the *heavy dashed line* is the imaginary part. These values are compared to calculation employing Pendry's equation offset by χ_{HDPE} and assuming our geometry and measured HDPE dielectric constant

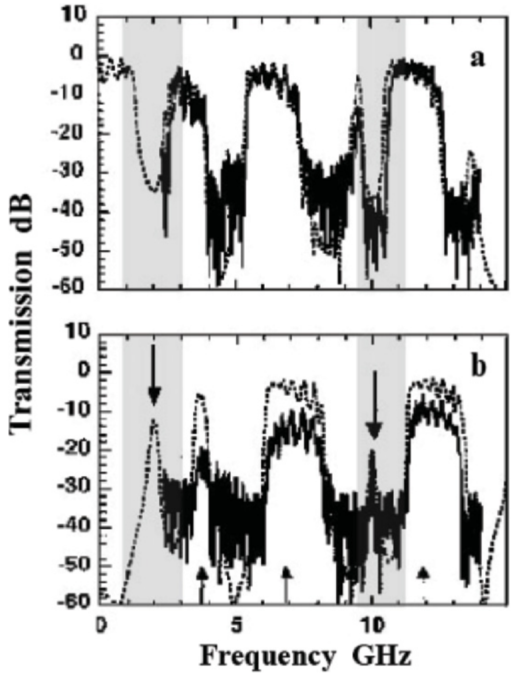

Fig. 9.6. Calculated (*dashed*) and measured (*dark*) transmission spectra for (**a**) stacks of square SRRs alone and (**b**) combined SRR and wire arrays in HDPE. Frequency regions near 2 and 10 GHz are high-lighted since they appear to behave as expected from simple theory; i.e., an absorption band in the ring-only structure yields transmission peak in the combined WSR structure. The *arrows* indicate frequencies at which detailed FDTD simulations were run following the time dependence of the wave propagation in the split ring alone and WSR composites

Table 9.1. Index of refraction at frequencies indicated in Fig. 9.6

F (GHz)	n
1.96	−3.6
3.57	1.6
6.93	1.0
9.98	−1.4
11.90	−0.9

These indices were deduced from analysis of single frequency FDTD simulations of this structure. The transmission peak at 9.98 GHz corresponds to the transmission peak appearing when wires are added to the SRR in HDPE stack

However, the progression of wavefronts in the simulated stack at 11.9 GHz also appears to show negative index. More confounding, transmission at frequencies below 9.98 GHz is strong and displays a positive index behavior. Whereas for the wires alone in HDPE, both measurement and simulation show strongly decreasing microwave transmission as frequency is reduced below 10 GHz, as is expected for a composite with negative permittivity and positive permeability. Clearly, though the simple model may explain the 9.98 GHz peak, it cannot adequately account for the wider frequency observations. It is notable that the early experiments were all restricted to narrow frequency band observations. In the following sections we explore structures without wire arrays and find that our SRR arrays can form negatively refracting photonic crystals.

9.5 Split-Ring Resonator Arrays as a 2D Photonic Crystal

As part of a program to measure SRR/wire composites, we measured arrays of SRRs without wires. Much to our surprise at the time, we found wide band focusing of divergent X-band radiation by a slab of stacked hexagonal SRR arrays on FR4 circuit board. At the time such focusing effects were touted as a hallmark of negative index behavior in SRR/wire composite structures. The SRR structure had dimensions summarized in Fig. 9.7.

Approximately 120 $10 \times 46 \times 0.32\,\mathrm{cm}^3$ circuit boards were stacked and microwave transmission was measured in a focused beam quasioptical fixture over several microwave waveguide bands. The electric field polarization impinging on the stacked SRR arrays was parallel to the plane of the hexagonal disk arrays.

In Fig. 9.8 we display the calculated (dots) transmission intensity of a plane wave propagating through our 4 in. thick array of hexagonal SRRs (see Fig. 9.7) vs. frequency at X-band. The calculation was performed using a FDFT code. We note two transmission peaks in this frequency band. The calculated response is very sensitive to the geometry and the griding in the FDTD calculation. Measured transmission (line) also shows two peaks in this

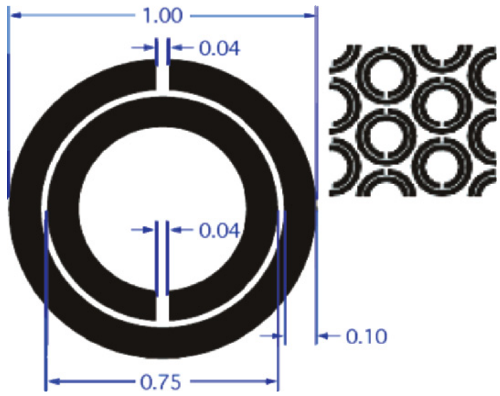

Fig. 9.7. Geometry of the split-ring resonator (SRR) used in this work. The SRRs are photoetched from metalized single sided FR4 circuit board (10 cm × 46 cm) in a hexagonal array. Spacing center to center of the SRRs in the array is 1.06 cm. The rings are 0.1 cm wide with a 0.025 cm spacing between inner and outer rings. The outside diameter of the outer ring is 1.00 cm. The gaps in the rings are 0.04 cm wide

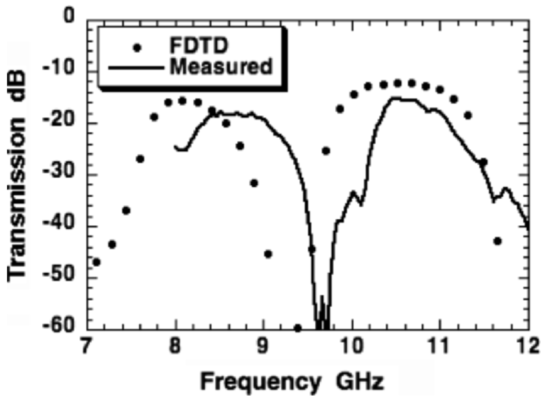

Fig. 9.8. The calculated (*dots*) and measured (*line*) microwave transmission intensity of our stacks of hexagonal arrays of copper SRRs on FR4 circuit board at X-band. The transmission units are relative dB

band, however, the measured peak are shifted up in frequency by approximately 0.5 GHz. Calculating the transmission with a coarser grid resulted in a similar transmission spectrum shifted to lower frequencies. We expect a further refinement in the FDTD grid would shift the calculated spectrum into closer agreement with experiment. We are restricted by computer memory limitations from testing this hypothesis.

The refractive properties of the 10 × 46 cm^2 stack were examined experimentally by placing an open ended waveguide in front of the stack to serve as a divergent source. A second open ended waveguide receiver was scanned

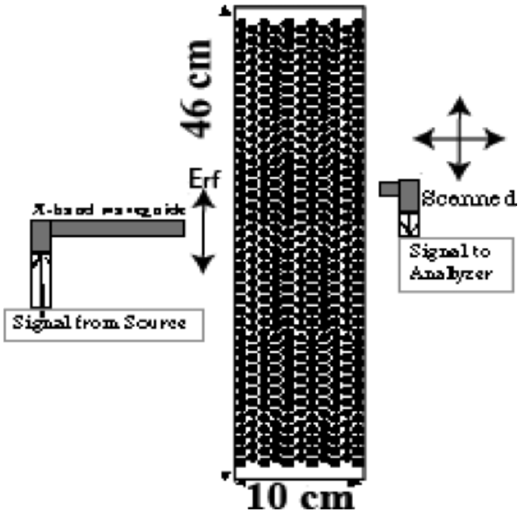

Fig. 9.9. Diagram of the disk array transmission scan experiment. An X-band waveguide source was aligned in the center of a stack of circuit boards with a hexagonal array of elements (SRRs or solid copper disks) with the microwave electric field in the plane of the circuit boards. A receiver was scanned in the same central plane behind the stack

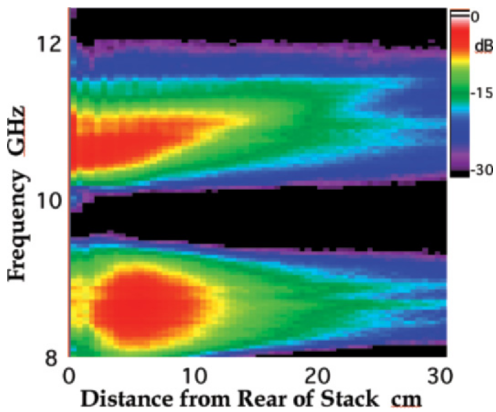

Fig. 9.10. A plot of the intensity of microwave radiation transmitted through a stack of hexagonal arrayed SRRs (color, relative dB) with respect to frequency and distance from the rear of the stack along the central axis of propagation

over an area $60 \times 60\,\text{cm}^2$ starting approximately 1 mm behind the stack (see Fig. 9.9). The scan plane was parallel to the plane of the central circuit board.

In Fig. 9.10 we plot the measured intensity of microwave power (color, dB relative scale) for frequencies swept through X-Band as a function of distance from the back surface of the stack along the central axis of propagation. The

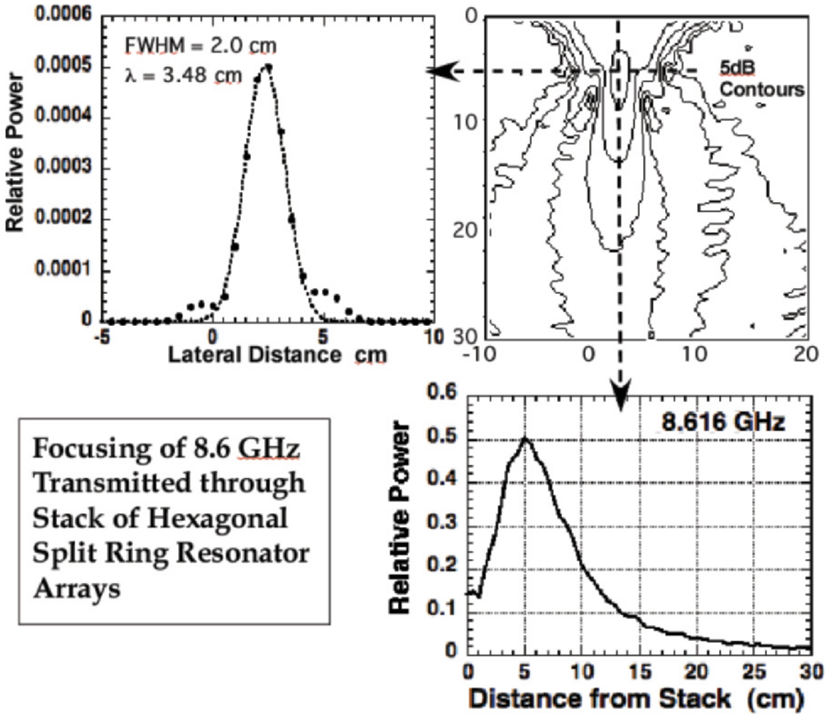

Fig. 9.11. Analysis of the focus of microwave radiation at 8.616 GHz by the stack of SRRs on FR4 circuit board. A well-defined focus occurs approximately 5–6 cm behind the stack. A contour plot in dB (relative) of the transmitted power vs. distance down range and cross range is shown with cuts taken along the central direction of propagation and laterally across the focus. The horizontal and vertical cuts through the focus are shown in the left and bottom plots. The cuts plot the power (linear scale relative) vs. distance across the focus. In the direction normal to the scan plane the radiation falls off as $1/r^2$ as expected for radiation from positive index material. The power vs. lateral distance plot has been fitted to a Gaussian. The Gaussian width is 1.275 or 2.0 cm full width at half maximum (FWHM). The free space wavelength at 6.616 GHz is 3.48 cm. The receiver aperture is 1 cm

experimental geometry is shown in Fig. 9.9. The transmission displays two intensity peaks. The lower peak, from ∼8.2 to ∼9.6 GHz shows focusing that remains spatially stationary, centered approximately 6 cm from the rear of the SRR stack. The upper band extends from ∼10.5 to 11 GHz and also displays focusing though not as apparent on this color scale. Radiation in the plane normal to the circuit boards diverges uniformly, as expected for microwaves emergent from a positive index slab.

Examining the transmission in detail in the center of the lower transmission band (8.616 GHz), we plot (Fig. 9.11) the transmission intensity in the X/Y plane behind the stack (5 dB contours). A focus is seen some 4–6 cm behind the stack. Lateral (cross range) and down range cuts through the data are plotted to the left and below the contours. Similar transmission peaks are seen in both passbands.

Fitting the lateral data at each frequency to Gaussians ($P = A\mathrm{e}^{-((x-x_o)/\mathrm{width})^{\wedge}2}$), we extract the focus width and distance of the focus from the rear of the stack. One such fit is shown in the top left plot of Fig. 9.11. The FWHM focus widths and focus distances from the rear of the stack derived from the whole data set are displayed in Fig. 9.12. The distance to the focus and the FWHM are normalized to the free space wavelength. Over most of this frequency range the free space wavelength is greater than the FWHM. The measured widths are convoluted with the 1 cm aperture of the receive antenna. The near field focus is seen to be quite sharp. A focus is observed to the limit of our scan resolution at the high end of the band; a distance exceeding ten free space wavelengths.

We find that the absorption between 9.5 and 10 GHz is due to the SRR resonance. The variation in focus width and location is attributable to a variation in negative index of refraction. Assuming Snell's Law we can estimate the index of refraction from the displacement of the focus as shown in Fig. 9.13.

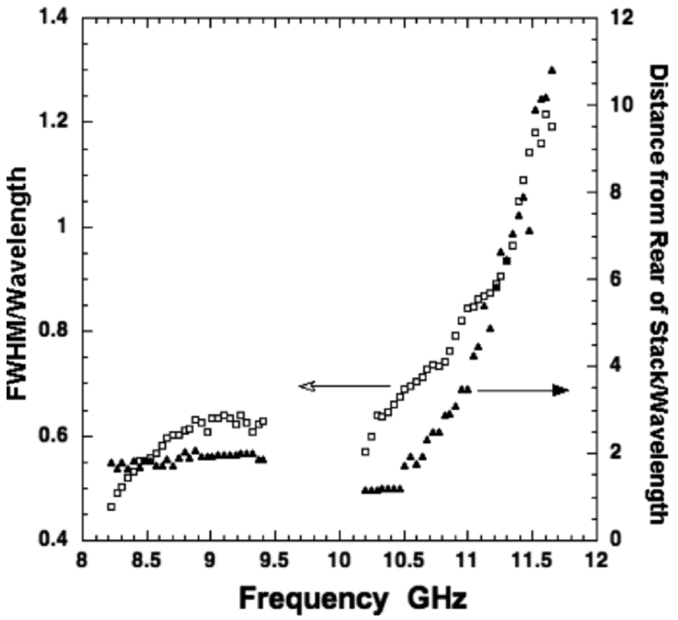

Fig. 9.12. Experimentally measured data from microwave transmission through a stack of SRRs. We plot the full width at half maximum normalized to the free space wavelength and distance of the focus point from the rear of the stack of hexagonal SRR arrays also normalized to wavelength vs. frequency. The source is fixed and the variation with frequency is later shown to be consistent with a frequency dependence of the (negative) index of refraction

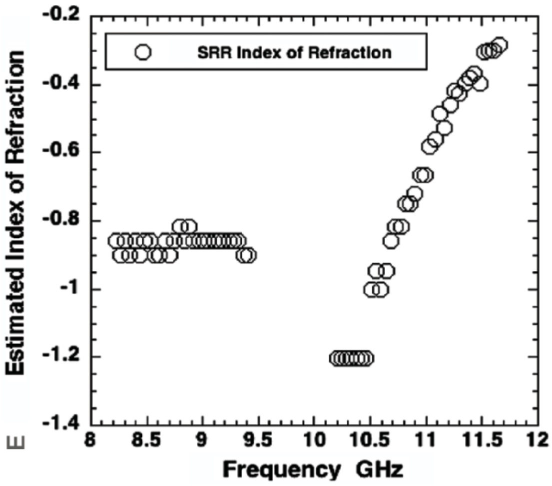

Fig. 9.13. Index of refraction estimated for the hexagonal SRR array described above from the displacement of the focus shown in Fig. 9.12

9.6 Hexagonal Disk Array 2D Photonic Crystal Simulations: Focusing

Simulations of electromagnetic wave interactions were performed using a thoroughly vetted FDTD code modified to handle negative index materials. Anticipating that interesting designs generated by computer simulation would be constructed and measured, we limited our calculations to designs to planar arrays of metal disks and strips on standard circuit board materials. In this paper we report simulations on metal disks arrayed in a hexagonal pattern on FR4 circuit board ($\varepsilon = 4.68 + 0.36\mathrm{i}, \mu = 1$). For these FDTD simulations 1 cm diameter disks are arrayed on and rationalized to a $0.025 \times 0.025\,\mathrm{cm}^2$ computational grid. The geometry of this disk array 2D photonic crystal is described in Fig. 9.14. The spacing between array planes is 3.2 mm (~1/8 in.). The geometry of the disks and their arrays were chosen to reproduce the SRR geometry investigated in Sect. 9.5 with the disk diameter equal to the outer diameter of the SRR. The overall transmission spectrum of the disk stack is similar to the SRR stack spectrum with the elimination of the SRR resonance absorption bands.

The calculated transmission spectrum and band structure for propagation in the x-direction are shown in Fig. 9.15. We focus our attention on the first two bands separated by a small bandgap from 5.6 to 6.1 GHz. From the band structure calculation the lower band has positive index whereas the second band has negative index. Fitting the band data and inverting we predict that the effective index in this band is negative varying between 0 and −2.5 (see Fig. 9.16). Single frequency plane wave simulations were performed at select frequencies in the first and second propagation bands. These movies confirm

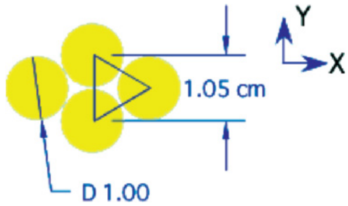

Fig. 9.14. A 1-cm diameter metal disk array. The hexagonal array is rationalized to conform to a $0.025 \times 0.025\,\mathrm{cm}^2$ computational grid in x–y plane and a 0.04 cm increment in the out-of-plane (z) direction

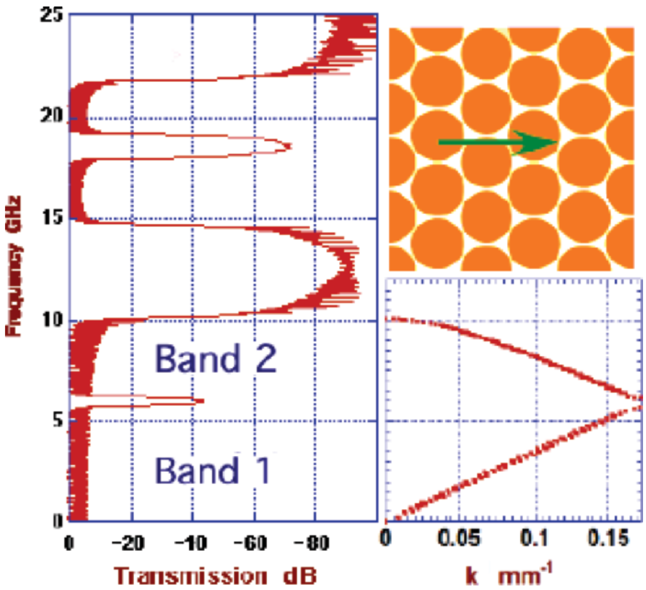

Fig. 9.15. Transmission spectrum and band structure of disk array for propagation along the X-axis (see Fig. 9.14). The first two bands are shown for propagation in the $\Gamma \rightarrow M$ direction. A similar structure is seen in the $\Gamma \rightarrow K$ direction. The negative slope of the valence band indicates the possibility of an effective negative index of refraction

the reversal of phase propagation in the second band and for longer wavelengths we can directly estimate the index by measuring the wavelength in the material and comparing it to the wavelength in free space. (See open triangles in Fig. 9.16.)

In order to study focusing we constructed a representation of a $46 \times 10\,\mathrm{cm}^2$ hexagonal array of our disks on 0.32 cm thick FR4 circuit board and located a radiating monopole a short distance in front of the stack. FDTD calculations where then run on this grided representation at frequencies from 2 to 14 GHz.

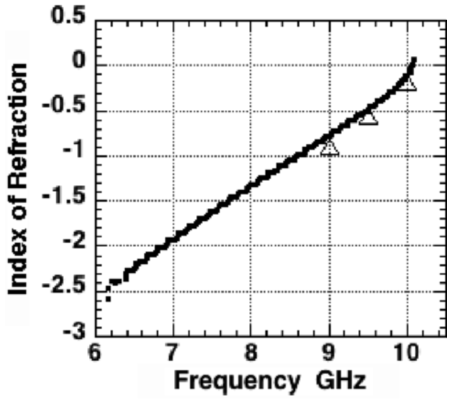

Fig. 9.16. Index of refraction of the second transmission band (*dots*) calculated from the band structure (Fig. 9.15). From single frequency propagation movies we directly confirm the reversed phase propagation and can measure the wavelength in the material and directly infer the index of refraction (*triangles*) in the material for sufficiently long wavelengths

In Fig. 9.17 we show representative views of the propagating rf electric field amplitudes for several frequencies. These snap shots were taken well into the steady state in the FDTD simulation. In the lower band the propagation in the disk array is consistent with an effective positive index of refraction. At 6 GHz the wave is highly attenuated as is expected in the first bandgap. At 8, 9, and 10 GHz focusing is seen in the transmitted wave with the external focus moving away from the array as the frequency is increased. The propagation is radiative, though anisotropic in the first two bands. The wavelength in the composite increases toward the high end of the second transmission band and is clearly larger than the external wavelength. This is clearly apparent at 10 GHz. The index in the forward direction of propagation can be estimated from this figure: $n \cong -0.2$, consistent with the band structure derived estimate in Fig. 9.16. At 11 GHz the wave is once again highly attenuated as is expected since at this frequency the array is in the second bandgap. At frequencies above the second bandgap, the propagation is highly diffractive with multiple beams propagating through the array and radiating away at odd angles on the far side.

In Fig. 9.18 we analyze the FDTD time averaged field radiated from a monopole source in proximity to our hexagonal disk array composite for two different frequencies (8 and 9 GHz) in the negative index passband. The E field amplitudes (solid curves) are given for a line passing through the monopole source, normally penetrating the composite and passing through the foci. The widths of the E field in the plane containing this line and parallel to the hexagonal disk array planes is also shown (dashed curves). The focus width at 8 GHz is 2.61 cm and the free space wavelength is 3.75 cm. The focal

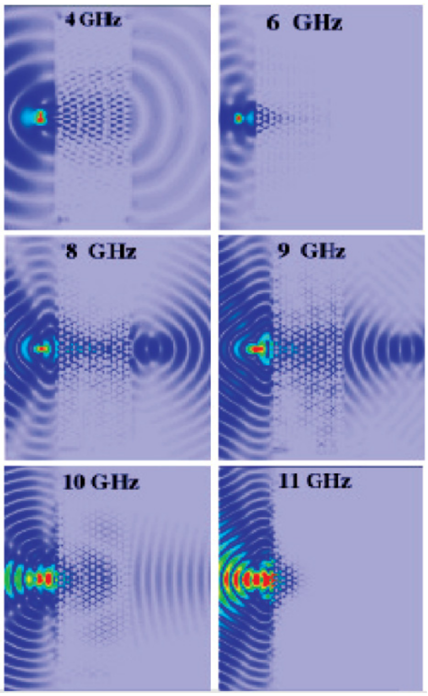

Fig. 9.17. FDTD simulations of radiation emanating from a microwave monopole traversing a photonic crystal slab. The slab is composed of a hexagonal metal disk array on FR4 circuit board. The disk geometry is the same as described above with periodic boundary conditions imposed in the out-of-plane dimension. Right-handed propagation is seen in band 1 (see Fig. 9.15) and focusing is seen in band 2. The structure transmits very little microwave radiation in the bandgaps (6 and 11 GHz). The focus within the stack moves toward the source, the transmitted focus away from the stack and the source as frequency increases in band 2. The propagation in the stack in the second band is nearly radiative, though anisotropic, with a wavelength larger than free space and increasing at higher frequencies. At higher bands the propagation can no longer be described by an (anisotropic) index and is clearly diffractive in nature

widths were approximately 0.7 times the wavelength at these two frequencies, consistent with the diffraction limit. No superfocusing [41] is seen (or expected for this lossy medium).

Another indication that our disk composite is acting like a negative index medium is the fact that the external focus moves with the placement of the source as predicted by Snell's law for negative refraction. The simulation and ray tracing sketch of Fig. 9.19 illustrates this effect. If the source moves by 1 cm the external focus moves by the same distance.

As discussed above for Fig. 9.17 we note that as the frequency increases to the top of the passband the external focus moves away from the slab.

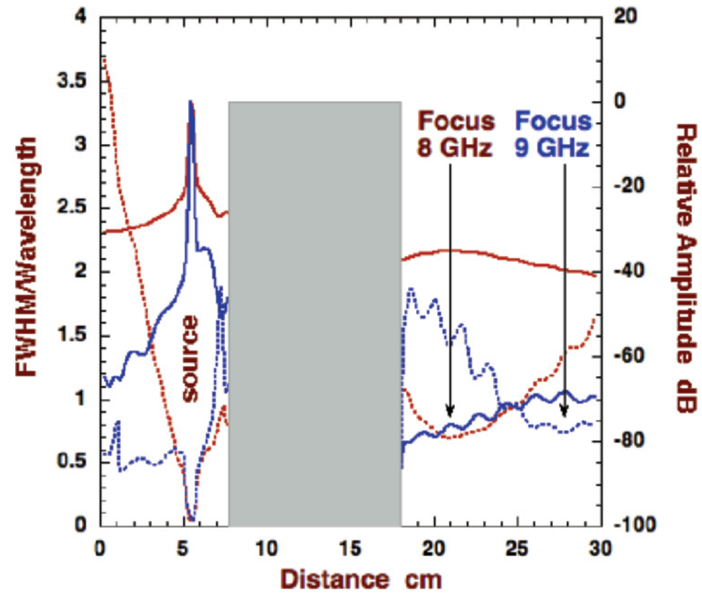

Fig. 9.18. Plot of the intensity (*solid lines*) and full width at half maximum (*dashed lines*) of 8 GHz (red) and 9 GHz (blue) radiation emerging from a monopole source, traversing the hexagonal disk medium and focusing on the far side. The FDTD simulation field was averaged after achieving a steady state. Note that the width at the foci is approximately 0.7 times the wavelength

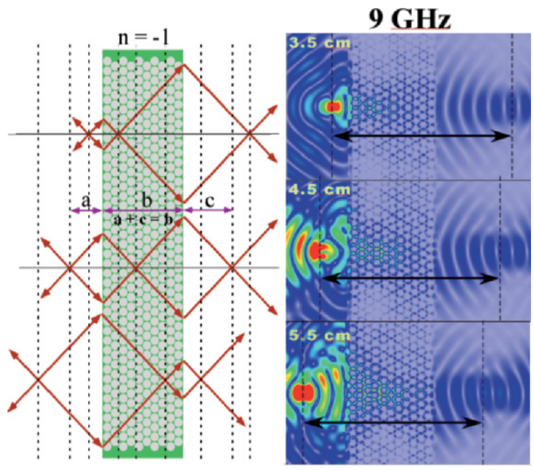

Fig. 9.19. Calculated 9 GHz electric field amplitude distribution for the hexagonal disk array. The monopole source is positioned to the left of the composite at 3.5, 4.5, and 5.5 cm from the front surface. The real focus tracks the displacement of the source as is expected for the real image produced by a negative index slab

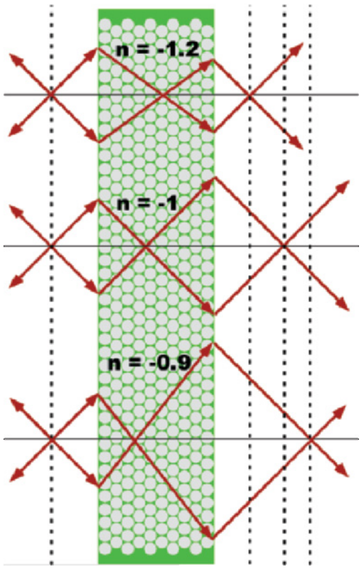

Fig. 9.20. Sketch of movement of focus with variation of the index of refraction. For $n = -1$ the distance of the external focus from the slab plus the offset of the source from the slab equal the thickness of the slab. For more negative index the external focus moves toward the slab. As n approaches zero the focus moves away from the slab

According to Snell's Law this implies that the index increases from a negative value as frequency increases. The optical rays drawn for different indices in Fig. 9.20 illustrate this point. The displacement of the focus is therefore a measure of the index of the slab. For small angles of incidence, the index can be estimated from the formula $n \approx -b/(a+c)$, where b is the thickness of the composite, a is the offset of the source from the composite, and c is the distance from the back side of the composite to the external focus. In Fig. 9.21 we plot estimates of the index from the displacement of the focus with frequency along with the index taken from the calculated band structure (Figs. 9.15 and 9.16) and the wavelength observed in the FDTD movie frames inside the composite. This observation gives us confidence that we can estimate the index for our measured samples by noting the position of the source and focal distances from the composite sample.

9.7 Modeling Refraction Through the Disk Medium

Another method to extract the effective index of refraction of our hexagonal disk medium is to note the displacement of an oblique beam impinging on the stack. Simulations were run for the experimental setup described in Fig. 9.22. The FDTD simulations closely match the experimental setup, however, due to

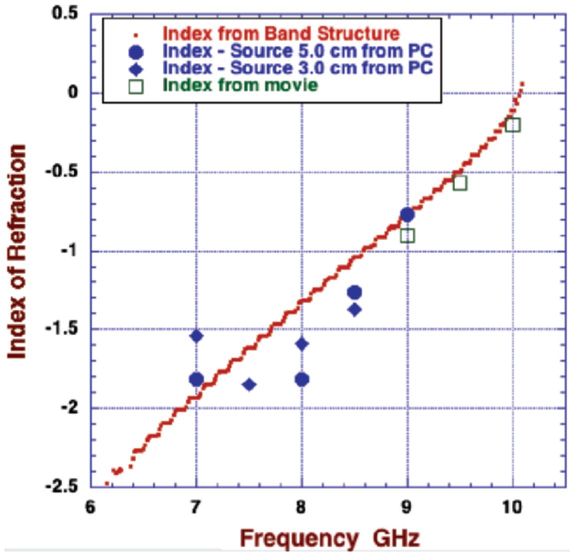

Fig. 9.21. Index of refraction estimates from source displacement and from inspection of calculated fields in the composite with the index derived from the calculated band structure for comparison

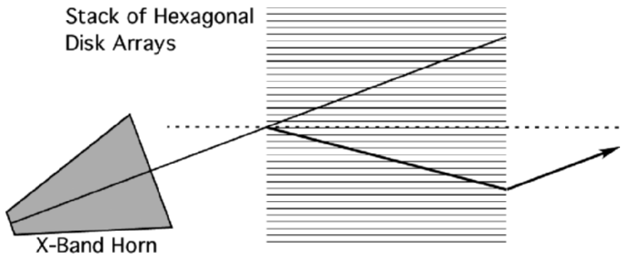

Fig. 9.22. Diagram of our refraction simulation and experiment. Microwave radiation is emitted from an X-band (8.2–12.4 GHz) microwave horn. It impinges on the stack of hexagonal disk arrays on circuit board at an angle of 20.5°. The refracted radiation is measured by two-dimensional scans of a microwave receiver on the other side of the stack. A sequence of Gaussian fits to the radiation pattern is used to extrapolate the radiation path to the point of emergence. The deflection of the beam then is used to calculate the effective index of refraction in the stack. The identical data analysis was also applied to FDTD calculated field patterns from simulations of similar spatial configurations

the size of the problem a coarser FDTD grid was employed which shifted the band structure to lower frequencies. In Fig. 9.23 we show plots of the FDTD calculation at various frequencies. As expected no radiation is transmitted in the first (5 and 6 GHz) and second (11 GHz) bandgaps. In the second transmission band the wave is negatively refracted and emerges with a downward

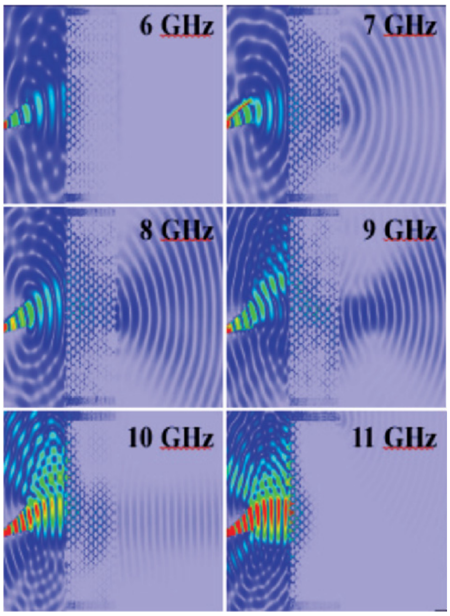

Fig. 9.23. Simulations of microwave radiation incident on a stack of hexagonal disk arrays at various frequencies. The radiation emerges from a horn at the left and impinges on the stack at an angle 20° to the normal. Some energy is reflected from the front surface due to the angle and frequency-dependent effective surface impedance of the stack. The remaining energy is refracted in the stack for frequencies 7–10 GHz. At 6 and 11 GHz a bandgap exists in the structure and the radiation is almost entirely reflected. Negative refraction is demonstrated by noting the center of the emerging radiation is "below" the center of the entering radiation. At 10 GHz the index of refraction can be estimated from the wavelength in the material

displacement from the entry position. Close to the composite two transmitted beams can be discerned, the main beam and the first side-lobe of the horn antenna. In the experiment, discussed in section 9.9, we find we were able to follow the beams 60 cm down range from the back of our sample. Computational limits did not allow us to fully separate the beams in the simulation, but the displacement effect is clearly evident. Experimentally we were able to accurately extrapolate the center of the main beam back to the point of exit from the composite as will be described in the experimental section of this chapter. The secondary beam identified as the antenna sidelobe actually extrapolates to exiting position above the exit of the main beam. This is consistent with the side lobe entering the stack at a downward slope, crossing the main beam in the stack and exiting above the centroid of the main beam at the rear of the sample.

Finally, we note that for indices approaching zero the entry of the wave into the composite is limited by "total internal reflection" into air at the front surface, $\Theta_{\mathrm{int\_refl}} = \arcsin(-n)$. This effect is apparent in the 10 GHz simulation

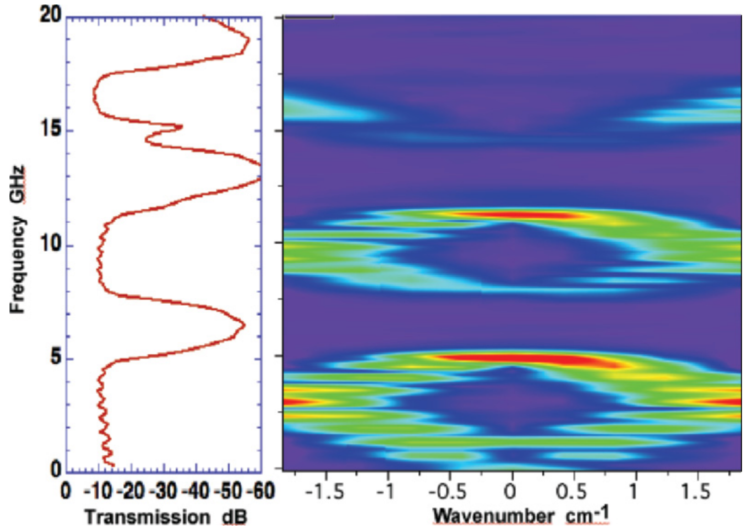

Fig. 9.24. Plot of calculated transmission spectrum and the frequency vs. wavenumber calculated for the hexagonal array of 1 cm diameter metal disks on FR4 circuit board. The transmission spectrum and band structure here (normal incidence) was calculated with a refined FDTD grid better approximating the real disk geometry

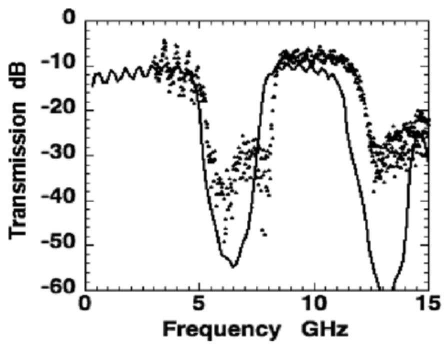

Fig. 9.25. Calculated (*line*) and measured (*small triangles*) microwave transmission through the stack of hexagonal metal disks on FR4 circuit board

seen in Fig. 9.23 at 9 GHz where only the near normal incident portion of the wave enters the composite.

The quasi-2D hexagonal disk simulations noted in figures such as Fig. 9.23 required calculations spanning FDTD grids 1,400 × 1,400 × 8 in size with base cell dimensions 0.025 × 0.025 × 0.08 cm^3. This cell size was chosen to expedite the 50 or so simulation runs. The coarseness of the grid lowered the frequency of the passbands while retaining their character from the measured geometry. Recalculating the band structure and transmission curves with a refined grid we find the results shown in Figs. 9.24 and 9.25. The refined grid cell dimension for these simulations was $0.005 \times 0.005 \times 0.01\,\mathrm{cm}^3$. (Experimentally, the observed depth of the transmission notches is limited by the noise floor, 30–40 dB). Although the transmitted intensity still does not quite match the measured data it is in good qualitative agreement. We are confident that further refinement of the grid will shift the passbands to higher frequency and bring closer agreement with the measurement.

9.8 Hexagonal Disk Array Measurements – Transmission and Focusing

A stack of approximately 120 aligned hexagonal arrays of 1 cm copper disks was constructed using standard photolithographic techniques on FR4 circuit board. The disk size and distribution corresponded to the calculation and is shown in Fig. 9.14. FR4 is fairly lossy over our target frequency band 8.2–12.4 GHz. We chose FR4 over lower loss (and higher cost) Teflon-based substrate because it minimizes internal microwave standing wave modes and Fresnel modulation that might complicate the interpretation of our data. The individual circuit boards were 0.32 cm thick and $45.7 \times 10\,\mathrm{cm}^2$ in the plane of the disk arrays. The arrays themselves were centered on one side of the circuit board, 43 cm long and 10 cm wide. Stacking aligned the disks in the vertical plane. The microwave radiation was polarized in the plane of the disks.

We studied the transmission through the stacks over two octaves, 4–16 GHz in our initial measurements. The measured spectrum is shown in Fig. 9.25. Reasonable agreement was found with FDTD calculations. These calculations employed a refined griding to better represent the hexagonal disk geometry of our arrays. In doing so the calculated spectrum moved significantly upward in frequency (compare Figs. 9.15 and 9.25). The measured second transmission band lies approximately 0.5 GHz above the calculated spectrum. The transmission is reduced by approximately 10 dB from free space, which is consistent with the calculation. The attenuation includes contributions from both front surface reflection and transmission losses. Some Fresnel modulations due to the presence of standing waves in the composite can be seen in both the measured and calculated transmission spectra. The first bandgap increased in width from the previous coarser grid calculations (Fig. 9.15) and now extends from 5.5 to 8.5 GHz.

The scanning of the stack of disk arrays was performed in the same manner as for the SRR arrays (see Fig. 9.8). An open-ended X-band waveguide served as the source with rf E-field aligned with the central circuit board/disk array plane. The X–Y scan was taken while the frequency was stepped through the band at each point. Several amplitude and phase plots are shown in Fig. 9.26. As the frequency increases the focus moves away from the stack (top of plots). A scan was also performed in the plane normal to the circuit board/disk array plane demonstrating the expected $1/r^2$ divergence in this plane. (The stack has a positive refractive index for radiation propagating in this plane.)

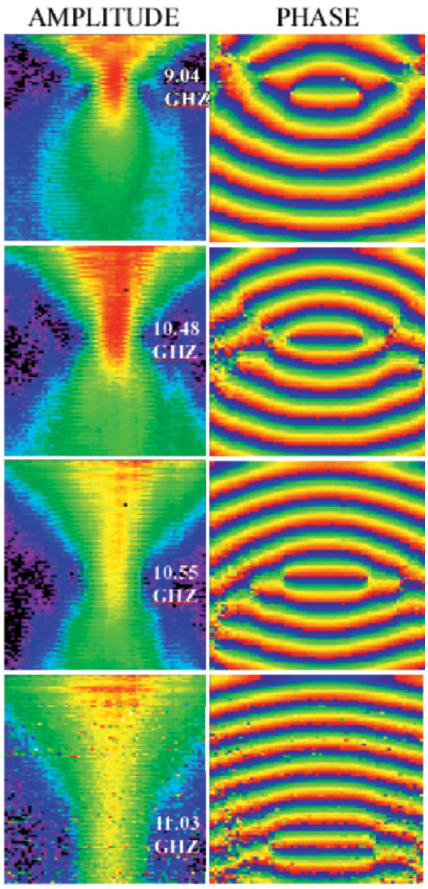

Fig. 9.26. Amplitude and phase X–Y scan plots at several frequencies in the second transmission band of the disk array stack. The scans traversed 15.25 cm in the lateral (X) direction and 23 cm in the down range (Y) direction. The amplitude relative color scale covers 40 dB from red to black. The phase color scale transition is 360°. As frequency increases the focus moves away from the rear of the stack (*top*). The planar hexagonal structure creates a 2D focus. The index is positive in the direction normal to the hexagonal array so the amplitudes before and after the focus are not symmetrical. The phase plots are perhaps more useful in locating the true foci

In Fig. 9.27, we plot the full width at half maximum (FWHM) of the focus and the distance of the focus from the rear of the stack, both normalized to the wavelength, vs. frequency. At the low frequency end of the band the FWHM is close to half the wavelength, increasing to slightly greater than the wavelength at the high end. The focus moves out from 1.5 times the wavelength at lower frequencies to 8 times the wavelength at the high end (limited by the range of our scan). Although the step increment in the scan

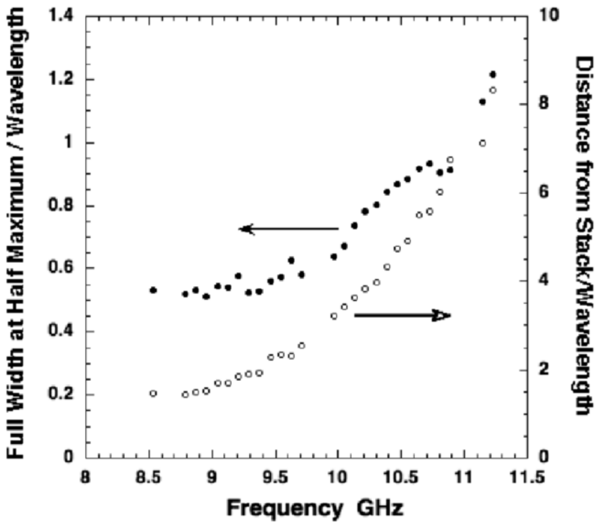

Fig. 9.27. Plot of the measured distance from the rear of the stack of hexagonal disk arrays and the full width at half maximum widths of the foci normalized to free space wavelength vs. frequency. The displacement of the external focus increases as the frequency increases through the second passband as expected for a negative refractive index decreasing in magnitude in the composite

was 0.25 cm, the resolution of the plots is further limited by the 1 cm aperture of both sending and receiving waveguides. The focus width appears to be diffraction limited even at the low end of the passband consistent with our expectations.

Using simple geometry we can estimate the frequency-dependent index of refraction from the displacement of the focus in our simulations knowing the distance of the source from the disk array stack. In Fig. 9.28 we plot the estimated index of refraction derived from experimental scans taken at three different source offsets: 1.9, 4.4, and 5.7 cm. There is more scatter in the data at short offsets (low frequencies) with good agreement at longer offset values. This trend in the data is consistent with small measurement errors existing in the positioning of the source and detector. The data is also consistent between independent data sets and with our expectations.

Examining the position of the focus for the three source offsets in Fig. 9.29, we note that the locus of foci move an equal distance (within error) as the source offset as is expected for a negative index material (see Fig. 9.20).

9.9 Hexagonal Disk Array Measurements – Refraction

In order to further demonstrate negative refraction in our hexagonal disk array medium we illuminated our stack with microwave radiation impinging

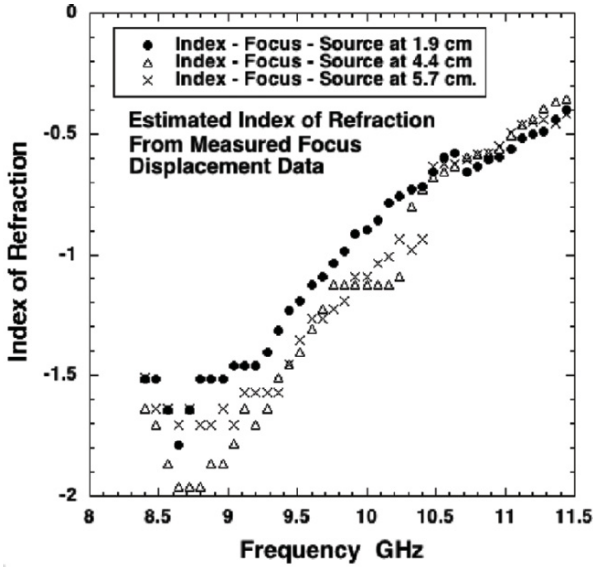

Fig. 9.28. Estimates of the index of refraction of our hexagonal disk stack for three different source offsets. The estimate employs data such as seen in Fig. 9.20 for the displacement of the external focus with frequency

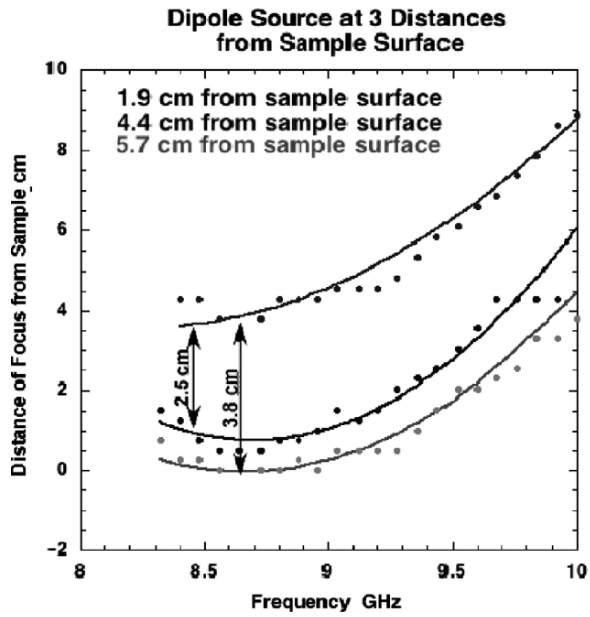

Fig. 9.29. Measured external focus displacement with frequency for three different source offsets. The external foci displacements track the source offsets as expected for transmission through a negative index slab

at a shallow angle (20°) to normal in an arrangement similar to the work of Moussa et al. [20]. Measuring the centroid of the radiation emerging from the rear of the stack allows us to estimate the effective index of refraction of our composite. Several problems contribute inaccuracies in this measurement scheme. The radiation illuminating the composite comes from a microwave horn in close proximity to the stack. The wavefront is spherical with the maximum occurring at the 20° incident angle. Since the impedance of the stack is expected to be angle dependent, the intensity center of the radiation inside the stack on the illuminated face need not be coincident with the maximum on the outside surface due to angle-dependent reflection at the boundary. It is not clear what the angle and frequency-dependent front surface impedance should be in this instance. Also the composite medium itself is lossy to radiation and longer path length in the material will suffer greater attenuation in the transit. With this understanding the magnitude of the index of refraction can be estimated from the angle connecting the center of illumination and center of emergence of the microwave energy. The refraction in the slab was simulated using FDTD code (see Fig. 9.23) and measured in X-band using our scanning detector.

In order to estimate the effective refractive index of our disk arrays we illuminated the stack with a beam of X-band microwave radiation impinging at an angle to the normal. See Fig. 9.22 for a schematic representation of the experimental setup. At each X–Y location, data was taken at multiple frequencies as the source was swept step wise ($\Delta f = 84\,\mathrm{MHz}$) across X-Band. The radiation emerging from the rear of the stack was detected in the X–Y scanner described above. A microwave power (dB relative) intensity plot of such a scan is seen in Fig. 9.30. This typical scan was taken at 10.72 GHz. Near the rear of the stack the main beam and a side lobe intersect. At greater distances the angle of the main beam propagation can be discerned. Microwave scalar power was plotted vs. lateral displacement at each distance step down range from the stack at each frequency step in the transmission band. Gaussian fits to these plots then located the beam max at each down range point for each frequency.

In Fig. 9.31 we plot the beam maxima vs. distance from the rear of the stack for 10.72 GHz as well as a linear fit (solid line) to the data. The crossing of the side lobe beam causes a deflection near the stack. But an accurate extrapolation can be made from the more distant down range data. Microwave attenuation of the stack medium with the increased path length for off-normal transmission skews the extrapolated estimate by shifting the beam maximum of the emergent radiation toward smaller displacements and larger absolute values of index of refraction. Consequently the magnitudes (but not the sign) of values of refractive index presented in Fig. 9.32 are overestimated. Negative refraction is indeed observed. It is interesting to note that the side lobe of the send horn also refracts negatively, crossing over the main beam in the stack and once again in free space on the far side. As frequencies are stepped the refracted angles of the main beam and side lobes increase

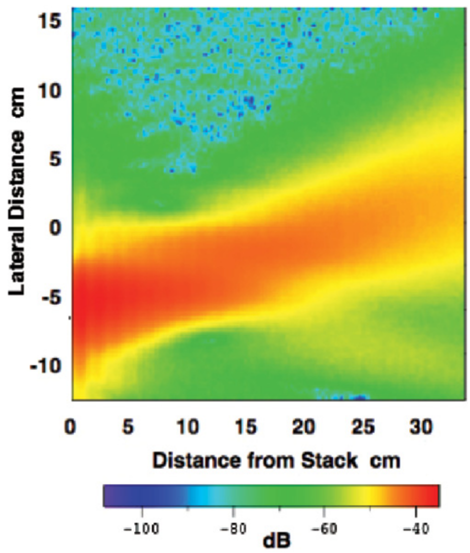

Fig. 9.30. A radiation intensity plot showing the measured scanned 10.72 GHz microwave beam emerging from the rear of the stack of hexagonal disk arrays. The color scale is relative in dB with red being the most intense and dark blue being the least

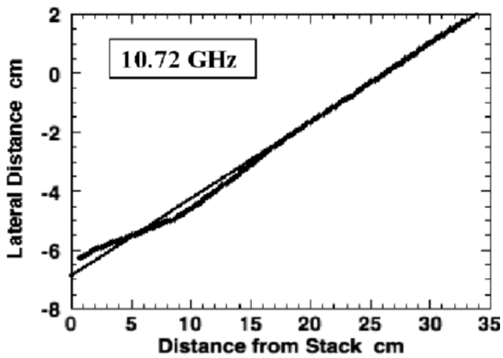

Fig. 9.31. Linear extrapolation of fitted beam centers of emergent radiation refracted by our planar stack of hexagonal disk arrays. Close in the center data is distorted by the side-lobe beam crossing over the main beam. The refractive index is then estimated from the displacement of the beam in the stack

continuously as expected. The scatter in Fig. 9.32 derives from uncertainty in the extrapolation.

Replotting these data (extracting outliers) with the previous estimates from the displacement we have Fig. 9.33. Good agreement is seen between the two methods of index estimation within experimental uncertainty. These data

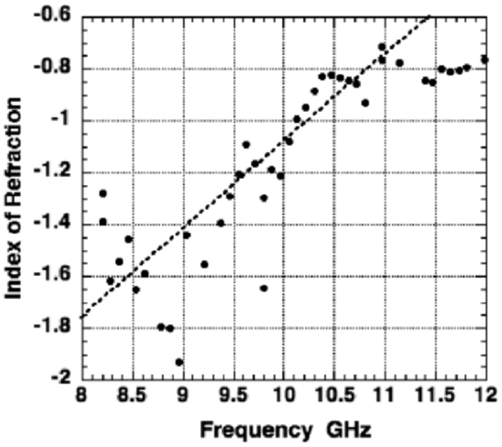

Fig. 9.32. Index of refraction inferred from the refraction experiment. The *dashed line* is a guide to the eye

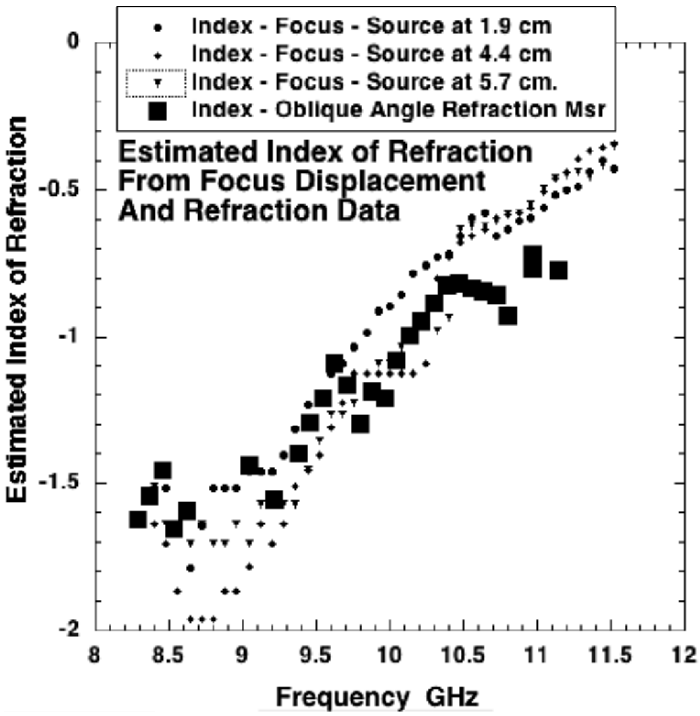

Fig. 9.33. Index of refraction estimated from the measured displacement of the focus with frequency for three different source offsets from the front of the hexagonal disk stack (*circles* 1.9 cm offset, *diamonds* 4.4 cm offset, and *triangles* 5.7 cm offset). Also plotted is the index vs. frequency from the oblique incidence analysis (*large squares*). Both types of estimates appear to be mutually consistent

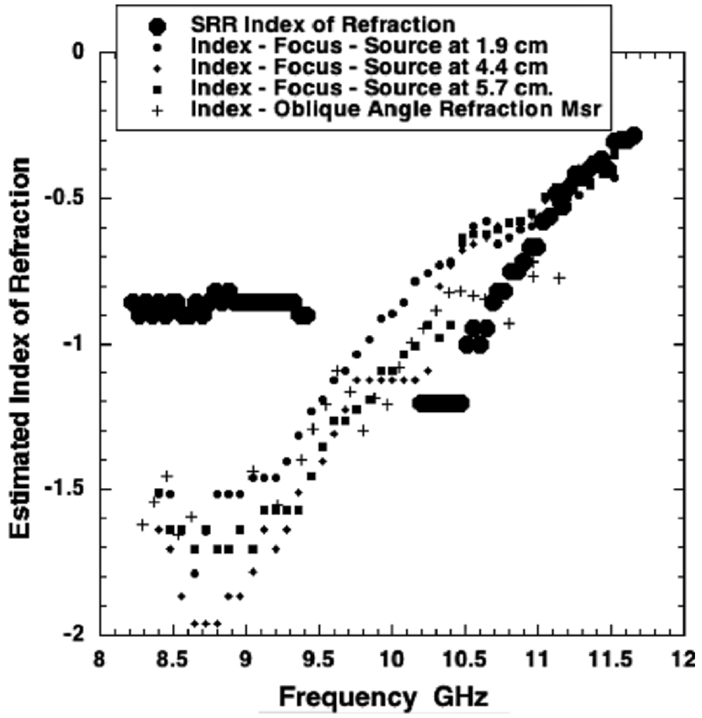

Fig. 9.34. Using the distance to focus information previously measured for transmission through our SRR array we infer an estimate for the index of refraction of this array (*large solid circles*). For comparison we replot the index inferred for the solid disk array. At frequencies greater than the SRR resonance (9.8 GHz) the index variation is similar to that found for the metal hexagonal disk array. The SRR resonance contribution to the composite permeability apparently shifts the index to larger (less negative values) below SRR resonance and to smaller values above

are also consistent with the expected variation of refractive index observed in our FDTD simulations of this structure.

With confidence obtained by the index analysis of the hexagonal disk structure summarized in Fig. 9.33 we now use the distance of focus method to estimate the effective index of refraction for the hexagonal SRR described in section 9.5 of this paper. The results are plotted in Fig. 9.34. For frequencies above the SRR resonance (~9.8 GHz) absorption gap we see that the frequency dependence of the index is similar to that of the disk structures. Below the SRR resonance the index appears to be flat at $n = -0.86 \pm 0.04$. It appears that the modulation of the SRR permeability at resonance shifts the composite index to larger values (less negative) below SRR resonance frequency and to smaller values (more negative) above.

We remain skeptical of procedures employing normal incidence S-parameter measurements for finding the effective complex permittivity and permeability of the disk or SRR media. The S-parameter to constituent parameter inversion routines are very sensitive to phase offsets. Choosing an effective front reflection plane and even effective thickness are not straightforward for such composite media with elements a third of the free space wavelength. It is remarkable that coherent radiative transmission is observed over the entire second transmission band.

Comparing the SRR and disk array results, it appears that the X-band negatively refracting regions in the SRR are related to the second band in the disks with a ring absorptive resonance splitting this negative refraction transmission band.

9.10 Conclusions

We have observed broadband focusing in photonic bandgap arrays of SRRs and disks. FDTD simulations demonstrate focusing similar to the observed data for the disk arrays. Griding compromises required to execute large scale simulations caused frequency shifts for the calculated transmission spectra of both the disk and SRR arrays and prevented implementation of FDTD refraction simulations for the SRR arrays where very fine scale resolution is necessary due to the small capacitive gaps between rings. The main features of the observed data are reproduced including the progression of the focus from the rear of the stack and a steady reduction in the amplitude of the negative refractive index as frequency is increased. Broad band negative index of refraction is demonstrated in hexagonal SRR and disk arrays.

Acknowledgments

The authors are grateful for the technical advice and support for the work by Dr. Donald Forester. This work was performed under contract from the DARPA DSO office, Dr. Valerie Browning program manager.

References

1. D.R. Smith, W.J. Padilla, D.C. Vier, S.C. Nemat-Nasser, S. Schultz, Phys. Rev. Lett. **84**, 4184 (2000)
2. D.R. Smith, D.C. Vier, N. Kroll, S. Schultz, Appl. Phys. Lett. **77**, 2246 (2000)
3. D.R. Smith, N. Kroll, Phys. Rev. Lett. **85**, 2933 (2000)
4. R.A. Shelby, D.R. Smith, S. Schultz, Science **77**, 292 (2001)
5. J.B. Pendry, A.J. Holden, W.J. Stewart, I. Youngs, Phys. Rev. Lett. **76**, 4773 (1996)
6. J.B. Pendry, A.J. Holden, D.J. Robbins, W.J. Stewart, J. Phys.: Condens. Matter **10**, 4785 (1998)

7. J.B. Pendry, A.J. Holden, D.J. Robbins, W.J. Stewart, IEEE Trans. Microw. Theory Tech. **47**, 2075 (1999)
8. D.R. Smith, N. Kroll, Phys. Rev. Lett. **85**, 2933 (2000)
9. J.B. Pendry, Phys. Rev. Lett. **85**, 3966 (2000)
10. F.J. Rachford, D.L. Smith, P.F. Loschialpo, D.W. Forester, Phys. Rev. E **66**, 036613 (2002)
11. C.G. Parazzoli, R.B. Greegor, K. Li, B.E.C. Koltenbah, M. Tanielian, Phys. Rev. Lett. **90**, 107401 (2003)
12. V.G. Veselago, Sov. Phys. Usp. **10**, 509 (1968)
13. P.M. Valanju, R.M. Walser, A.P. Valanju, Phys. Rev. Lett. **88**, 187401 (2002)
14. S.R.W. Ziolkowski, E. Heyman, Phys. Rev. E **64**, 056625 (2001)
15. S. Foteinopoulou, E.N. Economou, C.M. Soukoulis, Phys. Rev. Lett. **90**, 107402 (2003)
16. D.R. Smith, D. Schurig, J.B. Pendry, Phys. Rev. Lett. **81**, 2713 (2002)
17. M. Notomi, Phys. Rev. B **62**, 10696 (2000)
18. S. Foteinopoulou, C.M. Soukoulis, Phys. Rev. B **67**, 235107 (2003)
19. S. Foteinopoulou, C.M. Soukoulis, Phys. Rev. B **72**, 165112 (2005)
20. R. Moussa, S. Foteinopoulou, L. Zhang, G. Tuttle, K. Guven, E. Ozbay, C.M. Soukoulis, Phys. Rev. B **71**, 085106 (2005)
21. A.L. Efros, A.L. Pokrovsky, arXiv, Cornell University, Ithaca, NY, 29 Aug 2003, http:_arxiv.org/cond-mat/0308611
22. P.V. Parimi, W.T. Lu, P. Vodo, S. Sridha, Nature **426**, 404 (2003)
23. P.V. Parimi, W.T. Lu, P. Vodo, J. Sokoloff, J.S. Derov, S. Sridhar, Phys. Rev. Lett. **92**, 127401 (2004)
24. E. Cubukcu, K. Aydin, E. Ozbay, S. Foteinopoulou, C.M. Soukouli, Nature **423**, 604 (2003)
25. H. Kosaka, T. Kawashima, A. Tomita, M. Notomi, T. Tamamura, T. Sato, S. Kawakami, J. Lightwave Technol. **17**, 2032 (1999)
26. F.J. Rachford, D. Smith, P. Loschialpo, first DARPA Meta-materials PI Meeting presentation and conference CD June 2001, North Conway, NH
27. Finite Difference Time Domain simulations were performed using the program MAXTDA written at Georgia Tech Research Institute, Atlanta, GA, USA. MAXTDA was recently modified by GTRI to include the causal Lorentzian functional
28. D.R. Smith, Private communication
29. A.A. Houck, J.B. Brock, I.L. Chuang, Phys. Rev. Lett. **90**, 137401 (2003)
30. D.R. Smith, P. Kolinko, D. Schurig, J. Opt. Soc. Am. B **21**, 1032 (2004)
31. D.R. Smith, P.M. Rye, J.J. Mock, D.C. Vier, A.F. Starr, Phys. Rev. Lett. **93**, 137405 (2004)
32. Boeing DARPA Metamaterials Program Review, Hanscom AFB (2004)
33. B. D'Acunto, *Computational Methods for PDE in Mechanics* (World Scientific, Singapore, 2004), p. 192
34. J. Berenger, J. Comput. Phys. **114**, 185 (1994)
35. R.W. Ziolkowski, Opt. Express **11**, 662 (2003)
36. J.B. Pendry, Phys. Rev. Lett. **85**, 3966 (2000)
37. J.B. Pendry, S.A. Ramakrishna, J. Phys.: Condens. Matter **14**, 8463 (2002)
38. D.R. Smith, D. Schurig, M. Rosenbluth, S. Schultz, Appl. Phys. Lett. **82**, 1506 (2003)

39. P.F. Loschialpo, D.L. Smith, D.W. Forester, F.J. Rachford, J. Schelleng, Phys. Rev. E **67**, 025602 (2003)
40. P.F. Loschialpo, D.W. Forester, D.L. Smith, F.J. Rachford, C. Monzon, Phys. Rev. E **70**, 036605 (2004)
41. E. Cubukcu, K. Aydin, E. Ozbay, S. Foteinopoulou, C. M. Soukoulis, Phys. Rev. Lett. **91**, 207401 (2003)

10

Super Low Loss Guided Wave Bands Using Split Ring Resonator-Rod Assemblies as Left-Handed Materials

C.M. Krowne

Summary. SRR metamaterial is used as a substrate material in a microstrip guided wave structure to determine what the effect is of a material with potentially excessive dispersion or loss or both. A Green's function method readily incorporates the metamaterial permittivity and permeability tensor characteristics. Ab initio calculations are performed to obtain the dispersion diagrams of several complex propagation constant modes of the structure. Analytical analysis is done for the design and interpretation of the results, which demonstrate remarkable potential for realistic use in high frequency electronics while using the LHM for possible field reconfigurations. Bands of extremely low loss appear for several of the lowest order modes operating in the millimeter wavelength regime.

10.1 Introduction

It has been shown that very unusual field patterns occur for guided propagating waves in microstrip left-handed material (LHM) structures compatible with microwave integrated circuit technology [1]. Like for focusing, the most arbitrary control of the field pattern obtains when the substrate material can be isotropic, and then modified from isotropy to anisotropy to enhance certain features [2] if desired. For lenses, lack of isotropy can be disastrous, leading to serious wave distortion, and this holds true when studying LHM lenses. For the above reasons, only isotropic substrates will be analyzed in what follows. One of the looming major questions remaining to be answered using LHMs, is what effect does the substrate loss or dispersion have on the characteristics of guided wave propagation while reconfiguring the electromagnetic fields? For low loss or dispersion, or nondispersive LHMs, one can examine the dispersion diagram in [1] which was used to extract isolated eigenvalue points for making distribution plots. Of course, the use of such ideal crystalline substrates to make nondispersive devices is the goal, as in the negative refractive (NR) heterostructure bicrystal device creating field asymmetry [3] (such negative refraction without negative effective index has been studied in dielectric [4] and metal [5] photonic crystals in contrast to the more intensively studied cases of NR in LHM in dielectric photonic crystals [6]). However, significant dispersion may be present, even if the loss is low, in substrates fabricated from ordinary dielectric host right-handed materials (RHMs) with dielectric RHM inclusions, as in photonic crystals [7]. Finally, the use of metallic inclusions, such as split ring-rod combinations (SRRs) [8], may be used, which may have very sizable loss and dispersion.

Here it is shown, contrary to prevailing wisdom in the microwave community about the use of metallic inclusions and supported by the substantial losses seen in measurements on SRR prisms and other structures in the physics community [9–19], that even with extremely dispersive metamaterials, with potential for huge losses, a frequency band (or bands) may be found where the propagation is predominantly lossless, the wave behavior is backward (left-handed guided wave of reduced dimensionality), and the slow wave phase characteristic comparable to an RHM. This is nothing short of remarkable, and below we will design the metamaterial, highlighting its physics, and selecting reasonable values with which realistic simulations could be done. The low loss bands are a result of the 3D guided wave problem being reduced to a single 1D propagation direction, which apparently can be optimized, whereas the 3D lens focusing problem requires a multiplicity of propagation directions, all acting in 3D, which makes the acquisition of low loss propagation much harder.

10.2 Metamaterial Representation

Effective permittivity $\varepsilon(\omega)$ [20] and permeability $\mu(\omega)$ [21] of the metamaterial can be represented by

$$\varepsilon(\omega) = 1 - \frac{{\omega_{\mathrm{pe}}}^2 - {\omega_{\mathrm{oe}}}^2}{\omega^2 - {\omega_{\mathrm{oe}}}^2 + \mathrm{i}\omega\Gamma_{\mathrm{e}}} \tag{10.1}$$

$$\mu(\omega) = 1 - \frac{F\omega^2}{\omega^2 - {\omega_{\mathrm{om}}}^2 + \mathrm{i}\omega\Gamma_{\mathrm{m}}}. \tag{10.2}$$

Here ω_{pe}, ω_{oe}, and ω_{om} are the effective plasma, and electric and magnetic resonance radian frequencies. Γ_{e} and Γ_{m} are the loss widths in s^{-1}. Real part $\varepsilon_{\mathrm{r}}(\omega)$ of $\varepsilon(\omega)$ is

$$\varepsilon_{\mathrm{r}}(\omega) = \frac{\left(\omega^2 - {\omega_{\mathrm{pe}}}^2\right)\left(\omega^2 - {\omega_{\mathrm{oe}}}^2\right) + \omega^2{\Gamma_{\mathrm{e}}}^2}{\left(\omega^2 - {\omega_{\mathrm{oe}}}^2\right)^2 + \omega^2{\Gamma_{\mathrm{e}}}^2}. \tag{10.3}$$

As long as we are not too close to resonance, measured against the line width Γ_{e}, i.e., $|\omega^2 - {\omega_{\mathrm{oe}}}^2| \gg \omega\Gamma_{\mathrm{e}}$ (10.3) reduces to

$$\varepsilon_{\mathrm{r}}(\omega) = 1 - \frac{{\omega_{\mathrm{pe}}}^2 - {\omega_{\mathrm{oe}}}^2}{\omega^2 - {\omega_{\mathrm{oe}}}^2} = 1 - \frac{{\omega_{\mathrm{pe}}}^2}{\omega^2} \tag{10.4}$$

the last equality arising from having continuous rods making $\omega_{\mathrm{oe}} = 0$. For a desired $\varepsilon_{\mathrm{r}}(\omega)$ at a specific frequency (10.3) may be inverted to yield

$$\begin{aligned}\omega_{\mathrm{pe}} &= \sqrt{\left(\omega^2 + {\mathit{\Gamma}_{\mathrm{e}}}^2\right)\left[1 - \varepsilon_{\mathrm{r}}(\omega)\right]} \\ &\approx \omega\sqrt{1 - \varepsilon_{\mathrm{r}}(\omega)}.\end{aligned} \tag{10.5}$$

So if we wish to have $\varepsilon_{\mathrm{r}}(\omega) = -2.5$ at $f = 80\,\mathrm{GHz}$, then $\omega_{\mathrm{pe}} = \omega\sqrt{3.5} = 150\,\mathrm{GHz}$ by evaluating (10.5).

Imaginary part $\varepsilon_{\mathrm{i}}(\omega)$ of $\varepsilon(\omega)$ is

$$\varepsilon_{\mathrm{i}}(\omega) = \frac{\omega \mathit{\Gamma}_{\mathrm{e}}\left({\omega_{\mathrm{pe}}}^2 - {\omega_{\mathrm{oe}}}^2\right)}{\left(\omega^2 - {\omega_{\mathrm{oe}}}^2\right)^2 + \omega^2 {\mathit{\Gamma}_{\mathrm{e}}}^2} \tag{10.6}$$

Again for $\omega_{\mathrm{oe}} = 0$, (10.6) becomes

$$\varepsilon_{\mathrm{i}}(\omega) = \frac{\mathit{\Gamma}_{\mathrm{e}} {\omega_{pe}}^2}{\omega\left(\omega^2 + {\mathit{\Gamma}_{\mathrm{e}}}^2\right)} \approx \frac{\mathit{\Gamma}_{\mathrm{e}}}{\omega}\left(\frac{\omega_{\mathrm{pe}}}{\omega}\right)^2. \tag{10.7}$$

Since ω_{pe} has independence from rod metal electron carrier density, given by

$${\omega_{\mathrm{pe}}}^2 = \frac{2\pi {c_0}^2}{a^2 \ln\left(a/r_{\mathrm{e}}\right)} \tag{10.8}$$

for a chosen lattice spacing a to wire radius r_{e} ratio, a/r_{e}, a can be solved for in (10.8)

$$a^2 = \frac{2\pi {c_0}^2}{{\omega_{\mathrm{pe}}}^2 \ln\left(a/r_{\mathrm{e}}\right)}. \tag{10.9}$$

Setting $a/r_{\mathrm{e}} = 109.3$, inserting the free space light velocity c_0 and ω_{pe}, we find that $a = 0.690\,\mathrm{mm}$ corresponding to $r_{\mathrm{e}} = 6.313\,\mu\mathrm{m}$. With this same lattice spacing to wire radius ratio, one can determine $\mathit{\Gamma}_{\mathrm{e}}$ as

$$\mathit{\Gamma}_{\mathrm{e}} = \frac{\varepsilon_0}{\pi}\left(\frac{a}{r_{\mathrm{e}}}\right)^2 \frac{{\omega_{\mathrm{pe}}}^2}{\sigma_{\mathrm{r}}}. \tag{10.10}$$

One notices that the line width does indeed depend on the carrier density through metallic rod conductivity σ_{r}, and this is where potentially one can suffer tremendous ohmic losses, the bane of physicists and engineers trying either to reduce SRR based structure losses or circuit losses. If we use aluminum as had Pendry, taking $\sigma_{\mathrm{r}} = \sigma_{\mathrm{Al}} = 3.65 \times 10^7\,\Omega^{-1}\,\mathrm{m}^{-1}$, $\mathit{\Gamma}_{\mathrm{e}} = 0.1305\,\mathrm{GHz}$. Once $\mathit{\Gamma}_{\mathrm{e}}$ is known, by (10.7) the frequency variation of the imaginary part of the permittivity is fixed.

Turning our attention to the effective permeability, real part $\mu_{\mathrm{r}}(\omega)$ of $\mu(\omega)$ is

$$\mu_r(\omega) = \frac{\left(\omega^2 - {\omega_{\mathrm{om}}}^2 - F\omega^2\right)\left(\omega^2 - {\omega_{\mathrm{om}}}^2\right) + \omega^2 {\mathit{\Gamma}_{\mathrm{m}}}^2}{\left(\omega^2 - {\omega_{\mathrm{om}}}^2\right)^2 + \omega^2 {\mathit{\Gamma}_{\mathrm{m}}}^2}. \tag{10.11}$$

For a desired $\mu_{\mathrm{r}}(\omega)$ at a specific frequency (10.11) produces an equation for the magnetic resonance frequency

$$\left(\omega^2 - {\omega_{\mathrm{om}}}^2\right)^2 (\mu_{\mathrm{r}} - 1) + F\omega^2 \left(\omega^2 - {\omega_{\mathrm{om}}}^2\right) + \omega^2 {\mathit{\Gamma}_{\mathrm{m}}}^2 (\mu_{\mathrm{r}} - 1) = 0. \quad (10.12)$$

This is a quadratic equation in $\omega^2 - {\omega_{\mathrm{om}}}^2$ and so will generate a solution for ω_{om} once the correct root is determined since the squared root is displaced from the desired squared resonance value. As long as we are not too close to resonance, measured against the line width $\mathit{\Gamma}_{\mathrm{m}}$, i.e., $|\omega^2 - {\omega_{\mathrm{om}}}^2| \gg \omega\mathit{\Gamma}_{\mathrm{m}}$, we may reduce (10.11) directly with the result

$$\mu_{\mathrm{r}}(\omega) = 1 - \frac{\omega^2 F}{\omega^2 - {\omega_{\mathrm{om}}}^2}. \quad (10.13)$$

For a desired $\mu_{\mathrm{r}}(\omega)$ at a specific frequency, (10.13) may be inverted to yield the magnetic resonance frequency

$$\omega_{\mathrm{om}} = \omega\sqrt{1 - \frac{F}{1 - \mu_{\mathrm{r}}(\omega)}}. \quad (10.14)$$

So if we wish to have $\mu_{\mathrm{r}}(\omega) = -2.5$ at $f = 80\,\mathrm{GHz}$, then $\omega_{\mathrm{om}} = \omega\sqrt{0.8564} = 74.03\,\mathrm{GHz}$ by evaluating (10.14), using a value of $F = 0.5027$ obtained from using the ratio of cylinder radius to lattice spacing

$$F = \pi\left(\frac{r_{\mathrm{m}}}{a}\right)^2. \quad (10.15)$$

The F value quoted makes r_{m} 40% of a, i.e., $r_{\mathrm{m}}/a = 2/5$, giving $r_{\mathrm{m}} = 0.2761\,\mathrm{mm}$. For the sheets split on cylinders model, effective magnetic resonance frequency

$$\omega_{\mathrm{om}} = \sqrt{\frac{3d{c_0}^2}{\pi^2 {r_{\mathrm{m}}}^3}} \quad (10.16)$$

can be inverted to find concentric cylinder spacing d,

$$d = \frac{\pi^2 {\omega_{\mathrm{om}}}^2 {r_{\mathrm{m}}}^3}{3{c_0}^2}. \quad (10.17)$$

Inserting in the values already calculated, we find that $d = 0.1668\,\mathrm{mm}$. This model is like the SRR in that d will be like the gap in the split ring, and the ring radius is like the cylinder radius. Clearly the gap in the split ring has a capacitance dependent on the specific edge cross-section presented to the gap, whereas very short height cylinders look like rings with overlapping surfaces having length $2\pi r_{\mathrm{m}}$, and one only needs to adjust the parameters to make one model equivalent to the other.

Imaginary part $\mu_{\mathrm{i}}(\omega)$ of $\mu(\omega)$ is

$$\mu_i(\omega) = \frac{\omega^3 \Gamma_{\mathrm{m}} F}{(\omega^2 - \omega_{\mathrm{om}}{}^2)^2 + \omega^2 \Gamma_{\mathrm{m}}{}^2} \approx \frac{\omega^3 \Gamma_{\mathrm{m}} F}{(\omega^2 - \omega_{\mathrm{om}}{}^2)^2}. \tag{10.18}$$

One can specify line width which is required to get the exact frequency of $\mu_{\mathrm{i}}(\omega)$ using

$$\Gamma_{\mathrm{m}} = \frac{2R_{\mathrm{s}}}{r_{\mathrm{m}}\mu_0}, \tag{10.19}$$

where R_{s} is the surface resistance of the metal cylinders to electromagnetic waves [22,23]. It is an inverse function of metallic conductivity of the cylinders σ_{c}, allowing (10.19) to be written as

$$\Gamma_{\mathrm{m}} = \frac{1}{r_{\mathrm{m}}}\sqrt{\frac{2\omega}{\sigma_{\mathrm{c}}\mu_0}}. \tag{10.20}$$

Again using the conductivity of aluminum, $\sigma_{\mathrm{c}} = \sigma_{\mathrm{Al}}$, the magnetic line width is found to be $\Gamma_{\mathrm{m}} = 0.0853\,\mathrm{GHz}$.

10.3 Guiding Structure

The guiding structure to be simulated (Fig. 10.1) has a substrate thickness $h_{\mathrm{s}} = 0.5\,\mathrm{mm}$, an air region thickness $h_{\mathrm{a}} = 5\,\mathrm{mm}$, vertical perfectly conducting walls separation $B = 2b = 5\,\mathrm{mm}$ and a microstrip metal width $w = 0.5\,\mathrm{mm}$,

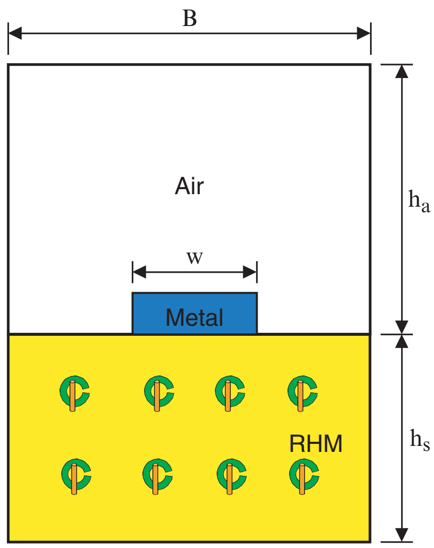

Fig. 10.1. Cross-section of guided wave structure

as in [1]. Certainly the lateral dimension of the structure B is substantially greater than the lattice spacing ($B/a = 7.25$), one requirement for the metamaterial to be used in our simulation. The longitudinal direction, for a uniform guiding structure, as this is, is taken as infinite, and automatically satisfies the metamaterial size requirement (i.e., $L \gg a,\ L \to \infty$). However, the substrate thickness is on the order of lattice spacing, which is not ideal, but we nevertheless accept it for purposes of needing some roughly useable value in order to perform simulations in what follows. Finally, the electromagnetic wavelength to lattice spacing ratio $\lambda/a = 5.43$, is substantial. Because of the logarithmic relationship entailed in solving for r_e in (10.9) once a has been selected, a noticeable reduction in a by small integer factors can have drastic affects on r_e, reducing by many orders of magnitude its size, moving from the μm range to the nm range, something still possible using conductive carbon nanotubes.

In the above calculations, we have been careful not to assume the metals of the split rings (or cylinders) are the same, $\sigma_\mathrm{c} \neq \sigma_\mathrm{r}$. In fact, one may be made out of gold, and the other out of aluminum, platinum, silver, or copper to name a few common metals. Range of conductivities of these metals is from 1.02×10^7 to $6.17 \times 10^7\,\Omega^{-1}\,\mathrm{m}^{-1}$ [20].

Also of interest for the effective permittivities and permeabilities, are their crossover frequencies. From (10.3), the electric crossover frequency ω_eco which satisfies $\varepsilon_\mathrm{r}(\omega) = 0$, obeys

$$\omega^4 - \omega^2 \left({\omega_\mathrm{pe}}^2 + {\omega_\mathrm{oe}}^2 + {\Gamma_\mathrm{e}}^2\right) + {\omega_\mathrm{pe}}^2 {\omega_\mathrm{oe}}^2 = 0. \tag{10.21}$$

When $\omega_\mathrm{oe} = 0$, which is our present case, it is easier to examine the numerator of (10.3) directly, than to solve (10.21), yielding

$$\omega_\mathrm{eco} = \sqrt{{\omega_\mathrm{pe}}^2 - {\Gamma_\mathrm{e}}^2} \approx \omega_\mathrm{pe}. \tag{10.22}$$

From (10.11), the magnetic crossover frequency ω_mco which satisfies $\mu_\mathrm{r}(\omega) = 0$, obeys

$$\omega^4(1-F) + \omega^2 \left[{\omega_\mathrm{om}}^2(F-2) + \Gamma_\mathrm{m}^2\right] + {\omega_\mathrm{om}}^4 = 0. \tag{10.23}$$

One of the solutions gives a value close to the resonance frequency when the line width is small, as we have seen it is for our case. For that limiting case, (10.23) considerably simplifies, and one may also readily find the solution by working with (10.11) directly, finding

$$\omega_\mathrm{mco} = \frac{\omega_\mathrm{om}}{\sqrt{1-F}}. \tag{10.24}$$

Placing the values already calculated into the right-hand side of (10.24), $\omega_\mathrm{mco} = 104.98\,\mathrm{GHz}$.

10.4 Numerical Results

For the LHM/NPV structure (NPV = negative phase velocity), in the limiting case of $\Gamma_{\mathrm{e}} \rightarrow 0$ and $\Gamma_{\mathrm{m}} \rightarrow 0$, two γ solutions exist which have $\alpha = 0$, and $\bar{\beta} = \beta/k_0 = 1.177647$ and 1.786090 (quoted values for number of current basis functions n_x and $n_z = 1$ and spectral expansion terms $n = 200$). One corresponds to a forward wave for nondispersive intrinsic LHMs ($\bar{\beta} = \beta/k_0 = 1.78609$) where the product of the integrated Poynting vector (net power through the cross-section) and phase vector in the z-direction is $\oint \mathbf{P}_z \bullet \beta\hat{\mathbf{z}}\, \mathrm{d}A > 0$ (dA is the differential cross-sectional element) or equivalently $\mathbf{v}_{\mathrm{gl}} \cdot \mathbf{v}_{\mathrm{pl}} > 0$. The other solution is a backward wave for nondispersive intrinsic LHMs ($\bar{\beta} = \beta/\mathrm{k}_0 = 1.177647$) where the product of the integrated Poynting vector and the phase vector in the z-direction is $\oint \mathbf{P}_z \bullet \beta\hat{\mathbf{z}}\, \mathrm{d}A < 0$ or equivalently $\mathbf{v}_{\mathrm{gl}} \cdot \mathbf{v}_{\mathrm{pl}} < 0$. Here $\mathbf{v}_{\mathrm{gl}}$ and $\mathbf{v}_{\mathrm{pl}}$ are, respectively, the group and phase longitudinal velocities. These modes are referred to as fundamental modes in the sense that as $\omega \rightarrow 0$, a solution exists.

As damping loss is turned on and becomes finite, only the larger guided wave eigenvalue solution will exist, and the smaller guided wave solution will cease to exist. One of the effects of utilizing a highly dispersive SRR like substrate is that it converts the forward wave nondispersive solution into a backward wave (at least up to 93 GHz, then it becomes a slightly forward wave until 103 GHz). The fundamental mode is shown in Fig. 10.2 (labeled R1: light blue $\bar{\alpha} = \alpha/k_0$ and green $\bar{\beta} = \beta/k_0$ curves), not extending beyond either 74 GHz on the low end or 105 GHz on the high end because $\mathrm{sg}[\varepsilon_{\mathrm{r}}(\omega)]\mathrm{sg}[\mu_{\mathrm{r}}(\omega)] = -1$, and that product causes evanescent propagation to occur where β is extremely tiny. Below f_{om} and above $f_{\mathrm{mco}}, \mu_{\mathrm{r}} > 0$ and $\varepsilon_{\mathrm{r}} < 0$. However, between these critical frequency points, $\mathrm{sg}[\varepsilon_{\mathrm{r}}(\omega)]\,\mathrm{sg}[\mu_{\mathrm{r}}(\omega)] = +1$ and the wave propagates with $\mu_{\mathrm{r}} < 0$ and $\varepsilon_{\mathrm{r}} < 0$. Out of the range plotted, above the electric cross-over frequency f_{eco} (near f_{pe} for low loss) where effective permittivity $\varepsilon_{\mathrm{r}} = 0$, $\mathrm{sg}[\varepsilon_{\mathrm{r}}(\omega)]\,\mathrm{sg}[\mu_{\mathrm{r}}(\omega)] = +1$ will occur again, with $\mu_{\mathrm{r}} > 0$ and $\varepsilon_{\mathrm{r}} > 0$ this time, being completely reversed from the region between f_{om} and f_{mco}.

Results for the two other modes R2 (dark blue $\bar{\alpha} = \alpha/k_0$ and orange $\bar{\beta} = \beta/k_0$ curves) and R3 (dark magenta $\bar{\alpha} = \alpha/\mathrm{k}_0$ and red $\bar{\beta} = \beta/k_0$ curves) are also shown in Fig. 10.2. They clearly have much higher attenuation than the fundamental mode. These modes do show forward wave behavior where the curve slopes go positive near 77.7 GHz and persist to 80 GHz.

The dispersion curves for the LHM/NPV substrate are plotted for the modes in Fig. 10.2 using $n_x = n_z = 5$ and $n = 500$ with frequency increments of $\Delta f = 0.0025$ GHz between eigenvalue points (only small differences with solutions at $n_x = n_z = 9$ and $n = 900$ and $n_x = n_z = 1$ and $n = 100$ have been found, on the order of less than a few tenths of a percent). At 80 GHz for the fundamental mode, $\bar{\gamma} = (\bar{\alpha}, \bar{\beta}) = (0.0320222, 1.79365)$ for $n_x = n_z = 1$ and $n = 100$, whereas for $n_x = n_z = 9$ and $n = 900$, $\bar{\gamma} = (0.0322745, 1.79116)$. Calculated values used the parameter settings mentioned above at room temperature, but note that Γ_{e} and Γ_{m} could be reduced further using superconductive

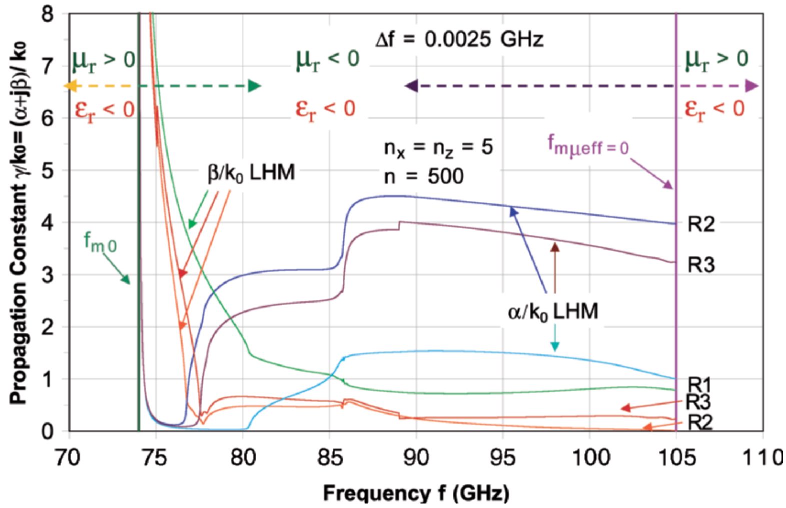

Fig. 10.2. Dispersion curves for LHM structure

metals at reduced temperatures. Permittivity and permeability at 80 GHz are $\varepsilon = (-2.5156, 5.77348 \times 10^{-3})$ and $\mu = (-2.4817, 2.5713 \times 10^{-2})$, corresponding to loss tangents ($\varepsilon_\mathrm{i}/\varepsilon_\mathrm{r}$ or $\mu_\mathrm{i}/\mu_\mathrm{r}$) of 2.28×10^{-3} and 1.04×10^{-2}. The reason why α rises and β falls after this frequency in Fig. 10.2 is that both ε_r and μ_r are becoming ever more positive, providing much less LHM advantage, with the relative rates of change of ε_r and μ_r determining the details of the curves. Of course, once the frequency f_mco is hit, any effective propagation ceases.

10.5 Conclusions

Examination of the fundamental mode at 80 GHz shows that the attenuation compared to the phase behavior is roughly two orders of magnitude smaller ($\beta/\alpha = 56$). This is truly a remarkable result, since by intuition alone, one might have thought that a metamaterial based upon metallic resonant objects would be extremely lossy. And indeed the guided wave structure does present huge losses below 75 GHz which is approaching the magnetic resonance point, while above 80.5 GHz one is entering the region where neither ε_r nor μ_r hold their simultaneous substantial negative real parts and the LHM behavior begins to die out. But between these two bounds, a sizable bandwidth exists where α is relatively tiny compared to β, giving us a freely propagating wave which is allowed by a substrate acting as an LHM, and propagating backward. It is easy to see that indeed in this band the wave is backward, since $v_\mathrm{gl} = \mathrm{d}\omega(k)/\mathrm{d}k = 1/[\mathrm{d}k(\omega)/\mathrm{d}\omega] = 1/[\mathrm{d}k(f)/\mathrm{d}f] < 0$, and inspection of the curve shows $\mathrm{d}k(f)/\mathrm{d}f < 0$.

Even the higher order modes R2 and R3 have low loss bands, but they are much smaller than the fundamental mode, existing between 75 and 76.7 GHz (R2) and 77.5 GHz (R3).

Results from this chapter are taken from [24], where a discussion of the Green's function methodology is presented, along with graphs of effective permittivity $\varepsilon(\omega)$ and permeability $\mu(\omega)$ of the SRR metamaterial.

References

1. C.M. Krowne, Phys Rev. Lett. **92**, 053901 (2004)
2. C.M. Krowne, arXiv.org/abs/cond-mat/0406219 (June 10, 2004)
3. C.M. Krowne, Phys Rev. Lett. **93**, 053902 (2004) γs in this work were $\alpha = 0$ and β(unrotated-stripline) = 2.30195 ($n_x = n_z = 1, n = 200$); β(rotated-stripline) = 2.24643 ($n_x = n_z = 1, n = 200$) and 2.24623 ($n_x = n_z = 5, n = 500$) all asymmetric basis set; β(rotated-microstrip) = 2.11530 asymmetric basis and 2.11604 symmetric basis ($n_x = n_z = 1, n = 200$)
4. C. Luo, S.G. Johnson, J.D. Joannopoulos, J.B. Pendry, Phys. Rev. B **65**, 201104 (2002)
5. C. Luo, S.G. Johnson, J.D. Joannopoulos, J.B. Pendry, Opt. Express **11**, 746 (2003)
6. S. Foteinopoulou, C.M. Soukoulos, Phys. Rev. B **67**, 235107 (2003)
7. P.V. Parimi, W.T. Lu, P. Vodo, S. Sridhar, Nature **426**, 404 (2003)
8. R.A. Shelby, D.R. Smith, S. Schultz, Science **292**, 77 (2001)
9. P. Markos, I. Rousochatzakis, C.M. Soukoulis, Phys. Rev. E **66**, 045601 (2002)
10. N.C. Panoiu, R.M. Osgood Jr., Phys. Rev. E **68**, 016611 (2003)
11. J.O. Dimmock, Opt. Express **11**, 2397 (2003)
12. N.C. Panoiu, R.M. Osgood Jr., Opt. Commun. **223**, 331 (2003)
13. P. Markos, C.M. Soukoulis, Phys. Status Solidi (a) **197**, 595 (2003)
14. P. Markos, C.M. Soukoulis, Opt. Express **11**, 649 (2003)
15. R.B. Greegor, C.G. Parazzoli, K. Li, B.E.C. Koltenbah, M. Tanielian, Opt. Express **11**, 688 (2003)
16. P. Markos, C.M. Soukoulis, Phys. Rev. E **65**, 036622 (2002)
17. D.R. Smith, S. Schultz, P. Markos, C.M. Soukoulis, Phys. Rev. B **65**, 195104 (2002)
18. L. Ran, J. Huangfu, H. Chen, Y. Li, X. Zhang, K. Chen, J.A. Kong, Phys. Rev. B **70**, 073102 (2004)
19. K.J. Webb, M. Yang, D.W. Ward, K.A. Nelson, Phys. Rev. E **70**, 035602 (R) (2004)
20. J. Pendry, A.J. Holden, W.J. Stewart, I. Young, Phys Rev. Lett. **76**, 4773 (1996)
21. J.B. Pendry, A.J. Holden, D.J. Robbins, W.J. Stewart, IEEE Trans. Microw. Theory Tech. **47**, 2075 (1999)
22. S. Ramo, J.R. Whinnery, T. Van Duzer, *Fields and Waves in Communication Electronics* (Wiley, New York, 1967)
23. C.M. Krowne, Int. J. Numer. Model.: Electr. Networks, Dev. Fields **12**, 399 (1999)
24. C.M. Krowne, IET Proc. Microwaves, Antennas & Propag. **1** (2007)

11

Development of Negative Index of Refraction Metamaterials with Split Ring Resonators and Wires for RF Lens Applications

C.G. Parazzoli, R.B. Greegor and M.H. Tanielian

Summary. Metamaterials are engineered ring and wire composites whose response to an incident electromagnetic wave can be described by an effective negative dielectric permittivity ε and magnetic permeability μ. Simultaneous negative ε and μ within a given frequency band of a metamaterial gives rise to a negative index of refraction n. This has been demonstrated via a Snell's law experiment. The electromagnetic properties of many metamaterial structures in the microwave region are investigated through numerical simulations and experiments. A negative index of refraction, n, allows lenses with reduced primary (Seidel) aberrations compared to equivalent positive index lens. This is demonstrated both for cylindrical lenses and spherical lenses, as well as for the gradient index lenses. Detailed field maps of the focal region of the metamaterials lenses are made and compared to a comparable positive index of refraction lens.

This chapter discusses the properties of negative index materials (NIMs), derived from numerical simulations, and compares them with experimental data for a Snell's law wedge and numerous lenses operating in the radio frequency (RF) range. Both cylindrical and spherical lenses are discussed. Specifically in Sect. 11.1, we discuss the physics of NIMs. In Sect. 11.2, we present the details of a Snell's law experiment that proves the existence of a negative refractive index. In Sect. 11.3 we describe the retrieval of the effective ε and μ from the scattering parameters. In Sect. 11.4, we discuss the testing of NIM structures. In Sect. 11.5 the optical properties of NIM lenses are discussed. In Sects. 11.6 and 11.7 the design, test and characterization of NIM lenses are elucidated.

11.1 Electromagnetic Negative Index Materials

The word *meta* is a Greek word meaning beyond. Metamaterials are artificial structures or composites with properties that are *not found or are beyond* naturally occurring materials or compounds. In 1968, Victor Veselago [1] described in a seminal paper the properties of materials where both their electrical permittivity ε and magnetic permeability μ are negative. The presence of simultaneous negative ε and μ gives rise to a negative refractive index. It reverses the Doppler shift and the Čerenkov effect. In 1996, John Pendry suggested a method of effectively obtaining negative permittivity by using an array of thin parallel wires. He did also suggest [2] an approach to obtain an effective negative permeability by using split ring resonator (SRR) patterns. In 2000, physicists at the University of California San Diego [3] demonstrated experimentally for the first time that a sample composed of wires and SRRs effectively displayed a negative index of refraction over a limited frequency range. This negative index material will be referred to as an NIM.

11.1.1 The Physics of NIMs

All known electromagnetic phenomena in a medium are described by the electric field $\mathbf{E}$, the magnetic induction $\mathbf{B}$, and the two auxiliary fields, $\mathbf{D}$, the electric displacement, and $\mathbf{H}$, the magnetic intensity, which describe the macroscopic response of the medium to the applied external fields. We assume harmonic time dependence for the electromagnetic field $\exp(-\mathrm{i}\omega t) = \exp(-\mathrm{i}k_o ct)$. Here k_o is the free-space wave number. The constitutive relations are $\mathbf{B} = \mu(\omega)\mathbf{H}$ and $\mathbf{D} = \varepsilon(\omega)\mathbf{E}$, where μ is the *magnetic permeability dyadic* and ε is the *electric permittivity dyadic*. With these assumptions Maxwell's equations read as

$$\nabla \times \mathbf{H} + \mathrm{i}k_o\varepsilon\,\mathbf{E} = 0, \tag{11.1}$$

$$\nabla \times \mathbf{E} - \mathrm{i}\,k_o\mu\,\mathbf{H} = 0, \tag{11.2}$$

$$\nabla \cdot (\varepsilon\;\mathbf{E}) = 0, \tag{11.3}$$

$$\nabla \cdot (\mu\;\mathbf{H}) = 0. \tag{11.4}$$

The detailed properties of a medium's electromagnetic response are thus contained in μ and ε, which we refer to as the *material parameters*. The range of possible values for these material parameters is limited by fundamental laws such as causality or thermodynamics, and it is broader than the range of naturally occurring materials. Natural occurring materials do not cover the full possible range, but new engineered materials do. When a material exhibits $\varepsilon_{\text{eff}}, \mu_{\text{eff}} < 0$ in a frequency band, it is referred to as a left-handed material (LHM) or NIM. The development of NIMs opens up a new region of parameter space for effective material parameters, as shown in Fig. 11.1. The lower left quadrant is where NIMs reside. NIMs are of particular interest, as a reversal in electromagnetic wave phase velocity takes place.

In an isotropic NIM the *index of refraction* $\mathbf{n}$, is negative. The quantitative statement of refraction is contained in Snell's law, which has the simple form

$$n_1 \sin(\theta_{\mathrm{I}}) = n_2 \sin(\theta_{\mathrm{R}}). \tag{11.5}$$

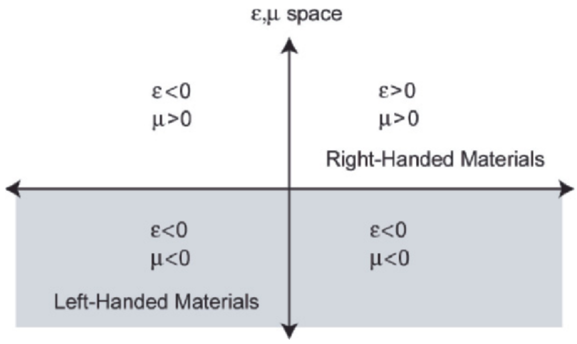

Fig. 11.1. Material parameter space can be conveniently visualized on the ($\varepsilon_{\mathrm{eff}} - \mu_{\mathrm{eff}}$) axes

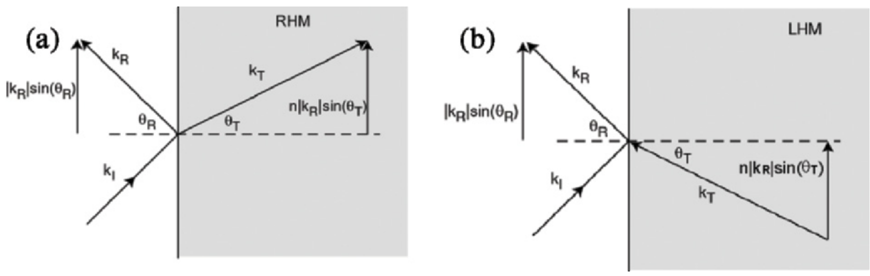

Fig. 11.2. (**a**) Snell's law illustrated for light transmission between two right-handed materials with different indices of refraction. (**b**) Snell's law illustrated for light transmission from a right-handed to a left-handed material

Here $n_{1(2)}$ is the index of refraction of the first (second) medium, and $\theta_{\mathrm{I(R)}}$ is the angle of incidence (refraction). A depiction of Snell's law for right-handed materials (RHM) and LHMs is shown in Fig. 11.2.

The index of refraction n is defined as the square root of the product of the material electrical permittivity and magnetic susceptibility $n^2 = \varepsilon_{\mathrm{eff}}\ \mu_{\mathrm{eff}}$. Most materials have $\varepsilon_{\mathrm{eff}}$ and $\mu_{\mathrm{eff}} \geq 1$; thus light rays are bent toward the normal to the interface, as shown in Fig. 11.2a. In determining the index-of-refraction for the material, we automatically took the positive square root of the product $\varepsilon_{\mathrm{eff}}\mu_{\mathrm{eff}}$, and this is always appropriate when dealing with RHMs. However, when dealing with LHMs, Veselago [1] showed that the *negative square root of* $\varepsilon_{\mathrm{eff}}\mu_{\mathrm{eff}}$ *should be taken.* Thus, NIMs have the unique property of displaying a *negative index of refraction*; i.e., the ray bends in an angle on the other side of the normal to the surface, thereby implying an entirely new regime of optics. This is illustrated in Fig. 11.2b. This property and its experimental verification are discussed in detail in Sect. 11.2 of this chapter. Note also that the direction of propagation of the refracted ray in Fig. 11.2b is drawn such that it propagates backwards. This is another consequence of the negative refractive index: The directions of the group and phase velocities are reversed from that of ordinary or RHMs.

Another unique property of NIMs is the ability to match the vacuum impedance. To illustrate this, we recall that the reflection coefficient of a linearly polarized electromagnetic wave from a surface has the form

$$r_{\perp} = \frac{E''_{\perp}}{E_{\perp}} = \frac{\sqrt{\varepsilon/\mu}\cos(\theta_{\mathrm{i}}) - \sqrt{\varepsilon'/\mu'}\cos(\theta_{\mathrm{r}})}{\sqrt{\varepsilon/\mu}\cos(\theta_{\mathrm{i}}) + \sqrt{\varepsilon'/\mu'}\cos(\theta_{\mathrm{r}})} \tag{11.6}$$

for the electric field perpendicular to the plane of incidence and

$$r_{\parallel} = \frac{E''_{\parallel}}{E_{\parallel}} = \frac{\sqrt{\varepsilon'/\mu'}\cos(\theta_{\mathrm{i}}) - \sqrt{\varepsilon/\mu}\cos(\theta_{\mathrm{r}})}{\sqrt{\varepsilon'/\mu'}\cos(\theta_{\mathrm{i}}) + \sqrt{\varepsilon/\mu}\cos(\theta_{\mathrm{r}})} \tag{11.7}$$

for the electric field parallel to the plane of incidence [4]. Here θ_{i} is the angle of incidence, θ_{r} is the angle of refraction, and the primed quantities refer to the NIM. Observe that the reflectivity vanishes for all incident angles if $\varepsilon = \mu = 1$ on the free space side and $\varepsilon' = \mu' = -1$ on the NIM side. The condition with $\varepsilon' = \mu' = -1$ can be used to build a first surface with zero reflection. This property is important for many applications where a minimum reflection is desired.

The NIM description via an effective ε and μ is predicated on the condition that λ/d ratio becomes large (e.g., >100), where λ is the wavelength of the radiation in the NIM and d the unit cell. We have found empirically that in most cases, even when $\lambda/d \sim 10$, the effective medium approach is quite satisfactory. The medium properties can be derived from single cell scattering parameters values. Thus, it is sufficient in most cases to design a unit cell and derive the effective medium parameters from its scattering parameters. Since the scattering parameters of a unit cell are a function of the geometrical dimensions of the ring(s) and wire(s) the frequency dependent effective medium properties, such as n and the impedance $Z(=\sqrt{\mu/\varepsilon})$, can be tailored to the designer requirements. In the following, we discuss the parameters associated with the unit cell design.

11.1.2 Design of the NIM Unit Cell

Several parameters are considered in the design of NIM unit cell, including dispersion and bandwidth, losses, unit cell size, and periodicity.

(a) *Frequency dispersion and bandwidth limitations.* The only constraints on the material parameter of LHMs are those set by causality. An analysis of the general analytic properties of $\varepsilon_{\mathrm{eff}}$ and μ_{eff} leads to the following conclusions:

$$\frac{\mathrm{d}\left|\varepsilon_{\mathrm{eff}}(\omega)\right|}{\mathrm{d}\omega} \geq 1 \quad \text{and} \quad \frac{\mathrm{d}\left|\mu_{\mathrm{eff}}(\omega)\right|}{\mathrm{d}\omega} \geq 1. \tag{11.8}$$

In work to date, we find that the bandwidth we obtain for the NIM response is typically 5–10% of the operating frequency. We are also generally able to find a frequency range in which $n = -1$ and with $Z = 1$, in all cases.

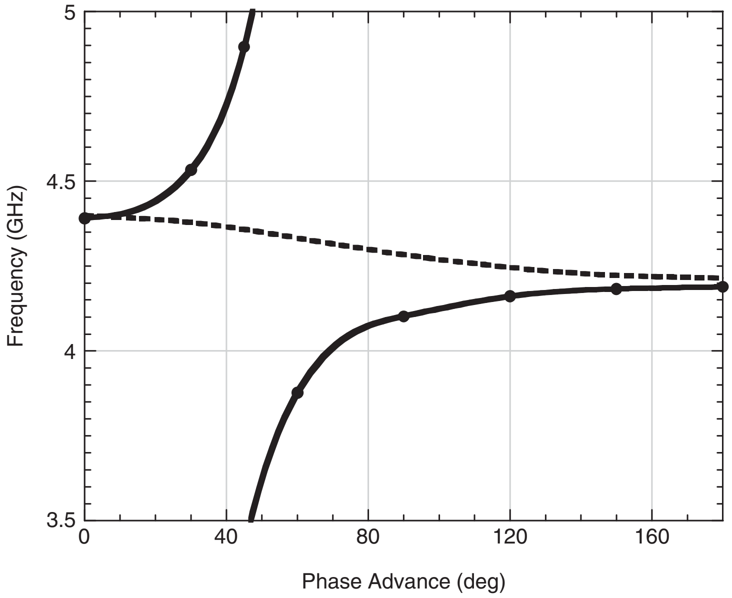

Fig. 11.3. Dispersion plot for left-handed material. The horizontal axis is the phase advance per unit cell, or kd, where k is the wave number

(b) *Losses*. Simulation and experiments show that LHMs exhibit losses. The origin of losses is discussed later in this section. It mainly arises from dielectric losses and ohmic losses. The generic frequency dependence of the effective refractive index for a typical LHM is Lorentzian with a region of negative index of refraction, as indicated in the phase advance diagram of Fig. 11.3, where the dashed line indicates the left-handed frequency band for LHM composed of straight wires and SRR.
The finite conductivity of the materials used for the patterns can lead to significant dissipative losses in LHMs. As is evident from Fig. 11.3, the group velocity ($\mathrm{d}\omega/\mathrm{d}k$), associated with the left-handed band, is very small. Waves propagating through this medium thus interact with the medium for a relatively long time. This phenomenon is similar to waves propagating in waveguides near cutoff, where the dissipative losses due to the low group velocity dominate.
(c) *Size*. The unit cell of an NIM is much smaller than the wavelength of interest. We found that typically it takes 3–4 cells for the effective medium description to be valid. Therefore a sub-wavelength structure can be well described in the effective medium approximation.
(d) *Periodicity*. The unit cell of the NIMs developed consists of conducting wires and SRRs. Because the wavelength of interest is much larger than the unit cells, there appears to be no basic requirement that the underlying structure be truly periodic, although certain elements within a unit cell

may need to have specified relative positions with respect to each other. We have found empirically that fabricated NIM samples are quite tolerant to small degrees of disorder, unlike photonic crystals where small degrees of disorder may lead to complete loss of the negative index of refraction behavior. However, indirect evidence seems to indicate that small degrees of disorder effectively contribute to a reduction in the transmission coefficient.

11.1.3 Origin of Losses in Left-Handed Materials

We define the structure loss as $l = 1 - (S_{11}S_{11}^* + S_{21}S_{21}^*)$. Sources of loss are in general the finite conductivity of the metallic (copper) layer and the loss tangent of the substrate, along with other materials that may be used to construct the sample, such as adhesives and binders. These losses can be minimized or amplified [5,6], depending on the type of resonant structure used. For instance, in Fig. 11.4 we calculate the losses for two different, identified as 402 and 901, ring and wire structures. The 402 structure is topologically similar to the 901, but is more compact (by a factor of ∼4–5) in the ring radial and azimuthal gap regions. What we find is that smaller rings gaps have higher losses because they tend to generate higher electric fields and which gives rise to increased dielectric loss.

The loss tangent is $l_t = \varepsilon''/\varepsilon'$, where ε' and ε'' are the real and imaginary part of the dielectric constant $\varepsilon = \varepsilon' - i\varepsilon''$, respectively. As shown in Fig. 11.4, the loss as expected increases with l_t. The loss is highest when the dielectric

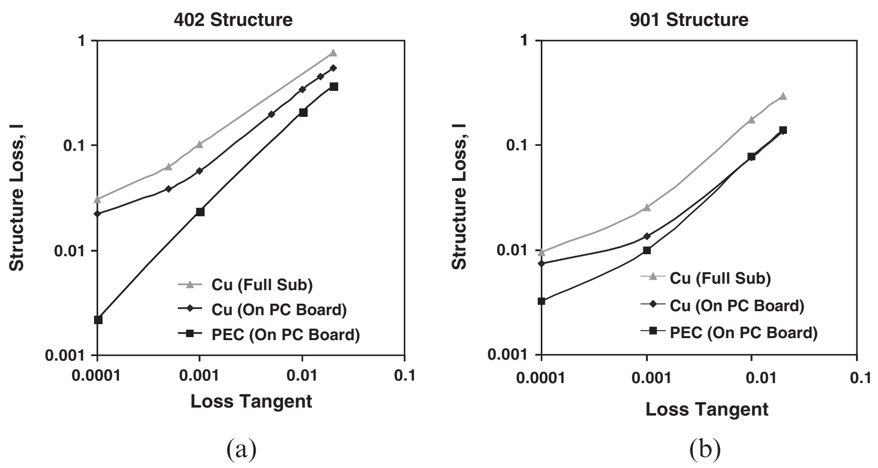

Fig. 11.4. Simulated losses at the pass-band peak for the (**a**) 402 and (**b**) 901 structures. The pass-band peaks are at ∼10 GHz for the 402 structure and at ∼13.5 GHz for the 901 structure. Full Sub refers to the copper patterns on a substrate without any voids and PEC is for a perfect electrical conductor

completely fills the cell. This corresponds to the upper curves (triangles). The loss decreases when the conductive elements are deposited on a thinner 0.025 cm substrate (PC board) as shown by the middle curves (diamonds). When the copper losses are omitted from the simulation, the results for a thin PC board substrate are given by the lower curves (squares). The copper conductive losses dominate, as expected, at low values of the dielectric loss tangent. The trends exhibited by these simulations have also been observed in our experiments.

As mentioned earlier, dielectric losses are concentrated in the high field regions. These numerical simulations are shown in Fig. 11.5. It is obvious from these results that the small gaps concentrate the fields more. It is also noticeable that the losses are limited to narrow regions surrounding the gaps. The 402 structure, which has an azimuthal gap 4.6 times smaller than the 901 structure, has a maximum power loss density $\sim$17 times higher. Therefore, one possibility in the fabrication would be to remove the dielectric in the region of high fields in order to significantly reduce the loss.

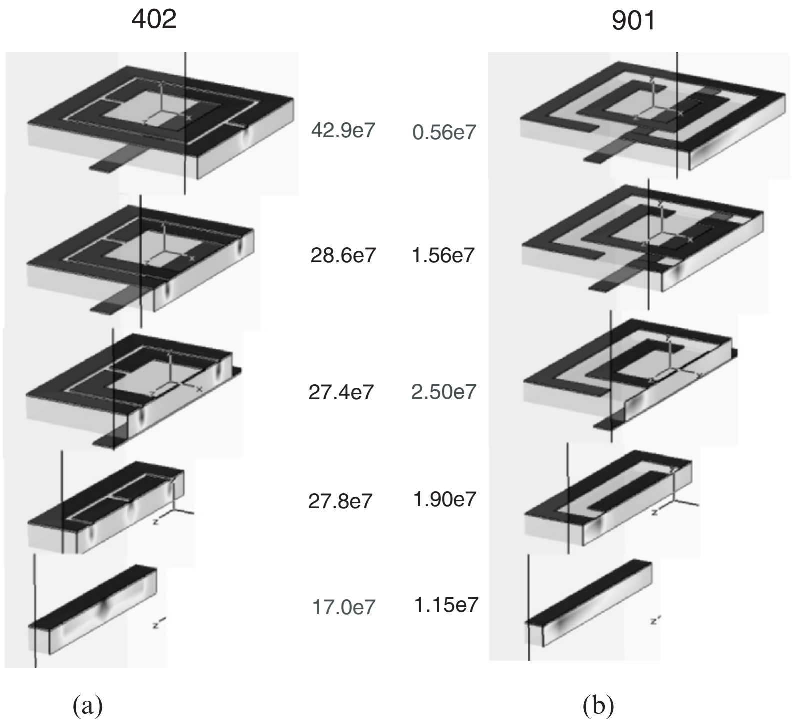

Fig. 11.5. Simulated power loss density in *gray* scale (**a**) the 402 structure and (**b**) the 901 structure. The numbers in the diagram indicate the maximum power loss density at the highlighted x = constant plane indicated. Note that the power loss density is greatest in the regions of the azimuthal gaps, and the structure with the smallest gaps (402) has the highest power loss density

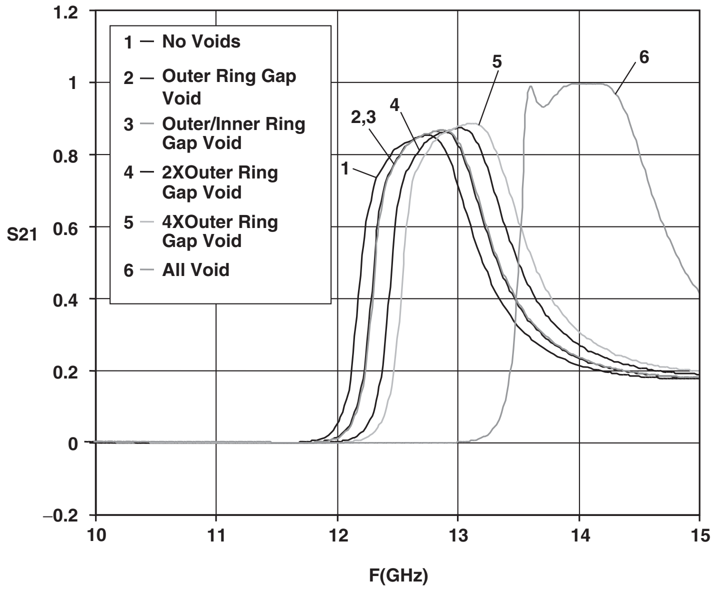

Fig. 11.6. Increase in transmission with the introduction of voids in the vicinity of the ring gaps in the 901 HWD structure. HWD (high wire density) refers to a structure having two wires per unit cell instead of the nominal one wire

The effect on S21 (transmission) of removing the substrate material in the vicinity of the outer ring gap is shown in Fig. 11.6. Here we show S21 for no voids, introduction of a void in the outer ring gap, voids in the outer and inner ring gap, doubling the size of the outer ring gap, quadrupling the size of the outer ring gap, and completely removing the substrate. The observed effect is to increase the transmission from approximately $\sim$0.83 to $\sim$1.00. It additionally shifts the pass band to higher frequencies due to the reduction in capacity of the structure.

When a lossy material, such as an adhesive, is placed on top of the rings in order to join one sheet of unit cells to the next sheet (high field region), even though the material is thin, the effect can be significant, as discussed earlier. This is shown in Fig. 11.7, where a 2 mil layer of adhesive was simulated on top of the ring structure. As the loss tangent of the adhesive layer was raised from 0.01 to 0.10 the transmission dropped from $\sim$0.95 to $\sim$0.70. Experimentally we observed this effect by removing the adhesive layer from the 901 HWD structure. In this experiment the adhesive used had a loss tangent of $\sim$0.016. When removed, the transmission increased from $\sim$0.80 to $\sim$0.90. This illustrates that care must be exercised in how NIM structures are fabricated. The use of low loss materials, especially around the ring gaps, is critical to lowering the losses.

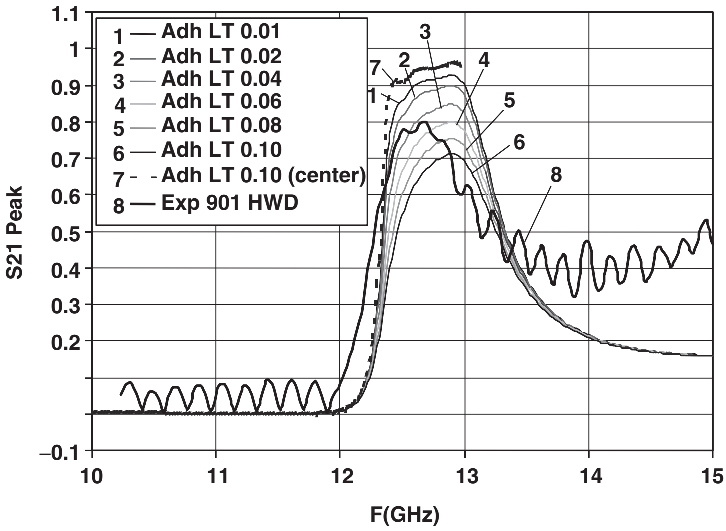

Fig. 11.7. Increase in transmission with the reduction of the loss tangent (LT) of the adhesive used to construct the 901 HWD structure. Curve 8 represents the experimental data

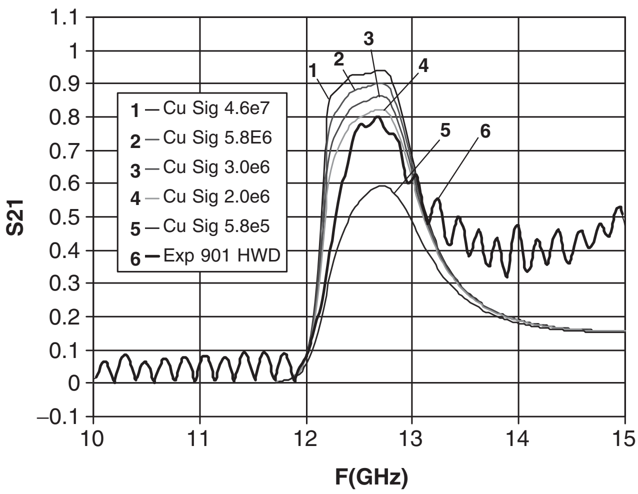

Fig. 11.8. Increase in transmission with the increase of metal conductivity (Sig in units of $\mathrm{S\,m^{-1}}$) used to construct the 901 HWD structure. Curve 6 represents the experimental data

In Fig. 11.8 we show the effect of changing the conductivity of the copper used for the rings and wires. In this simulation the transmission changed from $\sim$0.60 to $\sim$0.95 as the conductivity increased from 5.8×10^5 to $4.6\times10^7\,\mathrm{S\,m^{-1}}$. Finally, the thickness of the metallic layer also affects the structure loss, l.

Approximately five skin depths are needed to reduce the loss to acceptable values. The structure loss l, follows the empirical power law $l = 0.26t_h^{-0.56}$, where t_h is the layer thickness. This power law was obtained from the simulation results.

The above simulations and experiments have increased our understanding of the loss mechanisms in NIMs. These studies allow for the minimization of the NIM losses.

11.1.4 Reduction in Transmission Due to Polarization Coupling

We numerically calculated the transmission properties of a lattice of SRR for different polarizations and propagation directions [7]. As reported in the literature, we found that the incident electric field can couple to the magnetic resonance of the SRR when the incident electric field is polarized parallel to the sides of the SRR with the gaps. This is manifested by a dip in the transmission, T. This is shown in Figs. 11.9–11.12.

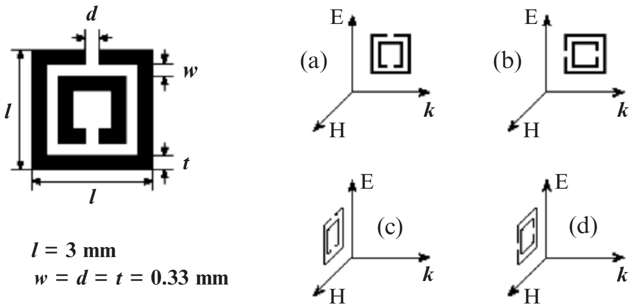

Fig. 11.9. The four orientations of the SRR with respect to the triad, k, E, H, of the incident EM field examined. Two additional orientations where the SRRs are on the H, k plane, produce no electric or magnetic response

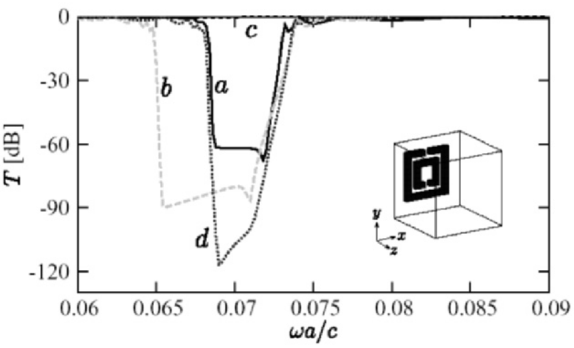

Fig. 11.10. Calculated transmission spectra of a lattice of SRRs for the four different orientations shown in Fig. 11.9. Curve c practically coincides with the axis

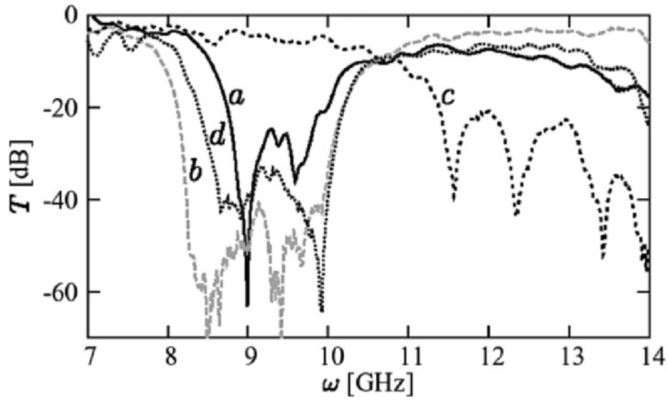

Fig. 11.11. Measured transmission spectra for a lattice of SRRs in the four different orientations shown in Fig. 11.9 and simulated in Fig. 11.10. There is reasonable qualitative agreement between theory and experiment

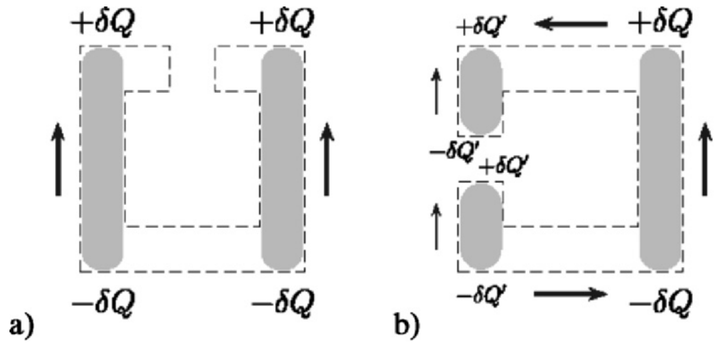

Fig. 11.12. A simple drawing showing the polarization currents in the two different orientations of a single ring SRR. In case (**a**) there is no net current, while in case (**b**) there is net current

Simulations with the gaps of the SRRs closed show that there is no dip in T. This is a standard technique we have used throughout, to verify that the dip in the transmission is due to the presence of the SRRs, rather than some other spurious effect. The discretization used in the calculation of one particular SRR is shown in inset of Fig. 11.10.

A simple explanation for the observed behavior is shown in Fig. 11.12. The external electric field produces opposing currents in the legs of the SRR. In case (a) there is no magnetic response because the two currents are balanced. However, in case (b) there is a difference in the magnitude of induced currents between the two sides of the wire, which allows a net current to flow around the ring and thus produce a magnetic response.

11.1.5 The Effective Medium Limit

The determination of the limit, in which the effective medium description is valid, is critical. This requires the identification of the minimum number of unit cells to which the effective medium theory can be applied. This question was addressed by simulating different numbers of unit cells in the direction of propagation and then observing the phase velocity reversal along those cells. The simulation model is shown in Fig. 11.13. The results for one, three, and six unit cells in the direction of propagation are given in Figs. 11.14–11.16, respectively. In these figures the phase velocity is given by $V_{\mathrm{p}} = \mathrm{d}z/\mathrm{d}t = c/n$, where a negative value corresponds to a negative index of refraction. From these figures it can be seen that the phase velocity is positive having a value of c before entering and after exiting the cell array. In the presence of a single cell, see Fig. 11.14, a definite sign reversal is already evident in the cell. Figure 11.15 shows that three cells behave like an effective medium. Henceforth, in the NIM designs, we have typically used at least four unit cells in the direction of propagation, to ensure that we are well within the effective medium behavior of the material.

11.1.6 NIM Indefinite Media and Negative Refraction

The most common type of NIM consists of a lattice of wires and SRRs on the same plane, which is the (E, k) plane of the incident electromagnetic wave. For this lattice the ε and μ dyadic have the form

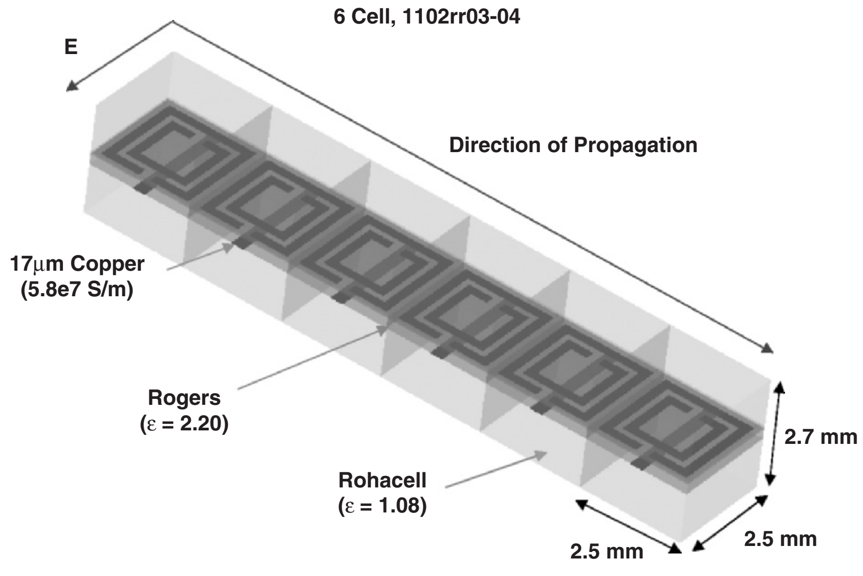

Fig. 11.13. Simulation geometry used for determination of the number of cells needed to produce a negative index of refraction

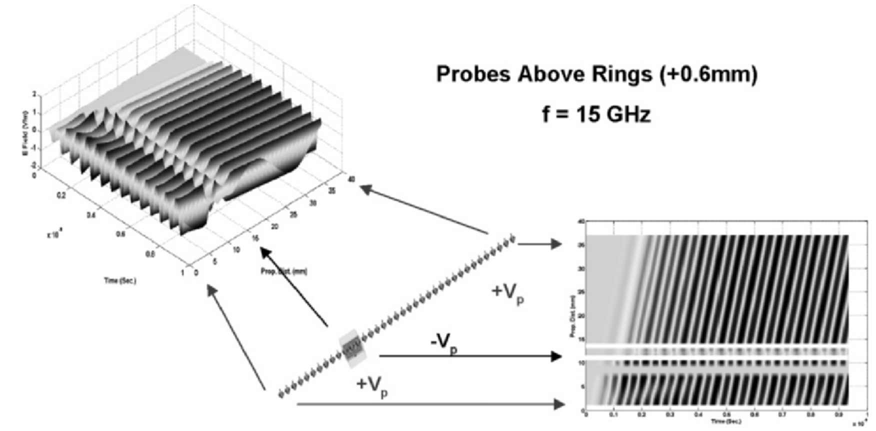

Fig. 11.14. E-field plots and phase velocity (V_p) for one cell in direction of propagation

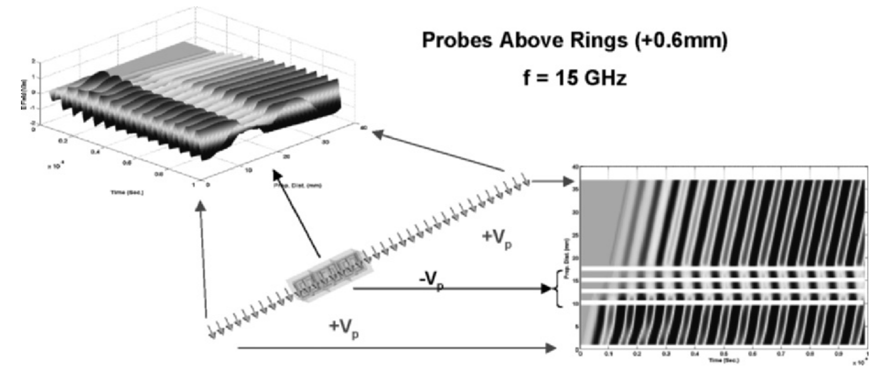

Fig. 11.15. E-field plots and phase velocity (V_p) for three cells in direction of propagation

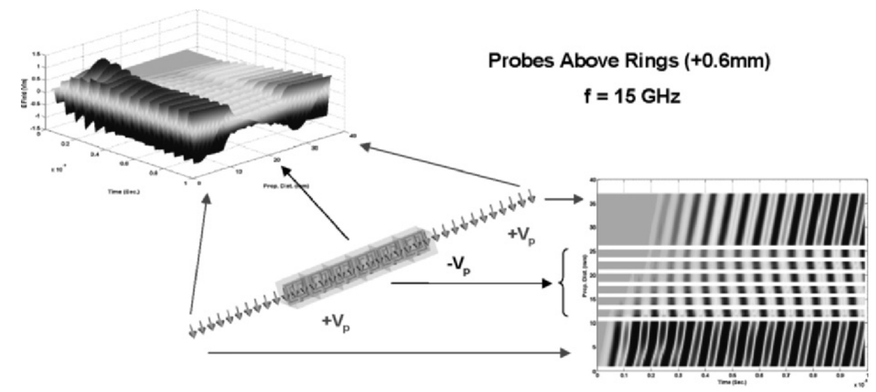

Fig. 11.16. E-field plots and phase velocity (V_p) for six cells in direction of propagation

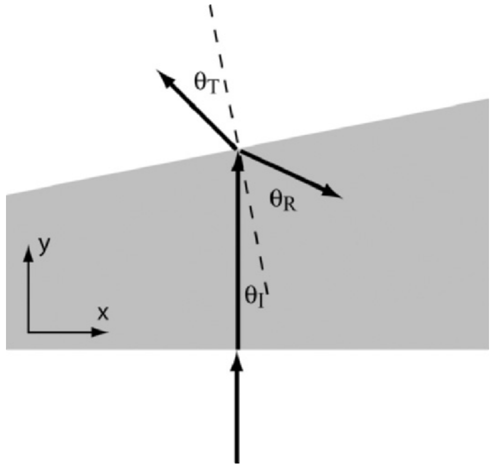

Fig. 11.17. In a typical negative refraction experiment in an anisotropic material, a wave from free space enters a wedge sample at the flat face, undergoing refraction at the second interface. There is in general a reflected wave in the material, although the wave vector associated with the reflected wave does not have to have the same magnitude as the wave vector associated with the incident wave. Nor is it necessary that $\theta_{\mathrm{R}} = -\theta_{\mathrm{I}}$

$$\overleftrightarrow{\varepsilon} = \begin{pmatrix} \varepsilon_x & 0 & 0 \\ 0 & 1 & 0 \\ 0 & 0 & 1 \end{pmatrix} \text{ and } \overleftrightarrow{\mu} = \begin{pmatrix} 1 & 0 & 0 \\ 0 & \mu_y & 0 \\ 0 & 0 & 1 \end{pmatrix} . \tag{11.9}$$

Thus, this material would have negative permittivity along the x-axis and negative permeability along the y-axis, but along the z-axis would have positive permittivity and permeability. This was the type of NIM used in the Snell's law experiment, which is discussed in Sect. 11.2.

The depiction of a typical negative refraction experiment is shown in Fig. 11.17. If the medium were isotropic, having a negative refractive index in all directions, then the phase and group velocities in the medium would be anti-parallel. Note that in the figure the arrows in the medium represent the direction of energy flow, not wave vectors.

For an anisotropic medium the material properties are described by tensors rather than scalars for the permittivity and permeability, i.e.

$$\overleftrightarrow{\varepsilon} = \begin{pmatrix} \varepsilon_{xx} & 0 & 0 \\ 0 & \varepsilon_{yy} & 0 \\ 0 & 0 & \varepsilon_{zz} \end{pmatrix} , \quad \overleftrightarrow{\mu} = \begin{pmatrix} \mu_{xx} & 0 & 0 \\ 0 & \mu_{yy} & 0 \\ 0 & 0 & \mu_{zz} \end{pmatrix} \tag{11.10}$$

It has been shown [8] that when the permittivity and permeability tensors of a material are *indefinite* (i.e. not all the tensor elements having the same sign) the resulting dispersion properties can be quite distinct from isotropic media. In particular, for the type of anisotropic material used in the Snell's law experiment to be discussed later, the dispersion is hyperbolic rather than elliptical, as would be the case for an isotropic material. The dispersion of a material at a given frequency can most easily be visualized by viewing its *isofrequency* surface. Figure 11.18 provides an illustration of negative refraction in both isotropic and anisotropic media, based on the isofrequency curves of the two types of media. We assume for these diagrams that a wave is incident from free space on the interface to either (a) an *isotropic* index medium, or (b) an *indefinite* index medium in which $\mu_x = -1,\ \varepsilon_z = -1$ and all other components are equal to unity.

The general relationship between the directions of energy and phase velocity for waves propagating within an indefinite medium can be found by calculating the group velocity, $\vec{\mathbf{v}}_{\mathrm{g}} \equiv \nabla_q \omega(\vec{\mathbf{q}})$. $\mathbf{v}_{\mathrm{g}}$ specifies the direction of energy flow for the plane wave, and is not necessarily parallel to the wave vector. $\nabla_q \omega(\boldsymbol{q})$ must lie normal to the isofrequency contour, as illustrated in Fig. 11.18.

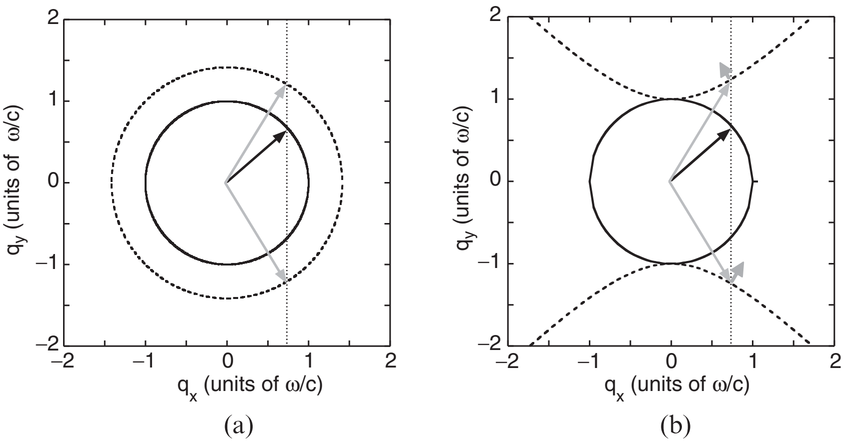

Fig. 11.18. (**a**) Refraction from free space into an *isotropic* material, illustrated using isofrequency curves. The wave vector of the incident wave, shown as the *black arrow*, must lie on a circle. The isofrequency curve of the medium, whose index has magnitude greater than unity, is represented by the dashed circle. Because the parallel component of the wave vector must be conserved, the wave vector solutions in the medium are those points on the isofrequency curve that intersect the parallel *dotted line* defined by the q_x value of the incident wave vector. If the index is negative, q_y is negative, so that the lower wave vector solution is taken. In this case the phase and group (not shown) velocities are anti-parallel. (**b**) Corresponding isofrequency curve for refraction from free space into an *indefinite* medium. Here the isofrequency contour is hyperbolic and the phase and group velocities are not anti-parallel as shown (*small arrows*)

The example of Fig. 11.18 does not correctly describe the actual Snell's law refraction experiment performed. In the experiment, the incident wave propagates within the medium along a principal axis (the wave does not refract at the first interface, but then refracts at the second interface into free space). The fact that the incident wave always travels along the principal axis makes the refraction experiment quite distinct from the scenario of Fig. 11.18.

Figure 11.19 shows the isofrequency diagram and the equivalent refraction diagram for refraction from the second interface. It shows that if an incident wave propagates within the indefinite material along the principal axis, then negative refraction always occurs at the outgoing interface to free space. In fact, the isofrequency curves show that the *angle of negative refraction from the indefinite medium is identical to that which would occur from an isotropic medium*. This means that the anisotropic wedge sample used in the Snell's law experiments can be expected to yield the exact refraction angles as if the wedge were isotropic.

It is of practical importance that an indefinite medium can yield refraction results identical to those of an isotropic medium. Anisotropic samples are much easier to design and fabricate than are isotropic structures. Thus, a plano-concave focusing lens made from an indefinite medium should have

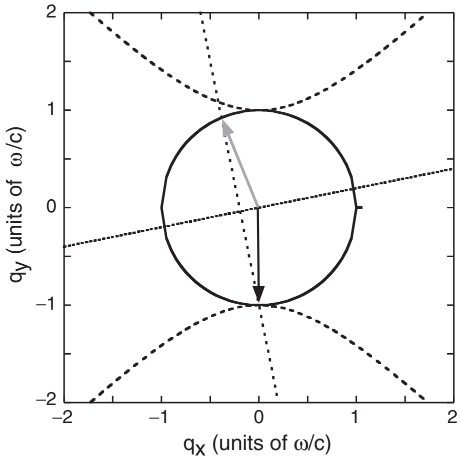

(a)

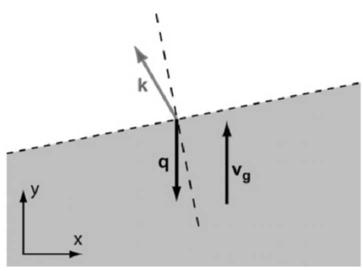

(b)

Fig. 11.19. (**a**) Isofrequency diagram showing refraction from an indefinite medium into free space. The incident wave propagates along the principal axis, for which phase and group velocities are reversed. See (**b**). The component of the incident wave vector parallel to the interface is conserved, leading to the dashed line shown in (**a**). The intersection of this line with the isofrequency curve for free space determines the outgoing wave vector, which is negatively refracted. Note that this construction clearly shows that the *angle of refraction from an indefinite medium is identical to that from an isotropic medium*

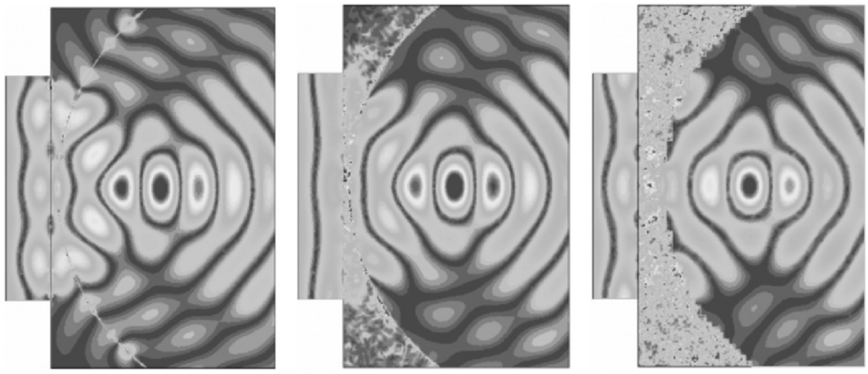

Fig. 11.20. (**a**) The field distribution at the focus of a left-handed (negative index) lens. In this case, the index has a value of $n = -1(\varepsilon = -1, \mu = -1)$. In this simulation, the radius of curvature of the lens was $R = 6\,\mathrm{cm}$, with a wavelength chosen at $\lambda = 3\,\mathrm{cm}$. (**b**) The field distribution at the focus of a concave lens made of *negative refracting* indefinite media, for which $\varepsilon_z = -1$ and $\mu_x = -1$. All other material parameters are equal to unity. The axes are such that z is out of the plane, y is along the direction of propagation, and x is perpendicular to the direction of propagation. The field is polarized such that the electric field is along the z-axis. (**c**) The field pattern for the same type of lens as in (**b**), but with a step pattern introduced to mimic the finite unit cell size of a typical NIM

about the same focal properties as the equivalent lens made from isotropic media at the polarization of the NIM media. The numerical results [9] are shown in Fig. 11.20. From the preceding analysis it becomes apparent how to design an anisotropic NIM lens that has focusing properties that are quite similar to those of an isotropic lens. This topic is discussed in detail in Sects. 11.6 and 11.7, where the solution of the eikonal equation in its most general case is given [10] e.g., in the case of an anisotropic, inhomogeneous sample. It is also confirmed by the ray tracing diagram of Fig. 11.21b for which either an isotropic or an anisotropic medium produce nearly the same focus. Note also that in either case, isotropic or anisotropic, the plano-concave lens has a reduced spherical aberration, which is another advantage specific to negative refracting materials.

11.2 Demonstration of the NIM Existence Using Snell's Law

A convincing demonstration for the existence of negative index of refraction in a metamaterial is a Snell's law experiment [11]. To this end, we first made simulations utilizing the ab initio Maxwell's equations solvers, Microwave Studio (MWS) and MAFIA [12], followed by material construction and free space

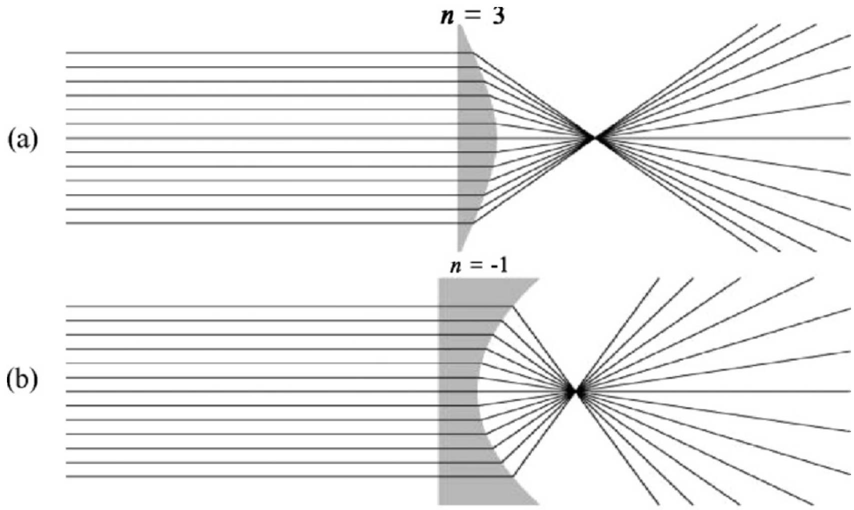

Fig. 11.21. (**a**) Ray tracing diagram for a positive index lens corrected for spherical aberration. (**b**) An $n = -1$ plano-concave lens, either isotropic or anisotropic, is inherently free from spherical aberration

testing. To save valuable computer time, the computational region was terminated in the proximity of the exit face of the wedge. To compute the fields at the various detector positions downstream from the wedge surface (so that we could compare the simulation results with the experimental data), we developed a propagator based on the Helmholtz–Kirchhoff theorem. This propagator requires as input only the MAFIA computed fields and their derivatives at the exit face of the wedge. It then evaluates the fields at a user-requested position.

In our experiments and unit cell numerical simulations a 1E1H NIM structure was used. A 1E1H structure is defined as a structure where the ring and wire patterns reside on one set of parallel planes only, whereas for a 2E2H structure the patterns are on two sets of orthogonal parallel planes. In general, we refer to a structure as having *mEmH* structure depending on the number of polarizations, m, of the electric and magnetic wave it couples with. Indeed, for the verification of NIM behavior using Snell's law, it is not necessary to use a 2E2H structure as discussed above. The elementary cell structure used for our investigations was the 901 high wire density (HWD) structure shown in Fig. 11.22. In a 1E1H NIM, the effective permittivity and permeability tensors, in the coordinate system of Fig. 11.22, where x is the direction of propagation, are given, respectively, by $\overleftrightarrow{\varepsilon} = (1, 1, \varepsilon_z)$ and $\overleftrightarrow{\mu} = (1, \mu_y, 1)$. Here the SRR generates the negative permeability μ_y, and the metal strip in the z-direction (the wire) generates the negative permittivity ε_z. The SRR and wire are deposited on a low loss dielectric substrate.

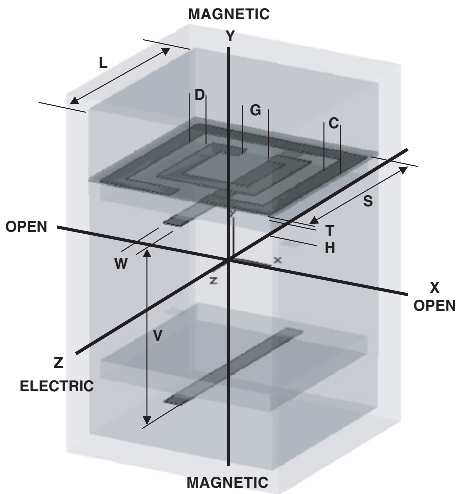

Fig. 11.22. Unit cell of the 901 HWD structure used in the numerical simulations showing boundary conditions. The direction of propagation of the electromagnetic field is along the x-axis, the electric field is oriented along the z-axis, and the magnetic field along the y-axis. $C = 0.025\,\text{cm}$, $D = 0.030\,\text{cm}$, $G = 0.046\,\text{cm}$, $H = 0.0254\,\text{cm}$, $L = 0.33\,\text{cm}$, $S = 0.263\,\text{cm}$, $T = 17.0 \times 10^{-4}\,\text{cm}$, $W = 0.025\,\text{cm}$, and $V = 0.255\,\text{cm}$

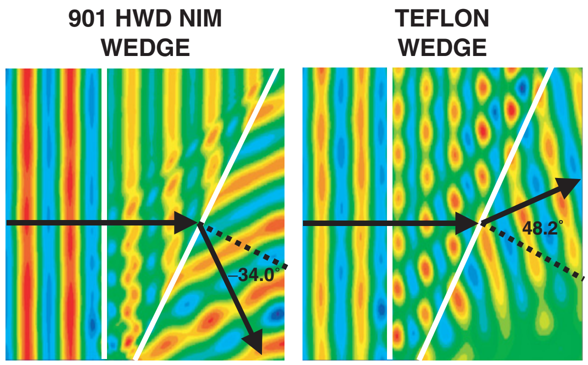

Fig. 11.23. Contour plots, in the $z = 0$ plane (medium plane of the experiment), of the E_z component of the electric field as computed by MAFIA at 12.6 GHz. The radiation propagates from left to right along the x-axis. The wedge angle = $32°.19$

The results of the MAFIA effective medium numerical simulations are shown in Fig. 11.23 for an NIM wedge and a control Teflon wedge. The pulse travels from left to right, in the positive x-direction. The contour plots of the E_z component of the electric field are shown for the Teflon (reference) and the NIM wedges. The wave fronts emerging from the wedge are clearly

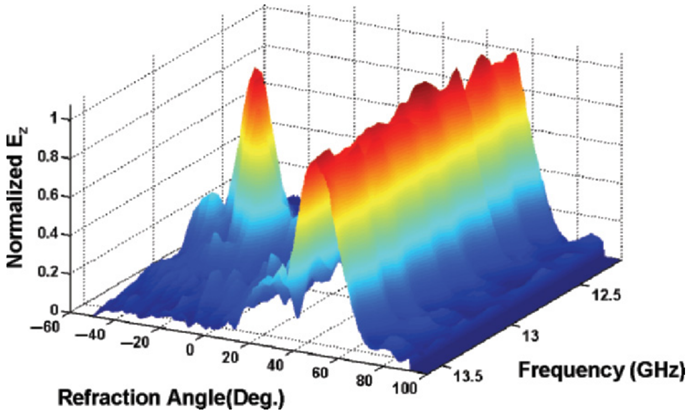

Fig. 11.24. Surface plot of the measured normalized peak amplitude of the electric field component $E_z\,(r, f)$ for the Teflon and 901 HWD NIM wedge. The electric field refracted by the Teflon wedge is independent of frequency at a positive refraction angle, while the electric field refracted by the NIM peaks at a negative refractive angle, which is a function of frequency. The two peaks are not normalized by the same factor. The non-normalized value of the peak electric field of the NIM sample is about 20% of the Teflon peak

deflected in opposite directions for the two materials. We explored numerically the effect of increasing the material losses. The losses were increased up to two orders of magnitude over the experimentally observed values. The computed refracted angle was unchanged.

The experimental data from the refraction experiments are shown in Fig. 11.24. One can clearly see that the data corresponding to the Teflon wedge are independent of frequency, as expected. Conversely, the data from the negative wedge shows the dispersive nature of NIMs.

We performed a quantitative comparison between the measured and computed $E_z(r, f) = 12.6\,\mathrm{GHz}$ angular profiles at constant frequency for two radial locations of the detector at 33 and 66 cm. This experiment was very important because initial critics of the existence of LHMs had argued that left-handed effects are near-field phenomena and are "unphysical" at the far field. We have shown experimentally that the angular distribution at 33 and 66 cm both show identical negative refraction angles. Furthermore, the peak values, normalized to the Teflon reference, show identical decay characteristics as one would expect from an RHM. These data clearly refute their assertions. The data is given in Fig. 11.25.

The simulations predict accurately the measured near-field angular distribution. The far-field angular distribution, as explained above, was based on the Helmholtz–Kirchhoff theorem. The simulation results are shown together with the experimental data in Fig. 11.26.

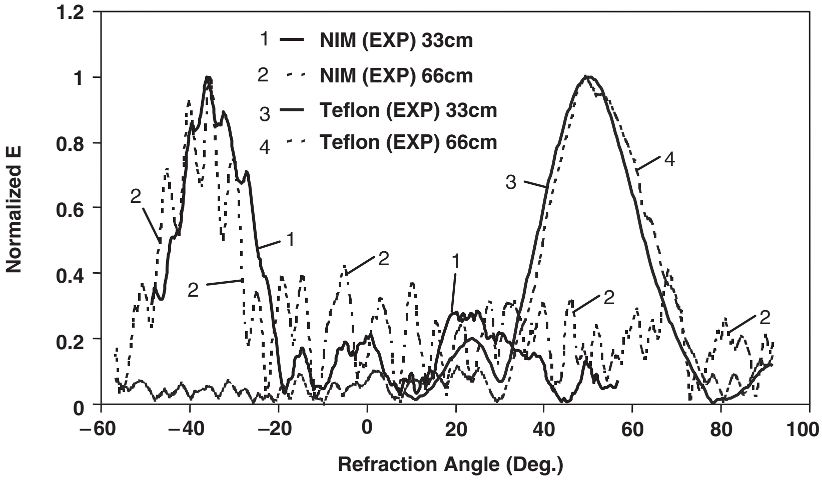

Fig. 11.25. Measured angular profile of the normalized electric field amplitude $E_z(r)$, at a constant frequency $f = 12.6$ GHz for detector distances of 33 and 66 cm both from the Teflon and 901 HWD NIM wedges. The intensity of the left-hand band at the two locations is normalized by the ratio of the intensity of the Teflon at those same locations

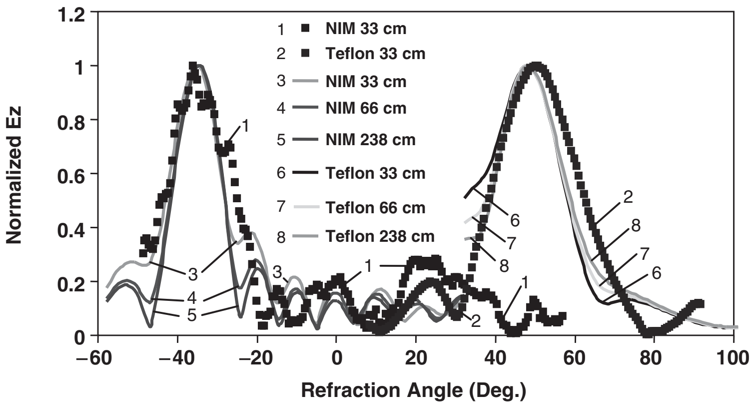

Fig. 11.26. Measured (*squares*) and MAFIA-simulated (*solid curves*) angular profiles of the normalized electric field amplitude $E_z(r)$, at constant frequency $f = 12.6$ GHz for detector distance of 33, 66, and 238 cm

11.3 Retrieval of ε_{eff} and μ_{eff} from the Scattering Parameters

When NIMs are exposed to electromagnetic radiation at wavelengths that are much larger than the unit cell dimensions, we expect that the electromagnetic waves do not "see" the details of the internal structure of the unit cell, but rather experience a homogeneous effective medium. In that case, effective material functions $\varepsilon(k)$ and $\mu(k)$, where k is the vacuum wave vector, might be attributed to NIMs. In the following we will derive the scattering amplitudes for a homogeneous slab at normal incidence and provide an inversion procedure to obtain material constants from the scattering amplitudes that satisfy the derived continuum scattering formulae. This allows the assignment of a set of effective material constants $\varepsilon(k)$ and $\mu(k)$ by considering the numerical scattering data of the NIM. This continuum scattering amplitude would then be subject to inversion using the continuum scattering formulae [13].

11.3.1 Homogeneous Effective Medium

For the transfer matrices T_0 for a single slice of vacuum and T_{slab} for a single slice of homogeneous material having thickness d, in wave-representation

$$T_0\,(d) = \begin{pmatrix} \mathrm{e}^{\mathrm{i}kd} & 0 \\ 0 & \mathrm{e}^{-\mathrm{i}kd} \end{pmatrix}, \qquad T_{\mathrm{slab}}\,(d) = \begin{pmatrix} \alpha\,(d) & \beta\,(-d) \\ \beta\,(d) & \alpha\,(-d) \end{pmatrix}, \tag{11.11}$$

where

$$\alpha\,(d) = \cos(qd) + \mathrm{i}/2(z + 1/z)\sin(qd), \tag{11.12}$$

$$\beta(d) = \mathrm{i}/\exp(z - 1/z)\sin(qd). \tag{11.13}$$

In the continuum formulation and for normal incidence the momentum q inside the slab is related to the momentum k in the vacuum by the index of refraction $n(k) = q/k$, the impedance z is defined by $\mathrm{z} = \mu(\omega)k/q = q/(\varepsilon(\omega)k)$ for the TE and TM mode, respectively. Here, $\mu(\omega)$ and $\varepsilon(\omega)$ denote the frequency-dependent complex permeability and permittivity of the homogeneous medium. Using the interrelation between the transfer matrix and the scattering matrix which defines the transmission $t_{\mp}$ and reflection $r_{\mp}$ amplitudes ($-$ right traveling wave, $+$ left traveling wave)

$$S = \begin{pmatrix} t_+ & r_+ \\ r_- & t_- \end{pmatrix}, \qquad T = \begin{pmatrix} t_+ - r_+ t_-^{-1} r_- & r_+ t_-^{-1} \\ -t_-^{-1} r_- & t_-^{-1} \end{pmatrix}, \tag{11.14}$$

we can calculate the transmission and reflection amplitudes for a sample composed of a left vacuum slice of length a, followed by N homogeneous unit cells of length L in the propagation direction, and terminated by a right vacuum slice of length b,

$$t_- = \frac{\mathrm{e}^{-\mathrm{i}kNL}}{\alpha\,(-d)\,\mathrm{e}^{-\mathrm{i}k(a+b)}}, \tag{11.15}$$

$$r_+ = \mathrm{e}^{-\mathrm{i}kNL}\beta(-d)\mathrm{e}^{-\mathrm{i}k(a-b)}t_-. \tag{11.16}$$

It is convenient to introduce the normalized scattering amplitudes T and R which, after N unit cells, take the form

$$T = -t_{-}\mathrm{e}^{\mathrm{i}kNL} = \alpha^{-1}(-d)\mathrm{e}^{\mathrm{i}k(a+b)} \tag{11.17}$$

$$R = \beta(-d)\mathrm{e}^{-\mathrm{i}k(a-b)}T \tag{11.18}$$

Now we can resolve the above scattering formulae with given amplitudes T and R obtained from the simulation (or measurement) of an NIM with respect to the material parameters, impedance $z(\omega)$, and index of refraction $n(\omega)$. If the solutions are (virtually) independent on the length of the sample, those parameters define the homogeneous effective medium (HEM) representation (or approximation) of the respective NIM. Then we have

$$z_{\mathrm{eff}}(\omega) = \pm\sqrt{\frac{(1+R)^2 - T^2}{(1-R)^2 - T^2}}, \tag{11.19}$$

$$n_{\mathrm{eff}}(\omega) = \pm\frac{1}{kL}\cos^{-1}\left(\frac{1 - R^2 + T^2}{2T}\right) + \frac{2\pi}{kL}m \tag{11.20}$$

with m an integer. Note that we obtain $\mathrm{z}_{\mathrm{eff}}$ and n_{eff} from the scattering amplitudes only, up to a common sign and the real part of the effective index of refraction, $\mathrm{Re}\, n_{\mathrm{eff}}$ only as a residue class. The relative sign of z_{eff} and n_{eff} is fixed by T and R. For known $n_{\mathrm{eff}}(\omega)$ and $z_{\mathrm{eff}}(\omega)$ the effective permeability and permittivity are defined as $\mu_{\mathrm{eff}}(\omega) = n_{\mathrm{eff}}(\omega) z_{\mathrm{eff}}(\omega)$ and $\varepsilon_{\mathrm{eff}}(\omega) = n_{\mathrm{eff}}(\omega)/z_{\mathrm{eff}}(\omega)$.

11.3.2 Lifting the Ambiguities

As shown above, the $n(k,d)$ and $z(k,d)$ obtained from the inversion of the transmission and reflection amplitudes are subject to certain degree of ambiguity. In general, this is the most information one can get from scattering data at normal incidence. However, one can exploit other available information to rule out some of the possible solutions obtained above. In the following, we discuss several of these possibilities.

Causality Arguments

The physical solutions we seek are a subset of the solutions of the Maxwell's equations that obey certain constraints. First of all, our NIMs at best absorb energy from the electromagnetic field penetrating it, i.e., they are passive. This requires that the imaginary part of n to be non-negative, $\mathrm{Im}\, n(k,d) \sim 0$. Further, the reflected power on a single interface cannot exceed the incident power. Therefore the real part of z has to be also non-negative, $\mathrm{Re}\, z(k,d) \sim 0$. These two conditions determine the remaining common sign in the inversion above, rendering $z(k,d)$ and $\mathrm{Im} n(k,d)$ unambiguous.

Length Independence

Now we are left with the ambiguity of the real part of n only. The solutions of the retrieval for the index of refraction constitute a residue class $n(k,d)$ $(\bmod 2\pi/(kd))$. As we have to eventually deal with data from numerical simulations and experimental measurements, we can safely assume that all numbers we will encounter are rational (complex). The main problem with the ambiguity of the real part of $n(k,d)$ is that the distance between two possible solutions (branches in k) gets rapidly smaller if the system length increases, rendering the selection of the "actual" $n(k,d)$ by external criteria virtually impossible for long systems. On the other hand, we need system lengths comparable to the applied radiation wavelength, in order to expect a behavior of an effective medium rather than a single layer of scatterers. For a homogeneous slab, $n(k)$ is clearly independent of the length of the slab. For the effective material we expect the same, at least asymptotically for sufficiently large lengths. Therefore, we consider the transmission data for different system lengths as simultaneous determinations of a single $n(k)$. This leads to a set of simultaneous congruences with different moduli,

$$n(k) = n_1 \left(\mathrm{mod}\frac{2\pi}{kd_1}\right) = n_2 \left(\mathrm{mod}\frac{2\pi}{kd_2}\right) = \cdots = n_N \left(\mathrm{mod}\frac{2\pi}{kd_N}\right). \quad (11.21)$$

We assume the lengths d_i to have a greatest common divisor $d = \gcd\{d_1, d_2, \ldots, \mathrm{d}_N\}$, i.e. that any available d_i is an integral multiple of d, we then multiply each equation in (11.21) with $kd/(2\pi)$ and introduce the abbreviation $x = kd\; n(k)/(2\pi)$. Thus we get a system

$$\left\{x(k) \equiv x_i(k) \cdots \left(\mathrm{mod}\frac{d}{d_i}\right) \cdots | \cdots d_i/d, \ldots i = 1 \cdots N\right\}. \quad (11.22)$$

By multiplication with some common multiple q of the d_i/d we find equivalent simultaneous congruences with integer moduli,

$$\left\{qx(k) \equiv qx_i(k) \ldots \left(\mathrm{mod}\frac{qd}{d_i}\right)\right\}. \quad (11.23)$$

Because the assumption of a length independent $n(k)$ guarantees the existence of a solution of (11.22), we know from the (rational) Chinese remainder theorem that this solution is some unique residue class $qx(k)(\bmod \mathrm{lcm}\{\mathrm{qd/d_i}\})$, where lcm is the lowest common multiplier. The theorem further provides an algorithm to effectively compute this solution. Since $d|d_i$ we have $qd/d_i|q$ for every i, hence $\mathrm{lcm}\{qd/d_i\}|q$. However, this does imply $\mathrm{lcm}\{qd/d_\mathrm{i}\} \equiv q$, independent on the actual choice of the set of lengths $\{d_1, \ldots, d_N\}$. Therefore the solutions of (11.21) are given as a unique residue class $n(k)$ $(\mathrm{mod}\, 2\pi\, m/(kd))$ with $m = \mathrm{lcm}\{qd/d_i\}/q \equiv 1$. Clearly, the least ambiguous $n(k)$ that could be extracted from the set $\{d_i\}$ of system lengths would be some $n(k)(\mathrm{mod} 2\pi/(\mathrm{kd}))$. How can we choose q and the set $\{\mathrm{d_i}\}$ to obtain m = 1? Because q has to be a common multiple of the d_i/d, the lcm$\{d_i/d\}$ is certainly a good choice. Then we may choose the d_i/d to be pairwise coprime, which renders their lcm simply their product. Further, the lcm of all the products $qd/d_j = \prod_{i \neq j} (d_i/d) = q$ becomes just $\prod_i (d_i/d) = q$ and therefore we get $m = 1$.

As we see, in order to get the maximum information from the length dependence of the scattering data, it is already sufficient to choose two coprime d_i/d with minimal d, e.g., two successive multiples pd and $(p+1)d$ for some $0 < p \in N$ and minimal d. As we may always assume rational data, including lengths, the gcd d is always guaranteed to exist, and if we have a smallest length step for the scattering data, which we certainly have for numerical data obtained from a lattice version of the transfer matrix algorithm, this length step is a lower bound for any gcd d above. Even worse, in most realistic cases of NIMs the length step has to be assumed to be the length of the unit cell in the propagation direction. However, since in those cases the wavelength also has to be larger than the unit cell, $2\pi/(kd) \approx \lambda/d$ would maintain the order O(1). We can summarize that exploiting the length independence of $n(k)$ for our systems, we can reach the theoretical least ambiguity

$$n(k) = n(k) \left(\mathrm{mod} \frac{2\pi}{kd} \right) \tag{11.24}$$

with d being the length of the unit cell in the propagation direction. The only way to remove this remaining ambiguity using the length independence would be to either use irrational ratios of lengths or to approach $d \in 0$. Both are virtually impossible since the sample can only have an integral number of unit cells.

Frequency Dependence

A second expected physical property of $n(k)$ that we may exploit is its continuity between resonances. Suppose that $\Delta n(k)$ is an upper bound $\left| \frac{\partial n(k)}{\partial k} \right|$ and for any given k we would be able to resolve $n(k)$ as a residue class $n(k)(\mod h(k))$. Then we may choose for each interval where $\Delta n(k)$ is finite a frequency discretization $\{k_i \in Q | i = 1 \cdots N_k\}$, such that $2\,|k_{i+1} - k_i|$ $\Delta_n(k_{i+1}, k_i) < \min\{|h(k_{i+1})|, |h(k_i)|\}\, 2|k_i{+}1{-}k_i|$ for every two $\mathrm{k_i}+1, \mathrm{k_i}$ from this discretization and further $\Delta_n(k_{i+1}, k_i) = \max_{k_i < k < k_{i+1}} \Delta_n(k)$. This way the upper bound $\Delta_n(k)$ guarantees that if we choose a certain representative of the residue class $n(k_i)(\mathrm{mod}\ \mathrm{h}(k_i))$ for one particular k_j from the discretization, we would have a unique continuation to all other $\mathrm{k_i}$ within the interval. Thus the ambiguity of $n(k)$ is further reduced from independent residue classes $n(k_i)(\mathrm{mod}\ h(k_i))$ for each k_i to the functional residue class $n(k)(\mod h(k))$ of piecewise continuous functions of k, interpolating the $n(k_i)$.

We now have a set of branches of a continuous $n(k)$ in each of the intervals which differ by an integral multiple of the function $h(k)$ and fixing one point in the interval would make $n(k)$ inside the whole interval unambiguous. Note, however, that this exploitation of the knowledge for several frequencies cannot reduce the residue class $n(k)(\mod h(k))$ for any given k. In practice, we usually "reverse" this method, which means that we make an educated guess for a discretization and derive an error upper bound for those "jumps" in $n(k)$ we might miss. With some experience, this works reasonably well, provided we choose the frequencies dense enough, near the resonances. From analytic models for our systems, we know in most cases how many (few) continuous intervals we expect. Apart from this, resonances will also have a signature in the unambiguous function $z(k)$. The frequency continuation method can be used concurrently with the length independence described above. The only remaining problem is that we need to know the "actual" $n(k)$ at least for one point inside each interval.

Information from Analytical Models

If we know from analytic models what kind of asymptotics or frequency dependence of $n(k)$ we would expect, we may use this information to further restrict the ambiguity of $n(k)$. Most useful is such information around resonances in $n(k)$, where the common continuity of this function is destroyed and the continuation method above inevitably looses coherence between the branches right and left of the resonance. For instance, when we calculate the dielectric function $\alpha(k)$ and the permeability $\mu(k)$ from $n(k)$ and $z(k)$, the character of the resonances is well known from analytical models. On the other hand, it depends on the choice of the branches for $n(k)$ right and left from the resonance. This can introduce some connection between the intervals used above.

11.3.3 Inversion for Lossless Materials

Under certain conditions we do not need the complete information from the complex scattering amplitudes to do the retrieval. For lossless materials, we can assume n, z to be real or purely imaginary if we exclude the isolated special cases $n = 0$ and $z = 0$. Note that this is a stronger demand than the no-loss condition $|T|^2 + |R|^2 = 1$ for a particular T and R. Then the index of refraction n is only related to the real part of the transmission amplitude

$$n = \pm\frac{1}{kd}\cos^{-1}(\mathrm{Re}\,1/T) \tag{11.25}$$

$$z = \sqrt{\frac{w \pm 1}{w \mp 1}}, \quad w = \sqrt{\frac{\sin^2(\arg T)}{1 - |T|^2}} \tag{11.26}$$

With the usual convention $\arg(z) \in (-\pi/2, \pi/2)$ we fix the positive sign and the branch-cut for the square root but we still have two solutions for z which are mutually reciprocal. As a consequence we could not distinguish the transposed pairs (μ, α) and (α, μ) in the μ, α space. This ambiguity of z could only be resolved knowing the phase, more precisely the sign of the reflection amplitude R. The phase of T cannot help; nor can the length dependence. Due to the ambiguity of the radicand in z, the sign of w does not matter and we may write even simpler $w = \sin(\arg T)/|R|$. Note that n is obtained again as a residue class mod $2\pi/(kd)$ only, the unambiguous solution can be found from the length dependence $0 < d \in R$ of the transmission amplitude. The sign in (11.25) is not ambiguous, because it is related to the sign of z by the scattering formulae for a given T, R. Only the common sign of n, z is arbitrary but can be fixed by the convention, $\arg(z) \in (-\pi/2, \pi/2)$.

11.3.4 Periodic Effective Medium

To study the impact of the periodicity, or more precisely the reduced translational symmetry of the sample in the propagation direction, we consider a sample composed of a repetition of the unit cell shown in Fig. 11.27, finite in the direction of propagation and infinite perpendicular to it [14].

The unit cell consists of a thin homogeneous core of thickness d characterized by arbitrary $\mu(\omega)$ and $\varepsilon(\omega)$, sandwiched by two slabs of vacuum with thickness a and b, which break the translational invariance. L is the length of one unit cell, N the number of unit cells in propagation direction. Now we can calculate the scattering amplitudes for this model and subject them to the HEM inversion discussed in Sect. 11.3.1.

The results show that this periodic medium can explain all the unexpected behavior like the resonance/anti-resonance coupling in the $\mu(\omega)$ and $\varepsilon(\omega)$ negative imaginary part, distorted resonances, and so on, observed in the HEM inversion that are here identified as periodicity artifacts. Once we derive the scattering formulae for such a periodic effective medium model, we can do the inversion to obtain the simulated scattering data. The description (or approximation) of the scattering amplitudes for a given NIM in terms of the effective parameters of such a periodic medium as defined in Fig. 11.27 will be denoted as a "periodic effective medium" (PEM). We found that for vacuum wavelengths down to almost the size of the unit cell the effective behavior

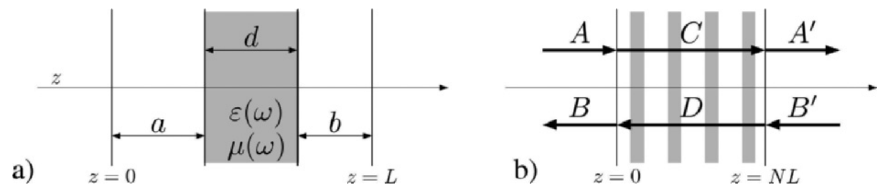

Fig. 11.27. The layout of the single unit cell (**a**) and of a finite slab of the model periodic medium are shown. The shaded regions indicate the homogeneous core of width d, which is characterized by the chosen appropriately model functions $\mu(\omega)$ and $\varepsilon(\omega)$ sandwiched by two vacuum slabs. L is the length of a single unit cell, N the number of unit cells in the slab in the propagation direction

of our NIMs can be decomposed into a "well-behaving" effective response of the resonances and a contribution of periodic structures described by the PEM.

11.3.5 Continuum Formulation

Using the interrelation between the transfer matrix and the scattering matrix, we obtain the (normalized) transmission and reflection amplitudes T and R after N unit cells, corresponding to those simulated for the real NIM

$$T = \left[\alpha(-d)\mathrm{e}^{-\mathrm{i}k(a+b)}U_{N-1}(p) - U_{N-2}(p)\right]^{-1} \tag{11.27}$$

$$R = \beta(-d)\mathrm{e}^{-\mathrm{i}k(a-b)}U_{N-1}(p)T. \tag{11.28}$$

Here, $U_n(z) = \sin\left[(n+1)\cos^{-1} z\right]/(1-z^2)^{1/2}$ are the Chebyshev polynomials of the second kind, taken at the argument $p = \cos(qd)\cos[k(L-d)] - \frac{1}{2}(z + 1/z)\sin(qd)\sin[k(L-d)]$.

The wave vector $q = n(\omega)\ k$ and the impedance $z(\omega)$ refer to the homogeneous core of the unit cell. We will now discuss what happens if we try to approximate the explicit periodic medium discussed earlier by a homogeneous effective medium. This corresponds to our previous attempts to describe the periodic NIMs by a homogeneous effective medium. We can show that if a homogeneous approximation is possible for a single unit cell of the periodic medium, then it holds for any number of unit cells and vice versa. Therefore, it is sufficient to consider a single unit cell. Furthermore, such a description as a homogeneous medium is only possible for $a - b = 0$. This implies that only NIMs that are inversion invariant in the propagation direction may possess a well-defined HEM approximation. In terms of the (normalized) scattering amplitudes T and R, for the single unit cell we then have the conditions

$$\alpha^{-1}(-d)\mathrm{e}^{\mathrm{i}k(L-d)} = T = \alpha_{\mathrm{eff}}^{-1}(-L), \tag{11.29}$$

$$\beta(-d)T = R = \beta_{\mathrm{eff}}(-L)T. \tag{11.30}$$

We already know how to invert the right-hand side of these equations. This is just what we did in the retrieval procedure for the HEM in the previous section. Defining renormalized scattering amplitudes $T' = T\,\mathrm{e}^{-\mathrm{i}k(L-d)}$ and $R' = R\,\mathrm{e}^{-\mathrm{i}k(L-d)}$, we could apply the same procedure to the left-hand side. Inserting the renormalized transmission and reflection amplitudes (11.29, 11.30) for a single unit cell into the inverted scattering formulae and using p defined above we obtain

$$n_{\mathrm{eff}} = \pm\frac{1}{kL}\cos^{-1}[p(n,z;k)] + \frac{2\pi}{kL}m \tag{11.31}$$

with m an integer. The problem with the signs of n_{eff} and z_{eff}, as well as with the ambiguity of $\mathrm{Re}n_{\mathrm{eff}}$ is similar, and can be resolved the same way as for the case of the homogeneous slab discussed above. Analogously, we can express the impedance z_{eff} of the effective homogeneous medium in terms of the n and z of the homogeneous core as

$$z_{\text{eff}}(k) = \pm\sqrt{\frac{2p^{+} + (z - 1/z)\sin(qd)}{2p^{+} - (z - 1/z)\sin(qd)}}, \qquad (11.32)$$

where $q = n(k)k$ and

$$p^{+} = \cos(qd)\sin[k(L-d)] + \frac{1}{2}(z + 1/z)\sin(qd)\cos[k(L-d)]. \qquad (11.33)$$

Equations (11.29) and (11.30) can be used with simulated scattering data for a real NIM to obtain the PEM approximation in terms of the core material parameters used in the periodic medium model. To obtain a reliable PEM approximation for simulated real NIMs, it turns out that a lattice version of the formalism above should be used [7].

11.4 Characterization of NIMs

11.4.1 Measurement of NIM Losses

We characterize the NIM designs by measuring the S-parameters in a free space setup [15] shown in Fig. 11.28. This setup allows characterization of

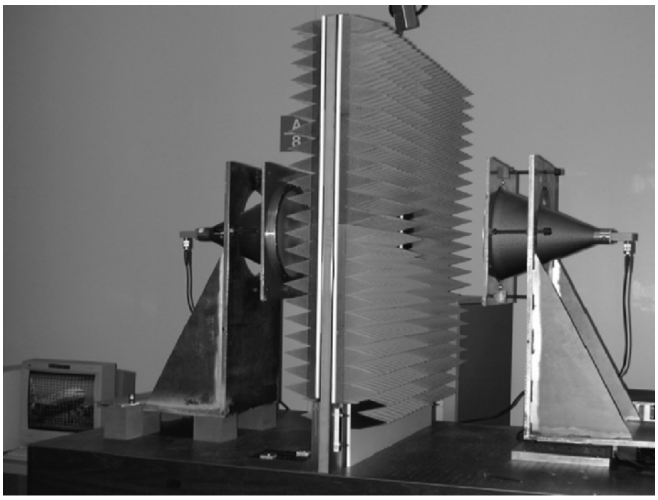

Fig. 11.28. A common setup we have used for S-parameter measurements. This particular system focuses the beam in the sample region to increase the signal to noise ratio

our unit cell designs without having to be concerned with grounding of the wires and other problems that can be associated with measurements made in a scattering chamber.

We measured the transmission and reflection of a slab sample made of Rogers 5880/Rohacell, having the 901-HWD pattern, in our free-space focused beam system. The slab was measured both with an adhesive between the Rogers and Rohacell and with no adhesive (taped at the ends only). What we found was that the insertion loss in the sample with the adhesive was quite significant compared to the one without the adhesive. The enhanced degree of loss is due to high field concentrations in the adhesive regions with high dielectric loss. The transmission and reflection data are shown in Fig. 11.29.

Simulations of this structure, using HFSS and periodic boundary conditions show excellent agreement. This is seen in Fig. 11.30. This agreement also validates that the use of a tapered-amplitude focused-beam with TRL calibration is pretty close to a plane wave incident on an infinite sample.

11.4.2 Experimental Confirmation of Negative Phase Shift in NIM Slabs

Far field range measurements were made to confirm the negative phase shift through a planar NIM sample (thickness L) as a function of frequency [16].

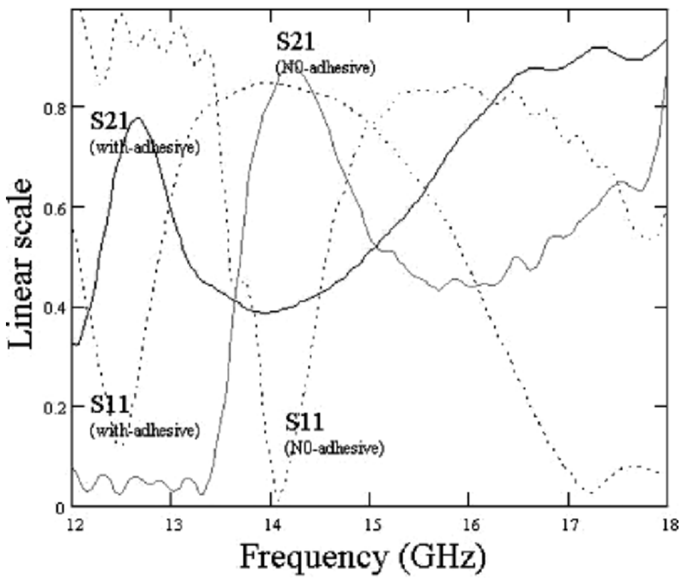

Fig. 11.29. The transmission and reflection of a slab of Rogers 5880 and Rohacell, with and without adhesive. S21 is not 100% is because of ohmic losses in the copper and the substrate loss tangent. The reflection is at -20 dB, it shows that the design is very well matched to free space

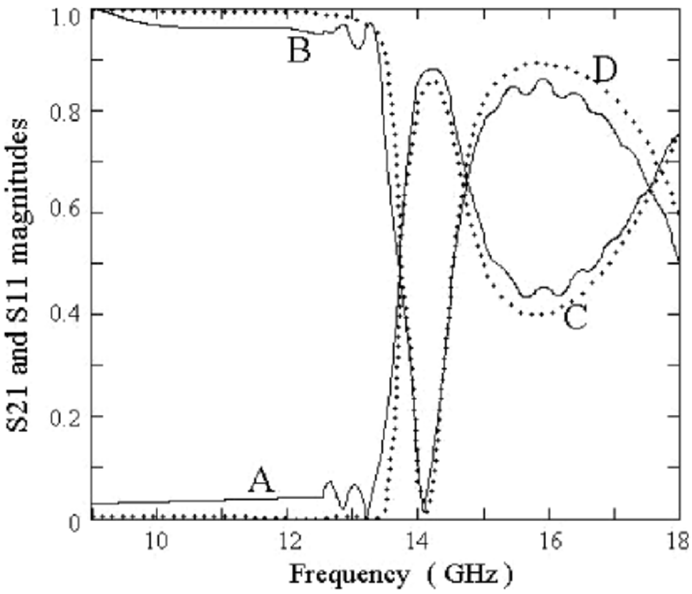

Fig. 11.30. Comparison between the measured S-parameters (*solid lines* A and B) and the HFSS simulated data (*dotted lines* C and D) for the sample with no adhesive. Curves A and C represent S21; Curves B and D represent S11. There are no adjustable parameters in this calculation. The loss is roughly 1 dB cm^{-1}

The sample studied is the 1E1H 0901HWD design. At the frequency for which the index $n = -1$ and the surface impedance $Z/Z_0 = 1$ we can determine the expected phase shift from the simple relation: $\Delta\phi = (n - 1)k_0L$. In addition to confirming the expected negative phase shift in the sample, we find that continuing to use the simple relationship for other frequencies results in a surprisingly good representation from $n = -2.5$ to -0.5. This illustrates that the simplification of only using the phase shift of the transmitted signal (normalized to free-space) can be a practical means of identifying (and in this case even quantifying) the existence of negative index in planar test samples.

A pair of horns spaced $\sim 75\lambda$ apart is used for the source and detection. The sample is placed between the horns on an aperture in a sheet of absorber as shown in Fig. 11.31. The measurements of the S-parameters as a function of frequency are obtained using an Agilent 8722ES Vector Network Analyzer.

In Fig. 11.32, we present an example of several studies that were conducted for calibration and verification of the measurements of the phase of the transmitted beam (S21). A series of Teflon sheets (0.25 in. thick) were tightly bound and inserted in the aperture. We must emphasize that what is measured is the phase change at each frequency relative to the "no sample" condition. As can be seen, the experimental points exhibit an excellent agreement between the Agilent data and the predicted change at 10 GHz for the index of 1.44 (Teflon).

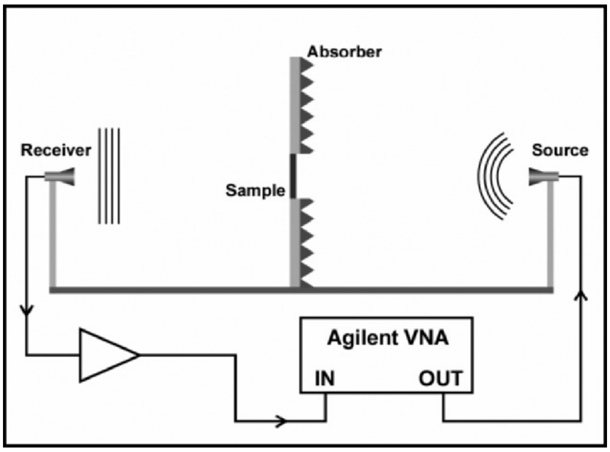

Fig. 11.31. A schematic representation of the measurement system

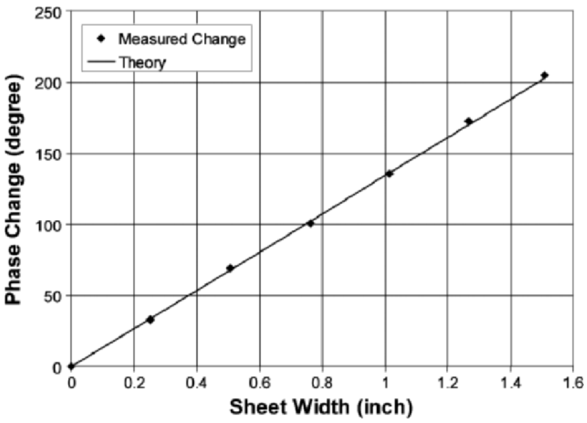

Fig. 11.32. Measured phase change as a function of dielectric thickness for Teflon sheets at 10 GHz

In Fig. 11.33, we present the experimental magnitude of the transmitted wave |S21| (Curve 1) vs. frequency from 13.5 to 16 GHz. The sample is made with a dual SRR and two wires per unit cell. For all data shown, the sample thickness is three unit cells (1 cm). *Solid* Curve 2 is a result of a numerical S-matrix calculation made utilizing Ansoft's HFSS v8.0 software. Except for the slight frequency shift, the experiment and simulation agree well as evidenced by the *dashed line* (Curve 3), which shows how the simulation results shifted by +0.15 GHz. Small frequency shifts between the numerical simulation and the measured properties for NIM samples are quite common. We note that

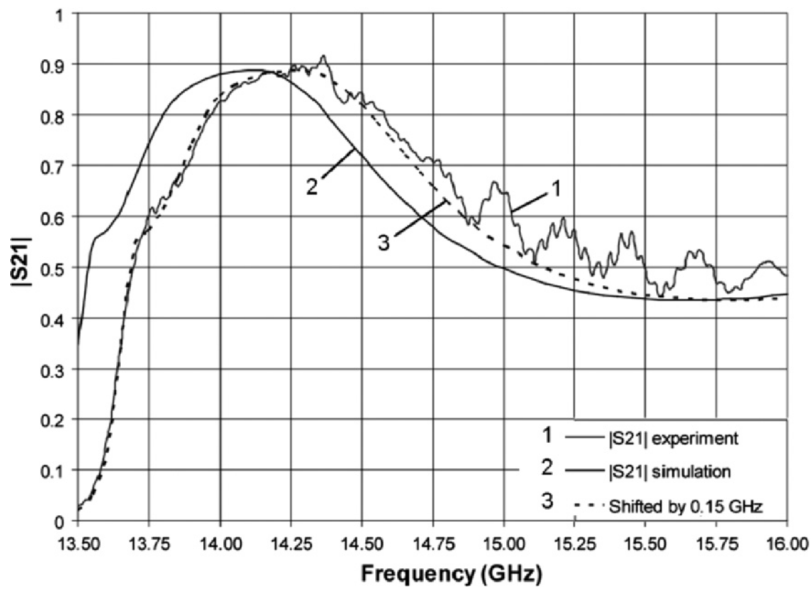

Fig. 11.33. The S21 parameter plotted vs. frequency. The thickness of the sample is 1 cm (three unit cells). The experimental curve closely approximates the simulation values. Furthermore, as the reflection coefficient is rather small for this particular sample, the difference from unity being almost entirely due to losses, it justifies using just the transmission coefficient to extract the value of n for this sample

the maximum in S21 is 0.9 indicating that in the region near 14.2 GHz the impedance match must be very close to 1 for normal incidence.

A rough estimate of the phase advance for different thicknesses of the NIM using the S21 data is shown in Fig. 11.34 after making the appropriate 2π corrections. Curve 1 corresponds to the experimental results, Curve 2 is the result of an HFSS numerical simulation of the phase difference. The main difference between the two curves of Fig. 11.34 is the 0.15 GHz shift mentioned.

In Fig. 11.35, we present the index of refraction vs. frequency determined three ways (1) (Curve 1) n is recovered using the experimental phase difference data of Fig. 11.34 from the relation $\Delta\phi = (n-1)k_0L$, (2) (Curve 3) the index is recovered from the full numerical simulation S-matrix via our standard retrieval method, and (3) (*diamonds*) the experimentally measured values of the index via Snell's law experiments on a 12-degree wedge sample (see Sect. 11.2). The very good agreement between the experimentally measured values of n (from the Snell's law experiments), the simulation results, and in the retrieval from the phase measurements described, indicates that this was a valid approximation.

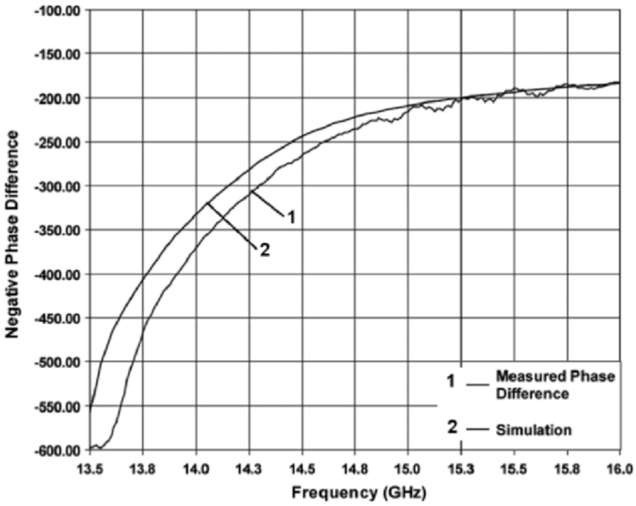

Fig. 11.34. Phase shift differences of S21 vs. frequency, which includes the 2π correction. The experimental data are represented by Curve 1, whereas Curve 2 is based on simulations using HFSS

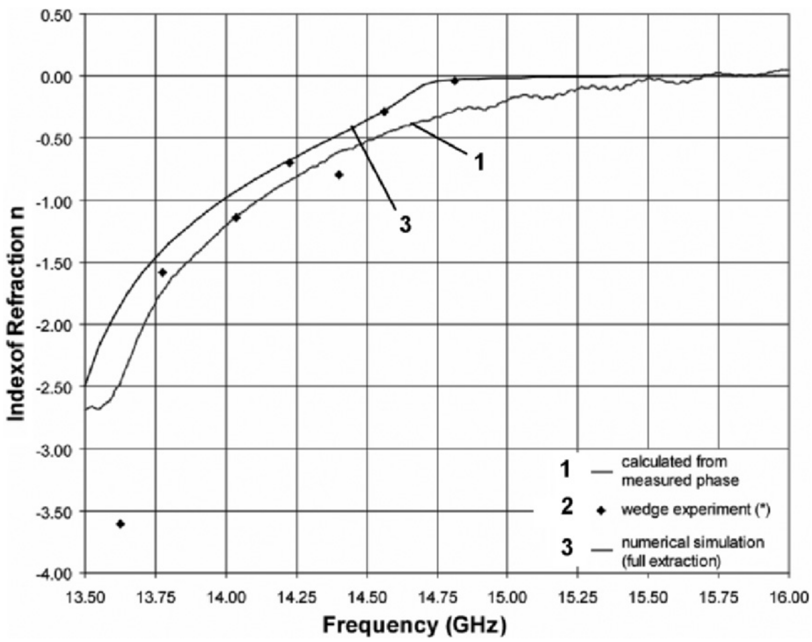

Fig. 11.35. Estimated values of the index of refraction n as a function of frequency, from the phase advance data

11.5 NIM Optics

It has been recognized that an NIM can be utilized as a lens material. An NIM lens serves as a vehicle to verify many of the material properties. In the following, we consider the potential advantages and properties of lenses made using NIMs.

11.5.1 NIM Lenses and Their Properties

A negative index lens with index of $n = -1$ can be used to either collimate or focus radiation, and offers the advantages of decreased reflectance and compactness, as compared to a positive index lens. One other aspect of NIM lenses was that they appear to be far superior to normal positive index material (PIM) lenses with respect to aberrations. To this end, a detailed evaluation of the aberrations of negative and positive index lenses was performed [17]. These calculations based on geometrical optics provide a strong indication that negative index lenses outperform positive index lenses for all imaging figures of merit. Of course, due to the frequency dispersion inherent in negative index materials, a negative index lens will exhibit more severe chromatic aberration than a positive index lens.

The aberrations of both positive and negative index lenses were estimated using standard analytical methods of geometrical optics and a generalized form of the eikonal equation that was developed specifically for this purpose [10]. We will not present the details of the calculations here, but note that the result of this process is to arrive at a set of expansion coefficients, which serve to quantify the imaging properties of a lens and are the accepted figures of merit for a lens. The lower order (fourth-order) expansion coefficients are well known as the five Siedel aberrations: spherical, coma, sagittal field curvature, astigmatism, and distortion. A plot of these aberrations as a function of index is shown in Fig. 11.36. As can be seen from the figure, while certain of the aberration coefficients are symmetric about $n = 0$, important aberration coefficients, such as coma, are symmetric about $n = +1$, which is a singular point for many of the aberrations. This asymmetry is understandable, as a lens with $n = +1$ does not provide any refractive power, and hence does not focus. Note also from the figure that the aberrations can be quite low near $n = 0$ and large $|n|$; however, an $n = 0$ is well outside of the regime of geometrical optics so that the results are not applicable, and for large $|n|$ there will be so much reflection that the lens will be unusable.

Figure 11.36 shows that for moderate values of the refractive index, a negative index lens has either significantly better or equal values of aberration coefficients as compared with a positive index lens. This is clearly true for the case of $n = -1$. The advantage of the negative index lens can be seen in Fig. 11.37, in which ray tracing diagrams are presented for positive and negative index lenses.

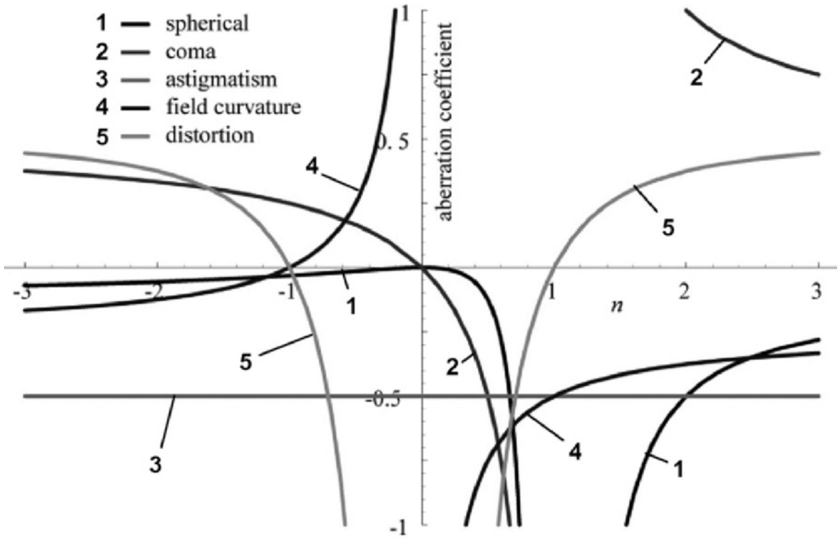

Fig. 11.36. The aberration coefficients as a function of refractive index. In all cases, a spherical lens is considered for which the focal length is kept constant

Table 11.1. Comparison of lens aberration coefficients for various indices of refraction

aberration	$n = -1$	$n = 1.5$	$n = 3$
spherical	-0.03	-1.13	-0.28
coma	0.25	1.50	0.75
astigmatism	-0.50	-0.50	-0.50
field curvature	0.00	-0.42	-0.33
distortion	0.00	0.28	0.44

The result of this study shows that negative index materials provide an inherent advantage for lens designs. We note that the conclusions drawn from this analysis do not include real material aspects such as loss and finite unit cell size; the impact of these issues on the aberrations needs to be evaluated on a case by case fashion. A comparison of aberration coefficients for lenses with $n = -1$, $n = +1.5$ and $n = +3$ is given in Table 11.1.

11.5.2 Aberration Analysis of Negative Index Lenses

Using the eikonal analysis of negative index lenses, we have also analyzed the spot diagrams for various types of lenses. Some of these results are summarized in Fig. 11.38. On the left top side of the figure, we show the aberrations, as a function of refractive index of a lens optimized so that the coma is always set at zero. The lens is assumed to focus rays from infinity. The incident

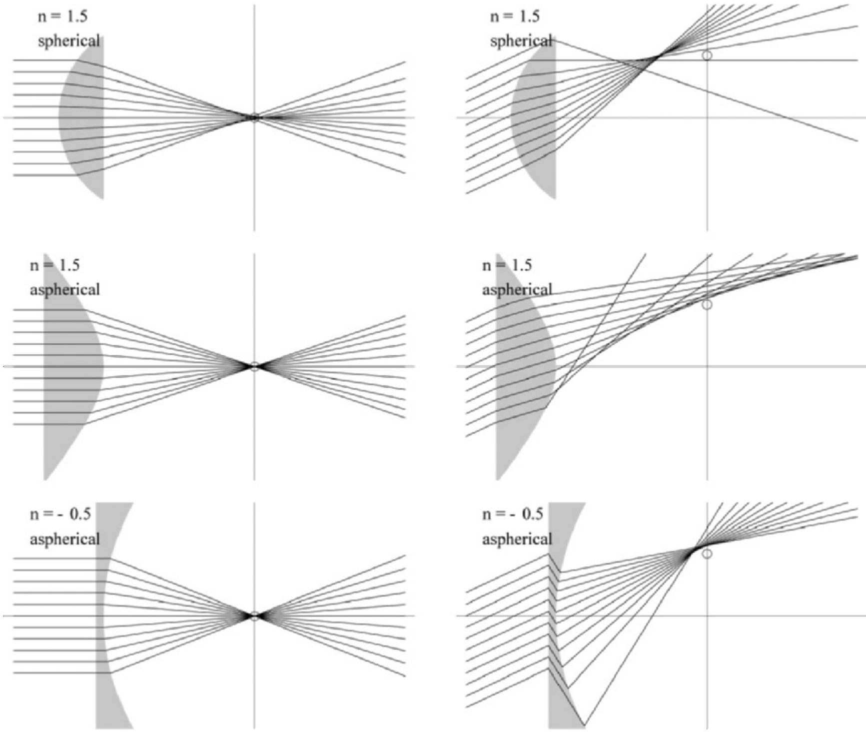

Fig. 11.37. Ray tracing diagrams of positive and negative index lenses. The left panel shows three diagrams corresponding to on-axis focusing. The upper two figures are spherical positive index lenses, the middle two figures are aspheric positive index lenses, and the lowest two figures are negative index aspheric lenses. The right panel shows the focusing of rays incident on the lens at a large angle of incidence. Note that the negative index lens exhibits far less coma than the positive index lenses

angle of the rays is 0.2 rad., and the lens is designed to have an F-number of $f/2$. Several negative index lenses are shown in comparison with the optimized positive index lens (lowest on the left). All of the negative index lenses display markedly improved imaging properties (note that the spot diagrams for the negative index lenses are multiplied by a factor of $\times 2$ or $\times 3$. The improvement in this case results from the lower field curvature (Curve 3) associated with the negative index lens. The right-hand side of Fig. 11.38 shows a similar analysis for a lens optimized so that spherical aberration is zero.

The analysis in Fig. 11.38 has been performed for isotropic NIMs. A similar analysis on anisotropic (or *indefinite*) NIM lenses also reveals improved imaging performance over positive index lenses. Doublets of indefinite media lenses can recover the full imaging benefits of isotropic negative index lenses.

Figure 11.39 shows the gain of a lens as a function of index, for various beam angles. Note that for shallow angles, the optimal positive and negative

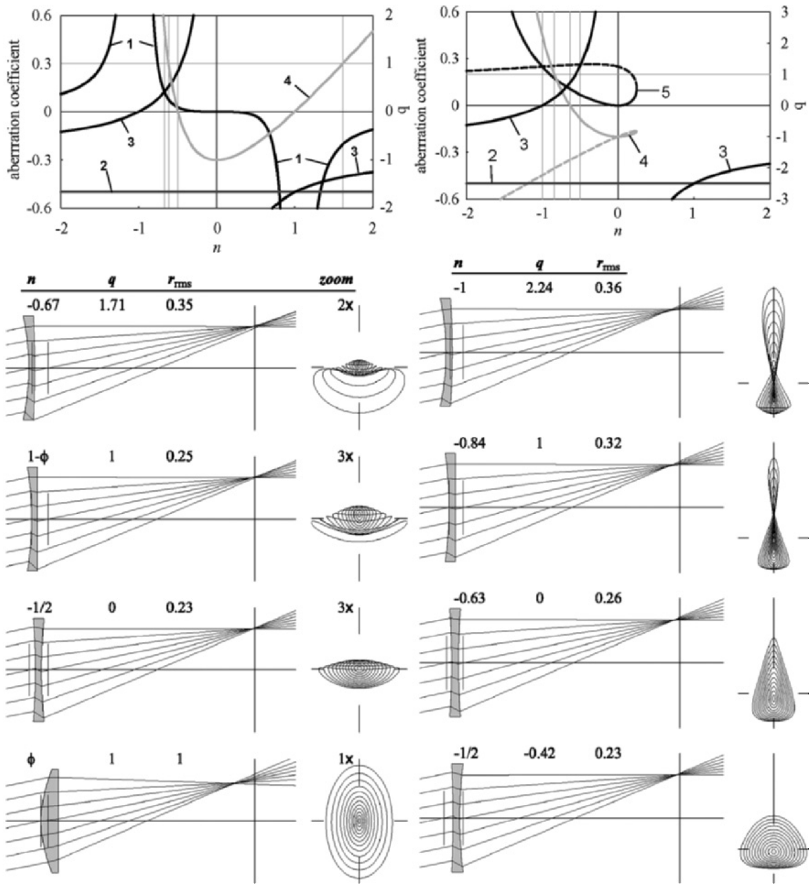

Fig. 11.38. (*Left*) The aberrations as a function of index (*top*) and several ray tracing diagrams for negative and positive index lenses optimized for zero coma. The aberrations shown are: spherical (Curve 1), astigmatism (Curve 2), and field curvature (Curve 3). Curve 4 is the shape factor. The *thin gray vertical lines* indicate the properties for the lenses shown in the ray tracing and spot diagrams below. (*Right*) Same as previous, except now the lens is optimized so that spherical aberration is zero. The numbered curves in the aberration plot is the same as in the *left panel*, except that coma is now indicated and shown as Curve 5. Note that spherical aberration cannot be eliminated from positive index lenses, thus leading to the unusual behavior shown for the coma (and shape factor) with two solutions existing in the negative index region. In this figure $\phi = 1.62$

index lenses perform equivalently well. However, for larger beam angles, the negative index lenses significantly outperform positive index lenses. This can also be seen in Fig. 11.40, which summarizes the optimal positive and negative index lenses as a function of beam angle and aperture size. In all cases, the negative index lens shows increased gain over a larger spread of angles.

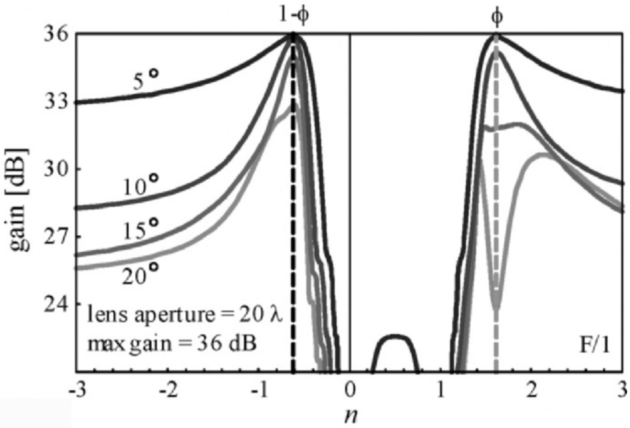

Fig. 11.39. Gain as a function of index, for varying beam angles

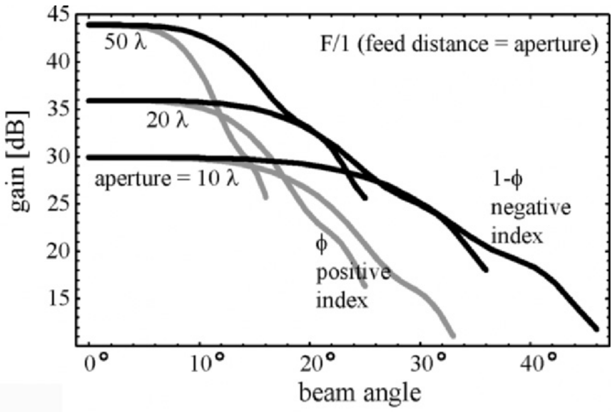

Fig. 11.40. Gain as a function of beam angle for the optimized negative (*black*) and positive (*gray*) index lenses. Curves are shown for several apertures. In this figure $\phi = 1.62$

11.6 Design and Characterization of Cylindrical NIM Lenses

As discussed in Sect.11.5, NIM lenses show promise as optical elements because they have unique properties that are not found in ordinary positive index materials. For simplicity the first NIM lens fabricated had a 1E2H cell type with cylindrical symmetry and the measurements were performed in waveguide geometry. The schematic and picture of the experiment are shown in Figs. 11.41 and 11.42

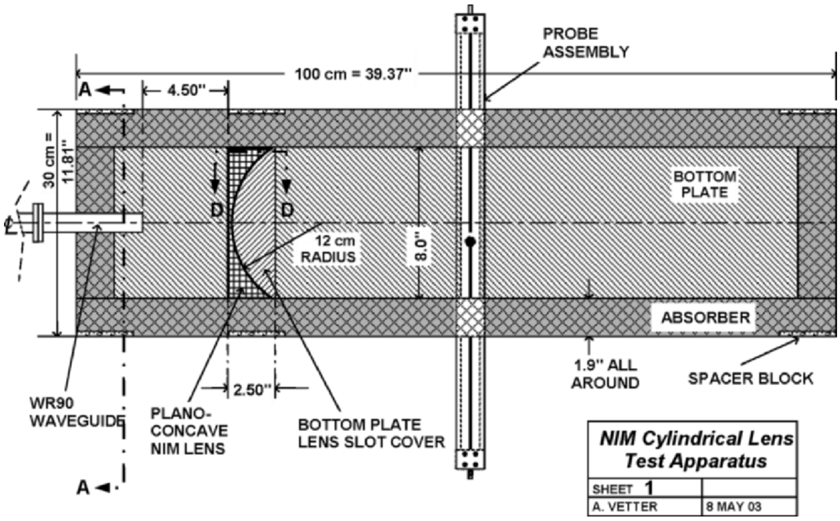

Fig. 11.41. Design drawing of the scattering chamber (*top view*)

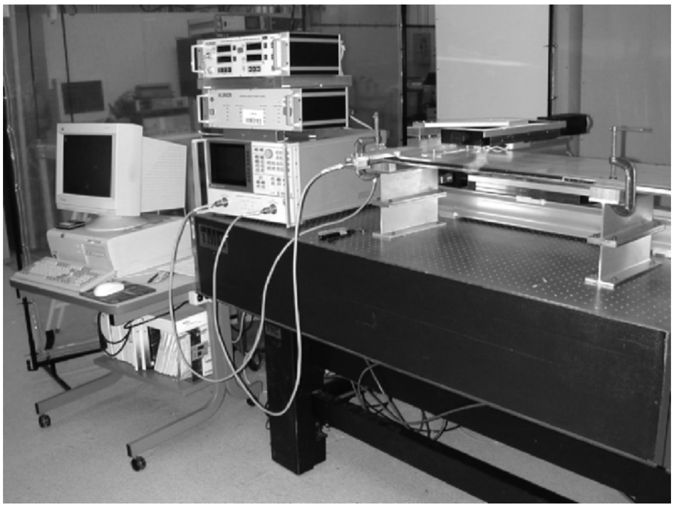

Fig. 11.42. Test-chamber and probe-scanner for the 2D-slab and lens measurement. It consists of a planar XY probe scanner, a waveguide source, a network analyzer, software control, and a data acquisition system

11.6.1 Cylindrical NIM Lens in a Waveguide

To assess how an NIM lens compares with respect to a positive index lens, we simulated and measured the performance of three types of cylindrical lenses [18]. Two lenses were made of positive index materials (Macor® and Teflon®),

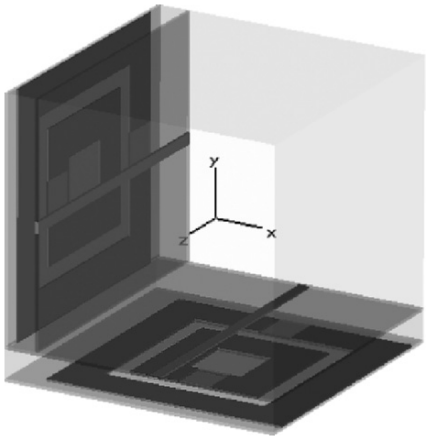

Name	Value (mm)	Description
cellx	2.51	cell x dimension
celly	2.51	cell y dimension
cellz	2.51	cell z dimension
gapa	0.30	gap azimuthal
gapr	0.15	gap radial
glut	.0279	glue thickness
off	0.1389	ring & wire offset
rngs	2.20	ring outer side length
rngt	.017	ring thickness
rngw	0.350	ring width
subt	.254	sub thickness
wret	.017	wire thickness
wrew	.100	wire width

Fig. 11.43. Unit cell for the 2D structure (1E2H) of the NIM lens

while the third one was made of a 1E2H NIM. The testing was performed in the scattering chamber described in Fig. 11.41. The results show excellent agreement between the simulations by MAFIA and the measurements done in the scattering chamber.

The unit cell for the NIM lens and its dimensions are given in Fig. 11.43. The wire elements of the NIM lens have been electrically grounded to the top and bottom plates of the scattering chamber. The lens is four cells thick in the direction of the wires and cylindrical axis (vertical). A drawing of the NIM lens design is shown in Fig. 11.44.

To evaluate the performance of the NIM lens, we first computed the amplitude of the electric field, $|E_x|$, in the empty scattering chamber using MAFIA. The computed electric field distribution as well as the computation geometry is shown in Fig. 11.45. The geometry of the simulation shows the position of the waveguide, the absorbing walls, and the position of the lens. The cylindrical wave fronts emanating from the exit of the waveguide are clearly visible. The electric field amplitude is shown in the right panel. The interference patterns emerging from the sidewall reflections are clearly visible.

In Fig. 11.46 the surface plots of the computed and measured normalized electric field amplitudes, $|E_x|$, for the empty scattering chamber are shown. The predicted and measured topologies of the electric field amplitude surface show remarkably good agreement. A more quantitative comparison is shown in Fig. 11.47. The line plots of the field amplitude along ($x = 0,\ y = \text{const},\ z$) and ($x = 0,\ y, z = \text{const}$) lines are given.

These results provided a high degree of confidence both in our simulations and testing procedures. The next step was to model and measure the behavior of a PIM lens in the scattering chamber. This comparison at $x = 0$ is shown in Fig. 11.48.

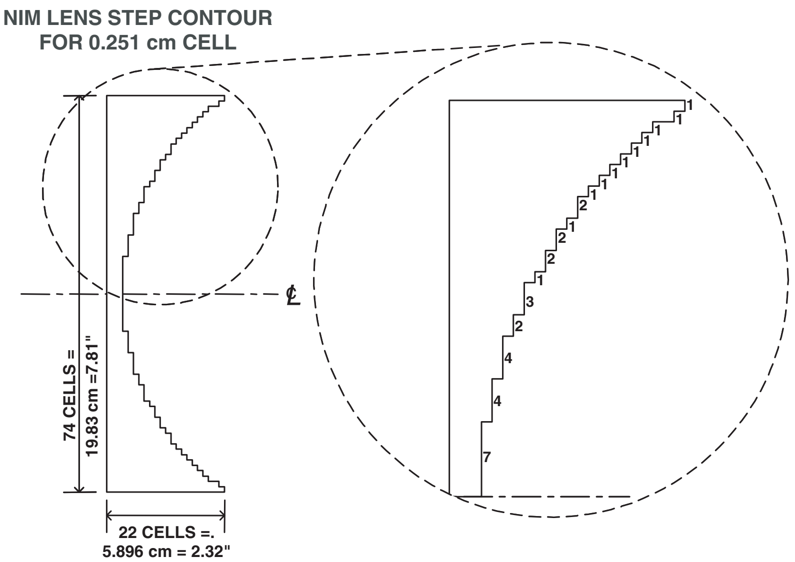

Fig. 11.44. Detailed drawing of the NIM lens. The numbers (*left* side expanded drawing) indicate the number of unit cells corresponding to the distance in the vertical direction

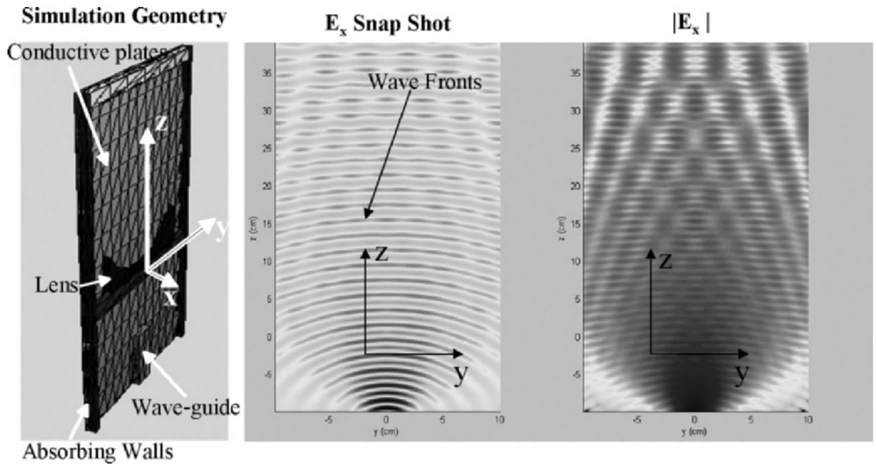

Fig. 11.45. (*Left*) Simulation geometry. (*Center*) A time-snapshot of the electric field in the empty chamber. (*Right*) Empty chamber, electric field $|E_x|$ amplitude as a function of position

The final step was to model and measure the performance of an NIM lens. It must be mentioned that grounding of the wires (in x the direction) of the NIM structure in a wave guide configuration is critical for obtaining a negative index of refraction. This was initially discovered experimentally

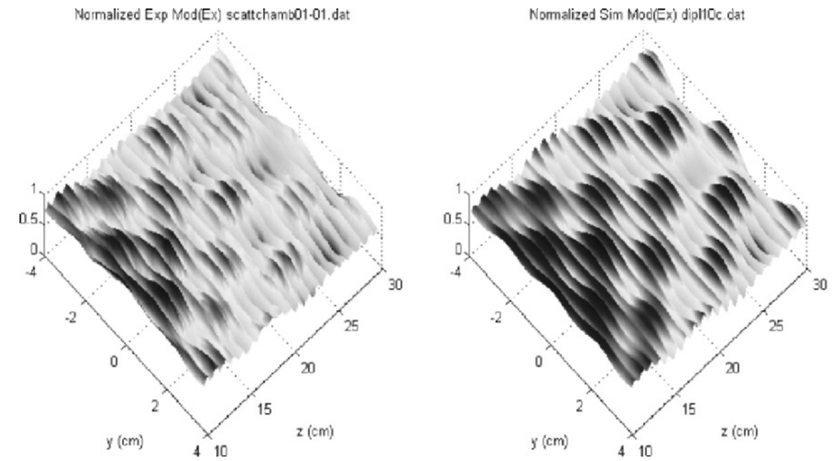

Fig. 11.46. Electric field amplitude for the empty scattering chamber. (*Left*) Measurement. (*Right*) Simulation

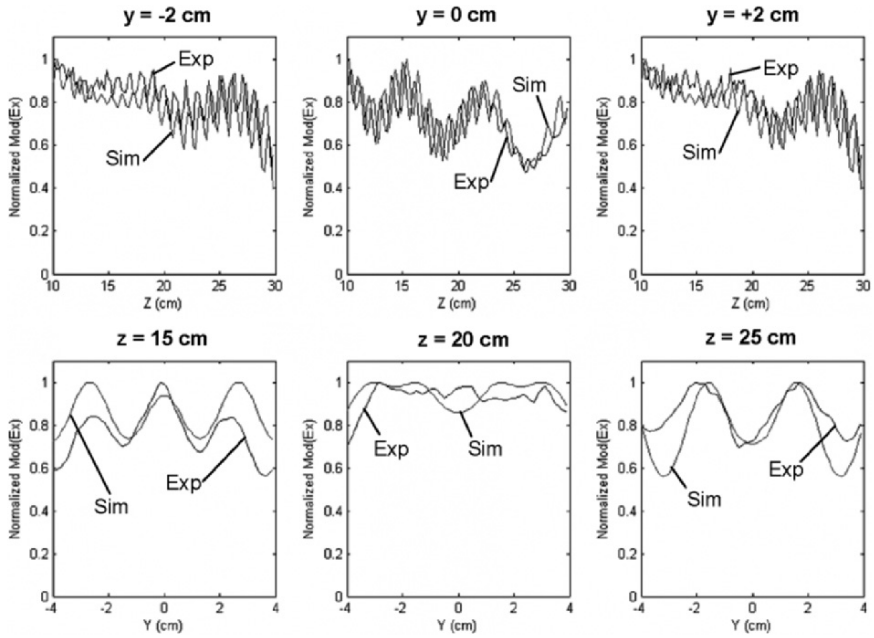

Fig. 11.47. Electric field amplitude, $|E_x|$, line plots for empty chamber

and later verified by simulation. To simulate the NIM lens, an effective ε and μ were obtained from MWS, based on the unit cell described earlier. The computed values for the dielectric constant and magnetic permeability are $\varepsilon = (-1.27 - \mathrm{i}0.291, 1, 1)$, $\mu = (1, -1.33 - \mathrm{i}0.562, -1.33 - \mathrm{i}0.562)$ at $\nu = 14.7$

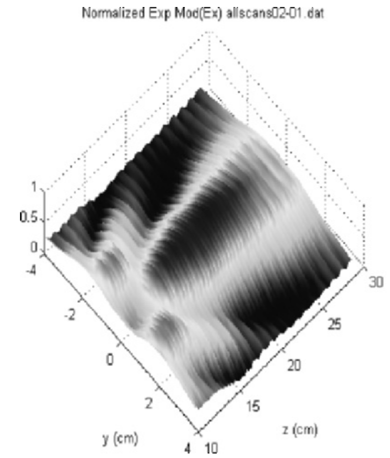

Fig. 11.48. Electric field amplitude, $|E_x|$, as function of position for the Macor lens. (*Left*) Measurement. (*Right*) Simulation. As in the case of the empty chamber, the agreement between the measured and computed topology of $|E_x|$ as a function of position is quite good

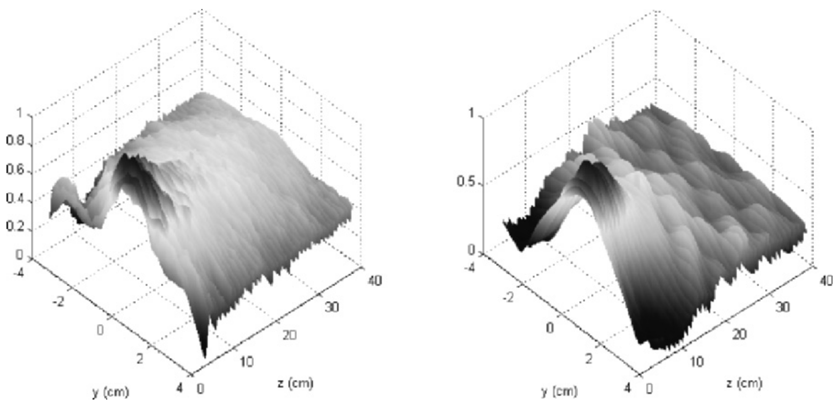

Fig. 11.49. Electric field amplitude, $|E_x|$, as a function of position in the scattering chamber for the NIM lens. (*Left*) Measurement. (*Right*) Simulation

(GHz). Using these values in the effective medium simulation, the computed and measured $|E_x|$ as a function of position is shown in Fig. 11.49. Again, we see excellent agreement between simulated and measured values. This also indirectly confirms the validity of the calculation procedure of the effective ε and μ.

11.7 Design and Characterization of Spherical NIM Lenses

In this section, we discuss the characterization of the free-space test setup for spherical lenses, the characterization of a positive index material (PIM) spherical lens, an NIM spherical lens, a negative index material gradient index (GRIN) lens, and compute and measure the aberrations of these lenses [19].

The empty lens aperture was modeled and experimentally characterized. This was important so that we could assess what its effect would be on the lens performance and the gain measurements. A standard PIM lens was designed and fabricated to experimentally assess the differences between PIM and NIM lenses. It was also used as a control sample. Additionally, we studied a GRIN version of the NIM lens because we expected that it would have lower losses; it is also thinner and lighter, as demonstrated for the case of a cylindrical GRIN lens [20]. All of the lenses were designed to have essentially the same nominal focal length ($\sim$12.7 cm) and aperture ($\sim$12.7 cm), giving an F-number approximately equal to 1.0. The fabricated lenses differ slightly from these values. All of the lenses were tested in the same setup having an aperture of 12.4 cm. A detailed comparison between the numerical and experimental results for all the lenses was made. In most cases the results were normalized to the maximum field amplitude, although absolute field comparisons are made. In general the agreement between experiment and simulation is excellent.

11.7.1 Characterization of the Empty Aperture

The experimental setup for the lens measurements was similar to those used previously, incorporating a network analyzer that is controlled by a computer running Labview. This setup is shown in Fig. 11.50. It has a source antenna illuminating a 6.20 cm radius aperture made of aluminum that is shielded by Eccosorb® to reduce reflections. The MWS simulation of this setup is given in Fig. 11.51.

Fig. 11.50. Experimental test setup for measuring PIM, NIM, and GRIN spherical lenses. The plane wave is generated at the right, travels through the aperture in the center panel, and is detected by the receiver on the left. The experiment is controlled by a computer running Labview shown in the center panel

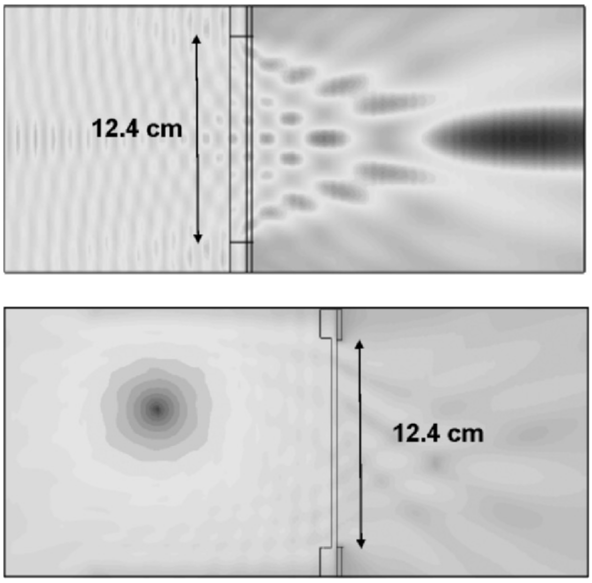

Fig. 11.51. MWS simulations of electric near-field amplitude for plane wave (*top*) and small dipole (*bottom*). The small dipole is 2.0 cm above the central optical axis illuminating an aluminum aperture having a 6.20 cm radius. The dipole is 10.8 cm to the left of the aluminum aperture

In this figure, the electric near-field amplitude is shown for two cases: (*top*) the aperture illuminated by a plane wave and (*bottom*) the aperture illuminated by a small dipole that is 2.0 cm above the central optical axis. The line plot comparison for the plane wave case of the MWS simulation and an analytical calculation is shown in Fig. 11.52 for the far field. For MWS the far field is calculated using the near field components in the computational volume as discussed previously using the Helmholtz–Kirchhoff theorem.

The analytical expression for the time-averaged plane wave, diffracted power per unit solid angle by a circular aperture is proportional to

$$\frac{\mathrm{d}P}{\mathrm{d}\Omega} \propto \left| \frac{2J_1(ka\sin\theta)}{ka\sin\theta} \right|^2 , \tag{11.34}$$

where J_1 is a Bessel function, k the wavevector, a the aperture radius, and θ the angle with respect to the propagation direction. Note that the far-field comparison between the FDTD and analytical methods are in good agreement. We estimate the far field to be at approximately $Z_{\mathrm{ff}} = 2D^2/\lambda = 2(2 \times 6.20\,\mathrm{cm})^2/(3\mathrm{e}10\,\mathrm{cm\,s^{-1}}/15\mathrm{e}9\,\mathrm{s^{-1}}) = 154\,\mathrm{cm}$, where D is the diameter of the aperture.

The near electric field downstream from the aperture was experimentally measured. The comparison of the MWS simulation to the experimental results is shown in Fig. 11.53 for plane wave illumination.

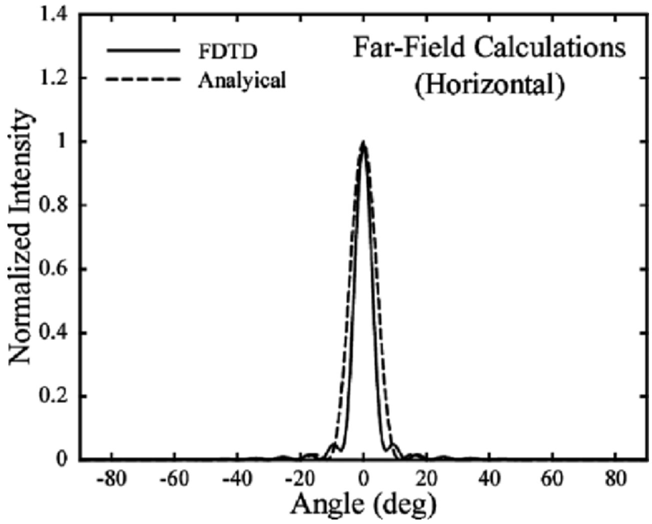

Fig. 11.52. Comparison of MWS and analytical calculation of electric field intensity in the far field for a circular aperture

Furthermore, to observe the effects of the aperture on steering, we moved a small dipole source off axis and measured the electric field as a function of angle in the far field at 1.75 m. The excellent comparison of these results to the simulation results is shown in Fig. 11.54.

11.7.2 Design and Characterization of the PIM lens

A PIM lens was fabricated as a reference for comparing the NIM and GRIN lens performances. This lens was made of Rexolite®, which has $\varepsilon = 2.53$ and $n = 1.59$. The designed focal length of the lens was 12.7 cm. This lens, along with a simple ray tracing analysis is shown in Fig. 11.55. Note that for the full aperture not all of the rays intersect at the same point due to aberration effects that cause the focal spot to be elongated.

The MWS simulation of the PIM lens is shown in Fig. 11.56. The simulation at the top was used to determine the focal point of the lens which occurs at $\sim$9.0 cm from the incident first surface of the lens. This simulation used a plane wave excitation source. Next, having determined the focal spot, a small dipole source was placed at this position but 2.0 cm above the central optical axis. This near-field simulation is shown at the bottom of Fig. 11.56.

A comparison of the experimental and simulated electric near-field focusing characteristics for the PIM lens is shown in Fig. 11.57. The line plots in this figure show excellent agreement between the experiment and simulation. The oscillations along the z propagation direction for the experimental data are due to interference between the receiving antenna and the mounting fixture.

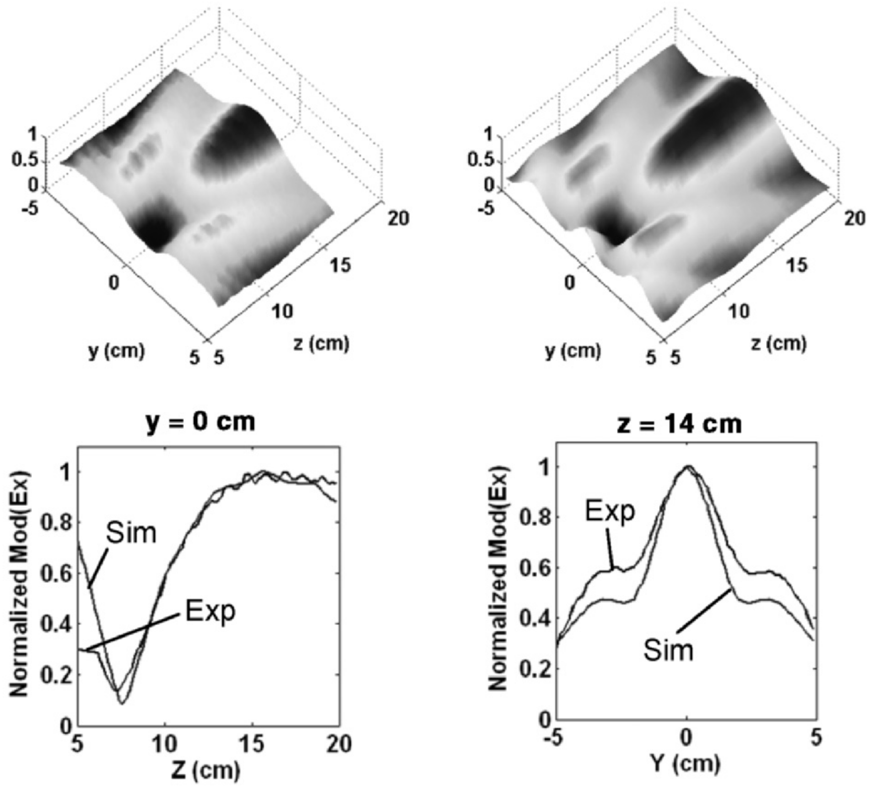

Fig. 11.53. Experimental (*top left*) and MWS simulated (*top right*) electric near field amplitude of the empty aperture at 14.6 GHz. The line plots (*bottom*) of the experimental and MWS simulated fields are in excellent agreement

Also, the experimental profile is broader than the simulated profile due to the finite dimensions of the receiving antenna.

The far-field steering characteristics of the PIM lens are shown in Fig. 11.58. These line plots correspond to moving a small dipole source off the optical axis, in a direction perpendicular to the propagation direction, at the focal spot (~9.0 cm). Again, we see excellent agreement between the simulated and experimental data.

11.7.3 Design and Characterization of the NIM Lens

We have fabricated an NIM lens with nominal focal length of 12.2 cm and a 24.4 cm radius of curvature. This design assumes that the NIM index of refraction $n = -1.0$ at an operating frequency of $\sim$14.8 GHz. The smooth radius of curvature is approximated by discrete steps, corresponding to the unit cell dimension of 0.254 cm, as seen in Fig. 11.59.

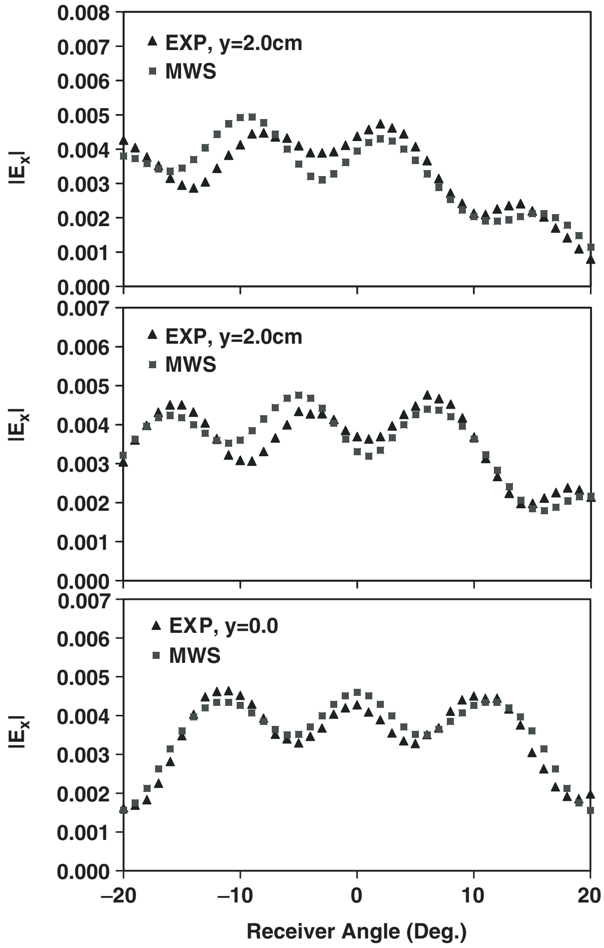

Fig. 11.54. Experimental (*triangles*) and MWS simulated (*squares*) normalized electric field amplitude of empty aperture when the source (10.8 cm in front of the aperture) is on and off the optical axis and the receiver is in the far field at 1.75 m. Starting at the bottom and moving upward, the source displacement is 0.0, 1.0, and 2.0 cm, respectively. The line plots of the experimental and MWS simulated fields are in excellent agreement

Note that this unit cell is indefinite so that $\varepsilon = \mu = (-1.0, -1.0, 1.0)$ at the designed operating frequency. Our eikonal (ray tracing) and effective media simulations have shown that this indefinite unit cell will perform nearly as well as a full 3E3H unit cell having $\varepsilon = \mu = (-1.0, -1.0, -1.0)$. The 2E2H unit cell lends itself to simpler fabrication techniques. As shown in Fig. 11.60, impedance matching with $Z = 1.0$ is achieved by designing $\varepsilon = \mu$ at the operating frequency of $\sim$14.8 GHz. A comparison of the simulated and measured

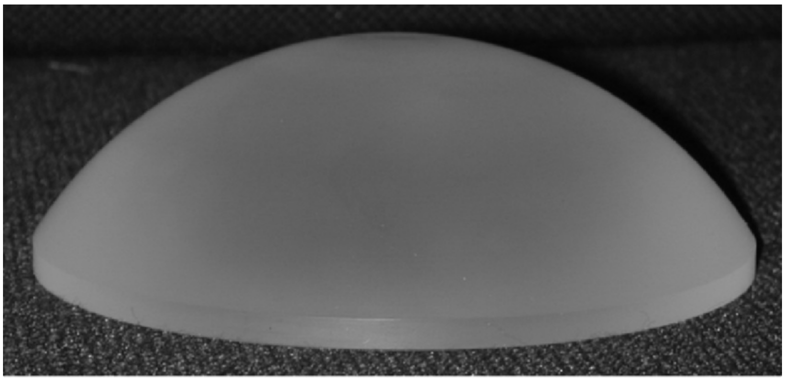

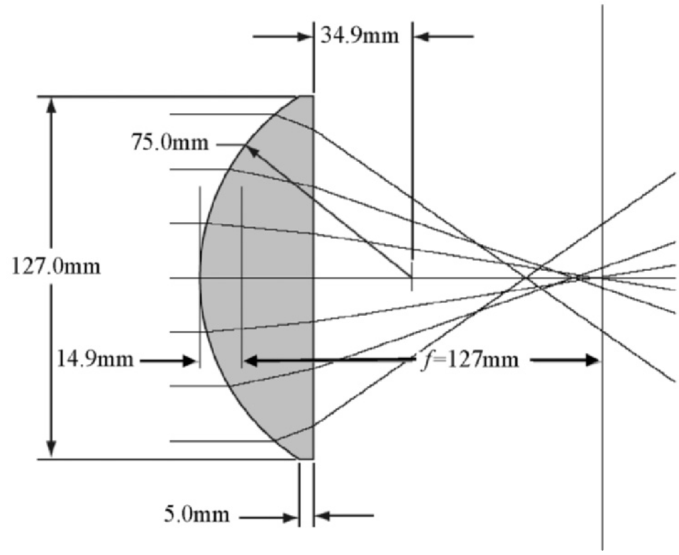

Fig. 11.55. Rexolite PIM lens (*top*) with dimensions shown in ray tracing diagram (*bottom*). The principal plane is shown from which the focal length is given

S21 for the pathfinder 2E2H unit cell is also shown in Fig. 11.60. Note that at the operating frequency the experimental transmission is approximately 0.90 for a single unit cell. This amount of loss/unit cell has an impact on the lens performance, where multiple unit cells are required in the propagation direction.

MWS effective medium near-field simulations for the NIM lens are shown in Fig. 11.61. In these simulations as before, we model the near-field focal region using a plane wave and then place a small dipole at this location but at 2.0 cm above the central optical axis at the focal distance to demonstrate collimation and steering. Note that the stepped lens surface approximating the smooth 24.4 cm radius of curvature produces a focal spot at approximately

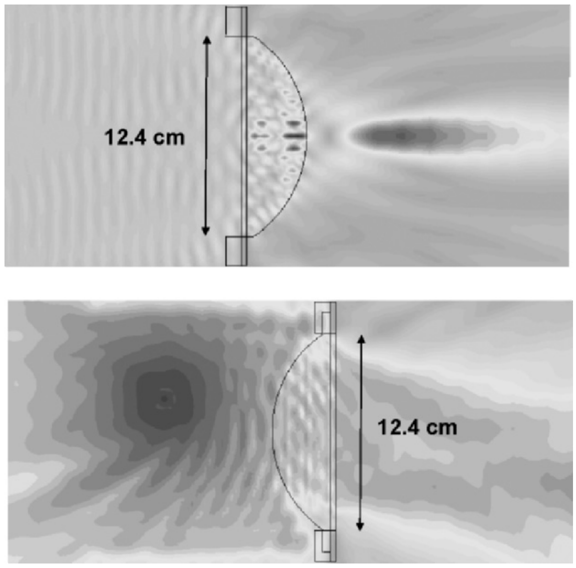

Fig. 11.56. MWS simulations of electric near-field amplitude for plane wave focusing (*top*) and small dipole (*bottom*), 2 cm above the central optical axis. The plane wave and dipole source illuminate the PIM lens in an aluminum aperture having a 6.20 cm radius

10.0 cm from the first surface of the NIM lens and also collimates and steers the field generated by the dipole source.

A detailed comparison between the MWS near-field simulation and experiment is shown in Fig. 11.62 for the NIM lens. The line plots in this figure show excellent agreement between experiment and simulation. Note that for the simulation the effective ε and μ were adjusted to $(-0.8, -0.8, 1.0)$, which is within our fabrication and experimental error. The oscillations along the z propagation direction for the experiment have been explained above for the PIM lens case.

The far-field steering characteristics at 1.75 m of the NIM lens are shown in Fig. 11.63. These line plots correspond to moving a small dipole source off the optical axis in a direction perpendicular to the propagation direction at the focal spot ($\sim$10.0 cm). Again we see excellent agreement between the simulated and experimental data.

Finally, the electric far-field pattern and gain with respect to the empty aperture are shown in Figs. 11.64 and 11.65, respectively. Note that the gain for the NIM lens is approximately 5.0 dB above the empty aperture.

11.7.4 Design and Characterization of the GRIN Lens

We have fabricated a GRIN lens with a nominal focal length of 12.7 cm, which is shown in Fig. 11.66. The principal advantage of a GRIN lens is its uniform

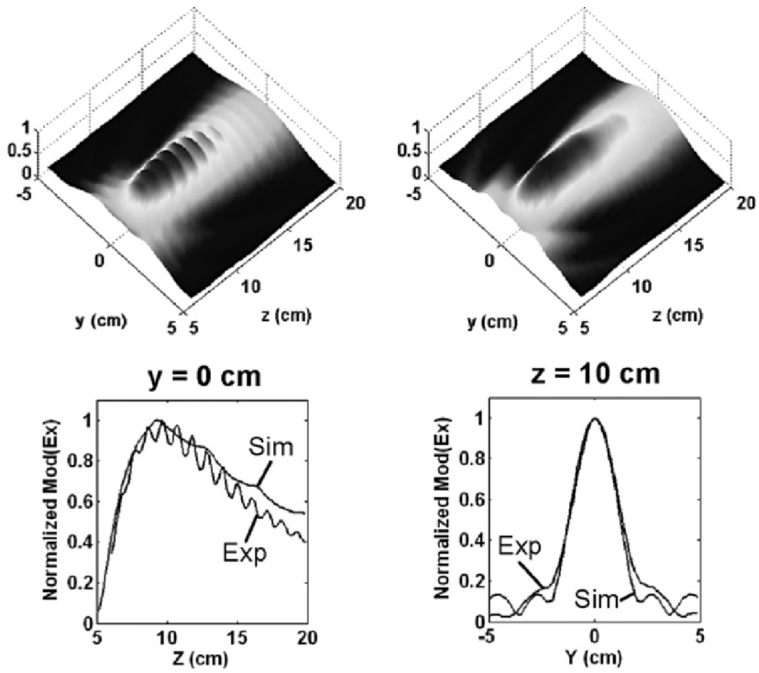

Fig. 11.57. Experimental (*top left*) and MWS simulated (*top right*) focusing electric near-field amplitude of the PIM lens at 14.6 GHz. The line plots (*bottom*) of the experimental and MWS simulated fields are in excellent agreement. Note that the focal spot is ∼9.0 cm for this lens

thickness, which on average is much thinner than a physically curved PIM or NIM lens. The GRIN lens is constructed by using a slab of NIM with a variable index of refraction in the radial direction. This lens was designed using the eikonal method [10].

The index of refraction gradient required for the 12.7 cm focal length lens is $\varepsilon = \mu = -1.1 - 0.0501\, r^2 + 0.0001\, r^4$. The unit cell stepwise approximation to this smooth gradient is also shown in Fig. 11.66. The GRIN lens has five unit cells in the propagation direction. Each unit cell is 0.20 cm in width for a total thickness of 1.0 cm. The number of unique unit cell types designed was 19. All the unit cells are impedance matched to free space at the operating frequency.

Using the eikonal equation and MWS we simulated the near-field effective medium focusing for a 3E3H-type NIM GRIN lens and compared it to a 1E1H-type NIM GRIN lens. This comparison is shown in Fig. 11.67. The analysis indicates that the 1E1H unit cell performs almost as well as its more complex counterpart for this application. However, the 1E1H unit cell has the distinct advantage of being very simple to fabricate and assemble compared with the 3E3H version.

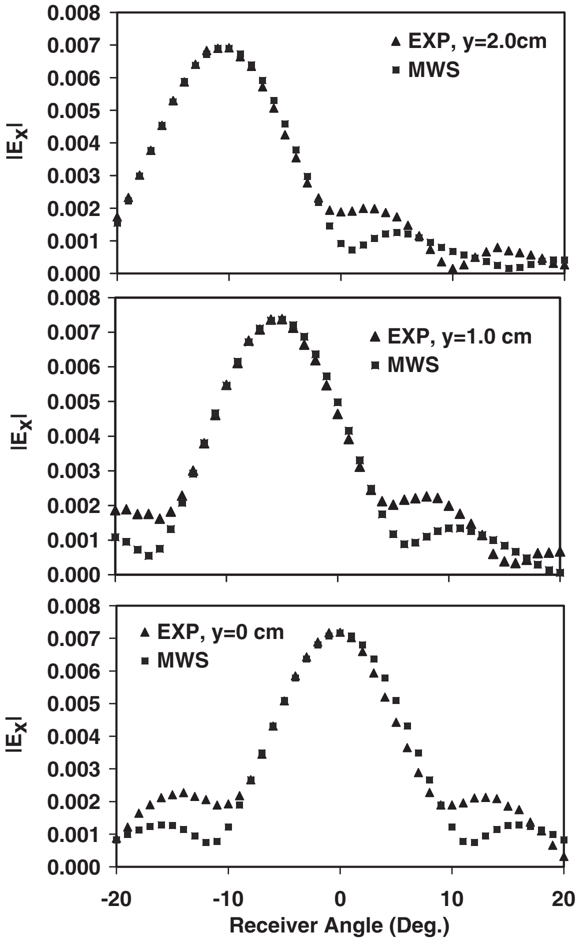

Fig. 11.58. Normalized experimental (*triangles*) and MWS simulated (*squares*) steering electric far-field amplitude at 1.75 m of PIM lens when the source is on and off the optical axis at the focal spot at ∼9.0 cm. Starting at the bottom and moving upward the source displacement is 0.0, 1.0, and 2.0 cm. The line plots of the experimental and MWS simulated fields are in excellent agreement

The MWS near-field effective medium focusing simulation and experimental data for a 1E1H unit are compared in Fig. 11.68. Note that the index gradient for the simulation was adjusted (i.e. $\varepsilon = \mu = -1.1 - 0.03r^2 + 0.0001r^4$) to match the experimental data. This effectively reduces the index gradient in the lens so that at the center A type unit cell the refractive index is -1.1 and at the edges the S type unit cell refractive index is ~ -2.4. This indicates that in the fabricated lens the gradient achieved was lower than the design goal shown in Fig. 11.66.

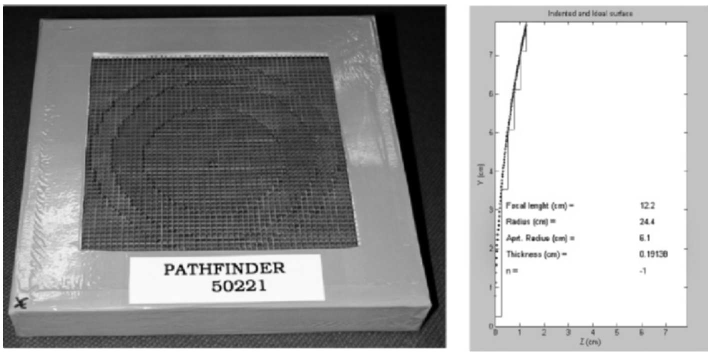

Fig. 11.59. Fabricated NIM lens (*left*) showing steps of the unit cell dimension (0.254 cm) used to approximate the smooth 24.4 cm radius of curvature (*right*) needed for a 12.2 cm focal length assuming an index of refraction $n = -1.0$ at the operating frequency of ~14.8 GHz. The unit cell dimensions of the 2E2H NIM lens (the unit cell couples with the E and H field along two orthogonal directions) are shown in Fig. 11.60

The far-field steering characteristics at 175 cm of the GRIN lens are shown in Fig. 11.69. These line plots correspond to moving a small dipole source off the optical axis in a direction perpendicular to the propagation direction at the focal spot (~10.0 cm). We see that the GRIN lens steers the beam similarly to the PIM and NIM lenses and again the simulation and experiment are in excellent agreement.

Finally, the electric far-field pattern and gain with respect to the empty aperture are shown in Figs. 11.70 and 11.71, respectively. Note that the gain for the GRIN lens is approximately 10.0 dB above the empty aperture and is comparable to the gain of the PIM lens.

11.7.5 Comparison of Experimental Data for Empty Aperture, PIM, NIM, and GRIN Lenses

We now compare the performance of our PIM, NIM, and GRIN lenses among each other at the approximate design frequency (14.8 ± 0.3 GHz) as well as below (13.1 GHz) and above (16.3 GHz) the design point. As shown in Fig. 11.60 (S21 magnitude vs. frequency for NIM unit cell) we expect the NIM lens to have little transmission at 13.1 GHz, perform best at ~14.8 GHz (where the unit cell is matched to free space), and have degraded performance at 16.3 GHz (where the NIM has good transmission but is not matched to free space). Indeed this is what we observe in our experimental measurements as shown in Fig. 11.72.

The aperture and lenses were illuminated by a small dipole placed approximately at the focal spot for each lens and the corresponding location for the empty aperture. Note that the electric field value for the NIM is approximately

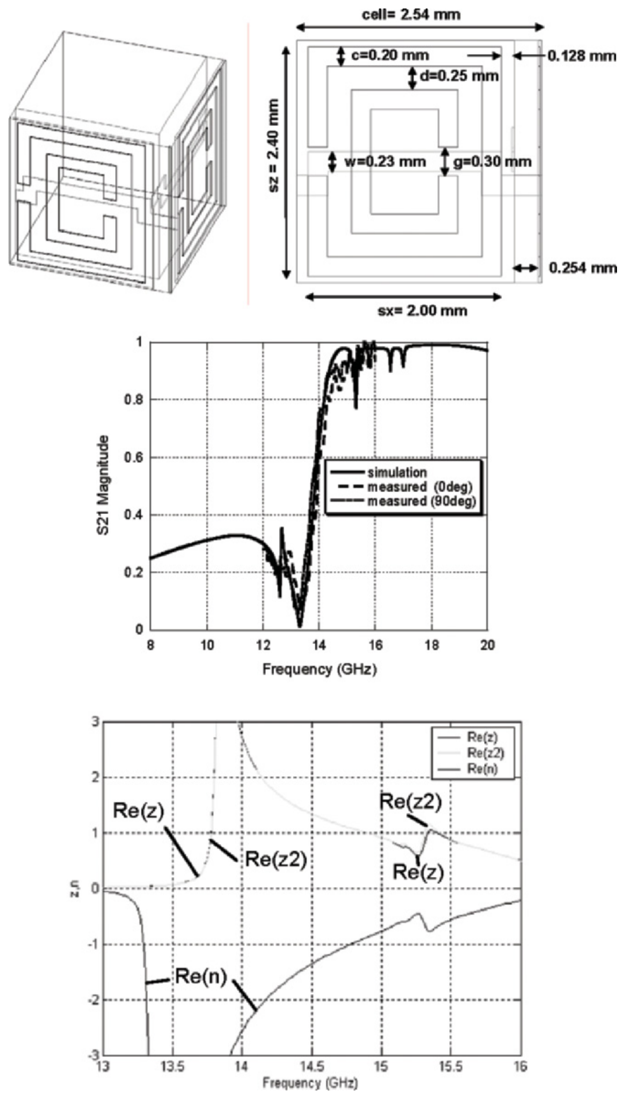

Fig. 11.60. NIM 2E2H unit cell design (*top*) and comparison of simulated and measured S21 values (*middle*) showing ∼0.90 transmission at the operating frequency of ∼14.8 GHz. The index of refraction (n) and impedance (Z) retrieved from the scattering parameters shows a match condition at ∼14.8 GHz (*bottom*)

50% of the value for the PIM lens at the design point of ∼14.8 GHz. This is due to losses in the NIM unit cell. If the transmission is ∼0.90 for a single unit cell at the designed frequency, then the transmission through the approximately five unit-cell thick NIM lens is $S21_{\mathrm{NIM}} \sim (0.9)^5 = 0.59$.

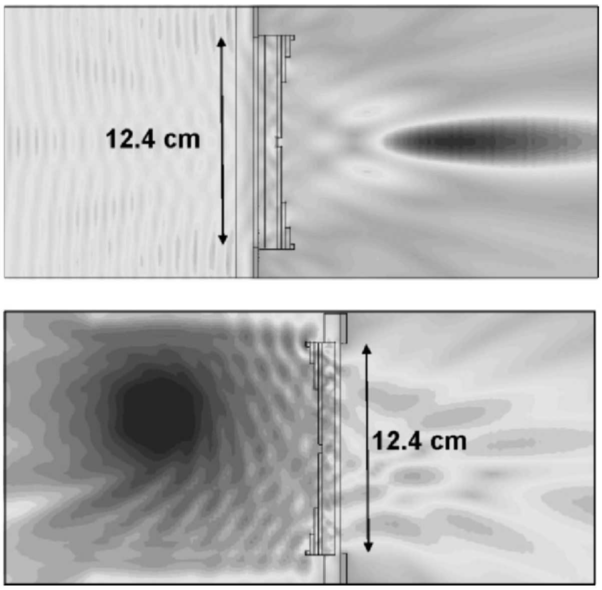

Fig. 11.61. MWS simulations of electric near-field amplitude for plane wave focusing (*top*) and small dipole (*bottom*) 2.0 cm above the central optical axis. The plane wave and dipole sources illuminate the NIM lens in an aluminum aperture having a 6.20 cm radius

For the PIM lens the transmission is much higher. For this case $S11_{\mathrm{PIM}} = E_{\mathrm{r}}/E_{\mathrm{o}} \sim (n-1)/(n+1) = (1.59-1.00)/(1.59+1.00) = 0.23$, where E_{o} is the incident field, E_{r} is the reflected field, and n is the refractive index of Rexolite. For one interface $S21_{\mathrm{PIM}} = (1-S11^2)^{1/2} = (1-0.23^2)^{1/2} = 0.97$, that becomes 0.94 for two interfaces, so we expect that $S21_{\mathrm{NIM}}/S21_{\mathrm{PIM}} \sim 0.59/0.94 = 0.63$ which is approximately what we observe experimentally. The experimental value (~ 0.50) is probably lower due to fabrication tolerances and the resulting increased impedance mismatch. We note however, that the FWHM of the NIM lens ($\sim 12.5°$) is smaller than the GRIN lens ($\sim 14°$) and PIM lens ($\sim 15°$) which is consistent with the aberration analysis discussed in the next section.

The GRIN lens exhibits a normalized electric far-field value that is approximately 75% that of the PIM lens. This is higher than the NIM lens due to the lower losses of the 1E1H unit cell structure. The GRIN lens FWHM maximum ($\sim 14°$) is smaller than the PIM lens but larger than the NIM lens. The experimental gain with respect to the empty aperture is shown in Fig. 11.73. Here, we see that the gain for the PIM is ~ 10 dB at each frequency 13.1, 14.8, and 16.3 GHz, whereas the gain for the NIM is ~ -30.0, 5.0, and 3.0 dB, respectively. The GRIN lens gain is ~ 9.0 dB at ~ 14.8 GHz, which is only slightly less than the PIM lens.

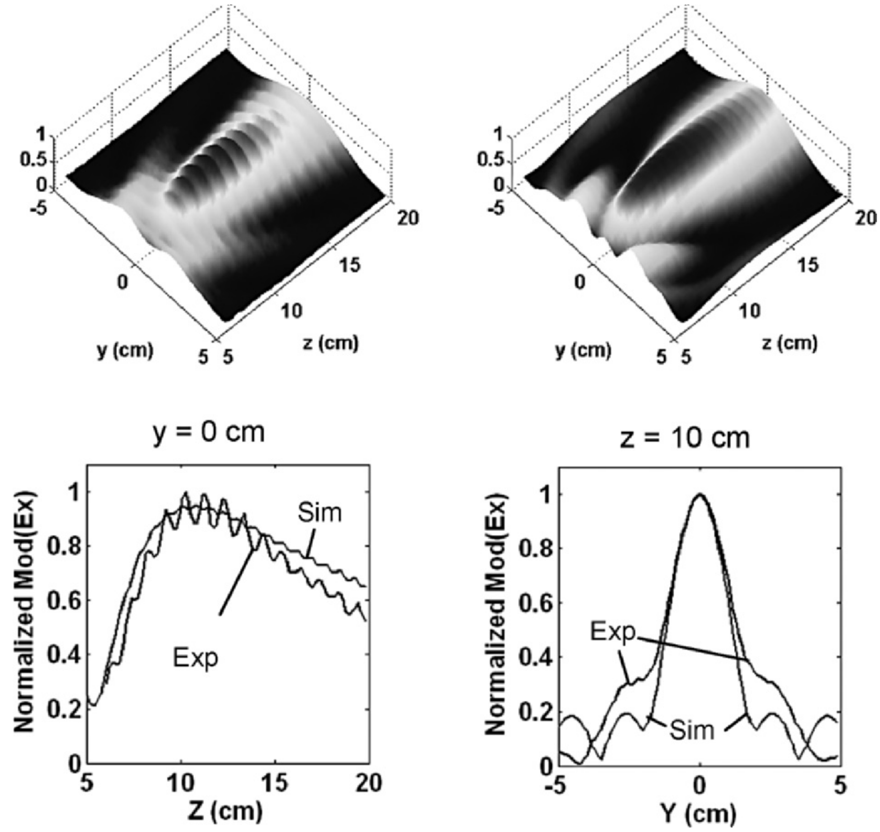

Fig. 11.62. Experimental (*top left*) and MWS simulated (*top right*) focusing electric near-field amplitude of NIM lens at 14.6 GHz. The line plots (*bottom*) of the experimental and MWS simulated fields are in excellent agreement. Note that the focal spot for this NIM lens occurs at ~10.0 cm

11.7.6 Comparison of Simulated and Experimental Aberrations for the PIM, NIM, and GRIN Lenses

In this section, we calculate the primary aberrations from the known eikonal surface ζ^{10}. The eikonal surface is simply the phase in a plane perpendicular to the wave propagation direction divided by the wave vector, k. The primary aberrations are defined as follows:

$$\text{Spherical Aberration} = \frac{1}{\sqrt{2}} A_{040} \left(6\rho^4 - 6\rho^2 + 1\right), \tag{11.35}$$

$$\text{Coma} = A_{031} \left(3\rho^3 - 2\rho\right) \cos\left(\theta\right), \tag{11.36}$$

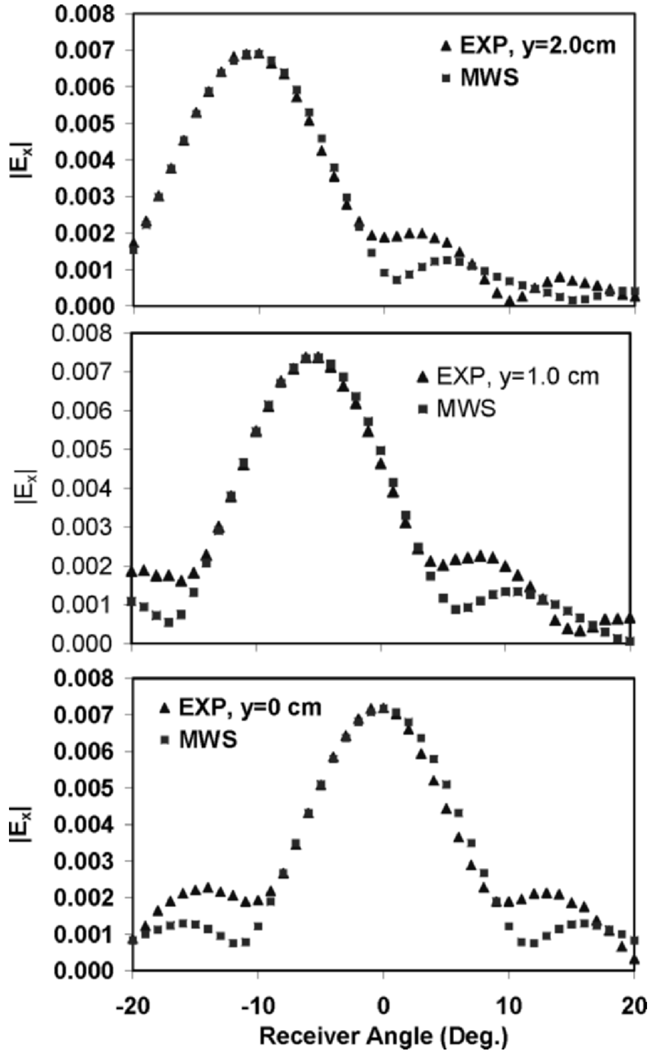

Fig. 11.63. Normalized experimental (*triangles*) and MWS simulated (*squares*) steering electric far-field amplitude of NIM lens when source is on and off optical axis. Starting at the bottom and moving upward, the source displacement is 0.0, 1.0, and 2.0 cm. The line plots of the experimental and MWS simulated fields are in excellent agreement

$$\text{Astigmatism} = A_{022}\rho^2 \left[2\cos^2(\theta) - 1\right], \tag{11.37}$$

$$\text{Curvature of Field} = \frac{1}{\sqrt{2}} A_{120} \left(2\rho^2 - 1\right), \tag{11.38}$$

$$\text{Distortion} = A_{111}\rho\cos(\theta). \tag{11.39}$$

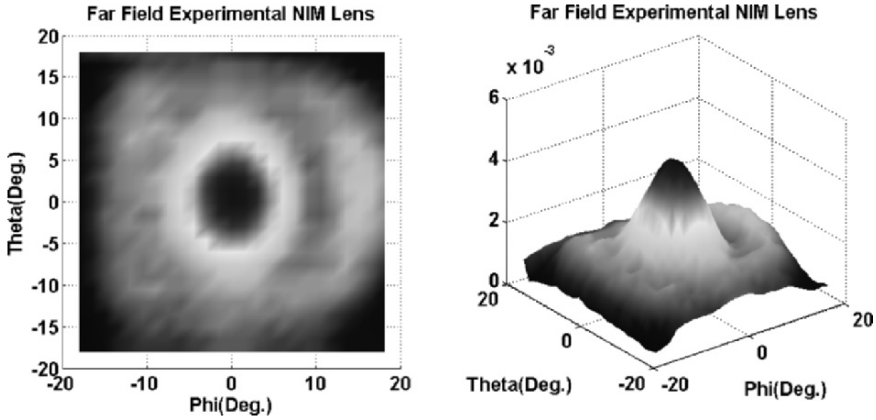

Fig. 11.64. Normalized electric far field at 2.0 m for the NIM lens illuminated by small dipole at the focal spot as a function of angle θ and ϕ

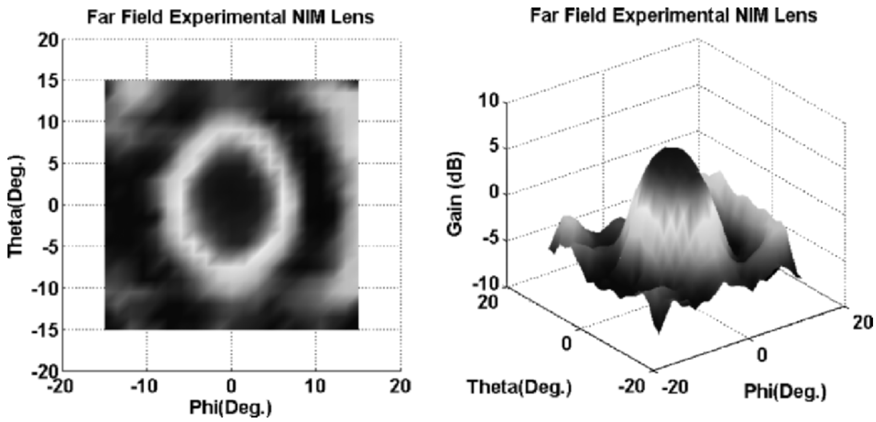

Fig. 11.65. Gain with respect to empty aperture in far field at 2.0 m for the NIM lens illuminated by small dipole at the focal spot (~10.0 cm) as a function of angle θ and ϕ

We also compute the normalized intensity

$$i = \frac{1}{\pi^2} \left| \int_0^1 \int_0^{2\pi} \mathrm{e}^{\mathrm{i}k_0\zeta} \rho \, \mathrm{d}\rho \, \mathrm{d}\theta \right|^2 . \tag{11.40}$$

Here we set $\rho = r/a$ where a is the pupil radius.

The Seidel coefficients A_{lmn} can be computed from the eikonal surface ζ with the help of the Zernike polynomials. The eikonal can be written as

$$\zeta(\rho, \theta) = \sum\nolimits_{n,m} \varepsilon_{nm} A_{\ln m} R_n^m(\rho) \cos(m\theta). \tag{11.41}$$

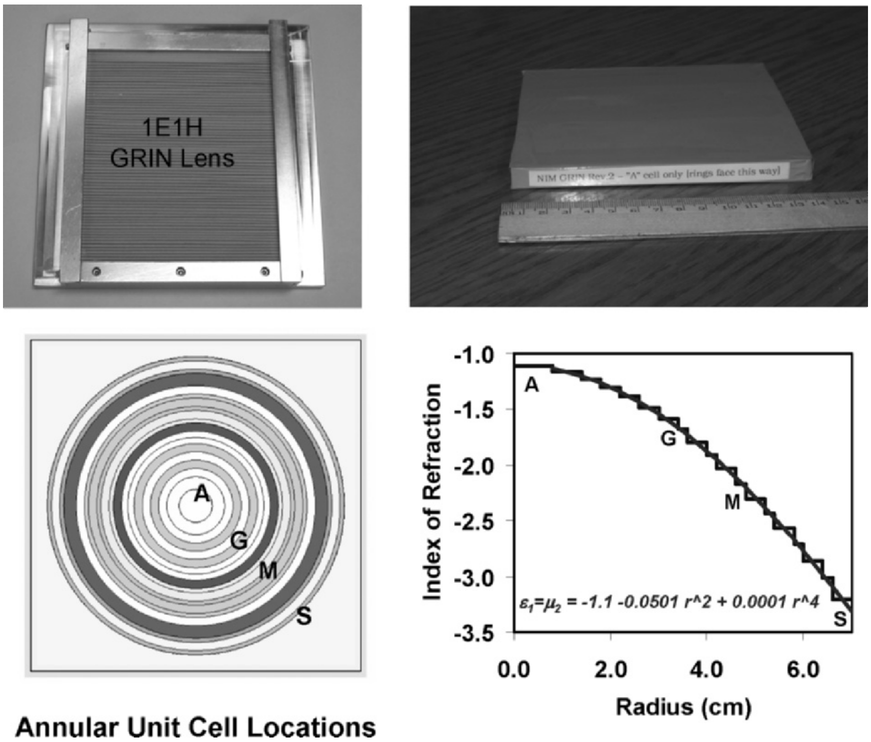

Fig. 11.66. Fabricated GRIN lens in its fixture and after completion (*top*), location of various cell types (*bottom left*), and stepwise approximation to smooth $\varepsilon = \mu = -1.1 - 0.0501\, r^2 + 0.0001\, r^4$ gradient (*bottom right*) needed for 12.7 cm focal length. Note that each unit cell, A–S, has a different index of refraction ranging from $n = -1.1$ to -3.2

For the Seidel aberrations:

$$2l + m + n = 4 \text{ and } \varepsilon_{nm} = \begin{cases} \dfrac{1}{\sqrt{2}}, & m = 0, n \neq 1 \\ 1, & \text{otherwise.} \end{cases} \tag{11.42}$$

We compute the A_{lmn} coefficients from (11.41) using the orthogonality properties of the Zernike polynomials and of the cosine functions:

$$\int_0^1 R_n^l(\rho) R_{n'}^l(\rho)\, \rho\, \mathrm{d}\rho = \frac{\delta_{nn'}}{2\,(n+1)} \text{ and } \int_0^{2\pi} \cos(m\theta)\cos(m'\theta)\mathrm{d}\theta = \pi\delta_{mm'}, \quad m > 0,$$

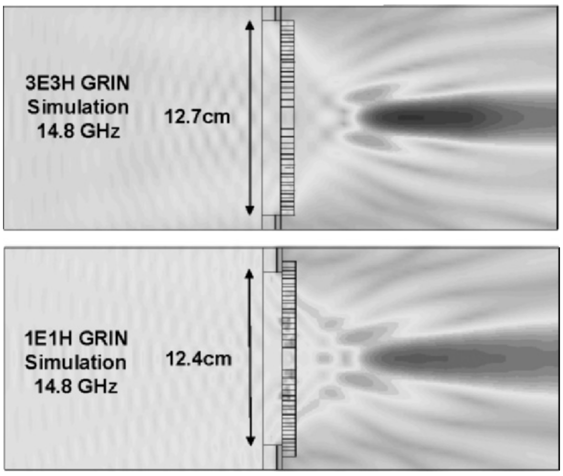

Fig. 11.67. Simulated electric near-field focusing for 3E3H (*top*) and 1E1H (*bottom*) GRIN lens. Note that the 1E1H effective medium performs essentially the same as the 3E3H medium for this application

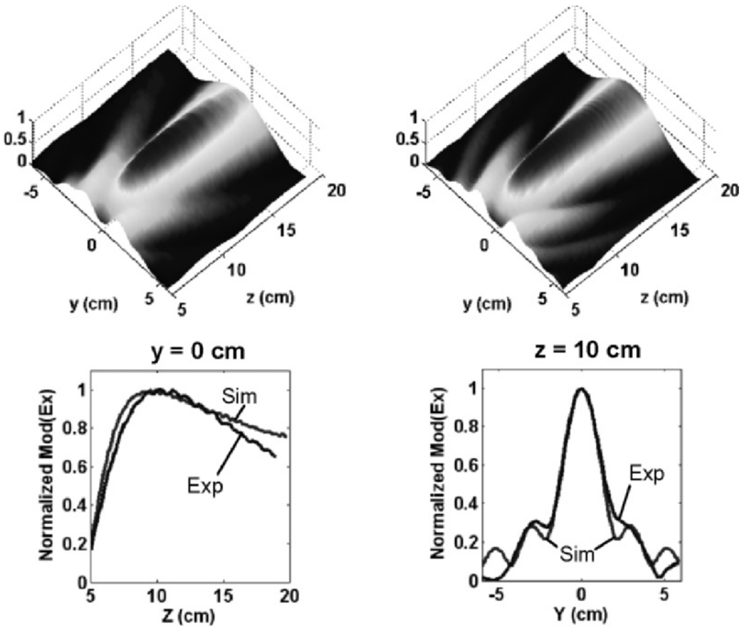

Fig. 11.68. Experimental (*top left*) and MWS simulated (*top right*) focusing electric near-field amplitude of the GRIN lens at 15.0 GHz. The line plots (bottom) of the experimental and MWS simulated fields are in excellent agreement. The focal spot for this lens is at ∼10.0 cm. Note that the index gradient for the simulation was adjusted to match the experimental data. This is most likely due to fabrication tolerances in ring and wire structures

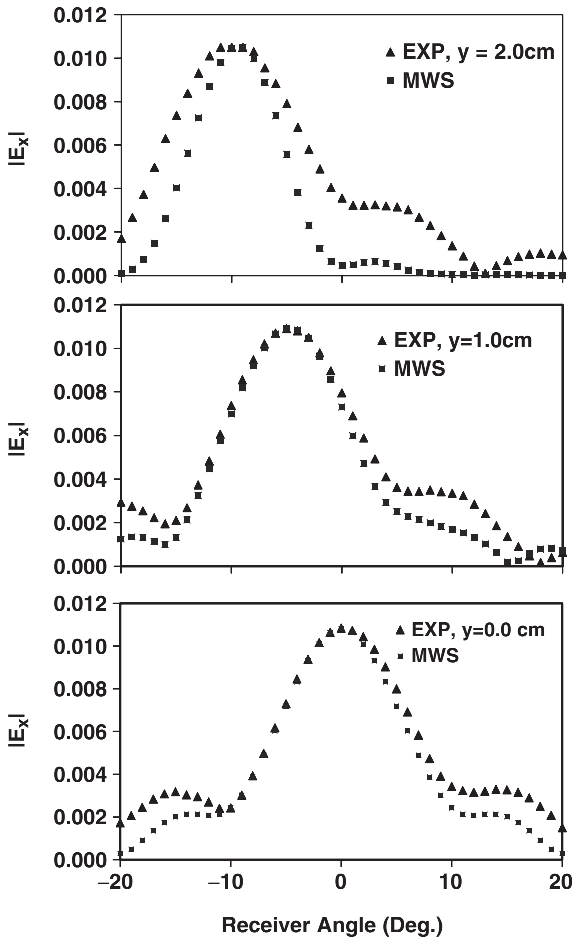

Fig. 11.69. Normalized experimental (*triangles*) and MWS simulated (*squares*) steering electric far-field amplitude of the GRIN lens when the source at the focal spot is on and off the optical axis. Starting at the bottom and moving upward the source displacement is 0.0, 1.0, and 2.0 cm. The line plots of the experimental and MWS simulated fields are in very good agreement

$$\int_0^1 R_{n'}^{m'}(\rho)\,\rho\,\mathrm{d}\rho \int_0^{2\pi} \zeta(\rho,\theta)\cos(m'\theta)\,\mathrm{d}\theta =$$
$$\sum\nolimits_{n,m} \varepsilon_{nm} A_{\ln m} \int_0^1 R_n^m(\rho)\,R_{n'}^{m'}(\rho)\,\rho\,\mathrm{d}\rho \int_0^{2\pi} \cos(m\theta)\cos(m'\theta)\,\mathrm{d}\theta. \tag{11.43}$$

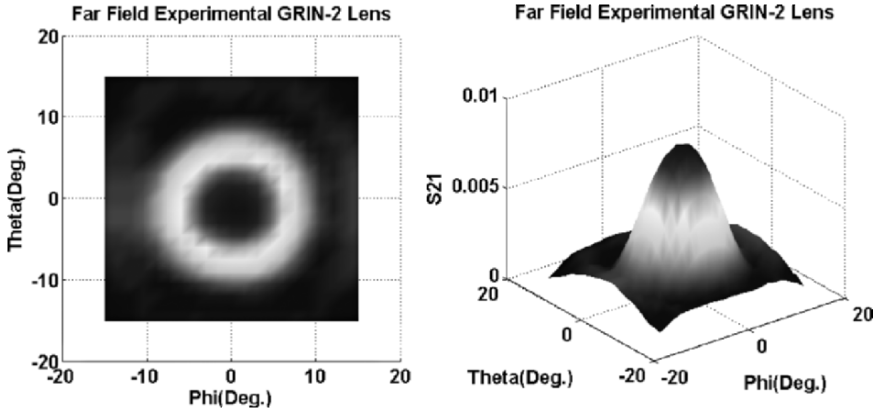

Fig. 11.70. Normalized electric far-field at 2.0 m for GRIN lens illuminated by small dipole at the focal spot (~10.0 cm) as a function of receiver angle θ and ϕ at 15.0 GHz

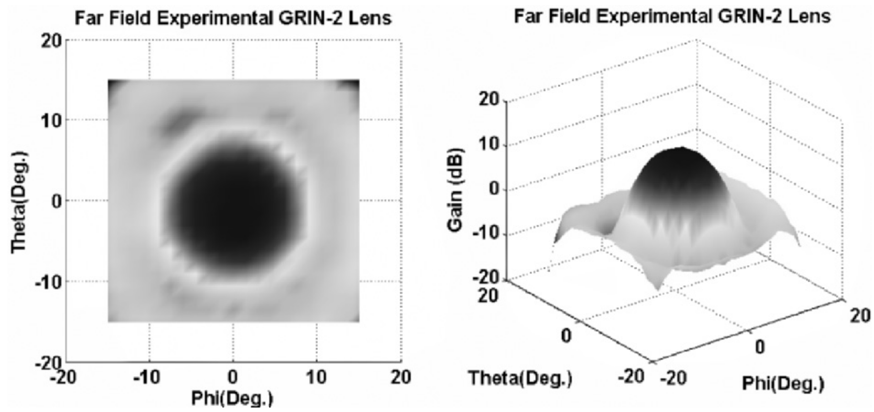

Fig. 11.71. Gain with respect to empty aperture in far field at 2.0 m for GRIN lens illuminated by small dipole at the focal spot (~10.0 cm) as a function of angle θ and ϕ at 15.0 GHz

It follows that:

$$\int_0^1 R_{n'}^{m'}(\rho)\,\rho\,\mathrm{d}\rho \int_0^{2\pi} \zeta(\rho,\theta)\cos(m'\theta)\,\mathrm{d}\theta = \sum\nolimits_{n,m} \varepsilon_{nm} A_{\ln m} \frac{\delta_{nn'}}{2(n+1)}\pi\delta_{mm'}$$

$$= \frac{\pi}{2(n'+1)}\varepsilon_{n'm'}A_{l'n'm'}.$$

$$A_{lmn} = \frac{2(n+1)}{\pi\varepsilon_{nm}}\int_0^1 R_n^m(\rho)\,\rho\,\mathrm{d}\rho\int_0^{2\pi}\zeta(\rho,\theta)\cos(m\theta)\,\mathrm{d}\theta. \qquad (11.44)$$

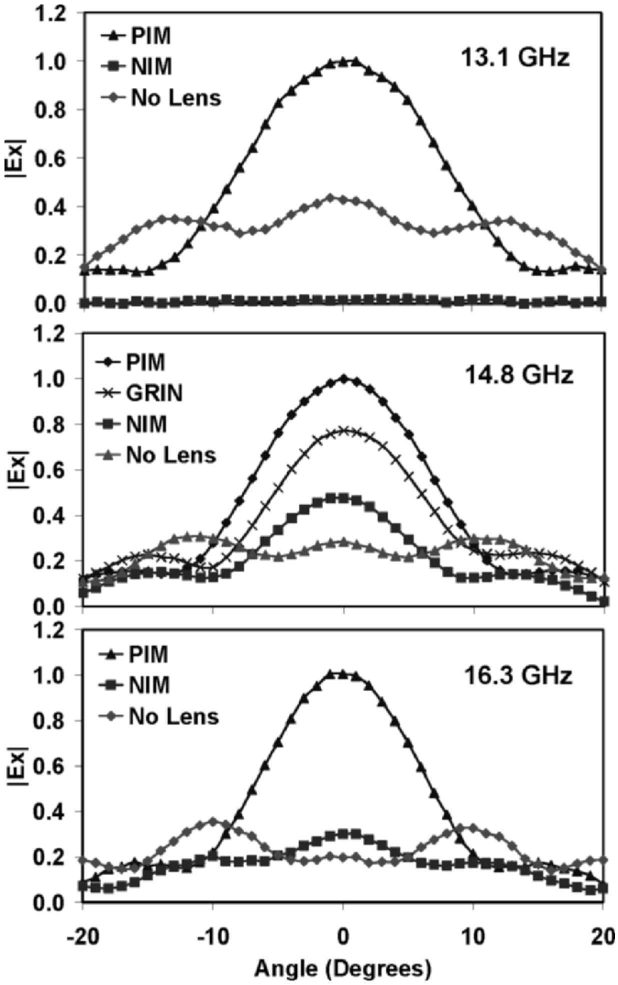

Fig. 11.72. Experimental normalized electric field magnitude for aperture, PIM, NIM, and GRIN lenses at 13.1 (below NIM resonance), 14.8 (at NIM impedance match point), and 16.3 (above NIM impedance match point) GHz for the source at the respective focal spot and the detector in the far field at 1.75 m

The eikonal surfaces of the PIM, NIM, and GRIN lenses based on MWS simulations and the corresponding experimental data are shown in Fig. 11.74. This figure shows reasonable agreement between the simulated and experimental data. From the eikonal surface the aberrations are calculated as outlined above. The normalized intensity i for the PIM, NIM, and GRIN lenses is shown in Fig. 11.75.

For both the simulated and experimental data we see that the NIM normalized intensity is higher than the GRIN and PIM. That is the NIM has

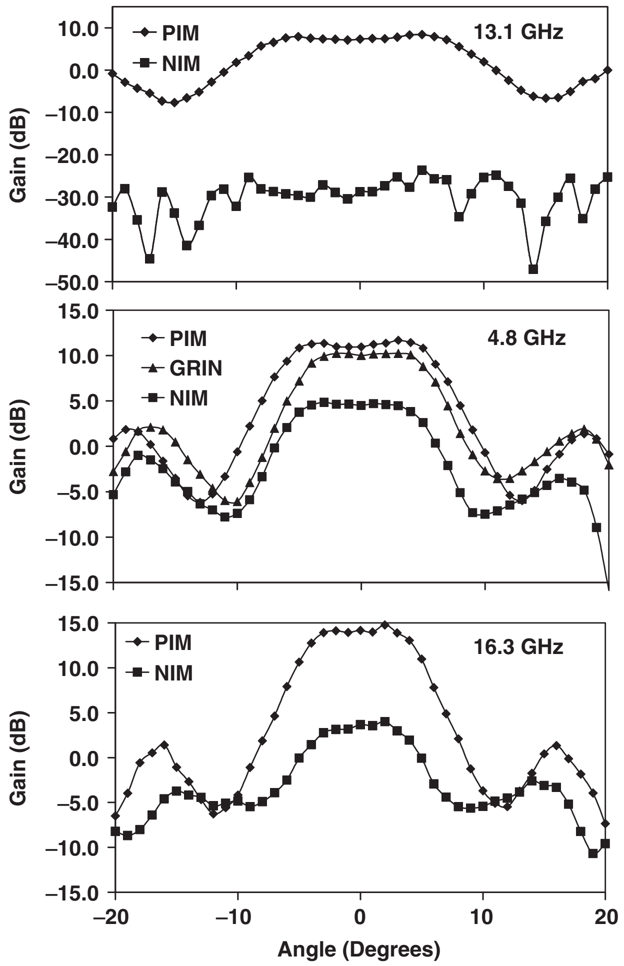

Fig. 11.73. Experimental gain with respect to empty aperture, for PIM, NIM, and GRIN lenses at 13.1, 14.8, and 16.3 GHz. Note that the gain of the PIM and GRIN lenses are very close

a narrower full width half maximum than do the GRIN and PIM lens. This is evident in the experimental data. The fact that losses are also incurred reduces the amplitude of the NIM lens with respect to the GRIN and PIM lenses even though the full width half maximum is narrower.

The corresponding field curvature (A120) using the MWS simulated and experimental phases for the NIM, GRIN, and PIM lenses is also given in Fig. 11.75. From this figure we see that the trends in the simulated and experimental data are the same. That is, on average, the field curvature (A120) is higher for the NIM than the GRIN and PIM lenses. On the basis of these criteria, the NIM lens shows superior performance with respect to the GRIN

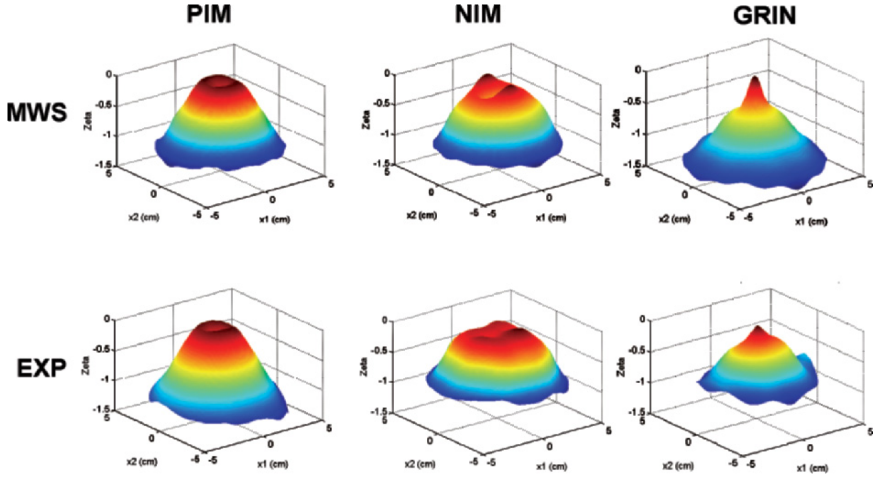

Fig. 11.74. Simulated (*top row*) and experimental (*bottom row*) eikonal surfaces computed from the phase in a plane perpendicular to the wave propagation direction, near the exit aperture for the PIM, NIM, and GRIN lenses. The eikonal surface is simply the phase divided by the wavevector k

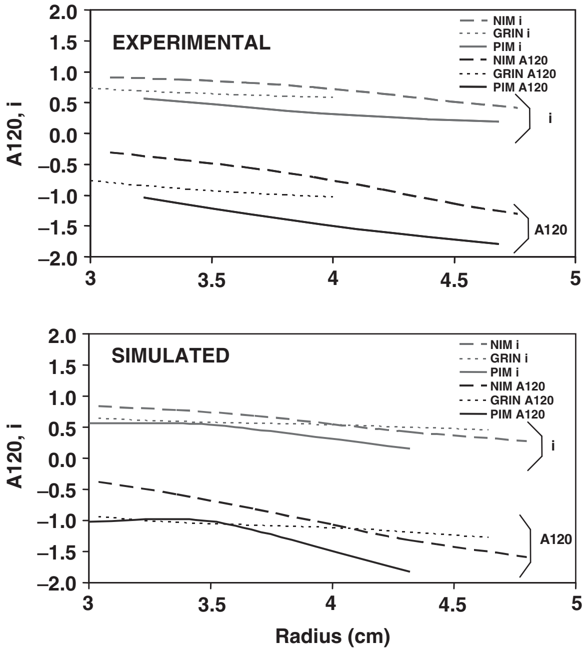

Fig. 11.75. Normalized intensity (i) and field curvature (A120) calculated using experimental (*top*) and MWS simulated (*bottom*) phase in a plane perpendicular to the wave propagation direction. Note that on average the normalized intensity (i) and the curvature of field (A120) are higher for the NIM than the GRIN and PIM lenses

and PIM lenses. Again it must be recognized that these criteria do not include losses. Of course, it may be possible to improve the performance of the GRIN and PIM lenses by adjusting the index gradient and using aspherical surfaces. If losses are included then, the PIM and GRIN lenses show favorable performances over the NIM lenses. Also, we note that much of the difference between the simulated and experimental aberrations is due to coupling between the experimental probe and the lens/setup.

11.7.7 Weight Comparison Between the PIM, NIM, and GRIN Lenses

We compared the weight of three types of NIM lenses as another metric of their physical properties. The respective weights are given below:

PIM	323.8 g
NIM Pathfinder Spherical Lens with 3-cell-thick bottom layer	229.5 g
NIM Pathfinder Spherical Lens with 1-cell-thick bottom layer	142.2 g
GRIN Lens	75.4 g

This data shows the obvious weight advantage of NIM lenses due to their honeycomb like fabrication structure.

11.8 Conclusion

Major advances in NIMs were made in (1) their design, such that they have a desired value for n and Z, (2) their characterization both in waveguides and free space, both in the near field and at far field, (3) the design of novel NIM optics, namely lenses, both with physical curvature and gradient index, (4) the characterization of such NIM lenses and in comparison with conventional PIM lenses, and (5) demonstrating that negative index lenses have inherently lower aberrations than their corresponding PIMs. NIMs can be made with properties that are attractive for practical applications, such as low loss and bandwidth of the order of 8–10% of the center frequency. Most of the work carried out has been in the microwave region but it is clear that many of the concepts used are applicable to other frequency domains.

Acknowledgements

The authors would like to acknowledge the contributions of the many individuals who helped in this effort. From the Boeing team, Ben Koltenbah, and later Tai Lam for the numerical simulations and theoretical calculations related to various NIM structures and lenses; Mark Thompson, Art Vetter, and Kin Li for metamaterial testing; Jean Nielsen for fabrication of the unit cell structures and lenses. From the Duke University team, David Smith and Dave Schurig for their many contributions to general NIM physics and lens properties. From the University of California at San Diego, Dave Vier for his detailed designs of unit cell structures and Sheldon Schultz for technical advice and experimental suggestions. From Iowa State University, Costas Soukoulis, Thomas Koschny, Lei Zhang, and Stavroula Foteinopoulou for analyzing some of the fundamental physics of NIMs and their implications. The authors would like to extend special thanks to Valerie Browning at DARPA for continuous encouragement, advice, and support during this effort that was supported under contract MDA972-01-2-0016.

References

1. V.G. Veselago, Sov. Phys. Usp. **10**, 509 (1968)
2. J.B. Pendry, A.J. Holden, D.J. Robbins, W.J. Stewart. IEEE Trans. Microw. Theory Tech. **47**, 2075 (1999)
3. D.R. Smith, W. Padilla, D.C. Vier, S.C. Nemat-Nasser, S. Schultz, Phys. Rev. Lett. **84**, 4184 (2000)
4. J.D. Jackson, *Classical Electrodynamics*, 3rd edn. (1999)
5. R.B. Greegor, C.G. Parazzoli, K. Li, M.H. Tanielian, Appl. Phys. Lett. **82**(14), 2356 (2003)
6. R.B. Greegor, C.G. Parazzoli, K. Li, B.E.C. Kotlenbah, M.H. Tanielian, Opt. Express **11**(7), 688 (2003)
7. P. Markos, C.M. Soukoulis, Phys. Rev. B. **65**, 033401 (2002); Phys. Rev. E **65**, 036622 (2002)
8. D.R. Smith, D. Schurig, Phys. Rev. Lett. **90**, 77405 (2003); D.R. Smith, P. Kolinko, D. Schurig, J. Opt. Soc. B **21**, 1032 (2004)
9. P. Kolinko, D.R. Smith, Opt. Express **11**, 640 (2003)
10. C.G. Parazzoli, B.E.C. Koltenvbah, R.B. Greegor, T.A. Lam, M.H. Tanielian, J. Opt. Soc. Am. B **23**, 439 (2006)
11. C.G. Parazzoli, R.B. Greegor, K. Li, B.E.C. Koltenbah, M.H. Tanielian, Phys. Rev. Lett. **90**(10), 107401 (2003)
12. MWS and MAFIA are commercial software packages available from CST
13. P. Markos, C.M. Soukoulis, Opt. Express **11**, 649 (2003); T. Koschny, M. Kafesaki, E.N. Economou, C.M. Soukoulis, Phys. Rev. Lett. **93**, 107402 (2004)
14. T. Koschny, P. Markos, D.R. Smith, C.M. Soukoulis, Phy. Rev. E **68**, 065602(R) (2003); T. Koschny, P. Markos, E.N. Economou, D.R. Smith, D.C. Vier, C.M. Soukoulis, Phys. Rev. B **71**, 245105 (2005)
15. K. Li, S.J. McLean, R.B. Greegor, C.G. Parazzoli, M.H. Tanielian, Appl. Phys. Lett. **82**(15), 2535 (2003); R.B. Greegor, C.G. Parazzoli, K. Li, M.H. Tanielian, Appl. Phys. Lett. **82**(14), 2356 (2003)
16. D. Vier, D.R. Fredkin, A. Simic, S. Schultz, M. Tanielian, Appl. Phys. Lett. **86**, 241908 (2005)
17. D. Schurig, D.R. Smith, Phys. Rev. E **70**, 065601(2004)
18. C.G. Parazzoli, R.B. Greegor, J.A. Nielsen, M.A. Thompson, K. Li, A.M. Vetter, D.C. Vier, M.H. Tanielian, Appl. Phys. Lett. **84**(17), 3232 (2004)

19. R.B. Greegor, C.G. Parazzoli, J.A. Nielsen, M.A. Thompson, M.H. Tanielian, D.C. Vier, S. Schultz, D.R. Smith, D. Schurig, Proceedings of the 2005 Antenna Applications Symposium, Monticello, Illinois, September 2005; R.B. Greegor, C.G. Parazzoli, J.A. Nielsen, M.A. Thompson, M.H. Tanielian, D.C. Vier, S. Schultz, D.R. Smith, D. Schurig, IET Microw. Antennas Propag. **1**, 108 (2007)
20. R.B. Greegor, C.G. Parazzoli, J.A. Nielsen, M.A. Thompson, M.H. Tanielian, Appl. Phys. Lett. **87**, 091114 (2005)

12

Nonlinear Effects in Left-Handed Metamaterials

I.V. Shadrivov and Y.S. Kivshar

Summary. We overview different types of nonlinear effects recently predicted for microstructured metamaterials which exhibit left-handed properties and negative refraction. We show that both magnetic and electric nonlinear response in such microstructured composites can be enhanced significantly compared to bulk media, since local electric fields in metallic microresonators may become extremely strong. We predict that nonlinear properties of metamaterials can allow for various applications, including a dynamic control and tunability of the electromagnetic properties of the composite structures, second-harmonic generation, intensity-dependent switches, and soliton generation.

12.1 Introduction

Novel types of microstructured materials that demonstrate many intriguing properties for electromagnetic waves such as negative refraction have been discussed recently in many theoretical studies [1–4], and currently such materials are being studied experimentally [5–7]. The simplest composite materials of this type are created by a mesh of metallic wires and split-ring resonators (SRRs), and their unique properties are associated with negative real parts of magnetic permeability and dielectric permittivity for microwaves. Such composite materials are often referred to as *left-handed materials* (LHMs) or *materials with negative refractive index*. Properties of LHMs were analyzed first theoretically by Veselago a long time ago [8], but such materials were demonstrated experimentally only recently. As was shown by Veselago [8], the LHMs possess a number of peculiar properties, including negative refraction for interface scattering, inverse light pressure, reverse Doppler and Vavilov–Cherenkov effects, etc.

Since the first days of the extensive studies of metamaterials and their properties, attention of most of the researchers was focused on linear properties of LHMs, when the parameters of the composites do not depend on the intensity of the electromagnetic field. However, the future efforts in creating *tunable structures* where, e.g., the field intensity can be used for dynamic control of the transmission properties of the composite structure would require the study of nonlinear properties of such metamaterials, which may be quite unusual. As we show in this chapter, this is because the fabricated metamaterials are composed of a mesh of conducting metallic components, namely wires and SRRs. The wires are used to provide negative dielectric permittivity, while SRRs give negative magnetic permeability. The dynamic control over metamaterials properties is nontrivial since they possess left-handed properties only in some finite frequency range, which is basically determined by the geometry of the structure. The possibility to control the effective parameters of the metamaterial using nonlinearity has recently been suggested in [9, 10]. The main reason for nontrivial behavior of nonlinear metamaterials is that the microscopic electric field in the vicinity of the metallic particles forming left-handed structure can be much higher than the macroscopic electric field carried by the propagating wave. This provides a simple physical mechanism for enhancing nonlinear effects in LHMs. We believe our findings may stimulate the future experiments in this field, as well as the studies of nonlinear effects in photonic crystals, where the phenomenon of negative refraction is analyzed now very intensively [11, 12].

In this chapter, we demonstrate that the dominant nonlinear properties of metamaterials arise from the hysteresis-type dependence of the magnetic permeability on the magnetic field intensity in the electromagnetic wave propagating through the material. It allows changing the material properties from left- to right-handed and back. Using the finite-difference time-domain simulations, we study the wave scattering from a slab of a nonlinear LHM and discuss a possibility of generation and propagation of spatiotemporal solitons in such materials. We demonstrate also that the nonlinear left-handed metamaterials can support both transverse electric- and transverse magnetic-polarized self-trapped localized beams, *spatial electromagnetic solitons*. We also discuss the physical mechanisms and novel effects in the parametric processes such as second-harmonic generation (SHG), which can take place in metamaterials. We demonstrate a novel type of the exact spatiotemporal phase matching between the backward propagating wave of the fundamental frequency (FF) and the forward propagating wave of the second harmonic (SH). We show that this novel parametric process can convert a surface of the left-handed metamaterial into an effective mirror totally reflecting the SHs generated by an incident wave. We derive and analyze theoretically the coupled-mode equations for a semi-infinite nonlinear metamaterial and a metamaterial slab of a finite thickness, and reveal the existence of multistable nonlinear effects. We also suggest the way to further enhance the SHG in metamaterials, by using *a double-resonant* metamaterial. We introduce somewhat exotic concept of nonlinear lens, which is capable of creating image of the source of electromagnetic waves being opaque at the FF, but transparent for the SH field.

This chapter is organized as follows. In Sect. 12.2, we present an overview of some nonlinear properties of left-handed metamaterials for the example of a lattice of SRRs and wires embedded in a nonlinear dielectric. Further in this section, we demonstrate the numerical model for the simulation of the nonlinear metamaterial by means of the finite-difference time-domain (FDTD) method. In particular, we study the wave scattering by a slab of a nonlinear composite structure. We also discuss the structure of electromagnetic solitons supported by the nonlinear LHMs with hysteresis-type nonlinear response. In Sect. 12.3, we discuss the metamaterials with Kerr-like nonlinear response, and study nonlinear surface waves as well as band-gap structures with LHMs. In Sect. 12.4, we study second-order nonlinear effects in metamaterials, such as SHG. We show the possibility of the nontrivial phase-matching which is possible in metamaterials, allowing for the creation of the SH reflecting mirror. We also suggest a way to enhance the efficiency of SHG by means of double-resonant metamaterials.

12.2 Nonlinear Response of Metamaterials

We consider a three-dimensional composite structure in the form of a cubic lattice of conducting wires and SRRs. We assume that the unit-cell size d_{cell} of the structure is much smaller than the wavelength of the electromagnetic wave propagating in the material, for simplicity, we choose the single-ring geometry of a lattice of SRRs. The results obtained for this case are qualitatively similar to those obtained in more involved cases of double SRRs near low-frequency resonance, for which the currents in both rings of the double SRR are in-phase.

The negative real part of the effective dielectric permittivity of such a composite structure appears due to the metallic wires whereas a negative magnetic permeability becomes possible due to the SRR lattice. As a result, these materials demonstrate the properties of negative refraction in a finite frequency range, i.e., $\omega_0 < \omega < \min(\omega_{\mathrm{p}}, \omega_{\|\mathrm{m}})$, where ω_0 is the eigenfrequency of the array of SRRs, $\omega_{\|\mathrm{m}}$ is some characteristic frequency, which we call the frequency of the longitudinal magnetic plasmon, ω_{p} is the effective plasma frequency, and ω is the angular frequency of the propagating electromagnetic waves, $(\mathcal{E}, \mathcal{H}) \sim (\mathbf{E}, \mathbf{H}) \exp(\mathrm{i}\omega t)$. The SRR can be described as an effective LC oscillator (see, e.g., [13]) with capacitance of the SRR gap, as well as an effective inductance and resistance.

If we embed the structure in a nonlinear dielectric, we expect it to exhibit quite unusual properties. The nonlinearity here must become complex in the sense that both the dielectric permittivity and the magnetic permeability will change with the variation of the external electromagnetic fields. Nonlinear dielectric response is determined by the bulk of the nonlinear dielectric, and frequency-dependant contribution will be provided by wires. Since we assume that the nonlinear dielectric does not possess magnetic properties itself, it seems that the magnetic response of the composite will still be determined by the array of SRRs. However, the response of the SRRs depends on the field pattern in the vicinity of the resonators, which, in turn, depends on the properties of the dielectric. Thus, both dielectric and magnetic responses of the composite are nonlinear.

As we just mentioned above, the nonlinear magnetic response will be determined by the dielectric which is close to the SRRs, and, in particular, in SRR slits where the electric field is the strongest. The dielectric response is due to bulk of the nonlinear dielectric. This suggests the way to *engineer the nonlinear response* of the composite structure. E.g., one can include small amount of nonlinear material to the SRRs, and the whole composite will have nonlinear magnetic properties only. Placing dielectric everywhere in the composite except the very vicinity of the SRRs will produce nonlinear dielectric properties, with linear magnetic response.

12.2.1 Nonlinear Magnetic Permeability

First, we assume that only the slits of the SRRs are filled with nonlinear dielectric with a permittivity that depends on the intensity of the electric field $|E|^2$ in a rather general form, $\varepsilon_{\mathrm{D}} = \varepsilon_{\mathrm{D}}(|\mathbf{E}|^2)$. For the calculations presented below, we take the dependence that corresponds to the Kerr-type nonlinear response, $\varepsilon_{\mathrm{D}} = \varepsilon_{\mathrm{l}} + \alpha|E|^2/E_{\mathrm{c}}^2$, where ε_{l} is the linear part of the dielectric permittivity, E_{c} is a characteristic electric field strength, $\alpha = +1$ for focusing nonlinearity, and $\alpha = -1$ for defocusing nonlinearity.

The nonlinear magnetic response of the composite material comes from the lattice of resonators since the SRR capacitance (and, therefore, the SRR eigenfrequency) depends on the strength of the local electric field in a narrow slit (we assume here that the capacitance of the SRR is due to its slit only). The intensity of the local electric field in the SRR gap, E_{g}, depends on the electromotive force in the resonator loop, which is induced by the magnetic field. Therefore, the effective magnetic permeability μ_{eff} depends on the macroscopic (average) magnetic field $\mathbf{H}$, and this dependence can be found [9, 14] in the three-dimensional case in the form:

$$\mu_{\mathrm{eff}}(\mathbf{H}) = 1 + \frac{F\,\omega^2}{\omega_{0\mathrm{NL}}^2(\mathbf{H}) - \omega^2(1 + F/3) + \mathrm{i}\Gamma\omega}, \tag{12.1}$$

where

$$\omega_{0\mathrm{NL}}^2(\mathbf{H}) = \left(\frac{c}{a}\right)^2 \frac{d_{\mathrm{g}}}{[2\pi r_{\mathrm{w}}\varepsilon_{\mathrm{D}}(|\mathbf{E}_{\mathrm{g}}(\mathbf{H})|^2)]}$$

is the eigenfrequency of nonlinear oscillations, $\Gamma = c^2/4\pi\sigma a r_{\mathrm{w}}$ the damping coefficient, $F = \pi^2 a^3/2d_{\mathrm{cell}}^3[\ln(8a/r_{\mathrm{w}}) - 7/4]$ the filling factor, a is the SRR radius, r_{w} the radius of the SRR wire, σ the conductivity of the wires, E_{g} the strength of the electric field in the SRR slit, c the speed of light. It is important to note that (12.1) has a simple physical interpretation: The resonant frequency of the artificial magnetic structure depends on the amplitude of the external magnetic field and, in turn, this leads to the intensity-dependent function μ_{eff}.

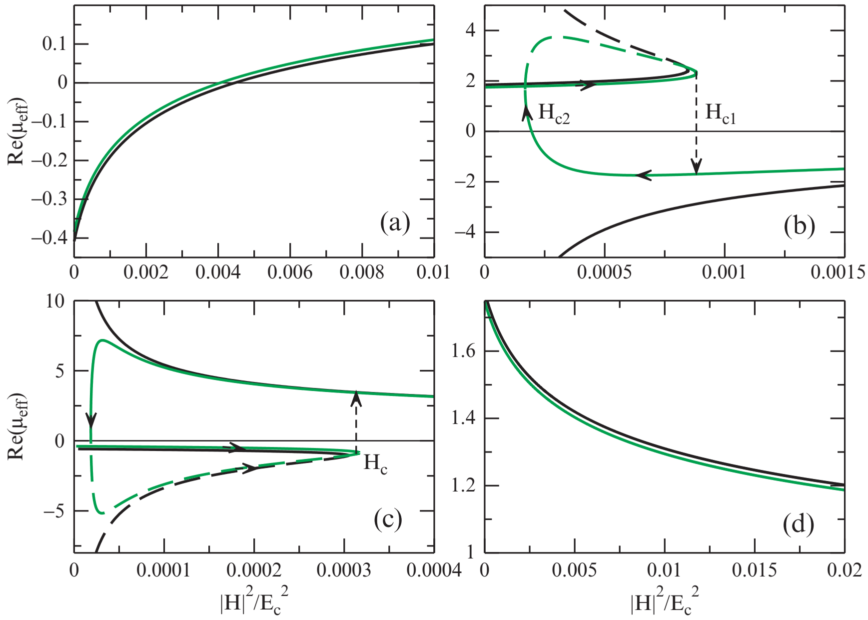

Fig. 12.1. *Solid green*: Real part of the effective magnetic permeability vs. normalized intensity of the magnetic field for $\Gamma/\omega_0 = 0.05$. (**a**) $\Omega > 1$, $\alpha = 1$; (**b**) $\Omega < 1$, $\alpha = 1$, (**c**) $\Omega > 1$, $\alpha = -1$; and (**d**) $\Omega < 1$, $\alpha = -1$. *Solid black*: lossless limit for $\Gamma/\omega_0 = 0$. Dashed: unstable branches [9]

Figures 12.1 and 12.2 summarize different types of nonlinear composites which are characterized by the dependence of the dimensionless frequency of the external field $\Omega = \omega/\omega_0$ for both *focusing* (Figs. 12.1a, b and 12.2a, b) and *defocusing* (Figs. 12.1c, d and 12.2c,d) nonlinearity of the dielectric. The actual value for Ω used in computations are 1.2 and 0.8.

Due to high amplitude of the electric field in the SRR slit as well as resonant interaction of the electromagnetic field with the SRR lattice, nonlinear effects in such structures can be enhanced dramatically. Moreover, the critical fields for switching between the LH and RH states, shown in Fig. 12.1 can be reduced to a desirable value by choosing the frequency close to the resonant frequency of SRRs. We want to emphasize that strong losses can suppress nonlinear resonance and multistable behavior. With low enough losses, even for a relatively large difference between the SRR eigenfrequency and the external frequency, as in Fig. 12.1b where $\Omega = 0.8$ (i.e., $\omega = 0.8\omega_0$), the switching amplitude of the magnetic field is $\sim 0.03E_c$. The characteristic values of the focusing nonlinearity can be estimated for some materials such as n-InSb for which $E_c = 200\,\mathrm{V\,cm^{-1}}$ [15]. As a result, the strength of the critical magnetic field is found as $H_{c1} \approx 1.6\,\mathrm{A\,m^{-1}}$. Strong defocusing properties for microwave frequencies are found in $Ba_xSr_{1-x}TiO_3$ (see [16] and references therein). The

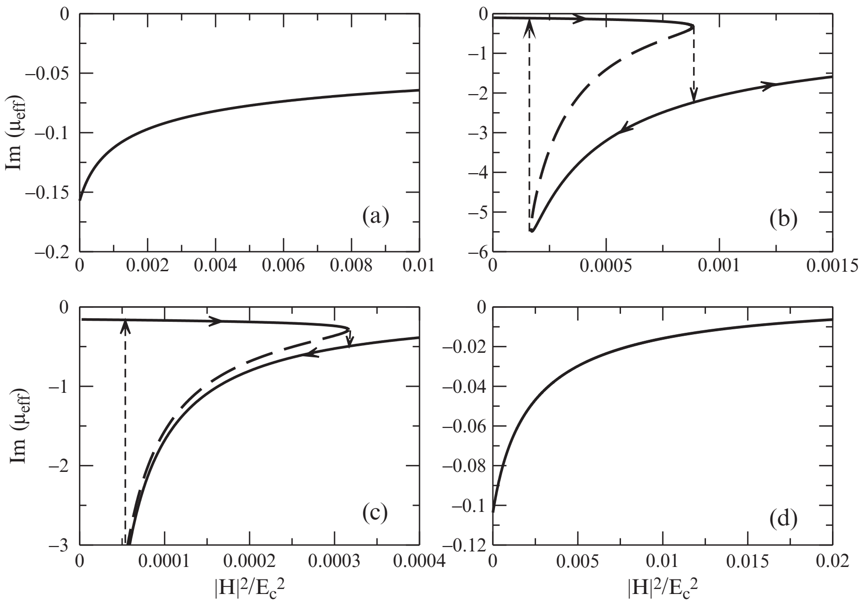

Fig. 12.2. Imaginary part of the effective magnetic permeability vs. intensity of the magnetic field for $\gamma = 0.05$. (**a**) $\Omega > 1$, $\alpha = 1$; (**b**) $\Omega < 1$, $\alpha = 1$, (**c**) $\Omega > 1$, $\alpha = -1$; and (**d**) $\Omega < 1$, $\alpha = -1$. *Dashed curves* show the branches of unstable solutions [9]

critical nonlinear field of a thin film of this material is $E_\mathrm{c} = 4 \times 10^4\,\mathrm{V\,cm^{-1}}$, and the corresponding field of the transition from the LH to RH state (see Fig. 12.1c) can be found as $H_\mathrm{c} \approx \sqrt{0.003} \times 4 \times 10^2/3\mathrm{CGS} = 183\,\mathrm{A\,m^{-1}}$.

The unique possibility of strongly enhanced effective nonlinearities (compared to the nonlinearities in dielectrics) in left-handed metamaterials revealed here may lead to an essential revision of the concepts based on the linear theory, since the electromagnetic waves propagating in such materials always have a finite amplitude. At the same time, the engineering of nonlinear composite materials may open up a number of their novel applications such as frequency multipliers, beam spatial spectrum transformers, switchers, limiters, etc.

12.2.2 Nonlinear Dielectric Permittivity

Now we analyze the dielectric properties of the composite. We suppose that contribution to the dielectric function given by the array of wires is much stronger then that from SRRs. In this case, we can obtain the following expression for the effective nonlinear dielectric permittivity [9]:

$$\varepsilon_\mathrm{eff}\left(|E|^2\right) = \varepsilon_\mathrm{D}\left(|E|^2\right) - \frac{\omega_\mathrm{p}^2}{\omega(\omega - \mathrm{i}\gamma_\varepsilon)}, \tag{12.2}$$

where $\omega_{\rm p} \approx (c/d)[2\pi/\ln(d/r)]^{1/2}$ is the effective plasma frequency, and $\gamma_\varepsilon = c^2/2\sigma S \ln(d/r)$, S is an effective wire cross-section. The second term on the right-hand side of (12.2) is in complete agreement with the earlier result obtained by Pendry and co-authors [1]. One should note that the low losses case, i.e., $\gamma_\varepsilon \ll \omega$, corresponds to the condition $\delta \ll r$, i.e, when the wires are thick with respect to the skin-layer depth.

12.2.3 FDTD Simulations of Nonlinear Metamaterial

To verify the specific features of the left-handed metamaterials introduced by their nonlinear response, in this section we study the scattering of electromagnetic waves from the nonlinear metamaterial discussed above. In particular, we perform the FDTD numerical simulations of the plane wave interaction with a slab of LHM of a finite thickness [17].

Following [17], we study the temporal dynamics of the wave scattering by a finite slab of nonlinear metamaterial. For simplicity, we consider a one-dimensional problem that describes the interaction of the plane wave incident at the normal angle from air on a slab of metamaterial of a finite thickness. We consider *two types of nonlinear effects* (i) nonlinearity-induced suppression of the wave transmission when initially transparent LHM becomes opaque with the growth of the input amplitude, and (ii) nonlinearity-induced transparency when an opaque metamaterial becomes left-handed (and therefore transparent) with the growth of the input amplitude. The first case corresponds to the dependence of the effective magnetic permeability on the external field shown in Fig. 12.1a, c, when initially negative magnetic permeability (we consider $\varepsilon < 0$ in all frequency range) becomes positive with the growth of the magnetic field intensity. The second case corresponds to the multivalued dependence shown in Fig. 12.1b.

In all numerical simulations, we use *linearly growing* amplitude of the incident field within the first 50 periods, that becomes constant afterwards. The slab thickness is selected as $1.3\lambda_0$ where λ_0 is a free-space wavelength. For the parameters we have chosen, the metamaterial is left-handed in the linear regime for the frequency range from $f_1 = 5.787\,\mathrm{GHz}$ to $f_2 = 6.05\,\mathrm{GHz}$.

Our simulations show that for the incident wave with the frequency $f_0 = 5.9\,\mathrm{GHz}$ (i.e., inside the left-handed transmission band), electromagnetic field reaches a steady-state independently of the sign of the nonlinearity. In the linear regime, the effective parameters of the metamaterial at the frequency f_0 are: $\varepsilon = -1.33 - 0.01\mathrm{i}$ and $\mu = -1.27 - 0.3\mathrm{i}$; this allows excellent impedance matching with surrounding air. The scattering results in a vanishing reflection coefficient for small incident intensities.

Reflection and transmission coefficients are qualitatively different for two different types of infilling nonlinear dielectric. For the defocusing nonlinearity, the reflection coefficient varies from low to high values when the incident field exceeds some threshold value. Such a sharp transition can be explained in terms of the hysteresis behavior of the magnetic permeability shown in

Fig. 12.1c. When the field amplitude in metamaterial becomes higher than the critical amplitude (shown by a dashed arrow in Fig. 12.1c), magnetic permeability changes its sign, and the metamaterial becomes opaque. Our FDTD simulations show that for overcritical amplitudes of the incident field, the opaque region of positive magnetic permeability appears inside the slab [17]. The magnetic permeability experiences an abrupt change at the boundary between the transparent and opaque regions.

For the focusing nonlinearity (see Fig. 12.3), the dependence of the reflection and transmission coefficients on the amplitude of the incident field is smooth. This effect originates, first, from a gradual detuning from the impedance matching condition, and, for higher powers, from the appearance of an opaque layer (see the inset in Fig. 12.3) with a positive value of the magnetic permeability that is a continuous function of the coordinate inside the slab.

Now we consider another interesting case when initially opaque metamaterial becomes transparent with the growth of the incident field amplitude. We take the frequency of the incident field to be $f_0 = 5.67\,\mathrm{GHz}$, so that magnetic permeability is positive in the linear regime and the metamaterial is opaque. In the case of self-focusing nonlinear response ($\alpha = 1$), it is possible to switch the material properties to the regime with negative magnetic permeability (see Fig. 12.1b) making the material slab left-handed and therefore transparent.

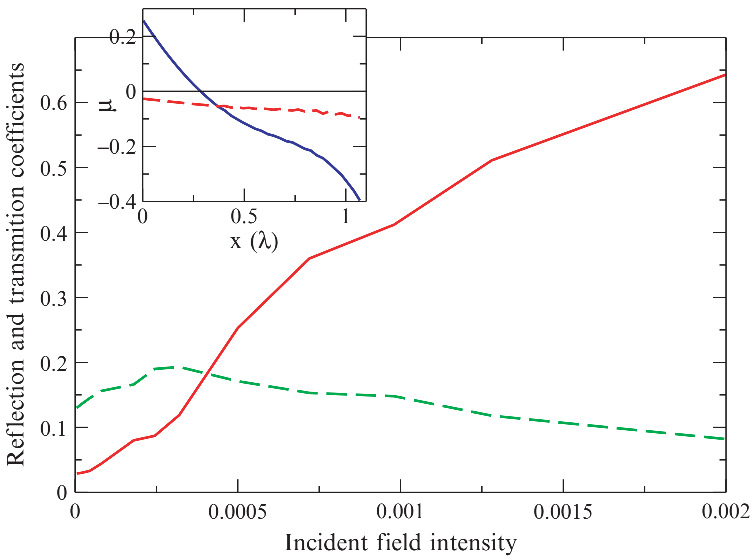

Fig. 12.3. Reflection (*solid*) and transmission (*dashed*) coefficients for a nonlinear metamaterial slab vs. the incident field intensity (H^2/E_c^2), for the focusing nonlinearity. *Inset* shows real (*solid*) and imaginary (*dashed*) parts of magnetic permeability inside the slab in one of the high-reflectivity regimes [17]

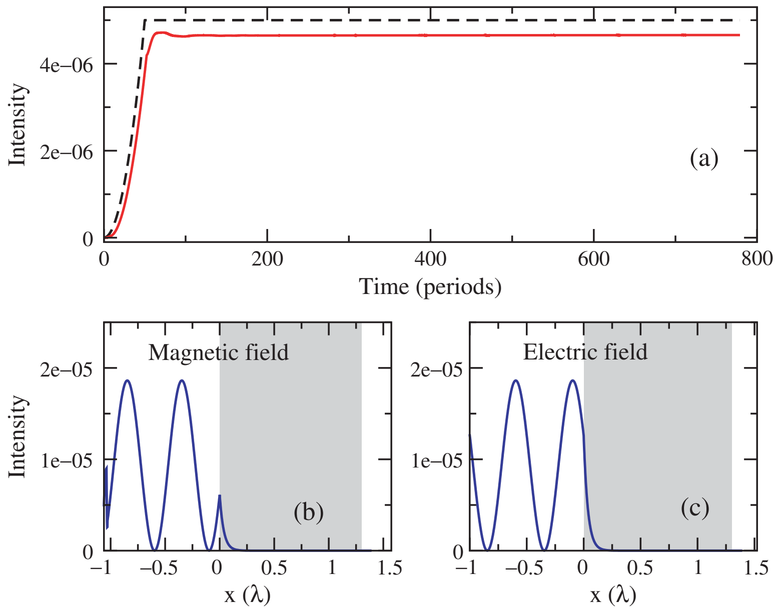

Fig. 12.4. (**a**) Reflected (*solid*) and incident (*dashed*) wave intensity, (H^2/E_c^2), for small amplitudes of the incident wave (i.e., in the linear regime). (**b**,**c**) Distribution of the magnetic and electric fields at the end of simulation time; the metamaterial is *shaded* [17]

Moreover, one can expect the formation of self-focused localized states inside the composite, the effect which was previously discussed for the interaction of the intense electromagnetic waves with over-dense plasma [18–20]. Figure 12.4a shows the temporal evolution of the incident and reflected wave intensities for small input intensities – this case corresponds to the linear regime. The reflection coefficient reaches a steady-state after approximately 100 periods. The spatial distribution of the electric and magnetic fields at the end of simulation time is shown in Fig. 12.4b, c, respectively.

In a strongly nonlinear regime, we observe the effect of the dynamical self-modulation of the reflected electromagnetic wave that results from the periodic generation of the self-localized states inside the metamaterial (see Fig. 12.5). Such localized states resemble *temporal solitons*, which transfer the energy away from the interface. Figure 12.5c shows an example when two localized states enter the metamaterial. These localized states appear on the jumps of the magnetic permeability and, as a result, we observe a change of the sign of the electric field derivative at the maximum of the soliton intensity, and subsequent appearance of transparent regions in the metamaterial. Unlike all previous cases, the field structure in this regime does not reach any steady-state for high enough intensities of the incident field.

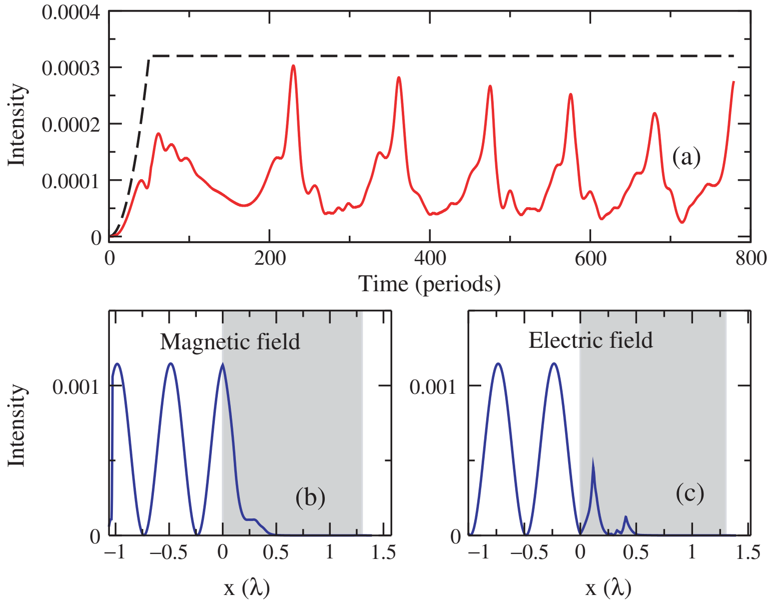

Fig. 12.5. The same as in Fig. 12.4 but for the overcritical regime [17]

12.2.4 Electromagnetic Spatial Solitons

Similar to other nonlinear media [21], nonlinear left-handed composite materials can support self-trapped electromagnetic waves in the form of *spatial solitons* [22]. Such solitons possess interesting properties because they exist in materials with a hysteresis-type (multistable) nonlinear magnetic response. Below, we describe novel and unique types of single- and multihump (symmetric, antisymmetric, or even asymmetric) backward-wave spatial electromagnetic solitons supported by the nonlinear magnetic permeability.

Spatially localized TM-polarized waves are described by one component of the magnetic field and two components of the electric field. Monochromatic stationary waves with the magnetic field component $H = H_y$ propagating along the z-axis and homogeneous in the y-direction, $[\sim \exp(\mathrm{i}\omega t - \mathrm{i}kz)]$, are described by the dimensionless nonlinear Helmholtz equation

$$\frac{\mathrm{d}^2 H}{\mathrm{d}x^2} + [\varepsilon \mu_{\mathrm{eff}}(|H|^2) - \gamma^2]H = 0, \tag{12.3}$$

where $\gamma = kc/\omega$ is a wavenumber, $x = x'\omega/c$ the dimensionless coordinate, x' the dimensional coordinate, and we assume that $\varepsilon < 0$ does not depend on the field intensity. Different types of localized solutions of (12.3) can be analyzed on the phase plane $(H, \mathrm{d}H/\mathrm{d}x)$ (see, e.g., [23]). First, we find the equilibrium points: the point $(0, 0)$ existing for all parameters, and the point $(0, H_1)$, where H_1 is found as a solution of the equation

$$\omega_{0\mathrm{NL}}^2(H_1) = \omega^2 \left\{ 1 + \frac{F\varepsilon}{(\gamma^2 - \varepsilon)} \right\}. \tag{12.4}$$

Below the threshold, i.e., for $\gamma < \gamma_{\mathrm{tr}}$, where $\gamma_{\mathrm{tr}}^2 = \varepsilon[1+F\Omega^2/(1-\Omega^2)]$, the only equilibrium state $(0,0)$ is a saddle point and, therefore, no finite-amplitude or localized waves can exist. Above the threshold value, i.e., for $\gamma > \gamma_{\mathrm{tr}}$, the phase plane has three equilibrium points, and a separatrix curve corresponds to a soliton solution.

In the vicinity of the equilibrium state $(0,0)$, linear solutions of (12.3) describe exponentially growing or decaying modes. The equilibrium state $(0,H_1)$ describes a finite-amplitude mode of the transverse electromagnetic field. In the region of multistability, the type of the phase trajectory is defined by the corresponding branch of the multivalued magnetic permeability. Correspondingly, different types of the spatial solitons appear when the phase trajectories correspond to the different branches of the nonlinear magnetic permeability.

The fundamental soliton is described by the separatrix trajectory on the plane $(H, \mathrm{d}H/\mathrm{d}x)$ that starts at the point $(0,0)$, goes around the point $(0,H_1)$, and then returns back; the corresponding soliton profile is shown in Fig. 12.6a. More complex solitons are formed when the magnetic permeability becomes

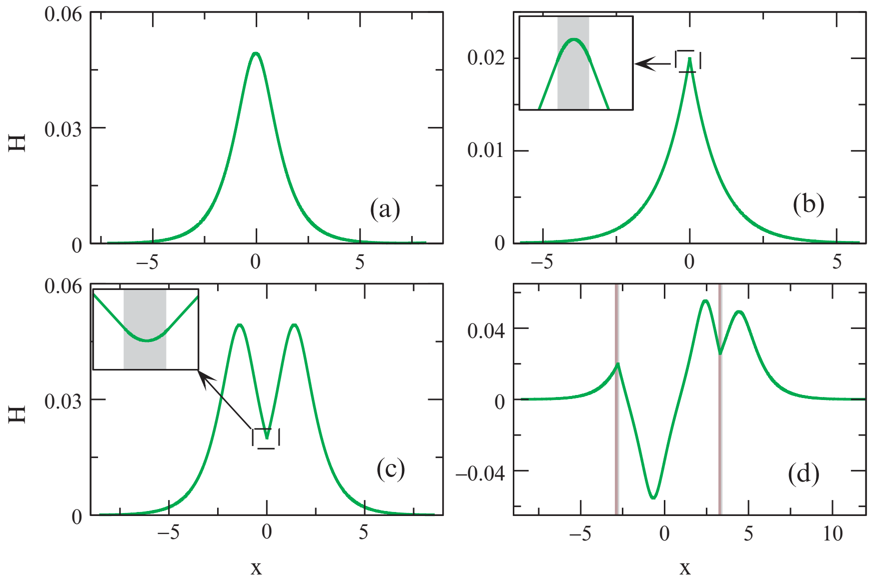

Fig. 12.6. Examples of different types of solitons: (**a**) fundamental soliton; (**b**,**c**) solitons with one domain of, respectively, negative and positive magnetic permeability (*shaded area* in the *inset*); (**d**) soliton with two different domains (*shaded area* in the *inset*). *Insets* in (**b**,**c**) show the magnified regions of the steep change of the magnetic field [22]

multivalued and is described by several branches. Then, soliton solutions are obtained by switching between the separatrix trajectories corresponding to different (upper and lower) branches of magnetic permeability. Continuity of the tangential components of the electric and magnetic fields at the boundaries of the domains with different values of magnetic permeability implies that both H and $\mathrm{d}H/\mathrm{d}x$ should be continuous. As a result, the transitions between different phase trajectories should be continuous.

Figure 12.6b, c shows two examples of more complex solitons corresponding to a single jump to the lower branch of $\mu_{\mathrm{eff}}(H)$ (see Fig. 12.1c) and to the upper branch of $\mu_{\mathrm{eff}}(H)$, respectively. The insets show the magnified domains of a steep change of the magnetic field. Both the magnetic field and its derivative, proportional to the tangential component of the electric field, are continuous. The shaded areas show the domains where the value of magnetic permeability changes. Figure 12.6d shows an example of more complicated multihump soliton which includes two domains of the effective magnetic permeability, one described by the lower branch, and the other one – by the upper branch. In a similar way, we can find more complicated solitons with different number of domains of the magnetic permeability.

We note that some of the phase trajectories have discontinuity of the derivative at $H = 0$ caused by infinite values of the magnetic permeability at the corresponding branch of $\mu_{\mathrm{eff}}(H)$. This is because we use a lossless model of left-handed nonlinear composites for the analysis of the soliton solutions. In more realistic models that include losses, the region of multistability does not extend to the point $H = 0$, and in this limit the magnetic permeability remains a single-valued function of the magnetic field [9].

For the multivalued nonlinear magnetic response, the domains with different values of magnetic permeability "excited" by the spatial soliton can be viewed as the effective induced left-handed waveguides which make possible the existence of single- and multihump solitons. Due to the existence of such domains, the solitons can be not only symmetric, but also antisymmetric and even asymmetric. Formally, the size of an effective domain can be much smaller than the wavelength and, therefore, there exists an applicability limit for the obtained results to describe nonlinear waves in realistic structures.

When the infilling dielectric of the structure displays *self-focusing nonlinear response*, and we consider frequencies $\Omega = \omega/\omega_0 < 1$, then we can find *dark solitons* in such a system, i.e., localized dips on the finite-amplitude background wave [21]. Similar to bright solitons, there exist both fundamental dark solitons and dark solitons with domains of different values of magnetic permeability. For self-defocusing nonlinearity and $\Omega < 1$, magnetic permeability is a single-valued function, and such a nonlinear response can support dark solitons as well, whereas for self-focusing dielectric, we have $\Omega > 1$ and no dark solitons can exist.

12.3 Kerr-Type Nonlinear Metamaterials

As we discussed in Sect. 12.2, metamaterials *can be designed* to exhibit nonlinear magnetic and/or electric properties in the controlled way. In this section we will focus on the metamaterials which exhibit dielectric nonlinear properties only, similar to those known in optics. This will give us an opportunity to see the difference between left-handed and right-handed materials which have the same nonlinearity. We will study surface waves, guided waves in nonlinear structures with metamaterials as well as wave scattering in left-handed Bragg gratings with nonlinear defects.

12.3.1 Nonlinear Surface Waves

In this section, we present a study of the properties of both *linear and nonlinear surface waves* at the interface between semi-infinite materials of two types, left- and right-handed ones, and demonstrate a number of unique features of surface waves in LH materials [24]. In particular, we show the existence of surface waves of both TE and TM polarizations, a specific feature of the RH/LH interfaces. We study in detail TE-polarized nonlinear surface waves and suggest an efficient way for engineering the group velocity of surface waves using the nonlinearity of the media. The dispersion broadening of the pulse can be compensated by the nonlinearity, thus leading to the formation of surface-polariton solitons at the RH/LH interfaces with a distinctive vortex-like structure of the energy flow. We must note here, that the presented study is based on the effective medium approximation, which treats the LH materials as homogeneous and isotropic. It can be applied to the manufactured metamaterials, which possess negative dielectric permittivity and negative permeability in the microwave frequency range, when the characteristic scale of the variation of the electromagnetic field (e.g., a field decay length and a wavelength of radiation) is much higher, than the period of the metamaterial.

Linear Surface Waves

Linear surface waves are known to exist, under certain special conditions, at an interface separating two different isotropic dielectric media. In particular, the existence of TM-polarized surface waves requires that the dielectric constants of two dielectric materials separated by an interface have different signs, while for TE-polarized waves the magnetic permeability of the materials should be of different signs (see, e.g., [25, 26] and references therein). Materials with negative ε are readily available (e.g., metals excited below a critical frequency), while materials with negative μ were not known until recently. This explains why only TM-polarized surface waves have been of interest over the last few decades. Recently, it was shown [24] that the LH/RH interface can support either TE- or TM-polarized surface waves. Region of existence of these waves

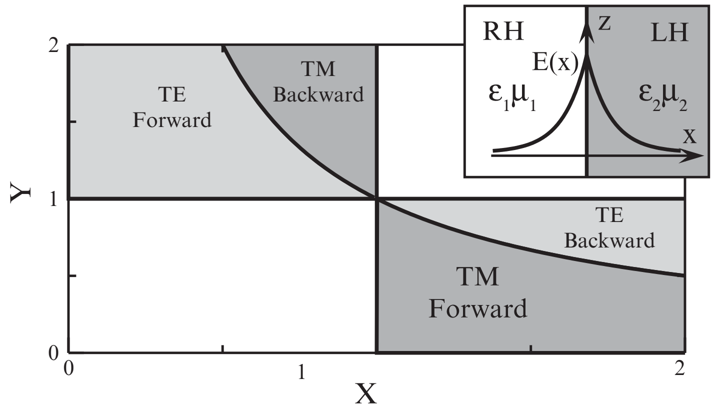

Fig. 12.7. Existence regions of *linear surface waves* on the plane (X, Y), where $X = |\varepsilon_2|/\varepsilon_1$ and $Y = |\mu_2|/\mu_1$. The *inset* shows the problem geometry [24]

is shown in Fig. 12.7. We note that there are no regions where both TE- and TM-polarized waves co-exist simultaneously.

One of the distinctive properties of the LH materials which has been demonstrated experimentally is their specific frequency dispersion. To study the dispersion of the corresponding surface waves, it is necessary to select a particular form of the frequency dependence of the dielectric permittivity and magnetic permeability of the LH medium. A negative dielectric permittivity is selected in the form of the commonly used function for plasmon investigations [26] and a negative permeability is constructed in an analogous form (see, e.g., [27]), i.e.,

$$\varepsilon_2(\omega) = 1 - \frac{\omega_{\mathrm{p}}^2}{\omega^2}, \quad \mu_2(\omega) = 1 - \frac{F\omega^2}{\omega^2 - \omega_{\mathrm{r}}^2}, \tag{12.5}$$

where losses are neglected, and the values of the parameters ω_{p}, ω_{r}, and F are chosen to fit approximately to the experimental data [5]: $\omega_{\mathrm{p}}/2\pi = 10\,\mathrm{GHz}$, $\omega_{\mathrm{r}}/2\pi = 4\,\mathrm{GHz}$, and $F = 0.56$. For this set of parameters, the region in which permittivity and permeability are both negative is from 4 to 6 GHz.

The dispersion curves of the TE-polarized surface wave (or surface polariton) with the wavenumber h along the interface ($\exp(\mathrm{i}\omega t - \mathrm{i}hz)$) calculated using (12.5) are depicted in Fig. 12.8 on the plane of the normalized parameters $\bar{\omega} = \omega/\omega_{\mathrm{p}}$ and $\bar{h} = hc/\omega_{\mathrm{p}}$. We note that the structure of the dispersion curves for surface waves depends on the relation between the values of the dielectric permittivities of the two media at the characteristic frequency, ω_1, at which the absolute values of magnetic permeabilities of two media coincide, $\mu_1 = |\mu_2(\omega_1)|$. The corresponding curve in Fig. 12.8 is monotonically decreasing for $\varepsilon_1 > |\varepsilon_2(\omega_1)|$, but it is monotonically increasing otherwise, i.e., for $\varepsilon_1 < |\varepsilon_2(\omega_1)|$. Only the first case was identified in the previous analysis reported in [27]. The change of the slope of the curve (the slope of the dispersion curve

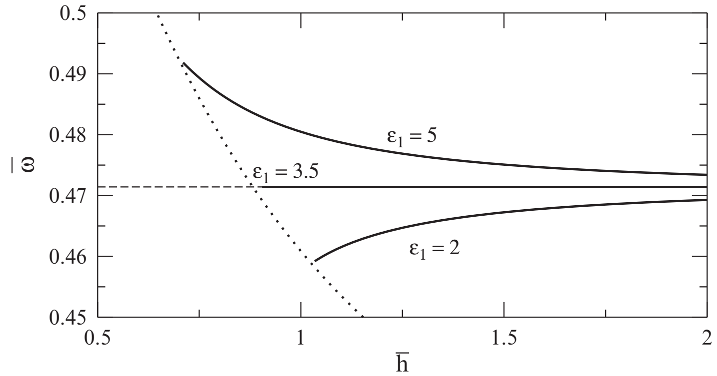

Fig. 12.8. Dispersion curves of the TE-polarized surface waves, for different values of ε_1, shown for the normalized values $\bar{\omega} = \omega/\omega_{\rm p}$ are $\bar{h} = hc/\omega_{\rm p}$. *Dotted curves* marks the dependence $\bar{h} = \bar{\omega}\sqrt{\varepsilon_2\mu_2}$. *Dashed line* is the critical frequency ω_1 [24]

represents the group velocity) with the variation of the dielectric permittivity of the RH medium can be used for group velocity engineering [24].

The critical value of dielectric permittivity $|\varepsilon_2(\omega_1)|$ for the case of a non-magnetic RH medium ($\mu_1 = 1$) is found from the dispersion relations for the surface waves, and it has the form [24]

$$\varepsilon_{\rm c} = |\varepsilon_2(\omega_1)| = \left(1 - \frac{F}{2}\right)\left(\frac{\omega_{\rm p}}{\omega_{\rm r}}\right)^2 - 1. \tag{12.6}$$

For the parameters specified above, this critical value is $\varepsilon_{\rm c} = 3.5$.

The change of the dispersion curve from monotonically increasing to monotonically decreasing, shown in Fig. 12.8, is connected with a change in the direction of the total power flow in the wave, as discussed later.

Nonlinear LH/RH Interface

Nonlinear surface waves at an interface separating two conventional dielectric media have been analyzed extensively for several decades starting from the pioneering paper [28]. In brief, one of the major findings of those studies is that the TE-polarized surface waves can exist at the interface separating two RH media provided that *at least one of these is nonlinear*, but that *no surface waves exist in the linear limit*.

In this section, we study TE-polarized nonlinear surface waves assuming that both media are nonlinear, i.e., they display a Kerr-type nonlinearity in their dielectric properties, namely

$$\varepsilon_{1,2}^{\rm NL} = \varepsilon_{1,2} + \alpha_{1,2}|E|^2, \tag{12.7}$$

where the first term characterizes the linear properties, i.e., those in the limit of vanishing wave amplitude.

For a conventional (or right-handed) dielectric medium, positive α_1 corresponds to a self-focusing nonlinear material, while negative α_1 characterizes defocusing effects in the beam propagation. However, this classification becomes reversed in the case of LH materials and, for example, a self-focusing LH medium corresponds to negative α_2. Indeed, taking into account relation (12.7), we write the equation for the case of the TE-polarized wave in nonlinear media as follows:

$$\frac{\partial^2 E}{\partial z^2} + \frac{\partial^2 E}{\partial x^2} + \left(\frac{\omega}{c}\right)^2 \left(\varepsilon\mu + \mu\alpha|E|^2\right) E = 0. \tag{12.8}$$

According to (12.8), the sign of the product $\mu\alpha$ determines the type of nonlinear self-action effects which occur. Therefore, in an LH medium with negative μ_2 *all nonlinear effects are opposite* to those in RH media with positive μ_1, for the same α. Later, we assume for definiteness that both LH and RH materials possess self-focusing properties, i.e., $\alpha_1 > 0$ and $\alpha_2 < 0$.

We look for the stationary solutions of (12.8) in the form $E_{1,2}(x,z) = \Psi_{1,2}(x)\exp(\mathrm{i}hz)$. Then, the profiles of the spatially localized wave envelopes $\Psi_{1,2}(x)$ are found as [29]

$$\Psi_{1,2}(x) = \left(\eta_{1,2}\sqrt{2/\alpha_{1,2}\mu_{1,2}}\right)\,\mathrm{sech}[\eta_{1,2}(x - x_{1,2})], \tag{12.9}$$

where $\eta_{1,2} = \kappa_{1,2}c/\omega$ are normalized transverse wave numbers, $x_{1,2}$ are centers of the sech-functions which should be chosen to satisfy the continuity of the tangential components of the electric and magnetic fields at the interface.

The total energy flow in the mode along the interface in this wave can be written in the form

$$P = P_0\gamma\left[\frac{\eta_1\alpha_2\mu_2}{\alpha_1\mu_1^2} + \frac{\eta_2}{\mu_2} + \frac{\eta_1}{\mu_1}\left(1 - \frac{\alpha_2\mu_2}{\alpha_1\mu_1}\right)\tanh\left(\eta_1 x_1\right)\right], \tag{12.10}$$

where $P_0 = c^2/4\pi\omega\alpha_2\mu_2$, and $\gamma = hc/\omega$ is the normalized wave number. We now consider the surface waves in the nondegenerate case when only $\alpha_1 = |\alpha_2|$. The dependence of the normalized energy flux P/P_0 on the parameter γ is shown in Fig. 12.9 for the cases when linear waves are forward or backward, respectively. Corresponding transverse wave structures (electric field amplitudes) are shown in the insets.

Nonlinear LH/Linear RH Interface

Next, we consider surface waves propagating along an interface between a linear RH and a nonlinear LH media (see the inset in Fig. 12.10) having a nonlinear coefficient α_2 which is negative and, thus, displaying the self-focusing properties. The transverse structure of the stationary surface wave has the form:

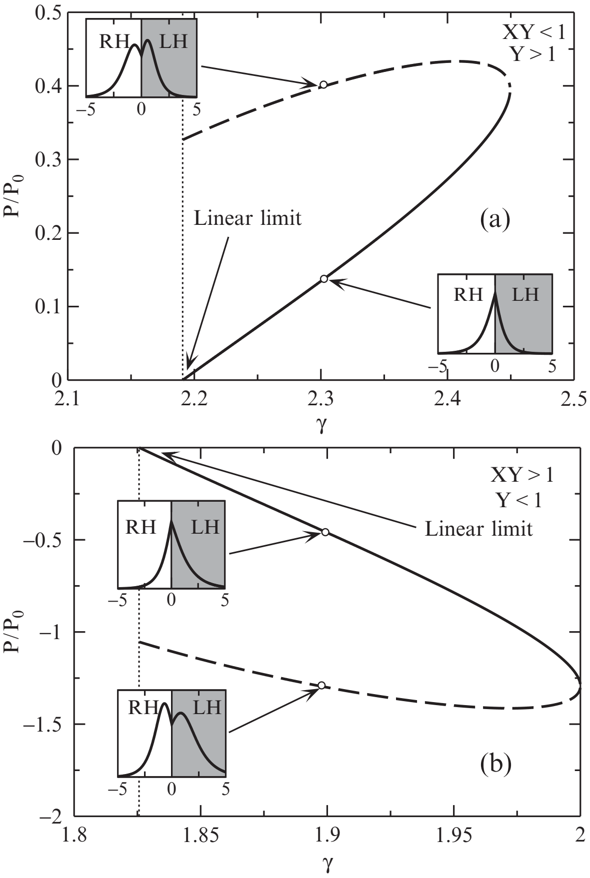

Fig. 12.9. Normalized energy flux vs. normalized wavenumber $\gamma = hc/\omega$ for the nonlinear surface waves between nonlinear LH and nonlinear RH media in two cases (**a**) $XY < 1$, $Y > 1$, and (**b**) $XY > 1$, $Y < 1$. *Solid curve* corresponds to a one-humped structure, *dashed* – double-humped structure. The *insets* shows the structure of the surface waves (electric field vs. normalized coordinate $x\omega/c$) at the points indicated by arrows. *Dotted lines* denote the linear surface wave wavenumber [24]

$$\Psi(x) = \begin{cases} E_0 \exp{(\eta_1 x)}, & x < 0, \\ (2/\alpha_2\mu_2)^{1/2}\, \eta_2 \,\mathrm{sech}\, [\eta_2(x - x_0)]\,, & x > 0, \end{cases} \tag{12.11}$$

where E_0 and x_0 are two parameters which should be determined from the continuity conditions at the interface for the tangential components of the electric and magnetic fields.

We find that a surface wave always has the maximum of field intensity at the interface. This is in a sharp contrast to the nonlinear surface waves excited at the interface separating two RH media, when the electric field has maximum shifted into a self-focusing nonlinear medium [30].

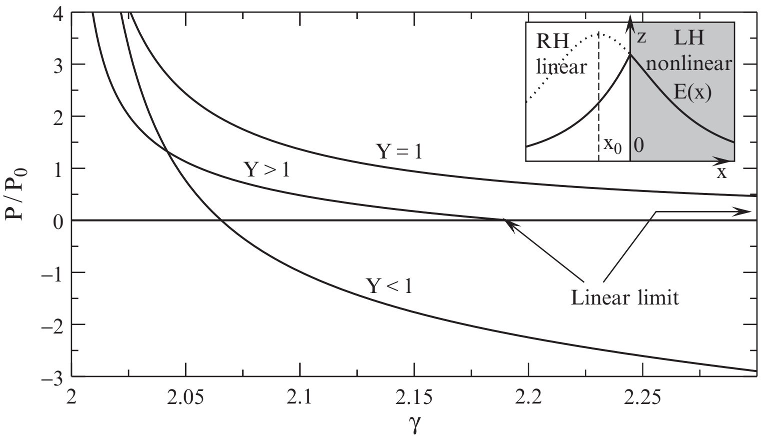

Fig. 12.10. Normalized energy flux vs. normalized wavenumber $\gamma = hc/\omega$ for surface waves at the nonlinear LH/Linear RH interface. Surface waves can be both forward (positive energy flux) and backward (negative energy flux). The *inset* shows the geometry of the problem. The *solid line* shows the transverse wave profile, *dotted line* shows the continuation of the solution in nonlinear medium (12.11) to the linear medium, *dashed line* indicates the position of the center x_0 of the sech function [24]

The energy flux P associated with the nonlinear surface wave can be calculated in the form

$$P = P_0 \gamma \eta_2 \left(1 + \frac{\mu_2 \eta_1}{\mu_1 \eta_2}\right) \left[\frac{2}{\mu_2} + \frac{\eta_2}{\eta_1 \mu_1} \left(1 - \frac{\mu_2 \eta_1}{\mu_1 \eta_2}\right)\right],$$

where P_0 is defined above.

As an example, we consider the case $XY < 1$ for which, as we have shown above, only forward surface waves can exist at the interface between two linear media. However, nonlinear surface waves can be either forward or backward, as demonstrated in Fig. 12.10. For $Y < 1$, there exists *no linear limit* for the existence of the surface waves, while in the other two regions the results for linear surface waves are recovered in the limit $P \to 0$. The point on the curve corresponding to $P = 0$ in the case $Y < 1$ describes the wave of finite amplitude in which the energy flows on the two sides of the interface are balanced. Such a wave does not exist in the linear limit.

Linear LH/Nonlinear RH Interface

Finally, we consider the case when the LH material is linear, while the RH medium is nonlinear. The dependence of the normalized energy flux on the wave number of the surface wave is shown in Fig. 12.11 for $XY > 1$. In contrast to the linear waves, the nonlinear surface waves can be either forward or backward (see Fig. 12.7). In analogy with the case $Y < 1$ for the nonlinear

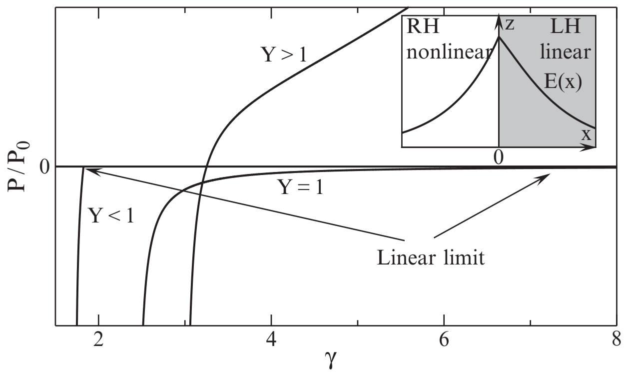

Fig. 12.11. Normalized energy flux vs. normalized wavenumber $\gamma = hc/\omega$ for the nonlinear surface waves at the linear LH/nonlinear RH interface. Surface waves can be either forward (positive energy flux) or backward (negative energy flux). The *inset* shows the geometry of the problem [24]

LH/linear RH interface, it can be shown that there exists no small-amplitude limit for the nonlinear surface waves for $Y > 1$. For $XY < 1$ only forward traveling waves exist when $Y > 1$, reproducing the property of the corresponding linear waves.

12.3.2 Nonlinear Pulse Propagation and Surface-Wave Solitons

Envelope Equation

Propagation of pulses along the interface between RH and LH media is of particular interest, since it was shown earlier [25] for TM modes that the energy fluxes are *directed oppositely* at either side of the interface. Therefore, we can expect that the energy flow in a pulse with finite temporal and spatial dimension has a nontrivial form [31] and, in particular, it can be associated with a vortex-like structure of the energy flow.

We analyze the structure of surface waves of both temporal and spatial finite extent that can exist in such a geometry. To obtain the equation describing the pulse propagation along the interface, we look for the structure of a broad electromagnetic pulse with carrier frequency ω_0 described by an asymptotic multiscale expansion with the main terms of the general form

$$\Psi(z,x,t) = \mathrm{e}^{\mathrm{i}\omega_0 t - \mathrm{i}h_0 z}\left[\Psi_0(x)A(\xi,t) - \mathrm{i}\Psi_1(x)\frac{\partial A(\xi,t)}{\partial \xi} + \Psi_2(x,\xi,t) + \cdots\right], \tag{12.12}$$

where $\xi = z - v_{\mathrm{g}}t$ is the pulse coordinate in the reference frame moving with the group velocity $v_{\mathrm{g}} = \partial\omega/\partial h$, the field Ψ stands for the components (E_y, H_x, H_z) of a TE-polarized wave, the first term $\Psi_0 = (E_{y0}, H_{x0}, H_{z0})$ describes the structure of the mode at the carrier frequency ω_0, Ψ_1 is the first-order term of the asymptotic series which can be found as $\Psi_1 = \partial\Psi_0/\partial h$, and Ψ_2 is the second-order term. Here A is the pulse envelope, h_0 is the wave number corresponding to the carrier frequency ω_0. Substituting (12.12) into (12.8) and using the Fredholm alternative theorem [32], one can obtain the equation for the evolution of the field envelope

$$\mathrm{i}\frac{\partial A}{\partial t} + \frac{\delta}{2}\frac{\partial^2 A}{\partial \xi^2} - \omega_2(h)|A^2|A = 0, \tag{12.13}$$

where the coefficient $\delta = \partial^2\omega/\partial h^2$ stands for the group-velocity dispersion (GVD) which determines the pulse broadening and can be calculated from the dispersion relations, $\omega_2(h) = \left(\partial\omega_{\mathrm{NL}}/\partial A^2\right)|_{A=0}$ is the effective nonlinear coefficient calculated with the help of the nonlinear dispersion relation. The nonlinear Schrödinger (NLS) equation has a solution in the form of a bright soliton localized at the interface, provided the GVD (δ) has the opposite sign to the sign of the nonlinear coefficient (ω_2) (see, e.g., [21] and references therein). The existence of the surface polariton solitons has been predicted in a number of structures supporting nonlinear guided waves (see, e.g., [33] and references therein).

The effective nonlinear coefficient for the case of an interface between the nonlinear LH medium and the linear RH medium, can be found in the form

$$\omega_2(h) = -\frac{\alpha\mu_1\kappa_1\kappa_2\omega^2}{4hc^2(\varepsilon_2\mu_2 - \varepsilon_1\mu_1)}\frac{\mathrm{d}\omega}{\mathrm{d}h}. \tag{12.14}$$

The signs of the group velocity $\mathrm{d}\omega/\mathrm{d}h$ and of the parameter δ can be determined from the Fig. 12.8. As a result, for any reasonable values of dielectric permittivity and magnetic permeability of the RH medium, there exists a range of frequencies for which $\omega_2 \cdot \delta < 0$, indicating the possibility of exciting surface polariton solitons.

To study the energy flow in such a surface-polariton soliton, we use the asymptotic expansions (12.12) for the field components, and we obtain the energy flow structure described by their components

$$S_z = \frac{c^2 h_0}{8\pi\omega_0\mu}E_0^2\,|A|^2\,, \tag{12.15}$$

$$S_x = \frac{c^2}{8\pi\omega_0\mu}\left[\frac{\partial E_0}{\partial h}\frac{\partial E_0}{\partial x} - E_0\left(\frac{\partial^2 E_0}{\partial h\partial x} - \frac{v_{\mathrm{gr}}}{\omega_0}\frac{\partial E_0}{\partial x}\right)\right]\mathrm{Re}\left(A\frac{\partial A^*}{\partial \xi}\right), \tag{12.16}$$

The structure of the Poynting vector in the surface-wave pulse is shown in Fig. 12.12, where it is clearly seen that the energy rotates in the localized region creating a vortex-type energy distribution in the wave. The difference between the Poynting vector $|S_z|$ integrated over the RH medium and that calculated for the LH medium determines the resulting group velocity of the surface wave packet.

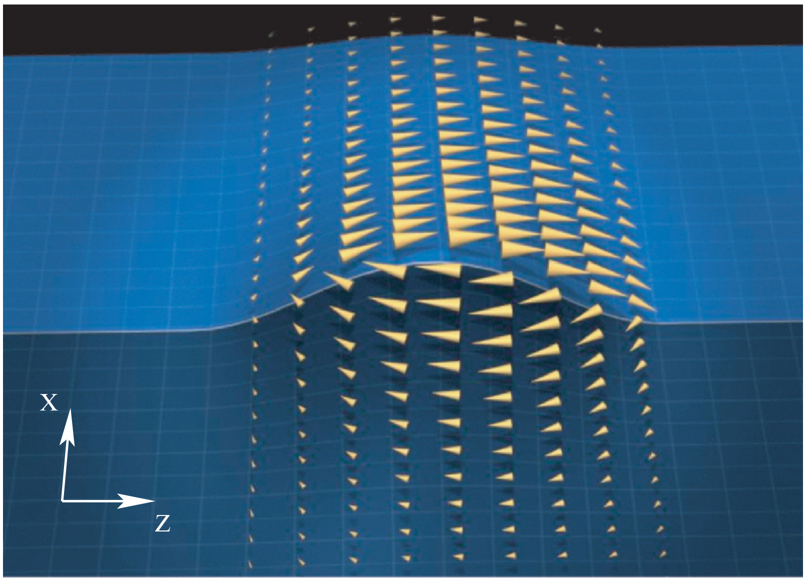

Fig. 12.12. A vortex-like distribution of the Poynting vector in a surface wave soliton propagating along the LH/RH interface [24]

We note the distinctive vortex-like structure of the surface waves at the interface separating RH and LH media follows as a result of the opposite signs of the dielectric permittivities of adjacent media for the TM-polarized waves or due to different signs of the respective magnetic permeabilities in case of TE-polarized waves. These conditions coincide with the conditions for the existence of the corresponding surface waves and, therefore, surface polaritons should always have such a vortex-like structure.

12.3.3 Nonlinear Guided Waves in Left-Handed Slab Waveguide

Previous studies of linear waves of an LH slab waveguide [31] has shown some of their peculiar properties, such as the absence of the fundamental mode, mode double degeneracy, and the existence of both forward and backward waves. In this section, we study *nonlinear* guided modes in a waveguide formed by a slab of linear LHM embedded into nonlinear dielectric, and we show that symmetric, antisymmetric, and asymmetric waves are supported by such a waveguide, and we study their properties. We predict in the nonlinear regime additional modes appear which do not exist in linear problem. We demonstrate that the propagation of the wavefronts (characterized by the phase velocity) with respect to the direction of the energy flow (Poynting vector) depends on the propagation constant, and the waves can be both forward and backward traveling, which is a distinct property of LH waveguides. We show that the type of the wave can be switched between forward and backward varying the wave intensity.

To study nonlinear guided waves in a nonlinear waveguide, we consider an LH slab with real negative dielectric permittivity ε_2 and real negative magnetic permeability μ_2 surrounded by a nonlinear dielectric (see inset in Fig. 12.13b) with constant magnetic permeability μ_1 and self-focusing Kerr-type nonlinear dielectric permittivity ε_1 [34]. To be specific, we consider TE-polarized guided waves, and we look for stationary guided modes in the form $E = \Psi(x) \exp(\mathrm{i}hz)$, where the transverse mode structure $\Psi(x)$ can be determined from the equation

$$\frac{\mathrm{d}^2\Psi}{\mathrm{d}x^2} + \left[\varepsilon\left(x, |\Psi|^2\right)\mu(x) - \gamma^2\right]\Psi = 0, \tag{12.17}$$

where we use the normalized wavenumber γ and normalized transverse coordinate x.

We separate the guided waves into *fast* and *slow modes*. The fast modes have the phase velocity larger than the phase velocity of light in a homogeneous medium of the core. For such modes, $\gamma^2 < \varepsilon_2\mu_2$, and their localization is caused by the total internal reflection of light from the cladding, resembling localization of waves in a dielectric waveguide. For the slow modes, $\gamma^2 > \varepsilon_2\mu_2$, and the wave guiding resembles localization of the surface waves.

Solutions of (12.17) for guided modes can be found in the form

$$\psi(x) = \begin{cases} \sqrt{2}\kappa_1 \mathrm{sech}[\kappa_1(x - x_1)], & x < -L, \\ A\sin(k_2 x) + B\cos(k_2 x), & |x| < L, \\ \sqrt{2}\kappa_1 \mathrm{sech}[\kappa_1(x - x_2)], & x > L, \end{cases} \tag{12.18}$$

where $\kappa_1^2 = \gamma^2 - \varepsilon_1\mu_1$, $k_2^2 = \varepsilon_2\mu_2 - \gamma^2$, and A, B, x_1, x_2 are constants determined from continuity of the tangential components of the electric and magnetic fields at the interfaces at $x = -L$ and $x = L$. The fast modes correspond to $k_2^2 > 0$, while for the slow modes $k_2^2 < 0$. Solutions (12.18) at $|x| > L$ have the form of sech-functions or solitons which are centered at $x = x_1$ and $x = x_2$ at either side of the slab. The modes with $x_1 < -L$ and $x_2 > L$ have the field maxima at the corresponding side of the waveguide. From the linear theory, it follows that solutions for the stationary modes can be found separately for the symmetric and antisymmetric modes. As has already been shown [35], even in a symmetric nonlinear dielectric waveguide asymmetric modes can exist due to the nonlinearity of the cladding. To find the asymmetric waves general solution (12.18) of the differential equation (12.17) should be considered here.

Inside the slab the energy propagates in the opposite direction (due to the negative μ_2) to that outside the slab, and the energy flow can be either positive or negative with respect to the wavevector. Also, we introduce the total energy flow circulating in the waveguide as

$$\Pi = |p_1| + |p_2|, \tag{12.19}$$

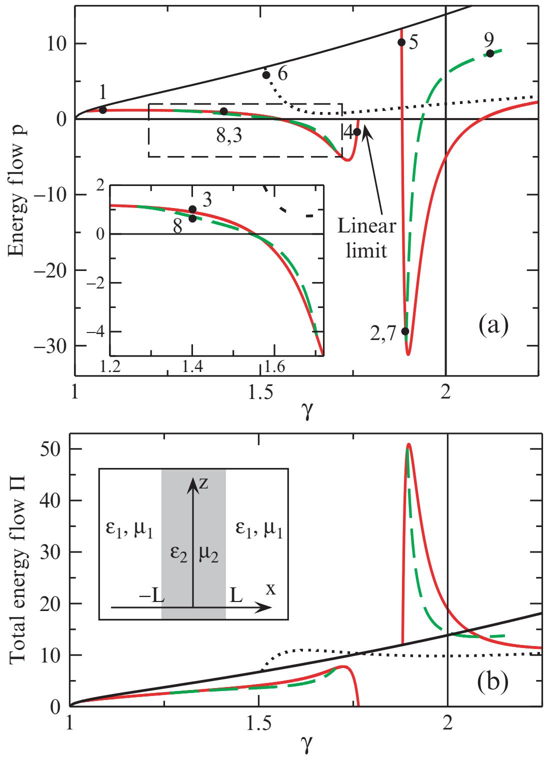

Fig. 12.13. (**a**) Dependence of the normalized power of guided modes p on the propagation constant γ. Parameters are: $L = 2$, $\varepsilon_1 = 1$, $\mu_1 = 1$, $\varepsilon_2 = -2$, $\mu_2 = -2$. *Vertical line* $\gamma = 2$ separates the fast (to the left of the line) and slow modes. *Bold solid curve*, symmetric mode; *dotted*, antisymmetric; *dashed*, asymmetric; and *thin solid line*, power of two solitons in nonlinear medium vs. propagation constant. *Dashed rectangle* is magnified in the *inset*. Numbers indicate parameters for which the mode structure is shown in Fig. 12.14. In the linear limit the only fast mode has the structure similar to that shown in Fig. 12.14 (4). (**b**) Dependence of the normalized total energy flow Π in the modes on the propagation constant. *Solid*, *dotted* and *dashed curves*, respectively, correspond to symmetric, antisymmetric, and asymmetric modes. *Inset* shows the schematic of the waveguide [34]

where $p_{1,2}$ are, respectively, the energy flow in the waveguide core, and waveguide cladding. The total energy flow Π characterizes the total energy circulating in the system, while $p = p_1 + p_2$ determines the energy which is being transmitted by the wave in some direction. This direction coincides with the direction of the wavevector for positive p, and such waves are called forward, while it is antiparallel to the wavevector when p is negative, and such waves are backward. We note, that in a conventional dielectric waveguide energy flows in the same direction inside and outside the waveguide core, and Π is identical to p.

Nonlinear dispersion diagrams are shown for both fast and slow modes in Fig. 12.13. The continuous dependence $\gamma(p)$ is a result of the intensity dependent index of refraction of the waveguide cladding. Parameters in the figure are chosen in such a way that only one fast mode (close to the point 4) exists in the linear case (at low intensities; for the solution of the linear problem and for the choice of parameters see, e.g., [31]). Figure 12.13b confirms that there is a single mode in the linear regime, which is characterized by a vanishingly small total energy flow. Thin solid curves in Fig. 12.13a, b shows the power of two solitons in a homogeneous nonlinear cladding vs. the propagation number. The mode structures are shown in Fig. 12.14, where each plot demonstrates the transverse wave profile corresponding to the numbered point in Fig. 12.13a.

The modes with the parameters close to the *thin solid line* (points 1, 5, 6 in Fig. 12.13a) resembles two in-phase and out-of-phase solitons at either side of the waveguide. Closer to the *thin solid line* the soliton centers in the nonlinear media move further away from the waveguide. The symmetry breaking bifurcation appears on the symmetric mode branch. The asymmetric mode curve in the fast region ends in the symmetric mode branch (see Fig. 12.13a), while in the slow wave region the asymmetric mode disappears, when the amplitude of the wave at one interface becomes the same as the amplitude of the soliton on the other side of the waveguide. Two structures (points 2, 7 in Fig. 12.14) obtained at the same value of the propagation constant show the point of the symmetry breaking, where a slight asymmetry can be seen in the

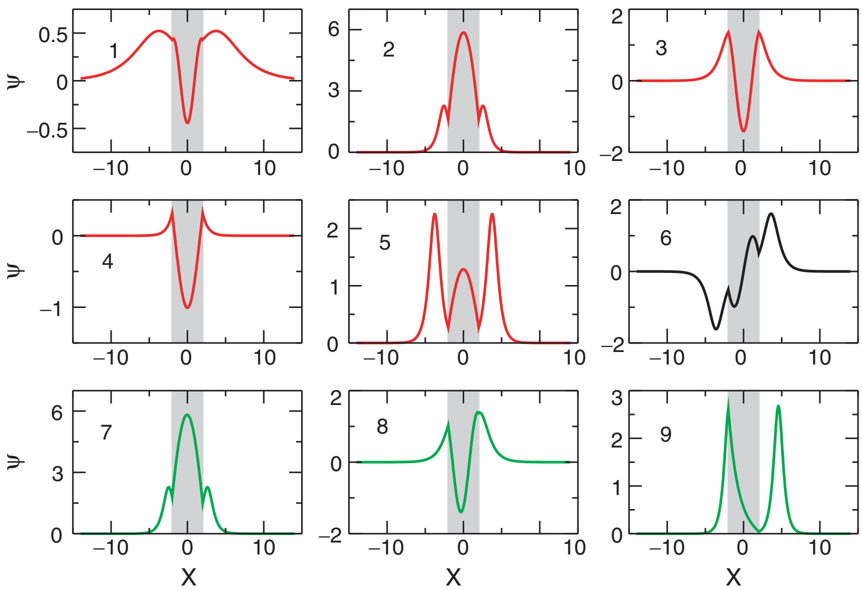

Fig. 12.14. Mode structure calculated for the parameters in Fig. 12.13a, b [34]

mode structure shown in the example 7 in Fig. 12.14. Symmetric and asymmetric modes can be both forward and backward traveling ($p > 0$ and $p < 0$, respectively). We note, that in contrast with nonlinear dielectric waveguides there is no threshold value of the mode power p transmitted in some particular direction for the asymmetric modes. However, it is the total energy Π, which determines the power of the source needed to excite the wave, and the asymmetric modes have a threshold value of Π (see Fig. 12.13b).

For the parameters indicated in Fig. 12.13, only one fast symmetric guided mode exists in the linear limit and the linear mode has a transverse structure similar to the one shown in Fig. 12.14 (4), while in the nonlinear regime the modes with zero, one and two nodes appear (see Fig. 12.14). At the intersection of the curves on the nonlinear dispersion diagram with $p = 0$ axes, apart from the linear limit, the energy flow inside the waveguide core exactly compensates that outside the core due to the structure of such modes. We note here, that with increasing the waveguide thickness, one more symmetry breaking point appears on the antisymmetric mode branch, when the slab parameter L exceeds some threshold value. Moreover, more high-order modes can be supported by the structure, and the nonlinear dispersion diagram becomes more complicated.

The presented nonlinear characteristics of the nonlinear waves in an LH waveguide surrounded by a Kerr-like nonlinear medium show the general nonlinear properties of the low-order fast and slow modes, which are qualitatively similar in other parameter regions.

12.4 Second-Order Nonlinear Effects in Metamaterials

Inclusion of elements with nonsymmetric current–voltage characteristics such as diodes into the SRRs will result in *a quadratic nonlinear response* of the metamaterial [10]. This quadratic nonlinearity is responsible for the recently analyzed parametric processes such as the SHG [34,36] and three-wave mixing [37]. In particular, the first analysis of SHG from a semi-infinite left-handed medium has been briefly presented by Agranovich et al. [36], who employed the nonlinear optics approach.

12.4.1 Second-Harmonics Generation

In this section we consider the problem of SHG during the scattering from a semi-infinite left-handed medium (or a slab of the LHM of a finite extent) and demonstrate the possibility of the exact phase-matching, quite specific for the harmonic generation by the backward waves. With this condition, we demonstrate that exact phase matching between a backward propagating wave of the FF and the forward propagating wave at the SH is indeed possible.

First, we will describe our model including both the electric and magnetic responses. Then, we analyze quadratic nonlinearity and the SHG process in metamaterials. Next, we develop the corresponding coupled-mode theory for SHG with backward waves and present the analysis of both lossy and lossless cases of this model. Then, we will present the results of numerical simulations of SHG process a slab of finite-extension.

Model

We consider a three-dimensional composite structure consisting of a cubic lattice of conducting wires and SRRs, shown schematically in the inset of Fig. 12.15. We assume that the unit-cell size of the structure d is much smaller then the wavelength of the propagating electromagnetic field and, for simplicity, we choose a single-ring geometry of the lattice of SRRs. The results obtained for this case are qualitatively similar to those obtained in more involved cases of double SRRs. This type of microstructured medium is known to possess the basic properties of left-handed metamaterials exhibiting negative refraction in the microwave region.

In the effective-medium approximation, a response of this composite metallic structure can be described by averaged equations allowing one to introduce the effective dielectric permittivity and effective magnetic permeability of the form

$$\varepsilon(\omega) = 1 - \frac{\omega_{\mathrm{p}}^2}{\omega^2}, \tag{12.20}$$

$$\mu(\omega) = 1 + \frac{F\omega}{(\omega_0^2 - \omega^2)}, \tag{12.21}$$

where ω_{p} is the effective plasma frequency, ω_0 a resonant frequency of the array of SRRs, F the form-factor of the lattice, and ω is the angular frequency of the electromagnetic waves. The product of permittivity ε and permeability μ defines the square of the effective refractive index, $n^2 = \varepsilon\mu$, and its sign determines if waves can $(n^2 > 0)$ or cannot $(n^2 < 0)$ propagate in the medium. Due to the medium dispersion defined by the dependencies (12.20) and (12.21), the wave propagation becomes possible only in certain frequency domains while the waves decay for other frequencies. Metamaterial possesses left-handed properties when both ε and μ become simultaneously negative, and such a frequency domain exists in the model described by (12.20) and (12.21) provided $\omega_{\mathrm{p}} > \omega_0$. In this case, the metamaterial is left-handed within the frequency range

$$\omega_0 < \omega < \min\{\omega_{\mathrm{p}}, \omega_{\mathrm{M}}\}, \quad \omega_{\mathrm{M}} = \frac{\omega_0}{\sqrt{1-F}}, \tag{12.22}$$

where ω_{p} is the plasma frequency introduced in (12.20).

We assume that $\omega_{\mathrm{M}} < \omega_{\mathrm{p}}$, and in this case we have two frequency ranges where the material is transparent, the range where the material is left-handed (LHM), and the right-handed (RHM) domain for $\omega > \omega_{\mathrm{p}}$, where both permittivity and permeability are positive (*shaded* domains in Fig. 12.15). For the frequencies outside these two domains, the composite material is opaque.

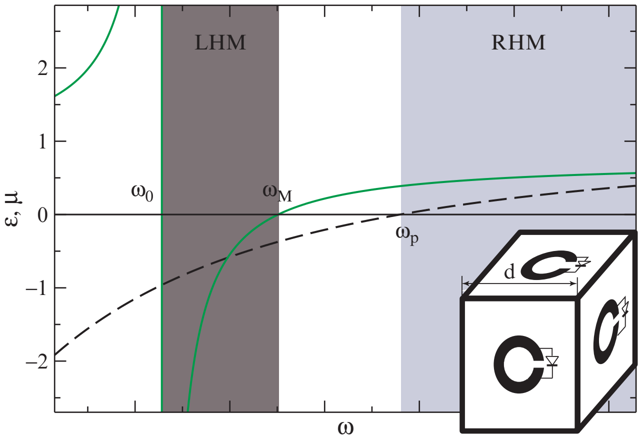

Fig. 12.15. Frequency-dependent magnetic permeability μ (*solid*) and electric permittivity ε (*dashed*) of the composite. Two types of the regions (LHM or RHM) where the material is transparent are *shaded*. For other frequencies it is opaque. Characteristic frequencies ω_0, ω_{M}, and ω_{p} are defined in (12.20) to (12.22). *Inset* shows the unit cell of the metamaterial [38]

Quadratic Nonlinearity and Basic Equations

The composite material becomes nonlinear and it possesses a quadratic nonlinear response when, for example, additional diodes are inserted into the SRRs of the structure [10], as shown schematically in the inset of Fig. 12.15. Quadratic nonlinearity is known to be responsible for various parametric processes in nonlinear media, including the frequency doubling and generation of the SH field. In dispersive materials, and especially in the metamaterials with the frequency domains with different wave properties, the SHG process can be rather nontrivial because the wave at the FF and the SH can fall into *different domains* of the material properties.

The most unusual harmonic generation and other parametric processes are expected when one of the waves (either FF or SH wave) has the frequency for which the metamaterial becomes left-handed. The specific interest to this kind of parametric processes is due to the fact that the waves in the left-handed media are *backward*, i.e., the energy propagates in the direction opposite to that of the wave vector. Both phase-matching condition and nonlinear interaction of the forward and backward waves may become quite nontrivial, as is known from the physics of surface waves in plasmas [39].

In nonlinear quadratic composite metamaterials, interaction of the forward and backward waves of different harmonics takes place when the material is left-handed either for the frequency ω or the double frequency 2ω. Under this condition, there exist two types of the most interesting SHG parametric processes in metamaterials [38].

Case 1. The frequency of the FF wave is in the range $\omega_0/2 < \omega < \omega_M/2$ and, therefore, the SH wave is generated with the double frequency in the LHM domain (see Fig. 12.15). For such parameters, the electromagnetic waves at the FF are nonpropagating, since $\varepsilon(\omega)\mu(\omega) < 0$. As a result, the field with the frequency ω from this range incident on a semi-infinite left-handed medium will decay exponentially from the surface inside the metamaterial. Taking into account (12.20) and (12.21), the depth δ of this skin-layer can be found as

$$\delta = \left(k_{\parallel}^2 - \varepsilon\mu\frac{\omega^2}{c^2}\right)^{-1/2} < \frac{\lambda}{17}, \tag{12.23}$$

where $k_{\parallel}$ is the tangential component of the wavevector of the incident wave, and λ is a free space wavelength. For the SH wave generated in this layer, the metamaterial becomes transparent. In this case, a thin slab of a metamaterial may operate as *a nonlinear left-handed lens* that will provide an image of the source at the SH [40], as it will be discussed in Sect. 12.4.3.

Case 2. The FF wave is left-handed, whereas the SH wave is right-handed. Such a process is possible when $\omega_p < 2\omega_0$ (see Fig. 12.15). What is truly remarkable here is the possibility of exact phase-matching of the SHG parametric process, in addition to the cases discussed earlier in [36]. The phase-matching conditions for this parametric process are depicted in the dispersion diagram of Fig. 12.16 for the propagating waves in the metamaterial where the dispersion of the plane waves is defined by the relation

$$D(\omega, k) = \left[k^2 - \varepsilon(\omega)\mu(\omega)\frac{\omega^2}{c^2}\right] = 0. \tag{12.24}$$

The exact phase matching takes place when $2k(\omega) = k(2\omega)$. Different signs of the slopes of the curves at the frequencies ω and 2ω indicate that one of the waves is forward, while the other wave is backward.

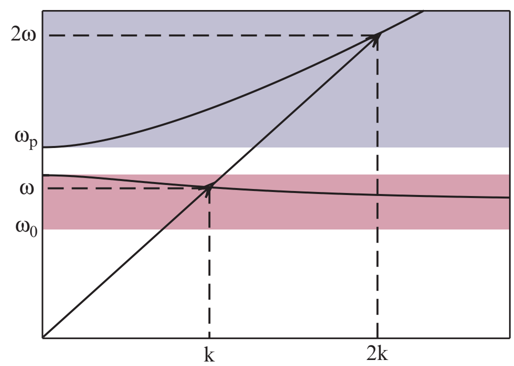

Fig. 12.16. Dispersion of plane waves $k(\omega)$ in the metamaterial. *Arrows* show the parameters of the FF and SH waves corresponding to the exact spatiotemporal phase matching [38]

To study the SHG process in metamaterials we consider a composite structure created by arrays of wires and SRRs. To generate a nonlinear quadratic response of the metamaterial, we assume that each SRR contains a diode, as depicted schematically in the inset of Fig. 12.15. The diode is described by the current–voltage dependence,

$$I = \frac{U}{R_\mathrm{d}}\left(1 + \frac{U}{U_\mathrm{c}}\right), \tag{12.25}$$

where U_c and R_d are the parameters of the diode, and U the voltage on the diode. Equation (12.25) is valid provided $U \ll U_\mathrm{c}$, and it represents two terms of the Taylor expansion series of the realistic (and more complex) current–voltage characteristics of the diode.

Following the standard procedure, we consider two components of the electromagnetic field at the FF ω and its SH 2ω, assuming that all other components are not phase matched and therefore they give no substantial contribution into the nonlinear parametric interaction. Subsequently, we write the general coupled-mode equations describing the simultaneous propagation of two harmonics in the dispersive metamaterial as follows:

$$\begin{aligned} &\Delta\mathbf{H}_1 + \varepsilon(\omega)\mu(\omega)\frac{\omega^2}{c^2}\mathbf{H}_1 = -\sigma_1\mathbf{H}_1^*\mathbf{H}_2, \\ &\Delta\mathbf{H}_2 + 4\varepsilon(2\omega)\mu(2\omega)\frac{\omega^2}{c^2}\mathbf{H}_2 = -\sigma_2\mathbf{H}_1^2, \end{aligned} \tag{12.26}$$

where the indices "1," "2" denote the FF and SH fields, respectively; Δ is a Laplacian, and other parameters are defined as follows:

$$\begin{aligned} \sigma_1 = \kappa/2R(\omega), &\quad \sigma_2 = \kappa/R^*(\omega), \\ \kappa = \frac{6\pi\left(\pi a^2\right)^3}{d^3c^5}&\left[\frac{\omega_0^4\omega^2}{U_\mathrm{c}R_\mathrm{d}R(\omega)R(2\omega)}\right], \end{aligned} \tag{12.27}$$

where $R(\omega) = \omega_0^2\omega^2 + \mathrm{i}\gamma\omega$, the asterisk stands for the complex conjugation, a and d are, respectively, the radius of the SRRs and the period of the metamaterial, and γ is the damping coefficient of the SRR. For simplicity, we assume that both FF and SH waves are of the same polarization, and therefore they can be described by only one component of the magnetic field. In this case, (12.26) become scalar. In the derivation of (12.26) we take into account the Lorentz–Lorenz relation between the microscopic and macroscopic magnetic fields [41]. Also, it is assumed that the diode resistance R_d is much larger than the impedance of the SRR slit, i.e., $R_\mathrm{d} \gg 1/\omega C$, so that the resonant properties of the composite are preserved.

SHG in Semi-Infinite Metamaterial

First, we consider a semi-infinite left-handed medium and the SHG process for the wave scattering at the surface. We assume that a TM-polarized FF

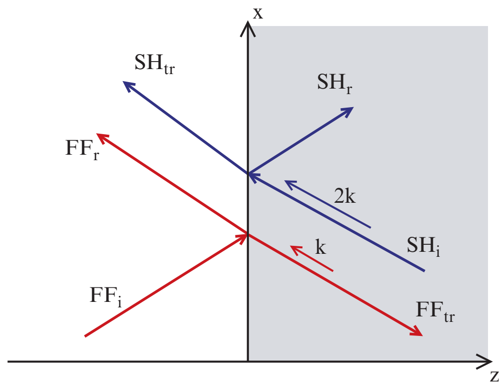

Fig. 12.17. Geometry of the SHG problem. Thick arrows show the direction of the energy flow, thin arrows – direction of wavevectors. Indices "i", "r", and "tr" stand for, respectively, incident, reflected, and transmitted waves [38]

wave is incident on an LH material from the vacuum, as shown schematically in Fig. 12.17. Inside the metamaterial, the wave at the FF satisfies the dispersion relation (12.24) which defines the wavenumber k. As was discussed above, the FF wave in the left-handed medium is backward, meaning that the normal component of the wave vector is directed towards the surface, i.e., in the direction opposite to the Poynting vector.

When the phase-matching conditions are satisfied, the generated SH wave has the wavevector parallel to that of the FF wave (see Fig. 12.17). However, the SH wave is forward propagating, so that the energy at this frequency should propagate towards the interface. When losses are negligible, the FF wave will be *transformed completely* into the SH wave with the energy flows in the direction opposite to that of the FF wave. This kind of the SHG process in a semi-infinite left-handed medium is characterized by two major features (1) the efficiency of the SHG process may become very high, and (2) the SH wave propagates in the direction opposite to that of the incoming FF wave.

Coupled-Mode Equations

To describe the SHG process analytically, we employ the coupled-mode theory and the slowly varying envelope approximation for the FF and SH fields, and present the magnetic fields in the material in the form:

$$H_{1,2}(t,z) = a_{1,2}(t,z)\mathrm{e}^{\mathrm{i}k_{1,2}z} + \text{c.c.}, \qquad (12.28)$$

where the amplitudes of the FF and SH fields $a_{1,2}(t,z)$ are assumed to vary slowly in both space and time, i.e., $\partial a_{1,2}/\partial t \ll \omega a_{1,2}$, and $\partial a_{1,2}/\partial z \ll k a_{1,2}$. Substituting (12.28) into Maxwell's equations and neglecting the second-order derivatives, we obtain the coupled equations

$$\begin{aligned}\frac{\partial a_1}{\partial t} + v_{g1}\frac{\partial a_1}{\partial z} &= \mathrm{i}\sigma_1 a_1^* a_2 - \nu_1 a_1,\\ \frac{\partial a_2}{\partial t} + v_{g2}\frac{\partial a_2}{\partial z} &= \mathrm{i}\sigma_2 a_1^2 + \nu_2 a_2 - \mathrm{i}\Omega a_2,\end{aligned} \tag{12.29}$$

where $v_{g1,2}$ are, respectively, the group velocities and $\nu_{1,2} = v_{g1,2}\mathrm{Im}(k)$ are linear damping coefficients of the FF and SH fields

$$\Omega = q_2 D(2\omega, 2k)/2\sigma_2 \tag{12.30}$$

is the phase mismatch, and

$$q_1 = \sigma_1\left[\frac{\partial D(\omega,k)}{\partial\omega}\right]^{-1}, \quad q_2 = \sigma_2\left[\frac{\partial D(2\omega,2k)}{\partial\omega}\right]^{-1}. \tag{12.31}$$

The coupled-mode equations (12.29) can be presented in the equivalent rescaled form,

$$\begin{aligned}\frac{\partial b_1}{\partial t} + v_{g1}\frac{\partial b_1}{\partial z} &= -q_1 b_1^* b_2 - \nu_1 b_1,\\ \frac{\partial b_2}{\partial t} + v_{g2}\frac{\partial b_2}{\partial z} &= q_2 b_1^2 + \nu_2 b_2 - \mathrm{i}\Omega b_2,\end{aligned} \tag{12.32}$$

where $a_1 = \alpha b_1$, $a_2 = \beta b_2$, $\alpha = \exp(\mathrm{i}\phi)$, $\beta = \exp[-\mathrm{i}(\pi/2 - 2\phi)]$, and ϕ is an arbitrary phase.

The incoming FF backward traveling wave has the group velocity in the z-direction, and the phase velocity – in the opposite direction. The generated SH forward wave has both the phase and group velocities in the $-z$-direction. The FF wave propagates inside the material, and it loses the energy due to SHG and also due to losses in the medium. As a result, the SH amplitude decreases in the z-direction, and the boundary conditions should be taken in the form $b_{1,2}(\infty) = 0$.

A Slab of Metamaterial

Next, we study the SHG process for a layer of thickness L (see Fig. 12.18) and employ a direct numerical approach to solve (12.26). First, we rewrite (12.26) in the dimensionless form:

$$\begin{aligned}\frac{\mathrm{d}^2 H_1}{\mathrm{d}z^2} + \left[\varepsilon(\omega)\mu(\omega) - k_x^2\right] H_1 &= -H_2 H_1^*,\\ \frac{\mathrm{d}^2 H_2}{\mathrm{d}z^2} + 4\left[\varepsilon(2\omega)\mu(2\omega) - k_x^2\right] H_2 &= -Q H_1^2,\end{aligned} \tag{12.33}$$

where the magnetic field is normalized by the value $\omega^2\sigma_1/c^2|\sigma_1|^2$, z is normalized by the value c/ω, and $Q = \sigma_1\sigma_2/|\sigma_1|^2$. We assume that a slab of the LHM is illuminated by the FF wave with the amplitude $H_\omega^{(\mathrm{i})}$, and the SH wave is

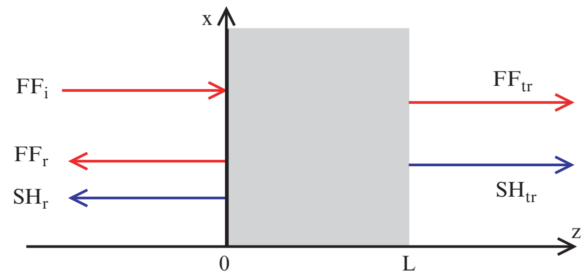

Fig. 12.18. Geometry of the SHG process for a finite-width slab of a nonlinear quadratic metamaterial (*shaded*). *Arrows* indicate incident, reflected and transmitted waves on FF ($\mathrm{FF_i}$, $\mathrm{FF_r}$, $\mathrm{FF_{tr}}$), as well as reflected and transmitted waves on SH ($\mathrm{SH_r}$, $\mathrm{SH_{tr}}$) [38]

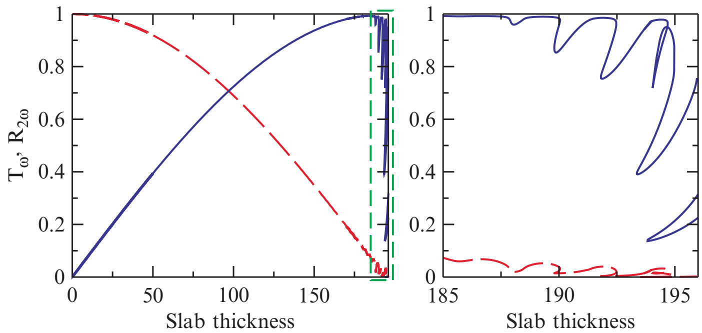

Fig. 12.19. Transmission coefficient of the FF wave (*dashed*) and reflection coefficient of the SH wave (*solid*) vs. the normalized slab thickness L, for a fixed amplitude of the transmitted wave, $H_1(L) = 10^{-2}$. *Right plot* shows a blow up region (*dashed box*) [38]

generated inside the slab, so that the reflected and transmitted waves of both the frequencies ω and 2ω appear (see Fig. 12.18), with the amplitudes $H_1^{(\mathrm{t})}$, $H_2^{(\mathrm{t})}$, $H_1^{(\mathrm{r})}$, $H_2^{(\mathrm{r})}$, respectively. Solving the coupled-mode equations numerically, we present our results for the reflection and transmission coefficients defined as $R_{\omega,2\omega} = H_{1,2}^{(\mathrm{r})}/H_1^{(\mathrm{i})}$ and $T_{\omega,2\omega} = H_{1,2}^{(\mathrm{t})}/H_1^{(\mathrm{i})}$.

In the calculations presented here we assume that the LHM is lossless, and we consider normal incidence. We take the following parameters of the composite: $\omega_0 = 2\pi \times 5 \times 10^9\ \mathrm{rad \cdot s^{-1}}$, $\omega_\mathrm{p} = 2\pi \times 7 \times 10^9\ \mathrm{rad \cdot s^{-1}}$, $F = 0.3$, $a = 3\,\mathrm{mm}$, $d = 6\,\mathrm{mm}$, $U_\mathrm{c} R_\mathrm{d} = 10^5$ CGS units. For such parameters the exact phase matching takes place at $f_\mathrm{pm} \approx 5.37\,\mathrm{GHz}$. Dependencies of the coefficients $R_{2\omega}$, T_ω and R_ω vs. the amplitude of the incident FF wave are shown in Fig. 12.19. One can see that the efficiency of the transformation of the incident FF wave into the reflected SH wave can be rather high. Larger intensities of the incident field result in the multistable behavior of the reflection and transmission coefficients.

Figure 12.19 shows the dependence of the transmission coefficient of the FF wave and the reflection coefficient of the SH wave vs. the slab thickness, for a fixed amplitude of the FF transmitted wave. We observe multistable behavior of the coefficients for thicker slabs.

SHG by Short Pulses

The overarching theme that characterizes all the works cited above is that SHG is efficient only if absorption inside the metamaterial is negligible. Although this constraint may not be crucial in cavity surroundings if metamaterial layers are relatively thin, the issue becomes critical in bulk environments. Naturally, this is a severe restriction that can raise serious questions in the minds of arbiters and ordinary readers alike, and may also lead one to question whether any proposed metamaterial-related phenomenon is observable in a bulk setting. Any predictions must in fact be ultimately reconciled with the fact that experimental observations strongly suggest that incident waves are significantly attenuated in NIMs. For this reason, Scalora et al. [42] considered the proposed phase-matched scheme for backward SHG discussed above and demonstrated that the process remains efficient even when the process employs pulses and absorption plays a significant role.

In particular, Scalora et al. [42] studied the pulsed SHG in metamaterials under the same conditions discussed above but in the presence of significant absorption. Tuning the pump in the negative index range, an SH signal can be generated in the positive index region, such that the respective indices of refraction have the same magnitudes but opposite signs. This insures that a forward-propagating pump is exactly phase matched to the backward-propagating SH signal. Using peak intensities of $500\,\mathrm{MW\,cm^{-2}}$, assuming $\chi^{(2)}$ $80\,\mathrm{pm\,V^{-1}}$, Scalora et al. [42] predicted the conversion efficiencies of 0.2% and 12% for, respectively, attenuation lengths of 5 and 50 μm.

Figure 12.20 shows the results for the conversion efficiency as a function of incident pulse duration, for two values of the effective damping coefficient $\tilde{\gamma}$. Changing $\tilde{\gamma}$ in this fashion leads to an order of magnitude increase in the imaginary part of the index, and reduces the attenuation depth down to 5 μm, with marginal effects to the real part of the index. Nevertheless, the conversion efficiency still reaches 0.2%. The figure also suggests that the efficiency improves by increasing pulse duration. This can be understood in terms of incident pulse bandwidth: as we increase pulse duration, more of the pulse comes into the phase matching condition, which is almost exactly satisfied at the carrier wavelength.

12.4.2 Enhanced SHG in Double-Resonant Metamaterials

In this section we suggest a novel type of composite metamaterials with *double-resonant response* and demonstrate that in the nonlinear regime such binary

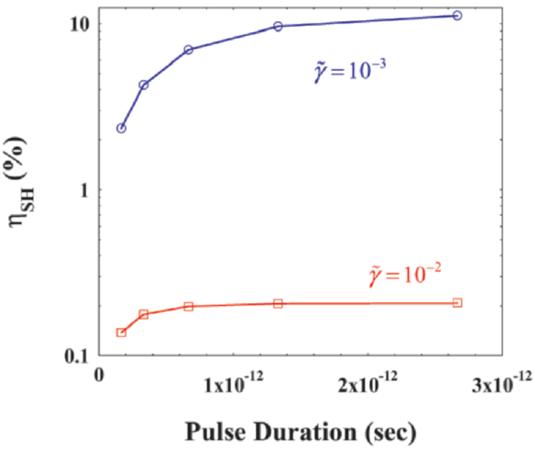

Fig. 12.20. SHG conversion efficiency (%) as a function of incident pulse duration, for $\chi^{(2)} \sim 80\,\mathrm{pm\,V^{-1}}$ and a peak intensity of $\sim$500 MW cm^{-2}. For $\tilde{\gamma} = 10^{-3}$, the attenuation depth is $\sim 50\,\mu$m. For $\tilde{\gamma} = 10^{-2}$, the attenuation depth is drastically reduced to 5 μm. Quasi-monochromatic pulses, i.e., pulse duration greater than 2.5 ps, yield conversion efficiencies of 12% and 0.2%, respectively [42]

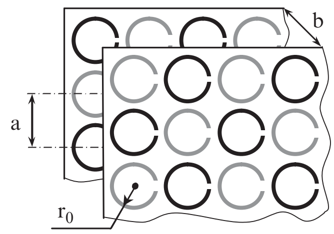

Fig. 12.21. Schematic structure of a binary metamaterial with the resonant magnetic elements of two types (shown by *black* and *gray* rings) [43]

metamaterials are ideally suited for enhanced phase-matched parametric interactions and SHG. Indeed, the quadratic nonlinear magnetic susceptibility is proportional to a product of linear magnetic susceptibilities at the frequencies of interacting waves. For conventional single-resonant nonlinear metamaterials, the magnetic susceptibility of the fundamental wave is relatively large, since it corresponds to the backward wave near the resonance [38] while the susceptibility of the SH wave is rather small. In the metamaterial with several resonances, it is possible to enhance the nonlinear response, so that both linear susceptibilities of interacting waves can become large.

To create a double-resonant metamaterial we suggest to mix two types of resonant conductive elements (SRRs) with different resonant frequencies, as shown schematically in Fig. 12.21 for the structure consisting of two lattices of different SRRs [43]. This idea is somewhat similar to what was suggested previously in [44]. Later, we present the results of numerical simulations of the SHG in a slab of realistic left-handed metamaterial and demonstrate that by introducing a double-resonant structure it is possible to enhance substantially the efficiency of SHG in a wavelength-thick nonlinear slab.

First, we study linear properties of the binary metamaterials. For large wavelengths, each SRR can be described as a resonant circuit (see, e.g., the approach outlined in [13, 45]) characterized by self-inductance L, capacitance C, and resistance R. We assume that the metamaterial consists of two types of SRRs of the same shape (i.e., with the same L and R), but with different capacitances C_1 and C_2, and, thus, different resonant frequencies.

In Fig. 12.22a, we plot the permeability dependence on frequency for double-resonant metamaterial. Parameters are: SRR radius $r_0 = 2$ mm, wire thickness $l = 0.1\,\text{mm}$, which gives self-inductance $L = 8.36\,\text{nH}$ (see [13]). To obtain SRRs of the type 1 with the resonant frequency of $\omega_{01} = 6\pi\times10^9\,\text{rad s}^{-1}$ ($\nu_0 = 3\,\text{GHz}$), we take $C_1 = 0.34\,\text{pF}$. The resonance frequency of the type 2 SRRs is chosen as $\omega_{02} = X\omega_{01}$ with $X = 1.75$, i.e., $C_2 = C_1/X^2$. The lattice constants are $a = 2.1r_0$ and $b = 0.5r_0$. The SRR quality factor, $Q = \omega_{01}L/R$, can reach the values up to 10^3 [46]. However, by inserting diodes this value may decrease, and therefore we take $Q = 300$.

Figure 12.22a confirms that indeed in such structures there exist two resonances and two frequency ranges with negative magnetic permeability. Positions of the macroscopic resonances are shifted from the resonant frequencies of individual SRRs; the shift is not the same for two resonances, and the resulting ratio of the resonant frequencies is about 2.17.

For the double-resonant medium, first we analyze the spectrum of electromagnetic waves, $\omega(k)$. We consider the waves with the magnetic field perpendicular to the planes of resonators and assume that the electric component of the metamaterial generates a plasma-like dielectric response, $\varepsilon(\omega) = 1-\omega_p^2/\omega^2$, where the plasma frequency $\omega_p = 1.2\omega_0$ is selected between

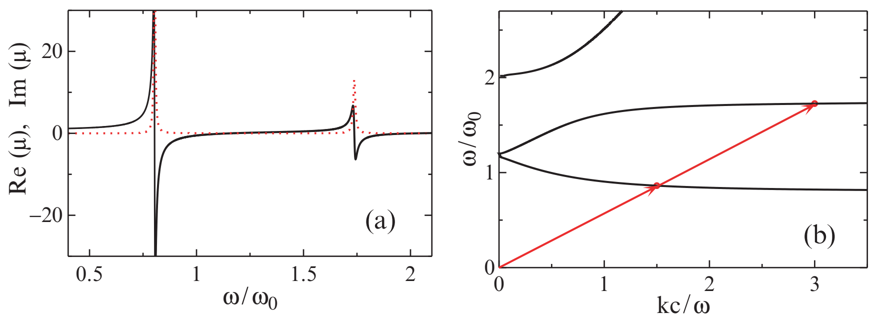

Fig. 12.22. (**a**) Real (*solid*) and imaginary (*dashed*) parts of magnetic permeability of the binary metamaterial. (**b**) Spectrum of electromagnetic waves. *Arrows* show the perfectly phase-matched SHG [43]

two magnetic resonances. The wave spectrum has three branches, as shown in Fig. 12.22b. Two branches, which are close to the magnetic resonances, correspond to large wavenumbers. Importantly, we can find the points of the exact phase-matching between fundamental and SH waves, for both waves close to the resonances.

We consider the case of a normal incident wave propagating along the z-axis and solve the problem numerically [43] with appropriate boundary conditions and obtain the dependence of the SH reflection coefficient, i.e., the ratio of the reflected energy flux of the SH to the incident wave, as a function of the ratio of the two resonant frequencies X, shown in Fig. 12.23a for three slab thicknesses. Calculating results shown in Fig. 12.23a, we were adjusting the frequency of the incident wave to satisfy the phase-matching conditions. Large X corresponds to the nonresonant limit, when the SH field is not in resonance. Decreasing X we drive both FF and SH waves closer to the magnetic resonances, and the conversion rate increases. At the same time, losses become stronger, and finally they dominate suppressing SHG efficiency. For small relative shifts (below $X = 1.75$), the phase matching cannot be archived. The incident field amplitude and nonlinear coefficients $\alpha_1 = \alpha_2 = 0.1$, and amplitude of the incident wave ($E_{\rm inc} = 0.12$) were chosen in such a way that maximum nonlinear modulation in simulations was $\chi^{(2)}(\omega; 2\omega, -\omega)H_\omega < 0.2$. Such modulation is expected in resonant nonlinear processes, since even in realistic nonresonant case [37], the nonlinear modulation of 0.01 was created by the external fields with amplitudes less then $1\,\mathrm{A\,m^{-1}}$. Our results demonstrate that for a one-wavelength-thick slab, the SHG enhancement due to the second resonance can become larger by at least one order of magnitude. The decrease of losses would allow increasing the efficiency.

Dependence of the maximum reflection coefficient of the SH wave and reflection coefficient in nonresonant case ($X = 3$) on the slab thickness is shown in Fig. 12.23b. One can see that the major relative increase of the

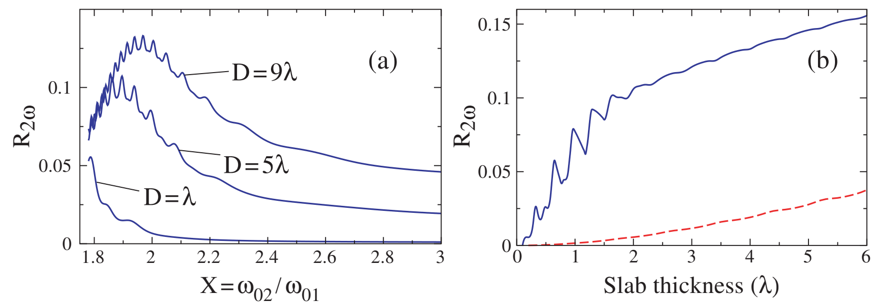

Fig. 12.23. (**a**) Reflection coefficient of the SHs as function of resonant frequency ratio X, for different slab thicknesses D. (**b**) Maximum reflection coefficient of the SH (*solid*) and reflection coefficient at $X = 3$ (*dashed*) as function of slab thickness [43]

SHG process in resonance, compared to nonresonant case, is observed for thin nonlinear slabs.

12.4.3 Nonlinear Quadratic Flat Lens

We consider a slab of a left-handed metamaterial with the thickness D (see Fig. 12.24), and assume that this slab is a three-dimensional composite structure made of wires and SRRs in the form of a cubic lattice. When the lattice period d is much smaller than the radiation wavelength λ ($d \ll \lambda$), this composite structure can be described in the framework of the effective-medium approximation, and it can be characterized by effective values of dielectric permittivity and magnetic permeability. For the specific structure these dependencies can be derived consistently, and in the linear regime they can be written as follows:

$$\varepsilon(\omega) = 1 - \frac{\omega_{\mathrm{p}}^2}{\omega(\omega - \mathrm{i}\gamma_{\mathrm{e}})}, \tag{12.34}$$

$$\mu(\omega) = 1 + \frac{F\omega^2}{\omega_0^2 - \omega^2 + \mathrm{i}\gamma_{\mathrm{m}}\omega}, \tag{12.35}$$

where ω_{p} is the effective plasma frequency, $\omega_0 = \bar{\omega_0}\sqrt{(1-F)}$, $\bar{\omega_0}$ the SRR eigenfrequency, F the filling fraction of SRRs, γ_e and γ_{m} are the corresponding damping coefficients, ω is the frequency of the external electromagnetic field (see details, e.g., in [47] and references therein). In the frequency range where the real parts of ε and μ are both negative and for $\gamma_{\mathrm{e}}, \gamma_{\mathrm{m}} \ll \omega$, this composite

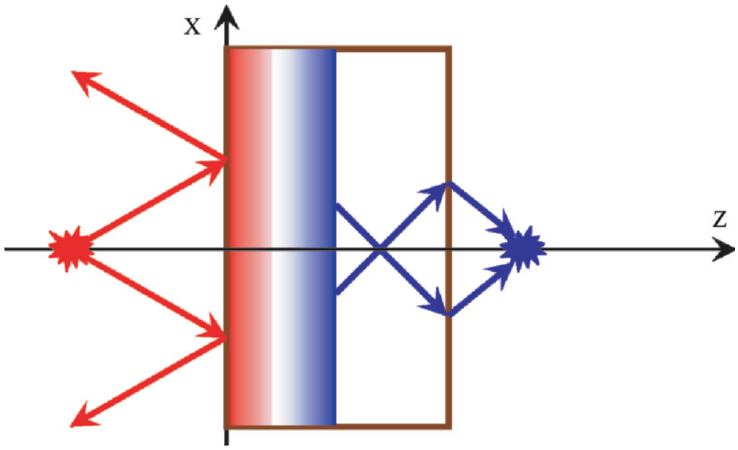

Fig. 12.24. Schematic of the problem. Electromagnetic waves emitted by a source at $z = -z_{\mathrm{s}}$ are reflected from an opaque left-handed slab of the thickness D. Inside the slab, the exponentially decaying field at the frequency ω generates the SH field at 2ω, which penetrates through the slab creating an image of the SH field [40]

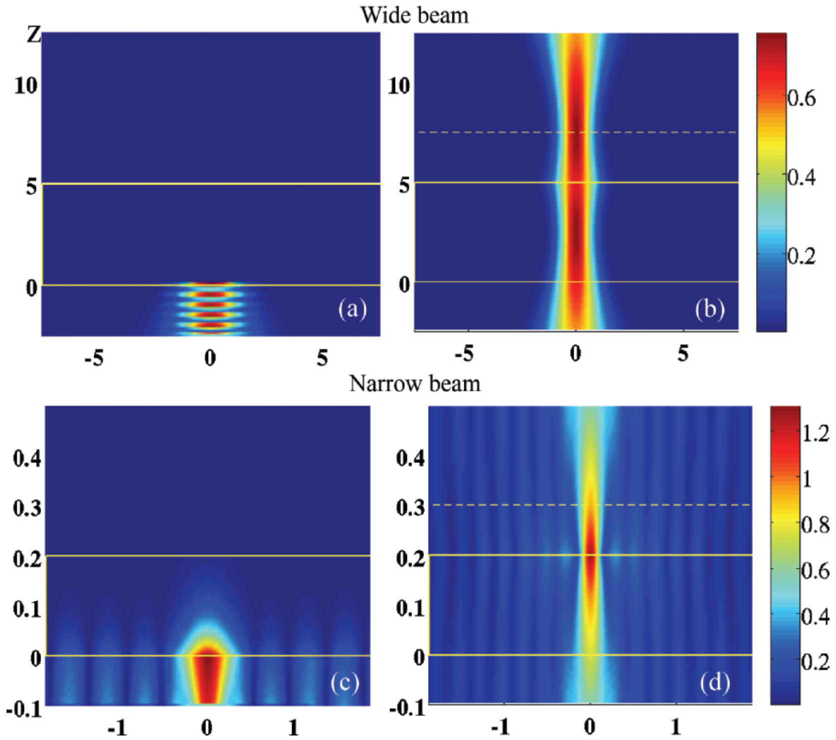

Fig. 12.25. Intensity of the fundamental (**a**,**c**) and SH (**b**,**d**)] beams (in units of the wavelength) for the problem of the SHG and imaging by a nonlinear left-handed lens. (**a**,**b**) Wide beam ($D = 5\lambda$, $z_s = 2.5\lambda$, and $a_0 = \lambda$) and (**c**,**d**) narrow beam ($D = \lambda/5$, $z_s = \lambda/10$, and $a_0 = \lambda/4$). *Solid lines* mark the flat surfaces of the nonlinear left-handed lens. *Dashed lines* show the predicted locations of the SH image [40]

structure demonstrates left-handed medium transmission, whereas for $\omega < \omega_0$, the slab is opaque because of the opposite signs of ε and μ.

Our idea is to satisfy the well-known conditions of Pendry's perfect lens at the frequency 2ω, i.e., $\mu(2\omega) = \varepsilon(2\omega) = -1$. From (12.34), (12.35) we obtain the parameters for the fundamental field in the low loss limit

$$\varepsilon(\omega) \approx -7, \quad \mu(\omega) \approx \frac{(3-F)}{(3-2F)}. \tag{12.36}$$

For this choice of the material parameters, a metamaterial is opaque at the FF ω, and the waves cannot penetrate through the slab. However, an effective nonlinear quadratic response of the metamaterial allows the process of the SHG. For the conditions (12.36) the metamaterial with the dispersion (12.34), (12.35) is transparent at the frequency 2ω, and we expect that the

SH field can propagate through the slab creating an image of the source behind the slab.

Using the so-called undepleted pump approximation, we can obtain the equation for the TM-polarized SH field $H_y^{(2\omega)}(x,z)$ inside the slab, which has the form well known in the theory of the SHG (see, e.g., [48])

$$\Delta H_y^{(2\omega)} + K^2(2\omega) H_y^{(2\omega)} = -16\pi k_0^2 \varepsilon(2\omega) M_{\mathrm{NL}}^{(2\omega)}, \qquad (12.37)$$

where Δ is the Laplacian acting in the space (x,z), $K^2(2\omega) = 4k_0^2\varepsilon(2\omega)\mu(2\omega)$, $k_0 = \omega/c$ is the free-space wavenumber, c is the speed of light and $M_{\mathrm{NL}}^{(2\omega)}$ is the nonlinear magnetization of the unit volume of the metamaterial at the frequency 2ω, which appears due to the nonlinear magnetic momentum of SRR, M_{NL}. We find [40] that the squared field at the FF acts as an effective source for generating the SH and, as a result, the image of the squared field is reproduced by the nonlinear left-handed lens. This image appears at the point $z_{\mathrm{im}} = D - z_{\mathrm{s}}$, this result coincides with the corresponding result for the linear lens [49].

When the source contains the spatial scales smaller than the wavelength, the imaging properties of the nonlinear lens depend strongly on the slab thickness D. Intensity distribution of the magnetic field in the fundamental and SH fields are shown in Fig. 12.25a–d for (a,b) large and (c,d) small (compared to the radiation wavelength) size of the source, respectively.

12.5 Conclusions

We have described several nonlinear effects recently predicted for microstructured metamaterials which exhibit left-handed properties and negative refraction. We believe that nonlinear properties of metamaterials can allow for much broader scope of future applications of such materials, including a dynamic control and tunability of the electromagnetic properties of the composite structures, SHG, intensity-dependent switches, and generation of self-localized pulses and beams.

Acknowledgments

During last years we have been collaborating with a number of people on the projects involving the theoretical studies of left-handed metamaterials and negative refraction, and we would like to thank all of them and especially those who made major contribution to the results reviewed in this chapter. In particular, we thank Alexander Zharov, Nina Zharova, Maxim Gorkunov, Andrey Sukhorukov, Costas Soukoulis, Allan Boardman, and Peter Egan. This work has been supported by a Discovery grant of the Australian Research Council.

References

1. J.B. Pendry, A.J. Holden, W.J. Stewart, I. Youngs, Phys. Rev. Lett. **76**, 4773 (1996)
2. J.B. Pendry, A.J. Holden, D.J. Robbins, W.J. Stewart, IEEE Trans. Microw. Theory Tech. **47**, 2075 (1999)
3. P. Markos, C.M. Soukoulis, Phys. Rev. E **65**, 036622 (2002)
4. P. Markos, C.M. Soukoulis, Phys. Rev. B **65**, 033401 (2002)
5. D.R. Smith, W.J. Padilla, D.C. Vier, S.C. Nemat Nasser, S. Schultz, Phys. Rev. Lett. **84**, 4184 (2000)
6. M. Bayindir, K. Aydin, E. Ozbay, P. Markos, C.M. Soukoulis, Appl. Phys. Lett. **81**, 120 (2002)
7. C.G. Parazzoli, R.B. Greegor, K. Li, B.E.C. Koltenbah, M. Tanielian, Phys. Rev. Lett. **90**, 107401 (2003)
8. V.G. Veselago, Usp. Fiz. Nauk **92**, 517 (1967) (in Russian) [English translation: Phys. Usp. **10**, 509–514 (1968)]
9. A.A. Zharov, I.V. Shadrivov, Yu.S. Kivshar, Phys. Rev. Lett. **91**, 037401 (2003)
10. M. Lapine, M. Gorkunov, K.H. Ringhofer, Phys. Rev. E **67**, 065601 (2003)
11. C. Luo, S.G. Johnson, J.D. Joannopoulos, Appl. Phys. Lett. **81**, 2352 (2002)
12. C. Luo, S.G. Johnson, J.D. Joannopoulos, J.B. Pendry, Phys. Rev. B **65**, 201104 (2002)
13. M. Gorkunov, M. Lapine, E. Shamonina, K.H. Ringhofer, Eur. Phys. J. B **28**, 263 (2002)
14. I.V. Shadrivov, A.A. Zharov, N.A. Zharov, Yu.S. Kivshar, Radio Sci. **40**, RS3S90 (2005)
15. A.M. Belyantsev, V.A. Kozlov, V.I. Piskaryov, Infrared Phys. **21**, 79 (1981)
16. H. Li, A.L. Roytburd, S.P. Alpay, T.D. Tran, L. Salamanca Riba, R. Ramesh, Appl. Phys. Lett. **78**, 2354 (2001)
17. N.A. Zharova, I.V. Shadrivov, A.A. Zharov, Yu.S. Kivshar, Opt. Express **13**, 1291 (2005)
18. K. Zauer, L.M. Gorbunov, Fiz. Plazmy **3**, 1302 (1977) (in Russian)
19. A.A. Zharov, A.K. Kotov, Fiz. Plazmy **10**, 615 (1984)
20. A.V. Kochetov, A.M. Feigin, Fiz. Plazmy **14**, 716 (1988)
21. Yu.S. Kivshar, G.P. Agrawal, *Optical Solitons: From Fibers to Photonic Crystals* (Academic, San Diego, 2003)
22. I.V. Shadrivov, Yu.S. Kivshar, J. Opt. A **7**, S68 (2005)
23. V.B. Gil'denburg, A.V. Kochetov, A.G. Litvak, A.M. Feigin, Zh. Éksp. Teor. Fiz. **84**, 48 (1983)
24. I.V. Shadrivov, A.A. Sukhorukov, Yu.S. Kivshar, A.A. Zharov, A.D. Boardman, P. Egan, Phys. Rev. E **69**, 16617 (2004)
25. J. Nkoma, R. Loudon, D.R. Tilley, J. Phys. C **7**, 3547 (1974)
26. A.D. Boardman (ed.), *Electromagnetic Surface Modes* (Wiley, New York, 1982)
27. R. Ruppin, Phys. Lett. A **277**, 61 (2000)
28. A.G. Litvak, V.A. Mironov, Izv. Vyssh. Uchebn. Zaved. Radiofiz. **11**, 1911 (1968) (in Russian)
29. V.E. Zakharov, A.B. Shabat, JETP **34**, 62 (1972)
30. A.D. Boardman, P. Egan, IEEE J. Quantum Electron. **21**, 1701 (1985)
31. I.V. Shadrivov, A.A. Sukhorukov, Yu.S. Kivshar, Phys. Rev. E **67**, 057602 (2003)

32. G.A. Korn, T.M. Korn, *Mathematical Handbook for Scientists and Engineers* (McGraw-Hill, New York, 1968)
33. A.D. Boardman, G.S. Cooper, A.A. Maradudin, T.P. Shen, Phys. Rev. B **34**, 8273 (1986)
34. I.V. Shadrivov, Photon. Nanostruct.: Fundam. Appl. **2**, 175 (2004)
35. N.N. Akhmediev, Zh. Éksp. Teor. Fiz. **83**, 545 (1982) (in Russian) [akhmediev:1982-299:jetp]
36. V.M. Agranovich, Y.R. Shen, R.H. Baughman, A.A. Zakhidov, Phys. Rev. B **69**, 165112 (2004)
37. M. Lapine, M. Gorkunov, Phys. Rev. E **70**, 66601 (2004)
38. I.V. Shadrivov, A.A. Zharov, Yu.S. Kivshar, J. Opt. Soc. Am. B **23**, 529 (2006)
39. A.A. Zharov, Fiz. Plazmy **17**, 20 (1991)
40. A.A. Zharov, N.A. Zharova, I.V. Shadrivov, Yu.S. Kivshar, Appl. Phys. Lett. **87**, 091104 (2005)
41. L.D. Landau, E.M. Lifshitz, *Electrodynamics of Continuous Media* (Pergamon, Oxford, 1963)
42. M. Scalora, G. DÁguanno, M. Bloemer, M. Centini, D. Ceglia, de, N. Mattiucci, Y. Kivshar, Opt. Express **14**, 4746 (2006)
43. M.V. Gorkunov, I.V. Shadrivov, Yu.S. Kivshar, Appl. Phys. Lett. **88**, 71912 (2006)
44. H. Chen, L. Ran, J. Huangfu, X. Zhang, K. Chen, T.M. Grzegorczyk, J.A. Kong, J. Appl. Phys. **96**, 5338 (2004)
45. R. Marques, F. Medina, R. Rafii El Idrissi, Phys. Rev. B **65**, 144440 (2002)
46. R.A. Shelby, D.R. Smith, S. Schultz, Science **292**, 77 (2001)
47. I.V. Shadrivov, N.A. Zharova, A.A. Zharov, Yu.S. Kivshar, Phys. Rev. E **70**, 046615 (2004)
48. Y.R. Shen, *The Principles of Nonlinear Optics* (Wiley, New York, 1984)
49. J.B. Pendry, Phys. Rev. Lett. **85**, 3966 (2000)

Index

Springer Series in

MATERIALS SCIENCE

Editors: R. Hull R. M. Osgood, Jr. J. Parisi H. Warlimont

40 **Reference Materials in Analytical Chemistry**
A Guide for Selection and Use
Editor: A. Zschunke

41 **Organic Electronic Materials**
Conjugated Polymers and Low Molecular Weight Organic Solids
Editors: R. Farchioni and G. Grosso

42 **Raman Scattering in Materials Science**
Editors: W. H. Weber and R. Merlin

43 **The Atomistic Nature of Crystal Growth**
By B. Mutaftschiev

44 **Thermodynamic Basis of Crystal Growth**
P–T–X Phase Equilibrium and Non-Stoichiometry
By J. Greenberg

45 **Thermoelectrics**
Basic Principles and New Materials Developments
By G. S. Nolas, J. Sharp, and H. J. Goldsmid

46 **Fundamental Aspects of Silicon Oxidation**
Editor: Y. J. Chabal

47 **Disorder and Order in Strongly Nonstoichiometric Compounds**
Transition Metal Carbides, Nitrides and Oxides
By A. I. Gusev, A. A. Rempel, and A. J. Magerl

48 **The Glass Transition**
Relaxation Dynamics in Liquids and Disordered Materials
By E. Donth

49 **Alkali Halides**
A Handbook of Physical Properties
By D. B. Sirdeshmukh, L. Sirdeshmukh, and K. G. Subhadra

50 **High-Resolution Imaging and Spectrometry of Materials**
Editors: F. Ernst and M. Rühle

51 **Point Defects in Semiconductors and Insulators**
Determination of Atomic and Electronic Structure from Paramagnetic Hyperfine Interactions
By J.-M. Spaeth and H. Overhof

52 **Polymer Films with Embedded Metal Nanoparticles**
By A. Heilmann

53 **Nanocrystalline Ceramics**
Synthesis and Structure
By M. Winterer

54 **Electronic Structure and Magnetism of Complex Materials**
Editors: D.J. Singh and D. A. Papaconstantopoulos

55 **Quasicrystals**
An Introduction to Structure, Physical Properties and Applications
Editors: J.-B. Suck, M. Schreiber, and P. Häussler

56 **SiO_2 in Si Microdevices**
By M. Itsumi

57 **Radiation Effects in Advanced Semiconductor Materials and Devices**
By C. Claeys and E. Simoen

58 **Functional Thin Films and Functional Materials**
New Concepts and Technologies
Editor: D. Shi

59 **Dielectric Properties of Porous Media**
By S.O. Gladkov

60 **Organic Photovoltaics**
Concepts and Realization
Editors: C. Brabec, V. Dyakonov, J. Parisi and N. Sariciftci

61 **Fatigue in Ferroelectric Ceramics and Related Issues**
By D.C. Lupascu

62 **Epitaxy**
Physical Principles and Technical Implementation
By M.A. Herman, W. Richter, and H. Sitter

Springer Series in
MATERIALS SCIENCE

Editors: R. Hull R. M. Osgood, Jr. J. Parisi H. Warlimont